THE INSTITUTE
OF MATERIALS

10th International Conference on

Deformation, Yield and Fracture of Polymers

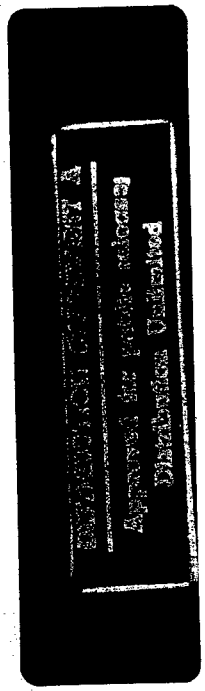

7 - 10 April 1997
Churchill College, Cambridge, UK

CONFERENCE PAPERS

In association with:

The British Society of Rheology
The Polymer Physics Group of
The Institute of Physics and
The Royal Society of Chemistry

REPORT DOCUMENTATION PAGE

Form Approved OMB No. 0704-0188

Public reporting burden for this collection of information is estimated to average 1 hour per response, including the time for reviewing instructions, searching existing data sources, gathering and maintaining the data needed, and completing and reviewing the collection of information. Send comments regarding this burden estimate or any other aspect of this collection of information, including suggestions for reducing this burden to Washington Headquarters Services, Directorate for Information Operations and Reports, 1215 Jefferson Davis Highway, Suite 1204, Arlington, VA 22202-4302, and to the Office of Management and Budget, Paperwork Reduction Project (0704-0188), Washington, DC 20503.

1. AGENCY USE ONLY (Leave blank)	2. REPORT DATE	3. REPORT TYPE AND DATES COVERED
	3 June 1997	Conference Proceedings

4. TITLE AND SUBTITLE

Molecular modelling
Elastomers
Specialty polymers
Environmental effects

5. FUNDING NUMBERS

F6170897W0083

6. AUTHOR(S)

Conference Committee

7. PERFORMING ORGANIZATION NAME(S) AND ADDRESS(ES)

Department of Engineering Science, Oxford University
Park Road
Oxford OX1 3PJ
United Kingdom

8. PERFORMING ORGANIZATION REPORT NUMBER

N/A

9. SPONSORING/MONITORING AGENCY NAME(S) AND ADDRESS(ES)

EOARD
PSC 802 BOX 14
FPO 09499-0200

10. SPONSORING/MONITORING AGENCY REPORT NUMBER

CSP 97-1027

11. SUPPLEMENTARY NOTES

19970624 029

12a. DISTRIBUTION/AVAILABILITY STATEMENT

Approved for public release; distribution is unlimited.

12b. DISTRIBUTION CODE

A

13. ABSTRACT (Maximum 200 words)

The Final Proceedings for 10th International Conference on Deformation Yield and Fracture of Polymers, 7 April 1997 - 10 April 1997

The Topics covered include: Molecular modelling
Elastomers
Specialty polymers
Environmental effects

14. SUBJECT TERMS

Materials, Structural Materials

15. NUMBER OF PAGES
582

16. PRICE CODE
N/A

17. SECURITY CLASSIFICATION OF REPORT	18. SECURITY CLASSIFICATION OF THIS PAGE	19. SECURITY CLASSIFICATION OF ABSTRACT	20. LIMITATION OF ABSTRACT
UNCLASSIFIED	UNCLASSIFIED	UNCLASSIFIED	UL

THE INSTITUTE
OF MATERIALS

10th International Conference on

DEFORMATION, YIELD AND FRACTURE OF POLYMERS

7 - 10 April 1997
Churchill College,
Cambridge, UK

The Churchill conferences on the deformation, yield and fracture of polymers, held triennially since 1970, have established this event as the leading conference on its subject worldwide. The 1997 conference reviews developments and identifies trends in the scientific understanding of deformation, yield and fracture of polymeric materials.

19970624 029

Registered with Charity No: 269275
Printed by The Chameleon Press Ltd

Committed to "Investors in People"
March 1997

ISBN: I-86125-041-X

ORGANISING COMMITTEE

CP Buckley (Chairman)	*University of Oxford*
CB Bucknall	*Cranfield University*
AM Donald	*Cambridge University*
RA Duckett	*Leeds University*
KE Evans	*Exeter University*
JWE Gearing	*Gearing Scientific*
JM Hodgkinson	*Imperial College of Science, Technology and Medicine*
AJ Kinloch	*Imperial College of Science, Technology and Medicine*
TCB McLeish	*Leeds University*
NJ Mills	*Birmingham University*
DR Moore	*ICI plc*
IM Robinson	*ICI plc*
K Thomas	*University of Wales*
JG Williams	*Imperial College of Science, Technology and Medicine*
RJ Young	*University of Manchester Institute of Science and Technology, UK*

INTERNATIONAL SCIENTIFIC COMMITTEE

HR Brown	*Wollongong University, Australia*
B Cherry	*Monash University, Australia*
M Dettanmaier	*Max-Plank-Institut für Polymerforschung, Germany*
RJ Gaymans	*Twente University, The Netherlands*
C G'Sell	*Ecole des Mines, Nancy, France*
HH Kausch	*EPFL, Switzerland*
EJ Kramer	*Cornell University, USA*
GB McKenna	*NIST, USA*
L Monnerie	*ESPCI, Paris, France*
EF Oleinik	*Russian Academy of Sciences, Russia*
A Pavan	*Politechnico di Milano, Italy*
B Pukanszky	*Hungarian Academy of Sciences, Hungary*
K Takahashi	*Kyushu University, Japan*
VI Vettegren	*Russian Academy of Sciences, Russia*
AP Wilczynski	*Warsaw University of Technology, Poland*
AF Yee	*Michigan University, USA*

ACKNOWLEDGEMENTS

The Institute of Materials and Organising Committee wish to thank the following companies for their generous support of the conference.

BP Chemicals Ltd
DSM Research
Gearing Scientific
ICI plc
US Airforce European Office of Aerospace Research & Development
US Army European Research Office

PROGRAMME

Monday 7 April 1997

11.00 Registration

12.30 Lunch

13.45 **Opening Remarks by the Conference Chairman**
CP Buckley (University of Oxford, UK)

SESSION ONE: MOLECULAR AND MICROMECHANICAL MODELLING
Chairman: RJ Young (University of Manchester Institute of Science & Technology, UK)

13.50 **Molecular modelling of aromatic ribbons, rings and sheets**
BL Farmer (University of Virginia, USA), R Pachter, DS Dudis, WW Adams (Wright Patterson AFB, USA)

14.15 **Tailoring the elastic constants of two and three dimensional molecular networks**
FR Attenborough, KE Evans (University of Exeter, UK), A Alderson (BNFL, UK), BR Eggen, MI Heggie (University of Sussex, UK)

14.40 **Molecular topology and crazing in glassy polymers: experiment and theory**
HZY Han, RA Duckett, TCB McLeish (University of Leeds, UK)

15.05 **A numerical study of craze growth**
J Lai, E Van der Giessen (Delft University of Technology, The Netherlands)

15.30 Tea

SESSION TWO: DEFORMATION IN SEMI-CRYSTALLINE POLYMERS
Chairman: AF Yee (University of Michigan, USA)

16.00 **Real-time simultaneous small- and wide-angle X-ray scattering during polyethylene deformation**
MF Butler, AM Donald (University of Cambridge, UK), AJ Ryan (University of Manchester Institute of Science and Technology, UK)

16.25 **Structural changes and stress relaxation following drawing of PET**
W Fuller, A Mahendrasingam, C Martin (University of Keele, UK), AM Adams, CP Buckley (University of Oxford, UK), DJ Blundell, DP Jones, DH MacKerron (Imperial Chemical Industries plc, UK)

16.50 **Polymers under mechanical stress: deformation of the nanostructure of isotactic polypropylene as revealed by SFM**
G Coulon, G Castelein (Université des Sciences et Technologies de Lille, France), C G'Sell (Ecole des Mines de Nancy, France)

17.15 **The effects of temperature and strain-rate on the deformation of polyethylene**
NW Brooks (University of North London, UK), AP Unwin, RA Duckett, IM Ward (University of Leeds, UK)

17.40 **Plastic behaviour and resistance to wear of ultra high molecular weight polyethylene**
C G'Sell, B Paysant-Le Roux (LMPSM, Ecole des Mines-INPL, France), A Dahoun (LPLI, Université de Metz, France), C Cunat (LEMTA, ENSEM-INPL, France), J Von Stebut (LSGS, Ecole des Mines-INPL, France)

18.05 Close of Day One

Tuesday 8 April 1997

SESSION THREE: DEFORMATION IN AMORPHOUS POLYMERS I

Chairman: GB McKenna (NIST, USA)

09.00 **Mechanisms of time-dependent and localized deformation in amorphous polymers**
MC Boyce (Massachusetts Institute of Technology, USA)

09.25 **Inelastic deformation of glassy PMMA: new experiments and computer modelling**
E Oleinik, S Rudnev, T Slavetskaya, M Kravchenko, O Salamatino (Institute of Chemical Physics RAS, Russia), C Gauthier, J Perez (GEMPPM-umr CNRS, France)

09.50 **Molecular approach of the deformation mechanisms in polymethylmethacrylate-based random copolymers**
JL Halary, L Monnerie (Laboratoire PCSM, France), L Tézé, P Tordjeman (Elf Atochem, France)

10.15 **On physical and mechanical behaviour of glassy polymers**
MS Arzhakov, SA Arzhakov (Lomonosov Moscow State University, Russia)

10.40 Coffee

SESSION FOUR: DEFORMATION IN AMORPHOUS POLYMERS II

Chairman: RA Duckett (University of Leeds, UK)

11.10 **Torque and normal force measurements in viscoelastic solids**
GB McKenna (NIST, USA)

11.35 **The onset of nonlinearity in the multiaxial viscoeleasticity of glassy polymers**
PJ Dooling, CP Buckley (University of Oxford, UK), S Hinduja (University of Manchester Institute of Science and Technology, UK)

12.00 **A viscoelastic fluid approach to deformation and yield of glassy polymers**
LE Govaert, PT Timmermans, ETJ Klompen (Eindhoven University of Technology, The Netherlands), TA Tervoort (Eidgenösische Technische Hochschule Zürich, Switzerland)

12.25 Lunch

SESSION FIVE: FATIGUE

Chairman: C G'Sell (LMPSM, Ecole des Mines INPL, France)

14.00 **Fatigue craze initiation in amorphous polymers and molecular approaches to enhancing fatigue life**
AF Yee, HA Hristov, DW Gidley (University of Michigan, USA)

14.25 **The microdeformation mechanisms of polyoxymethylene in static fatigue**
P Scaramuzzino, CJG Plummer, HH Kausch (Ecole Polytechnique Fédérale de Lausanne, Switzerland)

14.50 **The fatigue fracture of polyethylene**
JP Harcup, RA Duckett, IM Ward (University of Leeds, UK), G Capaccio (BP Chemicals Ltd, UK)

15.15 **POSTER SESSION ONE and Tea**

Wednesday 9 April 1997

SESSION SIX: FRACTURE

Chairman: AJ Kinloch (Imperial College of Science, Technology & Medicine, UK)

09.00 **The rate-sensitivity of impact fracture in thermoplastics**
PS Leevers, M Douglas, M Chong, JG Williams (Imperial College of Science, Technology and Medicine, UK)

09.25 **The contribution of plane stress and plane strain components in the fast fracture resistance of polyethylene pipe materials**
GP Marshall, EJ Ingham (Pipeline Developments Ltd, UK)

09.50 **Time-dependent ductile and brittle fracture in plastic pipe**
WL Bradley, SW Bradley, R Self (Texas A&M University, USA), D Register, M Lamborn (Phillips Petroleum Company, USA)

10.15 **Abnormal slow crack growth in polyethylene**
N Brown, X Lu (University of Pennsylvania, USA)

10.40 Coffee

SESSION SEVEN: DEFORMATION IN SPECIAL MATERIALS I

Chairman: RJ Gaymans (University of Twente, The Netherlands)

11.10 **Deformation and fracture of a polydomain liquid crystalline epoxy-based thermoset**
C Ortiz, R Kim, E Rodeghiero, EJ Kramer, CK Ober (Cornell University, USA)

11.35 **Morphology and fracture mechanisms in diglycidyl ether of 4,4'-dihydroxy-α-methylstilbene epoxies and composites**
HJ Sue (Texas A&M University, USA), JD Earls, RE Hefner Jr (The Dow Chemical Company, USA)

12.00 **Effects of ionic interactions on mechanical properties of polymers and polymer blends/composites**
M Hara, X Ma, JA Sauer, G Parker, W Chen, L Tsou, Y Xue (Rutgers University, USA)

12.25 Lunch

SESSION EIGHT: DEFORMATION IN SPECIAL MATERIALS II

Chairman: AM Donald (University of Cambridge, UK)

14.00 **Deformation micromechanics in model polyester-polyolefin blends**
PA Lovell, RM Casado, JL Stanford, RJ Young (University of Manchester Institute of Science and Technology, UK)

14.25 **Deformation mechanisms in closed cell LDPE foams**
NJ Mills, A Gilchrist, HX Zhu (University of Birmingham, UK)

14.50 **The effect of mechanical deformation on light transmission in polymeric optical fibres**
PM Pakhomov, SD Khizhnyak (Tver State University, Russia), AI Zubkov (Engineering Center of Polymeric Optical Fibers, Russia)

15.15 **POSTER SESSION TWO and Tea**

18.00 **Swinburne Lecture:**
THE MOLECULAR CONTROL OF POLYMER FRACTURE
EJ Kramer (Cornell University, USA)

19.00 **Conference Dinner**

Thursday 10 April 1997

SESSION NINE: TOUGHENING MECHANISMS I

Chairman: CB Bucknall (Cranfield University, UK)

09.00 **In-situ x-ray studies during deformation of rubber toughened amorphous polymers**
BJP Jansen, S Rastogi, HEH Meijer, PJ Lemstra (Eindhoven University of Technology, The Netherlands)

09.25 **Synchrotron studies of *in situ* deformation of rubber toughened PMMA**
C He, MF Butler, AM Donald (University of Cambridge, UK)

09.50 **Study of mechanical damage in rubber toughened polymethylmethacrylate by volume change, multiple scattering and coherent backscattering of light**
R Schirrer, R Lenke, C Fond (Institute Charles Sadron, France)

10.15 **Microdeformation in thin films of PP/EPR reactor alloys**
R Gensler, CLG Plummer, HH Kausch (Ecole Polytechnique Fédérale de Lausanne, Switzerland)

10.40 Coffee

SESSION TEN: TOUGHENING MECHANISMS II

Chairman: IM Ward (University of Leeds, UK)

11.10 **The effect of the rubber particle size on the brittle/tough transition of rubber toughened polypropylene**
A van der Wal, RJ Gaymans (University of Twente, The Netherlands)

11.35 **Improving the toughness of epoxy polymers by tailoring the properties of the elastomeric additives**
RA Pearson, HR Azini, R Bagheri, J Qian, Y-C Huang (LeHigh University, USA)

12.00 **Effects of rubber particle cavitation on dilatational yielding and fracture in toughened plastics**
CB Bucknall, D Ayre (Cranfield University, UK)

12.25 **Closing Remarks by the Conference Chairman**
CP Buckley (University of Oxford, UK)

POSTER SESSION ONE

P1 **Fracture kinetics of elastomer networks with chemical and physical junctions**
M Ye Solovyov, VA Kapranov, TN Nesiolovskaya, AG Galushko (Yaroslavl State Technical University, Russia), VI Irzhak (Institute of Chemical Physics in Chernogolovka, Russia)

P2 **New studies about deformation kinetics in polymers using laser interferometer**
PN Yakushev, NN Peschanskaya (Ioffe Physical-Technical Institute of the Russian Academy of Sciences, Russia)

P3 **Tensile yield of polyethylene and ethylene copolymers: evidence of two thermally activated rate processes**
V Gaucher-Miri, S Elkoun, R Séguéla (Université des Sciences et Technologies de Lille, France)

P4 **Mechanical properties of RIM copolymers**
AN Wilkinson, M Davallo (Manchester Metropolitan University, UK), JL Stanford (University of Manchester Institute of Science and Technology, UK)

P5 **Arrest and healing of a surface crack in poly(methyl methacrylate) due to case II diffusion of methanol**
M Kawagoe, J Qui, M Morita (Toyama Prefectural University, Japan), M Nakanishi (Toshiba Engineering Co Ltd, Japan)

P6 **Mechanical characterization of polymers using an inverse model**
Y Tillier, A Gavrus, E Massoni, N Billon (Ecole des Mines de Paris, France)

P7 **Compression test on a polycarbonate over a wide range of strain-rates**
ML Bissiliat, N Billon (Ecole National Supérieure des Mines de Paris, France), G Gary (Ecole Polytechnique, France), JR Klepaczko (Université de Metz, France)

P8 **About the structure of the physical network in polymer gels**
PM Pakhomov, VG Alekseev, NV Larionova (Tver State University, Russia)

P9 **Biaxial impact fatigue of PC/PBT blends**
DJ Dijkstra, A Karbach (Bayer Corporate Research, Germany), T Bartischies, G Hinrichsen (Technical University Berlin, Germany)

P10 **Mechanical properties through the thickness of polypropylene cast-films as a function of processing conditions**
F Jay, JM Haudin, B Monasse (Ecole des Mines de Paris, France)

P11 **Positron annihilation for the studies of structural transformations in polymers**
VP Shantarovich (Institute of Chemical Physics Russian Academy of Sciences, Russia)

P12 **A novel long term plane strain fracture test for tough polyethylenes**
DM Duan, JG Williams (Imperial College of Science, Technology and Medicine, UK)

P13 **Correlation between empiricism and the distribution of non-linear relaxations approach applied to creep of polymers**
P Marceron, Z Ayadi, C Cunat (LEMTA-URA-CNRS, France)

P14 **Inter-laminar delamination, matrix cracking and microfibrillar bridging in fatigued wood-pulp fibres**
WY Hamad (University of Manchester Institute of Science and Technology, UK)

P15 **Stress relaxation in cellulosic fibres: a micromechanics analysis**
WY Hamad, SJ Eichhorn (University of Manchester Institute of Science and Technology, UK)

P16 **Environmental stress cracking of PET in aqueous sodium hydroxide**
EJ Moskala (Eastman Chemical Company, USA)

P17 **Mechanisms of deformation of an amorphous polymer (polycarbonate) in the melt and in the solid state from a conformers interactive coupling point of view (EKNET model)**
JP Ibar (Eknet Research Corporation, USA)

P18 **Compressive cyclic behaviour and prediction of fatigue damage in elastomers**
A Plumtree (University of Waterloo, Canada), GX Cheng (Xi'an Jiaotong University, PR China)

P19 **Non-linear response of amorphous polymers: anelastic/viscoplastic components and strain hardening through Tg**
J Perez, C Gauthier, O Sindt (GEMPPM-umr CNRS, France)

P20 **A comparison of the effects of weathering and superficial abrasion on impact properties of plastic glazing materials**
SM Halliwell, D Gardiner (Building Research Establishment, UK)

P21 **Prediction of the failure of a polyethylene pipe with a defect under tension and internal pressure**
P Frontini, V Garcia Brosa, C Bernal, H Lopez Montenegro (INTEMA, Argentina)

P22 **Evaluation of dynamic fracture toughness in ductile polymers by the normalisation method**
P Frontini, L Fasce, C Bernal (INTEMA, Argentina), G Carcagno (Siderca, Argentina), H Sautereau (INSA, France)

P23 **Development of a process zone in rubber-modified epoxy polymers**
J Du, AF Yee, MD Thouless (University of Michigan, USA)

P24 **Indentation enhanced adsorption of aqueous zinc chloride prevents drawing of nylon 6**
JA Donovan, G Mitchell (University of Massachusetts, USA)

P25 **Mechanics of spider silk during and after contraction in selected solvents**
Z Shao, F Vollrath (University of Aarhus, Denmark)

P26 **Modelling of cavitation and yield in amorphous polymer rubber blends**
AC Steenbrink, E Van der Giessen (Delft University of Technology, The Netherlands), RJ Gaymans (Twente University, The Netherlands)

P27 **Viscoelastic behaviour of HDPE under tensile loading**
JGJ Beijer, JL Spoormaker (Delft University of Technology, The Netherlands)

P28 **Mechanical behaviour of nanocomposites with thermoplastic matrix and cellulose reinforcement**
L Chazeau, JY Cavaillé (CERMAV-CNRS, France), P Terech, JF Legrand (DRFMC-S13M-PCM, France), R Deridievel (INPG, France)

P29 **A fracture mechanics analysis of weld-line behaviour**
TJ Pecorini (Eastman Chemical Company, USA)

P30 **Tetrakaidecahedral cell model of foam mechanics**
HX Zhu, NJ Mills (University of Birmingham, UK)

P31 **A comparison of the deformation and fracture mechanisms in rubber toughened PMMA and in PU/PMMA interpenetrating polymer networks**
Ph Béguelin, HH Kausch (EPFL Laboratoire de Polyméres, Switzerland)

P32 **The effect of molecular structure and processing variables on the fatigue performance of medical grade polyethylenes**
L Bailey, D Crane, L Pruitt, M Goldman (University of California, USA)

P33 **The ESC initiation behaviour of polycarbonate in mixed environment systems**
JC Arnold (Swansea University, UK), JE Taylor (Rapra Technology, UK)

P34 **Strength properties of elastomers in high pressure CO_2**
JC Arnold (Swansea University, UK), OM Davies (Seals Group, BHR Ltd, UK), S Sulley (Nuclear Electric Ltd, UK)

P35 **Deformation behaviour of PA/PPO blends in relation to processing conditions**
M Quehen, JM Gloaguen, JM Lefebvre (UST Lille, France)

P36 **Instrumented ultramicrotomy - a method to study nano-scale crack growth**
ML Ericson, H Lindberg (Luleå University of Technology, Sweden)

P37 **Kinetics of craze tip advance in amorphous glassy polymers in the presence of liquid environments**
LM Yarysheva, L Yu. Kabal'nova, OV Arzhakova, AA Mironova, AL Volynskii, NF Bakeev (Lomonosov Moscow State University, Russia)

P38 **Structural and mechanical behaviour of polyamides with oxyaromatic compounds**
MS Arzhakov, AV Volkov, AL Volynskii, NF Bakeev (Lomonosov Moscow State University, Russia)

P39 **Specific features of fine structure of solvent crazes**
OV Arzhakova, AA Mironova, LM Yarsheva, AL Volynskii, NF Bakeev (Lomonosov Moscow State University, Russia)

P40 **Strain rate dependence of the tensile properties of injection moulded propylene-ethylene copolymer for different processing conditions**
JC Viana, AM Cunha (University of Minho, Portugal), N Billon (Centre de Mise en Forme des Matériaux, France)

P41 **Plastic deformation of aliphatic polyester: effect of rolling on the mechanical properties of poly (ε -caprolactone) sheets**
K Nakayama, AAJ Ketelaars (National Institute of Materials & Chemical Research, Japan)

P42 **Phase separation behaviour at weld line in PC/ABS injection moldings**
H Hamada (Kyoto Institute of Technology, Japan)

P43 **Fracture and deformation of LCP reinforced polymers**
H Hamada (Kyoto Institute of Technology, Japan)

P44 **Molecular modelling of siloxane-based side chain liquid crystalline polymers**
BL Farmer, GM Podojil (University of Virginia, USA), R Pachter, WW Adams (Wright Patterson AFB, USA)

P45 **Environmental influences on the mechanical properties of spider silks and webs**
L H Lin, DT Edmonds (University of Oxford, UK)

P46 **The hot compaction of spectra gel-spun polyethylene fibres**
RJ Yan, PJ Hine, IM Ward (University of Leeds, UK), RH Olley, DC Bassett, JJ Thompson Physical Laboratory, UK)

P47 **Effects of chemical environment on long term strength of polymers**
D Edwards, LJ Broutman (LJ Broughtman and Associates Ltd, USA)

P48 **New deformation mechanisms in poly(styrene-b-butadiene-b-methylmethacrylate) triblock copolymers**
R Weidisch, S Goerlitz, GH Michler (Martin Luther University of Halle-Wittenberg, Germany), R Stadler (Johannes-Gutenberg University, Germany)

P49 **The micro-hardness of crazed polymers**
M Ensslen, GH Michler (Martin Luther University of Halle-Wittenberg, Germany), FI Baltá Calleja (Instituto de Estructura de la Materia, Spain), L Könezöl, W Döll (Fraunhofer-Institut für Werkstoffmechanik, Germany),

P50 **Crack tip crazes created in bulk samples investigated by interference microscopy and transmission electron microscopy**
M Ensslen, G Schulze, GH Michler (Martin Luther University of Halle-Wittenberg, Germany), L Konczol, W Doll (Fraunhofer-Institut für Werkstoffmechanik, Germany)

P51 **The biaxial drawing behaviour of polyethylene terphthalate**
RG Matthews, RA Duckett, IM Ward (University of Leeds, UK), DP Jones (ICI Polyester, UK)

P52 **Microscopic in-situ characterisation of the constrained plastic deformation of a polymeric matrix in a composite**
C Briancon, S Chambaudet, P Sigety (ONERA, France), C G'Sell (Ecole des Mines-INPL, France)

P53 **Plane-strain tensile behaviour of biaxially drawn poly(ethylene terephtalate) sheets**
A Aubert, C G'Sell, JM Hiver (Ecole des Mines-INPL, France), M Aboulfaraj (Pechiney, France)

P54 **Application of relaxation thermodynamics to the modelling of polymers creep**
B Paysant-Le Roux, C G'Sell (Ecole des Mines-INPL, France), Z Ayadi, P Marceron, C Cunat (ENSEM-INPL, France)

P55 **Fracture behaviour of polymeric coatings on steel sheets**
G Robert, C G'Sell, S Etienne (Ecole des Mines-INPL, France) R Hellouin, C Bonnebat (SOLLAC CED, France)

P56 **A Monte-Carlo investigation of amorphous polymer deformation**
C Chui, M Boyce (Massachusetts Institute of Technology, USA)

P57 **Time-dependence of elastomeric materials: experiments and modelling**
J Bergstrom, MC Boyce (Massachusetts Institute of Technology, USA)

P57a **Modelling the compression of low density flexible cellular polymers (foams)**
SM Thorpe, AH Windle (University of Cambridge, UK)

POSTER SESSION TWO

P58 **Non-linear response of amorphous polymers: anelastic/viscoplastic components through Tg and thermostimulated strain recovery**
J Perez, C Gauthier (INSA, France)

P59 **Macroporous thermosets synthesized via chemically induced phase separation: a new approach towards void toughening**
J Kiefer, JG Hilborn (Swiss Federal Institute of Technology, Switzerland)

P60 **The effect of molecular weight on mechanical properties of polyimide**
M Notomi, H Inaba, K Kishimoto, T Shibuya (Tokyo Institute of Technology, Japan), A Morita, Y Yoshida (Mitsui Toatsu Chemicals Inc, Japan)

P61 **Deleted**

P62 **Characterisation of the large strain deformation response of polypropylene at low temperatures and high strain rates**
E M Arruda (University of Michigan, USA)

P63 **Time dependence in the stress optic response of crosslinked elastomers**
E M Arruda, PR Von Lockette (University of Michigan, USA)

P64 **Tensile behaviour of glassy polymers: description by a non-linear viscoelastic model**
N Heymans (Physique des Materiaux de Synthese, Belgium)

P65 **An investigation of yielding behaviour in drawn LDPE**
N Thavarungkul, I R Harrison (Pennsylvania State University, USA)

P66 **Measurement of an isochoric glass transition**
DM Colucci, G B McKenna (NIST, USA)

P67 **Reduced time concepts and the sub-Tg response of a polycarbonate glass**
PA O'Connel, G B McKenna (NIST, USA)

P68 **Volume recovery and physical aging in polycarbonate following temperature jumps**
CR Schultheisz, G B McKenna (NIST, USA)

P69 **Temperature and molecular-weight dependence of the strain hardening behaviour of polycarbonate**
L Govaert, K Van Aert, J Boekholt (Eindhoven University of Technology, The Netherlands)

P70 **Micromechanical modelling of time dependant failure in transversley loaded composites**
L Govaert, RJM Smit, T Peijs (Eindhoven University of Technology, The Netherlands).

P71 **Fatigue fracture and morphology in injection molded polyacetal.**
W Mizuno (Toyama Industrial Technology Centre, Japan), M Kawagoe, J Qiu, M Morita (Toyama Prefectural University, Japan)

P72 **The role of molecular weight in the hot biaxial drawing of amorphous PET**
J Shirodkar, CP Buckley (University of Oxford, UK), JL Harvie (ICI Chemicals and Polymers, UK)

P73 **Evolution of the crystalline texture of high density polyethylene under uniaxial drawing studied by video-controlled tensile testing and WAXD**
G Strobl, R Hiss (Faculty der Physik der Albert-Ludwigs-Universität, Germany)

P75 **The kinetics of dilatational bands and the interparticle distance effect in rubber toughened polymers**
A Lazzeri (University of Pisa, Italy)

P76 **Yielding kinetics in rubber toughened polymers**
A Lazzeri, D Giuliani, E Butta (University of Pisa, Italy)

P77 **Fatigue and Fracture in polyacetal resins**
A Lazzeri, A Marchetti, I Anguillesi (University of Pisa, Italy)

P78 **The impact toughness and morphological characteristics of modified PVC polymers**
EJ Ingham, GP Marshall (Pipeline Development Ltd, UK)

P79 **Evidence for particle cavitation as the precursor to crazing in high impact polystyrene**
HH Yang, CB Bucknall (Cranfield University, UK)

P80 **Criteria for cavitation in toughened plastics containing rubber particles with rigid cores**
CB Bucknall, D Ayre (Cranfield University, UK)

P81 **Criteria for fracture of high impact polystyrene under uniaxial tension**
B O'Connor, CB Bucknall (Cranfield University, UK), JL Hahnfeld (Dow Chemical Co, USA)

P82 **Computer simulation of crack propagation in rubber toughened polymers**
A Sauron, DJ Cleaver, CM Care (Sheffield Hallam University, UK) R Ettelaie (ICI Wilton, UK)

P83 **Characterisation of the surface deformation, yield and fracture of polymers during scratching**
BJ Briscoe, E Pelillo, SK Sinha (Imperial College of Science, Technology and Medicine, UK)

P84 **Amorphous polymers toughened with spherical rubber particles: a method to compute the mechanical interation between particles**
C Fond, R Schirrer (Institut Charles Sadron, France)

P85 **Analytical modelling of the deformation of auxetic polymers**
A Alderson (BNFL, UK) K Sasaki (Imperial College of Science, Technology and Medicine, UK) KE Evans (University of Exeter, UK)

P86 **Characterisation of toughening mechanisms in various impact modified semicrystalline polymer systems**
G-M Kim, GH Michler (Martin Luther University of Halle-Wittenberg, Germany)

P87 **Correlation between toughness and molecular relaxation behaviour in amorphous polymers**
R Lach, W Grellmann (Martin Luther University of Halle-Wittenberg, Germany)

P88 **Prediction of the mechanical behaviour of heterogeneous polymer systems, based on their microstructure**
RJM Smit, WAM Brekelmans, HEH Meijer, LE Govaert (Eindhoven University of Technology, The Netherlands)

P89 **Effects of water absorption and desorption on the strength of polymer/glass interface**
N Fuwa, M Kawagoe, J Qiu, M Morita (Toyama Prefectural University, Japan), Y Doi, T Yasuda, K Takada (Hitachi Kasei Unit Co Ltd, Japan)

P90 **Toughening of highly filled polypropylene: role of particle size and surface treatments**
G Orange (Rhone Poulenc Recherche, France)

P92 **Experimental study of deformation and fracture mechanisms of expanded polystyrene under bending loading conditions**
J-P Yvrard, A Imad (Hautes Etudes Industrielles, France) M Nait Abdelaziz, G Mesmacque (Laboratoire de Mécanique de Lille, France) B Beghin, R Daffara (Huntsman Chemical Company, France)

P93 **Study on the fracture strength and properties of polymeric materials v linear fractal dimensions of entangled networks and its dependence of strain energy release rate**
M Song, G Hu (Beijing University of Chemical Technology, PR China)

P94 **The high speed fracture of polymer compound material with dispersal contact layer**
AD Zjuzkov, PN Bogdanovich, BV Grunkin (Metal Polymer Research Institute, Belarus)

P95 **The effect of chlorine on the long term durability of cross linked polyethylene pipe**
SW Bradley, WL Bradley (Texas A&M University, USA)

P96 **Effective Young's modulus of a polymer composite**
R Wojnar (Polish Academy of Sciences, Poland)

P97 **Modelling of rapid crack propagation along pressurised plastic pipes**
A Ivankovic (Imperial College of Science, Technology and Medicine, UK)

P98 **The measurement and modelling of the strain dependent Poisson's ratio in microporous polyethylene**
RS Webber (University of Liverpool, UK), KL Alderson (Bolton Institute, UK), KE Evans (University of Exeter, UK)

P99 **Cavitational damage in PVDF strained at room temperature**
S Castagnet, J-L Gacougnolle (LMPM - ENSMA, France), P Dang (Elf Atochem, France)

P100 **IR and Raman Spectroscopic study deformation of chemical bonds under stress and temperature in volume and surface layers of polymer specimens**
V Vettegren (Technical Institute Russian Academy of Science, Russia)

P101 **Deleted**

P102 **Characterising fracture behaviour in rubber toughened polymers using the essential work of fracture**
F Dolan, D Taylor (Trinity College Dublin, Ireland), P Blackie (Regional Technical College, Ireland)

P103 **On the thickness dependence of toughness in short fibre reinforced polymers**
F Lumini, M Puricelli, A Pavan (Politecnico di Milano, Italy)

P104 **Influence of the environment on time dependence of crack propagation in polyester resins**
A Roy, X Nennig, JL Gacougnolle (LMPM - ENSMA, France)

P105 **Influence of the hydrostatic tensor on the deformation of the PA11 near Tg**
JL Gacougnolle, K Marchal, L Belec (LMPM - ENSMA, France), P Dang (ATOCHEM, France), Y Meimon (IFP, France)

P106 **Brittle-tough transition in high density polyethylene**
SJK Richie, P Davis, PS Leevers (Imperial College of Science, Technology and Medicine, UK)

P107 **The use of fillers to improve the dynamic fracture resistance of medium density polyethylene**
JC Graham, SJK Ritchie, X Dong (Imperial College of Science, Technology and Medicine, UK)

P108 **Statistical modelling of crack growth and reliability assessment of HDPE**
FS Qureshi, Z Khan, AK Sheikh, M Ahmad (King Fahd University of Petroleum and Minerals, Saudi Arabia)

P109 **Fracture of polymers at slow strain rate with UV exposure**
CT Kelly (University of Queensland, Australia), L Tong, JR White (University of Newcastle upon Tyne, UK)

P110 **An assessment of the defects damages in polyethylene gas pipes**
A Ouakka, K Dang Van (Laboratoire de Mécanique des Solides, France), D Gueugnaut, P Blouet (Gaz de France, France)

P111 **The properties of copoly(ester-ester)s/polystyrene system**
R Jeziórska, E Grzywa, W Zieliński (Industrial Chemistry Research Institute, Poland)

P112 Deformation behaviour of cubic block copolymer morphologies with discrete or tri-continuous glassy microdomains
EL Thomas, BJ Dair, E Prasman (Massachussets Institute of Technology, USA), M Capel (National Synchrotron Light Source, USA)

P113 Influence of molecular weight and mineral oil content on the fractuire toughness of commercial polystyrenes
J Pulda (Synthetic Rubber Research Institute, Czech Republic)

P114 Fracture toughness of core-shell particles modified polyepoxy networks
L Becu, H Sautereau (INSA, France), A Maazouz, JF Gerard (Laboratoire des Materiaux Macromoleculaires, France)

SESSION ONE:

MOLECULAR AND MICROMECHANICAL MODELLING

MOLECULAR MODELING OF AROMATIC RIBBONS, RINGS, AND SHEETS

B. L. Farmer*, R. Pachter†, D. S. Dudis† and W. W. Adams†

Molecular modeling techniques have been used to investigate the mechanical properties and behavior of aromatic ribbons, rings and sheets. Semiempirical molecular orbital calculations were used to examine the deformation behavior of small molecules representing the structural components of graphite and the modulus of a graphite sheet was determined. Energies for cyclic and mobius structures were also examined. Molecular dynamics simulations were used to examine the molecular motions in graphitic ribbons (polyacene) and sheets. Linear and planar structures all display considerable out-of-plane bending deformation at 300K. Correlations between the orientations of the component benzene-rings diminished with separation distance, most rapidly for ribbon-like molecules, but also for sheet-like geometries. Overall, the results demonstrate that these aromatic structures are susceptible to large bending deformations.

Previous molecular modeling studies [1,2] of rigid-rod polymers indicated that these polymers have considerably more flexibility than their linear bonding topology might suggest. This flexibility has been ascribed [1,2] to an out-of-plane bending deformation. Other semiempirical calculations suggest [3] that for small deformations (up to 15 ° C-C-C-C torsional rotations), benzene is not very much stiffer than cyclohexane. Experimentally, C_{60} and graphite tubes have substantially curved surfaces. Electron micrographs of graphite fiber morphology, while not yielding an atomistically detailed picture[4], show a great deal of convoluted folding in the graphite sheets comprising the fibers. These suggest that individual graphite sheets may be more flexible than might be surmised from the high modulus of carbon fibers.

METHODS

Semiempirical molecular orbital calculations were carried out with MOPAC 5.0 [5] using the AM1 Hamiltonian. Except for fixing the internal coordinates required to maintain the specified deformation, the molecular geometries were fully optimized. (The parameterization used for MOPAC AM1 was not developed for such highly strained structures and the results may therefore be less robust than found for minimum energy structures.) *Ab initio* calculations on the bending deformation of naphthalene were performed using GAUSSIAN 90 [6] and an RHF/6-31G* basis set. Molecular mechanics (MM) and molecular dynamics (MD) simulations on isolated molecules were carried out using SYBYL [7] and the Tripos force field [8]. MD trajectories were generated using a time step of 1 fs. Simulation times varied between 25 and 100 ps at a simulated temperature of 300 K. All atoms were considered explicitly.

The results of MM and MD calculations are intimately dependent on the force field parameters used. Therefore, prior to undertaking extensive modeling studies using the force field methods, results for small deformations using the Tripos force field were compared with those from *ab initio* and semiempirical molecular orbital methods. For bending naphthalene (in butterfly fashion) up to 15 deg, AM1 results indicate a slightly lower resistance to bending than do *ab initio* calculations. Molecular mechanics results give the greatest energy for a given

*Department of Materials Science and Engineering, University of Virginia
†Materials Directorate, Wright Laboratory, Wright-Patterson Air Force Base

deformation. It appears that any flexibility demonstrated in the MD results will represent an underestimation of the actual flexibility of the material.

RESULTS

Small Molecules

Figure 1 shows the energy (calculated using MOPAC) for deforming a benzene ring (folding it long a line connecting the mid-points of two opposite sides of the ring), a naphthalene molecule (butterfly fashion), and pyrene (butterfly fashion with respect to the central rings). Figure 2 shows orthogonal views of this latter structure when folded to 90 degrees. The resistance to bending implicit in the resulting geometry is remarkable. Comparison of the deformation of the component rings of pyrene suggests that two of the benzene rings are deformed roughly half as much as the benzene ring folded to 90 deg. The energy for folding pyrene is not very different from the sum of the energy for folding benzene plus that for folding naphthalene. It appears that when the requisite deformations are accounted properly, the mechanical behavior of deformed graphitic structures could be represented by simply considering the benzene and naphthalene component behavior.

Modulus of Graphite

We have also used semi-empirical calculations to examine the ultimate response to strain of a graphite model. In earlier work on rigid rod polymers, the predicted stiffness compared well with macroscopic stress-strain curves (9). The theoretical moduli are often higher than those determined experimentally, which may be rationalized by recognizing that solid material properties are limited by imperfection and morphology while the calculations are performed on models of idealized single polymer chains. Further, compared with *ab initio* results for polyethylene (10), the semiempirical method may systematically over-predict bond stiffness.

Within the quantum mechanical semi-empirical approach, the so-called cluster method [11] characterizes a polymer by a translation vector, resulting in a calculated magnitude that bounds the ultimate modulus and that minimizes effects of the finite size of the model. The equilibrium geometry of the cluster is optimized by energy minimization. The translation vector is thereafter incremented to impose molecular strain and the dependence of the heat of formation on tension (or compression) is established. This procedure was carried out for a graphite sheet in two directions - vertically and horizontally with respect to the section shown in Figure 3a.

The elastic modulus E for a model of the material is:

$$E = \sigma/\varepsilon = (F/A_{eq}) / (\Delta L/L_{eq}) = K\, L_{eq} / A_{eq} \qquad (1)$$

where σ is the stress, ε is the strain, K is the molecular force constant, L_{eq} is the equilibrium length (7.31 Å) of the polymer, and A_{eq} is the equilibrium cross-sectional area (43.87 Å^2) occupied by the polymer chain, obtained from the experimental density or X-ray unit cell dimensions. The force constant can be evaluated by fitting the dependence of the heat of formation, ΔH_f, on ΔL (in the region of small ΔL):

$$\Delta H_f = a_2(\Delta L)^2 + a_1(\Delta L) + a_0 \qquad (2)$$

$K = 2a_2$ at equilibrium at 0 K. The ΔH_f *vs.* ΔL dependence for deformation in the vertical direction (Fig. 3a) is shown in Figure 4. The results of fitting the energy-deformation curves for ΔL in the range ±0.25 gives a modulus of about 1600 GPa and Poisson ratio of 0.42. At large compression, the molecule succumbs to bending (as shown for vertical compression in Fig. 3b) and the energy is linearly related to the deformation. The energy increment for a given deformation is about one third larger for compression in the vertical direction than in the horizontal.

Ribbons, Rings and Sheets

Interest in structures of graphite cylinders, tubes and capsules, and the small radius of curvature seen in electron micrographs of graphitic sheets lead to questions of relative energies of planar *versus* curved sheets composed of fused benzene rings. The simplest of these would be ribbon like molecules, such as polyacene, one benzene-ring wide and of various lengths. We have also examined cyclic acenes and mobius acenes containing one twist in the ribbon-like molecule. For molecules comprised of 16 rings, the (MOPAC) energy for the mobius molecule is about 69 kcal/mol greater than that of the untwisted molecule, which is 101 kcal/mol higher in energy than the ribbon. The dynamic behavior of such structures is also of interest.

Figure 5 shows views of the polyacene ribbon after a few picoseconds of MD simulation. The ribbon undergoes twist by about 90 deg over a distance of less than 50 Å. This and wider ribbons (composed of 2, 4, 8 and 16 polyacene ribbons fused together - the latter being a fair representation of a graphite sheet) were also examined. All undergo substantial bending and twisting excursions from planarity. This is shown in Fig. 6 for the 4-wide ribbon. In this case, the molecule undergoes periodic bending excursions of 25 deg in about 9 ps. The behavior of the more sheet like molecules is similar in character to that of the ribbons, showing differences in time scale, but not in fundamental nature. Increasing the widths of the molecules apparently does not alter their fundamental flexibility.

The orientation parameter, S, is defined as $(<3\cos^2\theta>-1)/2$, where θ is the angle between two rings. It can be used to characterize the motions of the ribbons and sheets - specifically the correlations of the orientations of the rings as a function of the distance between them. In polyacene, for rings that are sixth neighbors, the value of S drops to a value indicative of isotropic relative orientations, and for 12^{th} neighbors, the value of the orientation parameter indicates that the rings are, on average, perpendicular to one another. Similarly, for ribbons which are 4-rings wide, S falls to about 0.1 at the 20^{th} neighbor. As the molecules become more sheet-like, the correlations between ring orientations appear to become more persistent (at least within the simulation times thus far investigated), but there is little reason to believe that the behavior should be fundamentally different for the sheets compared to the ribbons. Indeed for the 16-wide ribbon, S is 0.8 but tending downward at 20^{th}-neighbor distances and shows no sign of having reached a limit. For some pairs in the sheet, S has dropped to 0.2.

The mechanical properties of ribbon and sheet-like molecules are not much different from what might be expected for a two dimensional objects such as a sheet of paper. They are not inherently stiff because of their aromatic carbon network structure, and as a result, out of plane deformations in the form of wrinkles and ripples are facile. The stiffness exhibited by graphite fibers, then, must arise from some other feature of the structure such as the highly convoluted microstructure observed in electron micrographs [4]. The stiffness may arise from the corrugated nature of that microstructure.

REFERENCES

1. Farmer, B. L., Chapman, B. R., Dudis, D. S. and Adams, W. W. *Polymer* 1993, **34**, 1588
2. Socci, E. P., Farmer, B. L. and Adams, W. W. *J. Polym. Sci: Polym. Phys. Ed.* 1993, **31**, 1975
3. Lipkowitz, K. B. and Peterson, M. A. *J. Comp. Chem.* 1993, **14**, 121
4. Vezie, D. L., and Adams, W. W. *J. Mater. Sci. Lett.* 1990, **9**, 883
5. Stewart, J. J. P. MOPAC, QCPE Program #455
6. Gaussian 90, Gaussian, Inc. Pittsburgh, PA, 1986
7. Sybyl, Version 5.3, Tripos Associates, St. Louis, MO
8. M. Clark, R. D. Cramer III, N. Van Opdenbosch, *J. Comp. Chem.* 1989, **10**, 982

9. Klunzinger, P. E. and Eby, R. K. *Polymer* 1993, **34**, 2341
10. Shoemaker, J. R. M.Sc. Thesis, Air Force Institute of Technology, 1991
11. Klei, H. E. and Stewart, J. J. P. *Int. J. Quant. Chem., Quant. Chem. Symp.* 1986, **20**, 529

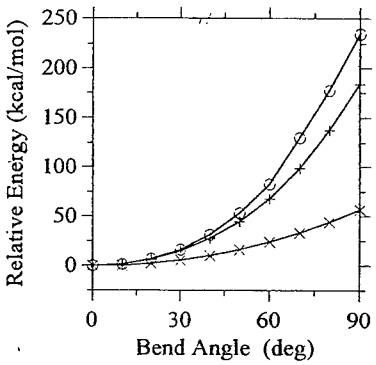

Fig. 1. Energy *versus* deformation for benzene (x), naphthalene (+) , and pyrene (o).

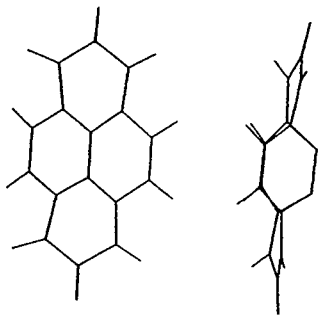

Fig. 2. Orthogonal views of pyrene molecule bent to 90 deg.

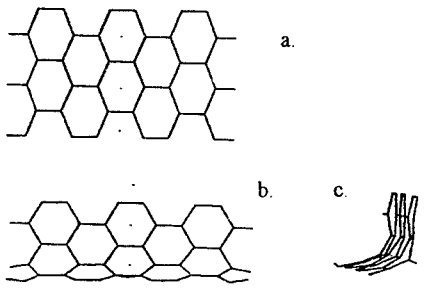

Fig.3 Views of deformed graphite sheet for tension (a) and compression (b and c, orthogonal views).

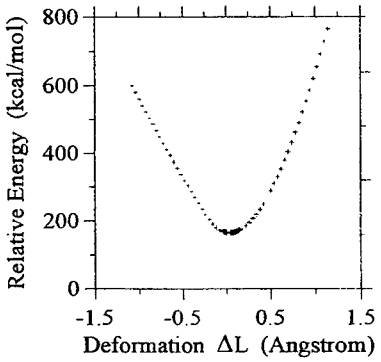

Fig.4 Energy *versus* deformation for graphite sheet.

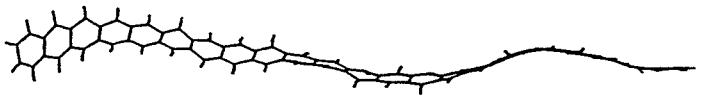

Fig. 5. Polyacene during MD simulation.

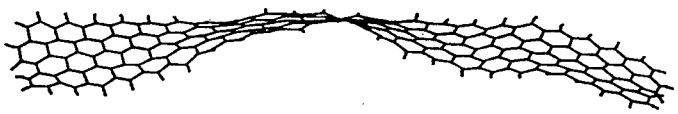

Fig. 6. Four-wide ribbon molecule during MD simulation.

TAILORING THE ELASTIC CONSTANTS OF TWO AND THREE DIMENSIONAL MOLECULAR NETWORKS

FR Attenborough* , KE Evans*, A Alderson*+, BR Eggen↑ , MI Heggie↑

ABSTRACT

Molecular modelling has been used to show that the mechanical properties of a network polymer can be tailored by simple rearrangement of the molecular geometry of the network. Use of molecular modelling offers an insight into the deformation behaviour of these networks, which we believe will be synthesised in the near future. The modelling describes, to a first approximation, how the network will behave before long and complex synthesis takes place thus allowing the screening of potentially poor networks. The results are comparable with those from simulations using *ab initio* (local density functional) techniques. By careful control of geometry networks with either large positive or large negative Poisson's ratios can be designed.

INTRODUCTION

Several materials showing the unusual mechanical property of a negative Poisson's ratio (in other words the material has a lateral expansion when stretched in a longitudinal direction) have been fabricated during the last ten years. Materials which have a negative Poisson's ratio are known as *auxetic* materials (1). Many auxetic materials owe their properties to deformation at a microstructural or even macrostructural level, and have a low Young's modulus as a consequence of the large free volume in the material at these length scales. A network, however, which has a mechanism causing auxetic behaviour at a molecular level will have a higher stiffness, and hence have better engineering properties (1). In this paper the Poisson's ratios, Young's moduli and shear modulus of two and three dimensional networks calculated using molecular modelling is reported and comparison with the preliminary results from local density functional techniques is made.

THE NETWORKS CONSIDERED BY MOLECULAR MODELLING

A series of two dimensional networks (described in detail in Evans *et al* (2)) was modelled using the POLYGRAF package (3) with the Dreiding force field (4). The minimisation technique is described in reference (2). The networks were constructed to have either a conventional hexagonal honeycomb cell structure (figure 1a), or a re-entrant honeycomb cell structure, (figure 1b). The networks consist of sub-units of benzene rings and acetylene bonds with the benzene rings at the junctions of the units and the connecting links formed by the acetylene bonds. Some of the networks had extra benzene rings along the vertical lengths of

* School of Engineering, University of Exeter, Exeter, EX4 4QF, UK

+ Now at Corporate Research Laboratory, BNFL, Springfields, Preston, PR4 0XJ, UK

↑ School of Chemistry, Physics and Environmental Science, University of Sussex, Brighton, BN1 9QJ, UK

the beams, which makes a more chemically stable network. It is hoped that these networks will be synthesised soon, either in the UK(5) or in the US(6).

Most recently three dimensional networks have been modelled using the CERIUS^2 package (3), also using the Dreiding force field. These networks have the geometry of the α-$ThSi_2$ structural motif and are also constructed of benzene ring junctions interconnected by acetylene bond links as in figure 2. Synthesis of a basic unit of one of these networks has recently been achieved by Wu *et al* (7). The networks were modelled to have either hexagonal style shape cell, in other words to have the exact α-$ThSi_2$ motif structure, or to have a re-entrant version of this cell shape.

Analytical models have also been developed for the two-dimensional networks (2) and the three dimensional networks (8).

RESULTS

Poisson's ratios between 0.24 and 1.33 were obtained for the two dimensional networks with a conventional honeycomb cell shape, whereas the Poisson's ratios lay between -0.22 and -1.04 for those networks with a re-entrant cell shape. Similarly, for the three dimensional networks, Poisson's ratios of between 0 and 0.77 were observed for those networks with the exact α-$ThSi_2$ geometry and between 0 and -0.78 for those with a re-entrant shape.

The Young's modulus of the two dimensional networks was measured to be between 19 and 220 GPa and for the three dimensional networks it was observed to be between 0.7 and 30 GPa. In comparison the Young's modulus of a foam structure is of the order of 20-400 kPa (9). The Poisson's ratios, ν_{ij}, for two three-dimensional networks can be seen in table I.

	ν_{xy}	ν_{xz}	ν_{yx}	ν_{yz}	ν_{zx}	ν_{zy}
(10,3) *b*- (1,2) -flexyne	0.2358	0	0.3564	0.5521	0	0.2327
(10,3) *b*- (1,4) -reflexyne	-0.1777	-0.0069	-0.2413	-0.2501	-0.0069	-0.1846

Table I The Poisson's ratios, ν_{ij}, of two three-dimensional networks calculated using CERIUS^2

Calculation of the shear moduli were also performed on the three dimensional networks giving a shear moduli between 74 and 676 MPa.

The nomenclature of the networks is as follows, for a two-dimensional network the first number in the bracket refers to the number of acetylene bonds in the diagonal link of the network, and the second number (or pair of numbers in the curly bracket) refers to the number of acetylene bonds in the vertical link of the network. The curly bracket refers to a stabilised network, in which there is an extra benzene ring in the vertical link - the numbers inside the bracket give the number of acetylene bonds between the benzene rings of the vertical link. The name reflexyne refers to a re-entrant shape cell, so for example the network in figure 1b) is (1,{2,2}) -reflexyne. For a three dimensional network the first bracket gives the geometry of the network using the notation devised by Wells (10) and the second bracket gives the number of acetylene bonds as in the two dimensional case.

Once all the elastic constants of a network have been calculated they can be used to calculate the properties of the network at all angles from the principal axis directions. This is done by substitution of the elastic constants into the standard transformation equations developed by Hearmon (11).One example of such a plot is given in figure 3. It is to be noted that such structures may be anisotropic, even when square symmetric.

As a further check on the validity of the calculations a comparison has been made with *ab - initio* quantum mechanical techniques using the local density functional method (12) This is

to ensure that the auxetic behaviour is not an anomaly due to an inappropriate choice of force field.

So far only two dimensional units have been considered, these are (1,4) -reflexyne and (1,{1,1}) -reflexyne; the results are given in table II:

	CERIUS[2] molecular modelling		*ab initio* calculations	
	ν_{yx}	E_x / GPa	ν_{yx}	E_x / GPa
(1,4) -reflexyne	-0.29 ± 0.02	124 ± 6	-0.343	141
(1,{1,1}) -reflexyne	-0.24 ± 0.01		-0.27 ± 0.016	

Table II Comparison of the elastic constants from molecular modelling and local density functional calculations.

The results show that the local density functional calculations on the 2D molecular units compare very well with the molecular modelling results for the full networks and confirm the proper physical behaviour of the molecular models used here.

ACKNOWLEDGEMENTS

The authors wish to acknowledge the support of the Engineering and Physical Sciences Research Council of the United Kingdom, and of Oxford Materials Ltd for the provision of a CASE award. The authors also wish to thank BNFL for support during part of this work.

REFERENCES

1 Evans, K.E., Nkansah, M.A., Hutchinson, I.J., and Rogers, S.C., 1991, Nature, 353, 124

2 Evans, K.E., Alderson, A., and Christian, F.R., 1995, J Chem Soc: Faraday Trans, 91, 2671

3 POLYGRAF / CERIUS[2], BIOSYM / Molecular Simulations, 16 New England Executive Park, Burlington MA 01803, USA

4 Mayo, S.L., Olafson, B.D., and Goddard III, W.A., 1990, J Phys Chem, 94, 8897

5 Leigh, D., Private Communication

6 Moore, J.S., Private Communication

7 Wu, Z., and Moore, J.S., 1996, Angew Chemie Int Ed Engl, 35, 297

8 Attenborough, F.R., PhD Thesis, The University of Liverpool

9 Chan, N., 1995, PhD Thesis, The University of Liverpool

10 Wells, A.F., Three Dimensional Nets & Polyhedra, John Wiley & Sons, 1977

11 Hearmon, R.F.S., An Introduction to Applied Anisotropic Elasticity, Oxford University Press, 1961

12 Jones, R. and Bridden, P.R., Identification of Defects in Semiconductors, Editor Stavola, M., Semiconductors and Semimetals, Academic Press, 1997

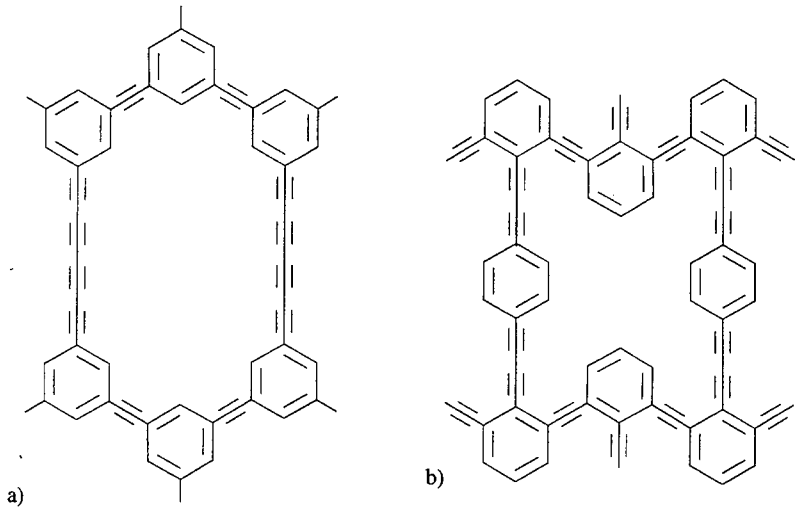

Figure 1 a two dimensional network with a) a hexagonal cell shape and b) with a re-entrant cell shape and extra benzene ring in the vertical link.

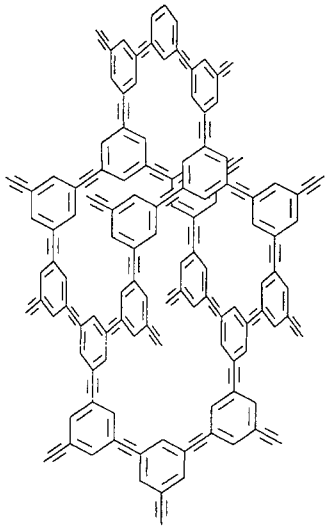

Fig 2 A three dimensional network

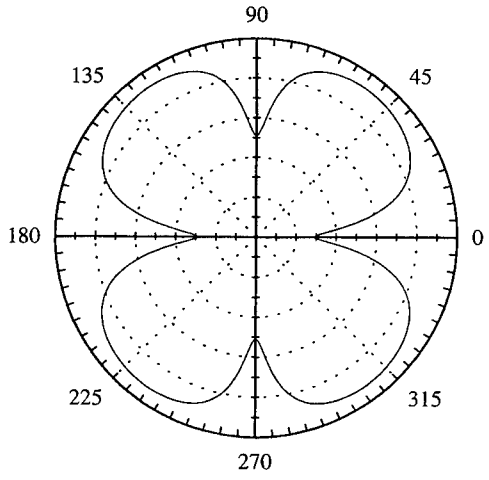

Fig 3 The Poisson's ratio v_{xy} at all angles of applied stress in the xy plane for the network shown in figure 2. The radius of the circle is 1, with each increment along the radial axis equalling 0.1.

Molecular topology and crazing in glassy polymers: experiment and theory

HZY Han*, RA Duckett*, TCB McLeish*, NJ Ward+ and AF Johnson+

We have incorporated the chain centre of mass (CoM) motion in the craze active zone, an inhomogeneous stress field, into previous tube models for crazing[1-3]. It is now able to distinguish molecules of different topologies and fits the experimental results. We found that effective stress field inhomogeneity acting on a chain or a segment (parameter β) is important in correctly describing the crazing process. There is a critical chain length (L_{crit}) at a given drawing condition. Chains longer than it break. Compare to the star chain of the same span molecular weight (*SMw*), L_{crit} of a linear chain can be the same or up to one-fifth longer; and the transition temperature, T_{tr} above which pure disentanglement crazing occurs, can be lower depending on β. Whereas the critical temperature, T_{cr} below which pure scission crazing occurs, is independent of both the *SMw* and molecular topology.

Introduction

Experiments and molecular theories describing craze growth for linear chains below the glass transition temperature (T_g) have been reported [1-4]. However, those for polymers with well-defined branched structure have not been reported. In our previous paper[3], we clarified a few physical concepts by introducing a general tube model and the discrete calculations in crazing. This paper is aimed at establishing the experimental crazing behaviours of monodisperse star polymers and expanding our previous calculations to molecules of different topologies. Previous rheology and orientation relaxation studies showed that properties of star polymers are comparable to the linear ones of the same *SMw*. Their differences in properties have been attribute to *CoM* motion effect[5]. Although using tailor made monodisperse polymers with defined molecular topology saves us from the mathematical complexity caused by molecular weight distribution and irregular molecular branching, to completely describe crazing in molecular level is still a complicated problem. Based on our previous calculations and experimental results, we have synthesised polymers which show the largest effective stress field inhomogeneity effect and chosen experimental strain rates in a theoretically clearly defined regime.

Experimental

Monodisperse linear and 3-arm star polystyrenes L110, S110, L210 and S210 (L = linear, S = star, numbers = molecular weight in thousands) were synthesised via anionic polymerisation. Thin films were made by dipping a glass slide into 5 wt.% toluene solution and withdrawing at 1 cm/min. They were floated off in a water bath after the solvent had evaporated and picked up by a copper mesh previously coated with a diluted solution. After drying overnight, the films were bonded to the copper grid by heating for 10 minutes at 125°C and then aged for 12 hours at 80°C under nitrogen. The film was then stretched on a Miniature Material Tester (Polymer Laboratories) at strain rates of $10^{-3}s^{-1}$ and $10^{-4}s^{-1}$ in a temperature controlled cell. A microscope was used to measure the strains at which crazes occurred.

Polymer IRC, *Department of Physics & Astronomy, +School of Chemistry,
University of Leeds, Leeds LS2 9JT, UK

Model

The maximum effect of *CoM* motion occurs when the centre of the low strain rate half sits at the void tip and that of the high strain rate half sit at the craze fibril centre (Figure 1). Assuming the maximum velocity gradient above the craze fibril centre is ∇v relative to 0 at the void tip (Figure 1), the average velocity gradient for the high velocity gradient half is $(3/4)\nabla v$ and that for the other half is $\nabla v/4$. That gives a ratio of 1/3 for the low stress half to that of the high stress half ($\beta_{min} = 1/3$). The maximum β value is 1 when both halves have the same average velocity gradient, *i.e.* the chain is either huge or very small comparing to the fibril spacing (D). To describe the physics described above, we chose the following functional form for the effective stress field inhomogeneity parameter:

$$\beta = 1 - \frac{16R_g}{3D} e^{-6R_g/D} \tag{1}$$

The radius of gyration (R_g) for both linear and 3-arm star polystyrenes can be calculated solely from their molecular weights[6]. Due to the stress field inhomogeneity the *CoM* in a linear chain moves at a velocity V relative to its environment (Figure 2). Thus the velocity at a point s in the chain takes the form:

$$v^L = \begin{cases} ks - V & s \geq 0 \\ \beta \cdot ks - V & s < 0 \end{cases} \tag{2}$$

From (2), the CoM velocity and frictional force acting on a chain can be calculated as:

$$V = \frac{1}{8} kL(1-\beta) \qquad f(s) = \int_{s}^{\pm L/2} \zeta kx dx \qquad 0 \leq |x| \leq L/2 \tag{3}$$

where ζ is the dynamic monomer friction coefficient, L the equilibrium tube length. Based the above model, the following equations can be arrived:

$$\frac{L_c^L}{L_c^S} = \frac{4}{3+\beta} = \begin{cases} 1.2 \\ 1 \end{cases} \qquad \beta = \begin{cases} 1/3 \\ 1 \end{cases} \tag{4}$$

$$\Gamma'' = \gamma + n_b \cdot \frac{M_e}{M} \cdot \frac{a\upsilon U}{4} + \left(1 - n_b \cdot \frac{M_e}{M}\right) \cdot \frac{a\upsilon b}{2} \cdot \langle f_{av} \rangle_t \tag{5}$$

where γ is the Van der Waals energy, M_e the entanglement molecular weight, M the *SMw* of the polymer, a the tube diameter, ν the entanglement density, U the energy to break the back bone chain, b the monomer length, $n_b = 2^n - 1$, the number of scission event per linear chain until the n-th scission, f_{av} the average force acting on the segments, and the time average is from the entanglement loss during stretching. In every 3 linear chains, there is one less scission event than the equivalent 3-arm star system (two star chains). This extra scission in the star is important when scission event is rare and becomes insignificant as crazing mechanism changing towards pure scission.

V is zero for a star chain. From Equations (3) to (5), when β equals 1, V is zero and there is no CoM motion, and L_{crit}, T_{tr} and Γ are irrelevant to the chain topologies. However, when β is 1/3 the CoM of a linear chain is maximum, L_{crit} of a linear chain is 20% longer than that of a star chain. From Table 1, increasing the strain rate by one order of magnitude leads to a 12 to 15°C increase in T_{tr} and T_{cr}.

Comparison of theory and experiment

In Figure 3, plots of Γ *vs.* temperature are shown for L110 and S110 at a strain rate of 10^{-4}. Little difference between monodisperse 3-arm star PS and comparable linear polymers have been observed at low temperatures. T_{cr} depends solely on the strain rate and is independent of the molecular topology and molecular weight. The difference occurs at high temperatures where disentanglement plays an important part in crazing. At room temperature Γ for L110 and S110 are the same. After 40°C, Γ begins to decrease for both samples. There is no apparent difference between the samples at lower temperatures of the mixed crazing region. But at the high temperatures of the mixed crazing region and in the pure disentanglement region Γ for the star is higher than that for the linear. In the star data there is a discontinuity at around 65°C whereas in the linear data there is a discontinuity at around 62.5°C.

Calculated results from our previous model are shown by the solid lines and these from the current model for linear chains are shown by broken lines and the star by dotted lines. In both of our calculations temperature is divided into three regions by T_{tr} and T_{cr} according to the crazing mechanisms. The pure scission region is the same in the two calculations. In the high temperatures of the mixed crazing region using the present model, the crazing behaviour of the star can be distinguished from the linear. The Γ for the star is higher than that of the linear, which implies a higher crazing stress for the star at this temperature range. It is also observed that star T_{tr} is around 2.5°C higher than that of the linear. The description of Γ has been improved in this calculation in low temperatures of the mixed region where the difference between a linear and a star becomes small as explained. In the pure disentanglement crazing region, the current calculation gives an improved description for the linear polymer. The Γ for the star is higher than that for the linear, again implying a higher crazing stress.

Coming back to the high molecular weight PS L1150 drawn at $4\times10^{-6}s^{-1}$, Figure 4 shows the experimental data [2], calculations from our previous model[3] (solid line), calculations from Berger and Kramer (broken line), Plummer and Donald (dotted line) and the present theory (dotted discrete line). The overall fit of the current theory is improved from those of previous theories. Generally speaking, considering the effective stress field inhomogeneity and CoM motion have improved $\Gamma$for linear chain from our previous calculations at high temperatures in the mixed region. Fitting to the same T_{tr}, the current theory gives a lower T_{cr} than our previous theory, which is closer to experimental data.

Acknowledgement

We thank the EPSRC(UK) for financial support and helpful discussions with Athene Donald.

Reference

1 McLeish, T.C.B.; Plummer, C.J.G. & Donald, A.M. *Polymer*, **1989**, 30, 1651.
2 Plummer, C.J.G. & Donald, A.M. *Macromolecules*, **1990** 23, 3929.
3 Han, H.Z.Y.; Duckett, R.A.; McLeish, T.C.B. *et al* submitted to *Macromolecules*.
4 Kramer, E.J. & Berger, L.L. *Adv. Polym. Sci.* **1990**, 90/91, 1.
5 Han, H.Z.Y.; Duckett, R.A.; McLeish, T.C.B. *et al Polymer*, **1997**, in press.
6 Khasat, N.; Pennisi, R.W.; Hadjichristidis, N. *et al Macromolecules*, **1988**, 21, 1100.

Table 1 Calculated transition and critical temperatures for PS crazing

$\dot{\varepsilon}$ (s^{-1})	$4x10^{-6}$	10^{-4}	10^{-3}
T_{cr} (°C)	24.4	44.6	57.3
L110	42.3	61.5	75.6
S110	44.2	63.6	78.0
L210	49.7	69.8	83.1
S210	51.2	71.5	86.5
L1150	69.7	94.1	111.2
S1150	69.8	94.2	111.3

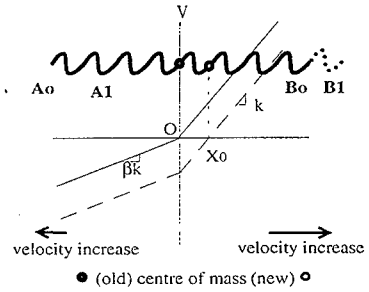

Figure 1 Effective stress field inhomogeneity parameter calculated in the craze active zone

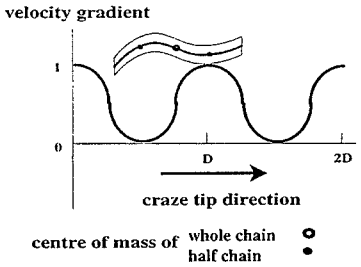

Figure 2 Velocity profiles of a star chain (solid line) and a linear chain with centre of mass motion (broken line) in an inhomogeneous stress field.

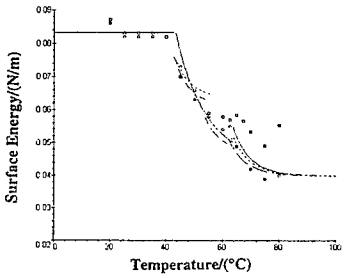

Figure 3 Craze growth surface energy of monodisperse linear and 3-arm star PS 110k thin films at a strain rate of $10^{-4}s^{-1}$. Experimental data: linear (circle) and star (square); This calculations: no centre of mass motion and effective stress field inhomogeneity (solid line), considering centre of mass motion and effective stress field inhomogeneity: linear (broken line) and star (dotted line).

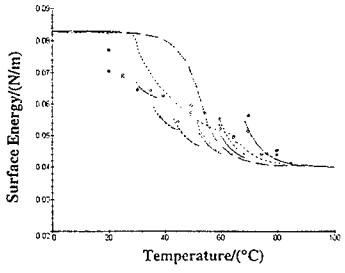

Figure 4 Comparison of the craze growth surface energy of monodisperse linear 1150k PS at a strain rate of $4\times10^{-6}s^{-1}$: this theory without centre of mass motion and effective stress field inhomogeneity (solid line), Berger and Kramer's theory (broken line), Plummer and Donald's theory (dotted line), this theory with centre of mass motion and effective stress field inhomogeneity (discrete dotted line).

A NUMERICAL STUDY OF CRAZE GROWTH

E Van der Giessen, J Lai [1]

The widening of a craze is studied numerically through an axially symmetric model of a fibril, using a three-dimensional constitutive model involving rate-dependent yield, intrinsic strain softening and progressive orientational hardening. Craze growth is found to occur by propagation of shear bands along the fibril.

INTRODUCTION

Although they have provided important qualitative insight, existing models for craze growth in the literature, due to Kramer [1] and Brown [2], are based on rather simplified constitutive models and on approximate, one-dimensional methods of analysis. This paper presents a refinement on these models by using a recent more advanced constitutive model for plastic flow in the craze material, which accounts for strain-rate and temperature dependent yield, intrinsic softening and progressive strain hardening due to molecular orientation. Currently, the model focusses on craze growth or widening, and involves an axisymmetric unit cell containing a single craze fibril, represented by the above continuum material model. A large deformation description allows to study the development of a craze fibril from an initial void by the drawing-in of bulk material. Full field solutions are obtained numerically by means of a detailed finite element discretization. A few results are included for parameters representative of styrene-acrylonitrile (SAN).

THE MODEL

The geometry of the model that we use is essentially similar to that used in (2), and is illustrated in Fig. 1. We consider a craze, much longer than its thickness, and are interested in the relationship between the average normal stress σ_n and the rate of change of the width δ_n of the craze. Further, we imagine a hexagonal periodic arrangement of fibrils with a mean spacing $2R$ (see Fig. 1a). The behaviour of each fibril can then be represented with good accuracy by an axisymmetric unit cell containing a single fiber, as shown in Fig. 1b. The material in the fibril and neighbouring bulk material (the active zone according to [1]) are described by a continuum model for elastic-viscoplastic deformations to be discussed below, including surface tension along the fibril surface with surface energy γ.

For the simulation of the development of the fibril, we use the following boundary conditions: (i) uniform, prescribed velocity $\dot{\delta}_n$ at a surface AB remote from the fibrils; (ii) periodic boundary conditions on BC such that the average stress over BC vanishes;

[1]Laboratory for Engineering Mechanics, Delft University of Technology, The Netherlands

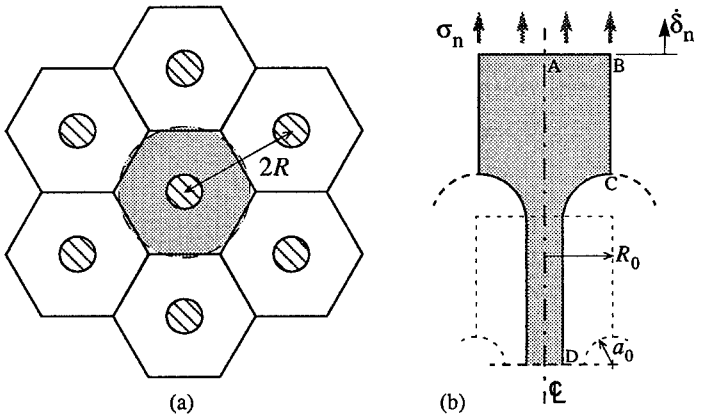

Figure 1: (a) Cross-section through craze with a hexagonal packing of fibrils. (b) Axisymmetric unit cell model of a craze fibril.

(iii) traction-free fibril surface CD. The initial condition for the simulation is taken to be a configuration with a small (toroidal) void with radius a_0 (dashed outline in Fig. 1b), representing the situation shortly after initiation of the craze. The computations are carried out using a large strain finite element technique, assuming isothermal conditions.

The constitutive model used for the fibril material draws on the three-dimensional elastic-viscoplastic model for amorphous polymers below T_g originally proposed by Boyce *et al.* [3], but with a few (conceptual and computational) modifications [4]. This model has also been used in recent studies of the growth of voids [5] and of crack tip plasticity [6]. It gives a description of rate dependent yield, followed by intrinsic strain softening, followed by progressive strain hardening. Yield is taken to be described by the Argon relation

$$\dot{\gamma}^p = \dot{\gamma}_0 \exp\left[-\frac{As_0}{T}\left(1-\left(\frac{\tau}{s_0}\right)^{5/6}\right)\right], \qquad (1)$$

for the equivalent shear rate $\dot{\gamma}^p$. Here, $\dot{\gamma}_0$ and A are material parameters, T is the absolute temperature, and α is the pressure sensitivity parameter. The strain softening that accompanies yield in glassy polymers is incorporated in (1) by replacing the annealed values s_0 of the shear strength with a plastic shear dependent shear strength s, which is initially equal to s_0 and which evolves with plastic shearing as $\dot{s} = h(1 - s/s_{ss})\dot{\gamma}^p$. The saturation value of s is s_{ss}, while the parameter h controls the rate of softening. The equivalent shear stress τ in (1) is derived from the effective stress $\bar{\sigma}_{ij} = \sigma_{ij} - b_{ij}$, where the back stress b_{ij} describes the orientational strain hardening. For the latter, we use the non-Gaussian random network model (see [4]), which involves the initial hardening modulus C^R and the parameter N which determines the locking stretch $\sqrt{N}$ of the network.

RESULTS AND DISCUSSION

We here present results for the following set of material parameters at room temperature ($T = 296\,\mathrm{K}$): $E = 1500\,\mathrm{MPa}$, $\nu = 0.38$, $\dot{\gamma}_0 = 1.06 \times 10^8\,\mathrm{s}^{-1}$, $s_0 = 120\,\mathrm{MPa}$, $\alpha = 0.25$, $A = 129\,\mathrm{K/MPa}$, $h = 1500\,\mathrm{MPa}$, $s_{ss} = 95\,\mathrm{MPa}$, $N = 12$ and $C^R = 4\,\mathrm{MPa}$. This parameter set is based on uniaxial compression experiments on SAN bulk samples. The elastic modulus E is chosen to match the ratio between yield stress and yield strain in uniaxial compression.

In order to emphasize the highlight the role of localized plastic deformations in the fibril deformation, the results presented here are for negligible influence of the surface tension ($\gamma = 0$). Then, there are no material length scales in the problem other than the geometrical dimensions, R_0 ($\approx R$), a_0 and, to a lesser extent, the total initial thickness of the craze. Upon closer examination, the solution in terms of δ_n/R_0 vs σ_n/s_0 is governed basically only by the nondimensional parameters a_0/R_0, $\dot{\gamma}_0/(\dot{\delta}_n/R_0)$, s_{ss}/s_0, As_0/T, C^R/s_0, h/s_0, N, ν, E/s_0.

The three snapshots in Fig. 2 demonstrate how the craze grows from the initial stage with $a_0/R_0 = 0.5$ at $\dot{\delta}_n/R_0 = 0.01\,\mathrm{s}^{-1}$. The corresponding σ_n vs δ_n curve in Fig. 3 shows that a threshold or yield stress must first be overcome before local plasticity is initiated between the initial 'voids'. Due to the intrinsic material softening, plastic flow strongly localizes (Fig. 2a). Subsequent strain hardening in the current plastic zone leads to propagation of the zone (or shear band) in the loading direction (Fig. 2b). Formation of the fibril by this shear band propagation mechanism continues but requires a continually increasing stress level. When the shear band approaches the dome of the void (Fig. 2c), further propagation becomes increasingly hindered.

At those stages of growth, substantial radial stresses σ_{11} develop along the edge BC near the void dome C (see Fig 1b), as seen in Fig. 4. According to [1], these stresses will lead to scission of network strands or disentanglement. The resulting crack may cause further craze growth.

ACKNOWLEDGEMENT

This work is part of a research program of the 'Stichting voor Fundamenteel Onderzoek der Materie (FOM)', which is financially supported by the 'Nederlandse Organisatie voor Wetenschapplijk Onderzoek (NWO)'.

REFERENCES

1. Kramer EJ, Berger LL, Adv. Pol. Sci., 91/92 (1990) 1
2. Leonov AI, Brown HR, J. Polym. Sci., 29 (1992) 197
3. Boyce MC, Parks DM, Argon AS, Mech. Mater., 7 (1988) 15
4. Wu PD, Van der Giessen E, Eur. J. Mech., 15 (1996) 799
5. Steenbrink AC, Van der Giessen E, Wu PD, LTM Rep. no. 1098, J. Mech. Phys. Solids (in print)
6. Lai J, Van der Giessen E, LTM Rep. no. 1105, Mech. Mater. (in print)

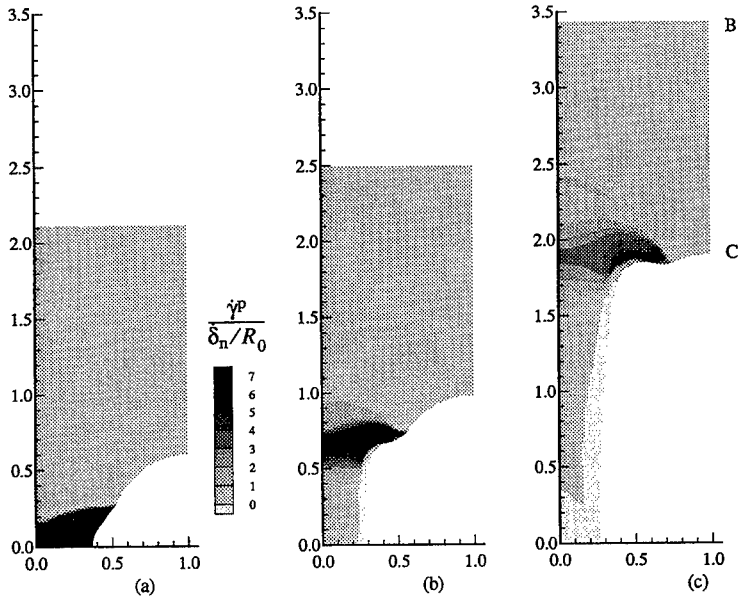

Figure 2: Contours of the normalized plastic shear rate $\dot{\gamma}^p$ at three stages during craze growth.

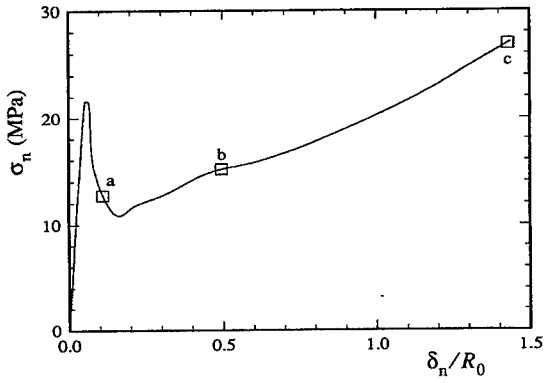

Figure 3: Average stress vs craze width corresponding to Fig. 2.

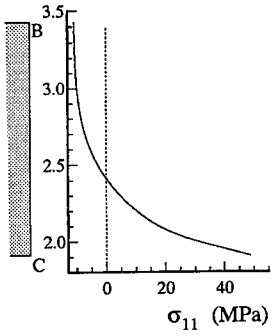

Figure 4: Radial stress distribution along edge BC, for the stage of Fig. 2c.

SESSION TWO:

DEFORMATION IN SEMI-CRYSTALLINE POLYMERS

REAL-TIME SIMULTANEOUS SMALL- AND WIDE-ANGLE X-RAY SCATTERING DURING POLYETHYLENE DEFORMATION

Michael F. Butler*, Athene M. Donald* and Anthony J. Ryan§[1]

2D small- and wide-angle X-ray scattering patterns have been simultaneously measured along with the load-extension curve for a variety of polyethylenes in both tension and compression. The macroscopic, lamellar and molecular deformation were correlated, revealing the microscopic events responsible for the shape of the load-extension curve.

Introduction

The mechanical properties of polyethylene (PE) are particularly important owing to its use in many applications where load-bearing ability is essential. Tailoring the molecular architecture by including short chain side branches to form linear low-density polyethylene (LLDPE) has been found to be a means of altering the mechanical properties (1). In this paper, data is presented from both high-density PE (HDPE) and LLDPE. Other influences (sample temperature, branch type, molecular weight and thermal history) are also mentioned. X-ray experiments were performed with a synchrotron source, which produces such a high flux of X-rays that real-time experiments are possible. The consequent elimination of sample relaxation provides an advantage over experiments performed using laboratory sources and *ex-situ* sample examination, where sample relaxation is inevitable.

Experimental

A range of HDPE and LLDPE grades were provided by BP Chemicals Ltd. They were selected to provide a series of samples possessing different molecular weights, densities, branch types and branch amounts. Some samples were annealed in order to alter their percentage crystallinity and microstructure. Tensile specimens, 20mm wide and 50mm long with two 8mm radius semicircular cutouts to act as stress concentrators, were cut from 0.9mm thick compression moulded plaques. Deformation was perfomed at 5.0mm/min in a Rheometrics Ltd. Miniature Materials Tester under PC control. Experiments were performed at 20, 40, 70, 90 and 110°C. X-ray scattering was performed on beamline 16.1 at the Synchrotron Radiation Source, Daresbury, UK. Two dimensional small-angle and equatorial portions of the two-dimensional wide-angle X-ray scattering patterns were collected simultaneously during deformation using two multiwire gas-filled electronic area detectors. The load-extension curve was collected with the scattering patterns.

* Cavendish Laboratory, University of Cambridge, UK
§ Manchester Materials Science Centre, UMIST, UK and CCLRC Daresbury Laboratory, UK

Results and Discussion

A series of simultaneously collected SAXS and equatorial WAXS patterns are shown in figure 1 for HDPE deformed at 110°C, along with the load-extension curve, on which is marked the points at which the scattering patterns were taken. The progression from a lamellar to a fibrillar morphology is clearly apparent from the SAXS patterns, in which the initial unoriented lamellar scattering pattern develops into an oriented one after the yield point. The lamellar normals orient away from the tensile axis until a strain is reached at which they fragment and a fibre pattern appears. The WAXS shows an increasing molecular orientation parallel to the tensile axis. Figure 2 demonstrates the value of simultaneously collecting the load-extension curve.

Figure 1. Simultaneously measured SAXS (bottom), WAXS (top) and load-extension curve data for an HDPE deformed at 110°C.

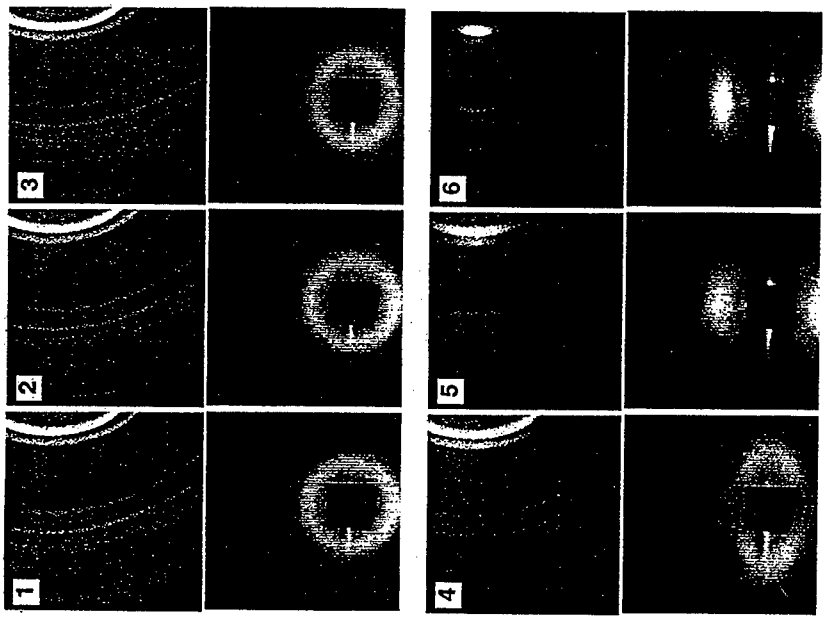

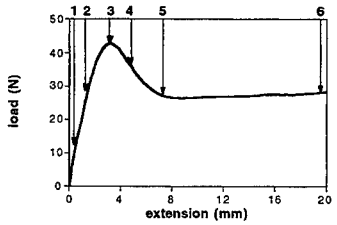

Figure 2. The correlation between SAXS (bottom), WAXS (top) and load-extension curve (middle) data for an HDPE deformed at 20°C (L) and 110°C (R).

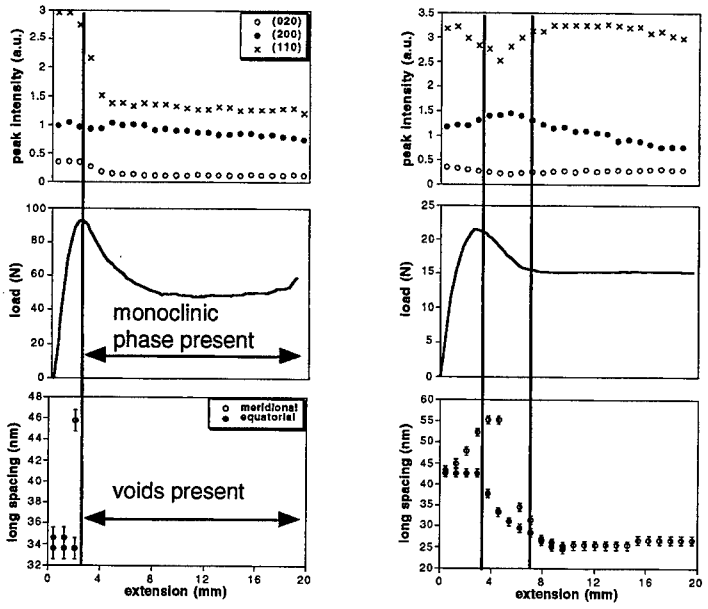

During elastic deformation the increase of the meridional long spacing reveals the occurrence of lamellar separation (2). The sudden decrease of the equatorial long spacing at the yield point is indicative of the onset of crystallographic deformation mechanisms in the form of fine chain slip (2). Analysis of the WAXS peak intensities leads to the suggestion that (100)[001] slip is the operative slip system (3). Strain softening can be seen to result from the conversion of the lamellar to the fibrillar morphology, since by the onset of the load-extension curve plateau the fibre pattern was established.

As the deformation temperature was lowered below 70°C two additional features occurred at the yield point, marked in figure 2, the first of which was for all types of PE but the second was only seen in the unbranched polyethylenes. Firstly, extra reflections due to the presence of a stress-induced metastable monoclinic phase (4) (via martensitic transformation), appeared in the WAXS patterns. Secondly, a dramatic increase in SAXS intensity, which completely overwhelmed the lamellar scattering, and whitening of the samples revealed the occurrence of cavitation. The appearance of the monoclinic phase, a crystallographic deformation mechanism, at the yield point suggested that the yield point corresponded to the onset of crystallographic deformation at all temperatures in the range studied, for all types of PE. It is known that high stress levels are required to activate the martensitic transformation. The absence of the martensitic transformation above 70°C is in accordance with the temperature of

the α transition, which occurs around 70°C (5) . This transition marks a weakening of the crystalline component (5). Stress levels must therefore be insufficient to activate the martensitic transformation. The absence of cavitation confirms that the structure is more compliant to deformation above 70°C.

Table I compares the strain at which the monoclinic phase and the yield point occurred for a high-density PE and a linear low-density PE. The higher strain at which the yield point occurred as well as the absence of cavitation in the less crystalline LLDPE suggests that a greater amount of deformation was borne by the amorphous component in this material, thus delaying the onset of crystallographic deformation. A study of branch amount revealed an increasing amount of interlamellar deformation with increasing branch density (hence decreasing percentage crystallinity and increasing tie molecule density). The role of percentage crystallinity was confirmed by studies of the molecular weight and thermal history dependence of the onset of crystallographic deformation. Tables II and III show results illustrating this behaviour for samples with different molecular weights and thermal histories respectively. In studies of materials with different branch types (ethyl, butyl, iso-butyl and hexyl), the branch length was found to unimportant. Percentage crystallinity was again the most important factor.

Table I. Effect of branches on the crystallographic deformation strain , ε_c

HDPE[a]	LLDPE[b]
0.170	0.189

Table II. Effect of molecular weight on ε_c

HDPE[c], $M_w = 385000$	HDPE[d], $M_w = 1500000$
0.144	0.170

Table III. Effect of percentage crystallinity (χ) on ε_c

HDPE[e], $\chi = 70.0\%$	HDPE[e], $\chi = 79.6\%$
0.170	0.095

a. M_W = 131,000 ; percentage crystallinity = 70.0%: b. M_W = 126,000 ; branch type= iso-butyl ; branch density = 21 branches per 1000 carbon atoms; percentage crystallinity = 35.2%; c. percentage crystallinity = 65.4%: d. percentage crystallinity = 49.8%; e. M_W = 131,000

References

1. Kennedy, M. A., Peacock, A. J., Failla, M. D., Lucas, J. C. and Mandelkern, L., Macromolecules 28 (1995) 1407
2. Peterlin, A. and Meinel, G., Makromol. Chem. 142 (1971) 227
3. Bartzcak, Z., Cohen, R. E. and Argon, A. S., Macromolecules 25 (1992) 4692
4. Lin, L. and Argon, A. S., J. Mat. Sci. 29 (1994) 294
5. Brady, J. M. and Thomas, E. L., J. Mat. Sci. 24 (1989) 3319

STRUCTURAL CHANGES AND STRESS RELAXATION FOLLOWING DRAWING OF PET

A.Mahendrasingam[1], C.Martin[1], W.Fuller[1], A.M.Adams[2], C.P.Buckley[2], D.J.Blundell[3], D.P.Jones[3], and D.H.McKerron[3]

Rapid hot-drawing of PET has been studied by in-situ wide-angle X-ray scattering and biaxial drawing experiments. Stress measurements after the cessation of drawing revealed a mode of stress relaxation not included in existing constitutive models of PET. The in-situ X-ray study showed that it was associated with stress crystallisation. The proposed mechanism is the relaxation of amorphous segments that results from auto-orientation of crystallising segments in a network polymer held at constant extension.

INTRODUCTION

In the production of fibres, films and bottles from poly (ethylene terephthalate) (PET) molecular orientation is introduced by drawing at temperatures above the glass transition. There is a practical need to understand the deformation mechanisms, and to model them. These tasks are complicated, however, by the well-known tendency of PET to stress crystallise when hot-drawn, and the question of how to incorporate the effects of this structural change in a constitutive model of PET is unresolved. Moreover, a further problem is that industrial drawing processes are both extremely rapid (strain-rates in the range 1 to $100s^{-1}$) and multiaxial in nature: relevant mechanical and structural measurements are therefore difficult to make in the laboratory. The present paper represents a collaborative effort to make progress by exploiting two recent developments in experimental technique.

Structural change on the time-scale of interest was studied by exploiting the high brilliance of the X-ray synchrotron radiation source at the European Synchrotron Radiation Facility (ESRF), Grenoble, together with a fast two-dimensional CCD detector for recording the scattering pattern and simultaneous video imaging of the specimen, to carry out in-situ wide angle X-ray scattering (WAXS) studies during rapid hot-drawing of PET[1]. Biaxial stress-strain data at the appropriate temperatures and strain-rates was obtained by using the Oxford Flexible Biaxial Film Tester (FBFT) that provided flexible control of biaxial strain and temperature[2]. In this paper we bring together results from the two techniques, to investigate how the stress in hot-drawn PET is affected by simultaneous crystallisation.

[1]Department of Physics, Keele University,[2]Department of Engineering Science, University of Oxford, [3]ICI plc, Wilton Centre, Middlesbrough

EXPERIMENTAL

The specimens of PET for the WAXS were strips approximately 1 cm long and 1 cm wide cut from a sheet of cast film ~ 840 μm thick. The x-ray camera used in the studies described in this report was constructed in the Keele Physics Department workshops[3]. The temperature of the oven could be controlled to within 1° C and the maximum temperature attainable was 350°C. Diffraction patterns were recorded using a Photonics Science CCD detector with an exposure times of 40 milliseconds. Over this period, the pattern was accumulated within the detector before being digitised by a Synoptic i860 framegrabber within an 8-bit word. The data acquisition system is capable of recording up to 128 frames "end-to-end" with essentially no dead-time between frames before the memory of the framegrabber is full. At this stage these frames were downloaded through a SCSI interface to a Pentium 100Mhz PC. Video camera measurements on changes in the position of reference marks on the specimen allowed the precise draw ratio and draw rate to be calculated at the point in the specimen from which x-ray diffraction data was recorded. WAXS data were recorded on the microfocus beamline at the ESRF beamline ID13 at the ESRF. The mirror/monochromator optics produced a highly collimated beam of ~ 30 μm diameter at the specimen with a wavelength of 0.92A. The sample of PET was clamped between two jaws attached to stepper motors which allowed uniaxial bi-directional drawing at rates up to 12 sec^{-1}.

Software routines have been developed to display both the TV and x-ray diffraction data from one whole experiment a single composite image and to highlight differences between successive frames. This software also performs data reduction and semi-automatic analysis in terms of specimen orientation and crystallinity.

Stress measurements were made in separate drawing experiments using the FBFT. This machine allowed drawing under biaxial stress conditions, at similar strain-rates to those employed for the X-ray scattering experiments. In all the experiments reported here, 0.25mm thickness PET specimens (average molecular weight M_e = 19000) were extended at constant rate to a pre-determined extension between 10% and 330%, in either one or two directions, held at that extension for a time of order seconds, and finally they were quenched to below the glass transition. In the results reported here the extension rate on at least one of the axes was always 100% s^{-1}, and draw temperatures varied between 86°C and 110°C.

RESULTS

Time-resolved WAXS data were recorded during the drawing of PET samples at four temperatures (80, 90, 100, and 110°C) with a nominal draw ratio of 4:1. Despite the differences in the development of the neck during drawing, there are broad similarities in the development of the diffraction patterns at different draw temperatures. In all four experiments there is a progression, starting from an unoriented amorphous halo, through a

gradual intensification of the halo at the equator which eventually gives the diffuse equatorial spots characteristic of a highly oriented amorphous structure the appearance of sharp diffraction spots from a highly oriented crystalline phase. From the detailed analysis of the WAXS diffraction data from these experiments, we can identify four important features about strain-induced crystallisation during the fast draw of PET. These are:

1. The start of crystallisation occurs essentially at the end of the draw;
2. The crystallisation follows first order kinetics (Avrami exponent = 1);
3. The rate of crystallisation is virtually independent of temperature;
4. Crystallisation does not occur below a critical draw ratio (in the range 80°C to 110°C), and increases with the draw ratio beyond this point.

The constant width drawing of PET at 92°C using the FBFT shows a pronounced strain-stiffening beyond a draw time of ~ 1.5s, and the rapid stress relaxation that follows cessation of drawing. The variation in shapes of the stress relaxation curves $\sigma(t)$ (defining the origin of time at the end of drawing) was investigated over the range of draw ratios and temperatures, by quantifying them empirically in terms of the Williams-Watts equation: $\sigma(t) = \sigma_o \exp[-(t/\tau)^q]$ where, σ_o, τ and q are constants. A good fit could be obtained throughout, but the value of exponent q was found to exhibit three regimes: q = 0.4 in regime I (low temperatures, strain < 0.4); q = 0.6 in regime II (high temperatures, before strain-stiffening commences); q = 0.3 in regime III (at high and low temperatures, in the region of strain-stiffening beyond a critical draw ratio in the range 1.4 to 2.5, increasing with temperature). A remarkable feature of stress relaxation in regime III was its insensitivity to temperature.

DISCUSSION

An amorphous polymer such as PET near the glass transition exhibits a thermally activated flow process due to segmental motion, constrained by entropy elasticity of the entangled molecular network. As shown elsewhere(2), each component of stress then has two contributions $\Delta\sigma_i^b$ and $\Delta\sigma_i^c$, where superscripts refer to the sources of free energy giving rise to the stresses: inter and intra-molecular bond potentials (*b*) and conformational entropy (*c*). Stress contributions are expressed here as their perturbations from the overall stress-free state. Comparing the observed stress relaxation data with such a constitutive model allows us to identify regime I with relaxation of the deviatoric part of $\Delta\sigma_i^b$ by segmental diffusion, and regime II with relaxation of the deviatoric part $\Delta\sigma_i^c$ of by reptation (slippage of entanglements). However, no constitutive model yet proposed can account for regime III. In terms of existing models it is inconsistent with the high rate of strain-stiffening preceding it, which is characteristic of a highly elastic network in which entanglement slippage has been arrested(4).

The paradox can be explained in terms of structural evolution as revealed by the in-situ WAXS study. Regime III stress relaxation clearly coincides with the crysallisation following drawing. They occur on the same time-scale. They both require the attainment of a critical strain before they are observed, and the values of critical strain in the two cases are close. They are both remarkably independent of temperature.

We conclude that regime III stress relaxation is a manifestation of the stress-induced crystallisation, and corresponds to the relaxation observed in stress-crystallising elastomers.

The present WAXS study showed a high degree of crystal alignment with molecular axes parallel to the draw direction. For fixed overall strain, it follows that the remaining amorphous segments are relaxed by the formation of crystals, leading to a relaxation of stress(5). Whereas proportionality between stress reduction and degree of crystallinity has been observed in rubbers, it is clear from that the time-dependencies of the two in PET are not identical. This possibly results from there being a contribution to stress relaxation arising from entanglement slippage even during regime III.

CONCLUSIONS

A mechanism of stress relaxation exists in PET following rapid hot-drawing, in addition to the two mechanisms encompassed in existing constitutive models. In-situ WAXS during similar drawing experiments reveals that this is associated with stress-crystallisation. Its origin is likely to be the relaxation of orientation of remaining non-crysallised segments, consequent upon the high degree of orientation of those that have crystallised, as proposed in the case of elastomers.

REFERENCES

1. Blundell, D.J., Fuller, W., MacKerron, D.H., Mahendrasinam, A., Martin C., Oldman, R.J., Riekel, C., Rule, R.J, *Polymer* 1996, **37**, 3303.

2. C.P.Buckley, D.C.Jones and D.P.Jones, *Polymer* 1996, **37**, 2403.

3. Mahendrasingam, A., Fuller, W., Forsyth, V.T., Oldman, R.J., MacKerron, D.H., Blundell, D.J. *Rev. Sci. Instrum.*, **63** (1992), 1087.

4. A.M.Adams, DPhil thesis, University of Oxford, 1995.

5. P.J.Flory, *J.Chem.Phys.* 1947, **15**, 397.

POLYMERS UNDER MECHANICAL STRESS : DEFORMATION OF THE NANOSTRUCTURE OF ISOTACTIC POLYPROPYLENE AS REVEALED BY SFM.

G.Coulon*, G.Castelein* and C.G'Sell†

Scanning Force Microcoscopy (S.F.M.) has been used to study the lamellar morphology of α and β spherulites in bulk intruded isotactic polypropylene (iPP) samples deformed under shear stress at room temperature. For permanent shear strains up to 1, no shear banding has been observed in both α and β spherulites. In contrast, the S.F.M. images show clearly the presence of either kinkings of the radial lamellae or nanocracks which go through the radial lamellae along the molecular axis.

INTRODUCTION

In the last years, much experimental work has been devoted to the mechanical behaviour of semi-crystalline polymers and elementary deformation mechanisms have been proposed (1). However, in most cases, the plastic deformation mechanisms have been evidenced by indirect experimental techniques such as X-ray diffraction or birefringence. In contrast with the case of single crystals or melt cast films, only few direct observations (T.E.M., S.E.M.) have been made on bulk samples (2).

One of the great advantages of Scanning Force Microcoscopy (S.F.M.) is to image directly surfaces in real space and previous experiments performed on smooth polymer surfaces have shown that technique was able to achieve nanometer-scale resolution (3). Up to now, most of the S.F.M. experiments have been performed on ultradrawn oriented polymers in order to characterize the nanofibrils (4); but, little attention has been given to clarify the local mechanisms of plasticity in the crystalline part of bulk semi-crystalline polymers.

The purpose of this work was to study by S.F.M. the lamellar morphology of α and β spherulites in bulk intruded isotactic polypropylene (iPP) samples deformed under shear stress at room temperature and to investigate the local plastic mechanisms which occur at moderate plastic strains in the iPP crystalline part.

EXPERIMENTAL

iPP was manufactured by Appryl (France). It is characterized by a broad molecular weight distribution with M_n=75940 g/mol. and M_w=262.000 g/mol.The iPP pellets were processed by intrusion in a thick mould designed for producing parallelepipedic iPP plates. Such intruded plates have no detectable orientation and possess much less chain degradation than injected ones.

* Université des Sciences et Technologies de Lille, L.S.P.E.S., 59655 - Villeneuve d'Ascq Cedex, France

† Ecole des Mines de Nancy, L.M.P.S.M., Parc de Saurupt, 54042 - Nancy, France

The iPP samples used in the shear test were cut out of the central area of the intruded plates. They have a parallelepipedic shape with a longitudinal notch in order to favour the localization of the plastic deformation within the predefined plane at the root of the notch. Due to the temperature gradient between the two external surfaces, the crystallisation kinetics varies across the thickness of the intruded plates : in the mid-thickness of the intruded plates, both α andβ spherulites are present, the fraction of β-spherulites is about 60% vol. and their mean size is 120 μm (5). Simple shear tests were performed in an Instron machine at room temperature with a strain rate of 5 10^{-4} s^{-1}. Two applied shear strain levels have been studied : $\gamma = 0.5$ and 1.

To enhance the presence of the crystalline phase, the samples were immersed for 40 minutes at room temperature in an acid solution (1.3 wt% $KMnO_4$, 32.9 wt% H_3PO_4 and 65.8 wt% H_2SO_4) which etches preferentially the amorphous phase. Then, the samples were rinsed in a dilute H_2SO_4 solution, in hydrogen peroxyde, in distillated water and in acetone.

SFM experiments were conducted on a Nanoscope III scanning force microscope (Digital Instruments). Measurements were carried out in the "Tapping Mode". Mean value of the repulsive normal force was about 0.1 nN.

RESULTS AND DISCUSSION

In the case of undeformed samples, the lamellar morphology of both α and β spherolites has been investigated and resolved by S.F.M. experiments. The β-spherolites are of β_{IV} type: there are only radial twisted lamellae; their mean measured thickness is about 25 nm. The α-spherolites are of α_I type: there are two families of lamellae, the radial and tangential ones. Their mean thicknesses are respectively about 22 nm and 19 nm, the angle measured between the radial and the tangential lamellae is about 85°. The amount of tangential lamellae is high and the α-spherolites appear as dense networks of radial lamellae with intertwinned tangential ones (6).

In the case of samples deformed to a permanent shear strain $\gamma = 0.5$, the resolution at the lamellar level is lost in numerous areas of the α-spherolites. However, where the lamellar resolution is achieved, the α-spherolites do not exhibit noticeable changes in the lamellar structure : no plastic events as lamellar kinkings, shear bands... have been detected. That "blurred" aspect of the S.F.M. images is confirmed at a higher permanent shear strain $\gamma = 1$ and is not well understood up to now. For $\gamma = 1$, the only salient feature is the presence of numerous nanocracks inside the radial lamellae which lie along the principal tensile strain axis. The nanocracks are parallel to the molecular axis.

Thus, in the case of the α-spherolites, the ability to deform plastically appears very limited; that behaviour can be related to the interlocking effect of the radial lamellae by the numerous tangential ones inside each spherolite.

In contrast, the S.F.M. experiments show that the β-spherolites deform more easily. At $\gamma = 0.5$, the more salient features are : few local kinkings of the lamellae which are parallel to the principal compressive strain axis, few collective nanocracks perpendicular to the principal tensile strain axis going through stacks of edge-on lamellae and flat-on lamellae as well, no trace of chain slips inside the lamellae, parallel or orthogonal to the shear direction.

When increasing the applied shear strain at $\gamma = 1$, the lamellar kinkings become cooperative and give rise to the formation of kinking bands perpendicular to the principal compressive strain axis (Figure 1); the number of collective nanocracks increases dramatically and, incidentally, the stacks of lamellae which are parallel to the principal tensile strain axis are broken up into smaller blocks (Figure 2). Nanocracks are also visible within the lamellae which are perpendicular to the shear axis, the nanocracks are parallel to the chain axis; but as for $\gamma = 0.5$, there is no trace of shear inside the lamellae parallel or orthogonal to the shear direction.

Comparing our data to those obtained in linear high density polyethylene (HDPE) deformed plastically either by uniaxial compression (7) or by simple shear (8), it has to be pointed out that, in HDPE, fine shear bands start to develop at $\gamma = 1$ in shear tests and at $\varepsilon = 0.82$ in compressive ones. In the latter case, T.E.M. experiments reveal clearly the presence of multiple and cooperative kinkings of radial lamellae and the authors assert that the kinking process acts as the precursor of the development of shear bands for higher permanent strains (7).

Here, the plastic deformation of the β-spherolites in bulk iPP is mainly characterized by the lack of local plastic shear. In other words, inside the β-spherolites, the local plastic deformation does not result only from the applied shear stress. The heterogeneous lamellar stacking inside each β-spherolite could induce locally internal stresses; besides, the β-spherolites are surrounded by the α-spherolites which do not deform easily; as a consequence, the stiffness of the α-spherolites could also impose additional local stresses inside the β-ones .Those local stresses could be responsible of the observed damaging events. Finally, it has to be noticed that the large size (about 100 μm) of both α and β spherolites should not favour the plastic deformation by local shear.

ACKNOWLEDGMENT

This research was supported in part by the Contrat de Plan Etat-Région 1994-98, by the FEDER (CEE program) and by the Ministère de l'Enseignement Supérieur et de la Recherche Français (MESR).

REFERENCES

1. Haudin J-M , in Plastic Deformation of Amorphous and Semi-Crystalline Materials, Escaig B. andG'Sell C.,eds., Les Editions de Physique, Les Ulis, France (1982)
2. Aboulfaraj M., Ulrich B., Dahoun A. andG'Sell C., Polymer, (1993), 34, 4817
3. Collin B., Chatenay D., Coulon G., Ausserre D. and Gallot Y., (1992), Macromolecules, 25, 1621
4. Cramer K., Schneider M., Mulhaupt R., Cantow H.J. and Magonov S.N., Polym.Bull., (1994), 32, 637
5. Aboulfaraj M., G'Sell C., Ulrich B.and Dahoun A., Polymer, (1995), 36, 731
6. Castelein G., Coulon G., Aboulfaraj M., G'Sell C. and Lepleux E., J.Phys.III France, (1995), 5, 547
7. Bartczak Z., Cohen R.E. and Argon A.S., Macromolecules, (1992), 25, 4692
8. Bartczak Z., Argon A.S. and Cohen R.E., Macromolecules, (1994), 35, 3427

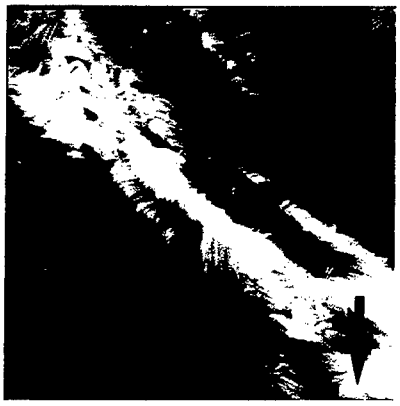

Figure 1 : Sheared intruded iPP sample ($\gamma = 1$) : a (5 μm x 5 μm) SFM image of the surface of a β-spherulite : kinking bands of edge-on radial lamellae . The black arrows indicate the shear axes. Height-range = 1 μm.

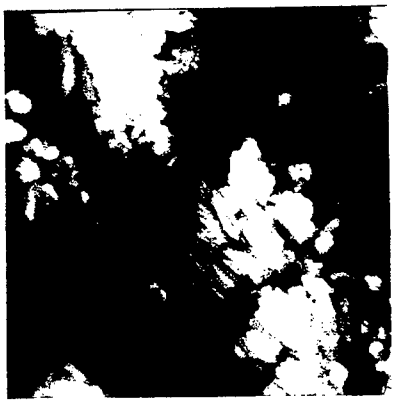

Figure 2 : Sheared intruded iPP sample ($\gamma = 1$): a (3.5 μm x 3.5 μm) SFM image of the surface of a β-spherulite. Collective nanocracks through edge-on radial lamellae.The black arrowsindicate the shear axes. Height-range = 5 μm.

The effects of temperature and strain-rate on the deformation of polyethylene.

N.W.Brooks *, A.P. Unwin[+], R.A.Duckett[+] and I.M.Ward[+].

Four slow-cooled polyethylene samples which differ markedly in their chemical structure have been subjected to extensive mechanical and structural examination. The details of these polymers are given in Table I. One of these (Material C) has been studied after different pressure annealing treatments.

In previous publications[1,2,3,4] we have established that under tensile deformation, above room temperature and at strain-rates lower than 10^{-2} s^{-1} , all four of these materials exhibited two yield points. The first yield point at strains around 5-10% is associated with the onset of plastic deformation, recoverable after a few days. The second yield point, generally at much higher strains, is linked to the onset of permanent plastic deformation. Wide Angle X-ray Scattering (WAXS) analysis of the materials[4,5] under load has shown that the first yield point marked the onset of recoverable reorientation of the lamellae and the second with the destruction of the lamellae by the process of c-shear.

The present work has extended these studies over a wider temperature range at strain-rates of 8.3 s^{-1} and 2.03×10^{-3} s^{-1}, combining mechanical measurements with WAXS studies of slow-cooled samples after unloading.

Analysis of the yield strain as a function of temperature has shown that there is a sudden transition in behaviour for each of the materials. The results for Material C are shown in Figure 1 (Strain-rate = 2.03×10^{-3} s^{-1}). The other three materials showed similar results; the yield strain is effectively constant at low temperatures, and then increases suddenly as the temperature is increased above a **transition temperature**. The transition temperatures identified for each of the materials (at the two differing strain-rates) are shown in Table II.

WAXS analysis of each of the materials after tensile deformation has shown that below the transition temperature there is no evidence of the lamellar reorientation which was observed for tensile deformation above the transition temperature. Below the transition temperature the materials are all transformed directly from the initial spherulitic structure into the oriented state. These results indicate that the observed transition in the yield strain behaviour is associated with interlamellar shearing of the initial spherulitic structure.

Analysis of the stress-strain curves for each of the polymer grades has shown that the deformation changes from non-linear visco-elastic behaviour above the transition temperature to elastic-plastic behaviour below[6]. The temperature and strain-rate dependence of the yield stress for each of these materials above the transition temperature have previously been modelled using a modified Eyring equation, the yield behaviour being considered to be velocity controlled[3]. Below the transition temperature it is believed that the yield process is nucleation controlled and so alternative methods of modelling the temperature and strain-rate dependence of the yield stress must be sought.

Argon[7] developed a theory to describe the yield behaviour of glassy polymers in

terms of the thermal activation of molecular kinks i.e. nucleation controlled approach. This theory predicts a linear relationship between $(\tau/\mu)^{\frac{5}{6}}$ and (T/μ), where τ is the shear yield stress, μ is the shear modulus and T is the absolute temperature. The results of plotting $(\tau/\mu)^{\frac{5}{6}}$ against (T/μ) for material C are shown in Figure 2 (Strain-rate = 2.03×10^{-3} s^{-1}). Similar results were obtained for all of the materials. The results show that this relationship holds over a certain temperature range for each of the materials, indicating that within this range the yield behaviour can be considered to be nucleation controlled. From these data the transition temperatures have been identified and are shown in Table II (compared to those found from analysis of the yield strain results). As can be seen from the table agreement between the two methods is very good, except for Material B at the higher strain-rate.

The Argon theory was developed for glassy polymers and, therefore, is not strictly applicable to semi-crystalline polyethylene well above Tg. A more appropriate nucleation controlled model to describe the yield behaviour of these materials has been developed by Young[8,9]. This is based on the thermal activation of screw dislocations within the lamellae in the c-axis direction and predicts that the yield stress is determined by the lamella thickness, l. Employing this approach we have fitted the yield stress against temperature data using l as the only fitting parameter. The results for Material C (strain-rate = 2.03×10^{-3} s^{-1}) are shown in Figure 3. It can be seen that the data are fitted exceptionally well by the theory and similar results were found for all of the materials. The best fit values for l are shown in Table III. In each case it can be seen that the lamella thickness predicted is much smaller than that measured using GPC analysis of nitric acid etched material. It is, therefore suggested that it is the thinner, in-fill, lamellae which yield initially at low strains.

The lamella thickness and the compressive yield stress (at -60°C, well below the transition temperature) were found for the four bulk crystallised materials and, additionally, three pressure annealed samples of Material C. The Young theory predicts that the natural logarithm of the yield stress should be linearly dependent on $1/l$. The data obtained have been plotted in this form in Figure 4. The results show that a good linear correlation is obtained. The value of the magnitude of the Burgers vector is calculated from the gradient, this was found to be 2.44Å, in very good agreement with the c-axis repeat unit length of 2.54Å.

* School Of Polymer Technology, The University Of North London, Holloway Road, London, N7 8DB.

+ I.R.C. In Polymer Science And Technology, The University Of Leeds, Leeds, LS2 9JT

References:

1) Brooks,N.W., Duckett,R.A. and Ward,I.M., Polymer, 1992, 33, No 9, Pp 1872.

2) Brooks,N.W.J., PhD Thesis, University Of Leeds, 1993.

3) Brooks,N.W., Duckett,R.A. and Ward,I.M., J.Rheol, 1995, 39(2), Pp 425.

4) Brooks,N.W., Unwin,A.P., Duckett,R.A. and Ward,I.M., J.Macromol.Sci-phys., 1995,

B34(1&2), Pp29.

5) Vickers, M.E. and Fisher, H, Polymer, 1995, 36, No 13, Pp 2667.

6) Brooks,N.W., Unwin,A.P., Duckett,R.A. and Ward,I.M., J.Polym.Sci. Part B: Polym.Phys (in press).

7) Argon,A.S., Phil Mag, 1973, 28, Pp 839.

8) Young, R.J., Mater Forum, 1988, 11, Pp 210.

9) Young,R.J., Phil Mag, 1974, 30, Pp85.

Table I.

	Mw	Mn	Branch content / 1000C
Material A.	126,000	30,300	21
Material B.	206,000	12,900	6.2
Material C.	131,100	19,100	<0.1
Material D.	395,000	32,800	<0.1

Table II.

	Transition temperature / °C.			
	From yield strain.		From yield stress (Argon).	
Strain-rate/ s^{-1}	8.33	$2.08x10^{-3}$	8.33	$2.08x10^{-3}$
Material A.	-60	-60	-40	-40
Material B.	20	-20	-40	-20
Material C.	20	20	0	0
Material D.	20	0	----------	---------- ------

Table III.

	Strain-rate / s^{-1}	Lamella thickness, l / Å	
		Best fit values.	Nitric acid / GPC.
Material A.	$2.03x10^{-3}$	49	110
Material A.	8.3	46	
Material B.	$2.03x10^{-3}$	54	132
Material B.	8.3	53	
Material C.	$2.03x10^{-3}$	61	343
Material C.	8.3	67	

Figure 1. Yield strain against temperature, Material C.

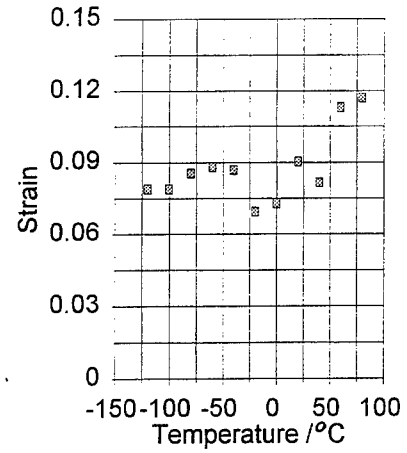

Figure 2. Argon plot for Material C.

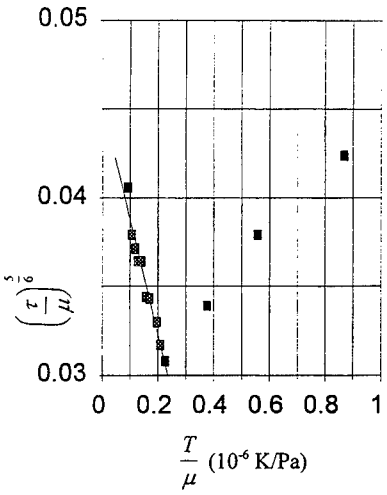

Figure 3. Yield stress against temperature, Material C.

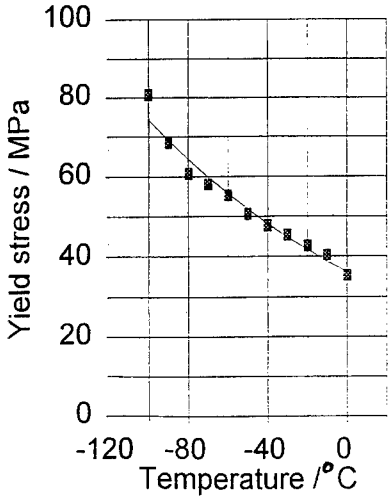

Figure 4. Natural logarithm of stress against reciprocal of lamellar thickness.

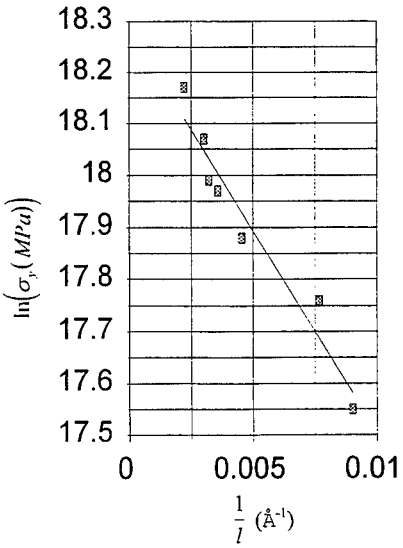

PLASTIC BEHAVIOUR AND RESISTANCE TO WEAR OF ULTRA-HIGH MOLECULAR WEIGHT POLYETHYLENE

C. G'Sell[*], B. Paysant-Le Roux[*], A. Dahoun[**], C. Cunat[+], J. von Stebut[++] and D. Mainard[↑]

Two polyethylene grades were investigated : i) high-density polyethylene (HDPE) and ultra-high molecular weight polyethylene (UHMWPE). For each material, the friction behaviour was investigated together with the intrinsic response up to large tensile strains. Although wear decreases with molecular weight, plastic strain under the indenter increases. This is correlated with the contrasted initial and ultimate regimes in tension : while yield stress is superior for HDPE due to higher crystallinity, strain hardening increases faster for UHMWPE resulting from the large density of tie molecules between crystallites.

INTRODUCTION

The development of polyethylene grades with average molecular weights higher than 10^6 g/mol have been essentially motivated by the need for low-friction, low wear, materials for sliding contact applications. In the domain of orthopaedic surgery, UHMWPE constitutes the nearly universal material for the fabrication of artificial joints, particularly for hip acetabular cups (1). However, the very high melt viscosity of this material makes its processing rather difficult with respect to more conventional HDPE grades. Furthermore, UHMWPE suffers significant creep compliance which limits its performances under high stress loading (*e.g.* knee prostheses) and may indirectly enhance the friction and wear in case of excessive plastic deformation. The aim of the present study is to analyse and interpret on a microstructural basis both plastic and wear resistance of UHMWPE by comparison to HDPE.

MATERIALS AND METHODS

The polyethylene grades investigated are obtained from industrial supplyers : i) general purpose HDPE extruded by Röchling in plates 15 mm thick (Röchling, D 500.000 min) and, ii) biomedical UHMWPE ram extruded in bars 50 mm diameter (Hoechst, GUR 415). The average molecular weights are $M_w = 2 \times 10^5$ g/mol and $M_v = 7 \times 10^6$ g/mol, respectively. From the density (0.956 and 0.935 respectively), the degree of crystallinity of each material could be assessed : 71 vol% for HDPE and 51 vol% for UHMWPE. Test pieces of two kinds were carefully machined and polished in each material : i) flat platelets 40 x 40 x 7 mm^3 for the friction-and-wear characterisation and, ii) hourglass shaped specimens with a minimum diameter $D_0 = 6$ mm for tensile experiments.

[*] Ecole des Mines-INPL, LMPSM (URA CNRS 155), Parc de Saurupt, 54042 Nancy, France
[**] Université de Metz, LPLI, 1 Blvd. Arago, 57070 Metz, France
[+] ENSEM-INPL, LEMTA (URA CNRS 875), BP 3, 54501 Vandoeuvre, France
[++] Ecole des Mines-INPL, LSGS (URA CNRS 1402), Parc de Saurupt, 54042 Nancy, France
[↑] Service de Chirurgie Orthopédique et Traumatologique, CHRU, 54035 Nancy, France

(Regional multidisciplinary program supported by the European Health Pole, Nancy, France)

The friction tests were run by means of two alternative methods : i) a pin-on-disk apparatus in which a 3 mm spherical steel indenter slides along a circular track at a speed of 94 mm/s, on the flat polymer disk in distilled water under a constant applied load of 10 N and, ii) a scratch-test system in which a 0.8 mm tip radius diamond indenter is displaced once along a 5 mm linear track at a speed of 0.17 mm/s under an applied load of 20 N. While the former technique favours polymer wear, the latter promotes plastic deformation. The friction tracks were characterised by laser profilometry and scanning electron microscopy.

For the determination of the stress-strain behaviour in uniaxial tension, we applied the VidéoTraction© testing system extensively described elsewhere (2). With this method, true strain at the mid-plane of the axisymmetric specimen is obtained in real time from the analysis of its digital image through the local diameter reduction : $\varepsilon = 2 \ln (D_o/D)$. Also, true strain-rate $\dot{\varepsilon}$ is kept constant by automatically adjusting the velocity of the servo-hydraulic tensile testing machine. As for true stress, it is given by $\sigma = (4 F / \pi D^2) \times F_T$, where the term in brackets is the local Kirchhoff stress and F_T represents the Bridgman triaxiality factor which corrects the perturbation to the ideally uniaxial stress field caused by the curvature of the sample.

EXPERIMENTAL RESULTS

The graph of Fig. 1 shows the evolution of the coefficient of friction in the pin-on-disk procedure for the two polymers. After an initial transient regime, the curves confirm the lower friction coefficient for the UHMWPE grade ($\mu \approx 0.05$) on which the steel ball slides easily, quite steadily and with minimum damage. Conversely, for HDPE, not only is μ higher (≈ 0.07) and erratic, but also the friction track shows important formation of wear debris and surface blisters. It is interesting to note, at least qualitatively at this step, that the good wear resistance of UHMWPE does not prevent the material from deforming under the pin.

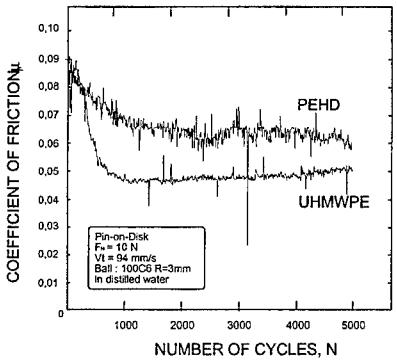

Figure 1 : *Evolution with time of the friction coefficient in the pin-on-disk tests*

However, this property is better identified in the one-way scratch test since plasticity is the only active mechanism (no removed debris are observed). We have displayed in Fig. 2 the shape of the track profiles after the indenter has swept along. It is remarkable that, for identical applied load and indenter velocity, the track is considerably deeper and wider for the UHMWPE than for the HDPE. Furthermore, inspecting these curves shows unambiguously that the volume conservation rule, obeyed in the HDPE, is not verified in the UHMWPE. For the latter material, the volume of the track under the baseline is 2.7 larger than the volume of total side up volume of the two rims above the baseline. This indicates that the plastic mechanisms are different for the two grades : i) in HDPE the ploughing process is such that all the material pushed out of the track flows into the lateral rims while, ii) in UHMWPE plastic flow is accompanied by significant density increase under the indenter. Based on the reasonable assumption that the plastically

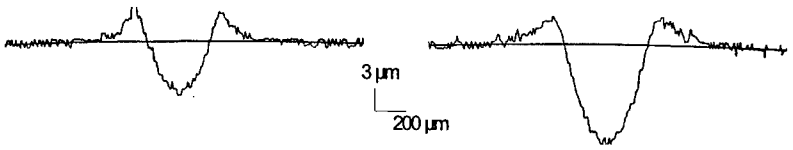

Figure 2 : *Track profiles after friction on HDPE and UHMWPE*

active zone has a depth about three times the penetration of the diamond under load, it is found that the local density change is of the order of - 5 % of the original density. This effect, particular to UHMWPE, could result presumably from two concurrent effects : i) the further consolidation of the powder processed polymer whose initial morphology is not fully cohesive (3) and, ii) the strain-induced orientation of the macromolecular chains under the effect of compressive plasticity. To date, no quantitative evaluation of any of those mechanisms is imagined.

Another approach toward a correct understanding of the structure-properties relationship in polyethylene consists in analysing the true stress-strain response of the materials up to large strains. It is now established that the intrinsic plastic behaviour of semi-crystalline polymers reveals the effect of microstructure evolution under load (4). In this scope, we analyse in figure 3 the results of video-controlled tensile tests run up to $\varepsilon \approx 2$ at the same rate $\dot{\varepsilon} = 5\,10^{-4}\,s^{-1}$. This graph shows outstanding features. At low strains, HDPE is clearly more resistant than UHMWPE. Both Young's modulus and yield stress of the former are larger. Furthermore, the flow stress remains a higher level than for UHMWPE up to $\varepsilon \approx 0.7$. Subsequently, as strain-hardening of the latter increases faster, the stress-strain curves eventually cross over and the flow stress of HDPE becomes much higher in the ultimate plastic stage (true stress for UHMWPE is nearly twice the value for HDPE at $\varepsilon \approx 1.5$).

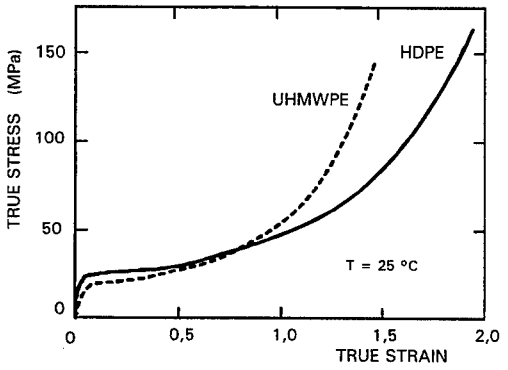

Figure 3 :
Stress-strain curves for the two polyethylene grades

It is interesting to note that this analysis of the plastic response of two polymer grades up to large strains is only rigorous in terms of true stress and true strain variables which are readily attainable by the application of the video-controlled tensile testing system. If conventional tensile tests were adopted, no comparison would be possible : for HDPE, the early occurrence of necking induces a very large yield drop in the nominal stress-strain curve while, for UHMWPE, deformation keeps more or less stable because of the larger hardening and no geometric softening is observed.

DISCUSSION

Although the relationship between the plastic behaviour of polyethylene grades and their resistance to wear is not straightforward, this work constitutes a firm basis to propose specific mechanisms in view of explaining the complex influence of the molecular weight on structure and mechanical properties. The first point concerns the influence on crystallinity. As the chain length increases, the melt viscosity gets larger and the formation of the crystalline lamellae becomes very difficult during the extrusion process. Since the crystallinity index is the dominating factor in both the elastic and plastic regimes, one understands easily why as intensive plastic deformation is observed at the indenter track in friction experiments. Additionally the imperfect consolidation of the UHMWPE powder structure during the forming process (3), due to the slow interdiffusion of polymeric chains in the melt, favours the observed compressibility of the plastically deformed material. By the way, the easier plastic flow of the UHMWPE grade causes unwanted creep compliance in some orthopaedic applications and complex metallic embedding structures are often required in order to keep the creep flow below a critical rate. However, a second point concerning strain-induced hardening and damage must be taken into consideration. As we showed in a previous study (4), the polyethylene crystallites are progressively tilted while strain increases, progressively loosing their capability of plastic accommodation. This results in a drastic fragmentation of the lamellae and in a stretching of the amorphous chains linking the remaining crystalline blocks. It is essentially at this step that the UHMWPE overrides the HDPE. The much higher density of tie molecules in the former grade does appear as the major cause of its plastic resistance at large strain. The problem remains of interpreting the influence of this enhanced plastic hardening on the wear mechanisms. Among various mechanisms proposed, microscopic fatigue cracking has been identified as an important cause of surface damage in cyclic friction. It is now well acknowledged (5) that the stress field in the craze at the tip of a growing micro-crack is essentially concentrated in the fibrils drawn from the parent material. The fibrillar material corresponds to a state of high strain, like in the ultimate plastic stage of figure 3. Higher stability of the fatigue micro-cracks in the UHMWPE grade is thus provided by the higher toughness of the fibrils and, in turn, by the highly cohesive network of the tie molecules. Other wear mechanisms, like ploughing the surface by a hard third-body mechanism, should be interpreted with the same arguments since, in all cases, the damage progresses in localised regions where the material failure is preceded (and often controlled) by plastic deformation mechanisms.

REFERENCES

1. Nusbaum, H.J., Rose, R.M., Paul, I.L. and Crugnola, A.M., 1979, "Wear Mechanisms for UHMWPE in the total hip prosthesis", J. Appl. Polym. Sci., 23, 777.

2. G'Sell, C., Hiver, J.M., Dahoun, A. and Souahi, A., 1992, "Video-Controlled Tensile Testing of Polymers and Metals Beyond the Necking Point", J. Mater. Sci., 27, 5031.

3. Rhambri, S. and Lin, S., 1996, "High Resolution Electron Microscopic Evaluation of Polyethylene", 5th World Biomaterial Congress, Toronto, Ont., may 29 - june 2, 1996, 510.

4. G'Sell, C. and Dahoun, A., 1994, "Evolution of microstructure in semi-crystalline polymers under large plastic deformation", Mat. Sci. Engn., A 175, 183.

5. Zhou, Y. and Brown, N., 1993, "Evaluating the fatigue resistance of notched polyethylene", Polym. Eng. Sci., 33, 1421.

SESSION THREE:

DEFORMATION IN AMORPHOUS POLYMERS I

Mechanisms of Time-Dependent and Localized Deformation in Amorphous Polymers

Mary C. Boyce
Massachusetts Institute of Technology
Department of Mechanical Engineering
Cambridge, MA
USA

Abstract

The mechanical behavior of polymeric materials has long been established to depend on time and temperature; the stress-strain behavior is also observed to be nonlinear prior to "yield". The nonlinear time and temperature dependent behavior is often modeled using nonlinear viscoelastic constitutive relationships. Nonlinear viscoelastic relations are integral equations relating stress to strain which typically contain multiple material time constants and/or strain dependent parameters. While some success has been achieved with fitting various nonlinear viscoelastic laws to actual polymer behavior, these models often fail to be predictive of data beyond the range of fit and also do not point to any underlying physics or structural origin responsible for the nonlinearity or the time dependence. On the other hand, the rate and temperature dependence of the "yield" point has been modeled using various approaches of plasticity, the most successful being the concept that yield or plastic flow is a thermally-activated process. The two schools of thought - *nonlinear viscoelasticy* and *viscoplasticity* - often appear at odds with one another in their attempts to describe similar aspects of material behavior yet provide no bridge or transition between what is commonly considered the viscoelastic regime of behavior and what is commonly called the plastic regime. In this research, we attempt to bridge these fields and provide a unified, continuous description of material response as it transitions from linear viscoelastic to nonlinear viscoelastic to viscoplastic. The general modeling methodology takes a mechanistic approach examining the material behavior over three length scales: mescoscopic network level modelling using Monte Carlo techniques; micromechanical modeling using the finite element techniques; and continuum modeling using internal state variable representation. This paper will specifically focus on micromechanical modeling of the inherently heterogeneous polymer microstructure. The model results reveal the local micro-shear banding mechanisms of deformation, energy storage due to distributed deformations, and the corresponding global continuum level response. The onset, growth and subsequent diffusion of microscopic shear bands is observed and linked to the macroscopic onset of nonlinear viscoelastic behavior and its transition to large scale viscoplastic flow. The nonlinear, time dependent nature of recovery during and after unloading is also predicted by the model. The modeling approach is motivated by earlier experimental results where positron annihilation spectroscopy reveals aspects of the distributed nature of the polymer microstructure, differential scanning calorimetry measures the energy storage which evolves with deformation, and mechanical evaluation shows the nonlinear loading and unloading behavior of the polymer as well as its nonlinear creep response. Comparison between simulation results and experiments are provided.

INELASTIC DEFORMATION OF GLASSY PMMA : NEW EXPERIMENTS AND COMPUTER MODELLING.

C.Gauthier*, J.Perez*
E.Oleinik**, S.Rudnev**, T.Slavetskaya**, M.Kravchenko**, O.Salamatina**,

Introduction

It is of great importance today, both, from technical and scientific points of view, to be able to understand and predict the mechanical response of glassy polymers. Recently quite a lot of new experimental data concerning viscoelastic and viscoplastic behaviour of glassy polymers, including PMMA, had appeared in literature (1-5). For deeper analysis and understanding of inelastic deformation mechanism operating in polymer glasses, there is a need for new type of experiments and for unified model which will permit to quantitatively describe the mechanical response of polymeric glasses. Such a model should allow to predict their response to different mechanical regimes (temperature, strain rate, deformation mode) and different thermal and mechanical history. Several constitutive models describing the behaviour of PMMA had appeared recently (e.g. 6-8). The main objective of this paper is the presentation of new experimental data concerning inelastic deformation behaviour of glassy PMMA and quantitative comparison with predictions by the modified model firstly introduced in (7).

We will model stress-strain behaviour of glassy PMMA at uniaxial compression, both, in loading and unloading regimes at different strains ε and T_{def}. We also will model the thermally-stimulated residual strain (ε_{res}) recovery of deformed samples at heating and will compare computed results with experiment (2,3). As far as we know, thermally-stimulated ε_{res} recovery processes were not modelled before.

Experimental results

Stress-strain curves for PMMA (Atochem, Mn = 10^6 g/mol, Tg (DSC)= 407K, dT/dt=20 °/min) are shown in Fig. 1. Cylinder samples (d=2mm,l=3mm) were tested in uniaxial compression ($\dot{\varepsilon}=7.10^{-4}$ sec^{-1}, T_{def}=287K) , recording both loading and unloading for different maximal strains ε_{def}. The amount of strain released during sample unloading ranges from 6,8 to 8,8% , depending on ε_{def}. During the test, the mechanical work of the stress (W) can be calculated and the heat (Q_ε) dissipated in the process is measured. The difference between the two values, $\Delta U = W - Q_\varepsilon$, gives the internal energy stored in the deformed sample the stored energy. Up to strain 15-20% , the main part of W is converted to stored energy ΔU.

Fig.2 represents residual strain ε_{res} recovery curves upon deformed sample heating. The curves show that two recovery peaks exist. One, sc. high temperature peak shows its maximum above but close to T_g. The other one shows its maximum a little higher than T_{def}, much lower than T_g. At low ε_{res} , only the low temperature recovery peak is observed. At high ε_{res} the intensity of low temperature recovery peak reaches the saturation. After the saturation of low temperature recovery peak, any changes of recovery curves at higher residual strains happen only by the changes of intensity of the high temperature recovery peak.

* I.N.S.A. de Lyon, Laboratory G.E.M.P.P.M. ura-341, Villeurbanne FRANCE
** Institute of Chemical Physics, Russian Academy of Sciences, Moscow RUSSIA

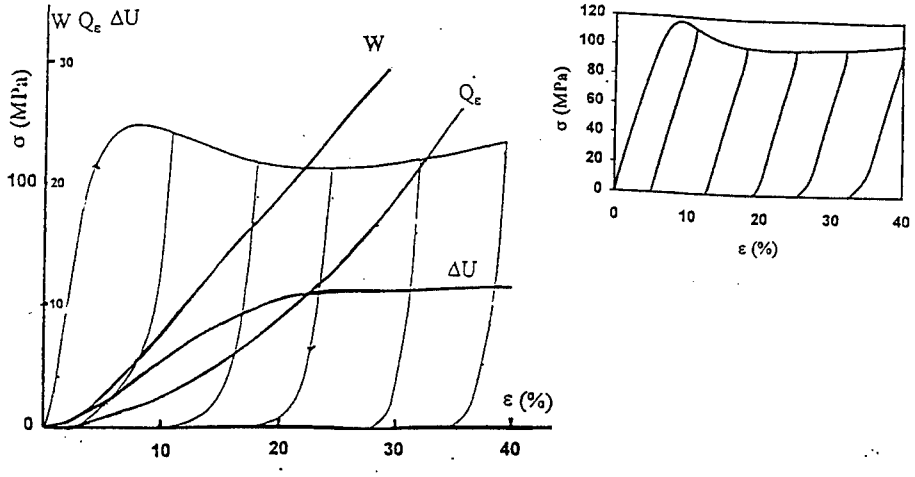

Fig.1 Experimental stress-strain curves for PMMA (Uniaxial compression, T_{def}=287K, Strain Rate = 7.10^{-4} sec^{-1}) - Insert : Calculated stress-strain curves

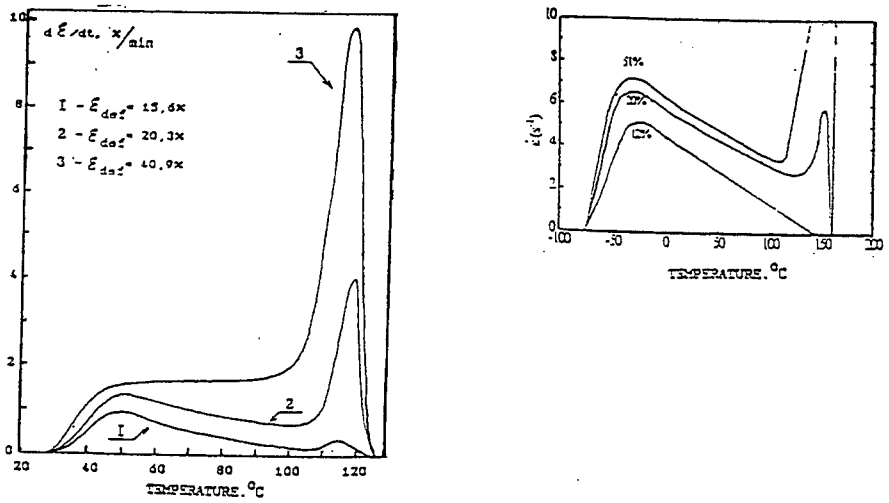

Fig.2. Residual strain recovery curves for PMMA deformed by uniaxial compression (strain rate 7.10^{-4} sec^{-1} at T_{def}=293K) up to ε_{def}=0.15 , 0.20 and 0.40%. Insert : Calculated recovery curves for PMMA deformed by uniaxial compression T_{def}=188 K)

Presentation of the modelling approach

The process of non-elastic deformation of glassy polymers is summarised in Figure 3. Under external stress σ, the nucleation and development of the specific defects (local shear transformations (3) or shear micro domains, smd (7)) occurs in isotropic glassy matter (Arrow

from (1) to (2) in Figure 3). These smd are the elementary carriers of the macroscopic anelastic strain (ε_{an}) in deformed glassy sample. The appearance of smd increases the internal energy (ΔU) of the sample as observed experimentally (3). Consequently, this stored energy results in a drawback force involving strain recovery in a temperature range $T_{def} < T < T_g$. When unloaded, the system returns to the equilibrium state by clearing the barrier from (2) to (1). With the constriction of smd, the microstructural state of the undeformed material is recovered. With further deformation, smd ultimately merge (arrow from (2) to (3), figure 3) and the stored elastic energy is dissipated. This last process is responsible for appearance of viscoplastic ε_{pl} component of macroscopic strain which can only be only recovered heating above T_g (5,9).

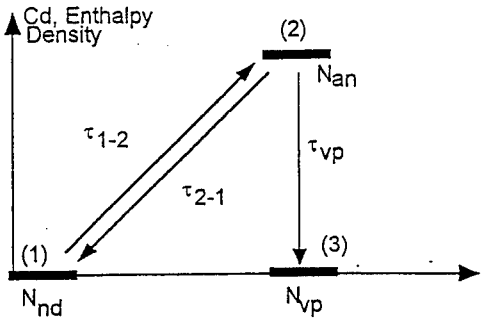

Fig.3. Schematic representation of deformation mechanism operating in glassy polymers.

The quantitative analysis of the experimental data has been performed on the basis of a molecular theory previously proposed (7) and further improved recently (8,11). The main features of this theory are : (i) the existence of quasi-point defects (dpd) corresponding to nanofluctuations of specific volume (concentration Cd) (ii) the hierarchically constrained nature of molecular dynamics (iii) under the application of a stress, the nucleation and growth of shear micro domains (smd) (anelastic strain) until they ultimately merge irreversibly with one another (viscoplastic strain). The molecular mobility in polymers can be given by the mean time τ_{mol} for a unit movement over a distance comparable to its size .

$$\tau_{mol} = t_0 \left(\frac{\tau_\beta}{t_0} \right)^{1/\chi} \qquad (1)$$

with t_0 : a scaling parameter, $0<\chi<1$: degree of hierarchical constraint in molecular motions (χ increases with disorder, i.e. with Cd between 0 (fully constrained situation) and 1 (constraint free situation). τ_β is characteristic time of a elementary molecular jump identified with the sub-T_g β relaxation. With thermomechanical activation of the jumps, we have :

$$\tau_\beta(\sigma) = \tau_{\beta o} \exp\left(\frac{U_\beta}{kT}\left(1-\frac{\sigma}{\sigma_0}\right)^{3/2}\right) \quad (2)$$

Finally, distribution effects are taken into consideration : random spatial distribution of disorder, that is Cd i.e. χ , results in a log normal distribution of $\tau_{vp} \approx \tau_{mol}(\sigma)$ related to ε_{vp}. On the other hand, τ_{an} related to ε_{an} is distributed from $\tau_\beta(\sigma)$ to $\tau_{mol}(\sigma)$. The details of such an analysis are given in another paper in this conference (11) .

Results of modelling

Calculated stress-strain curves in uniaxial compression for PMMA are shown in insert (fig. 1). One can see that calculation results semi-quantitatively reproduces experiments for loading and unloading regimes. Yield stress and strain and Young modulus coincide with experiment. For different maximal strains ε_{def}, the amount of strain released during sample unloading is quite well reproduced. Calculations also give the respective contributions of anelastic and viscoplastic strain during the test. The work of the stress (W) can be obtained from the $\sigma-\varepsilon$ curve and the stored energy in the deformed sample (ΔU) is proportional to ε_{an}. From these theoretical considerations, we can scale the variation of heat dissipation in the material with strain.

Calculated stress-strain curves for different T_{def} and $\dot{\varepsilon}_{def}$ also present a good agreement with experimental data (10). Quite reasonable changes of yield stress σ_y, Young moduli E and yield strain ε_y appear at different strain rates. The most important point to be underlined is that the same set of parameters is also used to performed calculation of residual strain recovery curves upon deformed sample heating (insert in Fig.2) : all main features of experimental recovery curves are quite well reproduced : (i) the existence of two recovery peaks at respectively high temperature (close to T_g) and low temperature (ii) the range of the recovery rates at these two recovery maxima for different ε_{def}.

All results show that the model is well representing the variety of experimental data for glassy PMMA in a quantitative manner. Now we are trying to use the model for an analysis of inelastic deformation of amorphous PET, PS and amine cured epoxy networks in the glassy state.

LITERATURE

1.O.A.Hasan, M.C.Boyce,S.Berko, Journ.Polym.Sci.B,V31,185-197 (1993)
2.E.F.Oleinik,O.B.Salamatina,S.N.Rudnev,S.V.Shenogin Polym. Science,A35,1819-1849 (1993)
3.O.Salamatina,G.Hoehne,S.Rudnev,E.Oleinik Thermochim.Acta (1994)
4.R.Quinson,J.Perez,M.Rink,A.Pavan,J.Mater.Sci.,V31, (1996)
5.L.David,R.Quinson,C.Gauthier,J.Perez Polym.Eng.Sci. 1996 (in press)
6.O.A.Hasan,M.C.Boyce Pol.Eng.Sci.V35,No4. (Febr.1995).
7. M. Mangion, J.Y. Cavaillé, J. Perez, Phyl. Mag. A66,773, (1992)
8.C.Gauthier,L.David,L.Ladouce,R.Quinson.Jo Perez, J. Appl. Sci. 1996 (in press)
9.E.F.Oleinik in book "High Performance Polymers" Eds. E.Baer and S.Moet, Hanser Verlag, Munchen (1990).
10. R. Quinson, Ph. D. These, I.N.S.A. LYON (1995)
11. O. Sindt, C. Gauthier, J. Perez, procd. Deformation, Yield and Fracture in Polymers, Cambridge, 1997

MOLECULAR APPROACH OF THE DEFORMATION MECHANISMS IN POLYMETHYLMETHACRYLATE-BASED RANDOM COPOLYMERS

J.L. Halary*, L. Monnerie*, L. Tézé+, P. Tordjeman*+

Mechanical measurements were carried out on two series of methylmethacrylate-based random copolymers, which include N-cyclohexyl maleimide and N-methyl glutarimide, respectively, as the comonomer. Viscoelastic measurements permit characterization of the β secondary relaxation motions and analysis of their possible coupling with the α relaxation motions, depending on their degree of cooperativity. Inspection of the stress-strain curves in the plastic deformation region shows that the cooperative β motions, whenever they exist, lead to a decrease of both yield stress and strain softening. In addition, crazing is shown to be the main deformation mechanism of most of samples prepared in the form of thin films. Diffuse deformation zones are detected only in the cases for which cooperative β motions have been found.

During the past decades, numerous studies have been devoted to such mechanical properties of glassy polymers as plasticity, shear banding, crazing and fracture. However, it is not yet understood how these properties depend on the chemical structure of the materials. Some encouraging attempts were made to elucidate macroscopic mechanical properties thanks to the knowledge of the polymer chain motions (1-4). In this context, we realized that methylmethacrylate-based random copolymers could be interesting systems for an approach of the relationships between molecular mobility and mechanical properties. Indeed, changes in the chemical nature and amounts of comonomer lead to significant modifications of both relaxational and deformation behaviours, as will be shown in this paper.

MATERIALS

The copolymers under study are based on methylmethacrylate (MMA) with either N-cyclohexyl maleimide (MIM) in the range 0-25 mol% (5) or N-methyl glutarimide (GIM) in the range 0-80 mol% (6) :

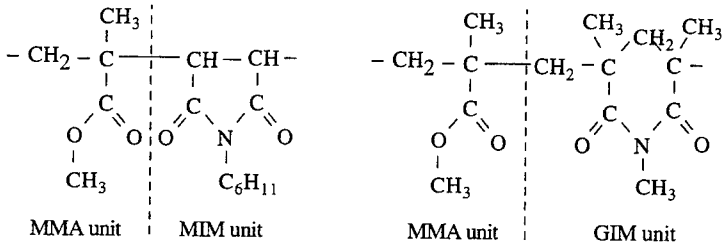

They will be referred as MIM x and GIM x, where x is the comonomer mole fraction. The MIM samples were kindly prepared for us by Drs P. Gaillard and S. Nowé (Elf Atochem, Lacq, France) and the GIM samples by Dr L. Canova (Enichem, Novara, Italy).

*Laboratoire PCSM (URA CNRS n° 278), Ecole Supérieure de Physique et Chimie Industrielles de la Ville de Paris, 10, rue Vauquelin, 75231 Paris Cedex 05, France
+Elf Atochem, CERDATO, 27470 Serquigny, France
*+Elf Atochem, Groupement de Recherches de Lacq, 64170 Artix, France

VISCOELASTIC MEASUREMENTS

Measurements were performed on a servohydraulic testing system MTS 831 operated in tensile mode. The samples were subjected to a static strain of 0.1% on which a sinusoidal strain of ± 0.05% was superimposed.The frequency range covered by the experiments was 0.04 to 70 Hz.

MIM copolymers. Inspection of the temperature dependence of the loss modulus, E", in the low temperature region (figure 1) shows a β relaxation (whose amplitude decreases with decreasing amount of MMA) and a low-temperature γ relaxation (whose extent increases with increasing amount of MIM). These dampings are assigned to MMA motions and chain-chain inversion of the substituted cyclohexyl ring, respectively. More interesting are the observations in the temperature domain between the β and α transitions (figure 2). An amount of 5 mol% of MIM units is sufficient to provoke a significant decrease of E". By comparing with the similar decrease of E" induced by physical ageing on PMMA, it is concluded that a MIM unit is able to decouple the β and α processes. In other words, the cooperativity between the ester group motions and the chain backbone, which develops in PMMA above 20°C and has been observed by ^{13}C NMR (7), is suppressed by the addition of MIM units.

GIM copolymers. The viscoelastic damping of the GIM copolymers in the sub-Tg region is more complex than that of the MIM copolymers, because of a substantial contribution of the GIM moieties (figure 3). As shown in a recent thesis (8), the contributions of the various groups to the loss compliance, J", of a copolymer are additive.Therefore, J" traces are more suitable than E" traces for analyzing complex mechanical relaxation spectra. It turns out that in the low temperature range (- 80°C to 0°C) the ester motion of MMA units is more dissipative in MMA/GIM than in MMA/MMA sequences, the GIM/GIM sequence having a very low dissipation. The opposite is observed in the high temperature range (30°C to Tg) : the cooperativity of the MMA motions is first hindered by the GIM units for GIM amounts lower or equal to 58 mol%, and then replaced by dissipative cooperative motions of GIM/GIM/GIM sequences at higher GIM contents.

STRAIN-STRESS MEASUREMENTS BELOW Tg

Measurements were performed on a servohydraulic testing system MTS 810 operated in compression mode. Usually, the imposed deformation rate was of 2.10^{-3} s^{-1} and the maximum strain considered was lower than 0.2.

The temperature dependence of the the yield stress, σ_y, was examined for the various copolymers. It is not easy to carry out direct comparisons, because of the differences in Tg of the materials. At low temperature, σ_y is very sensitive to the cohesion of the material and therefore to its modulus. Above room temperature, consideration of the modulus is not sufficient to account for the values of σ_y and the character of the sub-Tg motions plays also a role. This is unambiguously illustrated (figure 4) by the comparison of the temperature dependence of the yield stress for MIM 25 and GIM 76 which exhibit roughly the same Tg (160°C and 158°C, respectively). As a general rule, the cooperative β motions, either MMA/MMA in pure PMMA and MMA-rich GIM copolymers or GIM/GIM in MMA-poor GIM copolymers, are more efficient for initiating the plastic deformation than the non-cooperative ones, observed in most of the MIM copolymers.

The amplitude of plastic softening, (σ_y - σ_{pf}), defined as the difference between the yield stress and the plastic flow stress, was also examined (Table I).

TABLE I - Plastic strain softening at 50°C for the MIM and GIM copolymers

MIM mol%	0	3	5	10	15	20	25
σ_y - σ_{pf} (MPa)	2	3	8	12	17	23	27
GIM mol%	4	8	21	36	58	63	76
σ_y - σ_{pf} (MPa)	2	2	5	6	7	8	5

Systematically, very low values of (σ_y - σ_{pf}) are observed for the materials exhibiting cooperative β motions. On the other hand, lack of β motion cooperativity leads to a significant increase in the plastic softening.

MICRODEFORMATION MECHANISMS

The microdeformation mechanisms have been investigated by using the thin film technique (9). The temperature ranges in which crazing and shear deformation zones (SDZ) exist are sketched in figure 5a for MIM (10) and in figure 5b for GIM (11) copolymers. In the case of MIM copolymers, the spreading of crazing with increasing copolymer amount has been related to the parallel increase of the molecular weight between entanglements, M_e (10). This explanation is no longer satisfactory by looking at the series of GIM copolymers. In this case, indeed, M_e increases from 8000 g.mol $^{-1}$ for pure PMMA till about 12000 g.mol $^{-1}$ for 36 % of G units and then levels up. As a consequence, the results obtained on the whole set of copolymers cannot be accounted for by considering M_e changes only. On the contrary, the changes of σ_y can be consistently related to the extent of cooperativity of the β motions : the larger the cooperativity, the easier the shear deformation zones develop. As will be detailed in a forthcoming publication, these effects seem to be directly reflected in the fracture behaviour : the copolymers which exhibit highly cooperative β motions are less brittle than the others.

SYMBOLS USED

E', E" = storage modulus, loss modulus (MPa)
J" = loss compliance (MPa $^{-1}$)
M_e = molecular mass between entanglements, (g.mol $^{-1}$)
σ_y, σ_{pf} = yield stress, plastic flow stress (MPa)

REFERENCES

1. Bauwens JC, J Mater Sci 7, (1972) 577
2. Bauwens-Crowet CJ, J Mater Sci 8, (1973) 968
3. Lefebvre JM, Escaig B, J Mater Sci 20, (1985) 438
4. Schirrer R, Adv Polym Sci, 91/92, H.H. Kausch Ed., Springer (1990), p 215
5. Tordjeman P, Doctorat, Université Pierre et Marie Curie, Paris, 1992
6. Tézé L, Doctorat, Université Pierre et Marie Curie, Paris, 1995
7. Schmidt-Rohr K, Kulik AS, Beckham HW, Ohlemacker A, Pawelzik A, Boeffel C, Spiess HW, Macromolecules 27, (1994) 4733
8. Beaume F, Doctorat, Université Pierre et Marie Curie, Paris, 1996
9. Lauterwasser BD, Kramer EJ, Phil. Mag. A-39, (1979) 469
10. Tordjeman P, Halary JL, Monnerie L, Donald AM, Polymer 36, (1995) 1627
11. Plummer CJG, Kausch HH, Tézé L, Halary JL, Monnerie L,Polymer 37 (1996) 4299

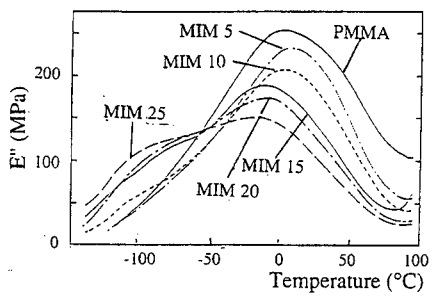

Fig. 1. E" at 1Hz for PMMA and MIM copolymers in the low temperature range

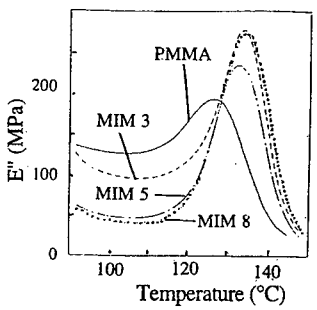

Fig. 2. E" at 1Hz for PMMA and MIM copolymers in the transition overlapping range

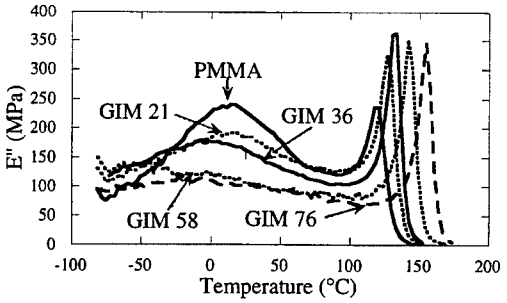

Figure 3. E'' at 1Hz vs temperature for PMMA and MIM copolymers

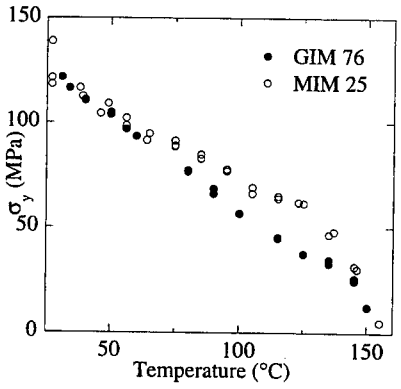

Figure 4. Yield stress vs temperature for the copolymers GIM 76 and MIM 25

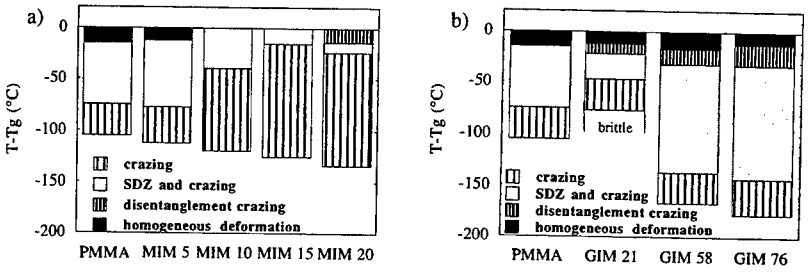

Figure 5. Schematic representation of the(T -Tg) dependence of the deformation micromechanisms in PMMA and (a) MIM and (b) GIM copolymers

ON PHYSICAL AND MECHANICAL BEHAVIOR OF GLASSY POLYMERS

M.S. Arzhakov* and S.A. Arzhakov*

Temperature-induced relaxation of residual plastic deformation of polymer glasses was discussed in terms of structural inhomogeneity of glassy polymers. Mechanical properties of glassy polymers were shown to be controlled by the ratio between low-temperature and high-temperature components of temperature-induced relaxation of residual deformation. This ratio was treated as a new physical parameter describing physical and mechanical behavior of polymer glasses.

Polymer glasses are widely used as modern materials (for example, engineering plastics) because of their unique properties, in particular, lowered brittleness and well-pronounced ductility as compared with low-molecular-mass glassy materials. For further development of advanced polymeric materials based on glassy polymers one should understand the origin of the specific properties of polymer glasses and, in general, the origin of their physical and mechanical behavior. To solve this problem, studying temperature-induced relaxation of residual plastic deformation in polymer glasses provides an important information. Temperature-induced relaxation of plastic deformation in polymer glasses involves low-temperature component at temperatures well below glass transition temperature T_g (ε_1) and high-temperature component at temperatures close to T_g (ε_2). Obviously, such complicated character of relaxation of plastic deformation is a manifestation of physical processes, which are responsible for and accompany plastic deformation. In this case, development of plastic deformation and physical and mechanical behavior of glassy polymers are likely to be controlled by the coexistence of the above components of relaxation.

In the present paper, for virgin poly(methyl methacrylate) (PMMA), PMMA plasticized with dibutyl phtalate (DBPh), and copolymers of methyl methacrylate (MMA) with butyl methacrylate (BMA), octyl methacrylate (OMA), and lauryl methacrylate (LMA), the correlation between the above components of relaxation and mechanical characteristics of polymers was studied.

*Polymer Department, Faculty of Chemistry, Moscow State University, Moscow, Russia

High-temperature component of relaxation is associated with the transition of excited chain conformations to their initial equilibrium state via segmental mobility in polymer sample. The appearance of low-temperature component of relaxation is treated by authors (1 - 3) in terms of structural inhomogeneity of glassy polymers. Within the framework of this approach, glassy polymer is characterized by a set of structural sublevels with different packing densities and ordering. Each of these sublevels is associated with its own relaxation time and activation energy of segmental mobility. As a result, at each temperature below T_g local segmental mobility in certain structural sublevels is allowed. With increasing temperature, structural sublevels with higher packing densities acquire segmental mobility, and finally at T_g, all polymer sample is involved in segmental mobility. Hence, a wide spectrum of segmental mobility in glassy polymer is provided by the existence of a set of structural sublevels with different packing densities and local ordering.

In the case of the deformed polymer samples, as temperature increases, the appearance of segmental mobility in structural levels with higher packing density is accompanied by a gradual recovery of local plastic deformation within the above structural sublevels. In other words, low-temperature relaxation of residual deformation is controlled by low-temperature fraction of the spectrum of segmental mobility because of temperature-induced segmental mobility within structural sublevels with lower packing densities at temperatures well below T_g. A complete relaxation of plastic deformation at T_g via high-temperature component is controlled by high-temperature fraction of the spectrum of segmental mobility. Hence, molecular mechanism of low-temperature relaxation is similar to that of high-temperature mode and involves transition of excited chain conformations to initial equilibrium state via segmental motion within certain structural sublevels.

Studying ratio between the components associated with low-temperature and high-temperature relaxation as a function of compression strain evidenced that, in the case of the samples with strains below yield strain ε_y, temperature-induced relaxation of plastic deformation proceeds via low-temperature component. At the strain corresponding to ε_y, component ε_1 is maximal, and further increase in compression strain is associated with appearance and growth in the high-temperature component ε_2 at constant ε_1.

The results obtained allowed us to advance the following structural pattern of the development of plastic deformation in glassy polymers. At strains below yield strain, deformation is controlled by the stress-induced segmental mobility within structural sublevels with lower packing densities. At temperatures well below T_g, temperature-induced relaxation of this portion of plastic deformation is controlled by low-temperature mode of the spectrum of segmental mobility. Obviously, a certain fraction of low-temperature mode of segmental mobility is able to relax during polymer loading. From

this viewpoint, low-temperature component ε_1 is likely to be associated with stored plastic deformation, which remained unrelaxed during loading. At strains above yield strain, plastic deformation is controlled by the stress-induced segmental mobility within densely packed structural sublevels. This portion of plastic deformation is able to relax at temperatures close to T_g, when all polymer sample is involved in segmental mobility. Experimental support of the mechanism proposed using positron annihilation lifetime spectroscopy can be found in reference (4). Note, that, from this standpoint, plastic deformation of glassy polymer may be described by the contributions from above components to total temperature-induced relaxation of deformation.

With respect to polymer strength properties, consideration of contribution of low-temperature component ε_1 to total relaxation $\varepsilon_1/(\varepsilon_1+\varepsilon_2)$ is of most interest. This parameter is responsible for the development of polymer deformation at initial portion of σ - ε curve, i.e., at strain less than ε_y, which is associated with such mechanical properties as elastic modulus E_0 and yield stress σ_y. This allows one to suggest the correlation between relaxation $\varepsilon_1/(\varepsilon_1+\varepsilon_2)$ and mechanical characteristics E_0 and σ_y.

To verify this correlation, PMMA samples were compressed to different strains at different temperatures. As deformation temperature T_{def} increases, the contribution from low-temperature component to relaxation of residual deformation is seen to decrease. On the other hand, as T_{def} increases, elastic modulus and yield point go down. This experimental evidence suggests an intimate correlation of elastic modulus and yield stress with the contribution from low-temperature component to total relaxation of plastic deformation $\varepsilon_1/(\varepsilon_1+\varepsilon_2)$. At any strains, similar tendency is observed: as contribution from component to relaxation of residual deformation decreases, both elastic modulus and yield stress tend to decrease.

With increasing T_{def}, the parallel decrease in both $\varepsilon_1/(\varepsilon_1+\varepsilon_2)$ and E_0 and σ_y is likely to be controlled by the fact, that, in this case, local segmental mobility in certain structural sublevels is enhanced. As a result, the higher fraction of low-temperature mode of the whole spectrum of segmental mobility is able to relax during deformation. Obviously, the enhancement of segmental mobility in polymer sample is controlled not only by increasing T_{def}, but also by decreasing T_g . Depression in T_g may be attained by either plasticization of PMMA or by copolymerization of MMA with methacrylic monomers. As was shown, with increasing concentration of DBPh in PMMA and increasing concentration of BMA, OMA, and LMA in copolymers with MMA, decrease in both σ_y and $\varepsilon_1/(\varepsilon_1+\varepsilon_2)$ takes place.

In other words, for copolymers of MMA as well as for PMMA deformed at different T_{def} and plasticized PMMA, a good correlation between σ_y and $\varepsilon_1/(\varepsilon_1+\varepsilon_2)$ is

observed. Note, that this correlation is independent of any variations in these parameters: either by varying T_{def} of PMMA, or plasticization of PMMA, or copolymerization of MMA with BMA, OMA, and LMA. This fact is likely to be associated with the difference between T_{def} and T_g, which is defined as $\Delta T = T_g - T_{def}$. Experimental evidence obtained allows one to conclude that, at a given ΔT, σ_y and $\varepsilon_1/(\varepsilon_1+\varepsilon_2)$ remain unchanged and are independent of any variations in ΔT: by increasing T_{def} at a fixed T_g or by decreasing T_g at a fixed T_{def}. Note, that such behavior is likely to be associated with the dynamics of segmental mobility in polymer glasses.

The dynamics of segmental mobility seems to be controlled not only by ΔT but also by strain rate. One could expect, that with increasing strain rate, the fraction of low-temperature mode of segmental mobility, which is able to relax during deformation, decreases. As a result, both σ_y and $\varepsilon_1/(\varepsilon_1+\varepsilon_2)$ should increase. To verify this idea, copolymers of MMA with BMA, OMA, and LMA were tested under the compression with different strain rates. For copolymer samples, with increasing strain rate from 0.1 to 100 %/min, increase in both σ_y and $\varepsilon_1/(\varepsilon_1+\varepsilon_2)$ is observed. In other words, in this case, a well-pronounced correlation between σ_y and $\varepsilon_1/(\varepsilon_1+\varepsilon_2)$ is also takes place.

Hence, studying temperature-induced relaxation of residual plastic deformation of polymer glasses was shown to provide an important information concerning development of plastic deformation and, in general, physical and mechanical behavior of glassy polymers. Mechanical characteristics of glassy polymers and the ratio between low-temperature and high-temperature components of relaxation were shown to be well correlated. This correlation is independent of any variations in the above parameters: either by varying deformation temperature and strain rate, or by physicochemical modification of polymer - plasticization and copolymerization. Such behavior is likely to be associated with the dynamics of segmental mobility within certain structural sublevels in glassy polymers. These speculations allowed us to treat the ratio between low-temperature and high-temperature components of temperature-induced relaxation of residual deformation as a new physical parameter describing physical and mechanical properties of polymer glasses.

REFERENCES

1. Arzhakov, S.A., Bakeev, N.F., and Kabanov, V.A., 1973, Vysokomol. Soedin., A 15, 1154 (in Russian)
2. Arzhakov, M.S. and Arzhakov, S.A., 1995, Intern. J. Polymeric Mater., 29, 249.
3. Arzhakov,M.S., Arzhakov, S.A., and Chernavin, V.A., 1996, New Polymeric Mater.,5, 43.
4. Shantarovich, V.P., Arzhakov, M.S., and Kevdina, I.B., 1995, Polym. Sci., B 37, 171.

SESSION FOUR:

DEFORMATION IN AMORPHOUS POLYMERS II

TORQUE AND NORMAL FORCE MEASUREMENTS IN VISCOELASTIC SOLIDS

Gregory B. McKenna*

INTRODUCTION

Since the late 1970's we have been exploring the possibilities in our laboratories of using torsional measurements in which the length of a right circular cylinder is held constant, suppressing the Poynting (1) effect and giving rise to large normal forces. The result is that we have been able to examine aspects of nonlinear viscoelasticity that reflect the multi-axial state of stress that arises in the torsion-normal force measurement in several ways that seem, at a minimum highly interesting, and more realistically as offering an important different way of interrogating a material's response that is more powerful in many aspects than simple uni-dimensional testing, such as uniaxial extension or simple shear. Here we give a flavor of the sort of result that can be obtained.

EXPERIMENTAL CONSIDERATIONS

While many devices are available that permit successful measurement of the normal force response in torsional deformations, we have had success with both tension-torsion servo-hydraulic testing equipment in which the axial displacement is controlled using a linear variable differential transformer in a feedback loop (2,3) as well as with conventional rotary rheometers (4-6) in which the system stiffness is sufficient to suppress the elongation of the sample.

It is important to understand that the errors in the measured normal forces arise from spurious length changes in the sample or the measurement apparatus that induce longitudinal strains in the samples which cause superposition of stresses that can either add or subtract from the measured normal force. An example of an extreme case of such an event was observed (6) in a rotary rheometer which had a load cell that heated upon application of the torque. In such an instance, the transducer got longer and the initial normal force relaxation of the sample was followed by an 'anomalous' increase as illustrated in Figure 1. Note also in Figure 1 that the torque relaxes monotonically in the expected fashion.

Finally, unlike many testing situations in which one searches to apply a homogeneous deformation to the entire sample, the fact that the torsional experiment creates a gradient in the deformation across the radius makes it possible to obtain extra information about the material response. This becomes obvious in the examination of the equations given below.

EQUATIONS

For a time dependent relaxing material (7) in the form of a right circular cylinder of radius R and length L subjected to a twist per unit length Ψ the torque T and normal force N

*Polymers Division, National Institute of Standards and Technology, Gaithersburg, MD 20899 USA.

responses at given values of time t (or strain rate) are written as (2,5,8):

$$T(t)=4\pi\Psi\int_0^R[W_1(t)+W_2(t)]r^3dr \quad (1)$$

$$N(T)=-2\pi\Psi^2\int_0^R[W_1(t)+2W_2(t)]r^3dr \quad (2)$$

And we note immediately that the information contained in the combined torsion and normal force measurement is greater than what would be obtained for a measurement of torque alone or, in fact, if one measured both shear and normal force, which each contains the same information. It is the inhomogeneity of the deformation (the gradient of the shear strain through the sample from inner to outer radius) that makes it possible to obtain the additional information. This was first recognized by Penn and Kearsley in 1976 (8) and they showed that simultaneous equations could be derived to solve for the strain energy function derivatives $\mathbf{W}_1$ and $\mathbf{W}_2$. Then, differentiating with respect to R and applying Leibnitz's rule:

$$W_1(t)+W_2(t)=\frac{1}{4\pi\Psi R^4}[3T(t)+\Psi\frac{dT(t)}{d\Psi}] \quad (3)$$

and

$$W_1(t)+2W_2(t)=\frac{-1}{\pi\Psi^2R^4}[N(t)+\Psi^2\frac{dN(t)}{d(\Psi^2)}] \quad (4)$$

Hence, from the torque and normal forces measured at different values of strain (and time) one can obtain the individual $\mathbf{W_i(t)}$ values.

SOME TYPICAL RESULTS AND DISCUSSION

When the torque and normal forces are measured in stress relaxation conditions, one can construct isochronal (constant t) 'stress-deformation' diagrams for both the torque and the normal force and then equations 3 and 4 can be applied to obtain values of the $\mathbf{W_i}$. Figures 2 and 3 show typical results of such an analysis for a polycarbonate polymer glass. The question that arises is what is the importance of such data? First, if similar data are taken in multiple step stress relaxation experiments (1,9,10) the normal force response can be used to check constitutive assumptions. For space reasons this is not discussed further. Furthermore, by extending the analysis in equations 1-4, which arise from rubber elasticity analogs for incompressible materials, it is possible to predict the response of compressible and viscoelastic materials to other deformation geometries (11,12). As seen in Figure 4 the tension and compression responses of polycarbonate, a highly nonlinear material, can be

reasonably well predicted from the data presented in Figures 3 with the additional assumption that one can use the Valanis-Landel (13) function to describe the time dependent strain energy function of the material. Space considerations prevent detailed discussion.

SUMMARY

Simultaneous measurement of Torque and Normal forces in torsion of cylindrical samples held at constant length provides an efficient means of testing solid-like polymers. Analogies with rubber elasticity theory allow determination of a time-dependent strain energy function and the inhomogeneous deformation field in a twisted cylinder is shown to provide more information than would be obtained in simpler testing geometries. Some typical results are presented for a polycarbonate material in which the strain energy function derivatives are obtained from the torsional measurements. An analysis, not presented here, was developed by Pesce and McKenna (12) to predict the tension and compression response from the torsional data and it is shown that the nonlinear response of polycarbonate is successfully described.

SYMBOLS USED

T = torque (N-m)
N = normal force (N)
L = cylinder length (m)
R = cylinder diameter (m)
t = time (s)
Ψ= angle of twist per unit length (radians/m)
W_i= derivative of the strain energy function with respect to the i^{th} invariant of the deformation tensor (N/m^2)
λ = stretch = ratio of length to initial length

REFERENCES

1. Poynting, J.H., Proc. Roy. Soc. London, Series A, 86, (1912) 534
2. McKenna, G.B. and Zapas, L.J. , J. Rheol., 23 (1979) 151
3 McKenna, G.B. and Zapas, L.J., J. Rheol. 24 (1980) 367
4. McKenna, G.B. and Kovacs, A.J. Polym. Eng. Sci. 24, (1984) 1131
5. McKenna, G.B.and Zapas, L.J., Polymer 24 (1983) 1495
6. Niemiec, J.M. , et al J. Rheol. 40 (1996) 323
7. Rivlin, R.S. Quarterly of Applied Math. Xx (1955) yyy
8. Penn, R.W. and Kearsley, E.A. Trans. Soc. Rheol. 20, (1976) 227
9. Venerus, D.C. and Kahvand, H., J. Rheol. 38, (1994) 1297
10. Brown, E.F. and Burghardt, W.R., J. Rheol. 40, (1996) 37
11. Kearsley, E.A. and Zapas, L.J., J. Rheol. 24, (1980) 483
12. Pesce, J.J. and McKenna, G.B. J. Rheol. (In press)
13. Valanis, K.C. and Landel, R.F., J. Appl. Phys. 38, (1967) 2997

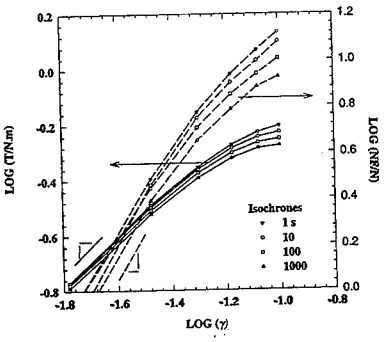

Figure 1. Double logarithmic representation of the isochronal Torque and Normal Force responses vs applied strain for glassy polycarbonate. [After reference 12.]

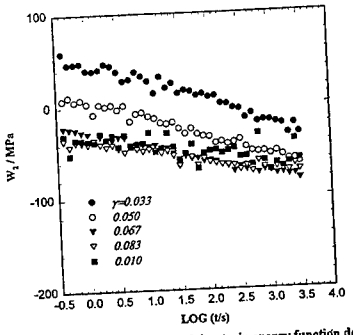

Figure 3. Time dependence of the strain energy function derivative W_2 (t) determined from torque and normal froce measurements at different strain values, as indicated. [After reference 12].

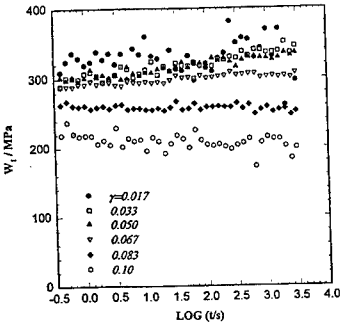

Figure 2. Time dependence of the strain energy function derivative W_1 (t) determined from torque and normal froce measurements at different strain values, as indicated. [After reference 12].

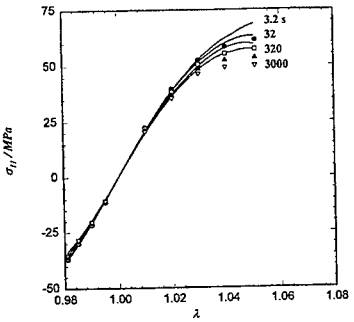

Figure 4. Comparison of isochronal (four times indicated) stress-strain response in tension and compression for polycarbonate with calculations from compressible Valanis-Landel strain energy function. Points represent data. Lines are calculated values. [After reference 12].

THE ONSET OF NONLINEARITY IN THE MULTIAXIAL VISCOELASTICITY OF GLASSY POLYMERS

P.J.Dooling*, C.P.Buckley* and S.Hinduja†

The applicability of an isostructural three-dimensional constitutive model was examined, for modelling the onset of nonlinearity in the viscoelasticity of glassy polymers. Nonlinearity entered through a spectral and multiaxial generalisation of Eyring rate process kinetics, with shear activation volumes varying across the relaxation spectrum, as expected from the "compensation rule" of polymer thermo-viscoelasticity. The model was fitted to and tested against uniaxial and biaxial creep data for poly(methyl methacrylate) (PMMA) in the region of its α-relaxation, and found to give good agreement. The data were not consistent with the onset of nonlinearity being caused by perturbation of the glass structure. The constitutive model proposed seems to exhibit the characteristic nonlinearities of creep in glassy polymers.

INTRODUCTION

There is great interest in applying stress-analysis software to load-bearing polymer components. A practical problem, however, is that accurate predictions cannot yet be made when deformations lie in the nonlinear viscoelastic range, whereas design strain limits for ductile polymers typically lie precisely in this range. The present work was aimed at constructing and validating a constitutive model to describe the multiaxial viscoelasticity of polymers, especially glassy polymers in the region of the α-relaxation process, for use in situations where nonlinearity is just commencing (typical strains are up to 2%), as needed in typical simulations of in-use performance.

EXPERIMENTS

Creep experiments were carried out on tubular specimens of cast ICI "Perspex" poly(methyl methacrylate) (PMMA) in the α-relaxation region. Care was taken to ensure specimens as tested were isotropic, stress-free and in a well-aged state. They were: normalised at 140°C prior to machining; annealed at 90°C and slow-cooled after machining; and finally aged for 100 hours at 70°C prior to mounting in the creep machine and testing, also at 70°C. All experiments were carried out with the biaxial tension/torsion creep machine described by Buckley and Resen(1). Results were interpreted in terms of the isostructural constitutive model outlined below.

* Department of Engineering Science, University of Oxford, Parks Road, Oxford, OX1 3PJ
† Department of Mechanical Engineering, UMIST, Manchester, M60 1QD.

Firstly, uniaxial creep tests were conducted in shear and tension in the linear viscoelastic range. Results were used to determine the linear viscoelastic shear compliance function $J_0(t)$, and the tensile compliance function $D_0(t)$. From $J_0(t)$ a discrete shear relaxation spectrum $G_j(\tau_j)$ and the apparent relaxed modulus G_R were computed, using a novel "intermediate model" described elsewhere (to be published). The bulk modulus K was calculated from J_0 and D_0 for a creep time of 30s and, as assumed in the model, this was taken to be independent of time and stress. The validity of these procedures is demonstrated in Figure 1, where measured compliances are compared with numerical solutions of the model in its linear viscoelastic limit.

Secondly, shear and tension+shear creep tests were conducted in the nonlinear range, to characterise the multiaxial response in terms of the dependence of the shear compliance function $J(t)$ on the first and second invariants of the total stress and deviatoric stress, I_1 and I_2' respectively, following the scheme proposed earlier(2). For creep under tensile stress σ and shear stress τ we have $I_1 = \sigma$ and $I_2' = \tau^2 + \sigma^2/3$. Two series of tests were carried out: shear creep tests in which I_2' was increased with $I_1 = 0$; and combined tension+shear creep tests in which I_1 was varied with constant $I_2' = 105$ (MPa)^2. In each series, J was determined from the axial shear strain in the tube wall, and a new specimen was used. Graphs of isochronal values for a creep time $t = 100$s may be seen in Figures 2 and 3 (data points). In these graphs the measured compliance has been normalised with respect to $J_0(100s)$, to remove the small scatter in compliance level (ca. 2%) found between different specimens.

In the course of these experiments evidence was sought for any perturbation of glass structure, as manifested by a change in linear viscoelastic response, caused by the application of stresses in the nonlinear regime. This was done by interposing small stress (2 MPa) shear creep tests between the larger stress tests. There was no discernible change in J_0 during either series of tests, even though the specimens were subjected to significant nonlinear excursions, as evidenced by Figures 2 and 3.

CONSTITUTIVE MODEL

As the present results clearly revealed no evidence for structural change, we applied an isostructural model to the data: a spectral generalisation of the glass-rubber model shown before to provide a good description of constitutive behaviour of amorphous polymers near the glass transition(3). Its basis is that the free energy is made up of two parts: perturbation of inter-atom potentials ("bond-stretching") and perturbation of chain conformational statistics. In the α-relaxation region the former can relax on the experimental time-scale, but is well-known to exhibit a spectrum of relaxation times. All six components of the stress are therefore represented by an equation of the form

$$\sigma_i = \sum_{j=1}^{N} v_j \sigma_{i,j}^b + \sigma_i^c \qquad (i=1..6) \qquad (1)$$

where $v_j(\tau_j)$ $(= G_j/\Sigma G_j)$ is the normalised relaxation spectrum. Assuming the hydrostatic response and, at the low strains of interest here, the deviatoric conformational response to be linear elastic, the mean stress and deviatoric part of the conformational stress are:

$$\sigma_m = \sigma_m^b + \sigma_m^c = K\phi\,, \qquad s_i^c = 2G^c e_i \qquad (2)$$

where ϕ is the dilation and s and e are deviatoric stress and strain. Invoking Eyring rate process kinetics leads to each deviatoric component of the bond-stretch stress being given by

$$\dot{s}^b_{i,j} + s^b_{i,j}/(a_{o,j}\tau_j) = 2G^b\,\dot{e}_i \qquad (i=1..6) \tag{3}$$

where nonlinearity intervenes through a time-stress shift factor

$$a_{o,j} = \frac{V_{s,j}\,s^b_{oct,j}}{2RT}\exp\left(\frac{-V_{p,j}\,\sigma^b_m}{RT}\right) \div \sinh\left(\frac{V_{s,j}\,s^b_{oct,j}}{2RT}\right) \tag{4}$$

and $s^b_{oct,j}$ is the octahedral shear stress in the j-th element and V_s and V_p are shear and pressure activation volumes.

There is growing evidence from thermally-stimulated creep and thermally-stimulated depolarisation current experiments that polymer relaxation processes, including the α-process in PMMA, do not have single activation energies but instead show spectra of values related linearly to the corresponding activation entropies, giving rise to the well-known "Compensation Rule". It follows that a spectrum of activation volumes would be expected:

$$V_{s,j} = V^*_s\left[1 + \beta\ln(\tau_j/\tau^*)\right] \qquad \text{where} \qquad \beta = \frac{R}{\Delta H^*_0}\left(\frac{1}{T} - \frac{1}{T_c}\right)^{-1} \tag{5}$$

and ΔH^*_0 and V^*_s are the activation enthalpy and volume applying to relaxation time τ^*. V^*_s and β were fitted to the data in Figure 2, giving the excellent agreement shown by the full line, while if V_s was forced to have a unique value ($\beta = 0$) the best fit was much poorer (dashed line). V^*_p was fitted to the data in Figure 3 (dashed line), but a marginally better fit could be obtained with a unique value for V_p (full line).

Finally, having fitted the three nonlinear parameters V^*_s, β and V_p to isochronal data, we tested the model by using it to simulate the time-dependence of nonlinear creep. Example results are shown together with experimental data in Figure 4. These and other comparisons with experiment showed that the model could replicate well the nonlinear creep of PMMA. It also showed the correct pattern of behaviour in response to load superposition. It was noteworthy, however, that the model was less successful in simulating creep recovery, unless an adiabatic cooling/heating cycle accompanies loading and unloading, as seen by some authors(4). At present, however, the literature is ambiguous on this point.

REFERENCES

1. Buckley, C.P. and Resen, A.S., in 'Nonlinear stress analysis' ed J.D.Clark, IoP (Bristol) 1990.
2. Buckley, C.P., Polym.Eng. and Sci. 27 (1987) 155.
3. Buckley, C.P. and Jones, D.C., Polymer 36 (1995) 3301.
4. Matsuoka, S. and Bair, H.E., J.Appl.Phys. 28 (1977) 4058.

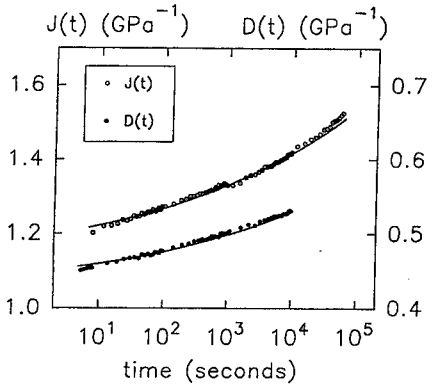

Figure 1. Linear creep compliances of PMMA at 70°C in shear and tension, as measured (points) and as calculated (lines).

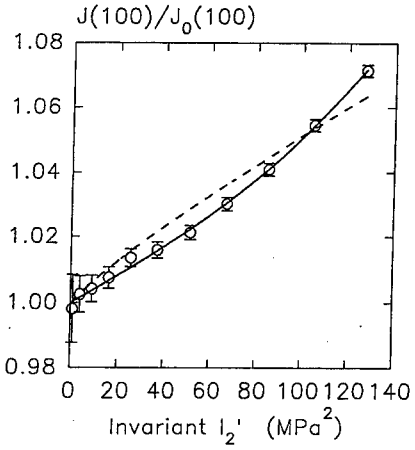

Figure 2. Normalised 100s shear compliance plotted versus I_2'.

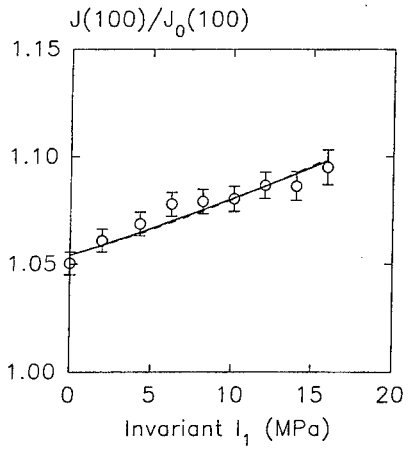

Figure 3. Normalised 100s shear compliance plotted versus I_1.

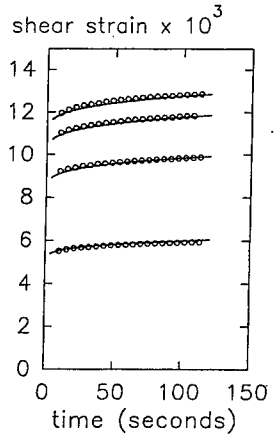

Figure 4. Shear strain as measured during combined tension+shear nonlinear creep tests, as measured (points) and as calculated (lines).

A VISCOELASTIC FLUID APPROACH TO DEFORMATION AND YIELD OF GLASSY POLYMERS

L.E. Govaert*, P.T. Timmermans*, E.T.J. Klompen* and T.A. Tervoort**

In this study a mathematical model is presented that covers the deformation behaviour of a glassy polymer from the linear viscoelastic range up to yield. In this approach the material is regarded as a viscoelastic fluid whose relaxation times are decreased under the influence of stress. The features of the model are demonstrated on a commercial grade of Polycarbonate.

Introduction

With respect to modelling of the deformation behaviour, glassy polymers are usually regarded as viscoelastic solids. A prime example being the approach to yield of these materials, using yield criteria of which the pressure modified Von Mises criterion appears to be the most successful. This "critical" stress approach inherently assumes that no irreversible "flow" deformation will occur below a certain stress limit, and hence a new deformation mechanism is activated above this level.

In the past decade several attempts have been made to come to an alternative approach to the deformation behaviour of polymeric materials [1-2]. In these models the yield behaviour is described using a single Maxwell element with a strongly stress dependent viscosity. In constant strain rate conditions, this results in a sharp transition from solid-like to fluid-like behaviour, almost identical to an elastic-perfectly plastic response employing a rate-dependent Von Mises criterion. At intermediate stress levels, however, the use of a single stress dependent relaxation time can not account for the multi-relaxation time viscoelastic response that is generally observed in glassy polymers. In this study a similar model is presented that can be combined into a "multi-relaxation time" expression that is also able to describe the spectrum of relaxation times required to describe the nonlinear behaviour at intermediate stress.

Basic approach: Time-stress superposition

In the case of a viscoelastic fluid the linear viscoelastic compliance D(t) may be represented by a generalised Kelvin-Voigt model:

$$D(t) = D_0 + \sum_{i=1}^{n} D_i \exp(-\frac{t}{\tau_i}) + \frac{t}{\eta_0} \qquad (1)$$

* Centre for Polymers and Composites, Eindhoven University of Technology

** Institut für Polymere, Eidgenösische Technische Hochschule Zürich

The prime difference with a viscoelastic solid being the presence of a flow-term, represented here by the viscosity η_0. In the constitutive approach stress is assumed to influence all retardation times in the same way, which, similar to time-temperature superposition, leads to time-stress superposition, in fact a simplification of the well known Schapery model [3]:

$$\varepsilon(t,\sigma) = \int_0^t D(\psi - \psi')\ \dot{\sigma}(t')\ dt' \qquad (2)$$

with the reduced time variables defined as:

$$\psi = \int_0^t \frac{dt''}{a_\sigma(\sigma)}\ ;\ \psi' = \int_0^{t'} \frac{dt''}{a_\sigma(\sigma)}\ ; \qquad (3)$$

where a_σ is a stress dependent shift function. In the case of stress activation according to Eyring it can be expressed as:

$$a_\sigma(\sigma) = \frac{\frac{\sigma v}{kT}}{\sinh(\frac{\sigma v}{kT})} \qquad (4)$$

where v is the activation volume, and k Boltzmann's constant..

For very low stress levels ($\sigma < kT/v$) $a_\sigma = 1$, and the model reduces to the classic expression for linear viscoelasticity. With increasing stress the shift function a_σ decreases, which leads nonlinear viscoelastic behaviour. At very high stress levels the material behaviour reduces to that of a nonlinear fluid, which displays the strain rate dependence of an Eyring dashpot that is typically observed in the yield behaviour of many glassy polymers. To be able to describe the post-yield behaviour a 3-D finite strain formulation was developed [4].

Experimental

All experiments were performed on injection moulded tensile bars (ISO R527) produced from a commercial grade of Polycarbonate (Lexan 161R, GE). Each of the experiments was performed on a new sample. all test samples had the same age, which exceeded by far the longest relaxation time in the experiments.

Results

To visualise the influence of stress the material was studied using creep tests at various stress levels (Fig 1). The curves were superimposed to the master curve shown in Fig.2 employing the shift function a_σ mentioned above (Eq.4), yielding an activation volume v of 2.96 nm^3. At this point it must be emphasised that the master curve in Fig. 2 is a "virtual" curve that, due to physical ageing effects, is very likely to deviate strongly from an experimental creep curve on the same time scale. Also the experimental time range covered in Fig.1 (3 decades) does not seem to justify the enormous extrapolation in time span. On the other hand, however, it seems encouraging that

the apparent shift of the curves correlates very well with Eq. 4.

The master curve was fitted using a generalised Kelvin-Voigt model with 14 retardation times. The prediction of nonlinear creep is also shown in Fig 1. It is shown that application of time-stress superposition to the master curve in Fig.2 yields a good description of the short term creep behaviour of polycarbonate. Also the tensile behaviour at various strain rates (Fig.3), seems to be represented quite well by the model. It can therefore be concluded that, within the range of experiments performed here, the phenomenological constitutive model presented here seems a promising approach.

References

1) Boyce MC, Parks DM and Argon AS, Mech. Mater. 7., (1988) 15
2) Wu PD, van der Giessen E, J. Mech. Phys. Solids 41, (1993) 427
3) Schapery, R.A., Polym. Eng 9, (1969) 295
4) Tervoort, TA, Klompen, ETJ and Govaert, LE, J. Rheol. 40, (1996) 779

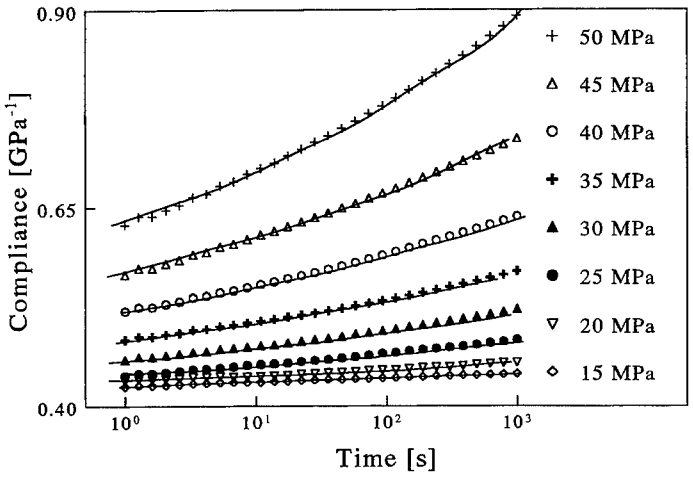

Figure 1 Creep compliance of polycarbonate at 22.5 °C and various stress levels (symbols) compared to model predictions (solid lines).

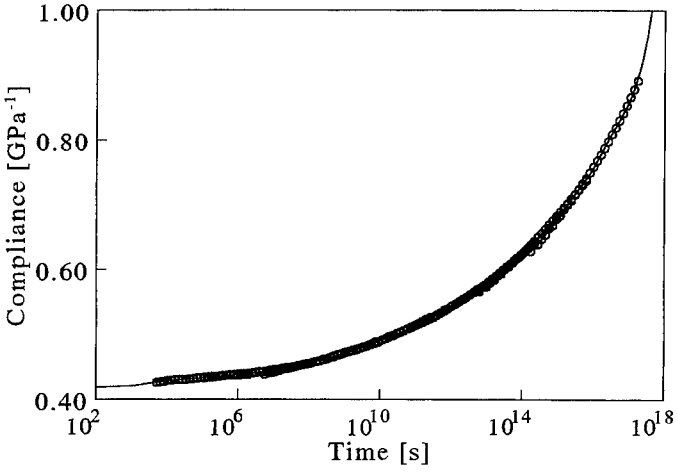

Figure 2. Master curve of the linear compliance obtained from the data in Figure 1

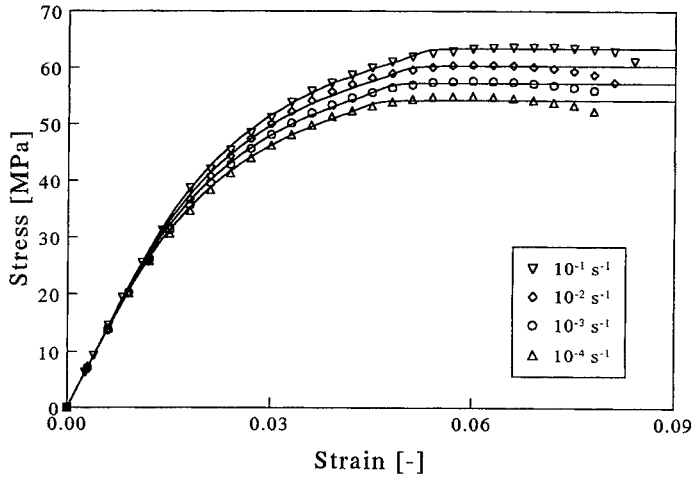

Figure 3 Tensile tests at various strain rates (symbols), compared to model predictions (solid lines)

SESSION FIVE:

FATIGUE

FATIGUE CRAZE INITIATION IN AMORPHOUS POLYMERS AND MOLECULAR APPROACHES TO ENHANCING FATIGUE LIFE

Albert F. Yee, Hristo A. Hristov, David W. Gidley, The University of Michigan, Ann Arbor, MI 48109, USA

INTRODUCTION

The increased use of polymers as structural components in various devices and systems is posing a challenge to scientists to understand the limitations to the durability of such materials. Fatigue failure, a major limitation to the durability of plastics, has been a subject of some investigation in the last twenty years. Investigators have found that in thermoplastics fatigue failure develops in two phases - the initiation phase, in which crazes and microcracks are formed, followed by the propagation phase, in which these crazes and cracks grow until final rupture of the specimen(1). Prior to the present series of studies(2-6) there exists very little information describing the structural changes characterizing fatigue craze initiation (FCI) in amorphous thermoplastics. In contrast the propagation phase has been studied much more extensively, and there is a fair amount of information with regard to the factors influencing the occurrence of various processes(7,8). In the propagation studies it was found that the lifetime of the polymers is strongly influenced by a number of experimental variables, such as stress amplitude, frequency, surface finish, presence of second phase particles, notches, plasticizers and others. Intuitively, the same factors should influence the FCI time (or the number of cycles for craze initiation), but there has not been a systematic study of these variables.

The goals of our work are to identify: [1] the microstructural changes leading to fatigue craze initiation in amorphous thermoplastics, [2] the factors influencing the early stages of fatigue failure and the molecular basis for the process.

EXPERIMENTAL TECHNIQUES

As a direct method for characterizing the initiation process, a combination of small angle X-ray scattering (SAXS) and transmission electron microscopy (TEM) measurements was chosen. To obtain a more detailed picture of the propagation phase, TEM and SEM investigations of fatigued specimens were combined with optical observations. In an earlier series of experiments we also used positronium annihilation lifetime spectroscopy (PALS) to detect the earliest stage of failure initiation. A servohydraulic testing machine fitted with a temperature chamber was used to apply the fatigue load. The loading was uniaxial tension and from 1.5 MPa to the indicated maximum stress. All fatigue loading was at 5 Hz and 24 °C. Humidity was not controlled. Craze initiation was detected visually with the aid of suitable illumination.

MATERIALS STUDIED

Most of the investigations were carried out on non-commercial laboratory grade polycarbonate (PC) resin supplied by GE Plastics. These resins have undergone a fractionation process and have molecular weights ranging from 18k to 102k and polydispersity ~2. A further series of PC with various end caps was also studied. Increasingly large end caps were used to test the hypothesis of disentanglement crazing. These PC's were synthesized in our laboratory. Their molecular weights were determined with a GPC using PS standard. For the same reason fatigue failure of polystyrene (PS) samples containing various levels of a crosslinking agent (from 0 to 9% divinylbenzene-DVB) was studied also. These were again synthesized in our laboratory. Unless otherwise indicated the specimens were cut from compression molded sheets, air quenched from above Tg, and carefully polished to remove visible scratches. Visual inspection using a low power microscope was used to reject flawed specimens.

EXPERIMENTAL RESULTS

The results from SAXS and TEM investigations show that FCI in PC specimens, with "standard" molecular weight (~30K), begins with the formation of elliptical voids with small dimensions 50 - 60 nm parallel to the stress direction. The aspect ratio of these voids was found to be 2-3 during the early stages. Increasing the number of cycles increases the size of the largest voids and generates new voids in a plane perpendicular to the fatigue stress. In Figure 1 are presented three stages of craze development: formation of initial voids (Fig. 1a), protocraze development (Fig. 1b), and the tip of a fine craze (Fig. 1c). It was found that high stress amplitudes and the presence of stress concentrating features such as notches of various shapes decrease the size of the initial voids and change their shape and spatial distribution.

Fig. 1a
(scale =100 nm)

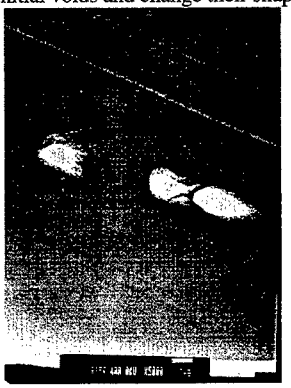

Fig. 1b
(scale = 1 μm)

Fig. 1c
(scale = 50 nm)

Molecular weight effect. It is important to note that the visual appearance of fatigue-induced crazes in PC (Fig. 1c) is quite similar to that of crazes produced under monotonic loading conditions at temperatures close to the glass transition of PC (~120°C)(9). It is known that craze fibril breakdown, and therefore the transformation of a craze to a crack, requires either scission of molecular chains or chain disentanglement in the craze fibrils(10). At low stress amplitudes the probability of chain scission is very small and, keeping in mind the observation that craze fibril breakdown at high temperatures is controlled by the disentanglement of polymer chains, it may be fruitful to explore the possibility that fatigue failure initiation under the range of testing conditions investigated is also dominated by chain disentanglement. If this is the case, the failure initiation time must strongly depend on the molecular weight of the material. Indeed, that was found to be the case. Figure 2 shows that the number of cycles for craze initiation changes as the 8th power of the molecular weight. This supports our hypothesis of chain disentanglement. Furthermore, Fig. 2 shows that the power law adequately describes the dependence of the initiation time on molecular weight.

End group effect. The power of 8 is reminiscent of the dependence of melt viscosity on molecular weight of highly branched polymers. This is presumably due to friction between chains as they slide past each other. Another way to increase inter-chain friction without changing the molecular structure is to give the chain larger end caps. Fortunately this can be done easily in the case of PC. (In fact chain capping agents are often used to control the molecular weight of condensation polymers.) We therefore synthesized PC's of very similar molecular weight and dispersity, but capped the chains with end groups of increasing size. Results on this series of PC's show that FCI time can be increased dramatically by increasing the size of the endcaps (Fig. 3).

Cross-link effect. Interchain friction can be increased even more effectively by introducing molecular crosslinks. This was demonstrated by fatigue initiation experiments on PS specimens with different amounts of DVB. These results demonstrate that after forming a 3D (infinitely large molecular weight) network, at ~1.6wt% DVB, the material becomes craze resistant at low stress amplitudes. As shown in Fig. 4 at 30 MPa the fatigue failure resistance of crosslinked specimens is approximately three orders of magnitude higher than the control PS specimens.

Discontinuous craze growth. TEM and SEM studies of more advanced stages of discontinuous craze growth (DCG) in PC revealed that fatigue craze propagation is achieved by the generation of several parallel crazes, one of which fails first and forms a fracture surface. We found also that a considerable number of crazes develop in front of the "main" craze/crack. From these observations we conclude that, at least in PC, during a significant portion of the DCG many crazes are formed before a single craze/crack jump.

CONCLUSION

Our investigations demonstrate that fatigue failure initiation in amorphous thermoplastics starts with the formation of nm-sized voids, which further grow, multiply and transform into visible crazes. The local stress state influences considerably the shape, size and location of the initial voids, which in turn affects the craze initiation time. Development of DCG zones is achieved through the simultaneous growth of several closely spaced crazes, in a plane perpendicular to the fatigue stress. There is substantial experimental evidence that the molecular mechanism of craze fibril breakdown is predominantly the disentanglement of polymer chains. Our studies also show that understanding of the molecular processes can lead to substantial improvement of the materials performance.

FINAL REMARKS

On the basis of the above observations we have developed a theoretical model to describe the molecular weight dependence of craze initiation time. The prediction is given in Fig. 2, and is seen to produce a rather good fit. Space limitations preclude a full description of the model. It will be described during the presentation if time allows.

ACKNOWLEDGMENT

This work was sponsored by the US Dept. of Energy, Grant #DE-FG02-88ER45366.

REFERENCES

1. Sauer, JA, and Hara, M., Adv. Polymer Sci. 1990, 91/92, 67.
2. Liu, LB, Gidley, D, and Yee, AF, J. Polym. Sci., Polym. Phys. Edn. 1992, 30, 231.
3. Liu, LB, Yee, AF, and Gidley, D, J. Polym. Sci., Polym. Phys. Edn., 1992, 30, 221.
4. Hristov, HA, Yee, AF, and Gidley, DW, Polymer, 1994, 35, 3604.
5. Hristov, HA, Yee, AF, Xie, L, and Gidley, DW, Polymer, 1994, 35, 4287.
6. Li, X, Hristov, HA, Yee, AF, and Gidley, DW, Polymer, 1995, 36, 759.
7. Hertzberg, RW, and Manson, JA, "Fatigue of Engineering Plastics", Academic Press, New York, 1980.
8. Takemori, MT, Adv. Polym. Sci. 1990, 91/92, 263.
9. Plummer, CJG, Soles, CL, Xiao, C, Wu, J, Kausch, H-H, and Yee, AF, Macromol. 1995, 28, 7157.
10. Kramer, EJ, Adv. Polym. Sci. 1983, 52/53, 1.

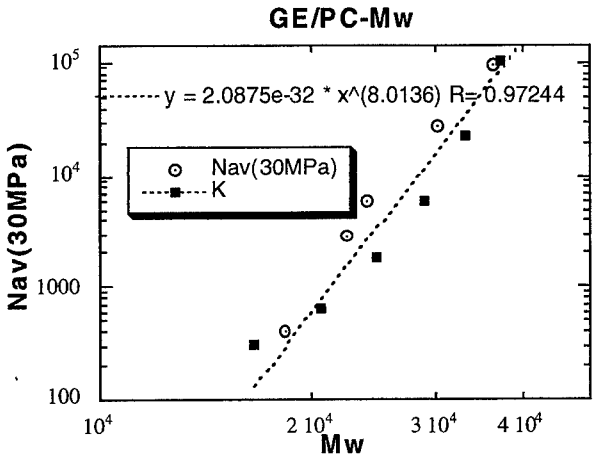

Fig. 2
Dependence of no. of cycles to craze initiation on MW of PC. The open symbols are experimental data. The solid symbols are the results of a theoretical model.

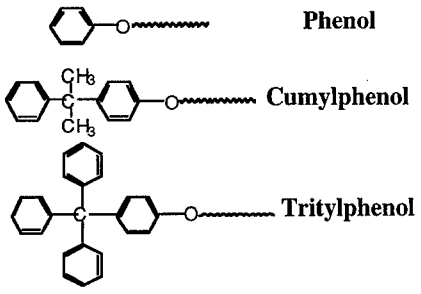

End Cap	MW	$N_{av}x10^3$
Phenol	29500	30
Phenol	31400	64
Trityl	29600	196
Trityl	18600	6
Cumyl	18200	0.38
Cumyl	26600	29

Fig. 3 Effect of chain end cap size on fatigue craze initiation time.

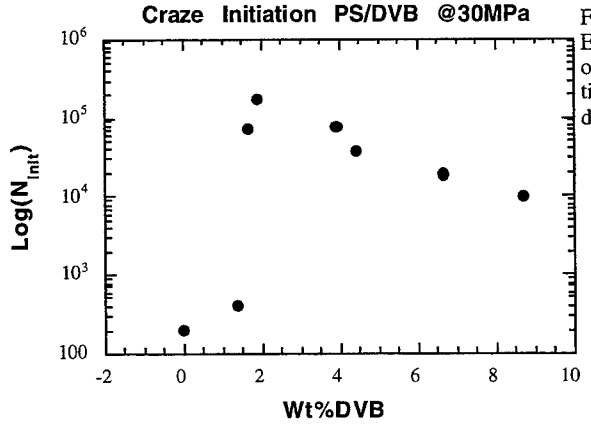

Fig. 4
Effect of cross-link density on fatigue craze initiation time in PS containing divinyl benzene.

THE MICRODEFORMATION MECHANISMS OF POLYOXYMETHYLENE IN STATIC FATIGUE

P. Scaramuzzino, C. J. G. Plummer, H.-H. Kausch*

Introduction

Polyoxymethylene (POM) is a semicrystalline engineering thermoplastic often used in load-bearing applications where good strength, toughness and durability are required. At room temperature and strain rates of the order of 10^{-3} s^{-1}, tensile deformation in POM is characterized by hard elastic behaviour arising from substantial internal cavitation. There is little macroscopic ductility in spite of the high strains to failure (up to 70 %), and fracture is qualitatively brittle. At higher temperatures or lower strain rates POM may nevertheless show ductile necking and drawing, and cavitation is reduced. Thus under dead weight loading, samples subject to stresses of around 80 % of the room temperature tensile strength at 10^{-3} s^{-1} deform to at least 200 %. However, at high temperatures a macroscopic ductile-brittle transition has been observed at low loads and indeed this can result in a decrease in the time to failure with decreasing load (in the region of the transition). Under these conditions, sub-critical deformation becomes localized to sparse planar craze-like defects extending perpendicular to the tensile axis. Such behaviour is similar to that giving rise to long term brittle failure in polyethylene (PE) gas pipes, which has prompted many detailed investigations of slow crack growth in PE [1-3].

The aim of the present study was to use a similar approach in order to characterize slow crack growth in POM. Three grades of POM with M_W of 33, 41 and 66 $kgmol^{-1}$, supplied as injection moulded plaques (10 mm thick) by DuPont de Nemours, were investigated at between 60 and 100 °C. The tests were performed using a Schenck tensile test machine and CT specimens with a/W = 0.5. The pre-crack was introduced by sliding a fresh razor blade along the notch tip prior to testing. To assess the microdeformation mechanisms ahead of the crack tip, TEM investigations were performed on a Philips EM 300 at 100 kV. Ultrathin sections were microtomed at -120°C from samples in which a certain amount of stable crack propagation had occurred, and in which the notch faces had been slightly wedged open. Prior to sectioning, the samples were embedded using a low viscosity crosslinkable resin, capable of penetrating and providing mechanical support to the crack tip damage zone. For fixation and to improve the bright field contrast, the sections were post-stained for about 8 hours in RuO_4 vapor.

Results and Discussion

Slow Crack Growth

Fig. 1 shows slow crack growth (SCG) behaviour in the three grades of POM tested at 100°C. The initial value of the applied mode I stress intensity factor K_{init} was 1.67 $MPa \cdot m^{1/2}$. To facilitate data acquisition, a pseudo-crack opening displacement (COD) was measured in the loading plane, rather than at the crack tip (direct observations confirmed this to be proportional to the true COD). The initial transient evolution of the COD as a function of time was similar in all the grades. The subsequent anelastic response could be described in terms of a two stage mechanism. The first stage involved crack tip

* Laboratoire de Polymères, École Polytechnique Fédérale de Lausanne
CH-1015 Lausanne, Switzerland

blunting accompanied by local stress whitening and the formation of a wedge-shaped fibrillar deformation zone directly ahead of the crack tip. The maximum width of the fibrillar zone increased with time up to a critical value δ_c at time t_b, both of which were molecular weight dependent. This point corresponded to a discontinuity in d(COD)/dt and the onset of stable crack propagation via breakdown of the fibrils at the crack tip. Finally, at time t_f, the crack propagation became unstable and the specimen failed. In addition to t_b and t_f, the crack growth rate is often used to characterize resistance to SCG [1-3]. In the present case, a measure of the slow crack growth rate was provided by the minimum value of d(COD)/dt.

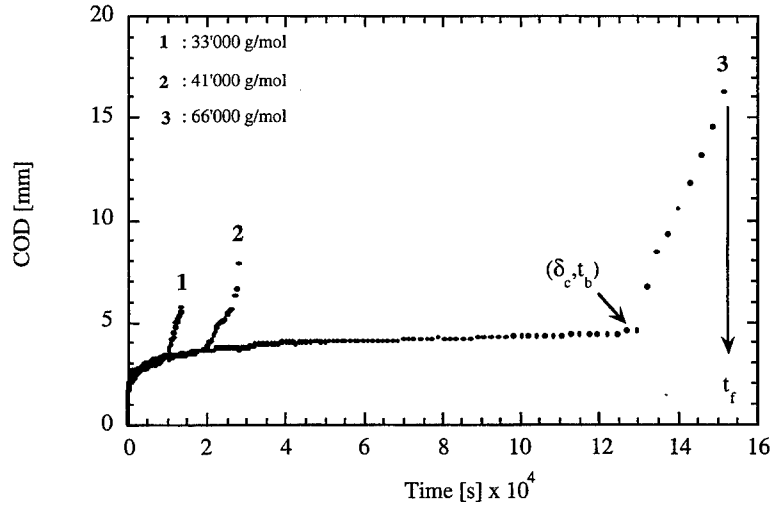

Figure 1. Plot of the COD versus time for the three grades of POM tested at 100°C.

For lifetime prediction $t_b(K_{init})$ is clearly a quantity of primary interest. It has been suggested in the literature [1-3] that t_b should depend on the rate of disentanglement of "tie molecules" in the fibrils, although this concept is somewhat ill-defined in the context of drawn material. In rapidly crystallized thin films deformed in tension, the observed draw ratios in localized micronecks are consistent with stabilization by entanglement, as in amorphous glassy polymers. It is therefore reasonable to assume stress transfer to take place at "entanglement points" and to consider crystalline regions to exert a frictional drag on the chains, opposing chain slip. This picture also implies a fringed micelle-type structure, which is admissible for the case of highly stretched chains, and hence total destruction of the chain folded lamellae in the undeformed material. A continuum model for forced disentanglement may therefore be appropriate, in which case one can invoke the simple molecular weight scaling laws derived from models for the kinetics of fibril breakdown in glassy polymers [4]. This accounts at least qualitatively for the increase t_b with M_W in the present case. By plotting the SCG rate versus 1/T in a semi-log scale, it was also possible to calculate an energy of activation Q, assuming a simple Arrhenius temperature dependence. A value of about 100 $kJmol^{-1}$ was determined for all three grades.

Similar activation energies have been determined for SCG in PE of different M_W by Lu and Brown [1], who suggested a link with the α transition. This in turn implies long range chain mobility in the crystalline regions, consistent with the previous discussion.

Given the presence of a relatively large plastic zone r_p at the crack tip during the different stages of SCG, the small scale yielding criterion for the application of linear elastic fracture mechanics was clearly inappropriate. In an attempt to make the study as quantitative as possible, we therefore calculated the J-integral as a function of crack-tip advance using the ESIS test protocol [5]. The implied fracture energy J_{IC} showed a systematic increase with M_W, ranging from 5 to as much as 12 kJm^{-2}. Although these values should be treated with caution, they are consistent with the extensive irreversible deformation associated with stable crack advance. It was also shown by confocal microscopic analysis that the roughness of the corresponding regions of the fracture surface was proportional to the measured J_{IC}, in agreement with observations in PE [6].

Results from dynamic fatigue (sine wave) tests for M_W = 66 $kgmol^{-1}$ at 80°C and 0.5 Hz with ΔK_{init} = 1.67 $MPa \cdot m^{1/2}$ showed a similar evolution of the COD as a function of N (number of cycles) (thermal fatigue effects were insubstantial under these conditions). Initially d(COD)/dN leveled off in a manner reminiscent of the static tests (stationary crack growth) and then increased sharply just prior to failure (tertiary growth). However, in contrast to the static behaviour, plastic deformation appeared to be limited to a small zone ahead of the crack tip, and the fibrillar zone was absent. This was reflected by the relatively smooth appearance of the fracture surfaces.

Microdeformation Mechanisms

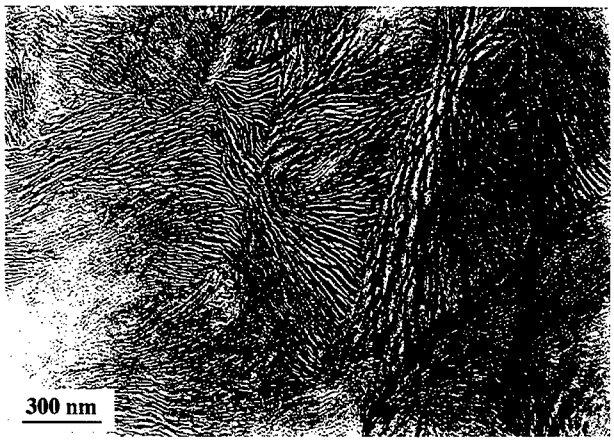

Figure 2. Micrograph of the initial morphology in POM obtained by cryomicrotomy.

Fig. 2. shows the internal morphology of an undeformed sample after RuO_4 staining. Optical microscopy indicates the overall structure to be spherulitic, but the local birefringence is highly non-uniform, as reflected by the apparently chaotic arrangement of the lamellae (the darker areas in Fig. 2 indicate lamellae roughly edge-on to the section,

whereas the lighter areas contain flat-on lamellae). The lamellae nevertheless appear to be organized locally into bundles of about 0.1 μm in thickness (this was confirmed by replication of etched surfaces).

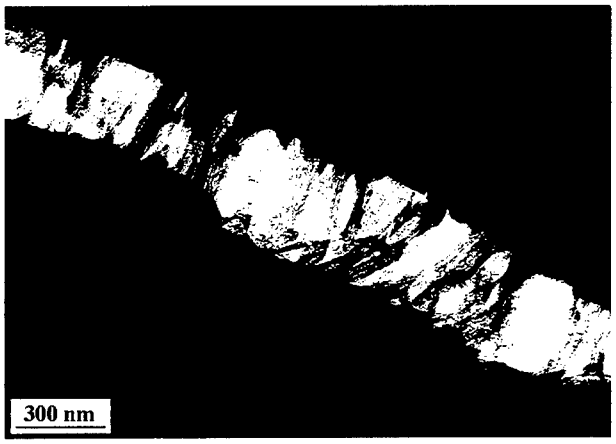

Figure 3. Micrograph of a craze-like feature observed in POM deformed in SCG.

Observation of the crack-tip deformation zones in the SCG specimens was complicated by the fact that the dimensions of the damage zone greatly exceeded those appropriate for cryomicrotomy, necessitating considerable retrimming of the sample.
Fig. 3 is a typical thin section, showing a region adjacent to the fibrillar zone in a sample of M_W = 66 $kgmol^{-1}$ deformed under the conditions of Fig. 1. The initial step in the irreversible deformation process appears to be the formation of craze-like features containing relatively fine fibrils, and originating in regions separating lamellar bundles running roughly perpendicular to the principal stress direction, as shown in the figure (such features are also thought to account for the stress whitening and hard elastic behaviour encountered in room temperature tensile tests). As deformation proceeds, these "crazes" break down, and the intervening regions are able to rotate towards the principal stress axis. Under conditions favouring shear deformation (high temperature, and in the case of sharp notches, low remote stress levels) further drawing results in the formation of the coarse fibrillar structure characteristic of SCG.

References

[1] Brown N., Lu X., Huang Y.-L., Qian R., Makromol. Chem., Macromol. Symp. 41 (1991) 55
[2] Lustiger A., Markham R. L., Polymer 24 (1983) 1647
[3] Brown N., Lu. X., Polymer 36 (1995) 543
[4] Kramer E. J., Berger L. L., 'Craze Growth and Fracture' Advances in Polymer Science, ed. Kausch H.-H, Springer-Verlag (Berlin), 1990
[5] ESIS Technical Committee, *A Testing Protocol for Conducting J-Crack Growth Resistance Curve Tests on Plastics* (1995)
[6] Lu. X., Qian R., Brown N., Polymer 36 (1995) 4239

THE FATIGUE FRACTURE OF POLYETHYLENE

IM Ward*, JP Harcup*, RA Duckett*, G Capaccio†

Fatigue Crack Growth (FCG) under two classes of waveform was investigated in a range of polyethylenes of various branch concentrations and molecular weights. It was found that the FCG rate depends upon the unloaded duration per cycle. It was found that the cause of this effect is the compressive stress associated with the viscoelastic recovery of the craze surroundings. The viscoelastic recovery characteristics are influenced by geometry and material. It was also found that the effects of cyclic loading become more severe in materials of higher branch concentration, suggesting that the craze damage process has a material sensitivity of its own.

INTRODUCTION

This work was primarily intended to enlarge the understanding of the dependence of Fatigue Crack Growth (FCG) in polyethylene on testing variables such as the waveform and material variables including branch concentration and molecular weight. A secondary goal was to examine the possibility that Slow Crack Growth rates could be predicted from FCG measurements.

EXPERIMENTAL

Materials and Specimens

The molecular weight and branch content of the polymers examined are shown in the first three columns of Table I. Samples A and E are homopolymers and samples B-D are hexene-ethylene copolymers. All materials were processed by slow cooling from the melt. Compact Tension specimens were used with dimensions meeting the ASTM criteria (1).

Waveforms

Two classes of waveform were used. First, Variable Mark Space Ratio (VMSR) waveforms for which the time under load was fixed at t_m=4s but the unloaded duration, t_s was varied. The stress intensity levels were fixed at K_{max}=1.0 MPa $m^{1/2}$ and K_{min}= zero.

In the second class of waveforms, t_m and t_s were both set to four seconds, but a compressive K_{min} was applied and R ratios (K_{min}/K_{max}) from 0 to -1 were explored.

*IRC in Polymer Science and Technology, University of Leeds, Leeds LS2 9JT UK

† BP Chemicals Ltd, Grangemouth, Stirlingshire, FK3 9XH UK

RESULTS AND DISCUSSION

VMSR Waveforms

FCG rate increased non-linearly with t_s, over a characteristic time, τ in each of the three samples tested, (*fig* 1). The crack growth rate per cycle a' (=da/dN), was given by

$$a'(t_s) = a'(t_s = 0).\left[1 + k\left(1 - \exp\left(-(t_s/\tau)^n\right)\right)\right] \quad (1)$$

where k, τ and n are material dependent (Table I). Separate measurements on Single Edge Notch tension specimens revealed that τ and n (but not k) are also geometry dependent.

Also as t_s was increased, the craze stress (determined from *post mortem* samples) decreased. Both of these results are consistent with craze damage being accumulated throughout the unloaded period (2,3) suggesting that the craze collapsed during this time. The thickness of the craze at its base is related to the measured crack opening displacement (COD) and *fig* 2 shows that upon unloading, the COD decreased as the bulk surrounding the craze viscoelastically recovered. The reduction in COD can be described by an expression of the form:

$$\Delta(t_s) = \Delta(t_s = 0)\exp\left(-\left(t_s/\tau^*\right)^{n^*}\right) \quad (2)$$

The plots of Δ in *fig* 2 are fitted well using the parameters τ and n taken from the crack growth data. Thus the same parameters describe both the kinetics of the increase in crack growth rate with respect to t_s and the closure of the crack under the recovery of the surrounding material during the unloaded period.

These results provide strong evidence that upon unloading, the surroundings first elastically, then viscoelastically recover causing the gradual collapse and damage of the craze which leads to the observed increase in crack growth rate.

The viscoelastic recovery characteristics are influenced by material and the geometry of the surroundings, as manifested in the geometry dependence of the quantities τ and n.

Compressive Cyclic Loading

Crack growth rates increased appreciably under waveforms containing a heavily compressive component (*fig* 3). The extent by which crack growth rate increased with the minimum load (measured by R) was represented by α', where

$$\frac{da}{dN} = \dot{a}t_m.\left[1 + \alpha'|R| + k'\right] \quad (3)$$

α' was found to increase appreciably with increasing butyl branch concentration, *fig* 4 and Table I. Indeed, so strong was the sensitivity of α' to branch concentration, that under sufficient compression, the more branched materials actually exhibited *higher*

crack growth rates than the less branched materials which is opposite to the slow crack growth ranking of these materials.
It was found that increasing the molecular weight, M_w at constant branch concentration appeared to cause a relatively small increase in α' although data for a wider range of materials reported by other workers showed that α' *decreases* significantly with increasing M_w for a wide range of homopolymers (4).

The sensitivity to branch concentration of the effects of the compressive step is such that FCG and SCG rates rank oppositely for some materials. This suggests that there is no *a priori* basis for a direct correlation between FCG and SCG, and that these quantities may only be confidently related where the material sensitivity of the craze damage process is understood.

CONCLUSIONS

The sensitivity of fatigue crack growth rates to the unloaded duration and the minimum applied load per cycle were investigated in an attempt to improve the understanding of the role of the applied waveform.
It was found that the dependence of FCG rate on unloaded duration per cycle depends upon material and geometry since these factors influence the viscoelastic recovery of the bulk material surrounding the craze. The viscoelastic recovery of the craze surroundings is important since it causes the craze to collapse and sustain damage, leading to the observed increase in crack growth rate.
The primary effect of applying a positive compressive stress was to increase the crack growth rate. The extent of the increase in da/dN was found to be greater in materials with higher branch concentration, suggesting that the craze damage process has a sensitivity to material variables of its own. This result indicates that there is no *a priori* basis for a direct correlation between FCG and SCG, and that these quantities can only be confidently related where the material sensitivity of the craze damage process is better understood.

REFERENCES

(1) ASTM E647-91
(2) Y. Imai and I.M. Ward J. Mater. Sci. (1985) **20** 3842-3852
(3) Y-Q. Zhou and N. Brown J. Mater. Sci. (1989) **24** 1458-1466
(4) Y. Zhou, X. Lu, Z. Zhou and N. Brown Pol. Eng. Sci. (1996) **36** 16 2101-2107

TABLE I

Sample	Mol. Wt M_W (g/mol)	Mol. Wt M_N (g/mol)	Butyl Branch Concentration (/1000 C)	τ (s)	n (-)	k (-)	α' (s)
A	131 000	19 100	-	3.12	1.02	5	3.3
B	156 000	17 000	1-2	2.1	1.36	1.7	27.3
C	155 000	18 000	2-3	0.8	0.64	18	210
D	206 000	12 900	6.2	-	-	-	1980
E	310 000	20 000	-	-	-	-	4.2

Fig 1 - Dependence of da/dN upon unloaded duration

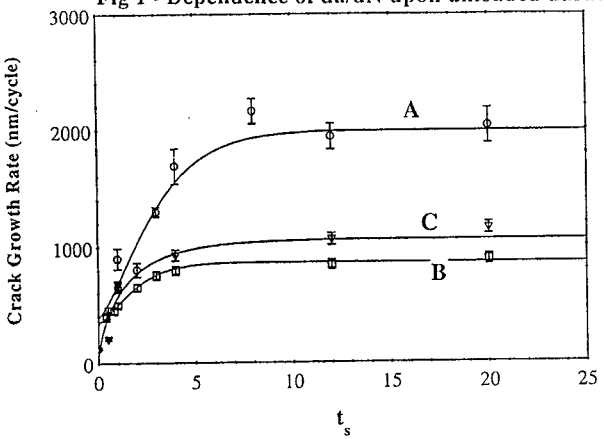

Fig. 2 - Variation in C.O.D. with time

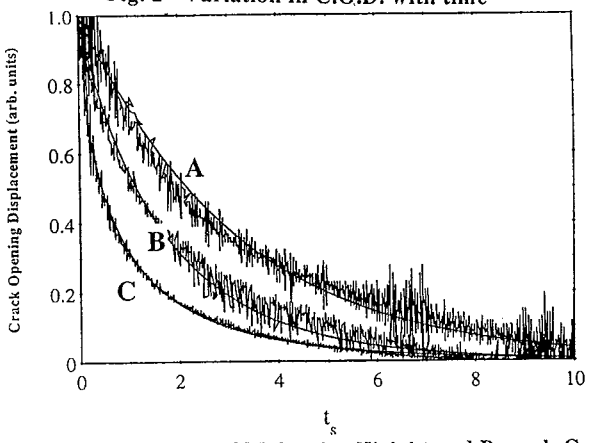

Fig. 3 - Effects of Minimum Load on da/dN

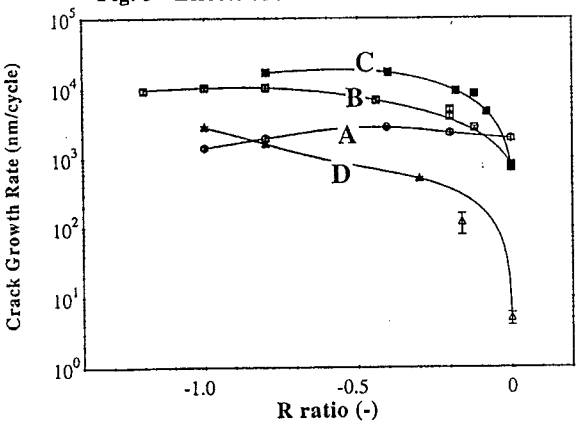

Fig 4 - Effects of Molecular Weight and Branch Content

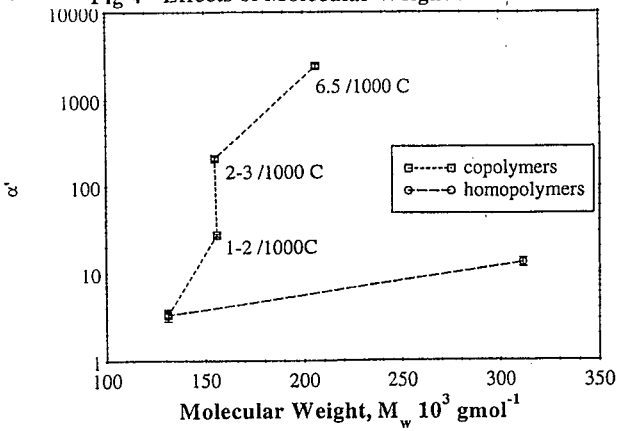

SESSION SIX:

FRACTURE

THE RATE-SENSITIVITY OF IMPACT FRACTURE IN THERMOPLASTICS

P.S. Leevers, M. Douglas, M. Chong and J.G. Williams*

Many tough thermoplastics, particularly if notched, suffer a transition to brittle behaviour under impact. Because the transition is primarily influenced by temperature and impact speed, fundamental understanding of the underlying mechanisms has previously been sought through the rate dependence of bulk viscoelastic-plastic properties. The mechanism advocated here, by contrast, attributes brittle fracture to localised adiabatic melting at the cohesive surface of a crack-tip craze. Using data for PVCu, PA6.6 and PP, we distinguish three regimes: plastic collapse (reflecting the positive rate exponent of the yield stress); initiation-limited adiabatic fracture (with a stronger negative rate-dependence) and dynamic fracture (for which, for most specimen geometries, impact rate effects arise only from inertia).

INTRODUCTION

The engineering use of tough crystalline thermoplastics is overshadowed by their tendency to revert to brittle behaviour, especially if notched. It is useful to distinguish 'quasi-static' modes (slow crack growth and fatigue), which involve long-time-scale disentanglement and are promoted by increasing temperature, from 'dynamic' modes (impact and rapid crack propagation) which are promoted by lower temperatures. A transition from tough to brittle behaviour is observed as a change in fracture surface and an order-of-magnitude decrease in fracture resistance G_c. Since Charpy and Izod tests are often the only quick way to provoke brittle fracture in tough plastics, they are widely used despite two major drawbacks. Firstly, impact fracture data cannot be extrapolated to other geometries, even (except for brittle glasses) using the tools of fracture mechanics. Secondly, there is little evidence that impact tests rank polymers or polymer grades with respect to the more insidious quasi-static failure modes.

Vincent [1] attributed the onset of brittle fracture in polymers at impact strain rates and low temperatures to the greater sensitivity of yield stress than of fracture stress to temperature, and Hiltner *et al* [2] went on to suggest that rate-sensitivity might be related through the usual shift factors. However, we will identify a regime in which impact fracture is by far the more rate sensitive process. As is often the case for both bulk [3] and fracture [4] processes in polymers, the exponents of scaling laws will prove to provide great insight into underlying mechanisms.

THE THERMAL DECOHESION MODEL

Recent papers [5, 6, 7] have argued that both impact crack initiation and fast fracture occur, in thermoplastics, by *thermal decohesion* in a Dugdale-Barenblatt line cohesive zone (i.e. a craze) at the crack tip. If this craze opens or translates sufficiently fast, drawing of craze fibrils from the adjacent bulk material causes intense local heating. The conditions at which adiabatic melting extends to a depth of one weight-average chain contour length, $\bar{s}_w$, thereby debonding the fibrils, define values for resistance G_{ca} to impact crack initiation and G_D to rapid crack propagation. As the crack speed approaches about 100 m s^{-1}, G_D falls steeply to a plateau,

$$G_{D\min} = \rho \bar{s}_w \left[5C_p(T_m - T) + 2\Delta H_f \right], \qquad (1)$$

where ρ is the mass density, C_p the specific heat, T_m the melting temperature and ΔH_F the latent heat of fusion. For crystalline polymers with a well-defined melting point, T_m effectively

* Mechanical Engineering Department, Imperial College, London SW7 2BX

defines structural collapse; for amorphous polymers, it requires more careful interpretation.

Resistance to impact is generally higher, because the running crack must be launched from a 'cold start'. For a linear material of dynamic tensile modulus E and thermal diffusivity κ, the G_c value at which the craze fails under a linearly increasing stress intensity factor K is given by

$$G_{ca} = \left[\rho C_p (T_m - T)\right]^{4/3} E^{1/3} (\pi\kappa)^{2/3} \dot{K}^{-2/3}. \qquad (2)$$

Three regimes of impact failure

It is very difficult to carry out high-rate tests under a linearly increasing load. Impact tests usually impose a constant load-point displacement rate $\dot{v}$. The transfer function to $\dot{K}$ involves both specimen inertia and specimen compliance — which depends strongly on crack length and is further affected by extension of the craze during loading [6, 7]. If the crack-length influence dominates, the apparent fracture resistance is

$$G_{ca} = E^{-1/3} (\pi\kappa)^{2/3} \left[\rho C_p (T_m - T)\right]^{4/3} \psi(\alpha) W^{1/3} \dot{v}^{-2/3}, \qquad (3)$$

so that as $\dot{v}$ increases G_{ca} falls indefinitely. Note that G_{ca} depends on specimen size W, crack-length to size ratio α and geometry (through ψ, a dimensionless function).

Impact 'fracture' is detected only when propagation follows initiation. If $G_{ca} \geq G_{D_{min}}$, this occurs immediately, and initiation remains the rate-determining process. If $G_{ca} < G_{D_{min}}$, however, fracture cannot proceed until $G_{D_{min}}$ is attained, and the rate dependence of G_D is parameterised by the driven crack speed $\dot{a}$ rather than $\dot{K}$. The predicted geometry-dependence of impact resistance therefore changes at the $\dot{v}_c$ at which $G_{ca} = G_{D_{min}}$. At *low* impact rates, on the other hand, G_{ca} becomes so high that impact specimens fail by *plastic collapse*.

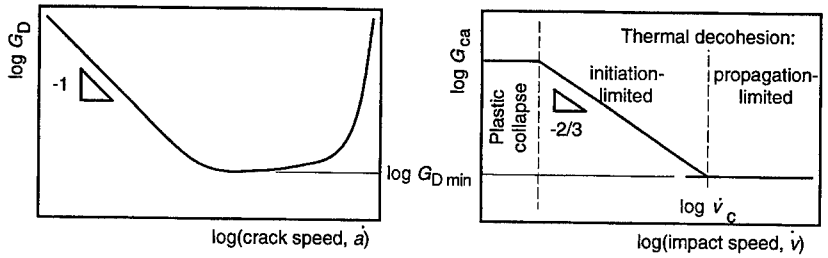

FIGURE 1: The crack speed dependence of dynamic fracture resistance and the impact speed dependence of impact fracture resistance (schematic)

Fig. 1 illustrates, in a simplified schematic form, the predicted rate-dependence of RCP and impact resistance. Dynamic fracture resistance tests on crystalline polymers readily access $G_{D_{min}}$ and generally support Eqn. (1) [8], but the falling region of $G_D(\dot{a})$ is dynamically unstable and relatively inaccessible. G_D is expected to rise steeply again at higher speeds only in very high MM polymers. This behaviour is known in cast PMMA, but evidence for a high-MM crystalline polymer is lacking.

Rate effects on impact fracture of compliant specimens

For impact resistance, the picture is more complicated but the evidence is more forthcoming. Compliant specimens have high ψ factors and thus, from Eqn. (3), high resistance to impact fracture initiation. The sharp-notched Charpy bend specimen is of this type, and a high impact speed is needed to reduce G_{ca} to $G_{D_{min}}$. Figs. 2 and 3 show $\log(G_{ca})$ *vs.* $\log\ \dot{v}$ data for an

unplasticised PVCu and a nylon 6.6. Like earlier results for polyethylenes [5], those for PVCu strongly support the inverse two-thirds power dependence predicted by Eqn. (3). This index comfortably exceeds any which could characterise a viscoplastic deformation process. The new data, however, also strongly suggests the existence of the expected G_{ca} plateau at high impact speeds. The measured G_{ca} is influenced by dynamic effects which can be factored out using a mass-spring model of the specimen. However, numerical simulations [7] suggest that these inertial effects originate partly in G_{ca} itself, due to periodic variations in the craze loading rate — and therefore the adiabatic heating rate. The model predicts an ultimate second-power climb in G_{ca} with impact speed, which is clearly visible in these data.

Given the low crystallinity of PVCu, its conformity to the thermal decohesion model is a little paradoxical. Crystalline nylon 6.6, on the other hand — stiffer, less lossy and more environmentally sensitive — generally yields more scattered results and a more complicated picture. The 'plastic collapse' regime is clearly defined and shows a rate exponent of about 0.2. Even for this tough material, the transition through initiation-limited to propagation-limited impact fracture involves an order-of-magnitude loss in fracture resistance.

Rate effects on impact fracture of stiff specimens

Stiffer specimens have lower ψ factors and lower resistance to impact fracture initiation. They therefore reach the rate-independent $G_{ca} = G_{D_{min}}$ 'dynamic' propagation-limited regime at a lower impact speed. Recent results [9] for PP homopolymer tested as single edge-notched tension specimens provide an interesting illustration. Five grades of various M_w were tested, across a range of temperatures, at an impact speed (1 m/s) which certainly escapes the initiation-limited regime. The results are plotted as peak stress *vs.* temperature in Fig. 4(a). The transition from brittle to tough behaviour corresponds to a change in the slope of each line, beyond which all five grades converge on a single 'plastic collapse' curve.

Fig. 4(b) shows the peak stress computed from $G_{D_{min}}$ as given by Eqn. (3). All of the other data required (including the plastic collapse locus but excluding a separately-measured dynamic modulus) are from Ref. [9]. Agreement is not perfect, but for the M_w = 164 000 grade it is good, and for all grades the main features of the data (in particular, the counter-intuitive fall in toughness with temperature and the temperature dependence of the brittle-tough transition) are well represented. It should be emphasised that increasing impact speed serves only to *reach* this regime; *within* it, $G_{D_{min}}$ is expected to be unaffected by impact speed and the high sensitivity of yield stress does, indeed, control the brittle-tough transition.

CONCLUSIONS

Thermal diffusion effects are primarily responsible for the loss in fracture resistance of thermoplastics with increasing impact rate. Above a low-rate regime in which plastic collapse intervenes, fracture resistance falls with the two-thirds power of impact speed. At high rates and in stiff specimens, fracture resistance settles near a minimum equal to the dynamic fracture toughness, which falls with increasing temperature.

REFERENCES

1. Vincent, P. I., Polymer 15 (1974) 111-116.
2. Hiltner, A. and Baer, E., Polymer 15 (1974) 805-815
3. De Gennes, P. G. 'Scaling concepts in polymer physics', Cornell University Press (Ithaca and London) 1979
4. Williams, J. G., 'Fracture of Polymers', Ellis Horwood (London), 1984
5. Leevers, P.S., Int. J. Fracture 73 (1995) 2, 109-127
6. Leevers, P.S. & Morgan, R.E., Engng. Fracture Mechs. 52 (1995) 6, 999-1014
7. Leevers, P. S. Polymer Eng. and Sci. 36 (1996) 18, 2296-2305
8. Greenshields, C. J. and Leevers, P. S., Int. J. Fracture 79 (1996) 85-95
9. Van der Wal, A., Mulder, J.J., Thijs, H.A. and Gaymans, R.J., submitted to Polymer.

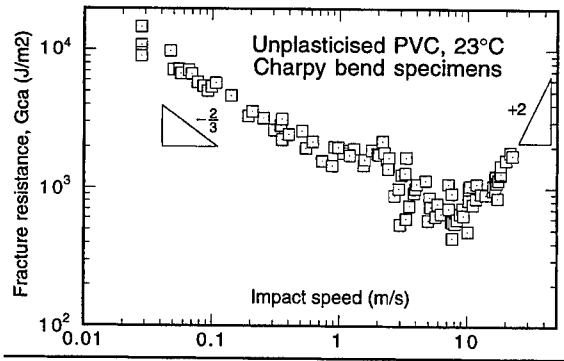

FIGURE 2: Fracture resistance as a function of impact speed for unplasticised PVC

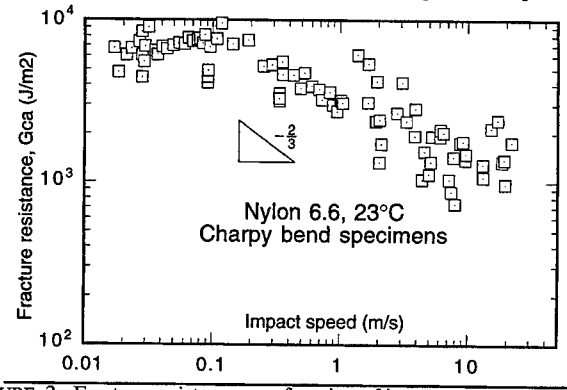

FIGURE 3: Fracture resistance as a function of impact speed for nylon 6.6

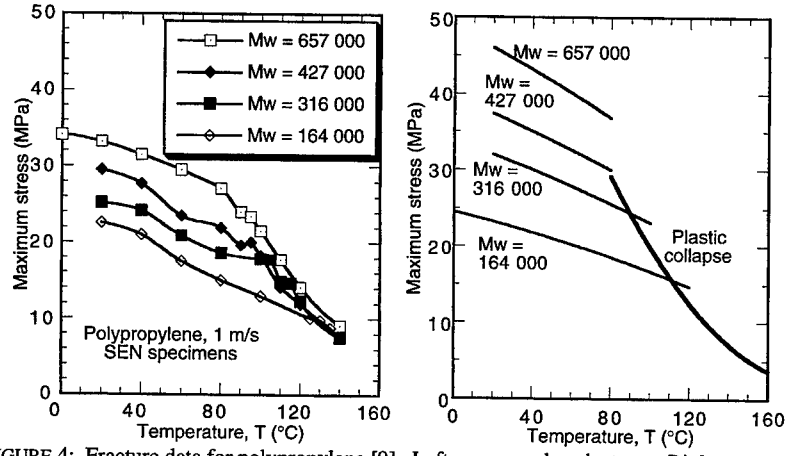

FIGURE 4: Fracture data for polypropylene [9]. Left: measured peak stress. Right: computed peak stress showing measured plastic collapse locus

The Contribution of Plane Stress and Plane Strain Components in the Fast Fracture Resistance of Polyethylene Pipe Materials

G. P. Marshall and E. J. Ingham[†]

Instrumented Charpy impact tests have been used to evaluate the dynamic toughness of existing and development grades of HDPE (PE 100) and MDPE (PE 80) pipe grade polymers. The data obtained have been shown to give excellent correlation with the subsequent resistance of these materials in large scale rapid crack propagation (RCP) tests, performed on large diameter water pipes.

The low RCP resistance of MDPE materials is believed to be caused by the low strength of the material, rather than lack of plane stress toughness. Unstable failure is initiated in the plane strain region when the crack tip net section stress achieves yield. A correlation between the yield stress and dynamic toughness has been observed in instrumented tests on a range of polyethylene grades.

Introduction

With welded polyethylene pipe systems it is important that the polymer used has not only high resistance to slow crack growth but also fast fracture. Although the new generation bimodal HDPE pipe grades appear to meet both of these requirements, both MDPE and HDPE polymers which are currently widely available often only satisfy one of the two criteria. In order that a pipe material may be used for a comprehensive range of pipe sizes in the Water Industry, the material must ultimately meet the required resistance to RCP, determined in the Spadeadam test operated by British Gas. This type of test is expensive and may not be adapted to study either the potential of new PE materials, or for the rapid evaluation of effects such as processing during production or geometry. An assessment of the RCP resistance of pipes up to 250mm diameter can be made using the S4 test by materials suppliers, as a type test for new PE materials.

With MDPE the low resistance to RCP has led to reductions in the permitted wall stresses for large diameter pipes by the U.K. Water Industry. MDPE pipes however have quite exceptional resistance to brittle slow crack growth (SCG), (the main precursor to RCP) and unlike most types of HDPE the material is extremely easy to weld and butt fusion joints have very high toughness. Hence, it is difficult to imagine under what conditions RCP would be initiated for MDPE. It should also be noted that the major consequence of the reduction in pressure rating with MDPE is that the use of thick wall sections is positively encouraged. Essentially this is undesirable since in thick sections it is easier to induce plane strain brittle cracking. In comparison to MDPE the slow crack growth resistance of HDPE grades is generally of a lower order. Although the RCP resistance may be improved for the base polymer, there is a danger that this may be compromised by variations in cooling during processing of thick section pipes, which encourage high crystallinity at the pipe bore. There is currently no test method which can be used during production to ensure that RCP resistance is maintained, and if the SCG characteristics are also prejudiced by enhanced crystallinity, then the initiation of fast fracture may be a possibility.

It has been the purpose of the present work to determine whether the use of notched sample impact tests has any relevance in determining toughness properties, which relate to resistance to unstable failure. The relative roles of plane strain and plane stress toughness have been examined in some detail.

[†]Pipeline Developments Ltd., Salford Quays, Manchester, England.

Experimental

Charpy impact samples were either machined from the walls of extruded pipe, or from compression moulded sheet. All testing was performed using an instrumented impact system, allowing determination of stresses and the energy to cause crack initiation and energy absorbed in causing complete fracture of the sample. In order to establish the contribution of the plane stress and plane strain components thick and thin samples containing both sharp and blunt notches were tested. Compression moulded sheets comprising of either an MDPE or HDPE core with HDPE skins were also used, in order to provide additional evidence of the role of shear lips on the enhancement of toughness.

Results and Discussion

Sharp notched Impact Tests

By testing HDPE and MDPE sections of various thickness containing sharp notches it was possible to derive an intrinsic plane strain fracture toughness (Gc_1) for each material. It was found that the plane strain toughness does not vary significantly between each material and is of the order of (5-6 KJ/m^2). It was found that the small differences in Gc_1 could not explain why there are considerable differences in the pressure required to cause RCP. In particular, the decrease in RCP resistance of MDPE over the range 20°C to 3°C could not be simulated.

However, when thin samples were tested there was found to be a substantial difference in the plane stress impact toughness (Gc_2) of HDPE and MDPE respectively. Moreover, when thin samples were tested at different temperatures and the plane stress toughness plotted as a function of temperature, excellent correlation with the change in RCP performance observed in the full scale tests is apparent as shown in figure 1. With the MDPE (PE80) the toughness is initially maintained as the temperature is reduced, with a ductile to brittle transition below 0°C. The HDPE materials however maintain both toughness and ductility at low temperature. The PE 100 (labelled HDPE 1) is known to just meet the acceptability criterion of the large scale RCP test and it is hence possible with development grades to use this data set to give an early indication of the large scale performance. The PE 100 (labelled HDPE 2), shown in figure 1 is a new generation bimodal polymer, which shows exceptional resistance to brittle cracking in both the Charpy and large scale tests.

The ability of the Charpy test as a swift method for assessing changes in toughness, caused by processing can also be seen from data presented for HDPE 3 also shown in figure 1. With this material it is clear that samples taken from the bore of the pipe exhibit a lower resistance to cracking, than samples taken from the external surfaces. With thick walled pipes in particular, the crystallinity of the bore is usually significantly higher than that of the exterior. It is therefore evident that the toughness developed in the HDPE 3 is extremely dependent on the amorphous content of the polymer, which can be greatly influenced by extrusion and cooling process used. With all these sharp notched, thin sample tests it would thus appear that the plane stress shear lips ultimately control the level of the critical crack initiation toughness of these materials.

Testing Thin Blunt Notched Samples

Because the use of sharp notches almost inevitably causes some plane strain crack growth, resort was made to use of blunt notched samples to further suppress brittle cracking and to allow a true comparison to be made of the plane stress toughness. With the HDPE 2 pipe grade, it was found that there was no significant reduction in toughness until the temperature was reduced to below -35°C as shown in figure 2. When the MDPE and HDPE 1 are compared over the same temperature range, it is evident that the shear lips developed in each material exhibit the same toughness. As expected, the true ductile toughness of the MDPE is of a reasonably high level. It is hence proposed that the loss in toughness of sharp notched samples of the MDPE as temperature is decreased is potentially due to the initiation of premature plane strain cracking.

Net Section Yielding

It is generally found that where a material fails in a ductile manner the crack only serves to remove material from the cross section. Cracking is initiated when the net section achieves the yield condition, with final failure at the peak load in bending occurring when the net section achieves the plastic collapse stress, which is at a loading 1.5 times that to achieve the tensile value. The analysis of instrumented impact data has shown that for both thick and thin samples of MDPE and HDPE 1 containing sharp notches, the peak net section stress is at the collapse condition as shown in figure 3. By using thin samples containing both sharp and blunt notches, it was possible to derive the toughness for materials of different yield stresses. The resulting plot of Gc_2 as a function of yield stress is shown in figure 4. The lower toughness of the MDPE materials would seem to derive from the fact that the potential capacity of the shear lips to absorb large amounts of energy is curtailed, because plain strain cracking occurs earlier. The lower density materials do not allow stresses to be elevated to the high levels needed, to allow the shear lips to develop sufficiently and absorb enough energy to arrest the plane strain crack growth.

The lower RCP resistance of the MDPE in comparison to HDPE 1 and HDPE 2 is simply a function of the lower yield stress of the MDPE and it is thus no coincidence that all PE materials so far developed to have resistance to RCP are high density polymers. High strength is a necessary condition for the generation of toughness.

Multilayer Polyethylene Composites

Further evidence for this theory was obtained by testing multilayer PE composites with either an MDPE or a low toughness HDPE core and HDPE 1 skins. Despite the apparent advantage of the tough HDPE 1 shear lips, the composite with the MDPE core gained only a slight increase in toughness, but failed to achieve the same toughness as the HDPE 1 section. However when the brittle HDPE core with HDPE 1 skins was tested, the toughness of the composite section was at least comparable to that of a section of purely HDPE 1. When used in the composite the higher yield stress of the low toughness polymer is an advantage, allowing the HDPE 1 shear lips to develop and arrest the advancing crack.

Conclusions

(1) The notched Charpy test using thin samples provides an excellent and rapid method for discriminating a measure of the potential fast fracture resistance of development grades of PE pipe materials in large scale tests.

(2) It is possible to use the toughness values from plane stress tests to determine the effect of changes in processing on RCP performance.

(3) The use of blunt notched tests provides evidence of a direct relationship between the net section yield stress at the onset of cracking and the observed impact toughness.

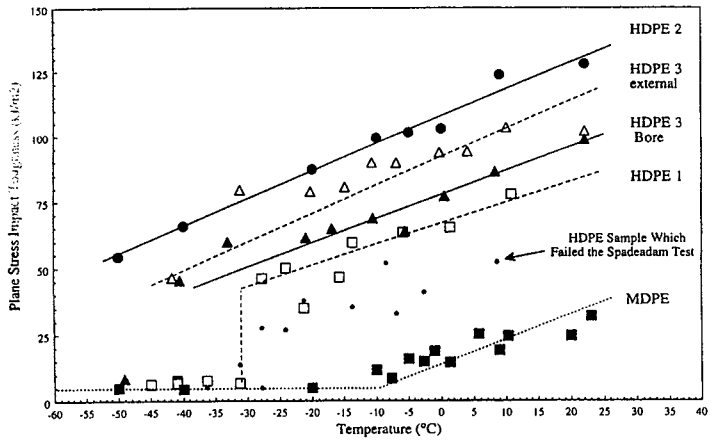

Figure 1. Thin Sample Plane Stress Impact Toughness for Sharp Notched Polyethylenes

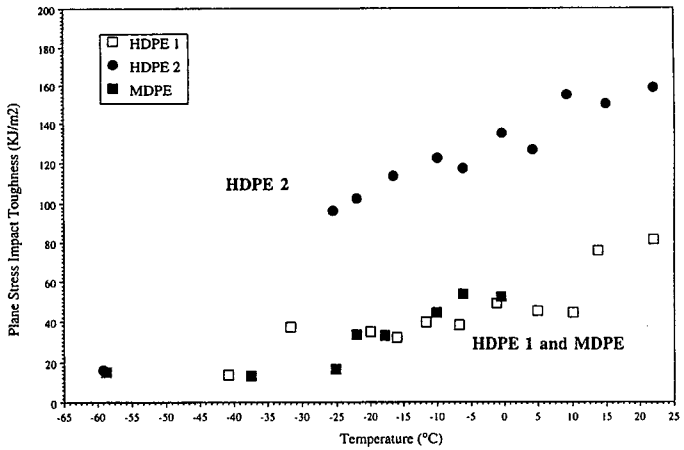

Figure 2. Effect of Temperature on the Crack Resistance of Thin Blunt Notched Polyethylenes

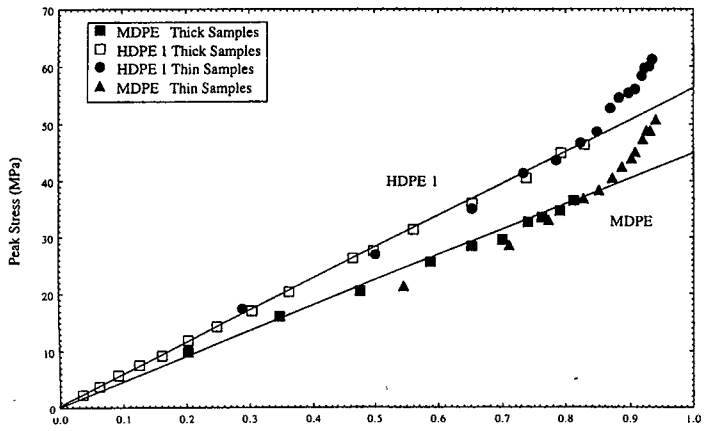

Figure 3. Net Section Yield Stress Data for Thin and Thick Samples of MDPE and HDPE 1 (1-a/D)2

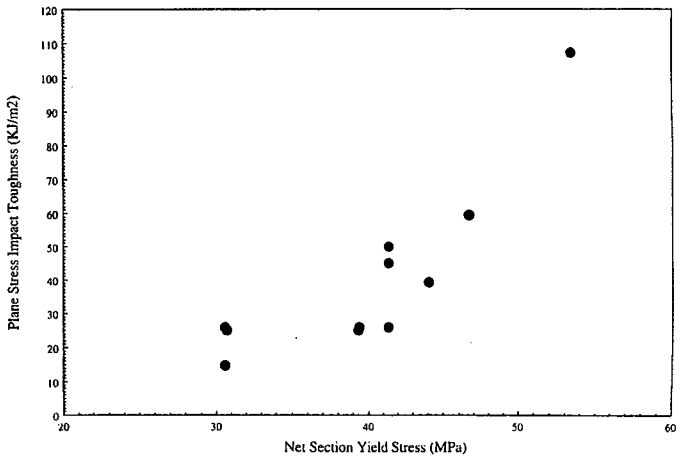

Figure 4. Relation Between Net Section Stress and Plane Stress Impact Toughness

Time-Dependent Ductile and Brittle Fracture in Plastic Pipe

Walter L. Bradley, Robert Self, and Steven W. Bradley, Texas A&M University, College Station, Texas; David Register and Mark Lamborn, Phillips Petroleum Company, Bartlesville, Oklahoma, USA

INTRODUCTION

The prediction of time-to-failure as a function of internal pressure, or hoop stress, in polyethylene pipe requires a significant number of tests to be conducted, some for quite long periods of time. This study seeks to predict both the brittle and ductile fracture portions of the "hoop stress versus time to failure" relationship for various grades of polyethylene pipe using data from the dead weight loading of a single, sharply notched three point bend specimen in which only the load-line displacement as a function of time is measured.

The initial portion of the load-line displacement prior to the initiation of crack growth is due to viscoelastic deformation in the specimen, allowing the compliance to be determined. Once crack growth begins, the additional load-line displacement this produces can be used to calculate the crack growth as a function of time. Stress intensity as a function of time can also be determined, allowing the relationship between stress intensity and crack growth rate to be established. This approach was first suggested by Chung and Williams[1].

Marshall and Williams[2] have developed a model for viscoelastic crack growth rate as a function of applied stress intensity which depends on the far field viscoelasticity and the rate dependence of the flow stress in the process zone, the critical crack tip opening displacement being assumed to be constant over a certain range of crack growth rates. For the case where the far field viscoelasticity is given by

$$D=D_0+D_1 t^n \qquad (1)$$

and the process zone flow stress is

$$\sigma_c=\sigma_0 t^{-n} \qquad (2)$$

then

$$\dot{a} = AK^{1/n} \qquad (3)$$

The brittle fracture portion the log hoop stress versus log time to failure behavior of pipe should in principle be predictable from the integration of the crack growth relationship Eq. 3 in combination with some knowledge of the usual incipient flaw size. Where the initial flaw size is small compared to the critical flaw size, which should usually be the case, the short time fracture toughness is not needed for the prediction of the brittle fracture portion of the curve. It should be noted that the fracture is only macroscopically brittle (no gross deformation preceding fracture) but microscopically ductile. Ideally, the crack growth rate data should be

run on C shaped specimens cut from actual pipe and razor notched. The use of the brittle fracture portion of the log hoop stress versus log time to failure from actual pipe failures in conjunction with the above described analysis should allow one to determine what is a typical incipient flaw size (from back calculations, knowing the actual time to failure at a given stress level) and to determine if one such test to determine an incipient flaw size then allows the prediction of the remainder of the log hoop stress versus log time to failure for the brittle fracture portion of the curve.

To predict the ductile fracture portion of the log hoop stress versus log time to failure curve is somewhat more problematic. The constitutive relationship which comes from the initial portion of the experimentally measured load-line displacement versus time curve, Eq. 1, could be used to easily predict time to ductile fracture if and only if the strain at which local bulging instability begins is independent of the hoop stress. Otherwise, the instability strain itself needs to be predicted with a model based on a constitutive relationship for biaxial deformation. Experiments are underway to try to determine how the local hoop strain adjacent to a bulge, which just precedes to ductile fracture, varies with hoop stress.

EXPERIMENTAL PROCEDURES AND RESULTS

Three-point bend specimens (see Figure 1) of a high density, low toughness polyethylene have been deeply notched using a fly cutter and subsequently sharpened with a serrated razor blade. While not shown in Figure 1, the specimens were side-grooved to a combined depth of approximately 20% of the wall thickness (10% on each side). Specimen testing consists of dead weight loading with the measurement of load-line displacement as a function of time, as seen in Figure 2. Note that tests 1 and 2 overlay each other almost perfectly. The load-line velocity is determined and the minimum point is assumed to be the point of initiation of crack growth. Initiation times for tests 1-4 shown in Fig. 2 are as follows: 52,300s, 57,900s, 57,600s, and 82,200s.

Standard compliance relationships for deeply notched three-point bend specimens have been used to determined the the time-dependent material compliance ($D=\epsilon(t)/\sigma$ in Eq. 1) and plotted to allowed a determination of the exponent "n", as seen in Fig. 3. The crack growth data has also been analyzed using standard compliance and stress intensity relationships and presented in Figure 4. Note the slopes of Figs. 3 and 4 should have inverse relationships to each others if both far field and process zone rate effects are important in the viscoelastic crack growth, as seen in Eq. 1 and 3. This is approximately the case. Even though the one of the initiation times vary significantly and two of the curves in Fig. 2 appear to be quite different from the other two, the crack growth rate versus stress intensity relationship for all four test specimens was quite consistent.

REFERENCES

1. W.N. Chung and J.G. Williams, 8th Conf. On Deform. Yield and Fracture of Polymers, Cambridge, 1991. London: Plastics and Rubber Institute. 28.
2. G.P. Marshall and J.G. Williams, *Proc. of Royal Society*, Vol. A342 (1975), pp. 55.

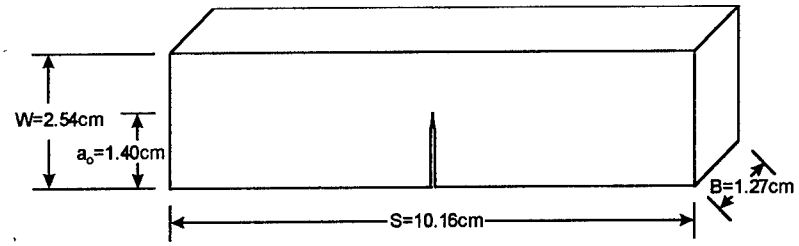

Figure 1

DISPLACEMENT VS. TIME

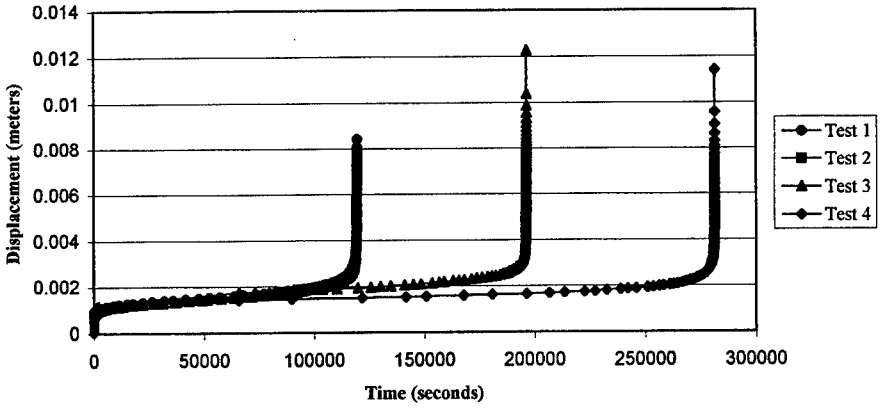

Figure 2

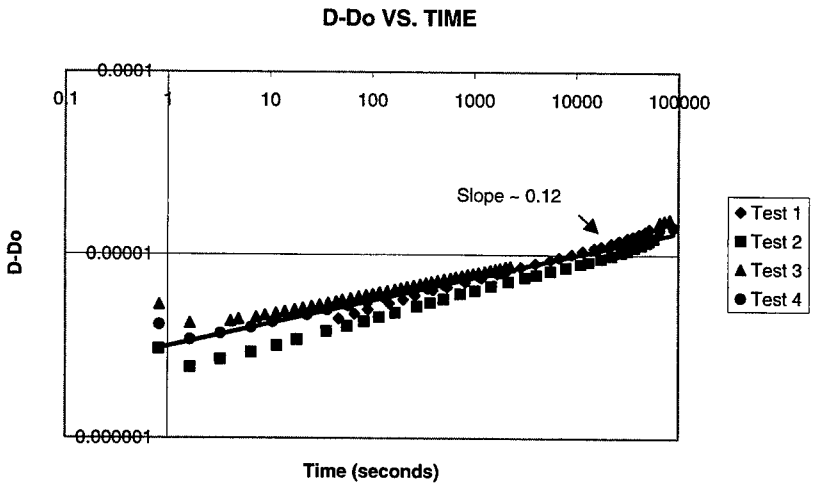

Figure 3

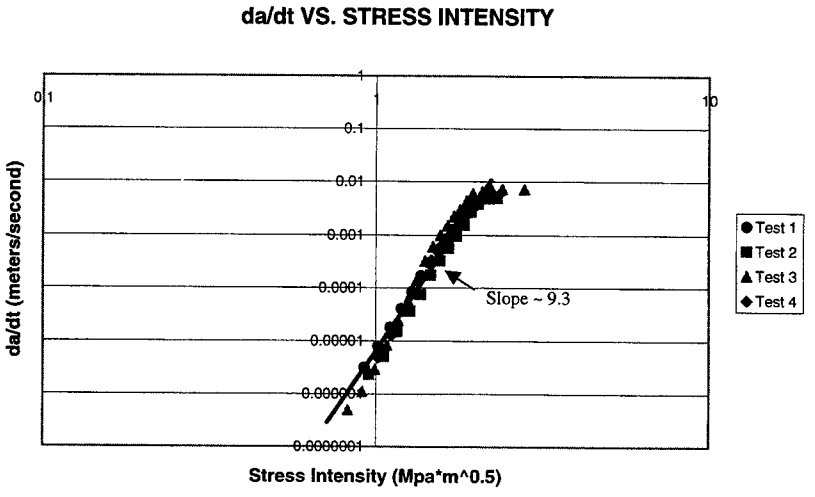

Figure 4

Abnormal Slow Crack Growth in Polyethylene

Xici Lu and Norman Brown*

The normal slow crack growth behavior of polyethylenes consists of a ductile- brittle transition where the transition to brittle fracture occurs below a critical stress and after a critical time. The curves of stress vs. failure time depend on temperature, but all curves can be superposed by shifting vertically and horizontally by well established shift functions. It has been observed that there are some polyethylenes whose stress vs. time to failure curves do not shift in the normal way and in some cases the time for brittle fracture does not change with temperature. SEM micrographs do not reveal any difference between the fibrillated fractured surfaces from the normal and abnormal specimens. Whereas the normal slow crack growth behavior has been attributed to disentanglement of molecules by sliding without chain scission, it is proposed that the abnormal fracture behavior involves disentanglement that consists of a combination of chain sliding and scission.

.. **NORMAL BEHAVIOR** The long time fracture behavior of polyethylene structures has been extensively investigated because PE is used in pipes, fittings, tanks, and electrical cables. Under a constant load, PE exhibits two general modes of failure: 1) ductile failure by homogeneous deformation, and 2) brittle failure which initiates at a point of stress concentration and the crack is proceeded by a craze . The long time failures in the field occur by the brittle mode. Thousands of tests have been done on pressurized pipes during the past 30 years whose typical behavior is shown in Fig. 1. [1] where the hoop stress, σ, is plotted against the time to failure, t_f, at various temperatures. This normal behavior is also shown in Fig. 2 [2] for specimens from a compression molded ethylene hexene copolymer (density 0.946) with a 3.5 mm razor notch and tensile loaded under plane strain conditions. Each curve consists of a region of ductile failure at high stresses and a brittle region at lower stresses.The slope of each region is given by

$$t_f \alpha \sigma^{-n} \qquad (1)$$

where typical values of n for ductile failure range from 20-27, and for the brittle region, 2.5-4.5. Generally, the transition stress is about one-half the yield point at the particular temperature.The entire curve at a temperature,T_1 , can by shifted to another temperature,T_2 by a horizontal and vertical shift as pointed out by Popelar, et al. [3] . The following shift functions based on detailed experiments by Lu and Brown [2,4] are modifications of those presented by Popelar, et al.

$$t_f(T_1) = t_f(T_2) \exp[Q_1/R\,(1/T_1 - 1/T_2)] \qquad (2)$$

$$\sigma(T_1) = \sigma(T_2) \exp[Q_2/R\,(1/T_1 - 1/T_2)] \qquad (3)$$

* Dept. Materials Science and Engineering University of Pennsylvania
Philadelphia, PA 19104

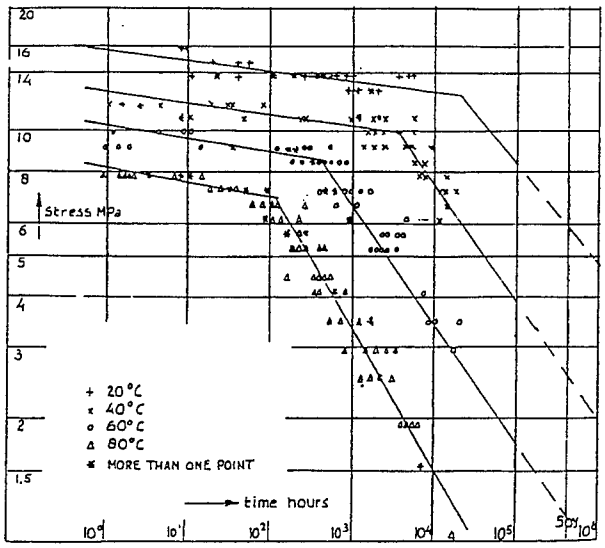

Fig.1. Log hoop stress vs. log time to failure at various temperatures for a pipe under hydrostatic pressure. Normal behavior.

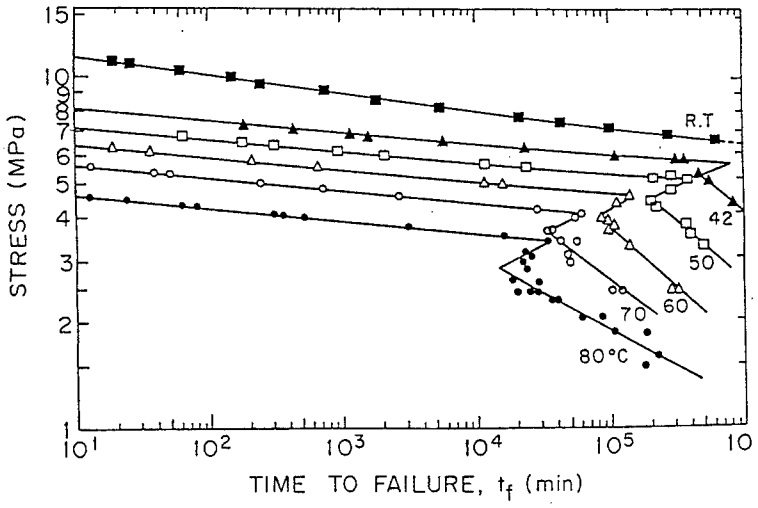

Fig 2. Tensile stress vs. time to failure with a 3.5 mm notch at various temperatures. Ethylene-hexene. Normal behavior

Q_1 and Q_2 are about the same for all polyethylenes that exhibits the normal behavior shown in Figs. 1 and 2, where $Q_1 \approx$ 80,000 J/mol and Q_2= 10,500 J/mol.

ABNORMAL BEHAVIOR Fig. 3 shows log σ vs. log t_f for a commercial ethylene-octene copolymer. The times for the ductile -brittle transition are indicated by the arrows. The abnormal behavior manifests itself by the fact that the times for the ductile -brittle transition are the same from 65 °C to 30 °C and that these times are less than that at 80 °C. However, the shift in stress with temperature is consistent with the normal behavior (equa. 2).

Fig. 4 shows the abnormal behavior for a commercial ethylene-hexene copolymer. The 80°C curve shows the normal behavior in that the slopes in the ductile and brittle regions correspond to n (equation 1) = 18 and 2.4 respectively. However, between 3 and 38 °C, all the data are brittle and no ductile-brittle transformation was observed, and the stresses did not shift with temperature. Also, the n in equation (1) for this brittle behavior is 18, which is much greater than the n values for the normal brittle behavior.

The fractured surfaces were observed with the SEM. The same fibrilla structure that is charachteristic of brittle fracture was observed in the normal and abnormal specimens In all the micrographs, the general trend is for the fibrilla structure to become finer the lower the temperature and the lower the stress. It was not possible to distinguish the normal from the abnormal fractured surfaces..

Discussion The normal fracture mechanism has been viewed as the disentaglement of the tie molecules from the crystals with no chain scission. It is speculated that the abnormal fracture involves a combination of scission and chain sliding. The molecular and morphological factors that determine whether normal or abnormal occurs are not known at this time.

References

1..W.. J. De Putter, 11'th Plastic Fuel Gas Pipe Symposium,1989, pub. Amer. Gas Assoc. p.378.

2.X. Lu and N. Brown,J. Materials Science,vol.25,(1990) p.411.

3.V. H. Kenner, C.H. Popelar, J. P. Wooster,12'th Plastic Fuel Gas Pipe Symposium 1991,p 130.

4. X. Lu and N. Brown, J. Materials Science vol.26,(1991) p.612.

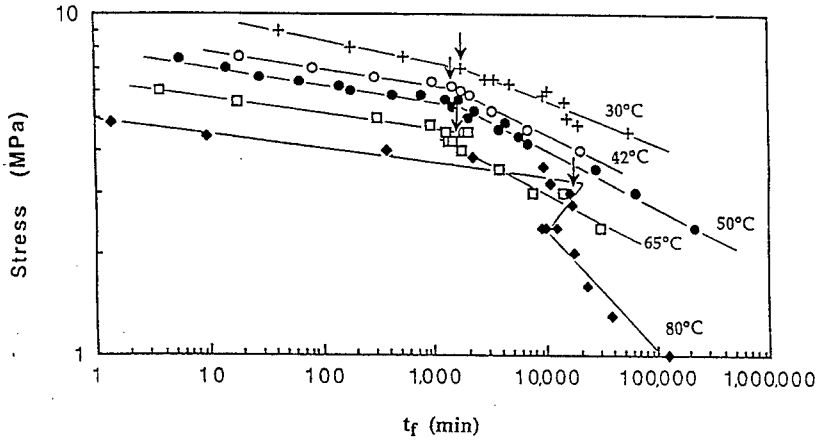

Fig 3. Same as Fig.2 except ethylene octene copolymer . Arrows indicate ductile -brittle transition. Abnormal behavior.

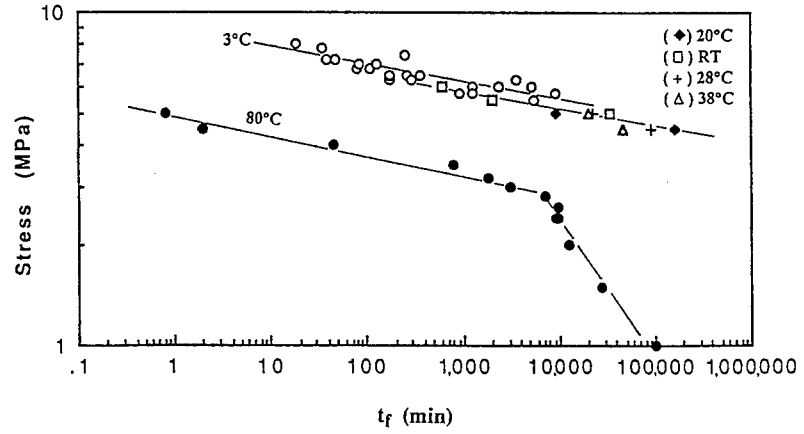

Fig.4. Same as Fig. 3. except ethylene -hexene. Abnormal behavior

SESSION SEVEN:

DEFORMATION IN SPECIAL MATERIALS I

DEFORMATION AND FRACTURE OF A POLYDOMAIN LIQUID CRYSTALLINE EPOXY-BASED THERMOSET

C. Ortiz, R. Kim, E. Rodeghiero, E.J. Kramer, and C.K. Ober*

Liquid crystalline thermosets (LCT's) are a new class of densely crosslinked network materials which have interesting and unusual mechanical properties due to their unique "polydomain" structure which consists of microscopic regions of uniform molecular orientation. The LCT's used in this study were prepared by curing the difunctional LC epoxy monomer, the diglycidyl ether of 4,4'-dihydroxy-α-methylstilbene (DGDHMS) [1], with stoichiometric amounts of the tetrafunctional crosslinker, methylene dianiline (MDA), according to a time-temperature-transformation (TTT) diagram.

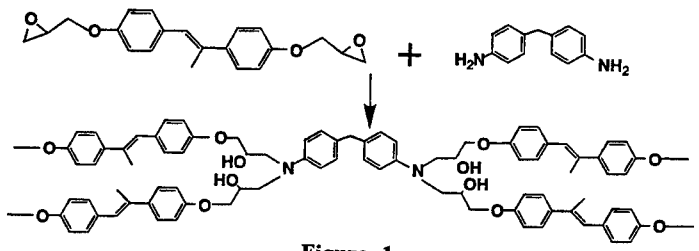

Figure 1.
Crosslinking reaction of DGDHMS and MDA to form a liquid crystalline thermoset

The crosslinking reaction "locked" the LC order into the network, thus preventing the disordering or "clearing" transition. The type of local molecular order (e.g. smectic, nematic, or isotropic, rigid-rod) depended on which phase the epoxy / amine mixture was reacted from and was controlled through the initial cure temperature. When viewed under the cross-polarized optical microscope, the LCT's exhibited a fine-scaled, high disclination density, Schlieren texture and hence, were further characterized by wide angle X-ray diffraction. A commercial, non-LC epoxy monomer, the diglycidyl ether of bisphenol A (DGEBA), of similar starting molecular weight was also cured with MDA to produce an amorphous thermoset for comparison. Mechanical properties were investigated using dynamic mechanical analysis (DMA), uniaxial compression, fracture toughness, and microdeformation testing of thin films.

DMA was performed while continuously heating thermoset beams using a Perkin Elmer DMA7 in 3-point bending configuration. The amorphous thermosets exhibited a typical glassy storage modulus, $E_g' \approx 10^9$ Pa, which exhibited a sharp drop at Tg (*see Figure 2.a) followed by the rubbery plateau with a modulus of $E_R' \approx 50$ MPa. The average molecular weight between crosslinks, $\langle M_X \rangle$, was calculated using the classical rubber elasticity equation, $3\rho RT/E_R$, and found to be consistent with that calculated from stoichiometry (≈1 monomer between crosslinks). The LCT's exhibited extremely high rubbery moduli which increased with increasing degree of local order (E_R': (isotropic) 60 MPa, (nematic) 80 MPa, and (smectic) 115 MPa) and decreased with temperature. The glass transition temperature and magnitude of the loss tangent peak, tan(δ), decreased with increasing degree of local order while the apparent breadth of the transition region increased (*see Figure 2.b).

*Department of Materials Science and Engineering, Cornell University

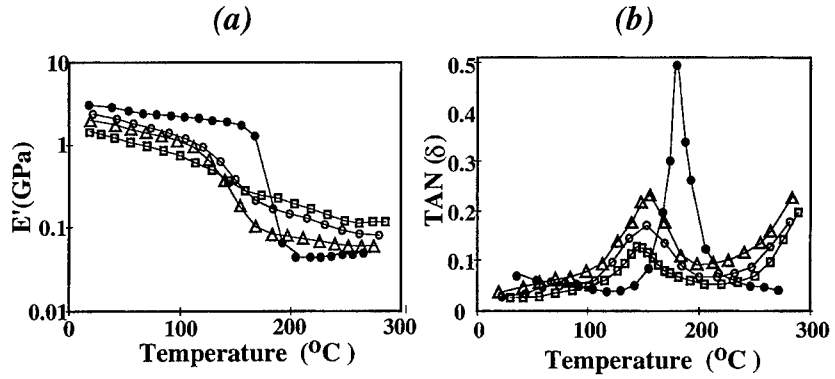

Figure 2: (a) Dynamic storage moduli, E', and (b) loss tangent, tan(δ), as a function of temperature for the DGDHMS / MDA LCT : smectic (□), nematic (○), and isotropic (△), compared to the amorphous, DGEBA/ MDA thermoset (●).

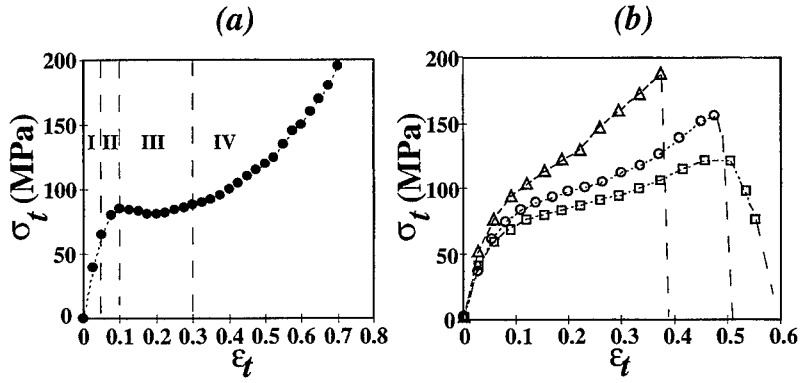

Figure 3: True stress versus true strain in uniaxial compression for the (a) DGEBA / MDA amorphous thermoset and the (b) DGDHMS / MDA LCT : smectic (□), nematic (○), and isotropic (△) LCT's

Figure 3.a is a plot of true stress, σ_t, versus true strain, ε_t, for the amorphous thermoset in uniaxial compression at room temperature. As for most glassy polymers, one can distinguish four distinct regions : (I) linear viscoelastic, i.e. glassy deformation, (II) homogeneous yielding, i.e. plastic deformation, (III) strain softening, and (IV) entropic strain hardening. Attempts to model the strain hardening region with the classical rubber elasticity equation for uniaxial deformation, $\sigma_t=E_R(\lambda^2-1/\lambda)/3$ where λ is the extension ratio, lead to a large overestimation in the prediction of the rubbery modulus. However, fitting the uniaxial compression data of Glad, et. al. [2] on DGEBA-based epoxy thermosets of various network strand densities leads to an E_R that decreased with increasing $<M_X>$. The flow curves of the LCT's, shown in Figure 3.b, show a similar compressive modulus (E≈2 GPa), no strain softening region, a reduced fracture strain (ε_f≈50%), and increased strain hardening compared to the amorphous thermoset. The strain hardening region could not be accurately modeled even qualitatively using classical rubber elasticity theory.

For all samples, the plastic strain was unrecoverable at room temperature, essentially "frozen" in the glassy phase. The deformed thermosets were sliced and polished into 25 μm films parallel and perpendicular to the compression axis, σ_C. Birefringence measurements indicated a macroscopically oriented material with a preferred molecular orientation for the LC director lying perpendicular to σ_C and random within this plane, i.e. a planar orientation distribution and negative order parameter, *S*. Upon heating, all of the samples exhibited a complete recovery of their macroscopic dimensions and original polydomain microstructure at temperatures well below Tg (≈80°C).

Fracture toughness tests were conducted using a chevron-notched 3-point bend sample. The amorphous, non-LC thermosets exhibited a linear force, F, versus displacement, δ, curve which led to sudden brittle, catastrophic fracture (*see Figure 4.a). All of the LCT's exhibited slow, stable crack propagation (*see Figure 4.b-d), resulting in increased fracture toughness with increasing degree of local order. The fracture toughness values, G_{Ic} (kJ/m^2), of the LCT's were measured as follows; (isotropic) 0.68, (nematic) 0.75, and (smectic) 1.62. Scanning electron micrographs of the fracture surfaces indicate strong differences in fracture mechanisms. The amorphous thermosets possessed a smooth, featureless fracture surface characteristic of brittle failure. The isotropic and nematic LCT's exhibited a more deformed, fibrillar structure, while the smectic LCT displayed extensive plastic deformation.

Free-standing thin films (30 μm) of the thermosets were bonded to annealed copper grids, strained in tension, and observed under the cross-polarized optical microscope. The results were consistent with the findings for the bulk fracture toughness experiments. At low strains, the amorphous films exhibited photoelastic birefringence and no visible plastic deformation. Further straining resulted in brittle, catastrophic failure which took place by the nucleation of a single microcrack which propagated quickly along a straight path perpendicular to the straining direction. The LCT films deformed by the nucleation of numerous microcracks which propagated slowly along curved paths and eventually interconnected, leading to failure of the film. The large crack tip opening displacements in these samples suggested that bulk plastic deformation had taken place in these samples.

[1] G.G. Barclay, C.K. Ober, K.I. Papathomas, and D.W. Wang, *J. Polym. Sci. Part A : Polym. Chem.* **30**, 1831-1843 (1992).
[2] M. Glad, Ph.D. Thesis, Cornell University, Ithaca, NY (1990)

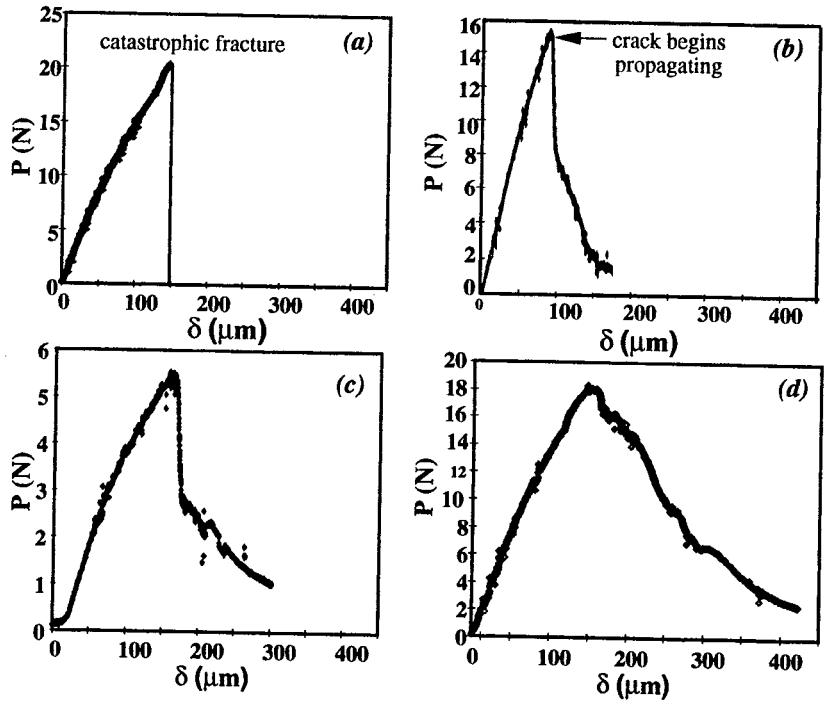

Figure 4 : Force versus displacement curves for chevron-notched 3-point bend fracture toughness tests (a) amorphous thermoset, (b) isotropic DGDHMS / MDA thermoset, (c) nematic LCT, and (d) smectic LCT.

MORPHOLOGY AND FRACTURE MECHANISMS IN DIGLYCIDYL ETHER OF 4,4'-DIHYDROXY-α-METHYLSTILBENE EPOXIES AND COMPOSITES

H.-J. Sue*, J.D. Earls, and R.E. Hefner, Jr.****

The morphologies and mechanical behaviors of various diglycidyl ether of 4,4'-dihydroxy-α-methylstilbene based liquid crystalline epoxy (LCE) blends and composites are studied. It is found that, depending on how the resins are cured and the level of mesogenic monomers are incorporated, the morphology in LCE may vary from being amorphous, to containing micro-domain of various size, and to the formation of preferred molecular orientation. Evidence of mesogenic molecular alignment along the fiber direction is detected in LCE composites. The LCE resins appear to exhibit higher fracture toughness than conventional epoxy resins. The fracture mechanisms observed in LCE resins are predominantly crack segmentation, crack branching, crack bridging, and crack blunting. The possible cause(s) for the unusual fracture behavior of LCEs is discussed.

INTRODUCTION

Recent research and development of the diglycidyl ether of 4,4'-dihydroxy-α-methylstilbene (DGE-DHAMS) based liquid crystalline epoxy (LCE) resin systems has shown that these LCEs possess extremely high tensile modulus and strength when molecularly oriented, high fracture toughness, high ductility, outstanding chemical and solvent resistance, high T_g, low water absorption, and ease of processing suitable for high performance automotive, electronic, and aerospace structural applications [1-5].

The chemical structures of the DGE-DHAMS and sulfanilamide curing agent to be used in this study are given below:

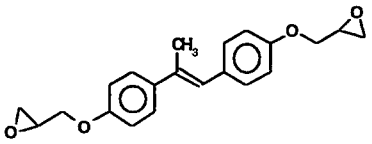

DGE-DHAMS

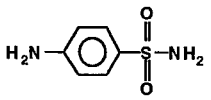

Sulfanilamide

The present work attempts to study the fracture behavior of the unoriented DGE-DHAMS/ sulfanilamide system using both fracture mechanics and microscopy tools. The effects of curing variations in the LC domain morphology and the corresponding fracture process are investigated. It is hoped that the source of toughening in the DGE-DHAMS/sulfanilamide system can be identified and the relationships between the LC domain, morphology, and fracture mechanisms in LCEs can be understood and established. Also, the morphology of the LCEs in graphite fiber composites is investigated. The potential of using LCE composites for high performance structural applications is discussed.

*Dept. of Mech. Eng., Texas A&M University, College Station, TX 77843-3123.

**Organic Product Research, The Dow Chemical Company, Freeport, TX 77541.

EXPERIMENTAL

To study how the curing conditions affect the morphology and mechanical property of LCEs, three different curing schedules were adopted on DGE-DHAMS/sulfanilamide system:

1) 4 hrs @ 120°C + 1 hr @ 140°C + 1 hr @ 160°C + 1 hr @ 180°C + 6 hrs @ 200°C **(LCE-1)**
2) 4 hrs @ 160°C + 1 hr @ 180°C + 6 hrs @ 200°C **(LCE-2)**
3) 4 hrs @ 200°C **(LCE-3)**

To investigate how monomer blends affect the morphology and mechanical property of LCEs, three LCE blends were considered. These LCE blends include (1) DGE-DHAMS : DHAMS : sulfanilamide (1 : 0.4 : 0.6 ratio by equivalent weight (E.W.)), (2) DGE-DHAMS : DHAMS : DEN 438 epoxy novolac resin : sulfanilamide (1 : 0.4 : 0.5 : 0.1 ratio by E.W.), and (3) DGE-DHAMS : TACTIX 556 epoxy resin : sulfanilamide (0.79 : 0.21 : 1.0 ratio by E.W.). It is noted that DHAMS, DEN 438 epoxy novolac resin, and sulfanilamide are utilized as crosslinkers. The curing conditions for the three blends are given as follows:

1) DGE-DHAMS/DHAMS/sulfanilamide: 4.25 hrs @ 120 °C + 1 hr @ 140 °C + 1 hr @ 160 °C + 1 hr @ 180 °C + 4 hrs @ 200 °C **(Blend-1)**
2) DGE-DHAMS/DHAMS/DEN 438 epoxy novolac resin/sulfanilamide: 4 hrs @ 135 °C + 1 hr @ 150 °C + 1 hr @ 175 °C + 2 hrs @ 200 °C **(Blend-2)**
3) DGE-DHAMS/TACTIX 556 epoxy resin/sulfanilamide: 4 hrs @ 120 °C + 1 hr @ 140 °C + 1 hr @ 160 °C + 1 hr @ 180 °C + 4 hrs @ 200 °C **(Blend-3)**

The uniweave graphite fiber (G30-500/8HS) LCE composites were prepared *via* resin flow molding. Four LCE resins were chosen to make the composite panels. These resins include LCE-1, LCE-3, Blend-1, and Blend-3. The curing schedule for the LCE composites follows that for the LCE resins given above.

The unoriented LCE blends with plaque thicknesses of 0.635 cm (0.25") and 0.3175 cm (0.125") were cast and slowly cooled to room temperature (25 _C) in the oven. The 0.635 cm plaques were machined into bars with dimensions of 12.7 cm x 1.27 cm x 0.635 cm (5" x 0.5" x 0.25") and dimensions of 6.35 cm x 1.27 cm x 0.635 cm (2.5" x 0.5" x 0.25") for the DN-4PB and the single-edge-notch three-point-bend (SEN-3PB) [6] experiments, respectively. The detailed experimental procedures are given elsewhere [6,7].

To determine whether or not the modulus of the LCEs is a strong function of temperature, the dynamic mechanical behavior of Blend-2 was studied using DMS (Rheometrics RMS-805) under a torsional mode, with 5 °C per step. A constant strain amplitude of 0.05% and a fixed frequency of 1 Hz were used.

The detailed procedures for preparing transmission electron microscopy (TEM) and transmission optical microscopy (TOM) samples of the damage zone around the survived DN-4PB crack in this study were the same as those described in the literature [6].

RESULTS AND DISCUSSION

(A) Dynamic Mechanical Spectroscopy

To demonstrate the strong temperature dependency of the LCE modulus, in comparison with conventional epoxies, the DMS spectra of Blend-2 as well as a formulated tough epoxy resin [7] were generated. As shown in Figure 1, the shear storage modulus (G') of Blend-2 clearly exhibits a much stronger temperature dependency than that of the formulated tough epoxy resin [7] over the entire temperature range investigated (except around the T_g region).

It is noted that the strong temperature dependency of the LCEs corresponds well to the relatively high magnitude of the Tan δ (ratio between loss modulus and storage modulus) curve of LCEs. This, in turn, implies that the sub-T_g molecular motion in LCEs is much more pronounced than that of the conventional epoxies. Unfortunately, there is no known method that can be utilized to characterize the crosslink density of LCEs. As a result, it is uncertain if the

high temperature dependency of LCE modulus is due to incomplete curing of LCE or due to the nature of LC molecular packing.

(B) Mechanical Properties

The SEN-3PB method was utilized for measuring the K_{IC} values of the LCE resins at 25 °C. As shown in Table I, the K_{IC} values of the LCE resins are higher than conventional epoxies [7], especially at low temperatures [1].

Table I. Mechanical Property of LCEs.

	E (MPa)	K_{IC} ($MPa \cdot m^{0.5}$)	G_{IC} (J/m^2)	T_g (°C)
LCE-1	4200	1.35±0.06	380	215
LCE-2	2900	1.43±0.08	580	235
LCE-3	3100	1.12±0.06	350	225
Blend-1	2700	1.65±0.10	1080	180
Blend-2	2400	1.89±0.04	1310	135
Blend-3	3300	1.11±0.08	330	224
Tough Epoxy [7]	3200	1.00±0.10	280	145

(C) Fracture Mechanisms

To effectively study the sub-fracture surface zone (SFSZ) of a damaged sample, it is desirable that the DN-4PB technique and the TEM and TOM methods are used. When TEM is utilized, it is shown that LC domains are present in LCE-1, LCE-2, Blend-1, and Blend-3. Although no LC domains were found in Blend-2, Blend-2 does exhibit high birefringence when viewed using TOM under crossed-polars. As for LCE-3, no signs of birefringence or LC domains were found.

In the SFSZ, it is found that all LCE resins, except for LCE-3, show signs of crack segmentation, crack bridging, crack branching, and crack deflection mechanisms upon fracture (Fig. 2). This type of fracture process is unique for LCEs. It is speculated that there exist numerous nanometer scale defects during the formation of LC in the LCE matrix. Thus, when the crack begins to open up, these defects initiate microcracks in front of the main crack tip. The process then repeats itself until unstable crack propagation ensues.

When LCE-1 is used as composite matrix, evidence of mesogenic molecular alignment along the graphite fiber direction is observed (Fig. 3). Limited data have indicated that the LCE composites exhibit superior physical and mechanical properties over the conventional epoxy composites.

CONCLUSION

The fracture toughness and failure mechanisms of LCE resins and composites based on DGE-DHAMS are studied using the SEN-3PB, DN-4PB, SEM, ROM, TOM, TEM, electron diffraction, X-Ray diffraction, and Micro-Raman techniques. Crack deflection, crack branching, segmented cracking, and crack bridging are found in all but LCE-3 resins. Evidence of mesogenic molecular alignment along the graphite fiber direction is found. It is possible that the LCEs may be utilized as a low cost alternative resins for high performance electronic and aerospace structural applications.

REFERENCES

1. H.-J. Sue, J.D. Earls, R.E. Hefner, Jr., *J. Mater. Sci.*, in press.
2. J.D. Earls and R.E. Hefner, Jr., P.M. Puckett, U.S. Patent 5,463,091, 1995.
3. J.D. Earls and R.E. Hefner, Jr., P.M. Puckett, U.S. Patent 5,218,062, 1993.

4. Q. Lin, Ph.D. Thesis, University of Michigan, Ann Arbor, 1994.
5. G.C. Barclay, C.K. Ober, K.I. Papathomas, and D.W. Wang, *J. Polym. Sci., Polym. Chem.*, 30, 1831 (1992).
6. H.-J. Sue, E.I. Garcia-Meitin, and D.M. Pickelman, "Toughening Concept in High Performance Epoxies", Chap. 18 in Elastomer Technology Handbook, CRC Press, Boca Raton, Florida, pp. 662-700, 1993.
7. H.-J. Sue, J.L. Bertram, E.I. Garcia-Meitin, and L.L. Walker, *Colloid & Polym. Sci.*, 272, 456(1994).

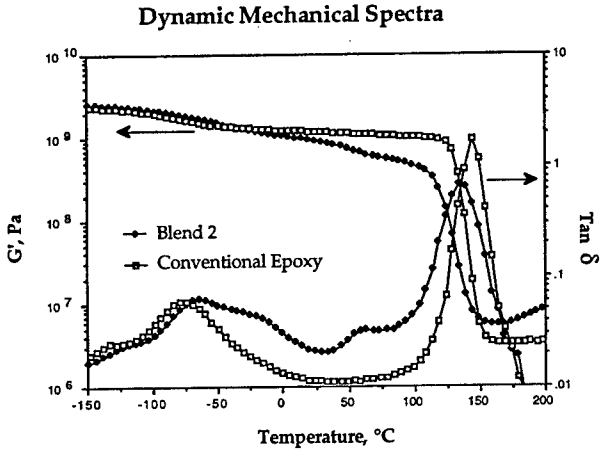

Figure 1. Dynamic Mechanical Spectra for Blend-2 and a conventional tough Epoxy Resins [7].

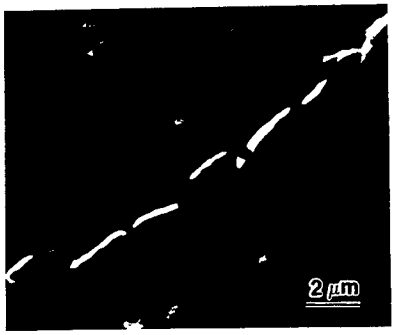

Fig. 2. TEM micrograph of DN-4PB-SFSZ of LCE-2. Segmental cracking, bridging, crack bifurcation, and crack deflection are found. These fracture mechanisms are typical of all LCE resins.

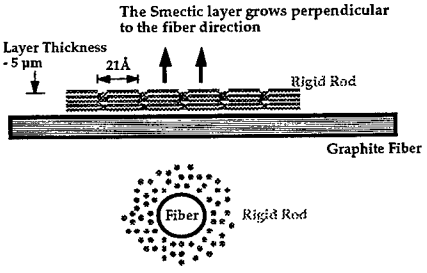

Figure 3. Schematic showing mesogenic molecular orientation of LC domains along the graphite fiber direction. The model is constructed based on TEM, Micro-Raman, and electron diffraction observations.

EFFECTS OF IONIC INTERACTIONS ON MECHANICAL PROPERTIES OF POLYMERS AND POLYMER BLENDS/COMPOSITES

X. Ma, J.A. Sauer, G. Parker, W. Chen, L. Tsou, Y. Xue, and M. Hara*

The effect of ionic interactions on mechanical properties, especially deformation and fracture properties, of polymers and polymer blends/composites, is discussed. Examples are given of the influence of ionic interactions on ionomers from flexible chain polymers, on ionic liquid crystalline polymers (LCPs), and on molecular composites of an ionic polymer and a polar polymer.

INTRODUCTION

Our research interest is exploitation of strong non-directional, *ionic bonds* in polymers (1,2) to develop new materials having superior mechanical properties and to understand such bonding in polymers. This can be achieved in two ways both of which involve enhancing inter-molecular interactions through strong ionic bonds: (i) in the same polymer molecules (creating ionic polymers); and (ii) in different polymer molecules (producing polymer blends and composites through ionic bonds between the components).

First, we discuss results on deformation and fracture of two types of ionomers (ionic polymers having a small number of ionic groups); one based on flexible chain polymers, such as polystyrene (PS) and poly(methyl methacrylate)(PMMA), and the other based on a semi-rigid liquid crystalline polymer, such as wholly aromatic polyester (Vectra®). Secondly, we discuss results on molecular composites made from a rigid reinforcing polymer and a flexible matrix polymer, in which miscibility (dispersity) is enhanced via strong ionic interactions between the component polymers.

EXPERIMENTAL

Ionomers based on PS or PMMA were made either by modification of parent polymers or by random copolymerization of component monomers (3-5). Ionic PPTAs, poly(p-phenylene terephthalamide), were made either by modification of Kevlar® pulp or by copolymerization of component monomers (6,7). Molecular composite samples were generally made as follows: an ionic PPTA and a matrix polymer, separately dissolved in dimethyl sulfoxide (DMSO), were mixed in solution, followed by precipitation into a nonsolvent, ether. After vacuum drying at high temperature, samples were characterized, and then compression molded into rectangular specimens for further mechanical testing. Characterization techniques are described elsewhere (6). Ionic LCPs were made by copoly-

* Department of Chemical and Biochemical Engineering, Rutgers University

merization of component monomers including ionic monomer, e.g., 5-sulfoisophthalic acid (8). Deformation modes were observed by transmission electron microscopy (TEM) as described elsewhere (5). Tensile testing was made on a Minimat Materials Tester (Polymer Lab) according to ASTM D-882. Fracture toughness, K_{Ic}, was measured by a 4 point bending test on single-edge-notched specimens. The observation of kink bands under compression was conducted as follows: several fibers were embedded in a matrix polymer, poly(hydroxypropyl methacrylate), which was post-polymerized after fibers were added. Then, these cylindrical samples were subjected to compressive loads of 100, 200, 300, and 400 lb. At each load, fibers were extracted by dissolving the matrix polymer in a solvent (DMSO) and observed by scanning electron microscopy to check if kink bands were formed.

RESULTS AND DISCUSSION

Ionomers (based on flexible polymers)

It is well established that, in flexible ionomers, ionic aggregates are made, which behave like ionic cross-links at low ion content and reinforcing fillers at higher ion content (2). As Figure 1 indicates, the formation of such *ionic aggregates* leads to an increase in the "effective" strand density; and, the deformation mode changes from crazing only for the unmodified polymer, e.g., PS or PMMA, to crazing plus shear deformation with an increase in ion content of the ionomers (3-5). This is somewhat similar to the situation of neutral polymers that contain (lightly) covalent cross-links (9). Such changes in the deformation mode are translated into enhanced tensile and fatigue properties of bulk ionomer specimens (5).

Ionic LCP

The introduction of ionic groups (and ionic bonds) into an LCP leads to enhancement in mechanical properties. For example, upon addition of 1 mol% ionic groups (Ca salt) into a polyester-based LCP, the modulus of the films increases from 13 to 23 GPa, the tensile strength increases from 142 to 351 MPa, and the elongation at break increases from 1.3 to 1.6 %.

One of the inherent problems of LCPs is their small compressive (and transverse) strength in contrast to a large longitudinal strength (10). An introduction of ionic groups (or bonds) into an LCP appears to lead to enhanced compressive properties. For example, nonionic LCP fibers (embedded in a matrix polymer) show *kink bands* under compressive load, while ionic LCP fibers (1mol%; Na salt) show no kink bands under the same conditions. Kink bands are a deformation mechanism of fibers which develop due to a low compressive strength. We speculate that the weak lateral cohesion between LCP molecules is enhanced by strong, non-directional, ionic bonds, leading to better compressive properties.

Molecular Composites (via Ionic Bonds)

Molecular composites have been made from an ionic PPTA and a polar polymer (e.g., poly(4-vinylpyridine)(PVP)), in which a good dispersion of the rigid molecules is achieved

via ionic (ion-dipole) interactions (6). Optical clarity, polarized microscopy, T_g measurements (both by DSC and DMTA), and TEM observation of ionic PPTA/polar polymer composites have indicated good dispersion of the PPTA molecules. Molecular composites based on amorphous matrix polymers (e.g., PVP) are all transparent and show no phase separation upon heating; therefore, they are melt-processable.

The deformation mode of the matrix polymer is modified significantly with the addition of rigid molecules: e.g., an addition of ionic PPTA molecules into PVP, which deforms only by crazing, induces shear deformation (see Figure 2). This is due to the interactions between rigid and coil molecules at the molecular (or microscopic) level. In conventional fiber composites, interactions between fiber and matrix polymer occur only at the interface during load transfer. The change in deformation modes is also reflected in the fracture properties of bulk materials. As shown by Figure 3, the stiffness, the strength, the ductility, and the energy to fracture are all enhanced for the molecular composite. The enhanced resistance to crack initiation and fracture upon addition of ionic PPTA is believed to be responsible for the improvement of tensile properties.

ACKNOWLEDGMENT

Acknowledgment is made to U.S. Army Research Office, ACS-PRF, and Hoechst-Celanese for support of this research.

REFERENCES

1. Holliday, L. Ed., 1975, "Ionic Polymers", Applied Science, London
2. Eisenberg, A. and King, M., 1977, "Ion-Containing Polymers", Academic Press, New York
3. Bellinger, M., Sauer, J.A., Hara, M., 1994, Macromolecules, 27, 1407
4. Ma, X., Sauer, J.A., Hara, M., 1995, Macromolecules, 28, 5526
5. Hara, M. and Sauer, J.A., 1994, J. Macromol. Sci., Rev. Macromol. Chem. Phys., C34, 325
6. Parker, G., Chen W., Tsou, L., and Hara, M., 1996, ACS Symp. Ser., 632, 54
7. Parker, G. and Hara, M. Polymer, in press
8. Xue Y. and Hara, M. Macromolecules, submitted
9. Henkee, C.S. and Kramer, E.J., 1984, J. Polym. Sci., Polym. Phys. Ed., 22, 721
10. Donald, A.M. and Windle, A.H., 1992, "Liquid Crystalline Polymers", Cambridge University Press, Cambridge

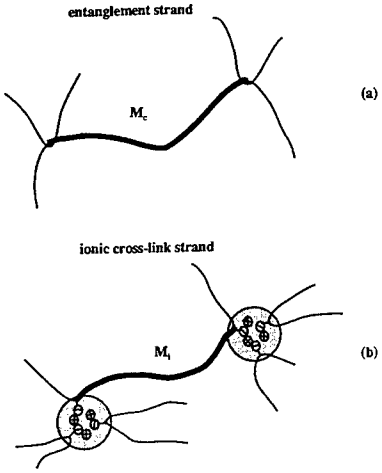

(a)

(b)

Figure1 Schematic figures showing (a) an entanglement strand and (b) ionic cross-link strand.

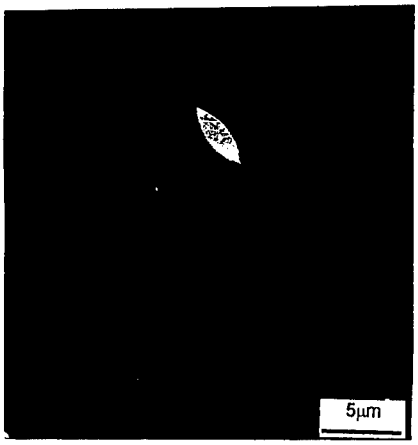

Figure 2 TEM micrograph of a deformed molecular composite thin film made from ionic PPTA (30 mol% ion content; Zn salt) and PVP, 10/90 mixing ratio.

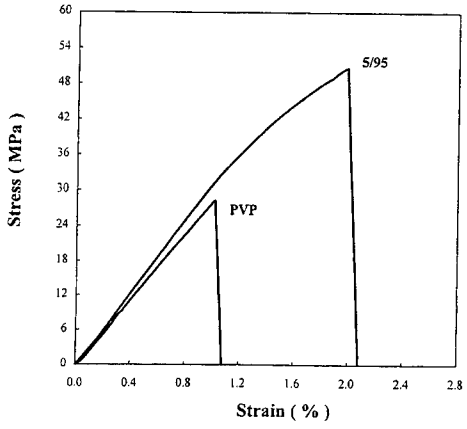

Figure 3 Stress-strain curve for a molecular composite made from ionic PPTA (100 mol% ion content; K salt) and PVP, 5/95 mixing ratio.

SESSION EIGHT:

DEFORMATION IN SPECIAL MATERIALS II

DEFORMATION MICROMECHANICS IN MODEL POLYESTER-POLYOLEFIN BLENDS

R.M. Casado, P.A. Lovell, J.L. Stanford and R.J. Young*

A range of diacetylene-containing polyesters have been prepared by polycondensation of terephthaloyl chloride with a series of diacetylene diols These polyesters were blended with isotactic polypropylene and the blends compression-moulded into dumbbell specimens, which then were exposed to ^{60}Co γ-radiation to effect cross-polymerization of the polyester phases. The dumbbell specimens were subjected to simultaneous tensile testing and resonance Raman spectroscopy, and the shift in wavenumber of the C≡C stretching band of the polydiacetylene crosslinks used to determine the local stress in the polyester phases independent of the overall applied stress, thereby facilitating determination of the efficiency of stress transfer in the blends.

INTRODUCTION

Solid-state topochemical *cross-polymerization* of conjugated diacetylene units in polymer chains was first reported [1,2] in 1970 and yields network materials with polydiacetylene crosslinks. Of particular relevance to the work presented here is the ability to study deformation micromechanics of such cross-polymerised polymers using the stress dependence of the wavenumber of the Raman band for stretching of C≡C bonds in the polydiacetylene crosslinks [3]. In a previous study, a diacetylene-containing polyester was prepared that was suitable for blending with a low-melting poly[ethylene-*co*-(vinyl acetate)] [4-6]. The blends were compression-moulded into tensile specimens with simultaneous thermal cross-polymerization of the polyester phases, and stress transfer between the phases during tensile testing was monitored by Raman spectroscopy [5,6]. In the present study, a range of diacetylene-containing polyesters have been prepared and those suitable for blending with higher-melting polymers identified. The properties and stress transfer in model blends of these polyesters with isotactic polypropylene are described.

EXPERIMENTAL

Preparation of Diacetylene-Containing Polyesters

A series of diacetylene diols of general structure $HO–(CH_2)_n–C≡C–C≡C–(CH_2)_n–OH$ were prepared as described elsewhere [7] by oxidative coupling of the corresponding acetylenic alcohol ($HO–(CH_2)_n–C≡CH$) [2]. Diacetylene-containing polyesters were prepared from each diacetylene diol by reaction in solution with terephthaloyl chloride in 1:1 stoichiometry for 5 h at 0 °C. Each polyester was obtained in the form of a white powder which was washed first with 0.1 M HCl and then with deionised water before drying. The nomenclature for the polyesters is exemplified by PE(n=3), which defines the polyester prepared from $HO-(CH_2)_3–C≡C–C≡C–(CH_2)_3-OH$.

* Polymer Science and Technology Group, Manchester Materials Science Centre, University of Manchester & UMIST, Grosvenor Street, Manchester, M1 7HS, UK.

Preparation, Moulding and Cross-Polymerization of Model Blends

Blends of PE(n=3) and PE(n=9) with isotactic polypropylene (Himont S30S), PP, were prepared as follows. In each case the polyester was first blended in the appropriate proportion with the PP by dissolution in boiling xylene, followed by co-precipitation into a large excess methanol [7]. After drying, the blend was compression-moulded directly into dumbbell specimens (gauge section 28 × 6 × 3 mm) in a pre-heated mould at 180 °C for a period of about 180 s before cooling to room temperature. The diacetylene-containing polyester phases were then cross-polymerised by exposure to ^{60}Co γ-radiation to a dose of 40 MRad, causing the specimens to attain the deep green/purple colour characteristic of polydiacetylenes.

Characterization Methods

Differential scanning calorimetry, DSC, was performed on a DuPont 2000 Thermal Analyst instrument with a DuPont 910 cell base equipped with a DSC cell. Powdered samples (~10 mg) were analysed over the range -50 to 400 °C at a heating rate of 20 °C min^{-1}. Resonance Raman spectra of cross-polymerised polyester powders were recorded using a Renishaw 1000 Raman spectrometer as described elsewhere [7].

Simultaneous Tensile Testing and Raman Spectroscopy

The cross-polymerised dumbbell specimens were subjected to simultaneous tensile testing and Raman spectroscopy measurements at 20±3 °C. The specimens were deformed to failure in a stepwise manner in a Polymer Laboratories Minimat miniature mechanical tester fitted with a 1 kN load cell. The overall strain on a specimen was measured using a resistance strain gauge (accuracy ±0.0014% strain) bonded to the specimen. Raman spectra containing the C≡C stretching band [7] were recorded immediately after each deformation step. At least 3 specimens of each material were tested and mean values of tensile properties determined.

RESULTS AND DISCUSSION

Preparation and Properties of the Diacetylene-Containing Polyesters

The diacetylene-containing polyesters were analysed by DSC to determine their melting points (T_m) and the temperature (T_{exo}) associated with thermal cross-polymerization of the diacetylene units. The results [7] showed that PE(n=1) did not melt, but underwent solid-state topochemical cross-polymerization with T_{exo} = 167 °C, in accord with previous observations [4-6]. Each of the other polyesters showed both a melting endotherm and a cross-polymerization exotherm, with T_m decreasing and T_{exo} increasing as the number of methylenes in the diacetylene unit increased. Thus, the objective of increasing the processing window (i.e., $T_m \rightarrow T_{exo}$) was achieved. However, the additional requirement that cross-polymerization should not occur during moulding required further evaluation of the polyesters. Hence, for each polyester, the susceptibility to solid-state topochemical cross-polymerization was investigated using three treatment methods: (i) heating below the melting point in the dark under N_2 for 15-90 h, (ii) exposure to radiation from a 9 W UV lamp at room temperature for 24 h, and (iii) exposure to ^{60}Co γ-radiation at room temperature to a dose of

Table 1. Susceptibility of the polyesters to cross-polymerization under different methods of treatment

Polyester	Method for Cross-Polymerization		
	Thermal	UV light	γ-radiation
PE(n=1)	•	•	•
PE(n=2)	•	•	•
PE(n=3)	×	•	•
PE(n=4)	×	(•)	(•)
PE(n=9)	×	•	•

40 MRad at approximately 0.2 MRad h^{-1}. The results are summarised in Table 1 and show that PE(n=3) and PE(n=9) have properties which make them suitable for blending with PP to give materials which can be moulded without simultaneous thermal cross-polymerization.

Preparation and Properties of the Model Blends

Two series of blends of PP with PE(n=3) and PE(n=9), respectively, were prepared and compression-moulded, without thermal cross-polymerization of the polyesters, using the procedures described in the experimental section. These materials comprised 20, 40, 60 and 80 wt.-% polyester and were a slightly off-white colour after moulding. The blends were analysed by DSC which showed the characteristic melting endotherms of the polyester and the PP (T_m = 167 °C), and the cross-polymerization exotherm of the polyester.

Exposure of the moulded tensile specimens to ^{60}Co γ-radiation led to solid-state topochemical cross-polymerization of the diacetylene units in the polyester phases. Each specimen was then subjected to tensile testing with simultaneous Raman spectroscopy. Cross-polymerised specimens of PE(n=3) and PE(n=9) were tested first in order to determine the variation of the wavenumber ($\Delta\nu^{C\equiv C}$) with applied stress (σ) for the C≡C stretching band of the polydiacetylene crosslinks. For both polyesters, $\{d(\Delta\nu^{C\equiv C})/d\sigma\}_{\sigma\to 0}$ was -0.11 ± 0.01 cm^{-1} MPa^{-1}. The measurements of $\Delta\nu^{C\equiv C}$ for the deformed blends were converted into local stresses in the polyester phases using the corresponding $\Delta\nu^{C\equiv C}$ versus σ curve for the cross-polymerised polyester. In this way the non-linear elastic behaviour of the polyesters was taken into account. The conventional stress-strain curves and the curves of local stress in the polyester phases versus overall applied stress (from the shift in $\Delta\nu^{C\equiv C}$ and the load cell response) are shown in Figures 1 & 2 for the PE(n=3) and PE(n=9) blend series, respectively. For the blends containing 80 and 60 wt.-% PE(n=3), the local stress in the polyester is equal to the applied stress, showing that the distribution of stress between the phases is uniform. However, stress transfer to the polyester phase is inefficient in the blends comprising 40 and 20 wt.-% PE(n=3) and diminishes as the applied stress increases, suggesting partial debonding of the polyester during deformation. In contrast, whilst the stress distribution in the blends comprising 20, 40 and 60 wt.-% PE(n=9) is uniform, the blend with 80 wt.-% PE(n=9) shows higher stress in the polyester phase as the applied stress increases, indicative of stress concentrations arising from debonding of the PP during deformation.

Thus, in conclusion, the results presented here clearly demonstrate that the approach described in this paper is capable of providing unique real-time information about stress-transfer between phases during deformation of polymer blends.

ACKNOWLEDGEMENTS

The authors express their thanks to the Royal Society, EPSRC and Basque Government (Spain) for funding the study. RMC-P would like to thank UMIST for a Mohn scholarship.

REFERENCES

1. G. Wegner, *Makromol. Chem.*, **134** (1970) 219
2. A.S. Hay, D.A. Bolon, K.R. Leimer and R.F. Clark, *J. Polym. Sci., Poly. Lett. Ed.*, **8** (1970) 97
3. X. Hu, J.L. Stanford, R.J. Day and R.J. Young, *Macromolecules*, **25** (1992) 672 & 684
4. P.A. Lovell, J.L. Stanford, Y-F. Wang and R.J. Young, *Polym. Int.*, **34** (1994) 23
5. P.A. Lovell, J.L. Stanford, Y-F. Wang and R.J. Young, *Polym. Bull.*, **30** (1993) 347
6. Y.-F. Wang, PhD thesis, Victoria University of Manchester, 1992
7. R.M. Casado, P.A. Lovell, J.L. Stanford and R.J. Young, *Macromol. Symp.*, in press.

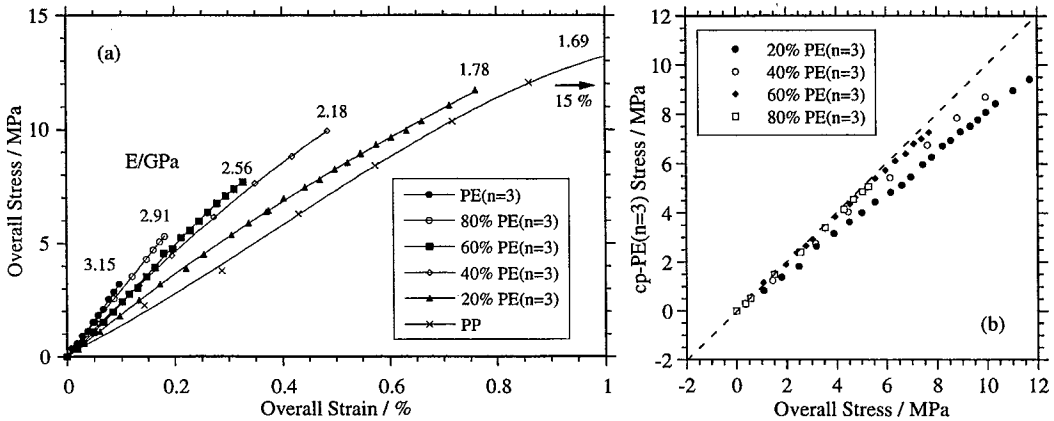

Figure 1 Data from simultaneous tensile testing and Raman spectroscopy of the PP/PE(n=3) blends after cross-polymerization of the polyester phases.
(a) Stress-strain curves (Young's modulus values are given against the curves for each of the materials).
(b) Local stress in the polyester phases plotted against the overall applied stress.

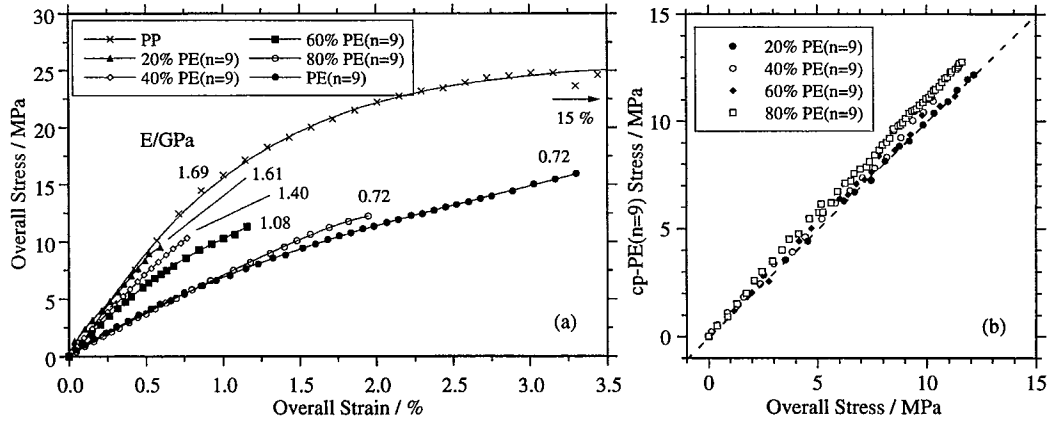

Figure 2 Data from simultaneous tensile testing and Raman spectroscopy of the PP/PE(n=9) blends after cross-polymerization of the polyester phases.
(a) Stress-strain curves (Young's modulus values are given against the curves for each of the materials).
(b) Local stress in the polyester phases plotted against the overall applied stress.

DEFORMATION MECHANISMS IN CLOSED-CELL LDPE FOAMS

N.J. Mills, A. Gilchrist and H.X. Zhu
School of Metallurgy and Materials, University of Birmingham

INTRODUCTION

Closed-cell low density polymer foams are used for packaging and impact protection. The average cell diameter in commercial foams ranges from 0.05 to 2 mm. Low density polyethylene (LDPE) foams, which recover well after compression, were categorised as 'elastomeric' by Gibson and Ashby[1]. Cell gas compression and polymer deformation are analysed to predict the compressive stress-strain curve.

GAS COMPRESSION

Gas pressure loss by diffusion through the cell faces does not occur for creep times less than 1 hour[2], so it will be ignored in the analysis. Cell gas compression has been assumed to be isothermal[1], or adiabatic on the time scale of an impact[3], without evidence. Burgess[4] considered these extreme cases, calculating the cushion curves (graphs of the maximum acceleration of the packaged object versus the gravitational stress on the foam, for a given drop height) for foams with a negligible polymer yield stress. He assumed natural convection inside the cells, and a zero foam Poisson's ratio. He showed that experimental data for LDPE foam of density 35 kg m^{-3} fell between the isothermal and adiabatic predictions, but was unable to solve the equations for intermediate conditions.

Assuming that the initial cell pressure is atmospheric p_a, and that the polymer structure has an initial yield stress σ_0, the foam compressive stress σ is related to the strain ε by

$$\sigma = \sigma_0 + p_a\left(\frac{1-R}{(1-\varepsilon)(1+\nu\varepsilon)^2 - R} - 1\right) \qquad (1)$$

where R is the foam relative density. If Poisson's ratio ν is zero, the term in brackets becomes $\varepsilon/(1-\varepsilon-R)$, a variable referred to as the *gas volumetric strain*. If eqn. (1) is obeyed, a graph of stress against $\varepsilon/(1-\varepsilon-R)$ is almost linear, with initial slope $p_a(1-2\nu)$. For adiabatic gas compression, the stress-strain relationship is predicted to be[2]

$$\sigma = \sigma_0 + p_a\left(\frac{1-R}{(1-\varepsilon)(1+\nu\varepsilon)^2 - R}\right)^{\gamma} - p_a \qquad (2)$$

where γ, the ratio of the constant volume and constant pressure specific heats, is 1.40 for air.

In general there is coupled deformation and heat transfer, since cell deformation affects the heat transfer time scale, and gas heating affects the gas pressure. Glicksman [5] argued that the Rayleigh number, for air in *undeformed* foam cells of diameter 0.5 mm, is so small (0.01) that natural convection does not occur. We assumed that forced convection did not occur, in spite of the rapid change of cell shape in an impact. The polymer properties are assumed to be temperature invariant; it is found later that polymer heating is minimal under the usual impact conditions. The thermal diffusivity of air at STP is 1.88 $mm^2\ s^{-1}$, and 0.1 $mm^2\ s^{-1}$ for LDPE. In the one-dimensional finite difference model, heat diffuses in a layer of air of varying thickness, connected to a polymer layer. As the cell face thickness is much less than the cell diameter, the Fourier number for the face is much smaller than that for the gas. The foam simulated was a 50 mm thick layer of LDPE of density 24 kg m^{-3}, of negligible initial yield

stress, which is compressed to 80% strain in an impact at 7 m/s. Its Poisson's ratio of 0.15, measured at small strains, is assumed to remain constant. For 0.2 mm diameter cells the conditions are predicted to be nearly isothermal(see table). An increase in cell diameter from 0.2 to 5 mm changes the conditions from nearly isothermal to nearly adiabatic, increasing the effective strain hardening rate of the LDPE foam (the p_0 factor) by 77%. Figure 1 shows that the hysteresis, in the stress-strain curve for a 1 mm cell diameter, is due to the time lag between the air temperature rise and the polymer temperature rise.

cell Diameter mm	Air Temp rise	Polymer temp rise	p_0 kPa
0.2	11	9	75
1	93	8	107
5	188	1	133

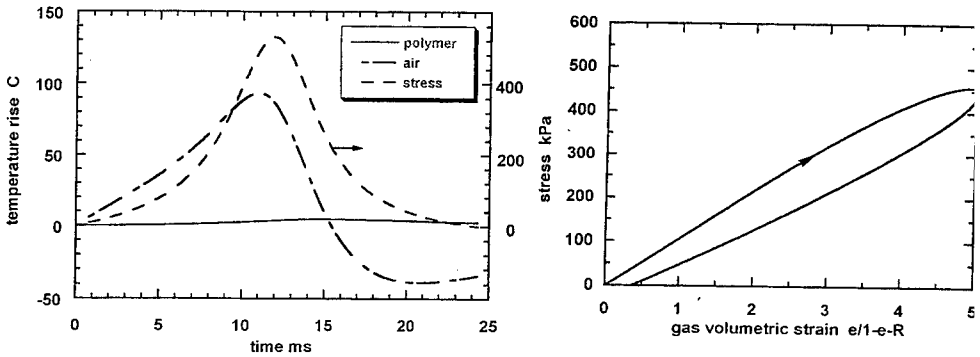

Fig. 1 a) predicted temperatures vs. time, b) stress-strain relation for LDPE with 1 mm cells.

An experimental impact compression curve for a LDPE with average cell diameter of 1.3 mm is shown in figure 2. The loading slope of 70 kPa (the value was 79 kPa at a lower strain rate of 4×10^{-3} s^{-1}) indicates that the heat transfer conditions are still nearly isothermal. The model predicts a greater loading slope; the inference is that there is forced convection in the cells. However it is difficult to estimate the effective heat transfer coefficient.

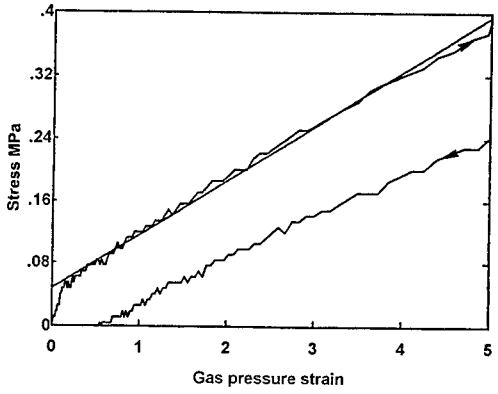

Fig. 2 Impact compressive stress of LDPE foam, vs. the gas compression strain.

FACE AND EDGE DEFORMATION IN THE FOAM

The unloading curve in figure 2 has a slightly lower slope, but considerably lower vertical position, than the loading curve. This implies that some 'yielding' process has occurred, rather than an elastic response, for which the curves should superimpose. This 'yielding' is a polymer, rather than an air, contribution. A lattice model of tetrakaidecahedral cells, developed for open cell foams[6], was modified by the addition of uniform thickness cell faces. The faces are assumed to be thin compared with the edges, which have Plateau border cross-sections(3 touching circular arcs), and the polymer is assumed to be linearly elastic. Compression was analysed for loading in the [100] lattice direction. Figure 3a shows the square and hexagonal faces in a structural cell in the deformed lattice, which has mirror boundaries. Slanting edges such as BC bend under the compressive force F, the moments which prevent its ends rotating, and the moments from the stretched faces(fig. 3b). The analysis requires an iterative numerical solution [7].

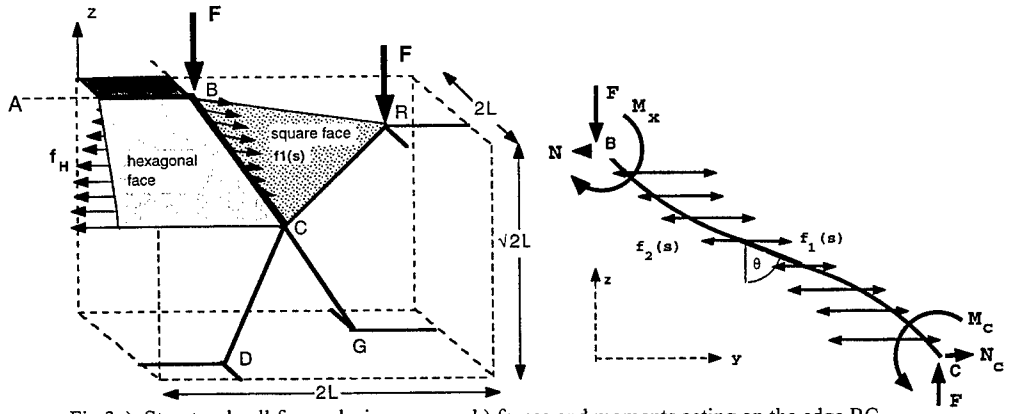

Fig 3a) Structural cell for analysis b) forces and moments acting on the edge BC

The LDPE Youngs modulus 300 MPa for a 0.01 s impact time-scale was extrapolated from creep compliance data for times from 0.1 to 10^6 s. The predicted stress-strain curve closest to experimental data for LDPE foam of density 24 kg m^{-3} (figure 4), is for cells with Plateau border edges of length 600 μm and radial distance to the cusps of 118 μm, face thicknesses 2.5 μm, and relative density 0.025. The real foam edge dimensions, a mean edge length of 620 μm and radial distance to the cusps of 36 μm, indicate that the face volume fraction ϕ_f = 0.93 is much higher than the 0.20 in the simulation. If a ϕ_f=0.4 value is used the predicted stress is 35% too high at 20% strain, but rejoins the experimental data at 50% strain. The calculation will not converge if ϕ_f>0.75. The polymer contribution for ϕ_f = 0.2, calculated by subtracting the gas pressure contribution, reaches a plateau for strains exceeding 30%, since the stretched faces exerting lower moments on the deformed edges. The predicted unloading response is the same as for loading, which is clearly wrong.

The vertical square face in figure 3 undergoes high tensile strains; the arrows indicate the form of the stress distribution, with maximum stresses across the face centres. High face strains also occur for [111] direction loading, in which the edges bend and twist. The model predicts that the foam initial Youngs modulus is given by

$$E_{001} = 1.05\,E\,R_e^2 + 0.22\,ER_f \qquad (3)$$

where R_e and R_f are the relative densities of edges and faces. The R_e coefficient justifies the value $\cong 1.0$, deduced by Gibson and Ashby by fitting a quadratic relationship to experimental data. The R_f coefficient is considerably smaller than the value $\cong 1$ that they inferred, but they made the unreasonable assumption that the proportion of polymer in the faces was > 0.6.

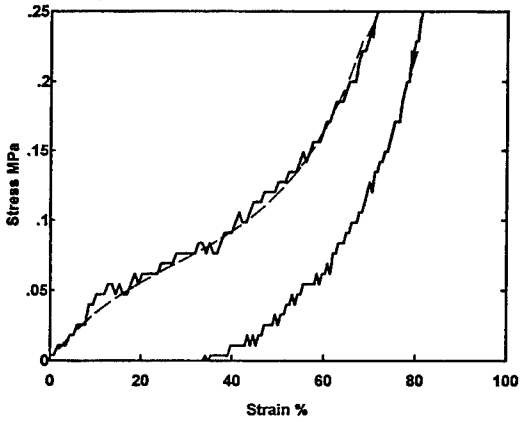

Figure 4. Stress-strain curve for a LDPE foam and the prediction of the closed cell model.

DISCUSSION

For LDPE closed cell foams, the gas pressure hardening equation (1) is an advance on the empirical equations of Gibson and Ashby and others. There is no need for a 'densification' term, starting at an arbitrary strain level when edges touch. Heat transfer from the cell gas to the polymer faces is so effective that the air remains nearly isothermal even for impacts at 5 m/s, a useful simplification. The contribution of cell faces to the compressive stress-strain curve has been predicted quantitatively for the first time; the effect on the initial Youngs modulus is large, but less at higher strains. For foam strains greater than 10% the analysis predicts high tensile strains in some faces; these probably undergo non-linear viscoelastic deformation. This explains why the unloading curves have negative intercepts on the stress axis. If the polymer has a non-linear response, this will affect the foam response at strains > 10%, so predictions for face contents $\phi_f = 0.9$ should be closer to the experimental data than the present linear elastic model. Analysis for loading the lattice in the [111] direction would be better since the edges both bend and twist. It is unreasonable to assert that LDPE foams are 'elastomeric', or that the initial 'yield' stress σ_o is due to elastic buckling. For the more rigid polystyrene closed cell foams, polymer yielding will be an essential part of the compressive analysis. This analysis has been started, but there are considerable problems.

References

1. Gibson, L.J. & Ashby, M.F., (1988), *Cellular Solids*, Pergamon, Oxford.
2. Mills N.J. and Gilchrist A. (1997) Cellular Polymers, **16**, to appear
3. Throne J.L. & Progelhof R.C. (1984), J Cellular Plastics, **20**, 437-442.
4. Burgess G.J.(1988) , J. Cellular Plastics, **24**, 56-69.
5. Glicksman L.R. (1994) Heat transfer in foam, in *Low Density Cellular Foams*, Eds. N. Hilyard and A.C. Cunningham, Chapman and Hall.
6. Zhu H.X., Mills N.J. and Knott J.F., submitted to J. Mech. Phys. Solids,.
7. Mills N.J. & Zhu, H.X., submitted to Cellular Polymers.

THE EFFECT OF MECHANICAL DEFORMATION ON LIGHT TRANSMISSION IN POLYMERIC OPTICAL FIBERS

PM Pakhomov*, SD Khizhnyak* and AI Zubkov**

The effect of mechanical deformation (bending, tensile drawing, compression) on light transmission in polymeric optical fibers with a PMMA core was studied by optical spectroscopy, microscopy and light scattering. Depending on bending curvature and static stress, reversible and irreversible changes in light transmission were observed. In all cases, irreversible changes were related to the appearance in PMMA of crazes, with scattering the light. The reversible changes were accounted for by violation of the law of total internal reflection on reversible geometrical changing the light guide.

INTRODUCTION

Polymeric optical fibers (POF) are widely used for the short-range transfer (to 100 m) of light and information. As compared to quartz light guides, POF offer a number of additional advantages, wich involve preparation of fibers with larger diameter, simplicity of their attachment, flexibility, etc. [1].

During their assemly and exploitation POF may be subjected to the action of many mechanical stresses (bending, tensile drawing, compression, etc.). In connection with this, the effect of such factors on the optical properties of light guides is of great interest. This work focuses on the effect of mechanical deformation on light transmission in POF.

EXPERIMENTAL

We used POF with a PMMA core coated with a reflecting lager based on poly (fluoroacrylate)

$$-[CH_2\text{-}C(CH_3)]_n-$$
$$\quad\quad\quad

In the case of bending tests, the dependence of the attenuation loss α on curvature R was presented as follows

$$\alpha = \frac{10}{2\pi\rho}\log\left(I_0/I\right). \qquad (2)$$

The relationship between static compressing stress σ and attenuation loss α was estimated using following formula

$$\alpha = \frac{10}{L}\log\left(I_0/I\right). \qquad (3)$$

Here, Δl stands for changes in the length of POF under stress σ; ρ=R+r (r is fiber diameter); L is length of POF; I_0 and I are intensities of monochromatic radiation passing through the sample before and after loading. The measurements were carried out using an instrument equipped with a light source, monochromator, and a light detector signal operating at 640 nm. To estmate the attenuation loss associated with light scattering, we used the equipment described in [3]. The density of the crazes was measured using a Leitz Artalux-2 optical microscope.

RESULTS AND DISCUSSION

We found that when POF samples are bent, attenuation loss appears to increase as bending curvature decreases according to the parabolic law (Fig.1, curve 1). At a bending curvature higher than R≅4 mm, no marked changes in the light transmission of POF were observed. A substantial attenuation loss was observed only after a further decrease in R. When the samples are relieved of the applied stress, and the free-standing fibers take their initial shape, light transmission partially recovers but does not attain the initial value (Fig.1, curve 2). With decreasing R, an increase in irreversible attenuation loss also follows the parabolic law. Hence, total attenuation loss α determined by formula (2) can be resolved into two components

$$\alpha = \alpha_r + \alpha_i , \qquad (4)$$

were α_r and α_i stand for reversible and irreversible loss, respectively.

Reversiblle attenuation loss is primarily associated with chnges in the geometry of POF. For some rays, the condition of total internal reflection does not hold (Fig.2, ray A), and the refracted rays leave the fiber. This results in light emission at the bending regions. A decrease in bending curvature is accompanied by an increase in both the fraction of the rays that leave the light guide and attenuation loss in POF.

Figure 3 shows the effect of tensile drawing (under static load) on the light transmission of POF. As in the case of bending, one can observe both reversible and irreversible components of attenuation loss. The dependence of attenuation loss on the applied stress is similar to that on bending curvature (Figs.1 and 3). Significant irreversible attenuation loss occurs at σ=40 MPa. The dependence of POF light transmittion on value of loading stress was similar to that presented in Figure 1 and 3.

We assumed that in all cases (bending, tensile drawing and compression) irreversible attenuation loss is related to the light scattering on microheterogeneities (crazes) arissing in the POF core under mechanical stresses. Actually, when POF samples are drawn, compressed or the bending curvature decreases, an increase in the intensity of the light scattering is proportional to the growth in irreversible attenuation loss. The linear dimensions of the

scattering defects (in our case, crazes) as estimated from the angular distribution of the indicatrix of the Rayleigh scattering [3] were ~100 nm.

In our case, reversible attenuation loss is also associated with scattering on crazes, the density of which increases with an increase in the static applied load. However, when the sample is relieved of the applied stress, such crazes are able to "heal" [2,4] and produce no scattering. Actually, in the stress-relieved samples, we observed a decrease in light scattering and crase density in the POF core. Direct microscopic observations showed an increase in craze density with a decrease in the bending curvature or with an increase in the strain and compression of POF samples. Figure 4 presents the dependence of craze density on bending curvature. At R=1.5 mm, craze density was 600 per 1 mm^3. The dependence of craze average dimension on bending curvature had parabolical character too [5].A comparision of Figs.4 and 1 reveals their qualitative similarity. A quantitative comparision of irreversible attenuation loss, craze density and average dimension reveals their linear dependence [6]. Irreversible attenuation loss appears to be proportional to the craze density and average dimension in the POF core. The effect of crasing on the mechanical and optical properties of POF was discussed in [7].

This approach can be applied in practice to estimate the quality of POF under certain operating conditions. This approach also allows one to monitor the quality of POF and to select optimal mechanical loading for assembling and operating POF.

REFERENCES

1. Gower J, "Optical Communication Systems", (London), 1984
2. Pakhomov PM, Dushkin AA and Chegolya AS, 1993, Mekhanika Kompozitnykh Materialov, 5, 732
3. Koike Y, Tanio N and Ohtsuku Y, 1989, Macromolecules, 22, 1367
4. Volynskii AL and Bakeev NF, "Highly Disperse Oriented State of Polymers", (Moscow), 1984
5. Khizhnyak SD, Zubkov AI, Levin VM and Pakhomov PM, 1996 , Physics-chemistry of polymers, 2, 89, TSU (Tver)
6. Pakhomov PM, Zubkov AI and Khizhnyak SD, 1994, Polymer Sci. (Russia), 36B, 1143
7. Dvoranec L, Machova L, Sorm M, Pelzbauer Z, Svatner J and Kubanek V, 1990, Angew. Makromol.Chem., 174, 25

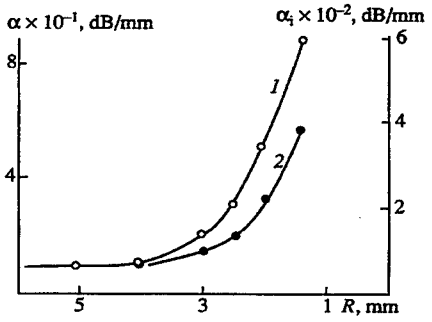

Figure 1. (1) Total and (2) irreversible attenuation loss in POF vs. bending curvature

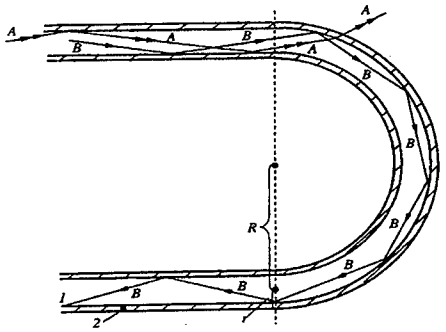

Figure 2. Development of reversible attenuation loss on bending POF. (A) light ray leaving POF, (B) light ray transmittiny along POF. (1) POF core, (2) reflecting POF outer layer. R - bending curvature, r - radius of POF

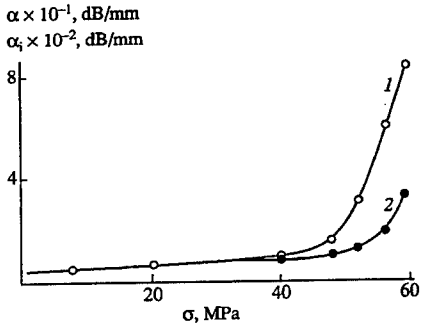

Figure 3. (1) Total and (2) irreversible attenuation loss in POF vs. tensile stress

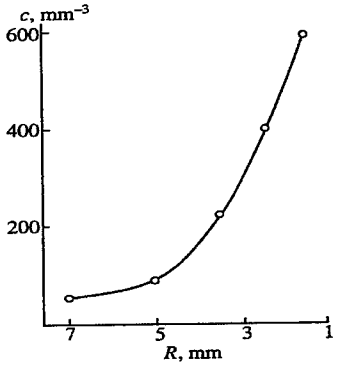

Figure 4. Crase density in POF vs. bending curvature

SESSION NINE:

TOUGHENING MECHANISMS I

59

IN-SITU X-RAY STUDIES DURING DEFORMATION OF RUBBER TOUGHENED AMORPHOUS POLYMERS

B.J.P. Jansen, S. Rastogi, H.E.H. Meijer and P.J. Lemstra *

The relationship between the morphology and the microscopic deformation mechanism in (toughened) amorphous polymers has been studied extensively for a variety of samples in our laboratory. We have demonstrated that polystyrene (PS) could be toughened via a transition in deformation mechanism from crazing, the common deformation mechanism in (high-impact) PS (2), to shear yielding. To achieve toughening, an extremely fine rubber morphology is required, ultimately resulting in extremely thin matrix ligaments, or alternatively, a small interparticle distance (1).

Presently we are aiming at heterogeneous polymer systems possessing a very finely dispersed rubbery phase, to achieve a small interparticle distance, at an as low as possible volume fractions in order to retain sufficient stiffness and strength. Since these nano-size morphologies cannot be prepared via conventional blending routes, two novel blending processes are developed. As a model material for the present study poly(methylmethacrylate), PMMA, was used.

In the first process, an aliphatic (rubbery) epoxy resin is used as a reactive solvent for PMMA. A homogeneous PMMA-epoxy solution is prepared which is subsequently cured causing chemical induced phase separation (CIPS). The final rubber morphology can be controlled via the curing temperature applied and, by preventing coalescence after CIPS occurred, an extremely fine dispersed rubbery phase can be realised in a continuous PMMA matrix.

Alternatively, a second process is developed to prepare PMMA/rubber blends possessing the required morphologies, starting with the monomer (MMA), mixed with epoxy resin and curing agent. The free radical polymerisation of MMA and curing of the epoxy resin are simultaneously performed resulting in a thermoplastic PMMA matrix phase and a rubbery epoxy phase. Via this route, transparent toughened blends can be prepared up to a rubber concentration of approximately 50 wt%. Given the maximum strain at break of PMMA (~10%) and that of the aliphatic epoxy (~30%), a remarkable synergy was found in this system, resulting in a maximum strain at break of ~150% for the PMMA/epoxy 60/40 composition (see figure1).

The relation between rubber morphology and deformation mode at a microscopic level was studied using *in-situ* small angle X-ray scattering (SAXS) during a tensile loading. These experiments were performed on the blends, prepared via the second route, and on high-impact polystyrene (HIPS) as reference material. In order to monitor the microscopic deformation and orientation during the drawing process, the SAXS patterns were analyzed by the integration over the azimuth angle (90 bins of each 4°) as presented in figure 2. The scattering

* Eindhoven Polymer Laboratories (EPL), Eindhoven University of Technology, P.O. box 513, 5600 MB Eindhoven, The Netherlands

perpendicular and parallel to the tensile direction is measured at an azimuth angle of respectively 0° or 180° and 90° or 270°.

In figure 3 the SAXS patterns as function of tensile deformation time are presented for the brittle PMMA/epoxy 90/10 blend. Since hardly any morphological scattering is present prior to tensile testing (figure 3a) all observed changes are attributed to the deformation on microscopic level. After some deformation time, sharp streaks in the tensile direction become visible (figure 3b). This is followed by the development of a star shape pattern as shown in figure 3c and 3d. A similar development in scattering pattern is observed for HIPS and is attributed to the development of crazes (3,4). In figure 4 the three-dimensional plots of the azimuth angle versus the intensity as function of deformation time are presented. For both the PMMA/epoxy blend and HIPS the scattering in the tensile direction is much stronger than the craze-fibril scattering observed perpendicular to the tensile direction.

The PMMA/epoxy 80/20 blend behaves more ductile during tensile testing which results in an enhanced strain at break. As can be observed in figure 4c, the deformation mode in the PMMA/epoxy 80/20 blend is clearly different to the previously described blends. During the early stages of deformation again an orientation in the tensile direction is observed. Next the overall scattering intensity suddenly increases accompanied by a further orientation in the tensile direction which can be explained by the development of small crack like cavities. At higher draw ratios, however, the scattering intensity in the tensile direction decreases while that at an azimuth angle of 180° is clearly developing. This is most likely the result of shear yielding which causes thinning of the sample and orientation of the formed cavities into the tensile direction. This is confirmed by the elliptical shaped scattering pattern as shown in figure 5c which has been monitored at the end of the deformation process prior to fracture.

At a rubber content to 30 wt%, the strain at break increases to values higher than 100%. From the SAXS pattern analyses, as shown in figure 4d, it is obvious that again a different mode of microscopic deformation occurs during tensile testing. Except from the minor maximum at the initial stages of the tensile experiment, sudden changes in the overall intensity as a result of processes involving dilation are not observed. At higher draw ratios the overall intensity is decreasing which is most likely the result of a reduction in cross sectional area. At the end of the drawing process the morphology is clearly oriented as can be concluded from the enhanced intensities at the azimuth angles parallel and perpendicular to the tensile direction. Therefore it can be concluded that this blend mainly deforms via shear yielding.

REFERENCES

1. M.C.M. van der Sanden, H.E.H. Meijer, P.J. Lemstra, Polymer 34 (1993) 2148
2. C.B. Bucknall, 'Toughened Plastics', Applied Science Publishers LTD (London), 1977
3. H.R. Brown, E.J. Kramer, J. Macromol. Sci.- Phys., B19 (1981) 487
4. R.A. Bubeck, D.J. Buckley, E.J. Kramer, H.R. Brown, J. of Mat. Sc. 26 (1991) 6259

ACKNOWLEDGEMENT

Authors wish to acknowledge the experimental facilities available at the beamline ID2-BL4 of the European Synchrotron Radiation Facility (ESRF) Grenoble France, especially Dr. P. Boesecke (ESRF).

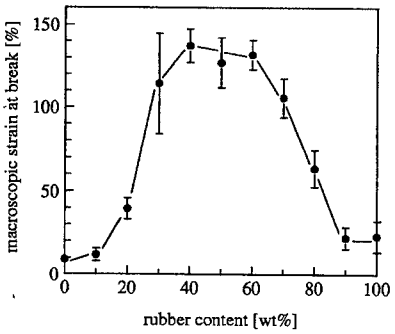

Figure 1: Strain at break vs. epoxy content of PMMA/epoxy blends.

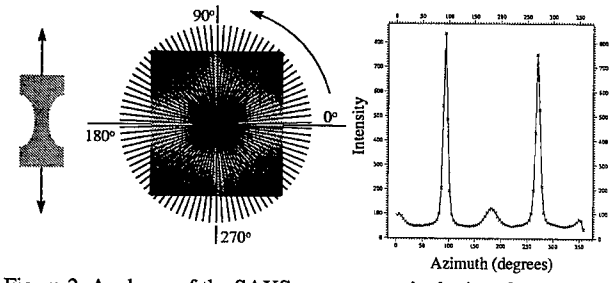

Figure 2: Analyses of the SAXS pattern at a single time frame.

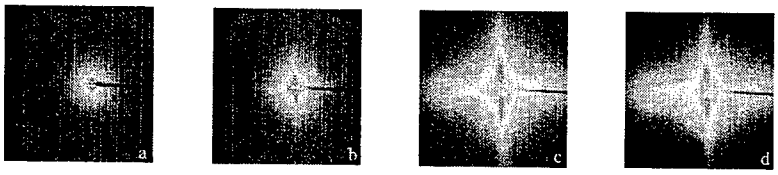

Figure 3: SAXS pattern development as function of deformation of PMMA/epoxy 90/10 blend.

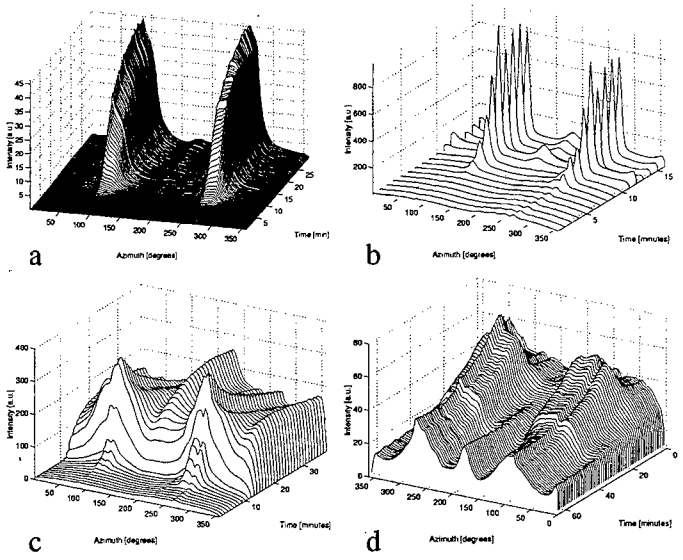

Figure 4: Intensity vs. azimuth angle as function of deformation time, a) HIPS and PMMA/epoxy b) 90/10, c) 80/20, d) 70/30.

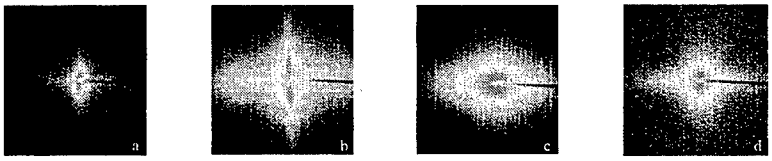

Figure 5: SAXS patterns measured during the final time frame, prior to fracture, a) HIPS and PMMA/epoxy b) 90/10, c) 80/20, d) 70/30.

SYNCHROTRON STUDIES OF *IN SITU* DEFORMATION OF RUBBER TOUGHENED PMMA

Chaobin He*, Michael F Butler* and Athene M Donald*

Synchrotron radiation has been used to permit real time studies of the deformation of rubber toughened PMMA, where the rubber particles have a core-shell morphology. The effect of particle concentration and rubber crosslinking density on the propensity for crazing has been quantitatively evaluated.

Introduction

The subject of rubber toughening has re-emerged in recent years as a subject of scientific controversy, with the realisation that crazing is far from the only toughening mechanism possible in many glassy polymer matrices (1-4), and indeed may not be a source of toughness at all (5). This finding originated with the observation made using *in situ* synchrotron deformation studies on high impact polystyrene (HIPS) that crazing only contributed a relatively small amount to the total deformation, and that other non-crazing mechanisms came into play before there was any crazing at all (1). In this paper we present data on core-shell rubber toughened PMMA investigating how the crazing density depends on both rubber particle loading and the characteristics of the rubber. This data has been obtained from *in situ* tensile testing at synchrotron sources.

Experimental

Rubber toughened PMMA was supplied by ICI plc with five different concentrations of rubber particles of 10 wt-%, 20 wt-%, 30 wt-%, 40 wt-% and 50 wt-%. The crosslinking densities of the rubber layer in this study are 0.5%, 1%, 2% and 5%. In total we had 20 samples in this study. The rubber particle has a three layer structure: a PMMA core of 80-85 nm radius, a rubber middle layer of 40-50 nm thickness and a thin outer PMMA layer. The rubber phase therefore only counts for about 50 wt-% of the total rubber particle. The samples were first extruded to ensure proper mixing of the core shell rubber particles and PMMA matrix, and then compression moulded to about 1.10 mm to 1.25 mm thick plaques, which were subsequently machined to an area of 20 x 50 mm^2. Two circular stress concentrators with a radius of 6 mm were machined opposite to each other in the middle of the sample to ensure that the X-ray beam passed through the region of deformation during tensile testing. Samples were studied at both the ESRF (Grenoble), beamline ID2-BL4, and at the SRS (Daresbury), beamline 2.1. Lower angles could be studied at ESRF. Polymer samples were stretched using a Minimat tensile testing machine, with a fixed extension rate of 0.5mm/min. The tensile curve and SAXS data were recorded simultaneously, although due to the non-uniform shape of the sample it was difficult to extract a true stress-strain curve from this. Data was collected at 6s intervals at the ESRF and 8s at the SRS, and around 40 frames were collected for each sample.

Results and Discussion

The standard way to extract the amount of crazing from SAXS data is via invariant analysis. As has been pointed out by Magalhaes (5) if additional deformation mechanisms are occurring within the particle itself (eg cavitation) this may affect the low q contribution to the analysis.

* Cavendish Laboratory, University of Cambridge, UK

Analysing the low q data obtained at the ESRF (typical scattering curves shown in figures 1 and 2 for 10 and 40% concentration of particles) it has been possible to show that this scattering only leads to an increase of ~10-20% in the invariant, as the particle itself deforms by up to 50% (as measured by the change in principal axes of the ellipse which defines the form factor scattering). Thus, for this family of toughened polymers at least, analysing the invariant by simply subtracting the undeformed sample scattering from the scattering at each stage of deformation is an adequate approximation.

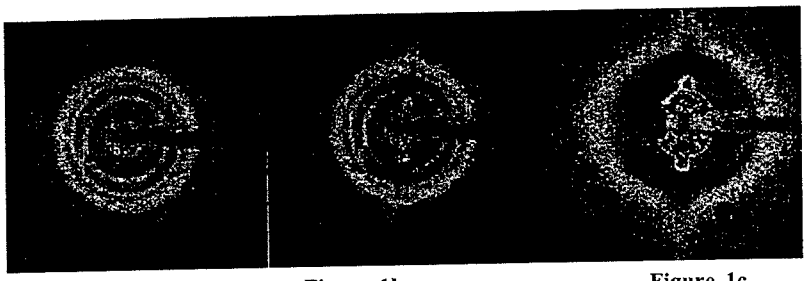

Figure 1a **Figure 1b** **Figure 1c**

Figure 1: 2-D SAXS of deformed rubber toughened PMMA with 10 wt.-% of rubber particles; a) undeformed; b) extension of 1 mm and c) extension of 1.75 mm. Tensile axis: vertical.

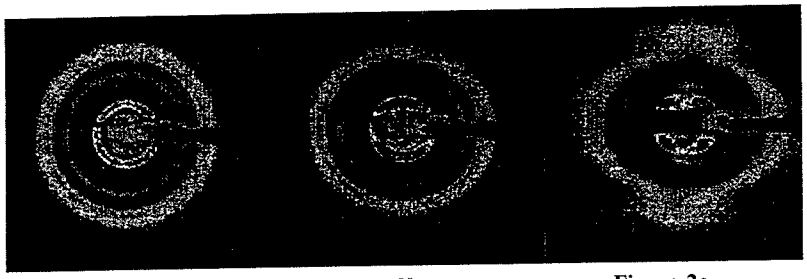

Figure 2a **Figure 2b** **Figure 2c**

Figure 2: 2-D SAXS of deformed rubber toughened PMMA with 40 wt.-% of rubber particles; a) undeformed; b) extension of 1 mm and c) extension of 1.75 mm. Tensile axis: vertical

Turning now to the effect of changing the crosslinking density of the rubber particles, figure 3 shows the results from invariant analysis for a family of samples for which the rubber particle content was kept fixed at 30 wt-%, as a function of extension of the sample. It can be seen that the maximum plastic strain due to crazing decreases with an increase in rubber crosslinking density. Table I shows the correlation between the extension of the sample with the extension at the maximum in the load-extension curve, defined as the yield point. It can be seen that the onset of crazing coincides with the yield point.

Figure 4 shows a similar set of results obtained for a family of samples for which the crosslink density was kept fixed at 2% but the concentration of rubber particles was varied from 10-50wt-%. For this family of samples the crazing onset again coincided with the maximum in the load-extension curve. In order to make the most useful comparison between

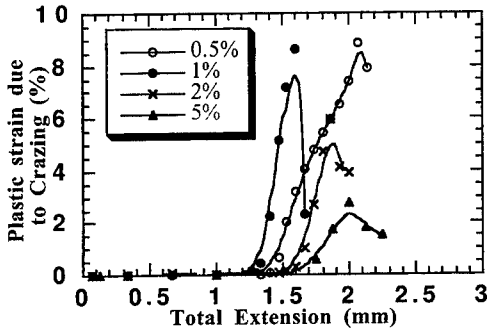

Figure 3 The relation between plastic strain due to crazing (derived from invariant analysis) and the total extension of the sample, for a family of samples with 30% rubber particles and different degrees of crosslinking.

Table I Comparision of the onset of crazing with the yield point of polymer samples

Crosslinking Density of Rubber Particles (%)	Total Extension of Sample at Onset of Crazing (mm)	Total Extension of Sample at Yield Point (mm)
0.5	1.2	1.2
1	1.2	1.2
2	1.4	1.4
5	1.5	1.5

samples, which eliminates inherent variability in parameters such as the distribution of particles, we have found it useful to evaluate the the density of crazes per unit plastic deformation, evaluated as the slope at the point of crazing onset. If a sample has a high value for this slope then it has a strong tendency to craze when deformed. Figure 5 shows that the value of this slope has a maximum at a particle concentration of around 30%, for 2% crosslinked rubber particles. Analysis of results for families of varying rubber particle concentration but (different) fixed crosslink density shows that this maximum occurs at the same particle concentration regardless of crosslink density.

It is not surprising that the tendency for crazing increases as the particle number density increases, since the particles would be expected to act as stress concentrators at which the crazes initiate. However it must also be remembered that the particles are more compliant than the matrix and as their number density increases they may start to modify the local stress fields. Ultimately it may be possible for this stress modification to drop the local stress below which crazing can be initiated.

A study by Gloaguen(6) et al shows that the yield stress strongly depends on particle volume fraction. It decreases monotonically as the concentration of rubber particle increases. More important is that their study shows there is a critical interparticle

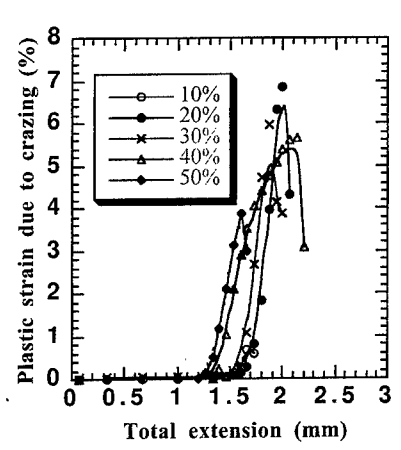

Figure 4 The relation between plastic strain due to crazing and the total extension of the sample for a crosslinking density of 2%.

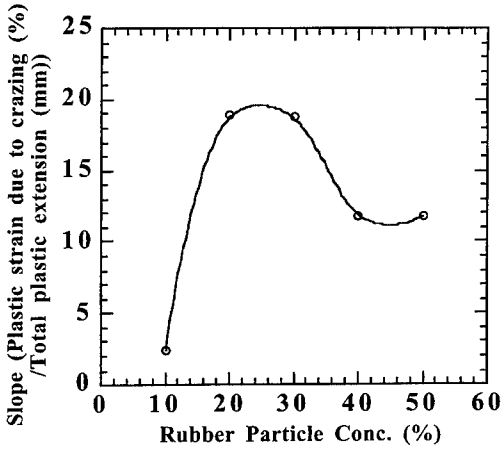

Figure 5 The relation between craze concentration and rubber particle concentration (data from figure 4).

distance of 50-60 nm (regardless of particle size) which facilitates the formation of shear bands. It is interesting to see that the critical interparticle distance suggested by Gloaguen occurs in our system at between 30 and 40 wt-% of rubber particles in our polymer system. This suggests that the fall-off in craze volume at high particle loadings arise because shear of the matrix is facilitated at these interparticle spacings. This of course does not necessarily mean that the material is less tough, only that the amount of crazing has decreased. Turning now to the effect of crosslink density, it seems that craze initiation efficiency is at its highest for a crosslink density of ~1%. Increasing the rubber crosslink density has the effect of decreasing the stress differential at the rubber/PMMA interface. The larger this differential is the more efficient the particle is at nucleating crazes; thus there is less crazing as the crosslink density is raised. The anomalous behaviour of the 0.5% crosslinked samples is thought to be due to a change in internal particle morphology (reflected in less clear form factor scattering at ultra low q).

References

1. Bubeck, R. A., Buckley, D. J., Kramer, E. J. and Brown, H. R., J Mat Sci 26 (1991) 6249-59
2. Lazzeri, A. and Bucknall, C. B., J. Mat. Sci. 28 (1993) 6799-6808
3. Lazzeri, A. and Bucknall, C. B., Journal of Materials Science 28 (1993) 6799-6808
4. Bucknall, C. B., Karpodinis, A. and Zhang, X. C., J. Mat. Sci. 29 (1994) 3377-3383
5. Magalhaes, A. A. M. and Borggreve, R. J. M., Macromols (1995) 5841-51
6. Gloaguen, J. M., Heim, P., Gaillard, P. and Lefebvre, J. M., Polymer 33 (1992) 4741-6

STUDY OF MECHANICAL DAMAGE IN RUBBER TOUGHENED POLYMETHYL-METHACRYLATE BY VOLUME CHANGE, MULTIPLE SCATTERING AND COHERENT BACKSCATTERING OF LIGHT.

by R. Schirrer, R. Lenke and C. Fond *

As glassy polymers are usually brittle materials, blending techniques are used to toughen these materials which are mostly opaque, which renders difficult any optical investigation of the damage process. If a body is highly opaque, an incident light beam is scattered successively by several scatterers before emerging again at the front surface of the body. There is a coherent backscattering interference enhancement of the randomly multiple scattered light in a small angle range around the exact reverse direction of the incident light. It can be analysed in terms of the size, shape and density of the scatterers. This technique is applied to the case of a rubber toughened PMMA, an initially transparent material which becomes progressively opaque during mechanical damage under stress.

1. INTRODUCTION

Light scattering is one of the easiest and least expensive experimental method to investigate microstructural changes occurring during damage. Howewer, in highly damaged and hence highly opaque materials, light is scattered randomly many times and the single diffraction pattern disappears. One way to study samples in the regime of multiple scattering is the so called « coherent backscattering ». Since light scattering in opaque materials has recently been much better described using coherent backscattering theory and experiments [1], the purpose of this paper was to apply the coherent backscattering technique to a study of the damage mechanisms in a rubber toughened polymethylmethacrylate (RT-PMMA) from Altulor (reference EI60), which consist of a glassy PMMA matrix (molecular weight 120,000) containing 40% particles of precisely 200 nm diameter. These particles comprise a hard core (PMMA) with a rubbery outer shell (butylacrylate styrene copolymer). Micromechanisms prevailing in this kind of material are not well known and appear to be complicated by the fact that the rubber layer around a particle in which the cavitation may take place is extremely thin (20 to 30 nm).

2. SCATTERING AND COHERENT BACKSCATTERING OF LIGHT

Light is scattered when the refraction index is not homogeneous in the material. In a medium where the index of refraction varies randomly, an incoming coherent light beam of intensity I_0 is attenuated after a distance d by: $I(d)/I_0 = e^{-d/L}$ where L is the scattering mean free path of the opaque material. If the dimensions of sample are large compared to the scattering mean free path L, the light is randomly scattered several times in the medium before emerging again.

* CNRS, Institut Charles Sadron, 6 rue Boussingault, F-67083 Strasbourg

The random propagation of the light can be described by a random walk model along a path on which the light is modified in amplitude and phase. The transport mean free path L^* is the average characteristic length in this random walk model. L^* is the propagation distance after which the light beam has lost the memory of its initial direction. Figure 1 shows a semi-infinite scattering medium illuminated with a planar coherent light beam. For each path followed by a beam between its entry and its output point, the reverse path is followed by another beam. In the backward direction $\theta=0$ the two paths are strictly identical , thus giving raise to an interference enhancement by a factor of two, the so-called coherent backscattering phenomenon. The cone $I(\theta)$ is the Fourier transform of the intensity distribution I(x). For example, for a sheet of white paper, the value of L^* is about 10 μm, which corresponds to a cone width of about 0.6 degree at a wave length of λ=633nm. An approximate formula for the shape of the cone is given by

$$I(q) / I_{incoh} = 1 + \frac{1 - e^{(-3.4qL^*)}}{3.4qL^*}.$$

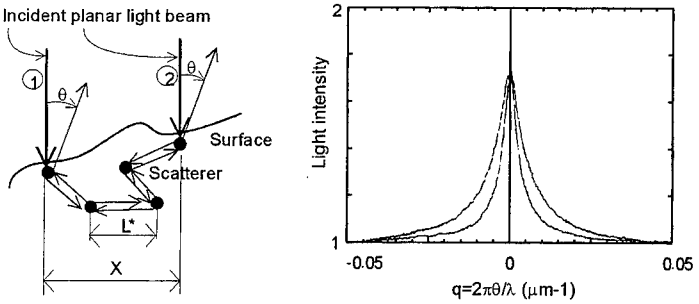

Figure 1: Left: The random walk of a light beam in a scattering medium. Right: 2 typical intensity curve $I_{\perp}(q)$ and $I_{||}(q)$ parallel and perpendicular to the axis for an anisotropic material (RT-PMMA at 10% strain). The peak level of the coherent backscattering is theoretically twice that of the incoherent scattering sphere.

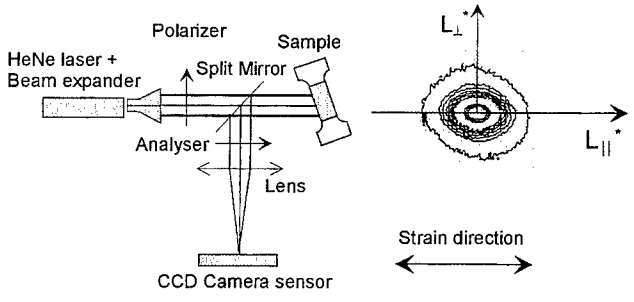

Figure 2: The optical system for light backscattering measurements and a typically anisotropic coherent backscattering cone in false colours.

3. EXPERIMENTAL PROCEDURE

A strip of transparent RT-PMMA is clamped in the tensile machine, which is housed in an environmental chamber set to the appropriate temperature. Strain gauges are fitted on the sample to record deformations and volume changes and the moving cross head of the machine is set in operation at constant speed until it attains a predetermined total strain. A laser beam (figure 2) traversing the sample allows instantaneous recording of the light transmission and scattering. The material becomes progressively blurred and finally opaque, the kinetics depending on temperature, strain and strain rate. Volume variations are deduced by means of the simple equation $\delta V/V = \varepsilon_x+\varepsilon_y+\varepsilon_z = \varepsilon_x + 2\varepsilon_y$. The strain rate may be varied from 10^{-1} to 10^{-5} s^{-1} and the temperature from -70 to 200°C. The originally transparent material becomes scattering at about 2 to 3% strain and fully opaque above 5 to 7% strain at room temperature, although as is usual in polymers, this phenomenon depends strongly on temperature and strain rate. At very low strain rate or high temperature, the material remains transparent and no mechanical damage occurs. Details and results of these experiments are given in reference [2].

4. MICROSTRUCTURAL MODELING OF THE SCATTERERS

In the case of rubber core particles, at a critical level of mean tensile stress, the hydrostatic stress component in the rubber leads to formation of a micro-void (10 to 20 nm diameter), the pressure drops instantaneously almost to zero and micro shear bands appear in the matrix near the particle [3,4]. In the case of core-shell (hard core) particles the mechanism is less well known. Nevertheless, the rubber wall around a particle may be considered to act like a shield for shear stresses, hydrostatic pressure appears in a similar manner in the rubber and cavitation then occurs in the rubber wall, most likely at the poles. The light scatterer close to the nature of the destroyed particle may be modelled as an equivalent homogenized particle of nearly spherical shape, occupying the volume of the particle plus its internal voids, and having an average optical index given by the Lorentz-Lorenz equation

$$\frac{<n>^2 - 1}{<n>^2 + 2} = (1 - v_f)\,\frac{n_0^2 - 1}{n_0^2 + 2}$$

where $<n>$ is the mean optical index of the scattering particle, n_0 the bulk index and v_f the void volume fraction in the particle. Once the scatterers have been defined, there exist two simple boundary cases for which the kinetics of the increase in opacity with damage can be analytically described:

i) the simultaneous particle destruction model, in which at a certain level of stress during damage, almost all particles cavitate simultaneously and acquire an initial void fraction v_f. The size of the voids subsequently increases with increasing external stress, as indicated by the macroscopic volume change. Figure 3 compares the calculated L values for homogenized equivalent scatterers with our experimental results derived from measurements of light scattering at the onset of damage. Clearly, the experimental values do not fit the predictions. In fact, the major feature of this model is that it offers no adjustable parameter to fit the experimental results: the number of scatterers is equal to the number of rubber particles in the material, which is 40% in volume in our samples.

ii) the successive particle destruction model, in which a very small number of particles cavitate at a certain level of stress. Cavitation is triggered by some accidental local stress fluctuation due to interactions between particles. A cavitated particle absorbs the elastic energy available in its vicinity until it attains a stable damaged state and the surrounding stress field is modified. Subsequently, as the external strain increases, another particle cavitates and reaches the stable state, probably at a location correlated with the sites of the previously damaged particle. Only

two types of particle exist: original transparent ones and damaged ones with the unique value of the void content. As shown in Figure 4, the theoretical plots for equivalent homogenized particles with a void content of about 8% in each particle correlate well with our experimental results. The void content is the tunable parameter of the model.

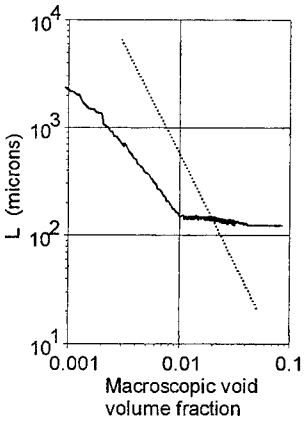

Figure 3: Experimental light transmission results (solid) compared to the theoretical predictions (dashed) of the simultaneous particle cavitation model. The noise level of the detector is reached above 0.01 void fraction.

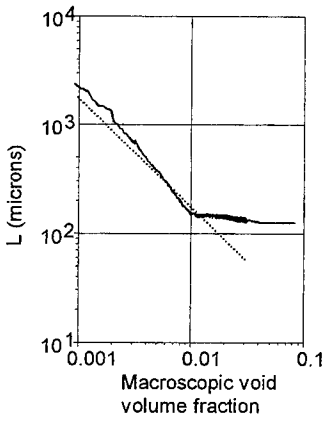

Figure 4: Experimental light transmission result (solid) compared to the theoretical prediction (dashed) of the successive particle cavitation model. The volume fraction of void in each particle is 8% in the model.

5. CONCLUSIONS

The onset of cavitation in rubber toughened polymethylmethacrylate containing core-shell (hard core) particles may be detected by light scattering. Analysis of the kinetics of light scattering during elongation of a sample in a tensile machine shows that each cavitated rubber particle changes suddenly from its original state to a stable cavitated state with about 8% void content. The macroscopic volume increase corresponds to an increase in the number of destroyed particles, whereas the void content of an individual damaged particle remains basically constant [5].

REFERENCES

1. Wolf, P.E. and Maret, G., Phys. Rev. Lett., 55(1985)2696
2. Schirrer R., Fond C., and Lobbrecht A., J. Mater. Sci. (1996), 1027-1042.
3. Lazzeri, A., and Bucknall, C.B. J. Mater. Sci. 28(1993)6799
4. Fond, C., Lobbrecht A., Schirrer, R. Int. J. of Fracture, 7(1996)141-159
5. Schirrer R., Lenke R., and Boudouaz J., Polymer Eng. Sci., in press(1996).

MICRODEFORMATION IN THIN FILMS OF PP/EPR REACTOR ALLOYS

R. Gensler, C.J.G. Plummer, H.-H. Kausch *

ABSTRACT

Microdeformation in thin films of PP/EPR reactor alloys at different temperatures has been studied by TEM. Details of deformation processes at the lamellar scale were observed by staining the samples in RuO_4-vapour. The particles of the dispersed EPR phase showed a core-shell structure, with a rubbery EPR shell and semicrystalline CH_2-rich inclusions. The average particle size and size distribution were dependent on the molecular weight of the PP matrix and the second phase content. On the basis of the TEM observations, a three-stage mechanism is proposed for room temperature deformation: 1. Formation of voids at the particle poles and/or initiation of matrix deformation in equatorial regions; 2. Matrix micronecking involving break-up and drawing of the lamellar structure; 3. Crack initiation and propagation by successive rupture of highly extended regions of the sample. Below -40°C, high aspect ratio craze-like defects were observed in all the blends, running perpendicular to the straining direction, and rubber particle cavitation appeared less effective in initiating matrix deformation.

INTRODUCTION

The low temperature impact resistance of polypropylene (PP) is improved by rubber modification, and ethylene-propylene copolymerisates (EPR) are frequently used as toughening agents (1). The EPR is either introduced by compounding, or formed in situ by multistep polymerization. This latter technique yields so-called "reactor alloys", which represent a new class of polyolefin blends with a wide range of performance (2).

In the current picture for toughness enhancement of impact PP, the rubber particles are thought to act as stress concentrators, which initiate energy consuming deformation processes over a large volume. Crazing is reported to dominate at low temperatures, high strain rates and low rubber contents, whereas higher temperatures, lower strain-rates and higher rubber contents favour shear banding (3). The role of rubber particle cavitation in initiating matrix deformation has also been discussed (4, 5), and recently quantitative models have been developed for the influence of particle size and interparticle distance on voiding and toughness, respectively (6, 7). Although TEM has been used previously to investigate microdeformation in PP/EPR blends (3-5), these studies have not provided details of the deformation processes at the lamellar scale. In view of the importance of impact modified PP, and the fact that the morphology of PP reactor blends may be considerably different to that of compounded blends which have been the principal object of earlier studies, we have re-examined the deformation mechanisms in PP/EPR reactor alloys as a function of temperature and matrix molecular weight.

EXPERIMENTAL

Three PP/EPR reactor blends, referred to as B1, B2 and B3, were supplied by PCD Polymere Austria. Basic characteristics of the materials are summarized in Table I. The blends had different matrix molecular weights as reflected by the variations in melt flow index. The volume fraction of the rubber phase was about 25 % in B1 and B3, and 30-35 % in B2. Films of 100 to 300 nm in thickness were cast on mica from a hot xylene solution. To obtain spherulitic samples with a well defined thermal history, the films were remelted on the mica substrate at 210°C, and isothermally crystallized at 120°C. They were then floated off the mica, mounted on annealed copper grids and deformed in tension using a Polymer Laboratories Minimat tensile

* Laboratoire de Polymères, École Polytechnique Fédérale de Lausanne, CH-1015 Lausanne, Switzerland.

machine at a strain rate of about 0.04 s^{-1}, and at temperatures between -100°C and +80°C. Prior to TEM observation, the samples were stained in RuO_4-vapour.

Blend	Matrix M_W (kg/mol)	Melt flow index (2.16 kg / 230°C)	Rubber volume fraction (%)	Number average particle diameter (nm)
B1	170	45	25	160
B2	560	3	30-35	136 *
B3	1000	0.2	25	85

Table I Characteristics of the PP/EPR reactor blends; * asymmetrical size distribution, about 65 % of the particles were less than 100 nm in diameter.

RESULTS AND DISCUSSION

Blend morphology

In B1 and B3, the second phase was homogeneously dispersed in the PP matrix in the form of disc-shaped particles as shown in Figure 1(a). Also visible in the figure are matrix lamellae in close to edge-on orientation, showing the characteristic cross-hatched α lamellar structure of unmodified iPP. In addition to the finely dispersed second phase particles, B2 also contained many large non-circular domains which extended over distances of 0.5 - 3 μm, and which presumably resulted from particle coalescence (Figure 1(b)). The number average particle diameters given in Table I were determined by image analysis of TEM micrographs of several samples cast under identical conditions and ranged from 85 nm in B3 to 160 nm in B1. In B2, the value of 136 nm includes the largest particles; as can be seen from Figure 1(b) most of the particle diameters were in the sub-100 nm range.

In each case, the rubber particles displayed a core-shell structure, with a CH_2-rich lamellar interior (essentially polyethylene (PE)) and an amorphous EPR shell. Matrix lamellae were widely observed to penetrate the EPR shells, provoking $(1\,0\,0)_{PE}//(0\,1\,0)_{PP}$ epitaxial growth in the PE core. This implies good interfacial adhesion between matrix and rubber phase.

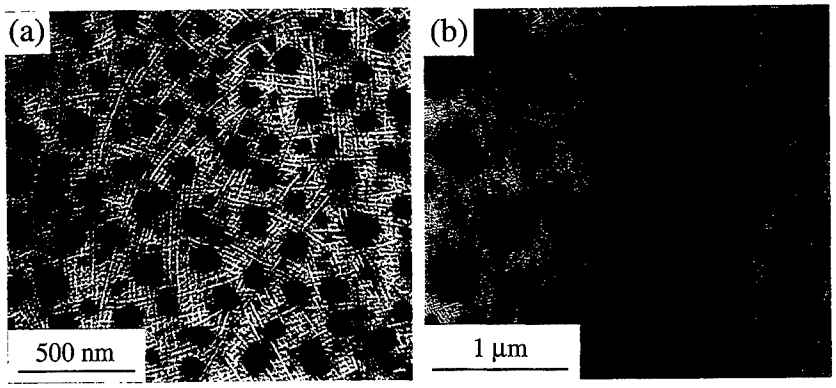

Fig. 1 Morphology of (a) B3 and (b) B2.

Deformation mechanisms at room temperature

Despite the differences in morphology and matrix molecular weight, the blends all showed the same basic deformation mechanisms, summarized here in terms of a three stage process:

(1) In the early stages of deformation, the particle shells are slightly stretched. Matrix deformation initiates at the particles equators and is visible in the form of enhanced staining of

interlamellar regions running roughly perpendicular to the stress axis (Figure 2(a)). Where the lamellar trajectories are inclined with respect to the tensile axis there is evidence for lamellar break-up by block shear. Cavitation of the larger modifier particles also intervenes at this stage, generally initiating in polar regions of the core-shell interface as shown in Figure 2(a).

(2) Further deformation results in further nucleation and growth of the intraparticular voids and generalized matrix micronecking in regions separating particles along their equators, to give large deformation zones connecting rows of voided particles. The lamellar matrix structure is progressively destroyed by surface drawing at the deformation zone boundaries as they widen. Any remaining uncavitated modifier particles tend to cavitate as they are engulfed by growing deformation zones, but the PE inclusions undergo little or no deformation (the lamellar structure of the PE remains intact within the deformation zones in spite of extensive stretching of the surrounding EPR).

(3) The formation and propagation of a crack by successive rupture of highly deformed regions of the film initiates the complete failure of the sample.

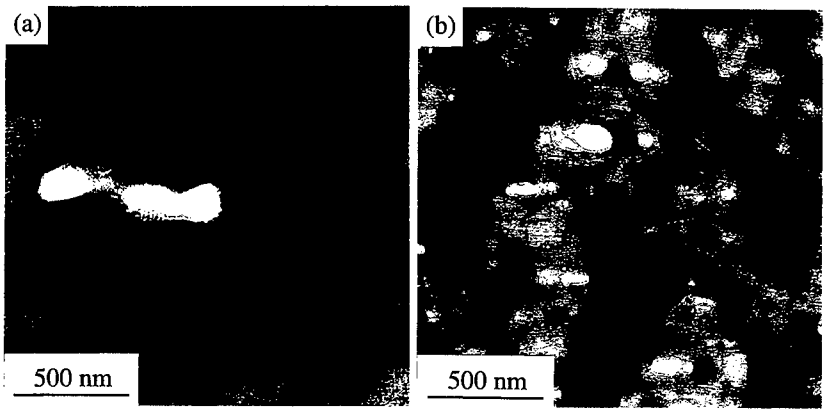

Fig. 2 (a) Particle cavitation, interlamellar separation and lamellar break-up in B2; (b) Mature deformation zones in a thin film of B3. Both samples were deformed at RT.

The influence of blend morphology and temperature on microdeformation

Although cavitation was observed in all the blends in the early stages of deformation, it was more pronounced in B1 and B2, which contained relatively large rubber particles. Moreover, in B2, voids appeared in the large agglomerates at significantly lower strains than in the smaller particles. This size effect may reflect the influence of the particle size on the critical volume strain required for cavitation as discussed, for example, by Dompas and Groeninckx (6), and simple energetic considerations suggest that sufficiently small rubber particles are unlikely to cavitate during tensile deformation of the surrounding polymer matrix (although such arguments generally involve triaxial stresses acting on spherical inclusions, they are easily extended to the present case of biaxial stresses acting on essentially two-dimensional, circular inclusions). Certainly, in B3 the particles appeared to be less prone to voiding, although they continued to provide sites for the initiation of widespread matrix deformation, such as shown in Figure 2(b).

At a given temperature, the drawability of the films was determined by the ultimate load bearing capacity of the deformed film regions. Although the rubber particle size influenced the structure of these latter (larger particles resulted in coarser internal voiding), their load-bearing capacity was also expected to depend on that of the highly drawn matrix. The observation that complete failure in B1 occurred at strains only a few % greater than those at which deformation zones first appeared may therefore be seen as a consequence of the low matrix molecular weight and hence reduced strength in the matrix ligaments in the deformed zones.

When the drawing temperature was increased to 80°C no qualitative changes in the deformation mechanisms were seen. However, deformation was found to be more homogeneously distributed over the whole sample volume, and the drawability increased markedly. Figure 3(a) shows a highly deformed sample of B1 showing extensive coalescence of the deformation zones. Conversely, as the temperature was decreased, deformation became more localized, and once a crack had initiated, rapid unstable failure of the film ensued. Below -40°C, the trajectories of the deformation zones were no longer strongly influenced by the presence of the modifier particles, as shown in Figure 3(b), remaining perpendicular to the tensile axis over distances much larger than the particle separation. Although the mature deformation zones showed details similar to that observed at room temperature, there was little evidence of deformation associated with individual modifier particles as observed during stage 1 of the room temperature deformation process. Indeed, the overall density of deformation zones was much lower than at room temperature, from which one may conclude that any toughening effect due to the presence of the particles is likely to be diminished below about -40°C. For comparison, the bulk EPR glass transition temperature is approximately -50°C, so that this regime probably corresponds to a decrease in modulus mismatch between the matrix and the modifier phase. However, the linearity of the deformation zone trajectories is also found to increase at low temperature in unmodified PP (8), which suggests that the matrix glass transition (-20°C) may play also an important role here.

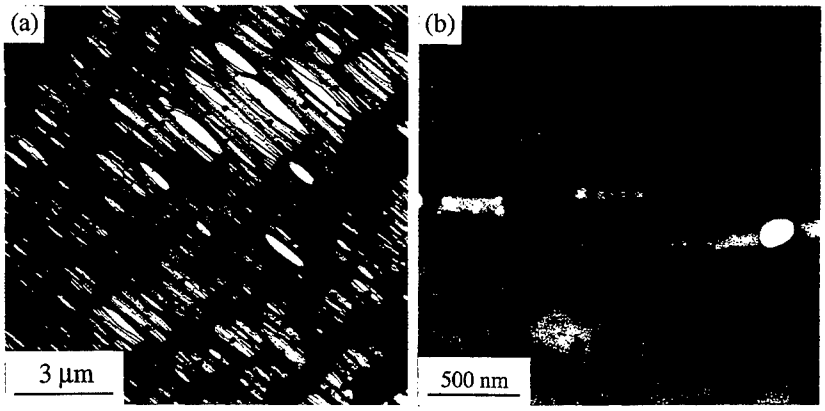

Fig 3 (a) Highly stretched thin film of B1 deformed at 80°C; (b) A sample of B2, deformed at -100°C.

Acknowledgments
This study was kindly supported by Ciba-Geigy AG, Basel, Switzerland. The TEM work was done at the Electron Microscopy Centre of the EPF Lausanne.

References

1. Phillips R.A., Wolkowicz M.D., in "Polypropylene Handbook" (ed. Moore E.P.) Chap. 3 (Hanser, Munich, 1996)
2. Galli P., Haylock J.C., Macromol. Chem. - Macromol. Symp. 63 (1992) 19
3. Jang B.Z., Uhlmann D.R., van der Sande J.B., J. Appl. Polym. Sci. 30 (1985) 2485
4. Kim G.-M., Michler G.H., Gahleitner M., Fiebig J., J. Appl. Polym. Sci. 60 (1996) 1391
5. Hayashi K., Morioka T., Toki S., J. Appl. Polym. Sci. 48 (1993) 411
6. Dompas D., Groeninckx G., Polymer 35 (1994) 4743
7. Wu S., Polymer 26 (1985) 1855
8. Plummer C.J.G., Kausch H.-H., Macromol. Chem. Phys. 197 (1996) 2047

SESSION TEN:

TOUGHENING MECHANISMS II

THE EFFECT OF THE RUBBER PARTICLE SIZE ON THE BRITTLE/TOUGH TRANSITION OF RUBBER TOUGHENED POLYPROPYLENE

Allard van der Wal, Reinoud J. Gaymans*

The effect of the rubber particle size (0.3 to 4 μm) on the brittle/tough transition of polypropylene/EPR blends was studied at low (0.02 s^{-1}) and at high (60 s^{-1}) strain rate. At high strain rate (impact conditions) the brittle/tough transition temperature (T_{bt}) increases upon increasing the particle size and a rough correlation between the T_{bt} and the interparticle distance (ID) is found. Surprisingly, at low strain rate the T_{bt} decreases with an increasing rubber particle size, and consequently there is no correlation between the T_{bt} and the ID. Based on these results a relation between the ID and the brittle/tough transition seems unlikely. The strain rate dependence of the rubber particle size effect may be related to the strain rate dependence of the temperature rise during fracture.

INTRODUCTION

Polypropylene (PP) can effectively be rubber toughened [1]. The fracture behaviour of PP/rubber-blends depends on the test parameters like temperature and strain rate as shown in *Figure 1* [2]. With decreasing temperature the fracture energy decreases and the fracture type changes from tough to brittle at the T_{bt} (*Figure 1*). With increasing strain rate initially the fracture energy decreases, analogue to the decrease with decreasing temperature, this decrease is surprisingly followed by an increase and finally the fracture type changes from tough to brittle at the brittle/tough transition strain rate (V_{bt}) (*Figure 1*). The increase in fracture energy with increasing strain rate was explained by a thermal blunting mechanism [2]. Evidence of such a mechanism is produced by the fact that the increase in fracture energy is accompanied by a relaxation of the deformation within the fracture zone [2]. This relaxation indicates melting of the material during fracture [3]. The temperature rise at the crack tip is due to adiabatic plastic deformation. The fracture behaviour and the occurence of the relaxation layer suggest that there is significant temperature rise at high strain rates and that this temperature rise affects the fracture behaviour. The increase in temperature rise with increasing strain rate was shown by infrared thermography for PP/EPR-blends [4].

In general the fracture behaviour of rubber toughened polymers depends on, besides the test parameters, the blend geometry: the rubber particle size and rubber content. The effect of the rubber content is straight forward, an increase leads to a higher resistance against fracture. The effect of the particle size seems to depend on the deformation mechanism. In the case of crazing materials such as HIPS, the impact energy increases upon increasing particle size [5]. In the case of yielding materials, such as rubber toughened nylon, the impact energy decreases with increasing particle size, or in fact the T_{bt} increases with increasing particle size [6]. Furthermore, the effect of the particle size seems to depend on the strain rate. As already mentioned, for rubber toughened nylon the T_{bt} increases with increasing rubber particle size at impact conditions. However, at low speed bending no effect in changing the rubber particle size on the T_{bt} was found [7]. The T_{bt} measured at low speed bending was close the T_g of the rubber phase, therefore these results may be affected by the underlimit exposed by the T_g of the rubber phase.

* Twente University, Dept. of Chemical Technology, P.O. Box 217, NL-7500 AE, Enschede, The Netherlands

For polypropylene the effect of particle size has been studied only under notched impact conditions. An increase in the impact strength was observed under crazing conditions [8], where as an increase was found under yielding conditions [9].

The effect of particle size on the brittle tough transition temperature for rubber toughened nylon and polypropylene has been described by the interparticle distance which is the distance between two neighbouring particles [6, 9]. Assuming regular lattice packing and a monodispersed rubber phase Wu [10] affords the following equation:

$$ID = d\left[k\left(\frac{\pi}{6\phi_r}\right)^{1/3} - 1\right] \qquad (1)$$

where d is the particle size, ϕ_r stands for the rubber content and k denotes a geometric constant which depends on the lattice type. The physical meaning of the ID is still a matter of debate.

We studied the effect of the rubber particle size on the brittle/tough transition of PP/EPR-blends at low and high strain rate.

EXPERIMENTAL

Specimen preparation. The materials used include a commercial polypropylene (GE 7100, Montell; MFI 0.8 (230 °C, 21.6 N)) and a series of experimental EPRs supplied by Shell (KSLA, The Netherlands). These EPRs differ in terms of their ethylene content and molecular weight as listed in *Table I*. The EPR was blended with polypropylene on a corotating Berstorff twin screw extruder. Blends containing 5, 10 and 20 vol% EPR were prepared. Rectangular Izod bars (74x10x4 mm) were injection moulded on an Arburg Allrounder injection moulding machine. A single edge V-shaped notch (45°, depth 2 mm) was milled in the bars. Particle size analysis. Samples for particle size analysis were taken from the core of the bars. The particle size was determined manually from SEM-micrographs using a graphic tablet. Fracture tests. The fracture behaviour at low strain rate (0.02 s^{-1}) was determined using a tensile test on the notched specimen, referred to as Single Edge Notch (SEN) tensile test; tensile speed 1 mm/s, clamp distance 50 mm. The fracture behaviour at high strain rate (60 s^{-1}) was determined using a notched Izod impact test. The strain rate given is the overall strain rate and not the strain rate at the crack tip.

RESULTS

Rubber particle size. The rubber particle size was changed by using EPRs differing in their ethylene content and molecular weight. The particle size of the blends is listed in *Table I*

High strain rate. *Figure 2* shows the effect of the particle size on the T_{bt} at high strain rate (60 s^{-1}) for the PP/EPR-blends containing different EPR-contents. The T_{bt} increases upon increasing particle size. The effect of the particle size seems to be independent of the rubber content and the ethylene content of the EPR-phase (*Figure 2*). *Figure 3* shows the T_{bt} as a function of the interparticle distance (ID). A correlation between the T_{bt} and the ID requires that all data point in *Figure 3* are on one line. As can be seen in Figure 3 this is not the case, and therefore there is only a rough correlation between the T_{bt} and the ID. Low strain rate. *Figure 4* shows the effect of the particle size on the T_{bt} at low strain rate (0.02 s^{-1}) for the 20 vol% PP/EPR blend. Surprisingly, the T_{bt} decreases with increasing particle size whereas it increases at high strain rate. This decrease in T_{bt} may be due to a decrease in cavitation stress of the rubber particle, since the cavitation stress decreases upon increasing particle size [11]. The T_{bt} values are close to the T_g of the E40 and E60 EPR of respectively -37 and -54 °C (*Table I*). The fact that large

particle size blends have a significant lower T_{bt} than their corresponding small particle size blends indicates that the T_{bt} values are not fully prescribed by the T_g of the EPR-phase.

DISCUSSION AND CONCLUSIONS

At low strain rate no correlation was found between the T_{bt} and the ID and at high strain rate only a rough correlation was found. Furthermore, there is no clear physical explanation of a relation between the ID and the brittle/tough transition. All in all, a relation between the brittle/tough transition and the ID seems unlikely.

The effect of the particle size on the brittle/tough transition of PP/EPR-blends depends on the strain rate. At both low and high strain rate the blends studied in this paper deforms during fracture by a yielding mechanism [15]. Therefore the test speed dependence of the particle size effect is not due to a difference in matrix deformation mechanism. We believe that the test speed dependence of the particle size effect is related to the test speed dependence of the temperature rise during crack propagation.

REFERENCES

1) Van der Wal A., PhD-thesis, Twente University, The Netherlands, Enschede, 1996, Ch. 5
2) Van der Wal A., PhD-thesis, Twente University, The Netherlands, Enschede, 1996, Ch. 7
3) Janik H., Gaymans R.J., Dijkstra K., Polymer 36 (1995) 4203
4) Van der Wal A., PhD-thesis, Twente University, The Netherlands, Enschede, 1996, Ch. 8
5) Donald, A.M., Kramer E.J., J. Mater. Sci. 17, (1982) 2351
6) Borggreve R.J.M., Gaymans R.J., Schuijer J., Ingen Housz J.F., Polymer 28 (1987), 1489
7) Lazzeri, A., PhD thesis, Cranfield Institute of Technology, UK 1991
8) Ramsteiner F., Acta Polymerica 42 (1991) 584
9) Wu, Xuanzheng, Zhu, Xiaogung, Qi, Zongneng, 8th International Conference on Deformation, Yield and Fracture of Polymers, London, April 1991, p78/1
10) Wu S., J. Appl. Polym. Sci. 35 (1988) 549
11) Dompas. D., Groeninckx G., Isogawa M., Hasegawa T., Kadokura M., Polymer 35 (1994) 4750
12) Van der Wal A., PhD-thesis, Twente University, The Netherlands, Enschede, 1996, Ch. 10

Table I. Properties of the EPR-rubbers and the particle size data for the PP/EPR-blends

EPR code	ethylene content [mol%]	intrinsic viscosity[a] [dl/g]	T_g[b] [°C]	rubber particle size (D_w[c]) [μm] 5vol%[d]	10vol%[d]	20vol%[d]
E40L	40	3.4	-37	0.28	0.33	0.37
E40M	40	6.9	-37	0.44	0.50	0.67
E40H	40	14.9	-37	0.80	1.20	1.34
E60L	60	4.3	-54	1.31	1.47	1.55
E60M	60	8.0	-54	1.38	1.59	2.08
E60H	60	14.1	-54	2.35	2.40	3.83

a) decaline 135 °C, b) DMA (torsion, 1Hz), c) $Dw = \sum n_i d_i^2 / \sum n_i d_i$, d) rubber content

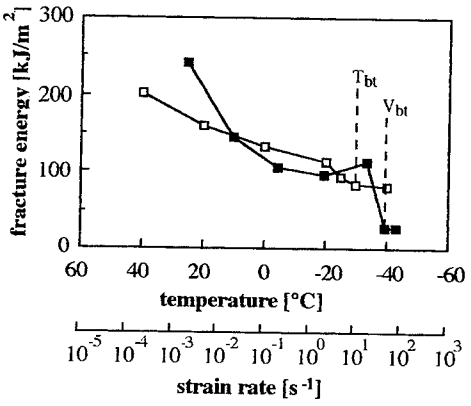

Figure 1 The fracture energy as a function of temperature (□) and strain rate (■) for a PP/EPDM-blend (80/20 vol%, dw = 0.5 μm)

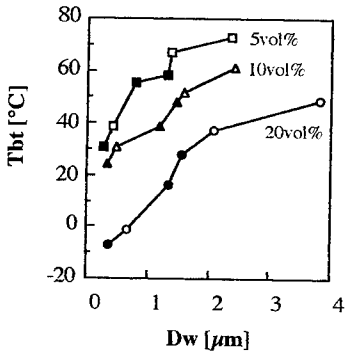

Figure 2. The brittle/tough transition temperature (T_{bt}) versus the rubber particle size for the PP/EPR-blends at high strain rate (60s^{-1}). Ethylene content: filled symbols: 40 mol%, open symbols: 60 mol%

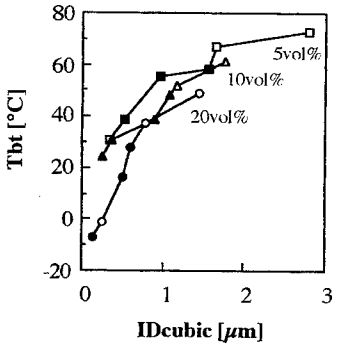

Figure 3. The brittle/tough transition temperature (T_{bt}) versus the inter particle distance (ID) for the PP/EPR-blends at high strain rate (60 s^{-1}). The interparticle distance was calculated for a cubic lattice (k = 1, Equation 1) and with the Dw (Table I) as a measure of the rubber particle size

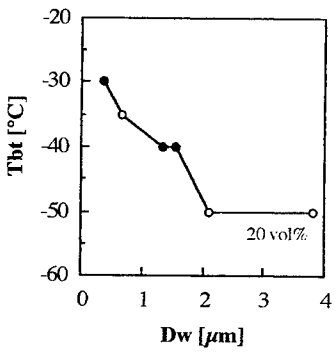

Figure 4. The brittle/tough transition temperature versus the particle size for the 20vol% PP/EPR-blend at low. strain rate (0.02 s^{-1}). Ethylene content: filled symbols: 40 mol%, open symbols 60 mol%.

IMPROVING THE TOUGHNESS OF EPOXY POLYMERS BY TAILORING THE PROPERTIES OF THE ELASTOMERIC ADDITIVES

R. A. Pearson*, H. R. Azimi**, R. Bagheri**, J. Qian**, and Y-C. Huang**

Over the years significant progress has been made in modeling the toughening mechanisms in rubber-modified epoxies. These efforts have led to an increased awareness of the roles of rubber particle bridging, rubber particle cavitation, matrix dilation, and matrix shear banding on the enhancement of fracture toughness. However, there are still many questions regarding rubber-toughening which remain unanswered. This presentation will focus on the importance of the interphase region between the epoxy matrix and the rubber particle, the overall particle morphology, and cavitation resistance of the rubber particles. It will be shown that additional toughness enhancement may be achieved by controlling the particle-matrix interphase, which in turn affects the overall blend morphology. It will also be shown that particles with no cavitation resistance can be effective toughening agents which suggests that rubber particles with improved cavitation resistance may not be necessary for some epoxy systems. Methods to incorporate these effects into existing toughening models will also be discussed.

INTRODUCTION

Toughening brittle epoxy polymers with soft, rubbery inclusions has existed since the late 1960s [1]. The pioneering work focused on the use of reactive, elastomeric oligomers to provide the toughening effect. Such elastomers were successful in toughening a number of brittle epoxy polymers. However, the understanding of the underlying toughening mechanisms that provided the improvements in toughness did not develop until some time later [2-4]. The elucidation of the toughening mechanisms led to mechanical models that attempted to quantify the toughening effect and in turn, could be used to facilitate the direction of future research.

Rubber-particle cavitation and concomitant matrix shear banding has been shown to be a very potent toughening mechanism. Therefore, an understanding of the material parameters affecting this mechanism is of keen interest. Presumably, such material parameters can be varied to optimize the toughening effect. For example, it known that the fracture toughness of rubber-modified epoxies can be further improved by lowering the crosslink density of the epoxy matrix [5, 6]. However, what happens if one is constrained to use a particular matrix? The focus of this paper is to evaluate the properties of rubber particles that influence their effectiveness in improving toughness.

EXPERIMENTAL

Materials

The role of rubber particle size, particle cavitation resistance, rubber-epoxy interphase, and overall morphology on fracture resistance will be elucidated using five series of model epoxy systems.

* Polymer Interfaces Center, Lehigh University, Bethlehem, PA 18015 USA
** Former students of the Polymer Interfaces Center.

SERIES I: The role of rubber particle size is examined using the diglycidyl ether of bisphenol A based epoxy cured with piperidine, DGEBA/PIP epoxy polymer, and modified with a carboxyl terminated copolymer of butadiene-acrylonitrile, CTBN rubber, or methacrylated copolymers of butadiene-styrene, MBS rubber. See reference 7.

SERIES II: The role of cavitation resistance is examined using a DGEBA/amino ethyl piperazine (AEP) epoxy polymer modified with either CTBN, MBS or hollow plastic spheres (HPS). See reference 8.

SERIES III: The role of the rubber-epoxy interphase is examined using a DGEBA/4,4'-diamino diphenyl sulfone (DDS) epoxy polymer modified with CTBN adducts containing DGEBA or DGEP. See reference 9.

SERIES IV: The role of the overall morphology is examined using DGEBA/PIP epoxy polymer modified with custom core/shell latex particles where the chemistry of the shell polymer can be varied to control the morphology of the blend. See reference 10.

SERIES V: The role of the overall morphology is examined further using DGEBA/PIP epoxy polymer modified with custom core/shell latex particles where the chemistry of the shell polymer is such that the particles are uniformly distributed. Epoxy spheres are added to cause either discontinuous or co-continuous segregation.

Mechanical Characterization

Several mechanical tests were used to evaluate these model systems. Uniaxial mechanical behavior was determined in tension and in compression. Tensile tests were performed using ASTM D638 guidelines. Compression tests were performed according to ASTM D695. Fracture toughness was determined using linear elastic fracture mechanics. Three-point bend, single-edge notched tests were performed according to ASTM D5045 guideline. Fatigue crack propagation resistance was determined using linear elastic fracture mechanics. Compact Tension (CT) tests were performed according to ASTM E647 guidelines. Constant load ratios of R=0.1 were used.

RESULTS AND DISCUSSION

Role of Particle Size

Previous work [11] had led to an empirical relation between the size of the particle and the inherent plastic zone size of the unmodified epoxy resin: *When diameter of the particle > inherent plastic zone of the matrix then no particle induced shear banding occurs at the crack tip.* The FCP behavior of unmodified and CTBN-modified epoxy polymers further support this empirical relation. Table 1 reveals that the fatigue crack growth rate is NOT retarded by the addition of CTBN particles at low ΔK values (for R-ratio = constant = 0.1). Azimi et al. [7] have explained this observation in terms of a particle size - process zone interactions. If the rubber particle size is less than the plastic zone size then the particles simply act as bridging particles which provide little improvement in FCP resistance. On the other hand, if the plastic zone is larger than the rubber particle size then the particles cavitate and induce shear bands which further increase the size of the plastic zone and improves FCP resistance. Micrographs of the fracture surfaces at low and high ΔK support this hypothesis.

Importance of Cavitation

The use of hollow plastic spheres (HPS) represents pre-cavitated particles with no cavitation resistance. Table 2 contains the results for the Series II epoxies. The analysis of the fractured specimens reveals that HPS toughens the epoxy in a manner similar to that of rubber particles. i.e. HPS induce shear banding and matrix dilation. The effectiveness of HPS as toughening agents decreases as the size of the particles increases. The use of acrylonitrile-butadiene or styrene-butadiene elastomers, which are more resistant to

cavitation, does not result in further improvements in fracture toughness. Therefore, one may conclude that cavitation resistance cannot always be used to optimize toughness and that some matrices may be insensitive.

Influence of the Rubber Epoxy Interphase

Unfortunately, no further improvements in fracture toughness were observed when CTBN is adducted with either a ductile or rigid epoxy. See Table 3. However, much can be learned from this study. The amount of matrix dilation around the rubber particles in the stress-whitened zone increased when CTBN-DGEP adducts are used. Correspondingly, the amount of matrix dilation around the rubber particles decreased when the CTBN-DGEBA adduct is used. TOM investigations shows that the plastic zone does not penetrate as deeply into the epoxy matrix when CTBN-DGEBA are used. Therefore, these results suggest that there is an interaction between matrix dilation and shear band propagation.

Importance of Blend Morphology

The original intent of this work was to vary the interphase region between the rubber particle and the epoxy matrix by varying the chemical composition of the shell polymer in core/shell latex particles. However, it was quickly realized that the changes in shell polymer chemistry could be used to control the overall morphology of the blend.

The influence of particle dispersion in the epoxy matrix has a dramatic effect on fracture toughness. Table 4 shows that the fracture toughness decreases as the shell AN content is increased. SEM analysis revealed that the uniformity of the blend increases with increasing AN content of the shell. TOM revealed that co-continuous microclustering allowed the plastic zone to grow deeper into the matrix. The larger plastic zones corresponds well to the increase in toughness.

The Series V epoxies were formulated to investigate the role of blend morphology in more detail. Uniformly distributed core-shell rubber particles were forced to segregate by the addition of epoxy spheres, which were prepared using emulsion polymerization methods. Epoxy particles containing segregated particles were also prepared. These results will be discussed during the presentation.

CONCLUSIONS

The following conclusions can be made:

- Rubber-particle size - plastic zone size relations can be used to predict the occurrence of shear banding, hence toughness improvement.
- Overall blend morphology strongly influences fracture toughness. Formation of co-continuous microclusters is beneficial.
- Increasing the cavitation resistance of the rubber particles did not result in increases in fracture toughness. This statement may not be true for all polymeric matrices.
- The presence of a ductile interphase around the rubber particle does increases the amount of plastic dilation in the matrix, however, there appears to be a negative relation between matrix dilation and shear band growth.

ACKNOWLEDGMENTS

This work was support by grants from the National Science Foundation, Petroleum Research Fund, and the Polymers Interfaces Center (An NSF- IUCRC program).

REFERENCES

[1] F. J. McGarry and A. M. Wilner, Org. Coat. Plast. Chem. 28 (1968) 512.

[2] A. J. Kinloch, S. J. Shaw, D. A. Todd, and D. L. Hunston, *Polymer* **24** (1983) 1341.

[3] A. F. Yee and R. A. Pearson, J. Mater. Sci., 21 (1986) 2462.

[4] R. A. Pearson and A. F. Yee, J. Mater. Sci., 21 (1986) 2475.

[5] R. A. Pearson and A. F. Yee, J. Mater. Sci., 24 (1989) 2571.

[6] A. J. Kinloch, C. A. Finch, and S. Hashemi, Polym. Comm., 28 (1987) 322..

[7] H. R. Azimi, R. A. Pearson and R. W. Hertzberg, J. Mater. Sci. Lett. 13 (1994) 1460.

[8] R. Bagheri and R. A. Pearson, Polymer, 37 (1996) 4529.

[9] R. Bagheri and R. A. Pearson, J. Appl. Polym. Sci., 58 (1995) 427.

[10] J. Y. Qian, R. A. Pearson, V. L. Dimonie, O. L. Shaffer, and M.S. El-Aasser, Polymer, 38 (1997) 21.

[11] R. A. Pearson and A. F. Yee, J. Mater. Sci., 26 (1991) 3828.

Table 1: The Series I epoxies showed that FCP resistance is improved at high ΔK levels.

DGEBA / Pip	K_{IC} (MPa√m)	ΔK@10-5 (MPa√m)	ΔK@10-3 (MPa√m)
0 % CTBN	0.86	0.4	0.56
1% CTBN	1.05	0.4	0.64
5 % CTBN	1.69	0.4	0.82
10% CTBN	2.02	0.4	0.86
10 % MBS	2.57	0.5	1.04

Table 2: The Series II epoxies demonstrated that toughness enhancement could be achieved with hollow plastic spheres (HPS).

Modifier Type	K_{IC} (MPa√m)	E (GPa)	σ_y (MPa)
None	0.85	2.8	76
10%CTBN (0.55 μm)	2.05	2.5	59
10% MBS (0.25 μm)	2.25	2.4	61
10% HPS-1 (0.40 μm)	2.30	2.4	--
10% HPS-2 (1.00 μm)	1.95	2.6	--
10% HPS-3 (15.0 μm)	1.30	2.8	--

Table 3: The Series III epoxies identified the interaction between matrix dilation and shear banding.

Modifier Type	K_{IC} (MPa√m)	Comments
CTBN standard	2.00	Particle cavitates matrix dilates plastic zone = 150 μm
CTBN-DGEP	2.00	enhanced matrix dilation plastic zone = 100 μm
CTBN-DGEBA	1.90	constrained matrix dilation plastic zone = 200 μm

Table 4: The overall blend morphology becomes more uniform as the AN content in the shell increases (toughness decreases).

AN/MMA Wt. Ratio	K_{IC} (MPa-√m)	E (GPa)	σ_y (MPa)
0/100	2.69±0.02	2.7	64.7
2.5/97.5	2.57±0.05	2.7	64.4
7.5/92.5	2.57±0.07	2.7	64.5
10/90	2.57±0.02	2.9	66.1
15/75	2.20±0.06	2.8	69.3
25/75	2.21±0.05	2.8	66.1

EFFECTS OF RUBBER PARTICLE CAVITATION ON DILATATIONAL YIELDING AND FRACTURE IN TOUGHENED PLASTICS

C. B. Bucknall and D. Ayre*

The energy balance model for cavitation of rubber particles is developed to include energy released from the matrix, and combined with criteria for temperature- and pressure-dependent shear yielding in polymers containing voids, in order to produce maps relating the behaviour of rubber-toughened plastics to the von Mises effective stress σ_e and the mean stress σ_m. The resulting 'cavitation diagrams' are compared with experimental data, and used to interpret the observed effects of particle and matrix characteristics on the deformation and fracture behaviour of toughened plastics.

INTRODUCTION

Cavitation of the rubber particles has long been recognised as making an important contribution to yielding of toughened plastics under critical conditions. Its role in relieving constraints on plastic deformation, especially at crack tips, has been stressed by several authors. On the other hand, the presence of voids in the matrix, due either to trapped air or to debonding at the particle-matrix interface, is known to weaken and embrittle most toughened plastics. The present paper addresses this and other aspects of rubber toughening, using the energy-balance model for cavitation of rubber particles.

MODELS FOR CAVITATION

Earlier papers on cavitation in rubber particles (1-3) concentrated upon the simplest case: a homogeneous spherical particle subjected to a fixed volume strain Δ_V. In this case, there is no exchange of energy with the surrounding matrix, and the energy U of the system can be written:

$$U(r) = \frac{2}{3}\pi R^3 K_r \left(\Delta_V - \frac{r^3}{R^3} \right)^2 + 4\pi r^2 \Gamma_r + 2\pi r^3 G_r F(\lambda_f) \qquad (1)$$

where G_r and K_r are the shear and bulk moduli of the rubber (subscript r), Γ_r = specific surface energy, $F(\lambda_f)$ = function of extension at break λ_f, and r = radius of void.

A necessary (but possibly not sufficient) condition for cavitation is that there is a value of r for which $U(r) < U(0)$, the initial energy of the particle. By applying this condition to eqn (1) it can be shown that the critical volume strain at cavitation is a function of particle size R and shear modulus G_r. However, while this relationship is qualitatively valid, it has obvious limitations. In order to develop a more accurate quantitative model, it is necessary to take account of other

* Cranfield University, Bedford MK43 OAL, UK

factors, specifically: (a) energy inputs from the surrounding matrix as the volume compliance of the particle increases; (b) stored elastic energy arising from differential thermal contraction as the material cools below the matrix T_g; (c) the presence of rigid inclusions embedded in the rubber phase; and (d) alternative criteria for cavitation, which are not based simply upon the condition $U(r) < U(0)$. Examination of eqn (1) shows that there is always a small energy maximum during the early stages of void formation, which could represent a barrier to void nucleation, in a manner similar to that seen in crystallisation. Each of the above factors has been addressed in a study of cavitation in a transparent grade of rubber-toughened PMMA, which is reported in more detail elsewhere at this conference (4). Comparison of the results with the energy-balance model indicates that $U(r)/U(0) > 1$ is not a sufficient condition for cavitation, and that the energy barrier at small r affects the process. The height of this energy barrier falls as the applied volume strain Δ_V increases, so that rates of cavitation at the yield point increase on decreasing the temperature.

In toughened plastics, cavitation of the rubber particles usually leads to dilatational shear yielding. Previous papers discuss the use of a modified Gurson equation to define the resulting yield envelope in terms of the effective stress σ_e and mean stress σ_m (1, 3), as follows:

$$\sigma_e = \sigma_o \sqrt{1 - 2f\cosh\left(\frac{3\sigma_m}{2\sigma_o}\right) + f^2 - \frac{\mu\,\sigma_m}{\sigma_o}\left(2 - \frac{\mu\,\sigma_m}{\sigma_o}\right)} \qquad (2)$$

where μ represents the pressure-dependence of the yield stress and f is the effective volume fraction of voids. In this context, each cavitated rubber particle is treated as behaving like a void, in that its initial resistance to volumetric expansion is very low, so that f can be equated with the volume fraction of cavitated particles. Figure 1 shows how the yield envelope changes as an increasing fraction of particles cavitates, in a rubber-toughened plastic containing 40 vol% particles. The dotted lines indicate uniaxial tension, equi-biaxial tension (σ, σ, 0) and triaxial stress at a crack tip (σ, σ, 0.8σ), where cavitation clearly has a marked effect on yielding. A second version of this diagram is presented in Fig. 2, which defines three regions of deformation behaviour, divided by an upper-bound curve for pressure-dependent shear yielding in the absence of cavitation, and a lower-bound curve for the case of complete cavitation of the rubber particles.

Calculated values for the mean stress required to cavitate particles of various sizes are marked on Fig. 3, which provides a basis for comparing criteria for cavitation with those for shear yielding. The largest particles cavitate within the elastic region under most stress conditions of interest, whereas the smallest particles cavitate well beyond the lower bound yield envelope. Obviously, the envelopes shown in the illustrations refer only to specific combinations of temperature and strain rate, and if these factors are altered, the relative positions of yield envelopes and critical stress for cavitation may change significantly, as shown in Fig. 4. Point A on this diagram marks a state of stress for which the rate of deformation changes from $10^{-5}\,s^{-1}$ before cavitation to $10\,s^{-1}$ after cavitation to $f = 0.4$.

It is now generally accepted that rubber particle cavitation precedes and accelerates shear yielding in toughened polymers, but the suggestion that particle cavitation is necessary for initiation of multiple crazing in HIPS and other polymers is more controversial. However, new evidence on this point has been obtained by Yang (5) in experiments on HIPS, in which tensile bars were pre-strained at 23°C, unloaded and annealed, then retested to failure at 23°C. Where

the rubber particles cavitate below the lower bound yield envelope, as in HIPS, thereby initiating multiple crazing, successful toughening is achieved only when the morphology of the rubber particles provides a mechanism of strain hardening, involving the stretching of rubber fibrils. This requires stabilising rigid sub-inclusions of the type found in salami or rigid-core/rubber-shell particles. Homogeneous or poorly-bonded rubber particles are much less effective as toughening agents because they do not provide stabilisation in this way.

This discussion suggests an explanation for the difference between pre-existing voids and well-bonded cavitating rubber particles. Voids that are present from the beginning constitute potential nuclei for crazes and cracks while the polymer is in the elastic region. By contrast, well-bonded rubber particles remain intact until they reach a critical stress/strain. If their sizes and moduli are chosen in such a way as to postpone cavitation until the material is above the lower bound yield envelope, the risk of producing craze-nuleation sites is drastically reduced. On the other hand, if the particles are too small, and cavitation is delayed to the point where a critical crack has grown from an external surface, their toughening effects will be minimised. The precise conditions for rubber particle cavitation are thus of crucial importance under certain conditions, and are currently being investigated using a range of techniques, including detection of shifts in the T_g of the rubber phase in response to thermally or mechanically induced dilatational stress: cavitation reduces or eliminates this stress, causing the relaxation to shift to higher temperatures.

CONCLUSIONS

This study has shown that the energy balance model provides a satisfactory basis for predicting the onset of cavitation in rubber particles under specified stress conditions. The model can be combined with yield envelopes calculated using eqn (2) to analyse the effects on deformation behaviour of materials characteristics (particle size, particle morphology, rubber content, particle-matrix adhesion) and test conditions (strain rate, temperature, specimen geometry). On the basis of this analysis, it can be seen that reduced toughness might result from premature cavitation (which leads to multiple crazing) or from delayed cavitation (which allows fracture to occur before significant yielding has occurred). Optimum toughness in critical situations is therefore associated with cavitation that takes place 'just in time', *i.e.* immediately above the lower yield boundary. The position of this boundary is a function of rubber content, temperature, strain rate, etc. At high rubber contents, high temperatures, and low strain rates, cavitation may be unimportant, because yield stresses are low enough to give plane-stress fracture even without cavitation.

ACKNOWLEDGMENTS

The authors thank the EPSRC for financial support of this programme, through grants GR/K24703 and GR/K99824.

REFERENCES

1. A Lazzeri and C B Bucknall, *J. Mater. Sci.* **28** (1993) 6799.
2. C B Bucknall, A Karpodinis and X C Zhang, *J. Mater. Sci.* **29** (1994) 3377.
3. A Lazzeri and C B Bucknall, *Polymer* **36** (1995) 2895.
4. D Ayre and C B Bucknall, Paper P80, this conference.
5. H H Yang and C B Bucknall, Paper P79, this conference.

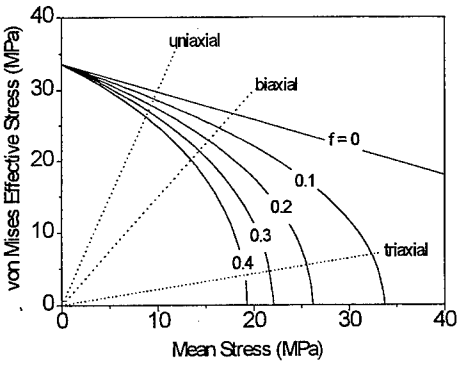

Fig. 1. Yield envelopes for RT-PMMA containing 40 vol% of rubber particles, for a range of values of f, the effective volume fraction of voids.

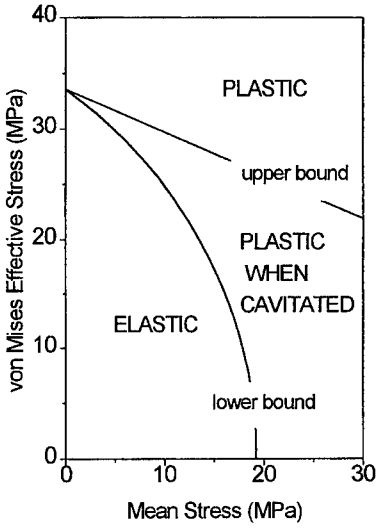

Fig. 2. Cavitation diagram based on Fig. 1, showing elastic, conditionally plastic, and unconditionally plastic stress conditions for one temperature and strain rate.

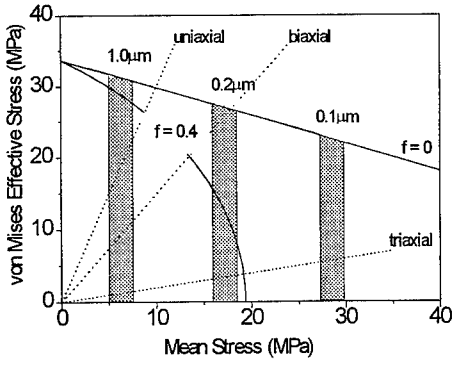

Fig. 3. Cavitation diagram based on Fig. 1, showing effects of varying rubber particle size and the onset of dilatational yielding.

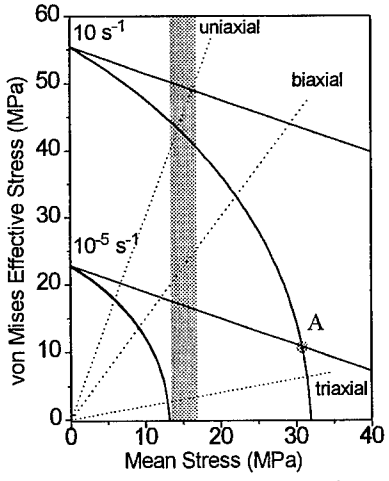

Fig. 4. Cavitation diagram based on Fig. 1, showing effects of varying strain rate. At point A, cavitation increases rate a million fold.

POSTER SESSION ONE

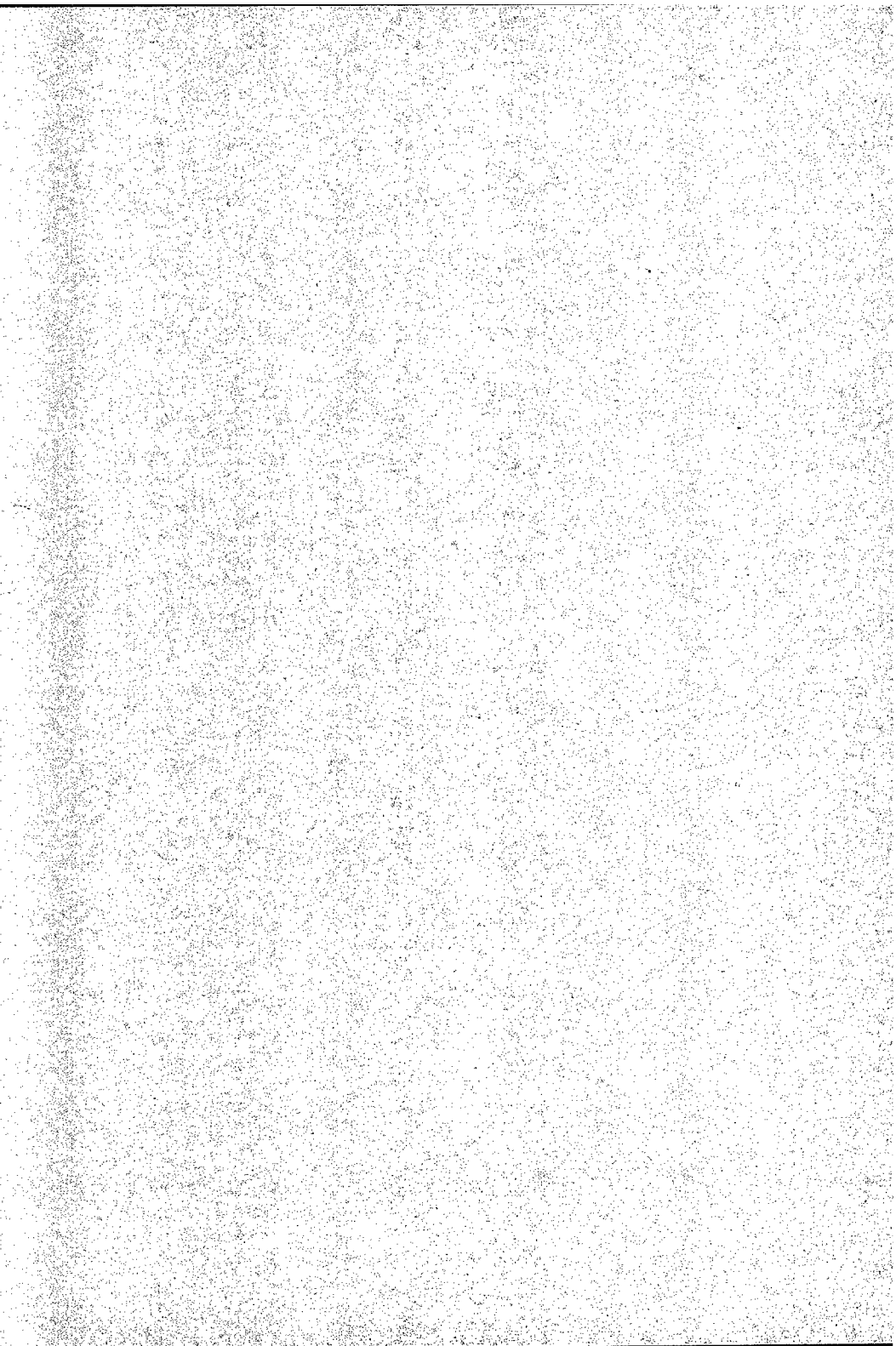

New studies about deformation kinetics in polymers using laser interferometer

P.N. Yakushev, N.N. Peschanskaya

Ioffe Physical-Technical Institute of the Russian Academy of Sciences, St Petersburg, Russia

The original method for precise creep rate measurements using laser interferometer has been developed. It gives the opportunity to investigate the activation parameters of deformation at any point of creep curve in the wide ranges of temperatures and deformation values.

New regularities of deformation kinetics for glassy polymers have been found. It has been shown that activation energy Q_o and activation volume α are the functions of temperature and deformation but their relation q_i is connected with cohesion energy E_{coh} :

$$q_i = \frac{Q_o V_m}{\alpha} = \frac{E_{coh}}{3},$$

where V_m is the volume of one monomeric unit.

The correlation obtained between these experimental kinetic parameters and E_{coh} confirmed the intermolecular non-chemical nature of potential barriers with deformation of isotropic polymers.

The influences of the molecular motion to the creep kinetics was also shown: because the activation parameters of deformation change in the relaxation transitions sharply.

The possibilities for studying of microplasticity in different materials including the brittle ones have been demonstrated. On this basis the creep -rate-spectra (CRS) method as a low-frequency and high resolution procedure of relaxation spectrometry has been offered.

Plots of the creep rate as a function of temperature under the small

fixed stresses have the appearance of spectra with peaks which determine the regions of relaxation transitions. The deformation method with nightly accurate rate measurements reveals the complex structure of the broad relaxation regions. It was shown that the heat treatment of polymers and other influences lead to changes of varying degree in characteristics of different transitions. Creep rate spectra can be used for faster prediction of critical temperatures of the most strong changes in the kinetics of deformation and fracture. By comparing the spectra of numbers of the polymer modifications we can choose the optimum conditions for using of every modification. The results of these studies demonstrate the connection between molecular mobility and mechanical properties.

TENSILE YIELD OF POLYETHYLENE AND ETHYLENE COPOLYMERS: EVIDENCE OF TWO THERMALLY ACTIVATED RATE PROCESSES

V. Gaucher-Miri, S. Elkoun, R. Séguéla*

The true-stress-strain characterization of the tensile yield as a function of temperature and cross-head speed is reported for three ethylene-butene copolymers having different crystal weight fractions in the range 0.69-0.35. Evidence is given of two thermally activated rate process operating competitively in relation to the draw conditions. Homogeneous and heterogeneous crystal slip are suggested on the basis of the concept of the mosaic block structure of the crystalline lamellae. Two crystal slip models are proposed, the competition of which relies on quite different dependencies on temperature and crystal thickness.

INTRODUCTION

Engineering stress-strain curves from polyethylene and ethylene copolymers under tensile loading usually display double yield points (1,2). The origin of this phenomenon is not clearly established, but it seems that several mechanisms are involved. True stress-strain measurements have been carried out in order to check if the double yield point is not a simple geometrical effect due to necking. The thermal activation of the phenomenon is studied through the influence of draw temperature and strain rate on the yield stress.

EXPERIMENTAL

Three ethylene-butene copolymers having nearly equal molar weights and various crystal weight fractions have been investigated. Their molecular and physical characteristics are reported in Table 1. The true-stress-strain curves have been determined using a video-monitored equippement developped for the study of strongly necking materials.

TABLE 1. Weight-average and number-average molar weights, M_w and M_n, ethyl group concentration, χ, weight-fraction crystallinity, α_c, and crystal thickness, l_c, of the polymers.

Materials	$M_w x10^{-3}$	$M_n x10^{-3}$	χ (ethyl/CH_2 in %)	α_c	l_c(nm)
A	157	30	0.4_0	0.69	17.8
B	136	31	1.3_5	0.55	12.5
C	146	27	3.8_0	0.35	8.0

RESULTS AND DISCUSSION

The true-stress-strain curves $\sigma(\varepsilon)$ of the three copolymers display one or two yield points, depending on the temperature and strain rate. This appears through two strain domains having different strain-hardening rates. Figures 1 and 2 show this effect in the case of copolymer B for different temperatures and for different strain rates. These findings give evidence that the double yield phenomenon is related to the occurence of two thermally activated rate processes of plastic flow, one of them being activated alone or the two of them being working consecutively as a function of strain.

* Laboratoire "Structure et Propriétés de l'Etat Solide", Université de Lille, Bat. C6, 59655 Villeneuve d'Ascq Cedex, France.

The true strain hardening rate versus strain (Figure 3) shows that in the case of copolymer C which displays a double yield point at 20°C, a significant homogeneous plastic deformation takes place ($\gamma>1$ for $\varepsilon<1.0$) prior to the occurence of a plastic instability ($\gamma<1$ for $1.0<\varepsilon<2.5$). In contrast, for copolymer A which gives a single yield point at 20°C, necking occurs readily at $\varepsilon=0.1$. Considering this homogeneous or heterogeneous character of the macroscopic deformation, and borrowing from pionnier structural studies of the mechanisms of plastic deformation on oriented polyethylene (3,4), homogeneous and heterogenous crystal slip processes are suggested to compete for predominance in plastic flow. To the homogeneous process are associated low values of the activation volume and activation energy in regard to the strong temperature and strain rate dependencies of the yield stress. A strong strain-hardening rate is also attributed. In contrast, the heterogeneous process is characterized with high values of the activation volume and activation energy in consideration of the low temperature and strain rate dependencies of the yield stress. A weak strain-hardening is considered in this case.

Figure 4 shows the principle of occurence of a single or a double yield point, depending on the temperature that can activate either of the two processes, owing to their different temperature dependency and different strain-hardening rate. At $T_1<T_2$, the heterogeneous process has the lower yield stress so that it occurs first, and owing to its low strain-hardening it remains the leading process of the plastic flow as strain increases. But this does not mean that the homogenous process is not active. Indeed, it may occur in parallel, but with a very low strain rate consistent with its own activation volume and the actual flow stress that is governed by the heterogeneous process. At T_2, the homogeneous slip has become more favourable thanks to its strong temperature dependency involving a larger drop of its yield stress compared to that of the heterogeneous slip. However, due to the stronger strain-hardening of the homogegeneous slip, this later becomes less favourable than the heterogeneous slip when the two $\sigma(\varepsilon,T_2)$ curves cross themselves. In this case, the homogeneous slip does not stop suddenly at the strain level for which the two curves cross, but rather slows down drastically at a strain rate consistent with the flow stress established by the heterogeneous slip.

Two models of plastic flow have been borrowed from the litterature to account for the homogeneous and heterogenous crystal slip processes. The model assuming thermally activated nucleation of screw dislocations in lamellar crystals (5) is used to account for the homogeneous crystal slip. According to this model, the flow stress writes (6)

$$\sigma = \frac{\mu b}{\pi r_o} \exp\left(-\frac{2\pi\Delta G}{\mu b^2 l_c} - 1\right)$$

where μ is the shear modulus of the slip planes, b the elementary slip length (Burgers vector), r_o the size of the dislocation core, and $\Delta G \approx 40kT$ the energy barrier for the dislocation nucleation which notably accounts for the dependency on strain rate. This model has a strong dependence on temperature through the shear modulus and the activation energy. The second process of heterogeneous crystal slip is the precursor of the plastic instability when the actual strain rate afforded by the stress-induced nucleation of dislocations at a given temperature is not high enough to match the macroscopic applied strain rate. Two hypothesis may be proposed for the occurence of heterogeneous or localized crystal slip. On the one hand, the defective regions in the mosaic block structure of the crystalline lamellae can be suspected to concentrate the slip owing to the reduced molecular interactions in the misfit interface. On the other hand, nucleation of partial dislocations propagating at lower shear stress than perfect dislocations may take place. But such partial dislocations leave behind them a stacking fault that is prone to play the same role as the above mentioned defective regions. The model proposed for the heterogenous slip is borrowed from an approach of the plasticity of amorphous polymers (7) through the glide of stacking faults. The yield stress is given by the following relation (6)

$$\sigma = \mu\,(h/d)^2$$

where h is the width of the stacking fault normal to the slip interface and d the length of the defect in the slip direction. Both factors have been estimated by assuming arrays of 2g1 kinks. The temperature dependency of the shear modulus is taken from McCullough and Peterson (8).

Comparison of the two models (Figure 5) clearly shows a stronger temperature sensitivity of the flow stress of the homogeneous slip together with a stricking crystal thickness dependence. The first feature makes the homogeneous slip become more favourable at high temperature. The second feature improves the ability of low crystallinity copolymers to develop homogeneous slip at low temperature. Both trends are actually observed (2).

The strain-hardening that mainly arises from the chain network stretching is suspected to be stronger for the homogeneous crytal slip owing to the chain loops bridging the slip planes that have a short contour length and get quickly fully extended (i.e. Langevin-type behaviour). In contrast, heterogenous slip turns into fragmentation of the crystalline lamellae accompanied by unfolding of the chains from the fracture surfaces of the crystal blocks that involves a low strain-hardening owing to the very large molecular strains (i.e. Gaussian-type behaviour).

CONCLUSION

Homogeneous and heterogeneous crystal slip processes are suspected to be the basic mechanisms of plastic flow in ethylene copolymers. The nucleation of dislocations and the glide of stacking faults are considered for modelling these two processes. In agreement with the experimental findings, the comparison of the two models predicts a stronger temperature dependency for the homogeneous slip together with an unequal crystal thickness sensitivity. This property is suggested to contribute to the greater propensity of low crystallinity copolymers for homogeneous plastic deformation.

REFERENCES

1 Brooks N W, Duckett R A, Ward I M, *Polymer* **1992**, *33*, 1872.
2 Séguéla R, Darras O, *J. Mater. Sci.* **1994**, *29*, 5342.
3 Takayanagi M, Kajiyama T, *J. Macromol. Sci.* **1973**,*B8*, 1.
4 Bowden P B, Young R J, *J. Mater. Sci.* **1974**, *9*, 2034.
5 Young R J, *Philos. Mag.* **1974**, *30*, 85.
6 Gaucher-Miri V, Séguéla R, *Macromolecules* to appear.
7 Escaig B, *Polym. Eng. Sci.* **1984**, *24*, 737.
8 McCullough R L, Peterson J M, *J. Appl. Phys.* **1973**, *44*, 1224.

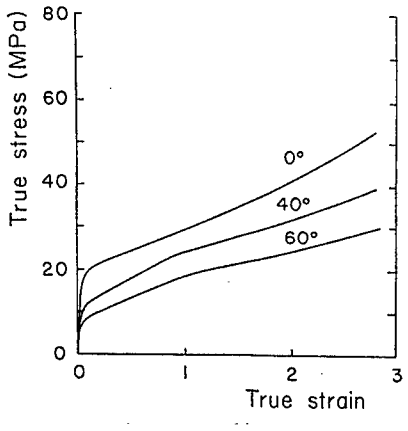

Fig. 1: Temperature effect on copolymer B at the strain rate $\dot{\varepsilon}_o=10^{-3}s^{-1}$.

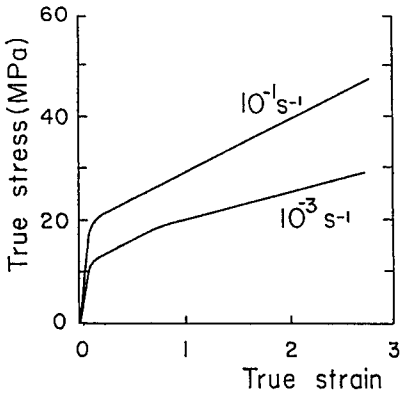

Fig. 2: Strain rate effect on copolymer B at the temperature 20°C.

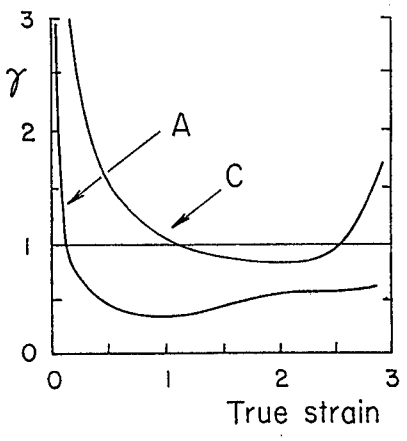

Fig. 3: True strain-hardening $\gamma=\left(\frac{\partial \mathrm{Ln}\sigma}{\partial \mathrm{Ln}\dot{\varepsilon}}\right)_{\dot{\varepsilon}}$ versus strain at 20°C and $\dot{\varepsilon}_o \approx 10^{-3} s^{-1}$.

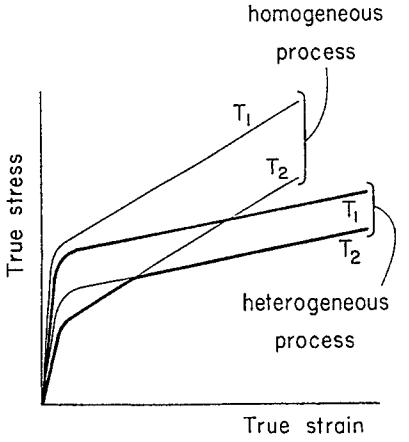

Fig. 4: Schematic drawing for the occurence of a single or a double yield point.

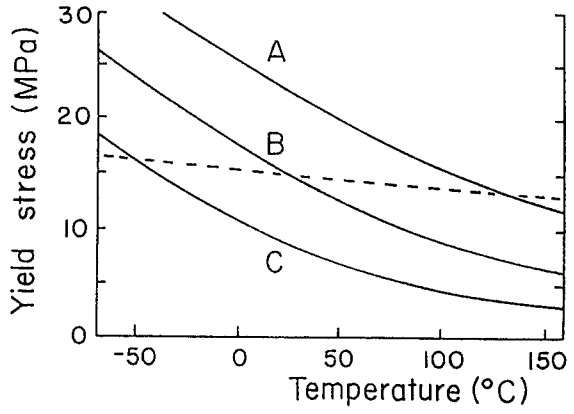

Fig.5: Predicted variations of the yield stress for the two models: (—) homogeneous slip; (----) heterogeneous slip.

MECHANICAL PROPERTIES OF RIM COPOLYMERS

A. N. Wilkinson*, M. Davallo* and J. L. Stanford†

The effects of formulation variables on the mechanical properties of RIM copolyureas (PUr) and copoly(urethane-urea)s (PUU) were determined using a simple demould toughness test, DMTA, tensile stress-strain and single edge-notch tensile fracture tests. Three formulation variables were investigated: (i) hard segment (HS) content; fracture and tensile stress-strain studies revealed a transformation in PUr behaviour with increasing HS-content from a flexible, tough elastomer to a rigid glass. (ii) polyamine or polyol prepolymer; a PUr exhibited superior tensile and thermal-mechanical properties but inferior demould toughness and fracture behaviour than an equivalent PUU, ascribed to morphological differences resulting from a change in copolymerisation behaviour. (iii) polyol functionality; the demould toughness of PUU increased significantly at higher polyol functionality, due to more rapid molar mass development during copolymerisation. However, thermal-mechanical, tensile and fracture behaviour showed a greater dependence on the resulting degree of phase separation.

INTRODUCTION

Copoly(urethane-urea)s (PUU) and copolyureas (PUr) formed by RIM are used extensively for large, complex components. Nominally, these materials are segmented block copolymers, with flexible, rubbery (or "soft") polyether segments linked to rigid, glassy (or "hard") polyurea segments, formed via random-step reactions of aromatic diisocyanates with mixtures of (hydroxyl- or amine-) functionalised polyethers and aromatic diamines. However, during copolymerisation, as the liquid reactants are rapidly converted to a solid, a combination of spinodal decomposition-induced phase separation [1] and vitrification effectively quenches the system to yield a mixture of reaction products comprising homopolymers, various AB-type block copolymers and free monomers. This solid mixture possesses a non-equilibrium morphology which arises from the competition between homo- and co-polymerisation kinetics and thermodynamic changes occurring during the RIM process. This morphology has been shown [1, 2] to comprise co-continuous, soft- (SS) and hard-segment (HS) phases, the degree of phase separation of which depends on HS content and thermal history.

This paper reports on the effects of three formulation variables on the thermal and mechanical properties of PUU and PUr copolymers, namely: (i) HS content, increasing HS% results in a greater proportion of the rigid, glassy polyurea in the copolymer (ii) Prepolymer reactive group (-OH or the more reactive -NH_2), the reactivity of the SS-prepolymer has a significant affect on copolymerisation kinetics and the resultant morphology of the copolymer (iii) polyol functionality, increasing functionality results in the development of higher molar mass copolymer before the reaction is quenched by vitrification [3, 4].

EXPERIMENTAL

Reactants. The RIM materials comprised up to four components. (i) a polyisocyanate, M340, a liquid MDI variant with an equivalent weight (E_n) of 143 g mol^{-1} and a functionality (f_n) of 2.15. (ii) a polyether prepolymer with an $E_n \approx 2000$ g mol^{-1}; either a polyoxypropylene triamine (T5000) or one of three poly(oxypropylene-oxyethylene) polyols, a diol (Do4000), a triol (To6000) and a tetrol (To8000). (iii) an aromatic diamine chain extender, 3,5-diethyltoluene diamine. (iv) the PUU systems contained dibutyltin-dilaurate to catalyse the hydroxyl-isocyanate reaction.

*Department of Materials Technology, Manchester Metropolitan University, John Dalton Building, Chester Street, Manchester M1 5GD, UK. †Manchester Materials Science Centre, University of Manchester and UMIST, Grosvenor Street, Manchester M1 7HS, UK

Moulding. Materials were moulded as narrow rectangular plaques (75 x 250 x 3.5 mm) using in-house RIM equipment. The copolymers produced are designated using a code referring to the SS-prepolymer used and the % hard segment. For example, Do450 is a 50% HS PUU formed using the diol Do4000. The demould-toughness of the copolymers was determined using an area-diagram approach; mouldings were produced at a series of mould temperatures between 50 and 120 °C, and demould times between 5 and 1200 s. On demoulding, each plaque was immediately subjected to a 90° bend at its midpoint, and its response was classified as either very tough (no visual damage), tough (visual damage but no break) or brittle (broke on bending). Plaques that broke in the mould were classified as being very brittle. These data were used to construct moulding-area diagrams (MAD's) as shown in Figure 1. Materials for mechanical testing were taken from plaques demoulded after 100 s, at typical mould temperatures of 70 and 120 °C for RIM-PUU and -PUr materials, respectively.

Thermal Analysis. DMTA data were obtained in the range -100 to 300 °C using a Polymer Laboratories apparatus operating at a frequency of 1 Hz and a heating rate of 5 °C min^{-1}. A double cantilever bending geometry was used for beam samples (3.5 x 10 x 45 mm) to obtain dynamic flexural moduli and mechanical damping as functions of temperature. The modulus-temperature dependence of the RIM copolymers at low and high temperatures is expressed as the ratio of moduli at -30/+65 °C and +65/+160 °C, respectively.

Mechanical Testing. Tensile data were obtained at 20±2 °C from dumb-bell specimens tested at an extension rate of 10 mm min^{-1}. The fracture properties of the copolymers were measured in a single edge-notch tensile (SENT) geometry using rectangular specimens of length 150 mm, width 10 mm and thickness 3.5 mm. Tests were conducted at 20±2 °C, an extension rate of 10 mm min^{-1}. At least twenty specimens were tested for each material and the nominal notch depth, a, was varied to give a/d ratios in the range $0.04 \leq a/d \leq 0.5$. Notches were cut approximately to pre-determined depths using a saw and finished with a fresh razor blade to sharpen the notch. During the tests, the onset of crack propagation was determined visually and marked on the force-time curve. The actual notch depths were measured, after fracture, to within 0.001 mm using a travelling microscope. Due to changes in formulation, RIM-copolymers vary from brittle glasses to yielding plastics and elastomers. Thus, the analysis of SENT data also varies [5, 6]; from an LEFM analysis to determine a value of fracture toughness, K_{Ic}, to determination of fracture energies, G_{Ic} or J_{Ic}, for materials which exhibit bulk, non-linear elastic behaviour or bulk plastic yielding, respectively .

RESULTS AND DISCUSSION

(i) Increasing HS% (35 → 50 → 65 % by weight). The MAD's determined for these three systems showed large reductions in demoulding area (defined as the combined area of very tough or tough behaviour) as HS% increased, which is attributed to more rapid vitrification in systems with high HS% resulting in a lower molar mass at demould. Tensile and fracture studies revealed a transformation in material behaviour with increasing HS%; from a flexible, tough elastomer to a yielding plastic and finally a rigid glass (Figure 2 and Table 2). DMTA (Figure 3, Table 1) showed an improvement in high temperature modulus with increasing HS%, due to the prescence of a greater proportion of the rigid, high-T_g polyurea.

(ii) SS functional group (i.e. -OH vs. $-NH_2$). In general, the PUr exhibited inferior fracture behaviour (Table 2) and a much smaller demoulding area than equivalent PUU, but superior thermal-mechanical and tensile properties (Figures 4 and 5). This behaviour can be attributed to differences in copolymerisation behaviour [4], which results in a lower degree of phase separation within PUr systems. Thus, at room temperature the PUr effectively contains a greater volume of glassy material, consisting of HS and mixed HS/SS, than the equivalent PUU resulting in a stiffer, stronger but less tough material.

(iii) SS-f_n. The demoulding areas of the PUU systems increased markedly at higher SS-f_n, due to more rapid molar mass development during copolymerisation [4]. The thermal-mechanical, tensile and fracture behaviour of both systems showed a greater dependence on the degree of phase separation resulting from the copolymerisation (Table 1).

Table 1. DMTA data for RIM-copolymers

Copolymer	PSR* / %	T_g^S / °C	T_g^H / °C	E'(-30°C) / E'(65°C)	E'(65°C) / E'(160°C)
HS%					
T535	63	-38	215	5.6	2.0
T550	68	-34	234	4.1	1.8
T565	59	-35	241	2.9	1.5
PUr vs PUU	(T550 vs To650)				
To650	72	-40	188	3.0	2.1
Polyol f_n	(Do450 vs To650 vs To850)				
Do450	81	-44	184	2.6	2.0
To850	66	-41	194	3.2	2.0

* PSR = phase separation ratio calculated from DSC studies [4]

Table 2 Tensile and SENT data for RIM-copolymers

Copolymer	E / MPa	σ_y[a] / MPa	ε_y / %	σ_u / MPa	ε_u / %	U_t / MJ m^{-3}	K_{Ic} / MPa m$^{0.5}$	G_{Ic} / kJ m^{-2}	J_{Ic} / kJ m^{-2}
T535	280	8.9	12	15.9	276	51	-	4.3	-
T550	496	16.3*	16	28.1	170	47	-	2.6	3.0
T565	1144	38.4*	11	37.6	17	9	1.5	1.9	-
To650	337	12.9		24.9	194	48	-	3.5	4.8
Do450	436	15.1*	15	27.9	249	68	-	3.7	5.1
To850	296	11.6		24.2	197	45	-	3.1	4.4

a Extrinsic yield points determined using Considere's construction, or intrinsic yield points marked*.

REFERENCES

1. Ryan, A.J., Polymer, 1990, 31, 707.
2. Ryan, A.J., Still, R.H., Stanford, J.L., Plast.Rubb. Proc. Appl., 1990, 13, 99.
3. Pannone, M.C., Macosko, C.W., Polym. Eng. Sci., 1988, 28, 660.
4. Stanford, J.L., Still, R.H., Wilkinson, A.N., Polymer, 1995, 36, 3555.
5. Ryan, A. J., Stanford, J.L., Still, R.H., Brit. Polym. Jnl., 1988, 20, 77.
6. Stanford, J.L., Still, R.H., Wilkinson, A.N., Polymer International, 1996, 41, 283.

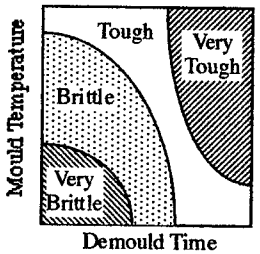

Figure 1. Schematic moulding -area diagram

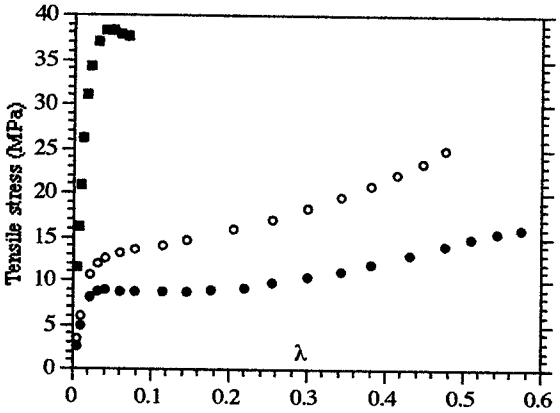

Figure 2. Tensile stress-strain (extension ratio) data for PUr of HS% (●) 35%, (○) 50% and (■) 65%.

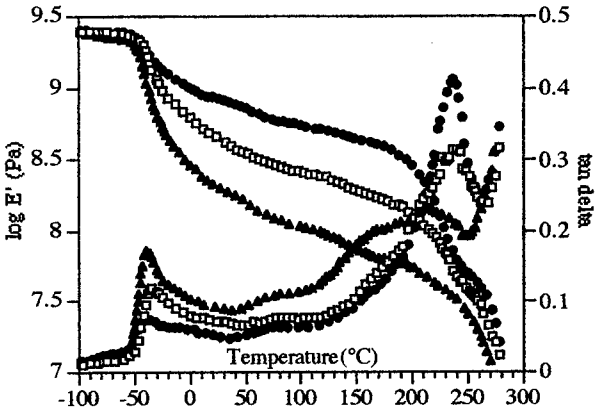

Figure 3. DMTA data for PUr of varying HS%: (●) HS% = 35, (□) 50%, (▲) 65%.

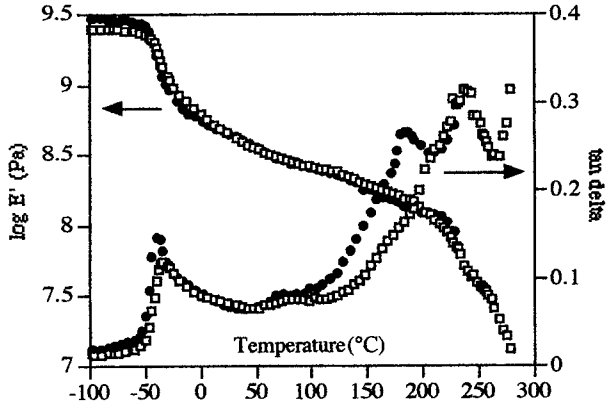

Figure 4. DMTA data for a 50% HS PUr (□) and an equivalent PUU (●).

ARREST AND HEALING OF A SURFACE CRACK IN POLY(METHYL METHACRYLATE) DUE TO CASE II DIFFUSION OF METHANOL

M. Kawagoe*, M. Nakanishi†, J. Qiu*, and M. Morita*

The behaviour of arrest and healing of a surface precrack due to case II diffusion of methanol in poly(methyl methacrylate) (PMMA) was examined in relation with the distribution of internal compressive stress in the surface swollen layer induced under constraint by the inner glassy core. It was demonstrated that the induced compressive stress clearly suppresses the growth of inserted precrack under applied tension, and also that the precrack is completely disappeared at 40°C for 3 min under no external load. Crack healing may be brought about both by high temperature above the glass transition temperature of swollen polymer and by the significant internal compressive stress.

INTRODUCTION

Case II diffusion is well characterized by the formation of a surface swollen layer clearly bounded by an inner glassy core [1]. The polymer in this layer is almost in equilibrium and highly softened as to show lower elastic moduli and shear flow stress. In addition, the internal compressive stress is induced near the boundary in this layer under constraint by the inner core [2]. Both the softening effects and the internal compression in the surface swollen layer are expected to exert considerable influences on the strength of polymer [3].

In this study the growth behaviour of a precrack inserted in the surface swollen layer is investigated for a PMMA - methanol system under static tension at 20°C. In addition, a possibility of crack healing [4] in the swollen layer is also examined for the same combination at 20 and 40°C. The crack growth and healing behaviour is discussed with reference to the distribution of internal compressive stress calculated by the finite element method (FEM).

EXPERIMENTAL

The material used is a commercially available PMMA sheet of 2mm thickness (Mitsubishi Rayon Co. Ltd). The rectangular specimens of 60x12x2mm^3 and 21x10x3 mm^3 were prepared for the measurements of the elastic modulus and the swelling strains, and for Poisson's ratio, respectively. The dumbbell-shaped specimen with gauge length of 15mm and width of 6mm were machined from the sheet for testing the tensile property and observing the behaviour of surface crack. Their cut surfaces were polished with a fine (#1000) abrasive paper. All the spesimens were annealed at 90°C for 2h in a forced-air oven.

The several mechanical properties were measured on the virgin and the swollen specimens, which were prepared by soaking in methanol at 20°C to equilibrium state showing a saturated weight gain. The elastic modulus was evaluated by the storage modulus, E', measured under a sinusoidal strain oscillating at 0.1Hz by means of a dynamic viscoelastic analyzer (Orientec Co. Ltd, VFA-1KNA). Poisson's ratios were obtained from the longitudinal and the lateral displacements of smaller rectangular

* Dept. of Mechanical Systems Engineering, Toyama Prefectural University
5180 Kurokawa, Kosugi, Toyama 939-03, Japan
† Toshiba Engineering Co. Ltd, 66-2 Horikawa, Saiwai-ku, Kawasaki 210, Japan

specimens under compression applied by a hydraulic-servo-controlled testing machine (Shimadzu Co. Ltd, FHF-FB10KN). All the measurements were made in air at 20±1°C applying methanol to the specimen surfaces for preventing them from drying, except for the virgin specimen. The tensile properties were evaluated in air at 20±1°C by using the same testing machine as the above at an elongation speed of 5mm/min.

The swelling strains were obtained from the changes in length, width and thickness of the rectangular specimen immersed in methanol at 20°C until equilibrium swelling.

The behaviour of a precrack inserted in the surface swollen layer was observed by using an equipment of our own making, which consisted of a loading system with a lever and a vessel filled with methanol, of which temperature was controlled by transporting methanol from and to a beaker placed in a thermo-controlled bath. The inserted precrack was monitored through the windows of the vessel under polarized light by use of a stereo microscope with a video camera, and recorded in a floppy disk by a still-video recorder (Olympas Co. Ltd, SR-300). A precrack of about 0.05mm length was immediately inserted in the surface swollen layer thicken to 0.5mm in methanol at 20°C by using a razor mounted a specially prepared device, perpendicularly to the longitudinal axis of specimen.

The behaviour of the crack grown under static tension to length of about 0.25mm in the surface swollen layer of 0.5mm thickness was observed after removing the tensile load in methanol at 20°C. A possibility of crack healing was also examined in methanol at 40°C, which was preliminarily confirmed to almost be an upper limiting temperature to allow case II diffusion in PMMA. At this temperature, however, the tensile load could not be applied, because the squeezing force between the specimen and the chuk faces was relaxed due to great softening of the swollen specimen surface. Thus the behaviour of precracks of about 0.2 - 0.25mm length was observed in the surface swollen layer of several thicknesses under no external load.

The glass transition temperature of the specimens swollen at 20 and 40°C were measured by a differential scanning calorimeter (MAC Science Co. Ltd, DSC 3100) using thin film samples of about 2mg in weight. The samples were once cooled to -20°C and then heated up at 10°C/min.

Three-dimensional FEM analyses of the induced stresses in the surface swollen layer and the inner glassy core were performed by use of a program for thermal stress analysis (Swanson Analysis Systems Inc., ANSYS 5.0A) by replacing the thermal expansion coefficients with the swelling strains. Considering the symmetrical geometry of the specimen, the calculation was done for the 1/8 part of the gauge region, which was divided into about 8000 elements of rectangular prism. In this calculation only the elastic stresses were estimated ignoring the viscoelastic responses of polymer, because of no adequate constitutive equation of dry and swollen PMMAs and of a capacity of our personal computer (NEC Co. Ltd, PC9821Xs). The absolute values thus seem to be overestimated, especially in the surface swollen layer, but the stress distribution necessary for interpreting the behaviour of inserted precrack may well be represented.

RESULTS AND DISCUSSION

Figure 1 shows a correlation among the longitudinal component of internal stress, σ_{yy}, calculated by the FEM, the concentrated stress at the crack tip, and the crack length varying with time under static tension. Just after loading, the precrack with initial length of 0.05mm rapidly advances to about 0.25mm. After that, however, the crack growth is almost arrested for long period. The opening displacement of arrested crack was observed to increase due to large creep deformation of swollen polymer. Subsequently the crack growth is accelerated. This accelerated crack took with the formation of a small sharp crack at the blunted crack front, and finally reached and passed through the boundary to cause the general fracture of glassy core. The internal stress, σ_{yy}, is in compression in the surface swollen layer and inversely in tension in the inner core, as indicated by a dotted line in the figure. It is also shown that the maximum value of compressive stress is not generated just at the bounday but near it in

the surface layer. The distribution of concentrated stress at the crack tip, represented by a solid line, was obtained by superposing the external stress amplified by a stress concentration factor at the crack tip to the internal stress field induced by surface swelling (the above dotted line). The external stress given by static tension also was simply calculated by the FEM neglecting the swelling deformation of the surface layer. The stress concentration factor at the crack tip was simply assumed to hold a constant of 7, supposing the arrested crack with shape approximated by a half ellipse. The actual stress at the entire surface thus will much higher than this calculation, because of much sharper tip of initial crack. It is clear that a position in the surface swollen layer where the crack growth is arrested for long time almost coincides with that where the tensile stress at the crack tip takes the minimum affected by the distribution of the induced compressive stress.

A crack grown to 0.22mm in length in the surface swollen layer of 0.5mm thickness at 20°C was gradually closed after unloading. The crack surfaces were almost in contact with each other after 30min, but still remained. The behaviour of inserted cracks at 40°C showed some interesting features, as shown in Figure 2. The cracks fairly shorter than the thickness of surface swollen layer did not completely disappear by soaking for long time of 30min, while the cracks reaching near the boundary in thinner swollen layer easily disappeared only for a few minutes (Figure 2a). In the overall swollen specimen, on the contrary, the crack was entirely closed, but remained for longer time preserving their initial length (Figure 2b). According to the tension tests, the tensile strength of the crack-healed specimen was completely recovered to that of the specimen without precrack. The FEM analyses indicate that the internal compressive stress in the longitudinal direction takes the maximum magnitude in the surface layer near the boundary, and also that its greater magnitude is obtained for thinner surface swollen layer. The phenomenon of crack healing shown in Figure 2a may take place with the aid of large internal compression acting on allover the crack in thinner swollen layer. The result for the entirely swollen specimen (Figure 2b), which is completely free of internal stress, also supports the necessity of the internal compression for crack healing. The DSC measurements revealed that the glass transition temperature, Tg, of the specimen swollen at 20°C is 43.5°C, while that at 40°C is lowered to 30.3°C. These results mean that the ambient temperature of 40°C causing crack healing obviously exceeds the Tg of the polymer in the surface swollen layer.

Therefore it is suggested that crack healing is brought about both by the formation of an interface by contact of crack surfaces under internal compression and by the self-diffusion of polymer chains across the interface to make the physical links of chains with the aid of thermal energy. These mechanisms may develop a smart material with a self-healing function in future.

CONCLUSIONS

The induced stresses due to case II diffusion were evaluated by the finite element method, and their effects on the behaviour of a precrack inserted in the surface swollen layer were examind for a combination of PMMA and methanol. It was demonstrated that the growth of precrack in the surface swollen layer under static tension at 20°C is almost arrested near boundary by the internal compressive stress, and also that the precrack inserted in thinner swollen layer is completely healed at 40°C only for 3min under no external load. The phenomenon of crack healing thus may result from sufficient contact pressure and promoted thermal motion of polymer chains.

REFERENCES

1. Windle, A.H., "Polymer Permeability" (Ed. J.Comyn), Elsevier, 1985, p.75
2. Alfrey, T., Gurnee, F.F. and Lloyd, W.G., *J. Polym. Sci.* (C), **12**, 249 (1966)
3. Kawagoe, M. and Nunomoto, S., *Polymer*, **32**, 3130 (1991)
4. Lin, C.B., Lee, S. and Liu, K.S., *Polym. Eng. Sci.*, **30**, 1399 (1990)

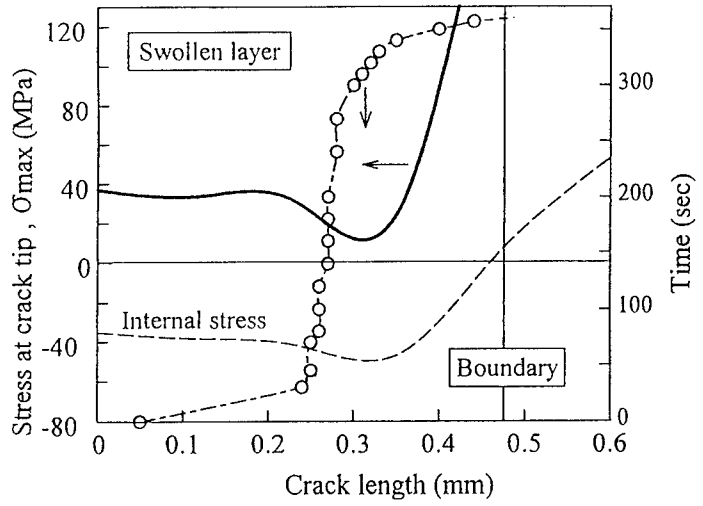

Fig.1 Correlation among the longitudinal induced stress, the stress at the crack tip, and the crack length varying with time under static tension at 20°C

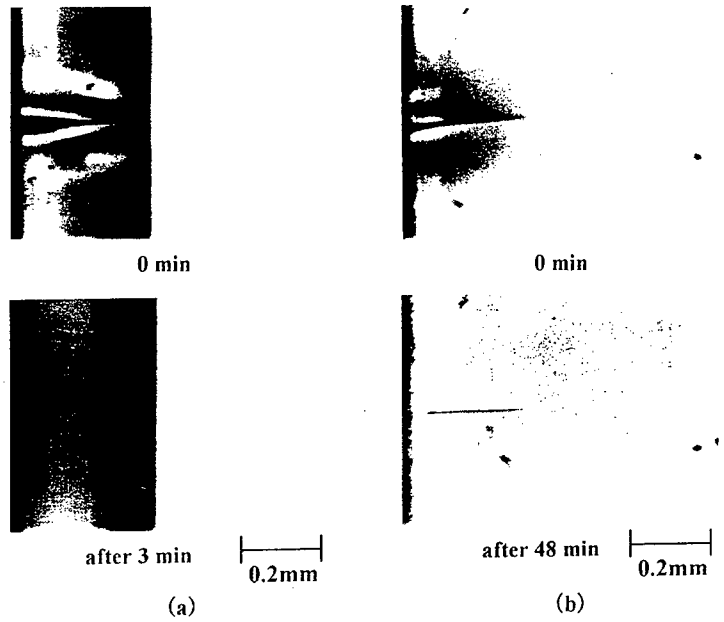

Fig. 2 Healing behaviour of precrack in methnol at 40°C :
(a) in the surface swollen layer ; (b) in the entirely swollen sample

MECHANICAL CHARACTERIZATION OF POLYMERS USING AN INVERSE MODEL*

Y. Tillier*+ , A. Gavrus*+, E. Massoni*+, N. Billon*+

INTRODUCTION

Good determination of the constitutive equations is required to obtain an accurate prediction of the impact resistance of polymers. Unfortunately, nowadays experimental characterization are not totally accurate in that field (Billon et al (1)). Data obtained during simple laboratory tests cannot be extrapolate to complex loading whereas complex tests (high strain rates or complex loadings) do not allow to determine intrinsic data. The development of inverse method based on the analysis of actual loading situations is of prime interest in that field. The aim of this study is to use such a numerical model coupled with multiaxial impact test. As a first step tensile test at intermediate strain rates are considered. In such a case, heat dissipation phenomenon makes it impossible to extract intrinsic data from experimental results using classical analysis.

THEORITICAL

The general purpose of rheological analysis is to express the evolution of stress σ within the material as a function of strain ε, strain-rate $\dot{\varepsilon}$ and temperature T :

$$\sigma = f(P, \varepsilon, \dot{\varepsilon}, T) \quad (1)$$

where f is the constitutive equation and P the constitutive parameters, respectively. Usually during tensile test, the only parameters being controled are the cross-head velocity and the initial temperature T^0. In parallel, the only parameters to be measured are the force, F^{ex}, and the cross-head displacement, Δl. In our case, using a video camera, it is possible to measure also the minimum diameter of the sample, d^{ex}. F^{ex}, Δl and d^{ex} are related to σ, ε and $\dot{\varepsilon}$ but not in a simple way (temperature can evoluate and strain are not homogeneous). Conversely, finite element simulation (Moal (2)) allows a precise modeling of tensile test providing that an exact expression of the constitutive equation (1) is known. Using the same operating conditions as experimental ones, the forces, F^c, and of the minimal diameter, d^c, can be calculated. Then the rheological problem is formulated as an inverse problem which consists in the determination of the constitutive coefficients P leading to the best fitting between computed data, M^c (F^c and d^c) and experimental measurements, M^{ex} (F^{ex} and d^{ex}).

THE DIRECT AND INVERSE NUMERICAL MODELS

The polymer is assumed to be isotropic, incompressible and to exhibit a plastic deformation well modeled using a Von Mises flow rule. That is, if s is the deviatoric stress tensor :

$$s = \frac{2}{3}\frac{\bar{\sigma}}{\bar{\dot{\varepsilon}}}\dot{\varepsilon} \quad (2)$$

* This work is done in cooperation with ELF-ATOCHEM and SOLVAY Companies

*+ *Centre de Mise en Forme des Matériaux, Ecole des Mines de Paris, URA CNRS 1374, BP 207, 06904 Sophia Antipolis Cedex, FRANCE*

In the case of polymer, the equivalent stress, $\bar{\sigma}$ is well approximated (G'sell et al (3)) by :

$$\bar{\sigma} = Kp\left(1 - \exp(-w\bar{\varepsilon})\right)\exp\left(h\bar{\varepsilon}^{n}\right)\dot{\bar{\varepsilon}}^{m} \tag{3}$$

where

$$\dot{\bar{\varepsilon}} = \frac{3}{2}\sqrt{\dot{\varepsilon} : \dot{\varepsilon}} \text{ and } \bar{\varepsilon} = \int_{0}^{t} \dot{\bar{\varepsilon}} dt \tag{4}$$

w takes into account viscoelastic deformation, Kp is a scale factor (consistency), h and n are related to strain-hardening process, whereas $\dot{\bar{\varepsilon}}^{m}$ characterizes a typical viscoplastic flow. The dependance of K upon temperature T is taken into account using an Arrhenius equation :

$$Kp = K\exp(a/T) \tag{5}$$

The finite element code allows to define the fundamental discretized equations associated to the mechanical equilibrium and the thermal balance. An incremental resolution procedure is used to solve the non-linear equations. The nodal coordinates and strain are updated following an explicit Euler scheme. The global quantities M^c (forces, diameters) are determined at the end of each increment using the computed values of the nodal state variables.

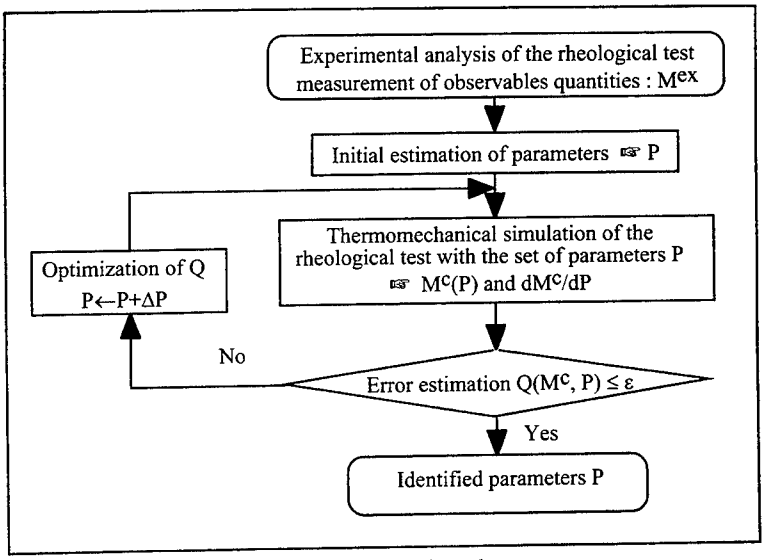

Fig 1 : The identification scheme

The identification of the parameters is based on an inverse approach. The difference between computed and experimental data is defined by a cost function Q formulated in a least squares sense :

$$Q(P) = \sum_{i=1}^{nbex}\left(\frac{\left(F_i^c - F_i^{ex}\right)}{F_i^{ex}}\right)^2 + \lambda\sum_{i=1}^{nbex}\left(\frac{\left(d_i^c - d_i^{ex}\right)}{d_i^{ex}}\right)^2 \tag{6}$$

where λ=0 for a cost function without geometrical terms or λ=1 if the experimental measurements of diameter are introduced. The number of experimental data, nbex, is the number of experimental measurement per experiment multiplied by the number of experiments. The problem is to find the set of parameters, P, which minimise the cost function Q. Fig. 1

illustrates the principle of the automatic sequence. An iterative Gauss-Newton method with line search algorithm is used. The numerical procedure requires the computation of the cost function derivatives with respect to all the parameters, P. Evaluation of forces and diameters sensitivity upon all rheological coefficients is then necessary. The main feature of the proposed technique is that sensitivity coefficients are calculated in close form using analytical differentiation of governing equations with respect to the parameters (Gavrus et al (4)). To solve the sensitivity system, the incremental resolution of the direct model is used.

COMPARISON BETWEEN ANALYTICAL AND INVERSE METHODS

A ductile high density polyethylene is used. Tests are performed on 6 mm-diameter cylindrical hour-glass-shaped samples at temperatures ranging from 23 °C to 90 °C. A video-controlled tensile testing system (G'sell et al (5)) enable us to determine the true strain in the sample, locally in the necking zone during the entire test and the actual shape of the zone of the sample where necking occurs. Rheological parameters are first determined during experiments performed at constant strain-rates ranging from 5 10^{-4} to 10^{-3} s^{-1} using classical techniques (3). Results are given in table I. These parameters do not allow to model tensile tests performed at strain-rates higher than 10^{-3} s^{-1}, since the global error is 25 %.

Parameters	Analytical identification		Computed Aided Rheology	
(Strain rates)	Initial values (low)	Analytical values (Intermediate)	Simple Q (Intermediate)	Mixed Q (Intermediate)
Kp (MPa s^m)	10	11	6	6.
w	30	31	287	322
h	0.5	0.5	0.9	1
n	2	2	1.3	1.2
a (K)	466	466	466	466
m	0.1	0.16	0.10	0.12
Δ_{global} (%)	**24.7**	**11**	**5.5**	**4.6**
(Δ_{force},$\Delta_{diam.}$)	-	(13.6%, 9.3%)	(2.9%, 9.2%)	(4.7%, 4.4%)

Table I : Parameters identification using classical and inverse methods (Δ=error) for a cross-head velocity of 2.5 mm/min.

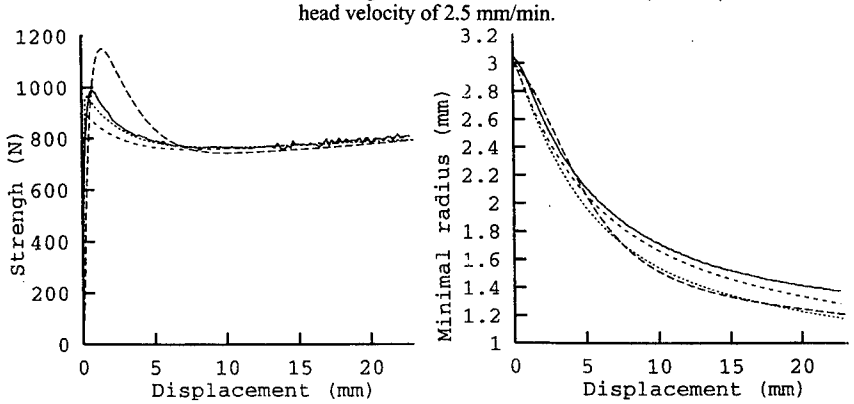

Fig. 2 : Evolutions of the force (left) and of the minimal diameter (right) versus the displacement in the case of a cross-head velocity of 2.5 mm/min. Comparison between analytical and inverse methods ; *Experimental measurements : ——, classical identification : ---- , Computer Aided Rheology with geometry : ····, without geometry : - - -*

So, measurements at higher strain rate are necessary. Unfortunately, in such a case, heat dissipation phenomenon induces important variation of temperature within the material (Tillier et al (6)).

If, despite this, classical analysis neglecting thermal effects, is used to estimate parameters from experiments performed at strain rates ranging from 5 10^{-3} to 2 10^{-2} s^{-1} (Tab. I), the resulting parameters allow to reproduce the force and the diameter with precisions of 14 % and 9 %, respectively (Fig. 2). Using our inverse method which takes into account heat dissipation, the deduced parameters are slightly different (Tab. I) and allow precisions of 3 % for the force and 9 % for the diameter. Results are different whether diameter is taken into account or not in the calculation (λ=1 or 0 in Eq. (6)). The error on the diameter (Tab. I) decreases with an antagonist effect on the force if experimental diameters are introduced in the cost function (Fig. 2). Final error are 5 % for the force and 4 % for the diameter.

CONCLUSIONS

A rheological identification procedure using a finite element simulation of the tensile test was developed. The method is based on the minimisation of a cost function depending on forces and possibly on the minimal diameters in the necking zone. The parameter sensitivity evaluation uses a direct differentiation of the discretized equilibrium equations. This study demonstrates the capability of the inverse method to be applied to actual experimental data. Application to a high density polyethylene clearly shows that characterizations of the mechanical behaviour of polymers performed at low strain-rate are inaccurate to model higher velocities tensile tests. Our code makes it possible to use higher strain rates experiments where thermal effects have to be correctly taken into account. It must be emphasized that thermal properties of the polymer (i.e., heat conduction, specific heat) have to be known. Further application to more complex loading situations will enable us to take into account specific strain-hardening.

NOTATIONS

$\dot{\varepsilon}$, σ, s = strain rate, stress and deviatoric stress tensors
$\dot{\bar{\varepsilon}}$, $\bar{\varepsilon}$ = equivalent strain - rate and the generalised deformation
p = the vector of nodal hydrostatic pressure
P = vector of rheological parameters
M^{ex}, M^{c} = experimental responses and computed quantities
Q = cost function

REFERENCES

1. Billon N., Maurin L., Germain Y., Proc. 1st International Conference on Mechanics of Time Dependent Materials, Ljubljana (1995)
2. Moal A., Massoni E., CHenot J.-L., Computer Methods in Applied Mechanics and Engineering 103 (1993) 417-434
3. G'Sell C., Jonas J. J., J. Mater. Sci. 14 (1979) 583
4. Gavrus A., Massoni E., Chenot J.-L., 'NUMIFORM'95', A. A. Balkema Edition, (1995) 563-568
5. G'Sell C., Aly-Helal N. A., Jonas J. J., J. Mater. Sci. 18 (1983) 1731
6. Tillier Y., Gandin E., Massoni E., Billon N., Proc. DEPPOS XIV, Grasse (1996)

We acknowledge Solvay and Elf Atochem companies for their support.

COMPRESSION TEST ON A POLYCARBONATE OVER A WIDE RANGE OF STRAIN-RATES.

M L Bisilliat*, G Gary+, J R Klepaczko*+, N Billon*

INTRODUCTION

The general purpose of this study is to characterise the mechanical behaviour of thermoplastics over a wide range of strain-rates, including impact loading. This paper focus on compression tests performed on a polycarbonate (Makrolon 3200) whose glass transition temperature is 150°C (measured using DSC analysis with a heating rate of 5°C/min) and whose average molecular weight is 31 027 g per mol.

EXPERIMENTAL PROCEDURE

Tests are performed at room temperature on 15 mm-diameter cylinder-shaped samples of height ranging from 3 to 15 mm. Specimens are machined from extruded rods. Their surfaces are lubricated to minimise friction effects. Depending on the strain-rate the experimental devices and, consequently, assumptions made to extract intrinsic data from measurements are different. For low strain-rates (up to 20 s^{-1}) a video camera continuously measures the current diameter, ϕ, of the largest section in the sample. Assuming the deformation to be *locally* homogeneous and the material to be isotropic and incompressible, stress, σ, and strain, ε, are :

$$\sigma = \frac{4F}{\pi\phi^2} \quad \text{and} \quad \varepsilon = 2\ln\frac{\phi}{\phi_0} \tag{1}$$

where F and ϕ_0 are the force and the initial diameter of the sample, respectively. Additionally, for very low strain-rate ($\leq 10^{-3}$ s^{-1}) a video-controlled system (1) allows tests at constant strain-rate whereas more rapid deformation are obtained at constant cross-head velocities.

Tests at high strain-rates (up to 5000 s^{-1}) are performed using the Split Hopkinson Pressure Bar (SHPB) technique (2, 3). Local measurements are no more possible, then the deformation is assumed to remain homogeneous in the sample. Let H_0 and H be the initial height of the specimen and its height at time t, respectively, then :

$$\sigma = \frac{4F}{\pi\phi^2}\frac{H}{H_0} \quad \text{and} \quad \varepsilon = \ln\frac{H}{H_0} \tag{2}$$

The latter assumption is valid only for strain lower than 0.36 (fig. 1) as already suggested using numerical simulations (4). Nevertheless, the value of yield stress, taken for convenience at the maximum of the stress vs. strain curve, is nearly not sensitive to these assumptions. To verify that stress wave propagation effects are negligible during SHPB measurements at high strain-

*: Centre de Mise en Forme des Matériaux, Ecole des Mines de Paris, URA CNRS 1374, BP 207, 06904 Sophia Antipolis Cedex, France.
+: Laboratoire de Mécanique des Solides, Ecole Polytechnique, 91 128 Palaiseau, France.
*+: Laboratoire de Physique et Mécanique des Matériaux, Université de Metz, Faculté des Sciences, Ile de Saulcy, 57 045 Metz Cedex, France

rate, samples of equivalent diameter and different heights, (5), have been used (fig. 2).

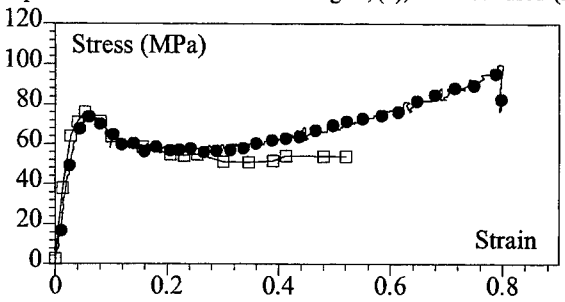

Figure 1. Stress vs. strain at 10^{-3} s^{-1}. Comparison between eqs. (1) (□)and (2) (•).

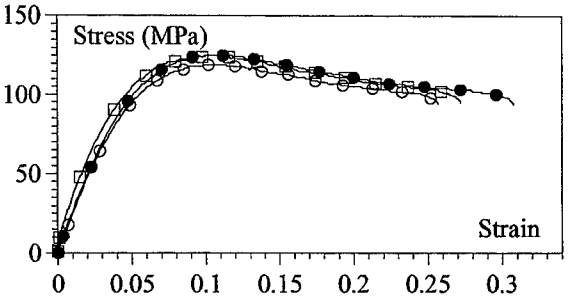

Figure 2. Stress vs. strain measured with the SHPB technique. Comparison between three samples : H_o= 9.6 mm (470 s^{-1}) (•), 8 mm (450 s^{-1}) (□) and 14.4 mm (400 s^{-1}) (O).

THERMAL AND STRAIN-RATE EFFECTS

Stress vs. strain curves significantly depend on strain-rate (fig. 3). In any case a peak appears as plastic deformation is initiated. This effect is rather common in amorphous polymers. Then, plastic flow occurs and an important strain-hardening process in observed at low strain-rate. Conversely, apparent strain-hardening decreases at high strain-rates. It can be shown that this observation can be correlated with heat generation due to energy dissipation.

Thermomechanical simulations (using a FEM code) of tensile tests coupled with Infra Red measurements (6), show that for this polymer, the adiabatic conditions are reached at strain-rates higher than 1 s^{-1}. Consequently, at high strain-rates the increase in temperature, ΔT, in the polymer can be estimated (assuming a complete conversion of mechanical work into heat):

$$\Delta T = \frac{1}{\rho C}\int \sigma(\varepsilon)d\varepsilon \qquad (3)$$

where ρ is the density, C the heat capacity and T the temperature, respectively.

In parallel to this increase in temperature, the consistency of the polycarbonate strongly depends on temperature. It is verified, using tests at controlled temperatures that its constitutive equation can be represented with a G'sell-Jonas law (7) : $\sigma = K \exp(a/T)\ f(\varepsilon, \dot{\varepsilon})$, where f is a function of strain and strain-rate only. The thermal coefficient, a, is 774 K(8).

Consequently the decrease of stress related to thermal softening is :

$$\Delta\sigma = -\frac{a}{T^2} K \exp\left(\frac{a}{T}\right) f(\varepsilon,\dot{\varepsilon})\Delta T = -\frac{a\,\sigma\,\Delta T}{T^2} \qquad (4)$$

RESULTS AND DISCUSSION

The thermal softening is important as soon as plastic strain is noticeable (fig. 4). Even if this calculation is not rigorous because it maximises heat dissipation and because the stress and strain are not totally accurate for strains higher than 0.36, it shows that the difference between strain-hardening at high and low strain-rates is mainly due to heat dissipation. Conversely, the yield stress does not depend on thermal effect. Because the yield stress depends neither on thermal effects nor on mechanical assumptions used to determine stress and strain and depends exclusively on strain-rate, it can be compared over the entire range of strain-rate studied.

Yield stress shown in fig. 5 increases with increasing strain-rate. Despite the fact that different techniques and different samples are used results are well organised in a "master" curve. Sensitivity to strain-rate is relatively low but seems to increase above a critical strain-rate of 50 s^{-1}. This is in agreement with previous observations (9-11).

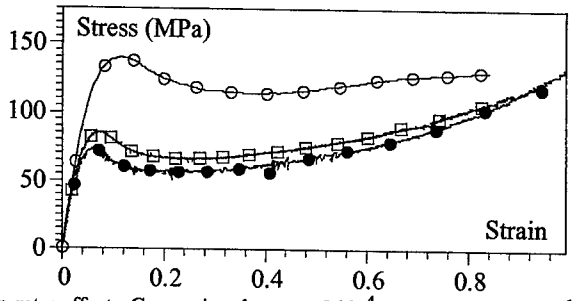

Figure 3. Strain-rates effects. Comparison between 5 10^{-4} (•), 1 (□) and 2500 s^{-1}(O).

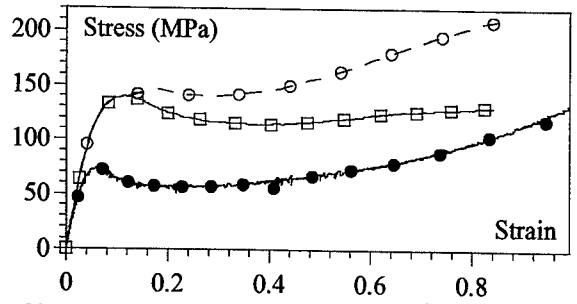

Figure 4. Effect of heat dissipation. Comparison between 5 10^{-4} s^{-1}(•) and 2500 s^{-1}without (□) and with corrections due to thermal effects (O).

In conclusion, the mechanical behaviour of a polycarbonate has been studied in compression over a wide range of strain-rates (from 5 10^{-5} to 5000 s^{-1}). Three experimental techniques have

been used : constant strain-rates tests for very low strain-rate, constant cross-head velocity hydraulic apparatus for intermediate strain-rate and SHPB technique for high rate tests. It was possible to minimise the gap between low strain-rate and high strain-rate measurements.

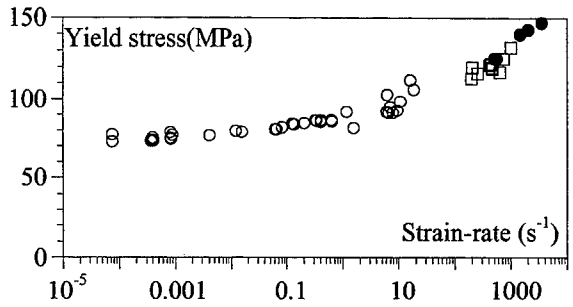

Figure 5. Yield stress vs. strain-rate. Measurements are performed using an hydraulic machine (O) or SHPB technique using 10 mm-thick samples (□) and 3 to 12 mm-thick samples (•)

The assumptions used to obtain intrinsic data are discussed and the main conclusions are :

- For low strains(≤ 0.36), deformations can be assumed homogeneous within the sample.
- Despite lubrication this assumption does not remain valid during the entire test ($\varepsilon > 0.36$).
- Stress wave propagation effects in the sample are negligible during high strain-rate experiments.
- Conversely, heat dissipation effects are responsible for a softening of the material for strain-rates higher than 1 s^{-1}.

Yield stress increases with increasing strain rates. Nevertheless the sensitivity to strain rates remains weak at low strain rate. At about 50 s^{-1} a change in the strain-rate sensitivity is a trace of a change in the physical processes involved in the plastic deformation of the polycarbonate.

SYMBOLS USED

ε, $\dot{\varepsilon}$ = strain and strain-rate (s^{-1}), ϕ, ϕo = diameter and initial diameter of the sample (mm),

ρ = density (kg/m^3), σ = stress (MPa)

a = thermal coefficient in the constitutive equation (K^{-1}), C = heat capacity (J/(kg °C)

F = force (N), H, Ho = height and initial height of the sample (mm), K = consistency of the material (MPa), T = temperature (°C)

REFERENCES

1. G'Sell C, Aly Helal N A, Jonas J J, J Mater Sci 18 (1983) 1731
2. Gary G, Klepaczko J R, Zhao H, J Phys 1 (1991) 403
3. Zhao H, Gary G, Ent. J Solid Structure 33 (1996) 3363
4. Haudin J M, Monasse B, Valla T, Glomeau S, Int Polymer Processing X 2 (1995) 179
5. Dioh N N, Ivankovic P S, Leevers P S, Williams J G, Proc Roy. Soc Lond A 449 (1995) 187
6. Tillier Y, Gandin E, Massoni E, Billon N, Proc DEPPOS XIV Grasse (1996)
7. G'sell C, Jonas J J, J Mat Sci 14 (1979) 583
8. Bisilliat M. L., Thèse de Doctorat, Ecole de Mines de Paris, (1997)
9. Bauwens J C, J Mater Sci 7 (1972) 577
10. Bauwens-Crowet C, Bauwens J C, Homes G, J Mater Sci 7 (1972) 176
11. Rietsch F, Bouette B, Eur Polymer J 26 (1990) 1071

BIAXIAL IMPACT FATIGUE OF PC/PBT BLENDS

DJ Dijkstra *, A Karbach **, T Bartschies †, G Hinrichsen †

The impact fatigue behavior of rubber modified PC/PBT blends was studied. The effects of this kind of mechanical loading, which is commonly encountered in daily use, were investigated for two blends, one of which is PC dominated and the other PBT.
For the PBT-rich sample, a rapid decrease in impact fatigue lifetime was found and an endurance limit for crack initiation was determined. For the PC-rich sample, the number of impact cycles for crack initiation was found to be almost independent of the impact energy imput. Even at very low energy input, no signs of an endurance limit could be seen. These preliminary experiments on biaxial impact fatigue are compared with static and cyclic fatigue data on the same blend systems.

To study the effects of biaxial tensile stresses on plate-like samples, samples held by an annular clamp were repeatedly impacted by a hemispherically-tipped plunger. Although this kind of mechanical loading is very common for polymers in daily use, only very few detailed studies on the biaxial impact-fatigue response of ductile polymers have been published (1). Less detailed studies exist for PMMA (2) and POM (3).

Experimental part

In our experiments we used an impact fatigue apparatus designed especially for this purpose (4). The plunger is accelerated horizontally by means of a linear drive. During the impact fatigue measurement, the impact energy input, the energy loss per cycle and the maximum force are calculated from the recorded force and displacement data. The impact fatigue lifetime was defined as the number of impacts at which a decrease in the peak load was first detected.

Two polybutadiene rubber modified PC/PBT blends were studied. Sample A was rich in polycarbonate and sample B was PBT dominated (Table I). The blends were injection moulded into disks ($\varnothing$ = 60 mm, thickness d = 3 mm) and multipurpose test specimens (ISO 3167 type A).

The stress-controlled cyclic fatigue experiments were performed using an Instron 8502 hydraulic tester at a frequency of 7 Hz; mean stress = 1/2 × stress amplitude.

The material properties of samples were characterized by means of dynamic-mechanical spectroscopy (Rheometrics RDS II, 1 Hz, torsion) and tensile testing (Instron 4502, 5 and 100 mm/min)

* Bayer Corporate Research, Leverkusen Works, D-51368 Leverkusen, Germany
** Bayer Corporate Research, Uerdingen Works, D-47812 Krefeld, Germany
† Technical University of Berlin, Institute of Non-metallic Materials, Polymer Physics, Englische Str. 20, D-10587 Berlin, Germany

Results and discussion

The results of the tensile tension characterisation are presented in Table I. The results of the dynamic-mechanical spectroscopy of the samples reflect the complicated morphology of the blends. Small amount of transesterification in the stabilized PC/PBT blend cause a LCST-type of phase diagramm (5). Crystallization of the PBT in both blend domains during the cooling cycle in the injection moulding process leads to an even more complicated morphology (6).

Table I:

	PC (% by wt.)	PBT (% by wt.)	BR (% by wt.)	E (GPa)	σ_y (MPa)
Sample A	60	27	12	2.2	49
Sample B	21	55	21	1.9	39

The results of the impact fatigue experiments are presented in Figure 1. The impact fatigue lifetime, defined by a decrease in the maximum force during an impact of the PC dominated sample A, is almost independent of the impact energy. At about 1200 to 1600 impacts, a decrease in maximum force is detected and a short brittle crack in the sample can be seen. Visible plastic deformation of the specimen in the impact fatigue experiment occurred at impact energies larger than 2.5 J. For this reason, the impact fatigue experiments were performed at impact energies below 2.5 J. The PBT-dominated sample shows a decrease in impact fatgue lifetime of about one decade with increasing impact energy from 1 to 2.5 J. For sample B, an endurance limit for impact fatigue behaviour between 0.5 and 1 J can be extrapolated.

Three different deformation regimes can be identified (1). During the first 20 to 30 cycles a rapid increase in maximum force is recorded, due to small amounts of local plastic deformation. The second regime is characterized by a small but steady increase in the maximum force during the lifetime of the sample in the impact fatigue experiment. The third regime starts with a decrease in the maximum force.

The increase in the maximum force of each impact cycle of the second regime is presented in Figure 2 as a function of the given impact energy. An increase in the maximum force at constant impact energy means an increase in stiffness of the specimen. Assuming a linear increase of the maximum force with an increasing number of impact fatigue cycles, the increase in the maximum force per impact cycle for sample A is predominantly larger than for sample B.

The behaviour of both samples in the third regime is totally different. For sample A an abrupt decrease in maximum force within one single impact cycle is recorded simultaneously with an audible and visible crack of a few millimetres in length. Sample B showns a steady decrease in maximum force, and a slowly propagating crack can be seen at the surface of the sample that is deformed in tension.

The results of the cyclic fatigue experiments on both samples are presented in Figure 3. Due to the higher yield stress of sample A, the Wöhler curves start at a higher stress level. A cross-over in tensile strength is found at about 50,000 cycles. For sample B an endurance limit of about 25 MPa can be extrapolated, whereas for sample A even at 10^7 cycles a decreasing stress in the Wöhler curve is found. The change in damping (tan δ) during

the fatigue experiment was calculated from the phase shift between stress and strain. An increase in tan δ during the fatigue experiment was found to be accompanied by a reduction in stiffness and ductile deformation before fracturing or necking of the sample. Brittle fracture of both samples is found at maximum (peak) stress level that is less than about 60% of the yield stress measured at a deformation rate comparable to that used in the tensile cyclic fatigue experiments, without any increase in tan δ during the fatigue experiment.

To gain insight into the mechanisms of crack initiation in these samples, specimens were stressed in cyclic fatigue at 50% of the yield stress and the tensile fatigue experiment was stopped at 50 % of the expected lifetime calculated from the Wöhler curves in Figure 3. These specimens were subsequently tested in a tensile experiment at -100°C, a temperature below the glass transition temperature of the polybutadiene modifier. At the fracture surface of sample B, a circular flaw, consisting of three concentric rings, was found that was not present in specimens tested at -100°C without preceding cyclic fatigue. An SEM study of the OsO_4 treated fracture surfaces showed agglomeration of the polybutadiene modifier in the center of these flaws.

Conclusions

Biaxial impact fatigue and cyclic fatigue experiments on PC/PBT blends showed, that, although the morphology of these blends is very complicated and by no means comparable with a simple two-phase system, the lifetime of the blends seems to be determined by the main component in the system. The tendency of the amorphous PC to craze at low stress levels (7) and the high resistance to fatigue-crack propagation of crystalline PBT (8) dominate the fatigue behaviour of the blends investigated.

Further conclusions are expected from complementary studies on the morphology of these blends.

References

1. Takemori MT, J. Mater. Sci. 17 (1982) 164
2. Lehmann V, Roltz W, Schneider M, Pastuska G, Materialprüfung 33 (1991) 135
3. Thieringer HM, Materialprüfung 38 (1996) 260
4. Dijkstra DJ, Busch KH, German patent publicaton LeA29539
5. Inoue T, Okamoto M, Polymer 34 (1994) 257
6. Pompe G, Häußler L, Winter W, J. Polym. Sci.: Part B: Polym. Phys. 34 (1996) 211
7. Takemori MT, Polym. Eng. Sci. 28 (1988) 641
8. Hertzberg RW, Manson JA, 'Fatigue of Engineering Plastics', Academic Press (New York), 1980

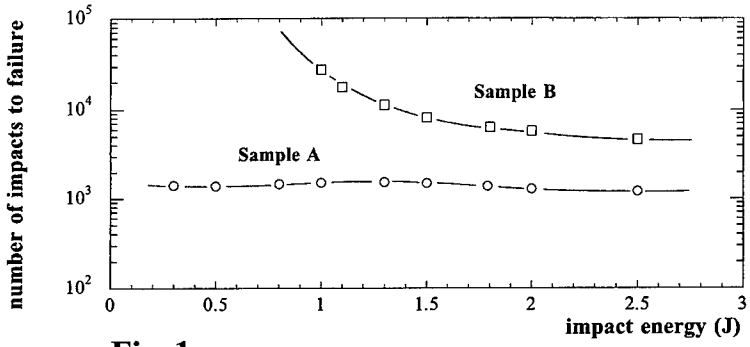

Fig. 1

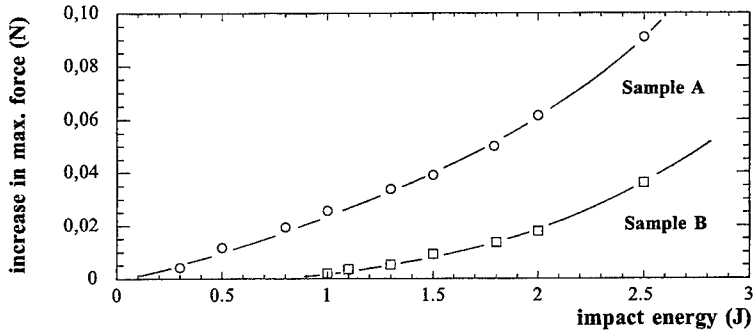

Fig. 2

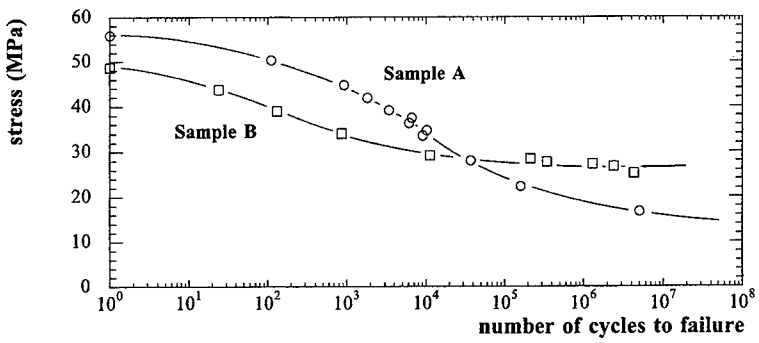

Fig. 3

MECHANICAL PROPERTIES THROUGH THE THICKNESS OF POLYPROPYLENE CAST-FILMS AS A FUNCTION OF PROCESSING CONDITIONS

F Jay*, JM Haudin*, B Monasse*

The local mechanical properties (Young modulus and yield stress) are measured on thin slices inside two extruded cast-films, differing by the chill-roll temperature. The local mechanical values and their gradient in the thickness widely depend on chill-roll temperature. They are discussed as a function of crystallization condition and of crystalline structure. An agreement is observed only with the crystalline content.

INTRODUCTION

Cast-film extrusion is a classical way to produce polypropylene films. The polymer is extruded through a slit die, stretched in air and cooled on a chill-roll where it crystallizes (Fig. 1). Various processing parameters control the mechanical and thermal conditions governing crystallization, and consequently the final morphologies. This problem was intensively studied in our laboratory from both experimental and theoretical point of view [1-3]. In the cross-section of 300-500 µm thick films, an inhomogeneous microstructure is observed, which leads to a heterogeneity of the local mechanical properties. The local mechanical properties are studied as a function of local crystallization conditions, measured and predicted in the thickness of the film.

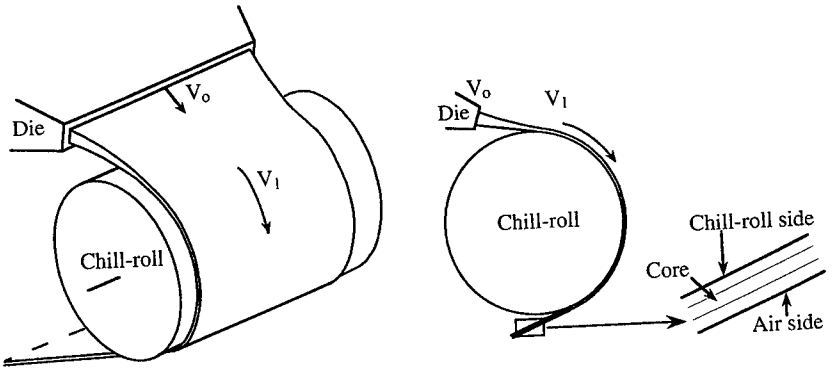

Figure 1 : Sketch of cast-film process

MATERIAL AND EXPERIMENTAL METHOD

A polypropylene homopolymer produced by Borealis A.S. was extruded on a cast-film pilot line. The main molecular parameters of this extrusion grade are : $\overline{M}_n$ = 77 000 g.mol^{-1}, $\overline{M}_w$ = 377 000 g.mol^{-1}, $\overline{M}_z$ = 1 087 000 g.mol^{-1}, isotactic content = 93.2% (NMR). Two films are considered here. All the thermomechanical conditions of the process are identical except for one, the chill-roll temperature. The polymer is extruded at 250 °C with a mean extrusion speed (V_o = 0.8 m.min^{-1}) stretched in air on 10 cm by the chill-roll (V_1 = 3.75 m.min^{-1}) and cooled on it. The films have almost the same thickness e (film 1 = 320 µm, film 2 = 332 µm). They differ only by the cooling condition imposed by the temperature of the chill-roll : film 1

* **Centre de Mise en Forme des Matériaux, Ecole des Mines de Paris, URA CNRS 1374, BP 207, 06904 Sophia Antipolis, France**

(Tcr = 30°C), film 2 (Tcr = 100°C) and then by the cristallization condition through the thickness of the films.

The gradient of structure and morphologies through the whole thickness was first observed by optical microscopy under polarized light on 5 µm-thick cuts. These cuts were done by an ultramicrotome along the extrusion direction. Generally three different layers were observed in the thickness of the films. Then three slices from 40 µm to 120 µm thick were prepared parallel to the film surface to measure local physical and mechanical properties through the thickness. They are defined as the chill-roll side, the core and the air-side layer, respectively (Fig. 1). Each layer was obtained by removing the two others by polishing. 4 cm long samples were obtained with no more than 5 µm thickness heterogeneity. The crystalline content was measured by DSC (Perkin-Elmer DSC7) from the melting peak recorded during heating at 10°C.min^{-1} and X-Ray diffraction (WAXS). The crystalline orientation was determined by the Debye-Scherrer method with a X-Ray 2-D detector and the crystalline long period by SAXS at the University of Bristol. The spherulite size and its gradient were deduced from microscopical observation of the microtomed sections.

Mechanical properties were measured on the thin layers with a Polymer Lab. Minimat tensile machine. The 5 mm-wide samples with a 15 mm gauge-length were tested under a strain rate $\dot{\varepsilon} = 2.3\ 10^{-3}\ s^{-1}$ at 100°C after a thermal stabilization during 5 min. The Young modulus and yield stress were measured assuming a homogeneous deformation up to the yield stress. The Young modulus was corrected for the small length effect of the sample and extrapolated to infinite length (Fig. 2). The correction seems to be independent of the sample width in the range $4\ mm \leq l \leq 10\ mm$ and unnecessary for the yield stress. This correction was applied to all the experiments.

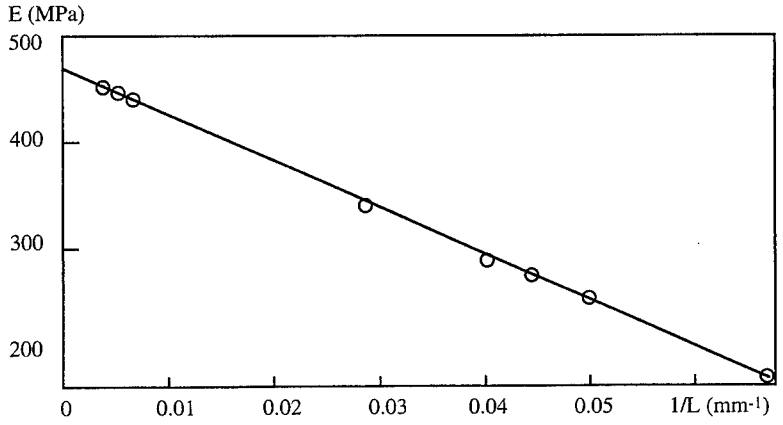

Figure 2 : Variation of the apparent elastic modulus as a function of the reciprocical sample length (Texperiment = 80°C)

RESULTS

The thickness e of the samples was adapted to reduce the mechanical heterogeneity inside the sample. Therefore, a thinner sample was prepared near the roll surface of film 1 (Tcr = 30°C) (Fig. 3). The various stress-strain curves derived from the force-displacement curves have a similar shape for most samples cut out from the films (Fig. 3). In most cases an instability is observed at the plastic yield, i.e., a drop of the force. Two exceptions are reported in figures 3 a and b (Roll-side and Core) where no drop of the force is observed at the plastic yield. Nevertheless all these curves mainly differ by the values of elastic modulus and yield stress. Their values are plotted as a function of the mean location of the samples in films 1 and 2 (Fig. 4).

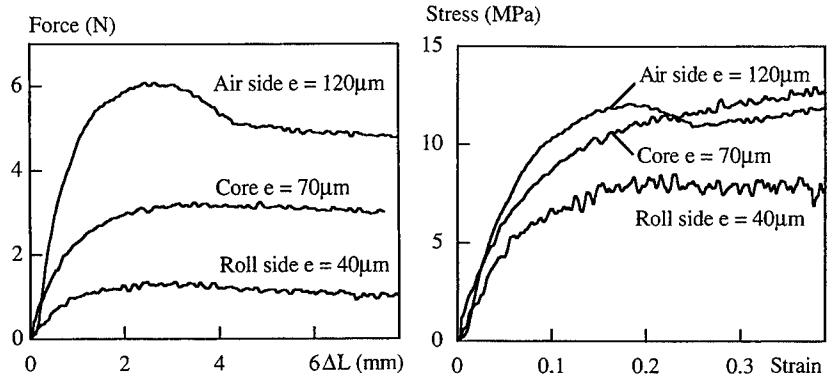

Figure 3 : Force-displacement and stress-strain curves measured in film 1 (Tcr = 30°C)

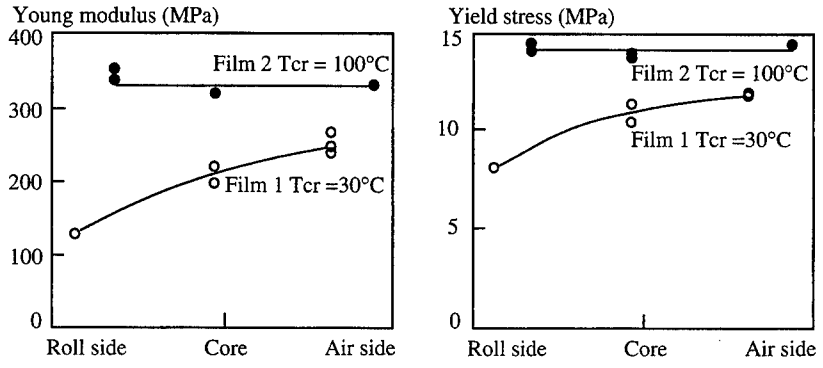

Figure 4 : Elastic modulus and yield stress at 100°C inside films 1 and 2

The yield stress and the Young modulus are always higher in film 2 (Tcr = 100°C) than in film 1 (Tcr = 30°C) (Fig. 4). The mechanical properties inside film 2 are high and almost constant through the thickness. On the contrary, a large gradient of mechanical properties (Young modulus and yield stress) appears in film 1. The lower properties are located near the surface in contact with the chill-roll during the extrusion process. This result will be further discussed using exprimental data.

A thermo-mechanical model of the cast-film process was developed in our laboratory [1-3]. It predicts the stretching of the polymer in air and the crystallization during the cooling on the chill-roll (Fig. 1). The crystallization is predicted by a kinetic law which depends on temperature, cooling rate and as demonstrated more recently on previous elongation rate [3]. The kinetic parameters depend on the polymer and are measured in laboratory experiments. The model predicts that stretching in air is almost isothermal while the crystallization appears under cooling in static condition. The crystallization and the resulting structures depend on this thermo-mechanical history inside the film. A low temperature of the chill-roll (Tcr = 30°C; Film 1) produces an efficient cooling of the polymer in contact with the metal, i.e., a high cooling rate and a low crystallization temperature. The cooling rate decreases continuously from the roll to the air side. Consequently, the crystallization temperature progressively increases from the roll side to the air side. On the contrary, a high roll temperature (Tcr = 100°C; Film 2) leads to a slow kinetics of crystallization and an almost constant high temperature of crystallization, i.e., a

low crystallinity gradient. The crystalline structure inside the films is fixed by these crystallization conditions and all the crystalline parameters (crystalline content, lamellar thickness, size and shape of spherulites) are modified. These structural modifications are actually observed in the final films and it is also possible to predict them. The model shows that the stretching in air must be taken into account to predict the main crystalline parameters. The molecular orientation is only slightly relaxed and acts on the subsequent static crystallization of the polymer on the chill-roll. Thus the model gives a qualitative prediction of the morphologies but the accuracy of the values is insufficient for various polypropylenes and processing conditions. Therefore, in the discussion of the mechanical properties only the experimental values characterizing the crystalline structure will be used.

Neither the lamellar thickness nor the dimensions of their aggregates, i.e., the sizes of deformed spherulites, can be correlated with the mechanical properties. The crystalline content seems to be the parameter able to describe the variation of the mechanical properties of the present films (Fig. 5). A linear approximation is used only to illustrate the variation of mechanical properties in this experimental range. A large deviation from linearity should appear for a low crystalline content.

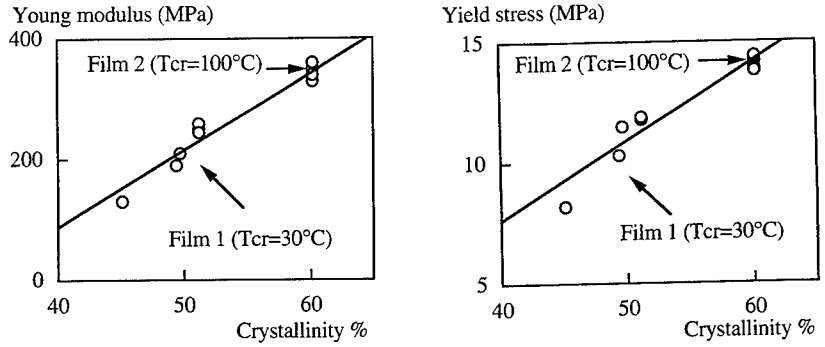

Figure 5 : Influence of the local crystalline content on elastic modulus and plastic yield stress inside films 1 and 2. Temperature of the test 100°C.

CONCLUSION

A heterogeneity of mechanical properties can be observed in thin extruded films, typically 300µm-thick. Measurements on very thin layers inside these films show out the local mechanical properties and a possible gradient through the thickness. The heterogeneity of mechanical properties comes from a high cooling rate from one surface during the cast-film extrusion process, which is responsible of the crystalline structures. The crystalline content acts more drastically on elastic modulus and yield stress than the lamellar thickness or the spherulite size. By the processing conditions it is thus possible to control the mean value of the mechanical properties and their gradient.

REFERENCES

1 Duffo P, Monasse B, Haudin JM, J. Polym. Eng. 10(1-3) (1991) 151
2 Cotto D., Duffo P, Haudin JM, Int. Polym. Proc. 4 (1989) 103
3 Jay F, Haudin JM, Monasse B, 12th Annual Meeting of the Polymer Processing Society, Sorrento (Italy), (May 1996)

We thank European Community for supporting this work as a part of the BRITE-EURAM contract n° BRE2-CT92-0331

POSITRON ANNIHILATION FOR THE STUDIES OF STRUCTURAL TRANSFORMATIONS IN POLYMERS

V.P.Shantarovich
Institute of Chemical Physics Russian Academy of Sciences, 117977 GSP-1 Moscow, Kosygin st.4, Russia.

The specific feature of the implementation of the positron annihilation technique, positron nondestructive testing, in studying polymers as nonhomogeneous structures are analyzed. The method is based on the studies of positron annihilation /1/ in materials, particularly on measurement of positron annihilation lifetimes in polymers. After fast slowing down, positrons are normally trapped by elementary free volumes. The larger are the defects and the higher is the number of these defects, the longer is positron lifetime and the higher is intensity of the long-lived component in the time-distribution of positron annihilation events. Furthermore, model experiments seem to show predominant localization and annihilation of positrons in the ordered and positronium (bound state e^+e^-)- in disordered regions of a polymer.

All these circumstances show that positron annihilation technique gives a unique possibility for the studies of microstructure transformations in ordered and disordered microregions separately. This selectivity reveals itself when nonhomogeneity characteristic size is below 100 nm. Contemporary development of the technique enables detection of 10^{15}-10^{19} cm^{-3} elementary free volumes with their effective diameter $\geqslant 6$ Å.

Particularly, structural changes induced by introduction of diethyl siloxane olygomers (plasticizer) to polymethylmethacrylate (PMMA) were studied. The effect of these structural changes on the mechanical response of PMMA is discussed in terms of structural inhomogeneity of PMMA: existence of structural sublevels with different packing density and ordering. Elastic modulus, yield stress, and contribution of low-temperature component of the temperature induced relaxation of plastic deformation were shown to be controlled by segmental mobility in structural sublevels with a lower packing density.

1. Yu.P.Yampolskii, V.P.Shantarovich, F.P.Chernyakovskii, A.I.Kornilov, N.A.Plate. Journ.Appl.Polym.Sci.1993, v.47, p.85.

A NOVEL LONG TERM PLANE STRAIN FRACTURE TEST FOR TOUGH POLYETHYLENES

D-M Duan , J G Williams*

A novel test method is described in this paper which is designed for craze generation and craze behaviour analysis under plane strain conditions. The test uses a specimen of circumferentially deep notched tension geometry. The test data of yield stress against time to yielding show a clear brittle ductile transition which implies different fracture mechanisms in short term fractures and long term fractures.

Due to the relatively low yield stress and low modulus, large craze zones occur at the crack tip in more recent pipe grade polyethylene materials which tends to invalidate the conventional fracture mechanics analysis. The need for knowledge on craze structure as well as craze degradation with time, which is essential for slow crack growth modelling (1,2), are thus crucial for understanding the controlling mechanism which operates in long term fracture problems. The purpose of this paper is to introduce a new test method for generating a craze zone in tough polyethylene and to analyse the craze behaviour under plane strain conditions.

Specimen and Test Apparatus

Circumferentially deep notched tensile (CDNT) specimens were fabricated from bars cut from the original compression moulded sheets (002-40). The bars have square cross sections (20 mm × 20 mm) and are either rectangular notched or roundly notched as shown schematically in Fig 1. The ligament area where a craze layer is produced upon loading is generally about one tenth of the original cross section. The notch angle is 45° for rectangular notches and is 20° for round notches. The tip radius of the cutter for round notches is about 70 μm while the rectangular notches are sharpened by sliding into the root of the notch with a fresh razor blade of a tip radius $\rho<20$ μm. The gauge length between the two grips is 40 mm. Extension in the gauge length is recorded against time by using an LVDT and the data are recorded by a computer.

Craze Zone Kinetics

A direct result for a constant speed test (Instron) is its stress against extension curve which includes both the craze thickness and the bulk deformation between grips in the recorded extension. From the comparison between the recorded extension and the simultaneously optically measured craze thickness, it has been shown that the bulk deformation is negligible and therefore the recorded extension can be regarded approximately as the craze thickness. A group of such curves for tests of identical 002-40 specimens are presented in Fig 2. It is apparent in the figure that although extensions at yielding and at failure stay almost unchanged at about 1.3 mm and 3 mm respectively at higher testing speeds, both of them drop remarkably at a low speed of 0.1 mm/min.

*Department of Mechanical Engineering, Imperial College, London SW7 2BX, UK

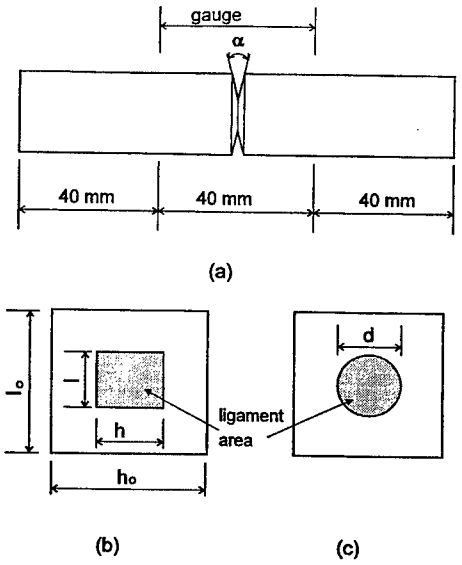

Fig 1 The specimen geometry for craze tests

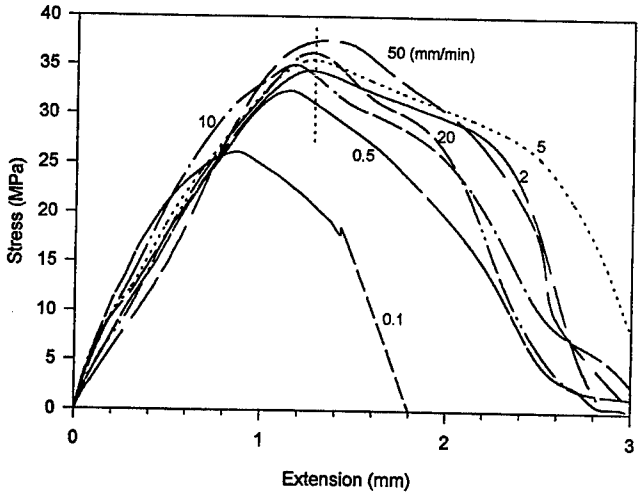

Fig 2 Traces for craze tests at different testing speed (Instron) for 002-40

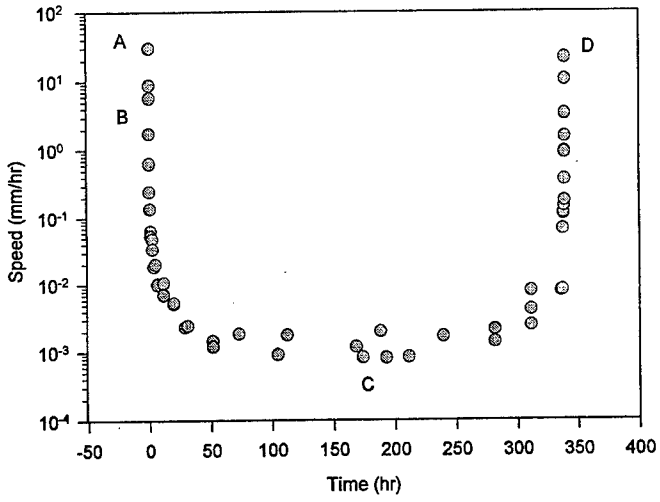

Fig 3 A typical curve of craze zone growth speed against time for 002-40

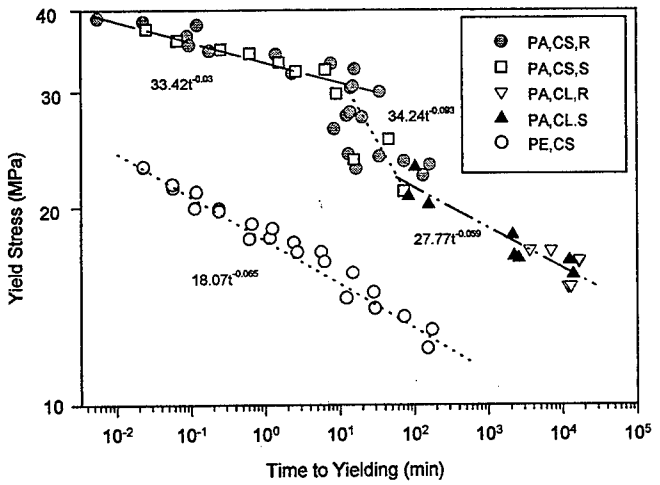

Fig 4 Yield stress against time to yielding for 002-40
(PA: plane strain; PE: plane stress; CS: constant speed; CL: constant load; R: round ligament; S: square ligament)

A typical craze growth speed against time curve for dead load tests is shown in Fig 3 which is obtained from the craze thickness data by using a local five point linear curve fitting. The striking feature of the curve is that the craze speed changes very slowly most of the time. The U shaped craze speed curve can be divided into two distinct parts AC and CD with speed decreasing and increasing respectively. The minimum speed point C corresponds to the yielding state in which the maximum resistance of the material at the speed is equal to the external load. Though the two parts are nearly equal, the post-yielding part of the curve with increasing speed may have different deformation mechanisms from the previous hardening part. There could be a competition between the yielding speed and the material resistance under the applied stress, and further craze damage and yielding lead to a continuing decrease in load bearing capacity of the material until the final failure.

Short Term Failure and Long Term Failure

The testing duration for most of the fixed speed tests performed on the Instron was less than 10 hours depending on the testing speed and these tests are here called short term tests. For most of the dead load craze damage tests, the life time was usually over 10 hours depending on the applied stress and the tests are accordingly called long term tests, though some of them with relatively high stresses had life times shorter than those of some Instron tests. Basically, in these two kinds of test, the materials exhibited different dependence of failure time on applied stress and also a different failure mode. A comparison of the dependence of time to yielding on net section stress between the long term tests and the short term tests is shown in Fig 4 where the stresses for short term tests are those corresponding to the maximum loads during testing. It is apparent that the data for short term tests at higher stress levels and the data for long term tests follow their own distinct dependence of time to yielding on stress despite of the difference in specimen ligament, and there is a clear transition between the two at intermediate stress levels. The difference in time to yielding against stress corresponds to a difference in failure mode. While for short term tests except for those at very low speeds (<0.2 mm/min), the failures are of ductile mode, for all long term tests except for those with high stresses (>20 MPa) the failures are of brittle mode. The difference between the two modes can be clearly seen from the fracture surfaces (3). Fig 4 also shows the results of yield stress against time to yielding for plane stress tensile tests for the same material which were obtained by using plain specimens of dimensions 100mm×10mm×4mm. From the data in Fig 4, it is easy to obtain the crack tip constraint factor for fracture tests, and also the long term fracture resistance of materials can be evaluated by computing the coefficients and indexes of the power law fits to the plane strain test data as shown in the figure.

REFERENCES

1. Cawood, M.J., Channel, A.D., and Capaccio, G., Polymer, 34, (1993) 423
2. Brown, N.,and Lu, X., Int'l J. of Fract., 69, (1995) 371
3. Duan, D-M., PhD Thesis , University of London, 1996

CORRELATION BETWEEN EMPIRICISM AND THE *D*ISTRIBUTION OF *N*ON-*L*INEAR *R*ELAXATIONS APPROACH APPLIED TO CREEP OF POLYMERS.

P. Marceron*, Z. Ayadi* and C. Cunat*

This work authenticates first of all our DNLR approach through certain empirical analyses on creep temperature and stress dependences. Futhermore, our modelling specifies and explains some limits of these empirical methods.

Several empirical methods have been proposed for creep behaviour of polymers. A new thermodynamic approach based on the phenomena of relaxation in continuous media called, "**D**istribution of **N**on-**L**inear **R**elaxations", has been developed in our group. This modelling can account for various unidirectional or three-dimensional mechanical behaviours as shown in Ayadi (1) and Loukil (2). This work is restricted to uniaxial creep at low loads, so that only primary and secondary creeps are concerned. This paper has two objectives : to authenticate our modelling through empirical methods and to analyse their discrepancies through DNLR aproach.

Presentation of our approach.

Our formalism is based on the processes relaxation theory extended to non-linear states and developed by Cunat (3). For creep tests at low stresses, the relaxation times τ^j are assumed to be independent of time. Their modelling, at constant temperature T, rests on the activation state theory :

$$\tau^j = \frac{h}{kT}\exp\left(\frac{\Delta G_r^{j+}}{RT}\right) \text{ avec } \Delta G_r^{j+} = \Delta H_r^{+} - T\Delta S_r^{j+} \qquad (1)$$

For creep test under a stress σ, analytical expression of strain is :

$$\varepsilon(t) = \varepsilon^u - (\varepsilon^l - \varepsilon^u).\left[\sum_j p_j^0 \exp\left(-\frac{t}{\tau^j}\right) - 1\right] - \left(\sum_j \frac{\varepsilon_j^l - \varepsilon_j^r}{\tau^j}\right).t \qquad (2)$$

- p_j^0 is the initial weight of the process number j linked to τ^j through an extension of Prigogine's theory of fluctuations ($p_j^0 = B\sqrt{\tau^j}$ and $\sum_j p_j^0 = 1$)

- $\varepsilon^u = \sigma / E^u = \sum_j \varepsilon_j^u$ is the unrelaxed strain and E^u the unrelaxed modulus of elasticity

- $\varepsilon^r = \sigma / E^r = \sum_j \varepsilon_j^r$ is the relaxed strain and E^r the relaxed modulus of elasticity

*LEMTA - URA - CNRS - Vandoeuvre-lès-Nancy, France

- ε^l is the limit strain for the transient creep given by :

$$\varepsilon^l = \sum_j \varepsilon_j^l = \sum_j \left(\tau^j . \left(\frac{\varepsilon_j^r}{\tau_1^j} + \frac{\varepsilon_j^u}{\tau_2^j} \right) \right) = \sum_j \left(\left(\frac{\varepsilon_j^r}{\tau_1^j} + \frac{\varepsilon_j^u}{\tau_2^j} \right) / \left(\frac{1}{\tau_1^j} + \frac{1}{\tau_2^j} \right) \right) \quad (3)$$

with τ_1^j and τ_2^j respectively relaxation times of strain and of recovery.

The four **DNLR parameters** are thus the two moduli of elasticity E^u and E^r and the two relaxation times τ_1 and τ_2 of the slowest process.

Temperature dependence.

This dependence is generally correlated with the « activation energy ». Two methods will be studied to work it out as exposed by Poirier (4), knowing the following kinetic law used for the creep rate:

$$\dot{\varepsilon} = \dot{\varepsilon}_0 . \exp\left(-\frac{Q}{RT} \right) \quad (4)$$

The first method exploits the derivate of equation (4) versus the inverse of temperature for secondary creep rate $\dot{\varepsilon}_s$. Thus, in case of uniaxial creep tests, for a given stress, the activation energy results from a slope analyse.
The second one is the well-known « reduced-times method ». In Figure 1 we compare both methods applied to Diacryl tests creep under 0.79 MPa for different temperatures.

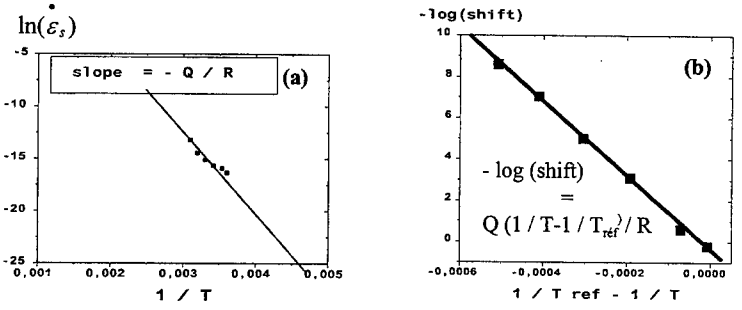

Figure 1 : a - Determination of Q for Diacryl by the derivative of the kinetic law.
b - Determination of Q for Diacryl by the reduced-times method.

The first method gives $Q \approx 60 kJ/mol$ whereas the reduced-times method gives $Q \approx 350 kJ/mol$. These results are all the more striking than these methods are supposed to be equivalent.

Our DNLR approach enables us to analyse and understand this discrepancy.
Indeed, on the one hand, all the experimental creep curves have been one after the other modelling, with DNLR parameters which depend on temperature : $E^r(T)$, $E^u(T)$, $\tau_1(T)$ and

$\tau_2(T)$. According to equation (1), ΔH_r^+ is deduced from $\tau_1(T)$ et $\tau_2(T)$ and is about 60 kJ/mol, as found by the first method (Figure 1-a).
On the other hand, we have simulated creep tests by keeping E' and E'' independent of temperature and by taking $\Delta H_r^+ = 60\,kJ/mol$. Under these conditions, the horizontal shift of the simulated creep curves leads to : $Q \cong 60\,kJ/mol$.

Thus, we can conclude that the difference between 60 and 345 kJ/mol is due to the evolutions of $E'(T)$ and $E''(T)$, which are disregarded when there is not a vertical shift in the reduced -times method.

Stress dependence.

For a given temperature, a powerful analysis about stress dependences was proposed by Garofalo, by means of an hyperbolic sine form to represent secondary and initial creep rates noted respectively $\dot{\varepsilon}_s$ and $\dot{\varepsilon}_i$. Figure 2 shows this behaviour for Polycarbonate.

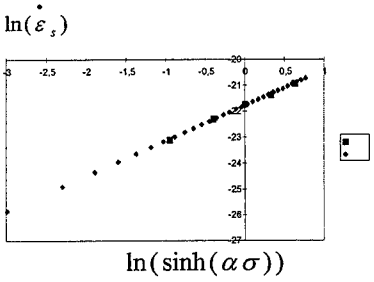

The squares symbolize the experimental data and the lozenges the modelling.

Figure 2 : Stress dependence of secondary creep rate for Polycarbonate at 60°C.

A simular evolution was observed for the initial creep rate $\dot{\varepsilon}_i$, for ε^l and for $(\varepsilon^l - \varepsilon^u)$.

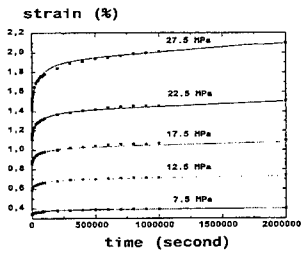

Figure 3 : Tensile creep curves for Polycarbonate at different stress levels at 60°C.
experimental data (●) and DNLR theoretical curves (straight line)

Therefore, a method for forecasting the values of the DNLR parameters has been outlined only thanks to experimental creep curves. Indeed, the previous empirical analyse links $\dot{\varepsilon}_s$, $\dot{\varepsilon}_i$, ε^l and ε^u to their analytical expressions correlated with the DNLR parameters (from equation (2)). The only thing to do is therefore to solve a four equations system with four unknown quantities : $E^u(\sigma)$, $E^r(\sigma)$, τ_1 et τ_2.
Simulations nicely fit the creep experimental data as shown in Figure 3.

Conclusion.

At the root, our approach is used in a very general thermodynamic framework and enables us to simulate multidimensional tests.
To obtain reliable forecasts for a kind of mechanical test, the study of empirical methods will confirm the validity of the hypotheses we have to do.

SYMBOLS USED

p_j^0 = initial weight of the process number j
τ^j = relaxation time of the process number j (s)
σ = applied creep stress (MPa)
ε = total strain
$\dot{\varepsilon}$ = total creep rate (/s)
ΔG_r^{j+} = free activation enthalpy (J/mol)
ΔH_r^+ = relaxed activation enthalpy (J/mol)
ΔS_r^{j+} = relaxed activation entropy of the process number j (J/K/mol)
h = Planck's constant (J.s)
k = Boltzmann's constant (J/K)
R = gas constant (J/mol/K)
B = constant for the relaxation spectrum ($1/\sqrt{s}$)
$\dot{\varepsilon}_0$ = constant rate-strain for the kinetic law (/s)
α = empirical constant of Garofalo

REFERENCES

1. Ayadi, Z., thesis, 1995, INPL, Nancy, France
2. Loukil, M., thesis, 1996, INPL, Nancy, France
3. Cunat, C., 1997, "Lois constitutives de matériaux complexes stables ou vieillissants", Rev. Gén. Therm. (to be published)
4. Poirier, J.P., 1976, " Plasticité à haute température des solides cristallins ", Ed. Eyrolles
5. Garofalo, F., 1965, " Fundamentals of creep and creep rupture in metals ", Macmillan Series in Materials Science.

INTER-LAMINAR DELAMINATION, MATRIX CRACKING AND MICROFIBRILLAR BRIDGING IN FATIGUED WOOD-PULP FIBRES

Wadood Y. Hamad[1]

When single wood-pulp fibres, which are concentrically-layered, laminated composite tubes of structural reinforcing material, are subjected to cyclic mechanical action, their morphological behaviour is characterized by the fatigue growth of micro-voids and surface damage which individually and collectively give rise to stress concentrations; and eventually crack development. The progressive damage phenomena are understood to be consequences of the cumulative material micromechanical degradation and subsequent microstructural breakdown of the cellulose microfibrillar framework. This structural breakdown is believed to effect the fibrillation and flexibilization of the fibres. Insight is further gained into the micromechanisms of damage accumulation, matrix cracking and microfibrillar bridging.

An analogy may be drawn between the structure of each layer of the fibre wall and that of a fibre-reinforced, composite shell in which the cellulose microfibrils represent the fibre reinforcement and the amorphous hemicellulose and lignin, the composite matrix (refer to Fig. 1). The latter polymer matrix serves to bulk, link and stabilize the microfibrillar framework; whereby the interaction of these framework and matrix components is analogous to anisotropic composite shell structures.

The atomic structure around the (microcrack) initiation point is deemed to determine the direction of crack propagation. Macrocracks advance longitudinally unless confronted by locations of natural bias. The imperfect alignment of the cellulosic microfibrils (with respect to the fibre axis) determines the orientation at which these (macro)cracks develop: The macrocracks propagate in a manner parallel to the orientation of the mechanically-superior cellulose chains — Hamad (1). The cohesion and, hence, the strength of the filamentary composite fibre are largely dictated by the strength of the cellulosic microfibrils: once the latter become structurally degraded, i.e. the crystalline structure is re-arranged, then the amorphous hemicellulose-and-lignin matrix can no longer hold the layers of the laminated tube together. Subsequently, inter-laminar delamination occurs. Adjacent layers delaminate, and external wall material peels off, after the development of dominant macrocracks in the highly-strained regions of the individual lamina — Hamad and Provan (2).

[1]Fibre Science and Technology Centre, Department of Paper Science, UMIST, Manchester, England. E-mail: wadood.hamad@umist.ac.uk.

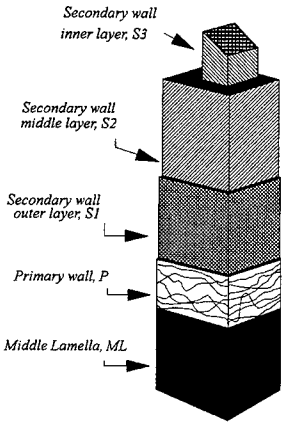

Figure 1: Cell wall organization of a typical native cellulose fibre showing fibrillar textures (after Forgacs, 1963).

EXPERIMENTAL TECHNIQUE

Twenty fibre samples, typically 1–3 mm long and 20–40 μm in cross-section, obtained from jack pine, loblolly pine and black spruce, were tested for each mode of loading and subjected to fatigue lives ranging from 300 to over 6000 cycles. Fatigue-testing was performed in three modes: shear, radial compression and longitudinal tension. All testing was performed in a specially-controlled room where temperature and relative humidity were maintained at 23±1°C and 50±5%, respectively. Testing frequencies were: 0.0262 Hz for shear, and 0.187 Hz for radial compression and longitudinal tension.

PROGRESSIVE MICROSTRUCTURAL DEGRADATION IN THE FIBRE WALL

It has been shown elsewhere, refer to Hamad and Provan (2), that the development of macrocracks in the wall laminae principally contributes to the localized volumetric expansion as the strength of the matrix is significantly decreased with increasing fatigue life. Commensurate with the level of damage accumulation, the microfibrillar structure progressively degrades leaving the matrix in an unstable state, thereby causing the random breakage of the cross-links in the inter-fibrillar matrix during the cyclic variation of load on the fibre.

Inter-laminar delamination and the unravelling of external laminae, depicted in Fig. 2, are typically seen when the fibre is subjected to a large number of cycles. This type of crack propagation leading to rupture may be explained in terms of the time-dependence behaviour of the viscoelastic cellulose fibres, and the concomitant stabilization effects of plastic deformation around the crack tip. The anisotropy of both the cell wall structure and the material properties of the fibre is clearly reflected in the latter statement.

The laminated brittle matrix composite spindle is seemingly prone to delam-

(a)

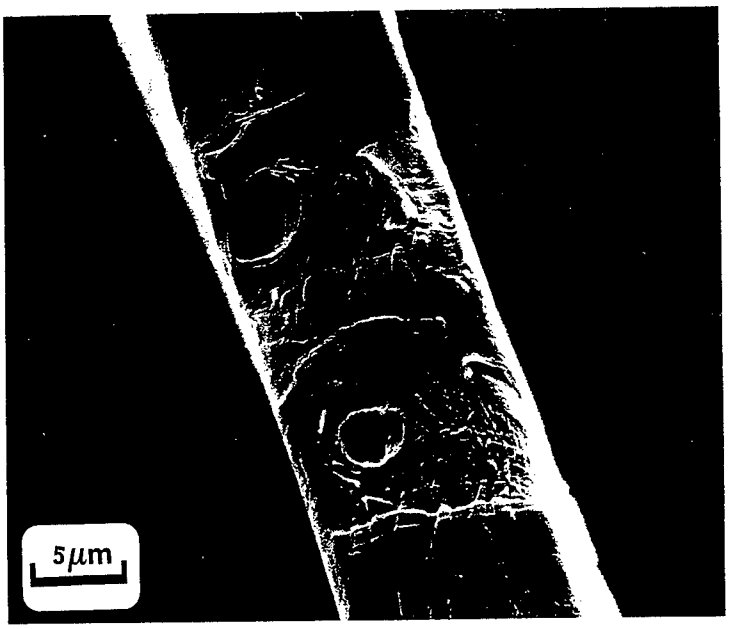

(b)

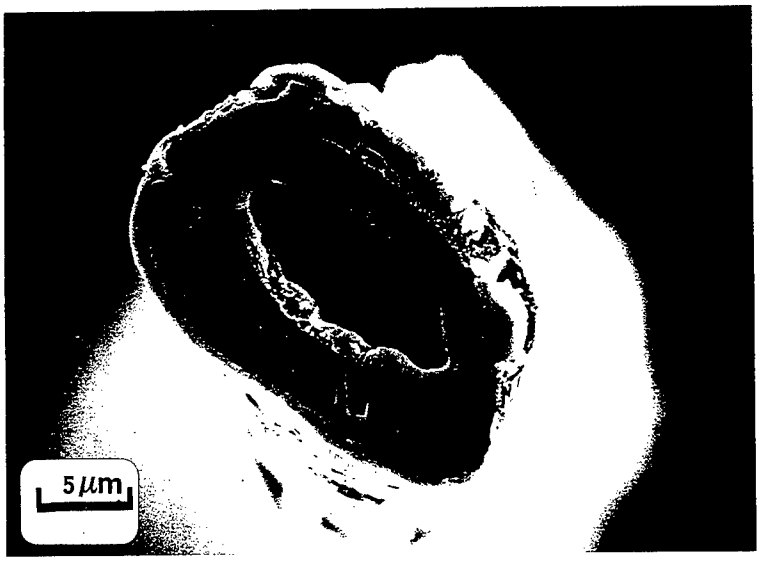

Figure 2: SEM micrographs depicting inter-laminar delamination and partial peeling-off of laminae, along (a) and across (b) the laminated composite fibre. Fibre sample: jack pine wood pulp subjected to 1200 cycles in shear at 0.0262 Hz.

ination cracking upon the application of fatigue loading. The susceptibility to this mode of damage is the direct result of the extreme anisotropy in fracture resistance parallel and normal to the microfibrillar orientation. Delamination cracking detrimentally influences the structural integrity of the framework-and-matrix composite system even though it does not directly constitute failure of the composite tube.

The fibre specimen's load response indicated a reduction at the inception of crack initiation and propagation. This may simply be attributed to the effects of hysteresis brought on by the strain-induced crystallization in the cell wall fibre under cyclic loading conditions, where the material is continually being stressed and recovering. The mechanical hysteresis giving rise to structural changes may, drawing upon polymer research terminology, be referred to as a "frozen stress-field" (4). The interaction of the successive cycles with this frozen stress-field may be considered to contribute to crack growth by a fatigue mechanism. The latter association seems apt in light of the significant structural changes and material degradation (at each cycle) in the fatigued fibres.

The micrographs of Fig. 2 reveal a range of mode mixities between pure opening (mode I) and pure shear (mode II) to categorize the inter-laminar delaminations. However, the former seemingly prevails since the delamination resistance in mode I occurs subject to the lowest fracture resistance. A substantive factor involved in the delamination crack growth resistance concerns the influence of the reinforcing microfibrils.

CONCLUDING REMARKS

It has been documented that external fibrillation of the fibre cell wall has a predominant occurrence in the fibres subjected to all modes of cyclic loading. Considerable economic advantage may accrue from the action promoting external fibrillation and structural modifications of the laminated composite fibre. The pulp would have yield retention properties, good strength and would make a sheet of paper in which the distribution of the fine material throughout the sheet thickness was uniform. The structural changes occurring during the application of cyclic action to wood-pulp fibres reflect a process whereby the fibres are believed to become more flexible due the breakdown in internal fibre structure.

Microfibrillar bridging probably contributes to the nonlinear response to cyclic loading. Microfibrillar alignment and placement relative to the crack plane significantly influence inter-laminar delamination.

REFERENCES

1. Hamad, W. Y. "Some microrheological aspects of wood-pulp fibres subjected to fatigue-loading," *Cellulose* (in press).
2. Hamad, W. Y., and Provan, J. W. (1995), *Cellulose*, **2**(3), 159.
3. Forgacs, O. L. (1963), *Pulp and Paper Mag. Can.* **64(C)**, T89.
4. Andrews, E. H. (1968), *Fracture in Polymers*, American Elsevier, New York.

STRESS RELAXATION IN CELLULOSIC FIBRES: A MICROMECHANICS ANALYSIS

Wadood Y. Hamad[1] and **Stephen J. Eichhorn**[1]

This paper reports investigations in to the phenomenon of stress-relaxation, which occurs in a variety of cellulosic fibres. In particular the band shifts upon straining in relation to the micromechanics, and the stress *versus* time characteristics, of fibres. These coupled with macro-measurements of stress relaxation are compared to elucidate the inter-dependence between macro- and micromechanical properties. Raman spectroscopy has further enabled the study of changes in *internal* strain associated with creep and recovery. The analysis of the mechanics of deformation of the fibres begins by following the response of the Raman-sensitive bands to external tensile loading. Moreover, this approach makes possible the modelling of single fibre properties using simple viscoelastic dynamics; thereby relating the macromechanical properties of stress and strain to those obtained at the microscopic level via spectroscopy.

Raman scattering is essentially the (small) portion of a beam of light that is inelastically scattered by a material — the majority of radiation which is scattered elastically at the same frequency as the incident light is the Rayleigh scattering. It is this inelastically scattered light that carries information about the molecular vibrations in the material, and hence it is useful in the characterization of non-metallic materials. There has been an increase in the use of Raman spectroscopy, over the last two decades, in analysing the molecular deformations of fibres and polymeric materials. Originally work was concerned with the deformation of single crystals of substituted diacetylene polymers (1-3), then followed by investigations into aramid fibres (4-6), rigid rod polymer fibres (7-9), gel spun polyethylene fibres (10-12) and more recently cellulosics (13). It has been documented that on the action of stress or strain the peak positions of certain bands, within the Raman spectra, shift to a lower wave number. This behaviour may be explained in terms of the macroscopic deformation being transformed directly into stressing the covalent bonds along the polymer backbone and changes in the bond angles as discussed many years ago by Treloar (14).

EXPERIMENTAL

Commercial grade 1.6 dtex tencel fibres, produced by solvent-spinning cellulose from wood-pulp (supplied by Courtaulds Fibres Ltd., U.K.), were employed for this study. Mechanical testing was performed on fibres that were individually

[1]Fibre Science and Technology Centre, Department of Paper Science, UMIST, Manchester, England. Correspondence should be addressed to W. Y. Hamad, e-mail: wadood.hamad@umist.ac.uk.

mounted — using a cyanoacrylate adhesive — into testing cards prior to being placed in the jaws of the series IX Instron mechanical testing machine (model 5564). Thirty specimens were used for ascertaining the mechanical properties for both the irradiated and unirradiated fibres (fifteen each).

Raman spectra were, on the other hand, obtained for the tencel fibres during deformation in a Raman microscope system. The Raman system is based upon a SPEX 1000M single monochromator with a holographic laser line filter. The 632.8 nm red line of a 7 mW He-Ne laser was used to excite the spectra to a 2 μm spot on the fibre using a modified Olympus microscope with a 50x objective. All experiments were performed at 23 $\pm$ 1°C and a relative humidity of 50 $\pm$ 2%.

RAMAN-BASED MICRODEFORMATION ANALYSIS

The stress-strain behaviour for tencel fibres typically exhibits no yielding and the response is principally nonlinear (visco)elastic. For regenerated cellulosics, the classes of internal motions associated with the different spectral features particularly fall in the regions below 1500 cm^{-1} which are the most sensitive to polymorphic change. Two peaks at 895 cm^{-1} and 1095 cm^{-1} prominently figure in the Raman spectrum for the structure of cellulose and the molecular deformation is ascertained by following these peaks as the fibres are subjected to external strain. The 1095 cm^{-1} peak is indicative of two principal modes: ring stretching together with C-O stretching motions. Whereas the 895 cm^{-1} peak indicates a contribution from angle bending coordiantes involving heavy atoms only (i.e. CCC, COC, OCC), however, ring and C-O stretches and the external modes of the methylene groups may also be major contributors (15).

The effect of deformation upon the dominant Raman bands due to skeletal modes is characterized by: bands shift to lower wave number, decrease in peak intensity and broaden somewhat upon the application of tensile strain (or stress). The shift is an indication of the straining of the fibre causing molecular deformation. The broadening, on the other hand, shows that there is a distribution of the stresses and strains over the molecules within the fibre. Figure 1 depicts the dependence of the peak positions of the 895 cm^{-1} and 1095 cm^{-1} Raman bands, respectively, upon strain. It can be seen that the peaks shift to lower wave number and that the dependence upon strain is approximately linear.

Figure 2 depicts a typical stress relaxation response for tencel fibres. The initial 30 seconds indicate a step drop in stress values. This has implications when testing fibres under the Raman microprobe system as the samples are held at constant strain for this period of time. The fitted curve is that of a standard Zener model (a spring and a Maxwell element). Applying the appropriate boundary conditions for stress relaxation (i.e. rate of change of strain in the system is zero), the resulting response equation is:

$$\sigma(t) = E_E \epsilon_0 [1 - (1 - \frac{E_Z}{E_E}) \epsilon^{-\frac{t}{\tau_M}}], \qquad (1)$$

where ϵ, σ, E and τ represent strain, stress, elasticity modulus and relaxation time, respectively; the subscripts E and Z denote the lone spring and Zener (total component) of the model.

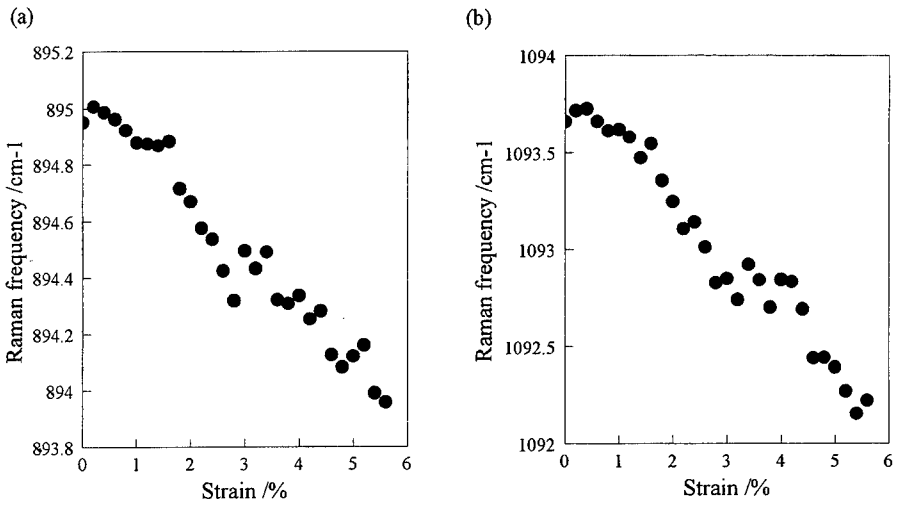

Figure 1: Dependence of the position of the 895 cm^{-1} (a) and 1095 cm^{-1} (b) Raman band peaks for tencel with strain.

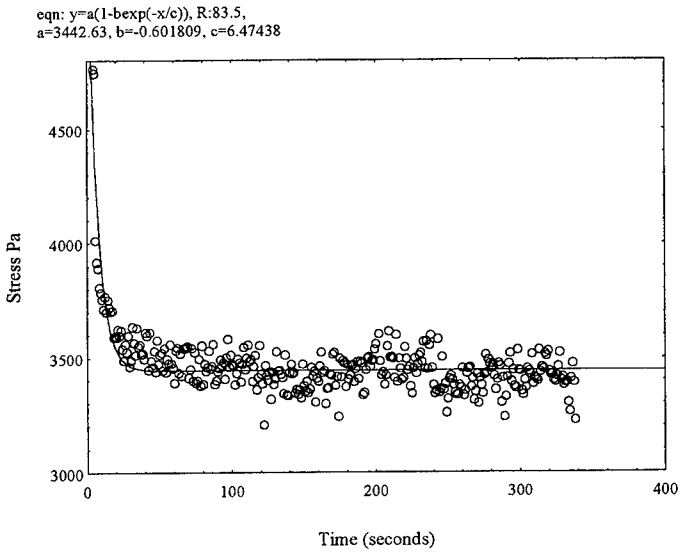

Figure 2: Stress relaxation response for tencel at $\epsilon = 2.903$ %.

CONCLUSIONS

It has been demonstrated that Raman spectroscopy is a powerful technique for explicating the deformation micromechanics of (single) regenerated cellulose fibres. The effect of bathing the fibres with He-Ne radiation has been found to have almost no effect on the mechanical properties of the fibres. The high tensile strength of tencel, σ_f=150 MPa, and elongation to failure, ϵ_f=13.5%, as compared with a Young's modulus value of 20.8 MPa reflect the highly viscoelastic behaviour of these fibres.

Significant shifts of 3.26 cm^{-1} and 1.98 cm^{-1} result in the 1095 cm^{-1} and 895 cm^{-1} Raman bands, respectively, upon the application of stress; resulting in both cases in strain sensitivities of -0.55 $cm^{-1}/\%$ and -0.39 $cm^{-1}/\%$, respectively. These values are comparable to reported results for other conventional polymers. The Raman technique was shown to give a direct measure of molecular strain; and that it could be calibrated to provide a microscopic strain gauge by which internal micro-strains/stresses could be monitored. The latter was used to shed light on the creep behaviour of these viscoelastic fibres. A phenomenological model, the Zener model, was proposed and is in good agreement with the experimental results.

REFERENCES

1. Mitra, V.K., Risen, W.M. Jr and Baughman, R.H.J. (1977), *Chem. Phys.* **66**, 2731.
2. Batchelder, D.N. and Bloor, D.J. (1979), *J. Polym. Sci.: Polym. Phys. Edn.* **17**, 569.
3. Galiotis, C., Young, R.J. and Batchelder, D.N.J. (1983), *J. Polym. Sci.: Polym. Phys. Edn.* **21**, 2483.
4. Young, R.J., Lu, D. and Day, R.J. (1991), *Polym. Int.* **24**, 71.
5. Young, R.J., Day, R.J., Dong, L. and Knoff, W. (1992), *J. Mater. Sci.* **27**, 5431.
6. Andrews, M.C. and Young, R.J. (1993), *J. Raman Spectrosc.* **24**, 539.
7. Day, R.J., Robinson, I.M., Zakikhani, M. and Young, R.J. (1987), *Polymer* **28**, 1833.
8. Young, R.J., Day, R.J. and Zakikhani, M. (1990), *J. Mater. Sci.* **25**, 127.
9. Young, R.J. and Ang, P.P (1992), *Polymer* **33**, 975.
11. Moonen, J.A.H.M., Roovers, W.A.C, Meier, R.J. and Kip, B.J. (1992), *J. Polym. Sci.: Polym. Phys. Edn.* **30**, 510.
12. Wong, W.F. and Young, R.J. (1994), *J. Mater. Sci.* **29**, 510.
13. Hamad, W.Y. and Eichhorn, S. (1996), *Proc. of CSME Forum 96-Mechanics in Design* vol.II, 853.
14. Treloar, L. R. G. (1960), *Polymer* **1**, 95.
15. Atalla, R. H. and Nagel, S. C. (1974), *Science* **185**, 522.

ENVIRONMENTAL STRESS CRACKING OF POLY(ETHYLENE TEREPHTHALATE) IN AQUEOUS SODIUM HYDROXIDE

Eric J. Moskala*

Environmental stress cracking of amorphous poly(ethylene terephthalate) in aqueous sodium hydroxide was studied using a fracture mechanics approach. Compact tension specimens were machined from injection-molded plaques and used to determine creep crack growth rate as a function of applied stress intensity factor. The effects of caustic concentration and polymer molecular weight on creep crack growth behavior were determined. Fractographic analysis of the fracture surfaces showed that crack growth proceeded by the formation of novel discontinuous growth bands. The structure and mechanism of formation of these bands are discussed.

INTRODUCTION

Environmental stress cracking refers to crazing and cracking that occurs when a polymer, under tension, is exposed to an aggressive chemical environment. The chemical reagent may cause crazing either by swelling the polymer or by chemically reacting with the polymer. For example, it is well know that poly(ethylene terephthalate) (PET) will be hydrolyzed by aqueous sodium hydroxide [1]. The concomitant reduction in polymer molecular weight caused by hydrolysis may lead to crazing and eventual catastrophic failure. The objective of this study was to determined the effect of a caustic environment on creep crack propagation in PET.

EXPERIMENTAL

Compact tension specimens of PET were machined from 3.2-mm-thick injection molded plaques. The specimen width, defined as the distance from the center of the loading pin holes to the back face of the specimen, was equal to 50.8 mm. Each specimen was notched with a band saw. The notch root was subsequently sharpened with a razor blade and immersed in an aqueous solution of sodium hydroxide (caustic). Loads ranging from 22-44 N were applied to the specimen. Crack length was determined from load-line displacement by using a compliance technique [2]. Crack growth rate (da/dt) was calculated by using the secant and seven-point incremental polynomial methods described in ASTM Standard E647. Crack growth rate was plotted versus stress intensity factor (K). Each set of crack growth data shown in this work was recorded from one specimen only. Repeat experiments gave values of da/dt at a given value of K that agreed to within ±20%. PET resin inherent viscosity (IV) ranged from 0.58 to 0.88 dl/g. IV was measured in a 60/40 phenol/tetrachloroethane mixture at 23°C.

RESULTS AND DISCUSSION

A plot of crack length versus time for PET (IV=0.71 dl/g) in 1% caustic is shown in Figure 1. From the grouping of crack length measurements, it is evident that crack growth occurs in a discontinuous, stepwise manner. This hypothesis was verified by an examination of the specimen's fracture surface which shows well-defined discontinuous growth bands. Each band corresponds to a grouping of crack length measurements from Figure 1. A possible mechanism for the formation of these bands is presented in Figure 2. At the tip of a newly

*Eastman Chemical Company, PO Box 1972, Kingsport, TN 37662, U.S.A.

formed crack (a_1), a craze begins to grow. Extension of the craze results in an apparent increase in crack length, although the actual crack tip is stationary. Since a typical craze is approximately 50% by volume [3] the length of the craze is about twice the amount of apparent crack growth. During extension of the craze, the caustic aggressively attacks the craze fibrils at the crack tip. After the crazed region is sufficiently damaged by hydrolysis, the crack jumps through the craze and is arrested when it reaches virgin polymer (a_2). The process then repeats itself until, at a critical stress intensity factor, the energy released during the jump is sufficient to cause catastrophic failure.

Crack growth rates were determined from Figure 1 using a secant method and are plotted versus stress intensity factor in Figure 3. The plot is fairly linear on a log-log scale as predicted by the Paris equation [4]. The apparent scatter at high values of K is a result of the formation of discontinuous growth bands. According to the crack propagation mechanism described above, the high values of da/dt correspond to when the crack jumps through the damaged craze zone. The subsequent low values of da/dt correspond to apparent crack growth resulting from extension of a newly formed craze.

The effect of caustic concentration on crack growth rate is illustrated in Figure 4. (Crack growth rates in Figure 4 were determined by using a seven-point incremental polynomial method in order to minimize the apparent scatter in the plots and to aid in visualizing the effect of caustic concentration on da/dt.) As expected, da/dt at a given value of K increases with increasing caustic concentration. Caustic concentration also affects the value of K at failure (K_c); K_c decreases with decreasing caustic concentration as indicated by the arrows in Figure 4. Crack growth rate in the specimen exposed to a 3% caustic solution reaches a plateau at high values of K instead of continuing to increase linearly. This plateau is a consequence of a transition in stress state at the crack tip from plane strain to plane stress resulting in the appearance of shear lips on the fracture surface [5].

The effect of caustic concentration on the size of the discontinuous growth bands in PET is shown in Figure 5. Note that for a given caustic concentration, band size increases with increasing crack length, or value of K. Band size should be indicative of the length of the plastic zone at the tip of the crack. According to Dugdale [6], the length of the plastic zone (r_p) is given by

$$r_p = \frac{\pi}{8}\left(\frac{K}{\sigma_y(t)}\right)^2 \qquad (1)$$

where $\sigma_y(t)$ is a time-dependent yield stress. The data in Figure 5 were best fit to equation (1) by using yield stress values of 31 MPa, 35 MPa, and 48 MPa for specimens exposed to 0.2%, 1%, and 3% caustic solutions, respectively. Note that yield stress increases with increasing caustic concentration since the time to form a band, and hence the time scale for craze growth, decreases with increasing caustic concentration. Furthermore, these yield stress values are reasonable considering that the yield stress of PET is 60.4 MPa as measured by ASTM Standard D638. Band size for the specimen exposed to 3% caustic deviates substantially from the predicted values above a crack length of about 30 mm due to the formation of shear lips as discussed above.

The effect of PET resin IV on crack growth rate in a 1% caustic solution is shown in Figure 6. IV has no effect on crack growth rate in the regime of stable crack propagation. However, the value of K_c does increase with increasing IV. It has been reported that increasing IV, or molecular weight, has no effect on the stress required to initiate a craze, but will increase the stress required to fracture a craze [7]. This may explain the effect of IV on K_c observed in this study.

SYMBOLS USED

K = stress intensity factor (MPa$\sqrt{m}$)
K_c = critical stress intensity factor (MPa$\sqrt{m}$)
da/dt = crack growth rate (mm/s)
a = crack length (mm)
r_p = plastic zone size (mm)
$\sigma_y(t)$ = yield stress (MPa)

REFERENCES

1. S.H. Zeronain, H.Z. Wang and K.W. Alger, *J. Appl. Polym. Sci.*, **41**, 527 (1990).
2. A. Saxena and S.J. Hudak, *Intern. J. Fract.*, **14**, 453 (1978).
3. A.J. Kinloch and R.J. Young, "Fracture Behavior of Polymers" (Elsevier, London, 1988).
4. P.C. Paris and F. Erdogan, *J. Bas. Eng. Trans. ASME Ser. D*, **85**, 528 (1963).
5. R.W. Hertzberg, "Deformation and Fracture Mechanics of Engineering Materials" (Wiley, New York, 1983).
6. D.S. Dugadale, *J. Mech. Phys. Solids*, **8**, 100 (1960).
7. J.F. Fellers and B.F. Kee, *J. Appl. Polym. Sci.*, **18**, 2355 (1974).

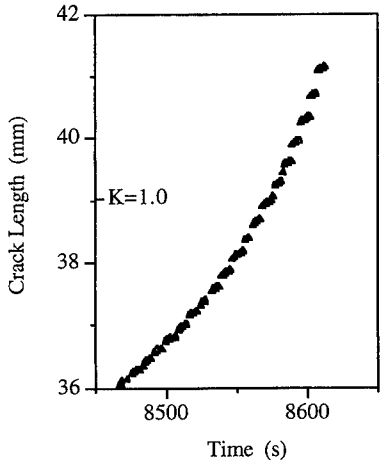

Figure 1. Crack Length Versus Time for PET in 1% Caustic.

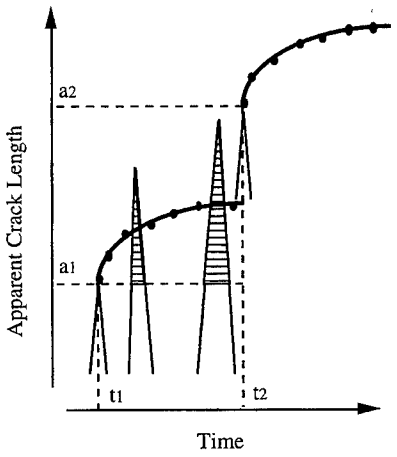

Figure 2. Schematic of the Relationship Between Craze Growth and Apparent Crack length.

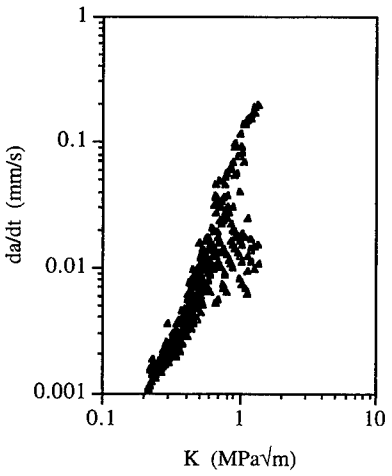

Figure 3. Crack Growth Rate Versus Stress Intensity Factor for PET in 1% Caustic.

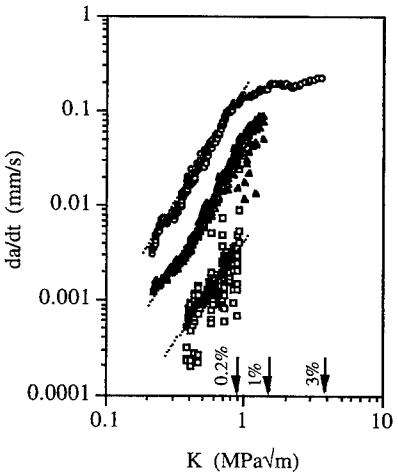

Figure 4. Effect of Caustic Concentration on Crack Growth in PET: Circles, 3% Caustic; Triangles, 1% Caustic; Squares, 0.2% Caustic. Arrows Indicate Failure Points.

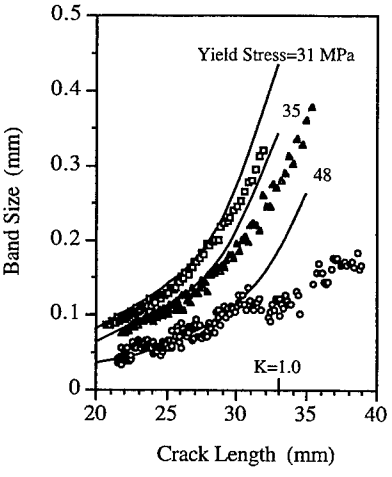

Figure 5. Effect of Caustic Concentration on Size of Discontinuous Growth Bands. Symbols Same as Figure 4. Solid Lines Represent Prediction From Equation (1).

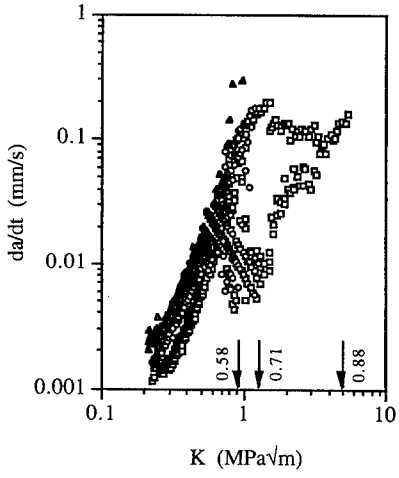

Figure 6. Effect of IV on Crack Growth in 1% Caustic; Triangles, 0.58 dl/g; Circles, 0.71 dl/g; Squares, 0.88 dl/g. Arrows Indicate Failure Points.

Mechanisms of Deformation of An Amorphous Polymer (Polycarbonate) in the melt and in the solid state from a Conformers interactive Coupling point of view (EKNET model). by J.P Ibar

ABSTRACT

We present the results of an extensive investigation of the mechanical deformation behavior of three Polycarbonate grades of different molecular weight, and explain the results in terms of the interactive coupling between conformers belonging to coiled macromolecules. Our investigation of the deformational behavior included viscous behavior, obtaining both capillary and dynamic shear viscosity, stress-strain tensile deformation at various strain rates and temperatures, flexural dynamic mechanical analyis from -150 C to Tg for quenched and aged Polycarbonate, and PVT curves from the higher melt region down to room temperature.

The results are consistent with a picture of amorphous polymers suggested by the EKNET model by which coiled up packs of conformers belonging to individual macromolecules interact with one another to create an interactive phase which behaves in many respects as a blended-in phase. The mechanisms of toughening and enbrittlement through physical aging are easily described in terms of the continuity or discontinuity (segregation) of the blended-in phase. The work also suggests a new definition for entanglements and a link between the localization of excess free volume and the blended-in phase due to inter-coils interactive coupling penetration.

Compressive Cyclic Behavior and Prediction of Fatigue Damage in Elastomers

A. Plumtree* and G. X. Cheng**

* Dept. of Mechanical Engineering, University of Waterloo
Waterloo, Ontario N2L 3G1, Canada
** Dept. of Chemical Engineering and Machinery, Xi'an Jiaotong University
Xi'an, Shaanxi Province 710049, P. R. China

Abstract

This work describes the results of cyclic experiments carried out on three elastomers and modelling of the data using a concept developed by the authors.

Cyclic compressive testing of three different elastomers was carried out to determine the fatigue behavior under simulated service conditions. The stress response was monitored continually and, for a given unidirectional cycle strain, the maximum stress decreased with number of cycles. Under conditions of two dimensional cyclic strain, the elastomers displayed similar behavior, although the stress response was higher. Damage occurring in the elastomers was assessed by measuring the changes in the maximum equivalent stress. Initially, the amount of damage was high and decreased gradually on further cycling. The damage then increased at a progressively faster rate, as the cross-links began to fail. The evolution of damage throughout fatigue life was described by a two stage model based on Continuum Damage Mechanics. Using this concept, damage development over the entire life could be predicted accurately.

NON LINEAR RESPONSE OF AMORPHOUS POLYMERS: ANELASTIC / VISCOPLASTIC COMPONENTS AND STRAIN HARDENING THROUGH Tg

O. Sindt, C. Gauthier, J. Perez*

The thermomechanical tensile behaviour of styrene-butyl acrylate copolymers are investigated and analysed in terms of anelastic and viscoplastic strain's components. Moreover, both rubber elasticity and chain orientation effects are taken into account, in order to describe the behaviour laws at large extensions (i.e. $\varepsilon \approx 1.2$).

INTRODUCTION

Since the comprehension of the mechanical behaviour of polymers is of high importance today, we propose an analysis of the polymer's response to an applied stress, in a large temperature domain, surrounding Tg.

In the past, different authors (1) have analysed the mechanical response of polymers below Tg as the sum of two terms: the first one corresponds to the anelastic response, followed by the viscous flow, and the second results from the rubbery effect (which is usually considered at temperatures higher than Tg). As experimental data has shown that strain hardening increases when temperature decreases, the contribution of rubber elasticity to this effect is not sufficient at temperatures lower than Tg. Hence, the authors had to modify the rubber elastic law's parameters (1), in order to better fit experimental data.

Since recent years, a theory (2) of non elastic deformation of polymers, based upon molecular mobility concepts, has been developed in our group. Such a description allows a good agreement between experiments and simulations for strain degrees about $\varepsilon \leq 25\%$. In order to describe higher strains (i.e., $\varepsilon \approx 1.2$), the effect of chain orientation, relied to the rubbery effect (3), is taken into account. Moreover, it appears that the molecular mobility, which is related to the disorder, decreases when macromolecules becomes oriented. This second effect is taken into account, in order to explain the high strain hardening observed at low temperatures.

THEORETICAL APPROACH

From a general point of view, a glassy (and amorphous) polymer can be considered as an homogeneous material, containing some nano fluctuations of density (4). These fluctuations are hereafter called quasi point defects (qpd), and occur in a concentration Cd in the material. On the other hand, when a stress is applied, the (nanoscale) polymer response is described in terms of nucleation and growth of sheared microdomains (smd). This phenomenon corresponds to the anelastic (ε_{an}) component of the strain (4,5). With further deformation, smd ultimately merge, and thus rise to viscoplastic deformation (ε_{vp}).

Previously, molecular mobility in polymers has been analysed in terms of hierarchically correlated movements (4), leading to an expression of the mean molecular mobility time τ_{mol} (see Eq. 1).

* G.E.M.P.P.M. INSA Lyon. 20 Avenue A. Einstein. 69621 Villeurbanne Cedex. France

$$\tau_{mol} = t_0 \left(\frac{\tau_\beta}{t_0} \right)^{1/\chi} \qquad \text{Eq.1}$$

In this expression (Eq.1), τ_{mol} corresponds to the time necessary for a structural unit to move on a distance equivalent to its length; τ_β is the time of the preliminary movement (taken as the β secondary process). Thermomechanical activation of this relaxation yields to:

$$\tau_\beta(\sigma) = \tau_{\beta 0} \exp\left(\frac{U_\beta}{kT} \left(1 - \frac{\sigma}{\sigma_0} \right)^{3/2} \right) \qquad \text{Eq. 2}$$

χ ($0<\chi<1$) is a correlation parameter related to the degree of disorder (i.e., Cd). Hence, $\chi = 0$ corresponds to a fully constrained situation and $\chi=1$ is a constrained free situation (perfect crystal and perfect gas, respectively). Thus, it appears that χ is constant ($=\chi_{(Tg)}$) when the microstructure is frozen ($T < Tg$) and increases as Cd with T when the system is in the metastable equilibrium ($T > Tg$).

Moreover, the anelastic times (related to the nucleation and expansion of smd) are distributed in-between the elementary time $\tau_\beta(\sigma)$ and $\tau_{mol}(\sigma)$. On the other hand, the viscoplastic times (corresponding to the motion of structural units over large distances) are distributed around $\tau_{mol}(\sigma)$, since the disorder is spatially distributed in the material (in practice, we have chosen to incorporate the disorder's characteristic through a gaussian distribution of the correlation parameter, which results in a log-normal distribution of the characteristic times).

From these basis, an incremental calculation (6) allows to determine the contribution (anelastic and viscoplastic) of each population to the macroscopic deformation. Such an approach has been improved, taking into account:

i) the evolution of the correlation effects during tests: first, the correlation parameter is varying with temperature when $T>Tg$ and a Taylor expansion has been used to describe such an evolution : $\chi_0 = \chi_{(Tg)} + a\,(T-Tg)$

Second, when a stress is applied, the nucleation and growth of smd (2,4,6) correspond to an increase of the disorder (Cd), and then an increase of χ with ε_{an}.

Lastly, the development of viscoplastic strain (introducing chain orientation) corresponds to a decrease of the molecular mobility which should results in a decrease of χ (6).

ii) the rubber elasticity: at high temperature, the polymer is in the rubbery state, which involves purely entropic effects. The description of rubberlike elasticity has been firstly developed considering an ideal network, constituted of freely jointed segments (7). Recently, refinements have been introduced to take into account finite elongation of chains. In that way, Arruda and Boyce (3) developed a certain topology of the network, in which the representative cubic cell contains 8 chains. Considering L(x) as the Langevin function of x, it yields to:

$$\sigma_1 - \sigma_2 = \frac{nkT}{3\lambda_c} \sqrt{N} (\lambda_1^2 - \lambda_2^2) L^{-1}\left(\frac{\lambda_c}{\sqrt{N}} \right)$$
$$\lambda_c = \frac{(\lambda_1^2 + \lambda_2^2 + \lambda_3^2)^{1/2}}{\sqrt{3}} \qquad \text{Eq. 3}$$

To sum up, when exploring high deformation domain, macromolecular orientation occurs and leads to i) entropic processes and ii) a decrease of molecular mobility due to a better organisation of the material. As we describe the entropic effect on the basis of ref. 3, we propose to relate the decrease of χ with the change of chains entropy, i.e., by using the same factor: $L^{-1}(\lambda_c/N^{1/2})$.

EXPERIMENTAL RESULTS AND COMPUTED DATA

The experimental data have been obtained from styrene-butyl acrylate copolymers films. Their main relaxation temperature (measured at 1 Hz) is 40°C. The tensile tests were performed on an Instron apparatus, on normalised samples at a constant crosshead speed (strain rate = 8.3 10^{-2} s^{-1}).

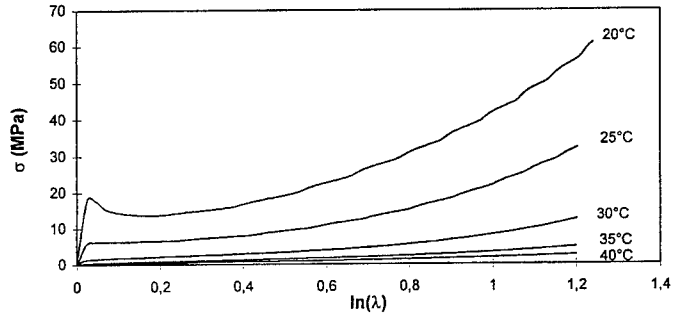

Fig. 1 a): Evolution of the experimental stress/strain curves between 20 and 40 °C.

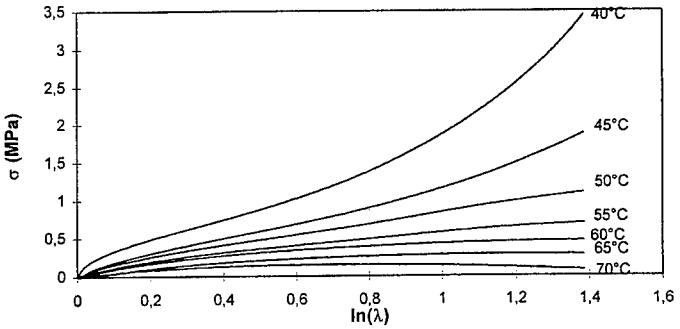

Fig. 1 b): Evolution of the experimental stress/strain curves between 40 and 70 °C.

When considering a tensile test (see Fig.1) performed on a polymer below Tg (for example T=20°C), we observe different domains on the stress/strain plot: first, beyond the linear viscoelastic response observed at low stress, the anelastic component (ε_{an}) occurs; about the yield stress (σ_y) the viscoplastic component (ε_{vp}) appears and results in strain recoverable only after annealing at T > Tg (5). For larger strain, the stress goes through a minimum, which

is the plastic flow stress (σ_p) and lastly, it increases with the strain (hardening of the material). At higher temperatures (i.e., T=40°C), the behaviour law changes toward a rubberlike one. Thus, the flow stress is dramatically decreased.

By comparing the experimental and simulated data concerning the evolution of σ_p as a function of temperature (see Fig. 2), a good agreement is observed. However, in the high temperature range, rather small discordance appears, this fact can be related to the flow of macromolecules, as it has been shown by dynamic mechanical spectrometry.

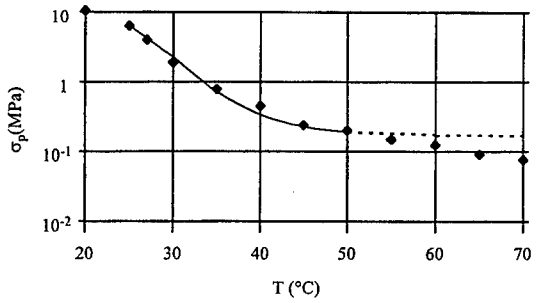

Fig. 2: Comparison between experimental (squares) and simulated (line) σ_p vs. temperature.

As a conclusion, the mechanical response of an amorphous polymer has been studied through the glass transition temperature range, i.e., in both glassy and elastomeric states. The simulation of the whole data has been developed in a unique frame, with only one set of parameters. The improvement of this approach appears to be necessary in a temperature range where chains flow occurs.

LITERATURE:

(1) **G'sell C., Souahi A.**, « *Deformation, yield and fracture of polymers* », Institute of materials, London, *Proceedings*, pp. 29/1-29/4 (1994)

(2) **Perez J., Ladouce L., Quinson R.**, « *Deformation, yield and fracture of polymers* », Institute of materials, London, *Proceedings*, pp. 25/1-25/4 (1994)

(3) **Arruda E.M., Boyce M.C.**, *J.Mech. Phys. Solids*, **41**, pp.389-412 (1993)

(4) **David L., Quinson R., Gauthier C., Perez J.**, *Polym. Eng. Sci.* (1997), in press

(5) **Gauthier C., Perez J., Oleinik E., Rudnev S., Slavetskaya T., Kravchenko M., Salamatina O.**, « *Deformation, yield and fracture of polymers* », Institute of materials, London, *Proceedings*, (1997)

(6) **Gauthier C., David L., Ladouce L., Quinson R., Perez J.**, *J. Appl. Polym. Sci.* (1997), in press

(7) **Mark J.E.**, « *Physical properties of polymers* », ACS Professional Reference Book, Washington, (1993)

A COMPARISON OF THE EFFECTS OF WEATHERING AND SUPERFICIAL ABRASION ON IMPACT PROPERTIES OF PLASTIC GLAZING MATERIALS

S M Halliwell* and D Gardiner*

This paper describes the use of an instrumented falling weight impact test to compare the effects of accelerated laboratory weathering and superficial abrasion on the impact resistance of plastic glazing materials. Examples of polycarbonate [PC], poly(methylmethacrylate) [PMMA] and poly(vinylchloride) [PVC] were studied. The materials lost impact strength as a result of both treatments, but abrasion does not predict the duration of weathering needed to produce the same effect.

INTRODUCTION

Transparent plastic materials, widely used for glazing, vary substantially in their impact resistance. Types with good initial impact resistance can experience loss in performance induced by surface damage associated with weathering or abrasion. This can impair service life and safety characteristics. It is well known that these sheet materials can be susceptible to the presence of edge notches. Biaxial impact tests, such as the Charpy (1) or Izod (2) methods, or uniaxial methods such as tensile impact (3) are well suited to investigate the effects of edge notching on impact strength. However, they are perhaps less well suited to the investigation of changes in the surfaces of sheet materials because all three methods require accurately machined test pieces (4), and there are unresolved questions as to whether machining and/or notching should be completed before or after exposure to weathering.

Therefore, as part of a wider investigation into the application of artificial weathering to plastic glazing materials (5), the use of an instrumented multi-axial puncture impact test was investigated. This allows relatively large areas of the test material to be exposed to weathering or abrasion from which test pieces can be cut without edge effects becoming significant. The method used differs in detail from the current ISO Standard procedure (6), but allows changes in impact parameters to be quantified. The observed modes of failure are also significant, ranging from ductile flow with splitting to brittle fracture producing undistorted shards. We consider that this approach relates most closely to practical circumstances. A full account of this work is being prepared.

EXPERIMENTAL

Details of the commercial products used are in Table 1. The results discussed here were obtained with 2mm thick sheets. Full details of the light exposure conditions are given elsewhere (5). Three light exposure conditions were used: xenon arc lamps with free access of air to both sides and a rainspray cycle; and fluorescent UV lamps using UV-A (340nm) lamps or UV-B (313nm) lamps both with a condensation cycle - this comprised 4 hours UV exposure at 45°C and 4 hours condensation at 50°C.

* Building Research Establishment, Watford, Hertfordshire, WD2 7JR.

Table 1: Glazing Materials Used

Polymer	Material Details
PMMA-1	cast acrylic sheet
PMMA-2	extruded acrylic sheet, impact modified
PVC-1	pressed sheet
PVC-2	calendered and pressed sheet, impact modified
PC-1	extruded sheet, indoor glazing grade
PC-2	extruded sheet, UV stabilised

Surface abrasion of unweathered material was carried out using the BRE abrasive impact pendulum as described by Rothwell (7). The effects of 10mm wide strips of Grade 0 and Grade 2 emery paper (8) as abrasive media were compared. The instrumented falling weight apparatus employed a dart of 10kg, falling 0.431m with an impact velocity of $3ms^{-1}$ and an energy of 45J. The hemispherical striker had a diameter of 12.5mm and the support ring 25mm. Samples were not clamped and were struck with the weathered or abraded face down, ie in tension on impact. Impact tests were carried out at 23 °C with at least 3 replicates for each test condition. Deflection and force at break and hence energy at break, generally taken at peak force, were determined.

RESULTS AND DISCUSSION

All materials tested had high initial impact resistance except PMMA-1 which failed in a brittle mode, at low deflection (ca 1.0mm) and at low energy to break (ca 0.1J). PMMA-1 tended to shatter into numerous sharp shards which were not distorted. Although PMMA-2 had high initial impact resistance, with deflection to break ca 5mm and energy to break ca 5J, it tended to shatter in a brittle manner yielding relatively large fragments which were distorted by ductile flow. Initially, all of the PVC and PC test pieces failed by ductile flow and splitting, the test pieces remaining in one piece. For 2mm thick sheets, the deflection to failure was ca 5mm and the energy to failure ca 5J, a relatively small fraction of the available 45J.

Surface abrasion had no significant effect on the impact resistance of the already brittle PMMA-1. However, PMMA-2 and both types of PVC were induced to fail in a brittle fashion with low extension to break (ca 0.8 to 1.8mm) and low energies to break (ca 0.1J to 0.3J); see Table 2. The two types of PC sheet were not significantly affected by superficial abrasion. The two grades of abrasive paper used produced essentially similar effects with no systematic differences evident between Grade 0 and Grade 2 paper. The reproducibility of the results was considered to be adequate considering the very large losses of impact energy to failure evident in susceptible materials. Data for three materials, on of each polymer type, in virgin condition and abraded with Grade 0 paper, using 9 replicates for each condition, are summarised in Table 3.

Artificial weathering using the xenon arc apparatus, like abrasion, produced little change in impact resistance either of the brittle PMMA-1 or of PC-1 or PC-2. The PC materials retained impact strength even after very prolonged exposure which caused visible surface erosion and loss of gloss. The initially tough PMMA-2 showed progressive loss of impact energy to failure, exceeding 50% by 1250 hours exposure, and increasingly brittle characteristics. After very

prolonged exposure the energy to failure fell to levels similar to PMMA-1 and abraded PMMA-2.

Both PVC-1 and PVC-2 were reduced to a brittle state on xenon arc exposure. However, unlike PMMA-2, individual test pieces of both PVC materials tended to fail either in a ductile mode or in a brittle mode with little evidence of intermediate behaviour. PVC-1 after 1000 hours and PVC-2 after 250 hours exposure were found to be in transition states in which some replicates remained fully ductile whilst others were essentially brittle in character. Beyond this point only brittle failures were observed, although the energy to failure levels were not so low as were produced by abrasion. All these three materials became brittle before showing visible warning of surface degradation caused by weathering.

Exposure to both fluorescent UV-A and UV-B lamps caused loss of impact strength in the same materials as did the xenon arc lamp. However, both fluorescent lamps appeared to be disproportionately severe in their effects on the exterior grade PVC-1, with this material becoming particularly brittle. The UV-B lamps, emitting shorter wavelengths than normally present in sunlight, were especially severe but, even so, had little effect on the impact resistance of the two polycarbonate materials. The effects of laboratory exposure on colour and gloss retention of these materials is described elsewhere (5). Overall, the xenon arc exposure is thought to come nearest to natural weathering in its effects.

CONCLUSIONS

The multi-axial instrumented puncture impact test appeared to be well suited for assessing the effects of superficial abrasion or light exposure on plastic glazing materials. At least for the six materials tested, superficial abrasion identified those glazing materials which either retained or lost high initial impact strength under three laboratory weathering test procedures. This information is useful in itself but gives no indication of the duration of exposure needed to induce embrittlement. In this respect, the xenon arc exposure probably comes closest to simulating the effects of natural weathering.

REFERENCES

1. ISO 179:1993 Plastics - Determination of Charpy Impact Strength.
2. ISO 180:1993 Plastics - Determination of Izod Impact Strength.
3. ISO 8256:1990 Plastics - Determination of Tensile-impact Strength.
4. Kreiter J and Knodel R. Kunststoffe, 83,11,889-893, (1993).
5. Halliwell S M and Gardiner D. Construction and Building Materials, 8, 4, 233-241, (1994).
6. ISO 6603-2:1989 Plastics - Determination of Multi-axial Impact Behaviour by the Instrumented Puncture Test.
7. Rothwell G W. BRE CP 4/82, A Method for the Determination of Abrasive-impact Resistance of Coatings on Galvanised Steel.
8. BS 871:1981 Specification for Abrasive Papers and Cloths.

Table 2: Summary of Energy to Break and % Retained of Affected Samples

	PMMA-2		PVC-1		PVC-2	
Condition of Test Pieces	Energy (J) mean±sd	% energy retained	Energy (J) mean±sd	% energy retained	Energy (J) mean±sd	% energy retained
Control	5.10±0.54	100	5.31±0.78	100	5.27±0.09	100
Abraded						
- grade 0	0.25±0.02	4.9	0.15±0.05	2.8	0.33±0.29	6.3
- grade 2	0.20±0.01	3.9	0.10±0.02	1.9	0.22±0.09	4.2
Xenon Arc						
250 hours	4.33±1.35	84.9			2.13±2.88	40.4
500 hours			6.35±0.11	119.6	0.53±0.13	10.1
750 hours	4.18±0.45	82.0	6.77±0.13	127.5		
1000 hours	3.86±1.16	75.7	5.11±3.61	96.5		
1250 hours	1.05±0.31	20.6	0.71±0.19	13.4		
8000 hours	0.13±0.04	2.5	0.35±0.07	6.6		
UV-A Lamps						
500 hours	4.78	93.7	4.69	88.3	1.34±1.28	25.4
1000 hours	2.56±0.36	50.2	0.14±0.05	2.6	0.88	17.0
1500 hours	1.28±0.69	25.1	0.10±0.01	1.9	0.34±0.09	6.5
UV-B Lamps						
250 hours	4.50±0.74	88.2	0.33±0.03	6.2	0.56±0.37	10.6
500 hours	0.93±0.07	18.2	0.10±0.03	1.9	0.71±0.02	13.5
1000 hours	0.83±0.79	16.3	0.25±0.02	4.7	0.71±0.30	13.5

Table 3: Reproducibility of Impact Test Data

	Force at Failure (N)		Displacement at Failure (mm)		Energy at Failure (J)	
Condition of test pieces	mean	C.of V. (%) *	mean	C.of V. (%) *	mean	C.of V. (%) *
PMMA-1						
Unabraded	298	5.0	0.85	5.9	0.11	9.1
Abraded	272	9.9	0.90	5.6	0.10	30.0
PVC-1						
Unabraded	2855	8.9	5.08	2.4	5.71	12.3
Abraded	357	20.2	1.28	19.5	0.20	35.0
PC-2						
Unabraded	2648	2.0	5.51	4.4	5.86	3.9
Abraded	2620	4.7	5.39	2.4	5.75	5.9

* C.of V. is coefficient of variation

PREDICTION OF THE FAILURE OF A POLYETHYLENE PIPE WITH A DEFECT UNDER TENSION AND INTERNAL PRESSURE

P Frontini*, V García Brosa*, C Bernal*, H Lopez Montenegro*

Ductile failure in structural components can be predicted using a methodology which combines the deformation characteristics of a material and structural geometry with the fracture properties. In this paper, a ductile methodology just developed for ductile fracture of metals pieces, is applied to predict the fracture performance of artificially flawed polyethylene pipes. Material Resistance curve is determined in arc-shaped samples directly obtained from methane gas pipes by the Modified Normalisation Method that combines the records of a blunt notched sample and a precracked sample.

The growing use of polymeric materials in engineering applications demands new methodologies in order to assess the material capability to bear loads. The use of PE in the construction of gas pipelines is one of the most common examples. This paper is concerned with the determination of PE J_R curves using samples obtained directly from the pipes without any additional processing stage and with the simulation of the failure of Polyethylene Pipes with a defect under uniaxial positive tension and internal pressure

Materials, sample preparation, and testing conditions

Specimens for mechanical characterisation were machined from 125 mm external diameter HDPE pipes filled with carbon black.

Fracture experiments were conducted on sharp and blunt notched arc-shaped side-grooved specimens in three-point. Tensile measurements were conducted on Dumbbell-specimens. Yield stress was determined at the maximum and the Young module from the initial slope of the true stress-deformation curve respectively. Mechanical testing was conducted at bending at 2 mm min^{-1} crosshead rate and room temperature.

Load separation

The methodology used here is based in the load separation principle which implies that for certain material , geometry and constraint, the load can be represented as follows:

$$P = G\left(\frac{a}{W}\right).H\left(\frac{v_{pl}}{W}\right) \qquad (1)$$

*Institute of Materials Science and Technology, CONICET-UNMDP, J. B. Justo 4302, (7600), Mar del Plata, Argentina.

Geometry calibration

J determination needs the knowledge of the η factors . η_{el} was experimentally from the specimen compliance using blunt notched specimens of varying a/W.

$$\eta_{el} = \frac{b}{C}\frac{dC}{da} \tag{2}$$

η_{pl} was evaluated experimentally using the analytical form of Sharobeam et al (1):

$$\eta_{pl} = \frac{W-a}{W}\frac{G'(W-a/W)}{G(W-a/W)} \tag{3}$$

G(a/W) was constructed from the experimental data by determine S_{ij} :

$$S_{ij} = \frac{P(a_i, v_{pl})}{P(a_j, v_{pl})} = \frac{G\left(\frac{a_i}{W}\right)}{G\left(\frac{a_j}{W}\right)} = constant \tag{4}$$

for different blunt notched specimen records, taking one as a reference and plotting S_{ij} vs. a_i/W. It can be demonstrated that:

$$G\left(\frac{(W-a)_i}{W}\right) = Constant \cdot \left(\frac{(W-a)_i}{W}\right)^{\eta_{pl}} \tag{5}$$

The η_{el} and η_{pl} resulted very close to the values traditionally adopted for normal bending specimens.

Pipes failure simulation

The material J_R curve determination was determined by the normalisation method using one precracked specimen and other blunt specimen load displacement records as explained in reference (2).

The solutions for structural components ductile failure in prediction are given in reference (3) and have the following general form: the plastic strain is related to stress by a simple power law:

$$\varepsilon/\varepsilon_0 = \alpha(\sigma/\sigma_0)^n \tag{6}$$

for any particular geometry the corresponding fully plastic values of J are expressed in terms of dimensionless h_1 functions as:

$$J = \alpha\, \varepsilon_0\sigma_0 L_1 h_1(a/b, n)(P/P_0)^n \tag{7}$$

the displacement conjugate to the load is expressed similarly in terms of dimensionless h_3 functions as:

$$v = \alpha\, \varepsilon_0\sigma_0 L_1 h_3(a/b, n)(P/P_0)^n \tag{8}$$

In this paper two specific problems were solved: a cylinder with an external circunferential crack under remote tension and an internally pressurised cylinder with an internal axial crack.

Using the expressions given in reference (3) for each particularly structure a J-Integral crack driving force diagram was generated from the material Power Stress-Strain Law Constants and the respective fully plastic solutions J vs. a curves having P as the parameter were simply constructed from eq. 7 varying a, J vs. a curves having displacement as the parameter were solved numerically from eq. 8. For a fixed value of displacement the equation was solved to obtain P as a function of a and then J computed from eq.7 varying a . The crack driving force diagram was used together with the J_R material curve to determine the complete crack growth and deformation behaviour of the cracked body and to simulate load-line displacement behaviour. The results are shown in Figure 3 to 5.

Further work is in progress in order to verify experimentally the predicted failure behaviour of PE pipes under internal pressure and uniaxial stress loading.

SYMBOLS USED

σ = stress
ε = strain
P = load
P_0 = normalising load
W = width
a = crack length.
v = displacement.
b = the section thickness
α, σ_0 , ε_0 and n = Power Law representation materials constants.

G(a/W) = crack geometry function
H (vpl/W) = deformation function
S_{ij} = separation parameter
C = specimen compliance,
η = geometry calibration factor
Subscripts:
pl = plastic
el = elastic
L1 =characteristic length of the structure

REFERENCES

1-M. H. Sharobeam And J. D. Landes, 1991, Int. J. of Fract., 47, 81.

2-C.R. Bernal, P.E. Montemartini and P.M. Frontini., 1996, J. Pol. Scie. Part. B. 34, 1869.

3-V. Kumadr, M. D. GErman and C.F. Shih. "An engineering approach for elastic-plastic fracture analysis". EPRI NP-1931, Project 1237-1 (July 1981).

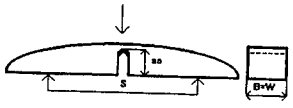

Figure 1. Fracture test specimen $\eta_{el} = 1.7$ and $\eta_{pl} = 2$.

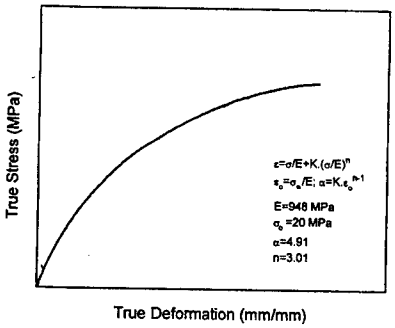

Figure 2. Stress-strain curve.

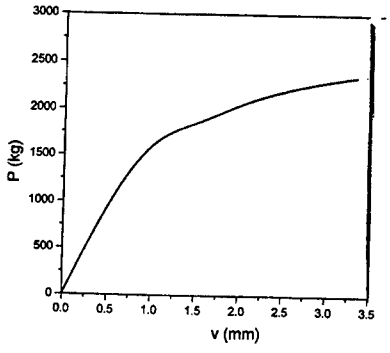

Figure 3. Load- displacement behaviour diagram for a circumferentially cracked PE pipe.

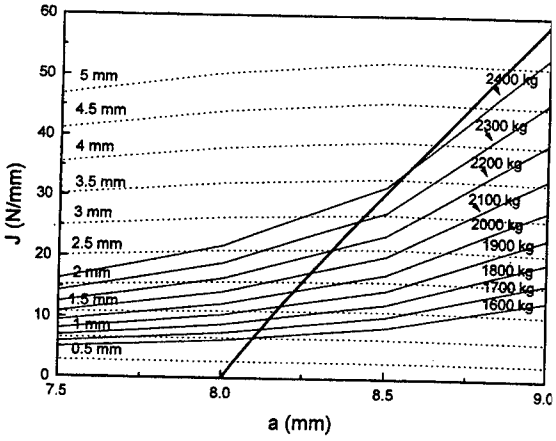

Figure 4. J-Integral Crack Driving force diagram for a circumferentially cracked PE pipe.

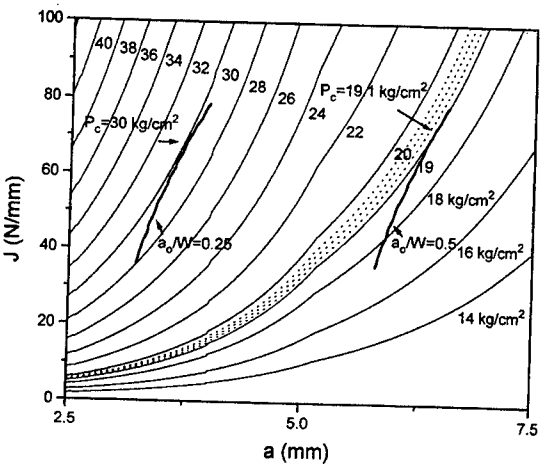

Figure 5. J-Integral Crack Driving force diagram for an axially cracked PE pipe.

EVALUATION OF DYNAMIC FRACTURE TOUGHNESS IN DUCTILE POLYMERS BY THE NORMALISATION METHOD

L.Fasce*, C.Bernal*, G.Carcagno**, P.Frontini* and H.Sautereau***

In the present work the applicability of two different methods, the Multiple Specimen Technique and the Normalisation Method, to determine the J-R Curve of Ductile polymers under impact conditions was evaluated. The J-R Curves obtained from the Multiple Specimen Technique and the Normalisation Method were generated by following the procedures proposed by Crouch and Huang (1) and Bernal *et al.* (2,3) respectively.

The measurements and analysis of the impact properties of polymers are still a controversial subject. Conventional Impact Tests (Izod and Charpy) involve the measurement of the energy to break a notched specimen but it is well known that such analysis is not satisfactory, particularly since the parameter has a strong geometry dependence and does not provide a measurement of a critical initiation parameter. Fracture mechanics theory provides the necessary theoretical framework to overcome these disadvantages. However, to employ this theory under impact conditions is not simple, because of dynamic effects, and because it requires sophisticated acquisition data instrumentation.

The purpose of this paper is the developing of a simple methodology capable of evaluate ductile fracture of polymers under impact conditions without the need of using sophisticated acquisition data instrumentation.

Experimental

Two commercial grade materials have been investigated: high impact rubber-modified polystyrene (HIPS) and ABS type resin.Pellets were dried under vacuum and then compression moulded into thick plates 7 mm thick. To release the residual stresses a post-moulding thermal treatment during was applied. Samples were machined to reach the final dimensions and improve edge surface finishing. Thickness to depth ratio (B/W) and span to depth ratio (S/W), were always kept equal to 0.5 and 4 respectively. Sharp notched specimens were prepared from the three-point bend specimens, as described in reference (2), keeping the crack to depth ratio (a/W) equal to 0.5.

Non-instrumented experiments were carried out on a conventional ASTM D 256 Charpy Pendulum Instrument at impact velocities in the range of 1.2-1.8m/s and at room temperature . The impact fracture energy was taken directly from the scale on the machine and corrected by kinetics effects following Ireland (4) recommendations.

*INTEMA - J.B.Justo 4302 - 7600 - Mar del Plata - Argentina
**Siderca - Dr. Simini 250 - 2804 - Campana - Argentina
***Insa - 20, avenue Albert Einstein - 69621 Villeurbane Cedex - France

Instrumented experiments were carried out in an instrumented Swick High Speed Universal Testing Machine at 1 m/s in order to obtain a digitalized load-displacement record at room temperature.

Methodologies

To generate the multiple-specimen resistance curve, the varying amounts of crack growth were obtained by using different initial angles in a non-instrumented Charpy pendulum, with the same impact weight. Crouch and Huang (1) suggested that the results should not be sensitive to the initial impact speed over this range. After impact, the specimens were fractured at high rate to produce a brittle break and the amount of crack growth generated during the impact was measured from the fracture surface. The J_R curve was constructed as explained in the J-integral protocols (5).

The geometry function, G, for bend specimens is equals to:

$$G = \left(\frac{W-a}{W}\right)^2 \qquad (1)$$

The deformation function or the "Material Key Curve" was obtained as a power law expression by normalising a precracked specimen load-displacement (P-v) test record by the geometry function. Only plastic displacement, v_{pl}, data points between the deviation from linearity and the maximum load point were used. The functional form of the deformation function, was assumed to be given by a simple power law:

$$P_N = \frac{P}{W^2 G} = \beta\left(\frac{v_{pl}}{W}\right)^n \qquad (2)$$

All these P_N data was regressed by one curve usually called the material key curve. Crack length, a_i, was estimated iteratively from the total displacement considering that plastic displacement can be evaluated from eq. 2 and the elastic displacement can be evaluated from the elastic compliance. From the instantaneous values of P_i, v_i and a_i J_R was constructed.

Results and Discussion

Figure 1 and 2 shows the J_R curves obtained by the Multiple Specimen Technique for two experiments carried out in the static and dynamic range respectively. Both J_R Curves, static and dynamic, are very similar. This result, even expectable, is in contradiction with the very high values of J_C obtained by indirect methods previously for the same material under impact conditions by Bernal and Frontini (6).

Figure 3 compares the Normalisation Method and the Multiple Specimen Technique Resistance Curves obtained under impact conditions for HIPS. Both methods lead to J-R curves that are in good agreement.

Although the Multiple Specimen Technique proposed by Crouch and Huang (1) has the inconvenience of the need of a large number of specimens it appears to be useful to obtain a valid J_R Curve to use as calibration of simplest by indirect methods and to characterise the toughness of polymers under impact loading conditions by using non-instrumented testing .

Regarding Normalisation Method, more work should be done to extent this method to other polymers like ABS. Up to this moment, it appears to be conditioned to the quality of the experiment plots. Further work is in progress to determine the crack blunting zone and the initiation crack growing point by following the procedure applied for toughened polymers under static loading conditions Bernal et al (2) and (3). It has the appealing advantage of not needing for crack length monitoring and for the use of a single specimen test experiment to determine the complete J_R Curve.

SYMBOLS USED

B = thickness sample

W = width sample

S = span

G = geometry function

P = load

v = diplacement

v_{pl} = plastic displacement

P_N = deformation function

a = crack length

REFERENCES

1- Crouch, B.A. and D.D.Huang, 1994, J. Mat. Sci., 29, 861.

2- Bernal, C.R., A.N.Cassanelli and P.M.Frontini, 1995, Polymer Testing, 14, 85.

3- Bernal, C.R., P.E.Montemartini and P.M.Frontini, 1996, J. Polym. Sci. Part B: Polym. Phys., 34, 1869.

4- Ireland, D.R., 1973, Instrumented Impact Testing, ASTM-STP 563, 7 .

5- G.E.Hale, "A Testing Protocol for Conducting J-R Curve Tests on Plastics, 1991, edited by ESIS Technical Committee for Polymers and Composites.

6- Bernal, C.R. and P.M.Frontini, 1995, Polym. Eng. Sci., 35, 1705.

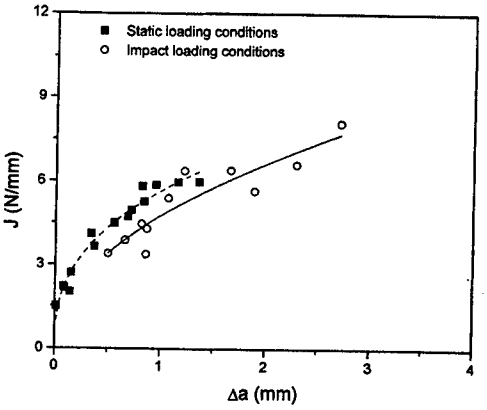

Figure 1. HIPS J_R Curves obtained from Multiple Specimen Technique under static and dynamic loading conditions.

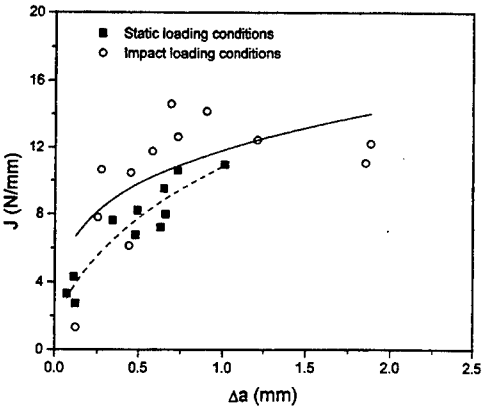

Figure 2.ABS J_R Curves obtained from Multiple Specimen Technique under static and dynamic loading conditions.

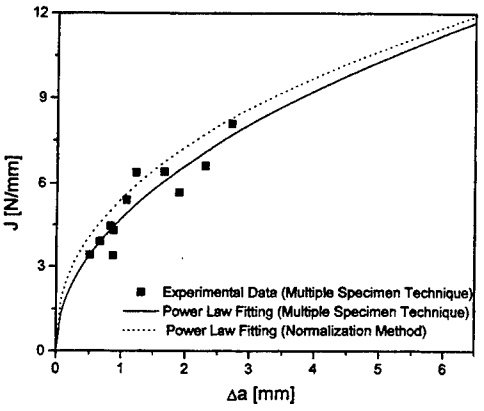

Figure 3. HIPS J_R Curves obtained from Normalisation Method and from Multiple Specimen Technique under impact conditions

DEVELOPMENT OF A PROCESS ZONE IN RUBBER-MODIFIED EPOXY POLYMERS

Jianguang Du*, Michael D. Thouless** and Albert. F. Yee*
* Department of Materials Science and Engineering, ** Department of Mechanical Engineering and Applied Mechanics, The University of Michigan, Ann Arbor, Michigan 48109, USA

INTRODUCTION

Epoxy resins can be substantially toughened by the incorporation of a rubbery phase. Investigations have revealed that, compared with unmodified epoxies, the successfully toughened versions have a considerably larger zone of plastic deformation. Within this zone there are localized bands of plastic deformation which are associated with cavitated rubber particles and enlarged cavities [1,2] It is generally accepted that cavitation of the rubber particles and enhanced plastic deformation of the matrix are the most important toughening mechanisms for rubber-toughened epoxies [1,3-6].

Micromechanics modeling of rubber-modified epoxy polymers has focused on exploring the effects of cavitation and flow in a process zone situated ahead of a stationary crack [7]. However, for toughened brittle materials it has been well established that the strengths of these materials depend critically on how the process zone interacts with a propagating crack [8-10]. As a crack passes through the process zone, it leaves a wake of inelastically deformed material behind the crack tip, and simultaneously creates a new region of deformed material ahead of the crack tip. This development of the process zone upon crack growth gives rise to an R-curve behavior [11,12] in which the toughness depends on the extent of crack advance. Typically, as an initial process zone forms ahead of the crack tip, an initial value of toughness similar to the intrinsic toughness of the matrix is expected. Since the material within the process zone ahead of the crack tip experiences monotonic straining and, hence, experiences no strain reversal, little toughening contribution is predicted for the frontal process zone when there is no crack growth [9]. As the process zone evolves with crack growth until a fully-developed, steady-state wake of uniform thickness is reached, the toughness rises rapidly to a steady-state, fully-toughened value which is independent of crack length. Since the material in the wake undergoes a nonlinear, irreversible unloading process and the consequent stress-strain hysteresis, significant contribution from the crack wake to the enhanced, steady-state toughness is unambiguously demonstrated for these materials [8-10].

Exploration of any wake effects in rubber-modified epoxy polymers appears to have been limited to cases in which bridging by rubber particles is thought to be the major toughening mechanism [13, 14]. However, the importance of the crack wake on toughening has been clearly substantiated for toughened brittle materials in the absence of any bridging mechanism [11]. No efforts have been devoted to understanding the wake toughening effects in the absence of bridging mechanism for toughened polymers. The present work deals with this unexplored area. Significant toughening contribution from the crack wake was experimentally demonstrated by R-curve measurements upon removal of the crack wake.

EXPERIMENTAL

The rubber-modified epoxy polymers used in this work were formed by combining (by weight) 100 parts of a liquid diglycidyl ether of bisphenol-A, 5 parts of piperidine, and 5, 10, 15, 20 and 25 parts of a carboxyl-terminated acrylonitrile-butadiene copolymer (HYCAR® CTBN 1300 X 8, produced by the B.F. Goodrich Co.). The materials were cured at 120 °C for 16 hours in a Teflon®-coated mold. The material properties are very similar to those obtained in previous studies [1,4-6]. Double-cantilever-beam specimens were machined. An initial crack was formed by machining a notch, and then tapping a razor blade into the tip of the notch to form a sharp crack prior to testing. R-curve measurements were performed using a screw-driven Instron testing machine with a crosshead speed of 0.5 mm/min. When, during

loading, *in-situ* optical observations indicated that some crack growth was occurring, the specimen was partially unloaded so as to arrest the crack. The sample was then reloaded to induce further crack growth, and unloaded again to mark the new position of the crack tip. This process was repeated until catastrophic crack growth caused rupture of the specimen. After this, the fracture surface was examined in an optical microscope, and successive crack lengths were measured from the striations. A typical R-cure for epoxy with 10 phr rubber is shown in Fig. 1

The evolution of the process zone in 10, 15, 20 and 25 phr rubber-modified epoxies was studied using a second set of identical specimens tested at the same crosshead-displacement rate. These tests were interrupted after about 25 mm of crack growth, but before unstable crack growth caused complete failure. A thin section at the mid-plane of the specimens and perpendicular to the crack surface was obtained by petrographic thinning. These thinned specimens were examined in transmitted light using a Nikon research microscope. A schematic depicting the process zone in 10 phr rubber/epoxy, which is typical, is shown in Figure 2.

The effect of the wake on the toughness was examined by repeating the R-curve measurements described above. Upon loading, a zone of "stress-whitened" material formed ahead of the starter crack at a certain load level. This "whitened" process zone extended with the crack advance, as a wake, over the crack surfaces. These tests were interrupted after about 20 mm of crack growth in which a fully-developed crack wake of uniform thickness was obtained. About 3 mm thick of the material within the wake region was then machined off. Consequently, all the preformed crack wake, up to the region about 2 mm behind the crack tip, was removed by this procedure. Further crack growth was obtained upon subsequent loading, and the R-curve was re-established. The resultant R-curve for 10 phr rubber/epoxy is shown in Figure 3.

RESULTS AND DISCUSSION

A significant R-curve behavior was observed for 10, 15, 20 and 25 phr rubber-modified epoxies. Upon a small crack growth of less than 1 mm, an initial fracture resistance of between 1 and 2 kJ/m^2 was obtained. The toughness then rose rapidly to an approximately steady-state value of about 7 kJ/m^2 for 10 and 15 phr rubber-modified epoxies or 5 kJ/m^2 for 20 and 25 phr rubber-modified epoxies after a crack growth of between 10 or 20 mm. These values should be compared with the toughness value of 0.2 kJ/m^2 for the unmodified epoxy [2]. This evolution in process zone shape can be directly correlated to the features of the R-curve. The presence of the crack wake provided an additional contribution to toughening, because materials within the wake experienced unloading and the attendant hysteresis.

Another important feature observed from Figure 2 was that the thickness of the steady-state process zone decreased from about 200 μm for 10 and 15 phr rubber-modified epoxies to about 150 μm for 20 and 25 phr rubber-modified epoxies. Because reaching a certain critical mean stress is a necessary condition for cavitation and subsequent hole growth to occur, the decreasing thickness of the steady-state process zone indicates that the mean stress ahead of the crack tip decreases with increasing rubber content. This mean stress reduction can be explained by the constraint relief effect of cavitation of the rubber particles. The greater the number of cavitated rubber particles, the greater is this constraint relief effect. Since the dilatational toughening associated with cavitation and subsequent void growth is process zone-size-dependent, i.e. increases with increasing the thickness of the steady-state process zone [2], the decrease of the steady-state fracture toughness from 7 kJ/m^2 to 5 kJ/m^2 is expected. Another reasonable explanation for the decrease of the steady-state toughness of these materials is the increase of cavitation density with increasing rubber content observed from the SEM micrographs of the steady-state fracture surfaces. Although cavitation of the rubber particles could enable extensive plastic deformation in the epoxy matrix, it also degraded the material in the process zone ahead of the crack, i.e. reduced the fundamental crack growth resistance of the material within this region proportionally to the volume fraction of the cavities

[2]. Therefore, lower steady-state toughness is expected for 20 and 25 phr rubber-modified epoxies in which the density of cavities was relatively high.

An interesting phenomenon observed in these materials is that instability of the crack growth occurred when the R-curves closely approached the asymptotic, steady-state toughness. This instability is characterized by the abrupt disappearance of the process zone at the point where instability occurred. Furthermore, the density of cavitation and the void size both decreased with an increase in crack velocity. This indicates that both the cavitation rate and the plastic flow in these materials are, to some extent, time-dependent phenomena.

ACKNOWLEDGEMENT

This work is supported by the National Science Foundation under Grant CMS-9523078. The authors are also thankful to Dr. J. Huang for his valuable help and discussions.

REFERENCES

1. R. A. PEARSON and A. F. YEE, *J. Mater. Sci.* **21** (1986) 2475.
2. A. F. YEE, D. LI and X. LI, *J. Mater. Sci.* **28** (1993) 6392.
3. W. D. BASCOM, R. L. COTTINGTON and C. O. TIMMONS, *Appl. Polym. Symp.* **32** (1977) 165.
4. A. J. KINLOCH, S. J. SHAW, D. A. TOD and D. L. HUNSTON, *Polymer* **24** (1983) 1341.
5. A. J. KINLOCH, S. J. SHAW and D. L. HUNSTON, *Polymer* **24** (1983) 1356.
6. A. F. YEE and R. A. PEARSON, *J. Mater. Sci.* **21** (1986) 2462.
7. Y. HUANG and A. J. KINLOCH, *J. Mater. Sci.* **27** (1992) 2763.
8. R. M. MCMEEKING and A. G. EVANS, *J. Am. Ceram. Soc.* **65** (1982) 242.
9. B. BUDIANSKY, J. HUTCHINSON and J. LAMBRAPOLOUS, *Int. J. Solids Struct.* **19** (1983) 337.
10. A. G. EVANS and K. T. FABER, *J. Am. Ceram. Soc.* **67** (1984) 256.
11. R. KNEHENS and R. STEINBRECH, *J. Mater. Sci. Lett.* **1** [8] (1982) 327.
12. M. V. SWAIN and R. J. H. HANNINK, *Adv. Ceram.* **11** (1984).
13. S. KUNZ-DOUGLASS, P. W. R. BEAUMONT and M. F. ASHBY, *J. Mater. Sci.* **15** (1980) 1109.
14. A. G. EVANS, Z. B. AHMAD, D. G. GILBERT and P. W. R. BEAUMONT, *Acta Metall.* **34** (1986) 79.

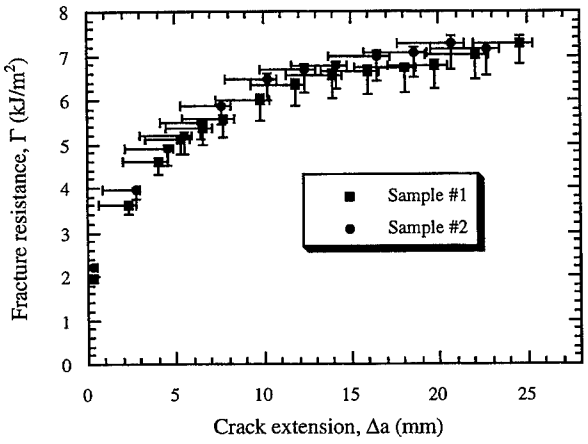

Fig. 1 Experimental R-curves for 10 phr rubber-modified epoxy.

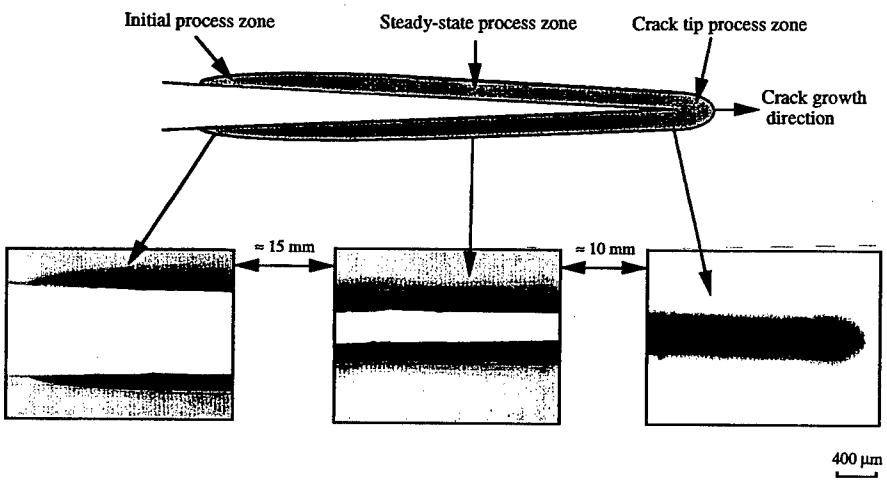

Fig. 2 TOM micrographs of evolution of process zone for 10 phr rubber-modified epoxy.

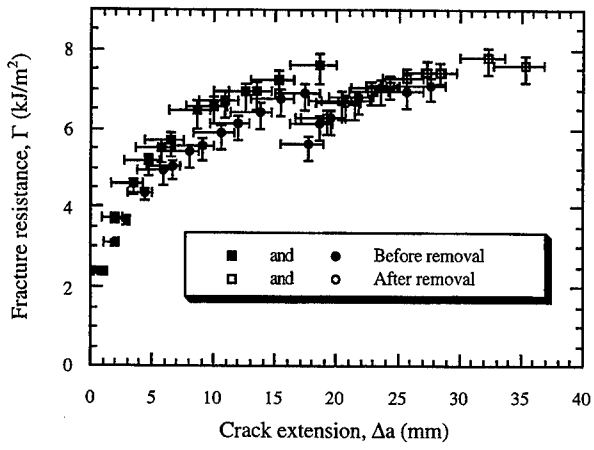

Fig. 3 Experimental R-curves upon removal of crack wake for 10 phr rubber-modified epoxy (■ and □ for sample #1, ● and ○ for sample #2).

INDENTATION ENHANCED ADSORPTION OF AQUEOUS ZINC CHLORIDE PREVENTS DRAWING OF NYLON 6

JA Donovan and G Mitchell*

Indentation, like in a hardness test, of a nylon 6 tensile specimen in the presence of an aqueous $ZnCl_2$ solution prevents drawing during subsequent tensile deformation, but the modulus and the yield stress are unchanged. A synergism between the plastic deformation and the aqueous $ZnCl_2$ solution enhances the uptake of the solution, as shown by X-ray analysis, that decreases the strain to failure by an order of magnitude. Out of plane plastic shear during indentation drags the hydrogen bonded solution into the plastically deformed region around the indent.. The mechanism that prevents drawing is not known, but the adsorbed aqueous Zn solution may interfere with the formation of inter- and intrafibrillar tie molecules.

INTRODUCTION

Environmental assisted crazing and crack growth in polymers have been extensively studied, for example by organic liquids of glassy polymers (1), detergent cracking of polyethylene (2) and salt solution cracking of nylons (3-6). The plasticization by the adsorption of aqueous inorganic salt solutions by nylon 6 and the embrittlement by the subsequent dehydration has recently been studied (7). The mechanisms of these interactions in the nylon \ aqueous electrolyte system are determined by the primary role hydrogen bonding has in determining the intrinsic mechanical properties of nylon 6 and other polyamides.

Plastic deformation of nylon (semicrystalline or amorphous) requires breaking these hydrogen bonds, and these broken hydrogen bonds will bond with other compatible species if they are available such as water or hydrated salt ions. Therefore, the simultaneous availability of a molecule or hydration cluster able to bind to the nylon

*Department of Mechanical and Industrial Engineering, University of Massachusetts, Amherst, Massachusetts, USA 01003-2210

amide group could be dragged with the nylon molecule during plastic deformation.

EXPERIMENTAL PROCEDURE

Injection molded nylon 6 ASTM tensile samples (6 mm wide, 3 mm thick with a gage length of 10 cm) considered to be dry, which means they contain about 0.5 percent water (8) were tensile tested at room temperature at a strain rate of 3.3×10^{-3} s^{-1} on a bench top Instron.

Prior to tensile testing the samples were in one of the following conditions:

1) Dry.

2) Indented to a maximum load of 1.5 kN with a 6.3 mm spherical indentor. The rates of indentation were 0.5, 1.5 or 3 mm per minute. The indent was placed on the center line and at the center of the gage length on the wide face of the tensile specimen. The local environment during indentation and unloading was either a) air, or b) a drop (about 0.5 cc) of water or c) of 4 molar $ZnCl_2$ aqueous solution. Before tensile testing the drop of liquid was removed by blotting with a paper towel.

3) Indented with the liquid present only during loading.

4) Indented without the liquid, but unloaded with the liquid present.

5) Drops of water or the $ZnCl_2$ solution were placed on a tensile sample that had been indented in air or had not been indented for the time required for the indentation, about 90 s, before tensile testing.

A sample fractured at LN_2 temperature after indentation in the presence of the $ZnCl_2$ solution at room temperature was examined in the SEM and the distribution of Zn and Cl were determined.

RESULTS

The stress strain curve for a dry nylon 6 specimen is shown in Figure 1. The yield region is broad and accounts for about 15 percent strain before the neck forms when the engineering stress drops abruptly. The neck propagates at a constant stress until it traverses the gage length of the specimen then work hardens until fracture. The stress strain curves for samples 1) indented in air or water, or 2) exposed to a drop of water or $ZnCl_2$ solution a) without indentation or b) only during unloading were the same as for the dry sample shown in Figure 1.

The stress strain curve for the nylon tensile specimen indented in the presence of the $ZnCl_2$ solution is also shown in Figure 1. The slope of the elastic region and the yield stress are the same as for the dry unindented specimen. But, the sample fails by highly localized ductile deformation without a stable neck developing. Therefore, the strain to failure was about 20 percent rather than 200+ percent.

DISCUSSION

Plastic deformation occurred in the region of the indent, and was constrained by the elastic field further away from the indent. The mechanics of the indentation test for elastic-plastic materials has been analyzed by Hill et al. and what follows is based on their analysis (9). For an elastic-plastic material there is an annulus just outside the contact perimeter where the circumferential stress and the radial stress are tensile. The planes of maximum shear stress are out of plane, which means that during loading the shear processes in this annulus are at approximately 45^0 to the surface, into and out of the surface.

In nylon 6, a semicrystalline material, yielding involves breaking the hydrogen bonds between the amide groups in the amorphous phase and the crystals. When these bonds are broken other compounds capable of forming hydrogen bonds like water or hydrated Zn or Cl or hydroxal ions could bind to the amide groups in the nylon and be dragged into the bulk by the shear process. The dragging of hydrated ions trapped by the amide groups whose hydrogen bonds with other amide groups have been broken by the shear process is compatible with the enhanced uptake; diffusion alone can not explain these data.

The appearance of the indents done in air, water, or $ZnCl_2$ solution were similar and the hardness was not affected by the local environment. Likewise the modulus and the yield stress of the indented or unindented tensile specimens were the same. This means that significant cracks or crazes or voids did not form due to the indentation because they would have decreased the elastic modulus, and probably be visible -- they were not. However, the strain to failure was reduced by about an order of magnitude, if the local environment was the $ZnCl_2$ solution during loading. The material in the region of the indent drew down in a ductile manner until separation occurred without forming a stable neck.

How the Zn solution interferes with this process is not clear at this time, but it is known that the adsorption of aqueous $ZnCl_2$ by nylon 6 without any applied stress causes decrystallization and plasticization (7). This suggests that the adsorbed Zn solution interferes with the recrystallization process or formation of tie molecules necessary for the development of a stable neck. Understanding the mechanism requires more work.

The process that prevents drawing (growth of a stable neck) occurs during the loading phase of the indentation process, but not during unloading when the maximum shear stresses now occur in plane, which means that they would not drag the local environment into the bulk. This explains why unloading the indenter in the presence of the solution does not affect subsequent deformation.

In conclusion, the simultaneous presence of the aqueous Zn solution and plastic indentation enhances the adsorption and transport of the solution that prevents drawing during a subsequent tensile test.

REFERENCES

1. R.P. Kambour, in Critical Reviews in Macromolecular Science, Vol. 1, E. Baer, ed., CRC Press, Chemical Rubber Co., Cleveland, OH, (1972).
2. P. Chang and J.A. Donovan, Poly. Eng. and Sci., 30, (1990) 1431.
3. M.G. Wyzgoski, and G.E. Novak, J. Mat. Sci., 22, (1987) 2615.
4. R.P. Burford, and D.R.G. Williams, J. Mat. Sci., 7, (1988) 59.
5. A.P. More and A.M. Donald , Polymer, 34, (1993) 5093.
6. C.C. Pai, R.J. Jen, S.J.Grossman and J.C. Huang, Advances in Polymer Tedhnology, 9, (1989) 157.
7. H. Li, Masters Thesis, University of Massachusetts, Amherst, (1995).
8. Y. Liu and J.A. Donovan, Poly. Eng. and Sci., 36, (1996).
9. R. Hill, B. Storakers and A.B. Zdunek, Proc. R. Soc. Lond., A423, (1989) 301.

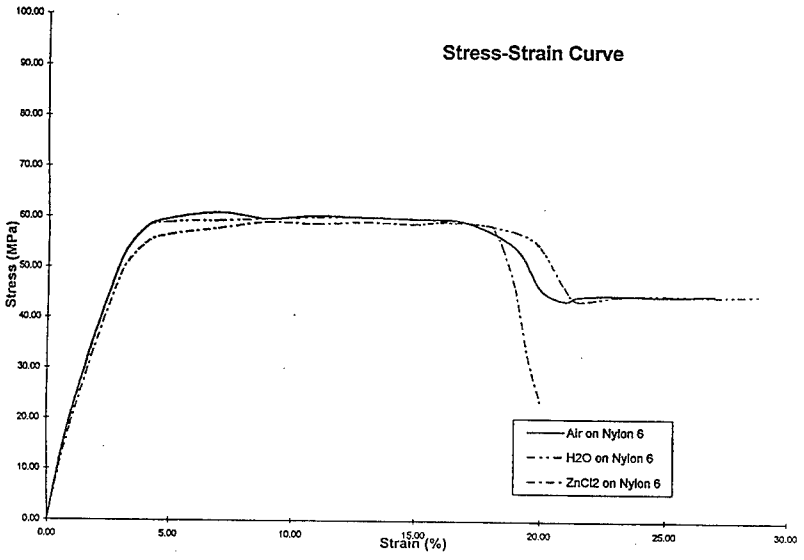

Figure 1. Stress strain curves for nylon 6 after being indented in air, water and $ZnCl_2$ solution. The specimens indented in air and water fail at about 200 percent strain.

MECHANICS OF SPIDER SILK DURING AND AFTER CONTRACTION IN SELECTED SOLVENTS

Zhengzhong Shao* and Fritz Vollrath*

Using a custom-built stress-strain gauge, we examined - during and after submersion in a range of solvents - the characteristics of major ampullate silk (MAS) reeled from the garden cross spider Araneus diadematus. The silk showed significantly different mechanical behaviour during and after supercontraction in (i) water, (ii) concentrated urea solution and (iii) a set of alcohol solvents. Apparently the solvents with their different polarity affect different regions of the silk's composite microstructure i.e. its molecular conformation. Evidence from recent ultrastructural studies would support such a conclusion. We hypothesise that the observed mechanical properties of MAS are a natural, hard elastic polymer.

INTRODUCTION

Spider silk is a most attractive biomaterial (1,2). Normally, the major ampullate silk (MAS) of a spider such as Araneus diadematus has the unusual combination of high strength and stretch, which leads to toughness values rarely observed in synthetic high-performance fibers (3). An additional feature (a constraint ? or an evolutionary adaptation ?) of MAS is its ability to supercontract when submerged in a solvent such as water. There are man-made polymers which exhibit supercontraction in organic solvents but virtually none which will supercontract in water alone (4). Here we report on the mechanical properties of reeled MAS studied during and after submersion in a range of solvents; and then we attempt to explain the mechanism of the supercontraction.

MATERIAL AND METHODS

All silk samples used in the experiments were reeled from 5 garden cross spiders Araneus diadematus with a drawing speed of 2 cm/s (at room condition, 24±3 °C, 25±3% rH). The spiders weighed 140 to 190 mg. The SEM-measured diameters of five threads per spider were 2.4 - 3.0 µm, and there was no correlation between spider weight and silk diameter because we used spiders of similar weight.

Using cyanoacrylate adhesive, a single thread was mounted on two hooks of our rapid response stress-strain gauge (transfer method in Köhler & Vollrath, 5). The gauge was set-up in such a way that we could measure fibers either in air or submerged full-length in a bath. The gauge (with a FORT 10 force transducer of World Precision Instruments) and extension mechanism (Pen Motor Assembly of Hewlett Packard) were driven and recorded using Lab View on Macintosh and had a time resolution of a few ms and a force resolution of 30 µN.

We measured the mechanical properties of fibers in air as well as submerged and calculated stress-strain characteristics after normalisation for fiber diameter. The samples were given 10 - 60 mins to reach equilibrium after submersion. The strain rate of the sample was 50% /min. The data shown give the average value of 3 - 10 measurement samples for each spider. Silks were measured either during submersion and without relaxation (Table 1) or during submersion (wet) and afterwards (dry) but with relaxation in the solvent (Table 2) .

*Department of Zoology, Aarhus University, Denmark

RESULTS

The first hysteresis cycles of restrained silk in various circumstances are shown in Fig.1 and their mechanical properties are listed in Table 1. Although some solvents such as water and methanol did reduce their modulus and strength because of plasticization, the MAS still displayed high initial modulus, no clear yielding point, large breaking strength, typical extendibility, good recoverability and "energetic" elasticity. Under a given strain (such as 18% extension, for instance), the stress of silk submerged in ethanol would relax to less than 40 % until equilibrium, whereas the same silk in air would relax to only about 20%. This is evidence for a hard elastic material, where such a behaviour has been explained using the mechanism of surface energy (6). Thus our experimental results suggest that the MAS of Araneus diadematus is a natural polymer with hard elastic properties in a specific range.

TABLE 1- Mechanical Properties of MAS from *Araneus diadematus* spider measured under restrained conditions.

	Initial Modulus ($x10^9 N/m^2$)	Breaking Strength ($x10^8 N/m^2$)	Breaking Elongation (%)
Water	1.6 ± 0.3	5.0 ± 0.5	25 ± 2
Methanol	3.5 ± 0.4	5.5 ± 0.6	24 ± 1
Ethanol	6.7 ± 0.5	7.5 ± 0.9	22 ± 2
Butanol	6.6 ± 0.4	8.0 ± 1.0	22 ± 3
Air	6.5 ± 0.4	8.1 ± 1.0	22 ± 2

Fig. 2 and Table 2 show the typical stress-strain curves and properties, as well as the shrinkage ratio of MAS during and after contraction in a range of solvents. There seemed to be a relationship between the contracting ratio (x) of length and the expanding ratio (y) of thread diameter ($y = 0.86x$); for practical reasons we used (for normalising) silk diameter and length before contraction. If we were to apply the real diameters and lengths of the silks after contraction in water, methanol or ethanol, then the initial modulus (dry) in Table 2 would have to be changed to about 2.0, 2.5 and $4.0x10^9 N/m^2$, respectively.

TABLE 2- Mechanical Properties of MAS after Contraction in a Solvent and Measured either during Submersion (wet state) or afterwards in Air (dry state).

Solvent	State	Initial Modulus ($x10^9 N/m^2$)	Breaking Strength ($x10^8 N/m^2$)	Breaking Elongation (%)	Shrinkage Ratio (%)
Water	wet	~ 0.1	6.5 ± 0.5	30 ± 3	
	dry	7.8 ± 0.8	6.2 ± 0.4	11 ± 2	55 ± 3
Methanol	wet	2.2 ± 0.3	6.3 ± 0.9	25 ± 3	16 ± 1
	dry	5.2 ± 0.4	7.3 ± 0.5	19 ± 2	27 ± 2
Ethanol	wet	6.6 ± 0.5	7.6 ± 0.7	22 ± 2	~0
	dry	5.1 ± 0.5	7.4 ± 1.0	21 ± 3	9 ± 2
Butanol	wet	6.4 ± 0.4	7.9 ± 1.1	22 ± 3	0
	dry	6.5 ± 0.3	7.8 ± 1.0	23 ± 2	0

The shrinkage ratio in water of silk is not given in Table 2 because there was no apparent initial modulus when the contracted thread was stretched in water (Fig. 2); but his shrinkage was about 45% (measured with light microscopy as reported by Work (7) (and confirmed by us). We noticed that silks wetted by submersion in water, methanol and ethanol

shrank somewhat more during subsequent drying in air. That means, that these solvents swelled the silk (to varying degrees). Highly concentrated urea solution (6 - 8M) had a very different effect: the silk lost its characteristic mechanical properties. Furthermore, after submersion in urea solution the silk surface became uneven (observed on SEM); and we conclude that such concentrated urea solution would partly dissolve the silk, inside and out. Last but not least, we found that guanidine hydrochloride totally dissolved our spider silk.

Discussion

Guanidine hydrochloride is a known destroyer of hydrogen bonds, these bonds (both within and between molecular chains) play a crucial role in the structure of proteins. When the spider spins its silk from its spinneret, most - if not all - of the molecular chains will be oriented - to varying degrees - along the fiber axis by the shear and stretch force of the spinning process. It seems that there is no clear boundary between the amorphous phase (with its poor orientation and lower density) and the so called crystalline regions (with their clear orientation and higher density). Since the glass transition temperature of spider silk is about -75 °C, we may assume that in room temperature the oriented chains would be fixed by some intermolecular hydrogen bonds. When these bonds are gradually destroyed, i.e. by the different actions of our solvents, the molecular chains would disorient step by step. Thus the essence of supercontraction of spider silk would be the disorientation of the molecular chains. We explain the different swelling action of our principal solvents (water, methanol, ethanol and butanol) by their differing impact on hydrogen bonds in the silk material. This could be due to solvent specific polarity and molecule size.

The more hydrogen bonds are destroyed, the larger the shrinkage until, finally and in a strong solvent, the silk is totally dissolved. It has been shown (7) that, in water, silk with high birefringence shrinks less than silk with low birefringence; we might assume that the former has more hydrogen bonds than the latter. Thus, the higher birefringence of a silk would mean higher molecular orientation and higher density, i.e. more so-called "ß-sheet crystal areas". We hypothesise that water molecules find it more difficult to enter these high density areas, resulting in fewer broken hydrogen bonds and lesser shrinkage than in the less dense surrounding regions. We have demonstrated that silk supercontracts in solvents other than water and urea. The stress-strain behaviour of supercontracted silk, in wet and dry state, gives us new indications as to the mechanism underlying the material properties. The plateau in the stress-strain curves (Fig. 2) could be interpreted as indicating that disoriented molecular chains reorient under the stretching force. As we assume shrinkage to be positively correlated with disorientation, pre-shrunk silks should display larger plateau, as they do. However, it seems that such disorientation has a cost: wet and pre-shrunk silk had lower breaking strength and elongation, maybe because of friction among chains and the reformation of some hydrogen bonds when drying.

REFERENCES

1. "Silk Polymers - Materials Science and Biotechnology", 1994, Ed. by Kaplan, D., Adams,W.W., Farmer, B., and Viney, C., ACS Symposium Series 544, Washington DC
2. Vollrath, F., 1992, Scientific American, 266, 70
3. Gosline, J.M., DeMont, M.E., and Denny, M.W., 1986, Endeavour, 10, 37
4. Work, R.W., 1977, J. Exp. Biol., 118, 379
5. Kohler, T., and Vollrath, F., 1995, J. Exp. Zoo., 271, 1
6. Walton, K., Moet, A., and Baer, E., 1983, Contemporary Topics in Polymer Science Vol.4. (Ed. by Bailey, W.J., and Tsuruta, T.), Plenum Press, New York, 977
7. Fornes, R.E., Work, R.W., and Morosoff, N., 1983, J. Polymer Sci., 21, 1163

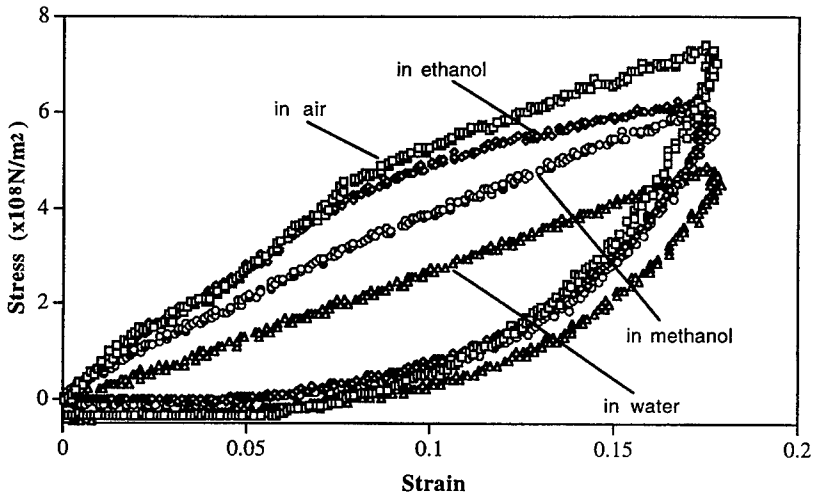

Fig 1. Loading-unloading cycles of major ampullate silk reeled from Araneus diadematus in air, ethanol, methanol and water

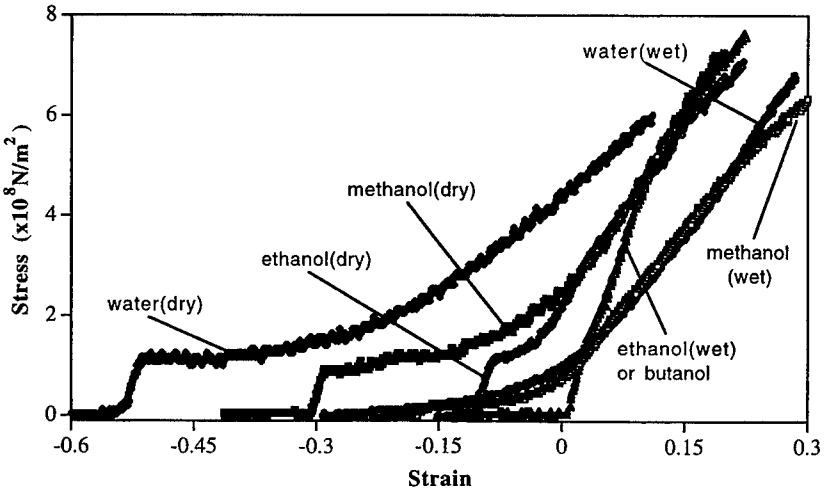

Fig. 2. Stress-strain curves of major ampullate silk during(wet) and after(dry) contraction in water, methanol and ethanol or butanol. The shrinkage was defined as negative strain, and diameter and length of silk before contraction were used for normalising

MODELING OF CAVITATION AND YIELD IN AMORPHOUS POLYMER-RUBBER BLENDS

AC Steenbrink* , E Van der Giessen* and RJ Gaymans**

INTRODUCTION

The phenomenology of deformation and fracture of rubber-toughened glassy polymers is quite well understood, owing to a large number of experimental studies. The key deformation mechanisms in such blends have been identified to be cavitation of the rubber particles, plasticity of the matrix, and/or crazing (1). This paper reports on results obtained from numerical studies based on a finite element method, in order to advance a quantitative description of these phenomena (and their interaction) in relation to the properties of the constituents. Analytical estimates for particle cavitation and the effect on matrix plasticity are also discussed.

MODEL FORMULATION

Similar to our previous work on porous polymers (2), the behaviour of polymer-rubber blends is investigated using an axisymmetric unit cell model. This model is an approximation for a material which consists of identical layers with a hexagonal closed packing of rubber particles. This approach allows us to employ a two-dimensional model which, to some extent, accounts for interactions between neighbouring rubber particles. The radial and axial directions are denoted by x_1 and x_2, respectively.

Loading is prescribed through a remotely applied axial strain-rate $\dot{E}_2$, which is taken to be constant. The macroscopic radial strain rate $\dot{E}_1$ is chosen such, that the overall stress ratio Σ_1/Σ_2 remains constant throughout the deformation process. This ensures that the overall stress triaxiality ratio Σ_m/Σ_e remains fixed during the process. Here, Σ_m denotes the remote hydrostatic (or mean) stress and Σ_e is the macroscopic Mises stress. For axisymmetric conditions, they are defined as $\Sigma_m = \frac{1}{3}(2\Sigma_1 + \Sigma_2)$ and $\Sigma_e = |\Sigma_2 - \Sigma_1|$, respectively.

The macroscopic state of deformation is specified in terms of the principal logarithmic strains E_2 and E_1. For future reference, we introduce the effective Mises strain $E_e = \frac{2}{3}|E_2 - E_1|$. The finite strain formulation of the boundary value problem is based on a Lagrangian description. The discretisation into finite elements requires a very fine mesh in order to resolve the localized shear bands that will be shown to occur.

It is of crucial importance to incorporate the characteristic features of the large deformation stress-strain behaviour of glassy polymers and rubbers in the analysis. The material model for the rubber is based on entropy elasticity and accounts for strain hardening of the cross-linked network. The description of the visco-plastic behaviour of the glassy polymer includes temperature and rate-dependent yielding followed by intrinsic softening. Subsequent strain hardening is described analogous to the nonlinear rubber elasticity model. Also the pressure dependence of yielding is incorporated. The effect of small strain visco-elasticity is neglected. The current material model does not account for crazing. For more details about the numerical procedures and the material models, we refer to (3). The material parameters have been chosen to represent to properties of styrene-acrylonitril at room-temperature ($s_0 = 120\,\mathrm{MPa}$).

*Delft University of Technology, Laboratory for Engineering Mechanics, Delft, The Netherlands
**Twente University, Department of Chemical Technology, Enschede, The Netherlands

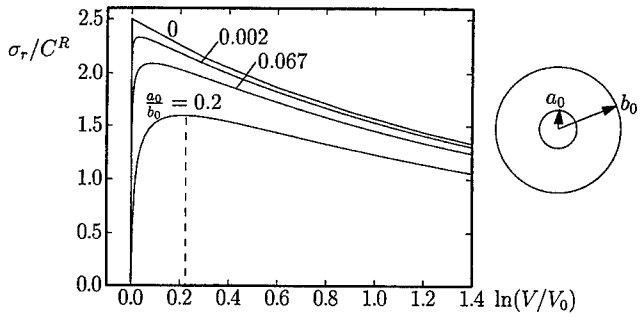

Figure 1: Radial expansion of a hollow Neo-Hookean sphere with various relative initial void sizes a_0/b_0, in terms of the normalized externally applied radial stress versus logarithmic volumetric strain.

CRITERIA FOR RUBBER PARTICLE CAVITATION

An issue of particular interest here, is the effect of cavitation of the rubber particle on plasticity in the matrix. Therefore we first try to establish some criteria for particle cavitation. Surface tension within the void may play an important role in the void *initiation* phase, i.e. if the void is very small ($\sim$ 10nm). Its contribution rapidly decreases if the void grows larger and here we neglect it at all. Thus, we implicitly assume that the resistance against void *growth* is the limiting factor controlling cavitation, irrespective of the void initiation process.

We consider the problem of spherical symmetric expansion of a hollow sphere, with an initial inner radius a_0 and initial outer radius b_0. Assuming incompressibility the problem is one-dimensional and the radial stress on the outer boundary can be found by directly integrating the equation of equilibrium (2). For Neo-Hookean material behaviour, the externally applied radial stress versus the logarithmic volumetric strain ($\ln(V/V_0)$) is depicted in Fig. 1. In the limit of an infinitesimal initial void we have a cavitation instability, for which the critical stress is $5C^{\mathrm{R}}/2$ (4,5), where C^{R} denotes the shear modulus. For a finite initial void size the peak stress is somewhat lower. However, the behaviour is essentially the same as in the case of an infinitesimal initial void; the resistance against dilatation is very high until a maximum in the hydrostatic stress is attained.

For cavitation in polymer rubber blends it is necessary to consider the effect of the matrix on particle cavitation, with arbitrary loading conditions. It was shown by Horgan *et al.* (5) that for a composite sphere of Neo-Hookean materials with different stiffnesses, the cavitation limit depends only on the stiffness of the core. In general, the stress state to which polymer-rubber blends are subjected is not purely hydrostatic. Hou *et al.* (6) showed that the critical stress for cavitation in a Neo-Hookean material depends on the remotely applied stress triaxiality. The analysis of Hou *et al.* (6) can easily be extended to a composite sphere of Neo-Hookean materials. For axisymmetric conditions, it can be shown that if the stiffness of the particle is much lower than the stiffness of the matrix, the cavitation limit hardly depends on the (macroscopic) deviatoric stress component, and also in the non-symmetric case only the properties of the particle are decisive.

Moreover, we note here that it shows from Fig. 1 that if the particle is expanded beyond the peak stress, it still sustains considerable radial tractions, up to large volumetric strains. *Therefore, the statement that a cavitated particle is equivalent to a void does not hold.*

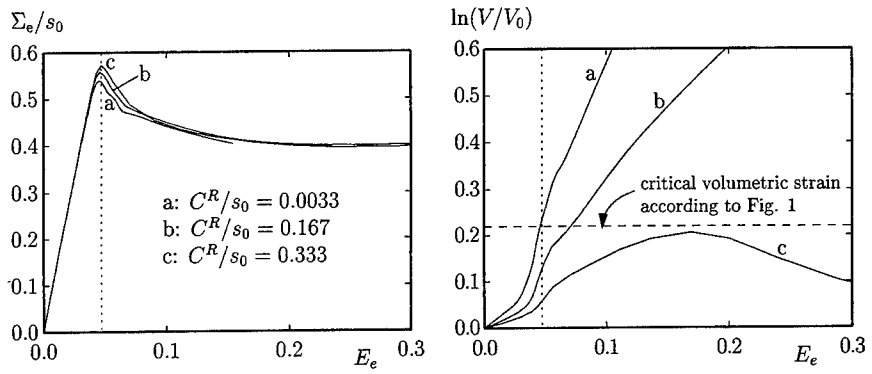

Figure 2: Macroscopic stress-strain response and logarithmic volumetric strain of the particle from cell model analyses.

RESULTS OF UNIT CELL MODEL COMPUTATIONS

The effect of the stiffness of the rubber particle on the macroscopic stress-strain response and void growth in the rubber particle is illustrated here by means of numerical results of cell model analyses, using an initial rubber volume fraction of $f_0 = 0.00533$ (corresponding to a particle diameter of 0.2 relative to the particle spacing), under loading conditions with an intermediate triaxiality ($\Sigma_m/\Sigma_e = 1.0$). For computational reasons, an initial void (0.2 times the particle diameter) is assumed in the particle in the cell model. Clearly, this does not imply a serious limitation since the essential features of the behaviour of the particle are not affected by the presence of an initial void (see Fig. 1).

The macroscopic response in terms of the effective true stress Σ_e versus the effective logarithmic strain E_e is shown in Fig. 2. At this stress triaxiality and with this low rubber volume fraction, the macroscopic yield stress apparently is not very sensitive to the differences in stiffness of the particle. However, the particle stiffness has a strong effect on the void growth behaviour, expressed here in terms of the logarithmic volumetric strain

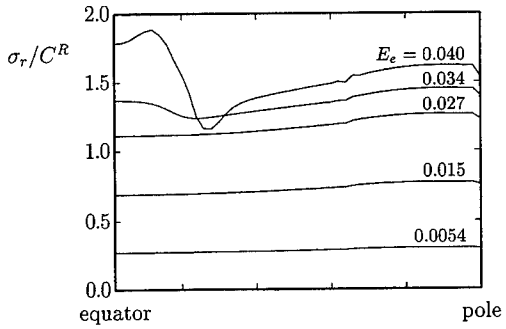

Figure 3: Radial stress components along the particle-matrix interface, from unit cell analysis with $C^R/s_0 = 0.167$.

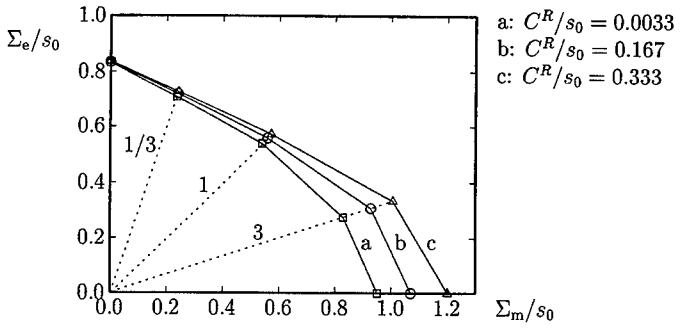

Figure 4: Yield contours from cell model analyses for different triaxialities Σ_m/Σ_e (the triaxiality is indicated along the dotted lines).

of the particle. For a very low value of the rubber modulus ($C^R/s_0 = 0.0033$) the critical volumetric strain is reached before macroscopic yield. For $C^R/s_0 = 0.167$ it is close to this value, and after macroscopic yield the void continues to grow. For a high particle stiffness ($C^R/s_0 = 0.33$) the void growth resistance is too high and at some point the volumetric strain of the particle decreases again. The hydrostatic stress which the particle exerts on the matrix (associated with the particle expansion) can be estimated from Fig. 1.

As a check, we monitored the interfacial stresses for $\Sigma_m/\Sigma_e = 1.0$ and $C^R/s_0 = 0.167$. The tangential components are small, so only the radial components are depicted in Fig. 3 at various instants of the overall effective strain E_e. The distribution of the radial stresses over the interface is uniform as long as the matrix is elastic, and does not exceed the peak value for a particle with a relative initial void size of $a_0/b_0 = 0.2$ ($\sigma_r/C^R \approx 1.6$ see Fig. 1). Matrix plasticity is initiated slightly before macroscopic yield (roughly at $E_e = 0.03$) and, since this involves the initiation and propagation of localized shear bands (2), the uniformity of the radial stresses is destroyed.

The effect of the stiffness of the rubber particle on the macroscopic yield stress in a wide range of triaxialities is shown in Fig. 4. The dotted lines indicate loading paths of constant triaxiality. It is seen that in shear ($\Sigma_m/\Sigma_e = 0$) the macroscopic yield stress is essentially the same in all cases, whereas under hydrostatic tension ($\Sigma_m/\Sigma_e = \infty$) the differences are most notable. Note that the negative slope of the yield contour at low triaxiality is caused by the intrinsic pressure dependence of the yield behaviour of the matrix.

ACKNOWLEDGEMENT

The work of A.C. Steenbrink is part of a research project funded by the Netherlands Technology Foundation (STW).

REFERENCES

1. C.B. Bucknall, *Toughened Plastics*, Applied Science Publ., London, (1977)
2. A.C. Steenbrink, P.D. Wu, E. van der Giessen, LTM Rep. no. 1098, J. Mech. Phys. Solids (1997) in print
3. P.D. Wu, E. van der Giessen, Eur. J. Mech., A/Solids, 15 (1996) 799
4. A.N. Gent, P.B. Lindley, Proc. Roy. Soc. Lond., A249 (1958) 195
5. C.O Horgan, T.J. Pence, J. Elasticity, 21 (1989) 61
6. H.-S. Hou, R. Abeyaratne, J. Mech. Phys. Solids, 40 (1992) 571

VISCOELASTIC BEHAVIOUR OF HDPE UNDER TENSILE LOADING

J.G.J. Beijer* and J.L. Spoormaker*

Creep experiments on HDPE tensile bars were performed at different loads covering a time span of one week. The measured strain was modeled with the Leaderman model with a plastic strain term added for higher stresses. The creep strain could be adequately described for stresses up to 14 MPa. However the model predictions of the creep-recovery experiments compared with measurements indicate that even at low stresses plasticity is present and that the plasticity at higher stresses is overestimated.

INTRODUCTION

Due to the increasing use of plastics in load bearing constructions an understanding of the mechanical behaviour of these materials is becoming more important. One major feature of many thermoplastics is their creep behaviour, meaning that the strain increases in time when loaded with a constant stress. A good and simple description of creep and other viscoelastic phenomena like creep-recovery is important for designers of plastic constructions.

To find a description of viscoelasticity, first creep experiments at different load levels and some creep-recovery experiments were performed. The results of the creep tests were modelled after which the model prediction for the creep-recovery experiments was compared with the results. Finally conclusions about further improvement of the model were drawn.

MATERIAL AND EXPERIMENTAL

High Density PolyEthylene was chosen as research material since its use in products is various. HDPE 7058S delivered by DSM is an injection mould grade used for instance in crates and containers. ISO 527 tensile bars were injection moulded from this material at relatively high temperatures and low cooling rates as to decrease the effect of internal stresses. After production the specimens had been stored at 23 °C for 16 weeks before testing at that same temperature.

The creep experiments, with a total time range from 10 seconds till 1 week, consist of two series of tests: the first series involves creep experiments of two hours performed on a ZWICK tensile tester and the second involves dead weight creep experiments of one week. All tests of the first series were in threefold whereas the dead weight experiments were in duplicate for 2, 4 and 8 MPa and in singular for the others. In figure 1 for both series the averages are shown. The agreement between the two series is good.

Additionally some creep-recovery experiments were done. The creep time amounted half an hour and the recovery was measured for one and a half hour. These tests were conducted in duplicate with loads of 2, 4, 8, and 12 MPa only.

*Laboratory of Mechanical Reliability, Delft University of Technology, the Netherlands

RESULTS AND DISCUSSION

In figure 1 it can be seen that the slope of the strain curve is decreasing and that the bending point hardly changes in time with different loads. This makes time-stress superposition, see Leaderman (1) and Schapery (2), unlikely to be helpful in describing these results. Since the shape of the creep curves is similar at low stresses it seems that the creep curves can be described by shifting one master curve vertically on logarithmic scale. The model for creep will therefore be the generalized Leaderman model, Leaderman (3), meaning that the creep strain ε_c is the product of a function of time t and a function of the stress σ:

$$\varepsilon = \varepsilon_0 + \varepsilon_c = D_0(\sigma)\sigma + g(\sigma)D(t)\sigma \tag{1}$$

Here the first term is the elastic response and the second term the viscoelastic one.

A simple way to see whether this model is applicable, is to look at the strain rate vs time curves, see figure 2. The elastic strain has no contribution to the strain rate and this clarifies the picture. It can be seen that at higher stresses other mechanisms appear but for 1 to 8 MPa the principle of vertical shifting is applicable. Only at very long times for 1 and 2 MPa a deviation is found. An explanation for this cannot be given so far since the information of the creep curves is not sufficient. Therefore this effect will be disregarded.

The strain rate belonging to the 4 MPa creep curve will be fitted now with the generalized Kelvin-Voigt model, see Findley et al (4). The model gives the next strain rate:

$$\dot{\varepsilon}_c = g(4)\dot{D}(t)4 = g(4)\sum_{i=1}^{10}\frac{D_i}{\tau_i}\exp\left(-t/\tau_i\right)4 \tag{2}$$

Since the terms with a small retardation time τ_i have no influence on the strain rate at longer times, the determination of the D_i can be done easily backwards. Shifting the 4 MPa creep rate curve vertically on the data of the 1, 2, 6, and 8 MPa measurements together with the condition that $g(0) = 1$ yields the values of the g-function.

Even for the short creep experiments of two hours it can be seen that after a long period of time (months) deformation is still present. This deformation, even at 8 MPa, can therefore be attributed to plasticity. With plasticity it is now attempted to model a larger part of the upper three curves where an upward curvature is present and to gain a better fit for the 8 MPa curve. The strain rate for the 8 - 14 MPa tests is fitted additionally with a plastic strain rate term obeying a power law as found in Lai et al (5):

$$\dot{\varepsilon}_p = D_p m t^{m-1}\sigma \tag{3}$$

where D_p and m are a function of the stress.

The final description of the creep strain is presented in figure 1. The modulus of elasticity is determined by shifting the creep strain curves of the model on the measured data, meaning that this E-modulus is a ten seconds modulus.

The prediction of this model for the creep-recovery curves shown in figure 3 is not completely satisfying. It can be seen clearly that the plasticity for 12 MPa is overestimated. On the other hand it seems that plasticity is already present at low stress levels. This will make the fitting procedure somewhat more difficult since no direct fit to $D(t)$ is possible.

The predicted recovery strain minus the measured recovery strain is almost constant, especially for the lowest load levels. The description for the recovery strain will therefore be more accurate if plasticity were modeled better. Creep-recovery experiments with different creep times are needed for this.

CONCLUSIONS

From this discussion it can be concluded that the description of the creep at low stress levels can be done by the Leaderman model with good results. For the behaviour at higher stresses and for a good description of recovery after creep more tests are needed to find a good separation of viscoelasticity and plasticity. This can be done by performing creep-recovery experiments with different creep times.

REFERENCES

1 Leaderman H, "Elastic and Creep Properties of Filamentous Materials and Other High Polymers", The Textile Foundation (Washington D.C.), 1943

2 Schapery R A, Pol. Eng. Sci. 9 (1969) 295

3 Leaderman H, Trans. Soc. Rheol. 6 (1962) 361

4 Findley N F, Lai J S, Onaran K, "Creep and Relaxation of Nonlinear Viscoelastic Materials", NHPC (Amstardam), 1976

5 Lai J, Bakker A, Pol. Eng. Sci. 35 (1995) 1339

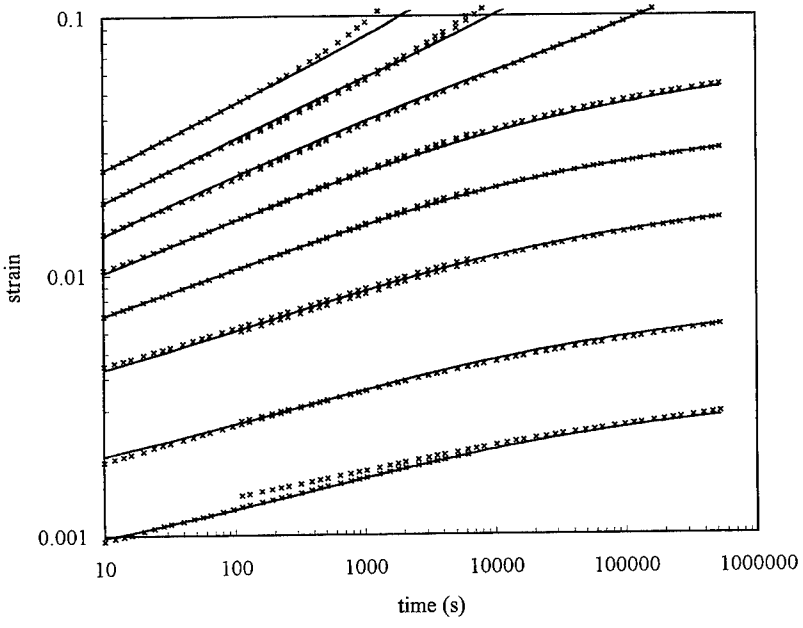

Figure 1. Strain of HDPE 7058 during creep experiments at 1, 2, 4, 6, 8, 10, 12 and 14 MPa (markers) and the model fit (lines).

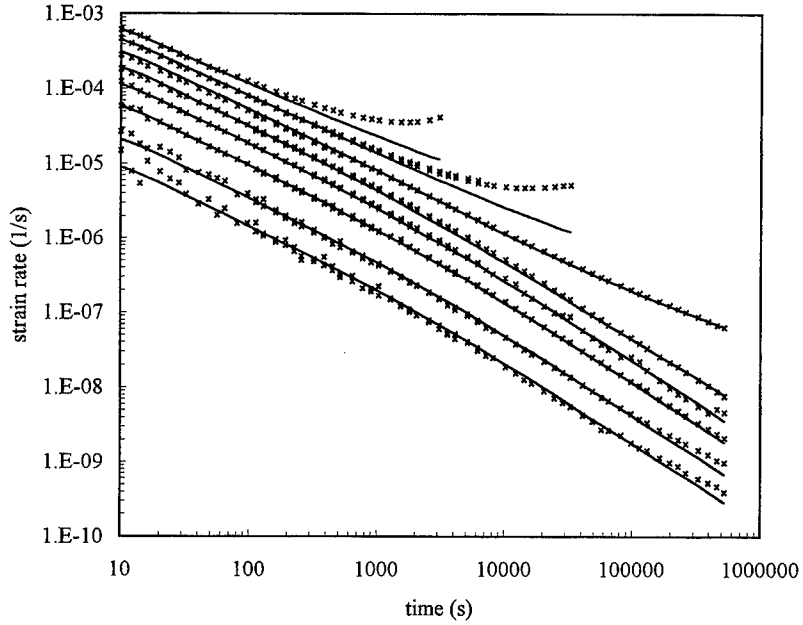

Figure 2. Strain rate of HDPE 7058 during creep experiments at 1, 2, 4, 6, 8, 10, 12 and 14 MPa (markers) and the model fit (lines).

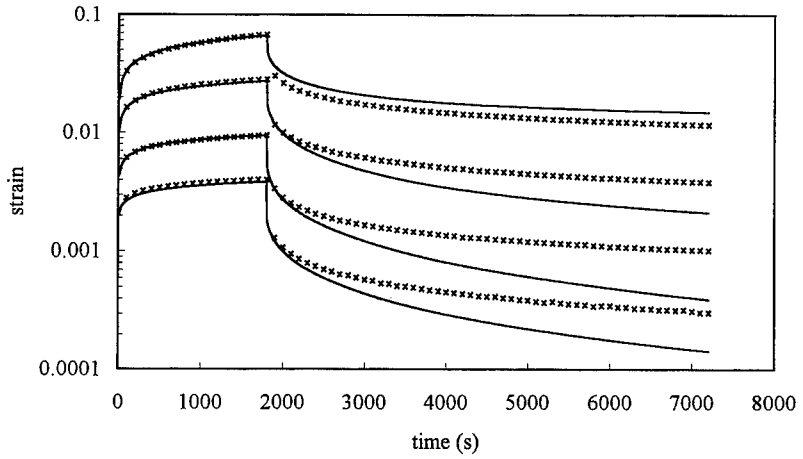

Figure 3. Strain of HDPE 7058 during creep-recovery experiments at 2, 4, 8 and 12 MPa (markers) and the model prediction (lines).

MECHANICAL BEHAVIOUR OF NANOCOMPOSITES WITH THERMOPLASTIC MATRIX AND CELLULOSE REINFORCEMENT

L. Chazeau*, J.Y. Cavaillé*, P. Terech, J.F. Legrand**, R. Dendievel*****

Nanocomposites of plastified PVC matrix reinforced by cellulose whiskers have been prepared. S.A.N.S. and S.A.X.S. experiments showed a good dispersion of the whiskers and the homogeneity of the composites. Mechanical tests were carried out below and above Tg and showed an important reinforcement effect of the whiskers. Damage was observed at all temperature and was studied by multiple tensile tests.

INTRODUCTION

New nanocomposites materials have been processed with micro-crystals (or whiskers) of cellulose dispersed in synthetic polymer matrix. Such whiskers are obtained from the biomass and have typical dimensions of one μm in length and about 15 nm in diameter (Favier et al.(1)). Their small dimensions allow to process pieces with very small thickness, a good transparency, a low density ($d_{cellulose}$=1.58) and a high modulus by comparison with classical glass short fibres composites where fillers have usual dimensions of 10 μm length by few mm.

Up to now, the behaviour of such composites is not well understood. Indeed, the important improvement of the mechanical properties could be partly explained by the large interface area (more than 100m^2/g of cellulose) which might lead to a significant modification of the molecular mobility of the polymer matrix at the interphase. It could also find explanations in effects of geometric percolation which occurs even at very low reinforcement concentrations.

Due to the nanoscopic aspect of the fillers, the difficulty of structural characterisation of those composites lead us to use several techniques, and peculiarly the Small Angle Neutron Scattering and Small Angle X-rays Scattering techniques, to have information on the dispersion of the cellulose whiskers in the matrix. Knowing the morphology of these material, the question is actually to understand their behaviour under compression, in the glassy state, or under tensile stress-strain, above the glassy transition temperature, i.e. to explain the plastic or visco-elastic response and the damage phenomenon that we observed at all temperature.

EXPERIMENTS

The cellulose whiskers were obtained from a sea animal, *Halocynthia Roretzi,* after a

* CERMAV, CNRS et Université Joseph fourier, Grenoble
** DRFMC-SI3M-PCM, CEA Grenoble
*** Génie Physique et Mécanique des Materiaux, I.N.P.G, Grenoble

treatment described in Favier et al.(2). The final aqueous suspension of whiskers does not sediment or flocculate thanks to the electrostatic interaction between the surface sulphate groups created during the sulphuric acid treatment. For both industrial and fundamental interest, plastified PVC has been chosen as matrix. The films were made by freeze-drying of the aqueous suspension of whiskers mixed with PVC supplied as micro-suspension by Elf-Atochem. The blend of this freeze-dried powder, 30 phr (i.e. *per hundred ratio* of PVC) plastifier D.O.P, 4.5 phr heat stabiliser and 1.5 phr lubricant was compounded by hot-mixing at 180°C for 5 min. Then this mixture was pressed into sheets or into cylinder by compression moulding at 200°C for 3 min.

Mechanical tests were performed on a Rheometrics Scientific Minimat machine for tensile stress-strain tests or on an INSTRON serie 30 for compression tests. The crosshead speed was fixed so that the strain rate was $1.3\ 10^{-2}\ s^{-1}$. The parallel faces of cylinder were polished and lubricated.

S.A.N.S. and S.A.X.S. experiments were carried out at the Laue-Langevin Institute in Grenoble and at the Leon Brillouin Laboratory and the L.U.R.E. in Saclay.

RESULTS AND DISCUSSION

SANS and SAXS were performed on seven different whiskers suspensions in D_2O with concentrations ranging between 0.032% g/g and 1.37% g/g. The 2D SANS data showed in all cases the isotropy of the suspensions. The Guignier method with the POROD correction allows the calculation of a mean radius of 83±1 Å which is in good agreement with literature. A more accurate calculation with the assumption of parallelogram-shaped whiskers give dimensions of 88 by 182 Å which improve the precision of the observation made by Von Daele and coworkers (3). Curves obtained for plastified PVC reinforced with 6.6%vol. of reinforcement confirm the isotropy of the composite. Then after the extraction of the signal only due to the whiskers from the whole composite signal, we observed that it was similar to the scattering of the whiskers D_2O suspension (cf. Fig. 1). Therefore we can conclude that there are no aggregates and that the whiskers are homogeneously dispersed in the matrix.

Compression tests were performed on plastified PVC samples reinforced with whiskers concentration from 3%vol. up to 12.4%vol., at -20 °C, below Tg (cf. Fig.2). The whiskers increase the modulus and the yield strength. The most interesting point is the hardening part of the curve which shows up a strong effect of the whiskers and the increase of the ultimate tensile strength. Tensile stress-strain tests were performed on films with the same whiskers concentrations at 60°C, i.e. above Tg. We noticed a high increase of the stress for the same deformation level, when increasing the whiskers concentration. For example, we have a strength increased by 30 times for a 12.4%vol. whiskers content.

For both compression tests (below Tg), and tensile test (above it), we observed a whitening of the material when containing whiskers. It is attributed to the appearance of mesoscopic damage. The question is to determine if it is only due to the dewetting of the whiskers by the matrix or to a cavitation phenomenon inside the matrix which could occur at the contact between whiskers. After noticing that the behaviour of our composites is close to that of a reinforced rubber, we firstly studied the damage above Tg by multiple tensile tests. It is one of

the test described by Heuillet (4) to quantify the « damage energy ». It consists of stretching the sample up to a certain deformation level at 60°C, letting it relax at 80°C, and then stretching again up to a higher deformation level. The stress-strain area between the first curve and the second one give directly the damaging energy density, since the visco-elastic effects of the matrix have been annihilated after relaxation. We made such tests for whiskers concentration of 3%vol. , 5%vol. and 6.6%vol.. Damaging energy density as a function of nominal deformation level is shown in Figure 3. The energy increase as a square power law of the deformation. So the damage energy seems to be linked with the increase of the surface, either at the interface, or into cavities created at singular points with a high stress concentration such as whiskers contact or whiskers ends. The calculation of the adhesion failure energy, using the surface energy we found with contact angle techniques at 25 °C, give a value of 10^6 J/m^3. This value is a rough approximation of the energy necessary for the total dewetting of the whiskers, since it uses a surface energy value at equilibrium which does not take into account visco-elastic behaviour of the interface. This result has the same order of magnitude than the values measured in multiple tensile tests. However, it is noteworthy that it is much higher than values calculated for classical composites by Lepie et al. (5) because the much larger interface area.

CONCLUSION

We prepared homogeneous nanocomposites with a very good dispersion of the cellulose whiskers in the plastified PVC matrix. The behaviour of these new materials have been studied above and below Tg. We have now to complete the analysis, taking into account several problems. The influence of the whiskers on molecular mobility, that we studied previously, might be significant because of the very important interface area. We have to consider the geometric percolation of the whiskers and the nature of the network they form from very low whiskers concentration. Finally, we have to understand the damage mechanism and its role in the behaviour of our composites.

ACKNOWLEDGEMENTS

We would like to thank the G.E.M.P.P.M. of the INSA in Lyon and especially C. Gauthier et P. Hajji for having allowed us to make compression tests in their laboratory, and B. Ernst of Elf-Atochem for his support. This work is supported by Elf-Atochem, the CNRS-Ecotech Program and the A.D.E.M.E.

REFERENCES AND NOTES

1. Favier, V. Canova, G., Cavaillé, J.Y., Chanzy, H., Dufresne, A., and Gauthier, C., 1994, Polymers Adv. Technol., 6, 351-355.
2. Favier, V.,Chanzy, H., and Cavaillé, J.Y., 1995, Macromolecules, 28, 6365-6367.
3. Von Daele, Y.,Revol, J.F., Gaill, F., Goffinet, G., 1992, Biol. Cell.,76, 87-96.
4. Heuillet, L., « Caractérisation de l'endommagement des propergols solides composites », 1992, Thesis of the Université Technologique de Compiègne, France.
5. Lepie, A.H., and Adicoff, A., 1974, J. Appl. Polymer Sci., 18, 2165-2176.

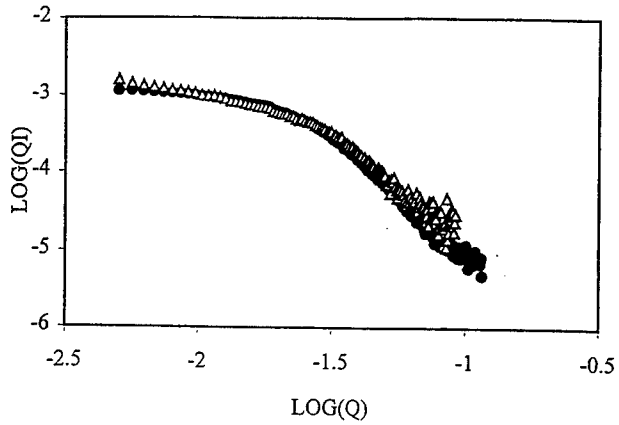

Fig 1 : SAXS signal of whiskers in aqueous suspension (●) and in plastified PVC matrix (Δ).

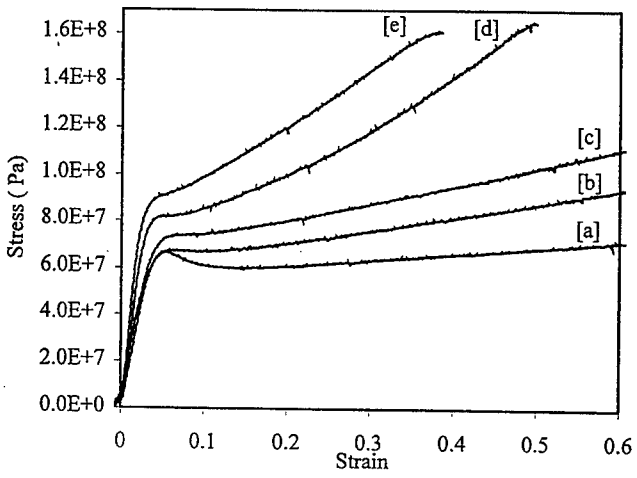

Fig. 2 : Compression tests at -20°C, strain rate of 0.013 s-1, on plastified PVC not reinforced [a], or reinforced by a whiskers content of 5%vol. [b], 6.6%vol. [c], 8.4%vol. [d], 12.4%vol. [e].

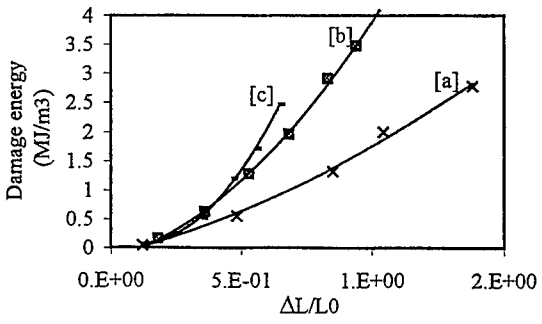

Fig. 3 : Damage energy of plastified PVC with a 3%vol.[a], 5%vol.[b], 6.6%vol.[c] whiskers content, T=60°C.

A FRACTURE MECHANICS ANALYSIS OF WELD-LINE BEHAVIOR

TJ Pecorini *

The fracture properties of molded articles containing weld-lines have been analyzed by a fracture mechanics approach. In the region of the welded zone nearest the mold wall, polymer chain mobility freezes too rapidly to allow sufficiently interdiffusion across the mated melt fronts. This region of insufficient interdiffusion can, therefore, be considered to be a sharp crack, whose "length" can be estimated by simultaneously solving equations relating the cooling of the polymer melt with simple equations describing polymer interdiffusion. Weld-line "crack" lengths estimated in this way are found to be in excellent agreement with "crack" lengths calculated from the fracture loads of impacted bars.

INTRODUCTION

It is well known that the presence of a weld-line may lead to undesirable embrittlement of a molded part. The weakness is commonly attributed to lower entanglement at the weld-line than is found in the bulk material, due to poor interdiffusion across the interface. In support of this view, changing the processing conditions (such as by increasing melt temperature) so as to enhance interdiffusion will improve weld-line strength (1). It is also known, however, that milling off the outer layer of the part with a weld-line will also improve the strength of the molded article (2,3). This evidence suggests that the region of poor interdiffusion exists only at the surface of the weld, whereby a weld-line can be treated as an ideally sharp surface crack. It is possible, then, to model the failure properties of a weld-line using fracture mechanics principles.

Segregation of this poorly entangled weld region to the surface of the part is due to the non-uniform through-thickness cooling of the polymer during molding. Rapid cooling near the mold surface leads to less diffusion in the outer skin of the molding than in the more slowly cooled center of the molding. The length of a weld line "crack" can, therefore, be theoretically estimated by combining a simple heat transfer analysis of the cooling profile through the thickness of the part with a calculation of instantaneous polymer self-diffusion rate. Assuming that the chilled mold affords an infinite heat sink, and that heat transport is much slower through the polymer than through the mold, the cooling profile in a flat plate (i.e. a tensile bar) can be readily estimated as a function of time and depth from the mold wall.

$$\frac{T_{x,t} - T_{mold}}{T_{melt} - T_{mold}} = \mathrm{erf}\left(\frac{x}{2\sqrt{\alpha t}}\right) \qquad [1]$$

* Eastman Chemical Company, P.O. Box 1972, Kingsport, TN 37662

where $T_{x,t}$ is the instantaneous temperature at x and t, T_{melt} is the initial melt temperature, T_{mold} is the mold temperature, erf is the Gauss error function, α is the thermal diffusivity of the polymer, x is the depth from the mold wall, and t is the time after contact between the melt and the mold. The depth of interpenetration across a mated flow front can be related to time and the polymer's self diffusion coefficient (4,5) by

$$<s^2> = 2D_s t \qquad [2]$$

where s is the interpenetration distance, t is time and D is the polymer's self diffusion rate. Integrating equation 2 with respect to time will then yield the total interdiffusion distance

$$< s^2 >= 2\int_0^t D_s(x,t)dt \qquad [3]$$

during cooling at any location in the bar, whereby a plot of interdiffusion distance can be created as a function of depth from the mold wall. The "crack length" of the weld-line can then be calculated as the depth from the mold wall at which the interdiffusion distance becomes large enough to produce sufficient entanglements; this interdiffusion distance is commonly accepted to be 1/2 of the polymer's radius of gyration (6). The weld-line "crack" lengths calculated by this method can then be incorporated into standard fracture mechanics equations to predict failure conditions.

RESULTS AND DISCUSSION

In order to demonstrate this concept, the data required to calculate weld-line "crack" lengths were measured on a commercially available cellulose acetate propionate, Eastman CAP 482-20 (CAP). Bis(2-ethylhexyl) adipate (DOA) was added to the CAP as a plasticizer. All data were measured by standard procedures (7). The self diffusion coefficient, D_s, was estimated from

$$D_s = \left(\frac{\rho RT}{270}\right)\left(\frac{Mc}{M}\right)^2\left(\frac{R_g^2}{M}\right)\left(\frac{1}{\eta_{Mc,T}}\right) \qquad [4]$$

where ρ is the melt density, T is the processing temperature, R is the gas constant, Mc is the critical molecular weight, M is the absolute molecular weight, R_g is the radius of gyration, and $\eta_{(Mc,T)}$ is the zero shear viscosity at critical molecular weight and processing temperature (8). Note that $\eta_{Mc,T}$ is related to melt temperature through an arrhenius relation (using the activation energy of flow), whereby small differences in melt temperature will greatly affect the diffusion constant and weldability through this viscosity term. The instantaneous polymer self diffusion rate ($D_s(x,t)$) for any combination of x and t were then estimated from $T_{x,t}$. Interdiffusion distances were then calculated per equations 1, 2 and 3 and are plotted in Figure 1 as a function of depth from the mold wall. Weld-line crack lengths were then calculated as the depth from the mold wall at which the interdiffusion distance equaled 1/2 the radius of gyration of the polymer. For this CAP material, the radius of gyration is 20 nanometers. It is immediately apparent from Figure 1 that increasing the melt temperature dramatically decreases the weld-line length by increasing the extent of polymer interdiffusion. Because of these shorter crack lengths, weld-line toughness should, and does, increase with temperature.

For direct comparison, molded bars containing weld-lines were fractured using an instrumented impact tester. Samples were prepared from double gated tensile bars molded using injection barrel temperatures (T_{melt}) of 200, 220, 240, 260, and 280°C. The mold temperature was 50°C. The final cut specimen dimensions were: width = 12.5 mm, thickness = 3.1 mm and length = 65 mm. Apparent fracture loads and energies for three point bend weld-line specimens were measured at 23C on a Dynatup drop tower instrumented impact tester moving at 1m/sec. The specimens were not notched, but were positioned in the frame such that the weld-line was directly under the striker. The specimens were all struck on the 3.1 mm edge. Twenty bars from each molding condition were tested in this way. The fracture toughness of the specimens containing a sharp surface notch can be calculated as;

$$K_c = \sqrt{\pi}\sigma_f\sqrt{a} \qquad [5]$$

where K_c is the fracture toughness, σ_f is the apparent fracture stress and a is the crack length (9). The standard fracture toughness of CAP (without weld-lines) at impact rate (1m/sec) had been previously calculated to be 1.10 MPa$\sqrt{m}$. Using this value, weld-line "crack" lengths were calculated using equation 5 from the apparent fracture loads obtained from impact testing of the weld-line three point bend specimens. These values are shown in Table I along with the weld-line lengths estimated from the heat transfer/diffusion analyses. Agreement is found to be excellent among the three techniques, confirming that weld-lines are, essentially, a type of surface crack.

It is important to note, however, that if the weld-line crack is very short, then the material's yield strength may be lower than the fracture strength associated with that crack length, whereby the part may yield instead of fracturing. (Recall that σ_f is proportional to Kc/$\sqrt{a}$.) At impact speeds, the yield strength of CAP was measured to be 65 MPa, whereby the critical crack length a_c is 0.091 mm. For the bars molded at 280°C, the weld-line length was calculated to be slightly less than 0.091mm, whereby many of these bars yielded instead of fracturing. In addition, milling away the outer 0.2 mm from each face and 0.4 mm from each edge of some of the bars from each molding condition caused all bars except those molded at 200°C to become ductile, while the measured weld-line "crack" length of the milled bars molded at 200°C reduced to 0.25 mm.

Finally, it should be noted that impact fracture toughness values were also measured on weld-line bars which were subsequently sharply notched. Regardless of the temperature at which the bar was molded, the weld-line fracture toughness values were found be 1.10 MPa$\sqrt{m}$, identical to the non-welded material. This is not surprising when it is recognized that the preparation of a fracture toughness specimen introduces a deep notch into the specimen (to an a/w value of 0.5) which is subsequently sharpened with a razor. This deep sharp notch, therefore, erases the effect of the sharp but shallow surface weld, and provides a measurement of only the well entangled core material. Weld-lines are, therefore, confirmed to be purely a surface phenomenon related to the freezing of non interdiffused polymer in the outer skin of the molding.

REFERENCES

1. Malguarnera SC, Polym. Plast. Tech. Eng. 18 (1982) 1

2. Tomari K, Tonogai S, Harada T, Hamada H, Lee K, Morii T and Maekawa Z, Poly. Eng. Sci. 30 (1990) 931
3. Tomari K, Harada T, Maekawa Z, Hamada H, Iwamoto M and Ukai A, Poly. Eng. Sci. 33 (1993) 996
4. Tirrell M, R. Chem. and Tech. 57 (1984) 523
5. Wool RP, Yuan B-L and McGarel OJ, Poly. Eng. Sci. 29 (1989) 1340
6. Jud K, Kausch HH and Williams JG, J. Mat. Sci. 16 (1981) 204
7. Pecorini TJ, Poly. Eng. Sci. 37 (1997) in press
8. Graessley WW, J. Poly. Sci., Poly. Phys. 18 (1980) 27
9. Hertzberg RW, 'Deformation and fracture mechanics of engineering materials', John Wiley & Sons, New York, 1989

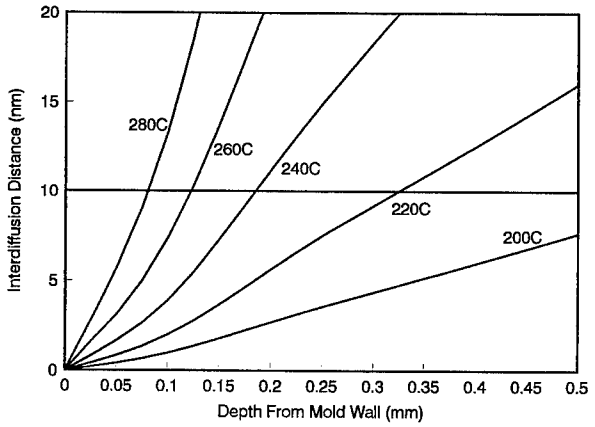

Figure 1. Calculated interdiffusion depths plotted as a function of depth from the mold wall for CAP molded at various melt temperatures and a 50°C mold temperature. Weld-line lengths are taken as the intersections of each curve with the line a 10 nm (1/2 the radius of gyration of CAP).

Table I. Calculated and measured weld-line lengths (with standard error of the mean).
* Some of the bars molded at 280°C yielded instead of fracturing.

Melt Temperature	Weld length (a_w), estimated	Weld Length (a_w), from Kc
200°C	0.60 mm	0.58 ± 0.05 mm
220°C	0.32 mm	0.31 ± 0.07 mm
240°C	0.18 mm	0.14 ± 0.01 mm
260°C	0.12 mm	0.16 ± 0.02 mm
280°C	0.08 mm	0.06 ± 0.01 mm *

TETRAKAIDECAHEDRAL CELL MODEL OF FOAM MECHANICS

H X Zhu and N J Mills,
School of Metallurgy and Materials, University of Birmingham

INTRODUCTION

A lattice of tetrakaidecahedral cells was proposed by Lord Kelvin(1) as minimum surface energy partitioning of space. Four edges meet at each tetrahedral vertex, but the square and hexagonal faces are non-planar. Modified tetrakaidecahedra with planar faces, with the cells packed in a BCC array, were used by De'mentev and Tarakanova(2) to model open-cell polymer foams. They calculated the Young's modulus in the [001] direction, but neither the elastic anisotropy nor the high strain behaviour have been analysed.

MODELLING THE FOAM GEOMETRY

Reticulated polyurethane (PU) foam is solidified with closed cells, then the thin cell faces is removed in a subsidiary process. The edge cross-sections are Plateau borders, consisting of three circular arcs, meeting at angles close to 10°(figure 1a). A BCC lattice of tetrakaidecahedral cells(figure 1b) has an initial Youngs modulus that is isotropic within 5%(3). The loaded chains of square faces, joined corner to corner in the [001] direction, are stiffer but wider spaced than the 3_1 helices of load bearing edges in the [111] direction. For Plateau border edge sections with the arcs meeting at a zero angle, the model predicts the modulus E_{100} of a foam of relative density R is related to the polymer modulus E by

$$E_{100} = \frac{1.009\,ER^2}{1+1.514\,R} \qquad (1)$$

which agrees with experimental data.

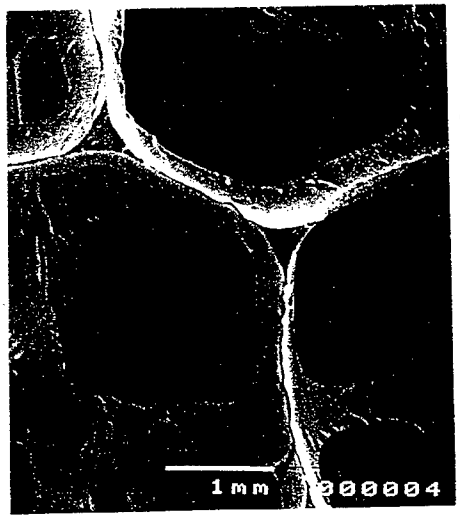

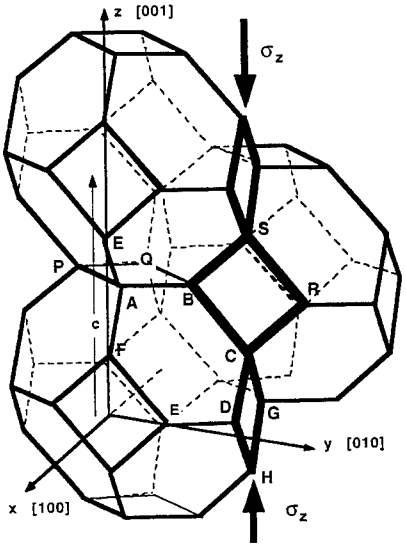

Fig. 1 a) PU foam microstructure, b) tetrakaidecahedral model.

MODELLING THE CELL EDGE DEFORMATION

High strain compression was analysed for loading in the [100] and [111] lattice directions. The edge length change was shown to be negligible for low relative density foams(3), hence the deformation mechanisms are **edge bending** and **torsion**. Reinforcing webs between the edges(figure 1a) prevent vertex deformation, so restraining bending moments are applied to the ends of the edges.

For [001] compression, in-plane forces act on square faces, so no edge torsion occurs. The edge shape, given by a modification of Timoshenko and Gere's (5) elliptic integral analysis, is shown at a range of foam strains in Figure 2a.

For [111] compression a triangular prism within the lattice, with a central 3_1 screw axis, was analysed. The generalised moment vector **M** on the slanting edges is not perpendicular to the unit vector **s** along the edge. The twist increment $d\phi$ in an element ds of edge is

$$d\phi = \frac{T}{GJ}ds = \frac{1}{GJ}(\mathbf{M} \bullet \mathbf{s})ds \qquad (2)$$

where T is the torque, G is the polymer shear modulus and J is the effective polar moment of area of the cross section. Edge curvature $d\theta/ds$, about an axis parallel to the bending component $\mathbf{M_B}$ of the generalised moment **M**, is given by

$$\frac{d\theta}{ds} = \frac{\mathbf{M}_B}{EI} = \frac{\mathbf{M} - T\mathbf{s}}{EI} \qquad (3)$$

This curvature vector is resolved into components along the x, y and z axes. The edges were treated as 100 segments, and their shapes were calculated by iteration. Figure 2b shows a deformed slanting edge and two near-horizontal half edges, which forms the motif of the structure. There is significant twisting at high strains but buckling does not occur until 70% foam strain. The largest restraining moment M_y prevents the vertices rotating about the y axis. The moments are given in table 1 in dimensionless units 10^{-3} E R^2 L^3, and the force P as 10^{-3} E R^2 L^2, where L is the edge length.

Table 1. Predictions for [111] direction compression, for two edge cross-section shapes

edge section	stress / E R^2	foam strain %	twist degrees	M_x	M_y	M_z	P
equilateral	0.058	9.9	4.1	16	-46	-12	136
Plateau 0^0	0.082	10.2	4.4	21	-65	-19	189
equilateral	0.127	40.3	19.4	22	-122	-46	285
Plateau 0^0	0.166	40.6	20.3	21	-164	-68	384

The experimentally observed edge cross-section shapes lie between the cases in table 1; the equilateral triangular section is a Plateau border with arcs meeting at an angle $\theta = 30°$. The angle θ is related to the surface energies of the face γ_F and the polymer/air phase boundary γ_{PA} by

$$\theta = 2\cos^{-1}(\gamma_F/\gamma_{PA})$$

Hence the predicted stress should lie between the values in Table 1 for the two edge shapes.

Table 2 gives the foam compressive strain, for the [001] axis compression, at which the maximum edge strain reaches 7.5%, for a range of foam relative densities(6). For an elastic/ideally-plastic solid, although the edge curvature vs. bending moment relation becomes non-linear at this strain, plastic hinges will not form until the bending moment is 2.3 times higher. Most commercial polymer foams have relative densities in the range 0.02 to

0.1, so a non-linear polymer response will affect the compressive stress-strain curves at strains in the range 5 to 10%.

Table 2 The foam strain causing the maximum edge strain to be 7.5%.

Relative Density R	0.012	0.025	0.070
Foam Strain e(%)	15	9.8	5.8

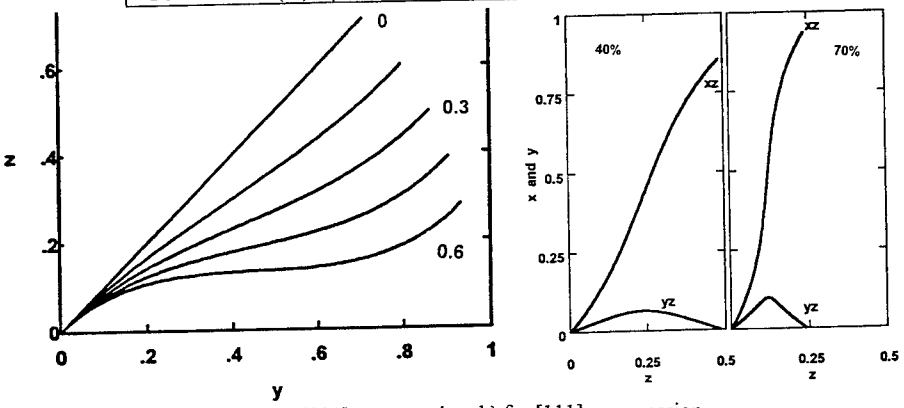

Figure 2. a) edge shapes for [001] compression, b) for [111] compression

MATERIAL RESPONSE

A semi-rigid PU open cell foam of density 31 kg m^{-3} was supplied by Recticel, Belgium. The stress-strain curve for compression of the solid PU indicates considerable non-linearity if the strain exceeds 5%(Figure 3). The PU is viscoelastic but, if the timescale of the compressive measurements is the same for both the foam and the solid, this should not influence the comparison. The foam Poisson's ratio changed from an initial value of 0.09 to a value close to zero(no further lateral expansion) when the compressive strain exceeded 12%, with the relationship having no hysteresis on unloading.

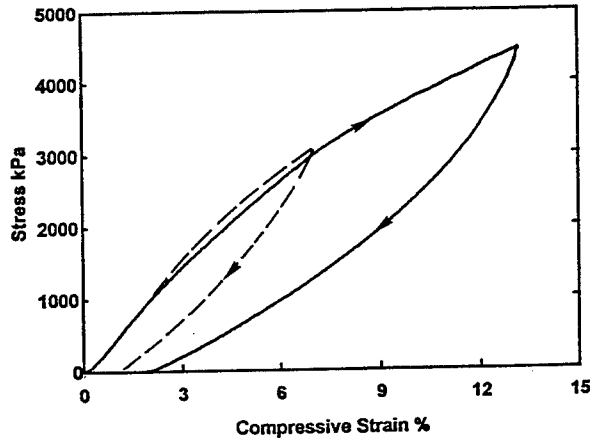

Figure 3 The compressive response of the solid PU

COMPARISON OF PREDICTIONS WITH EXPERIMENT

The stress strain curve of the PU foam was measured in a direction parallel and perpendicular to the foam rise direction. This is compared in figure 4 with the model predictions for [111] direction compression, using the measured Youngs modulus of 54 MPa for the 1229 kg m^{-3} density solid PU. The prediction is close to the experimental data, whereas the [001] direction prediction is higher. In a real foam no face is likely to contain the compression axis.

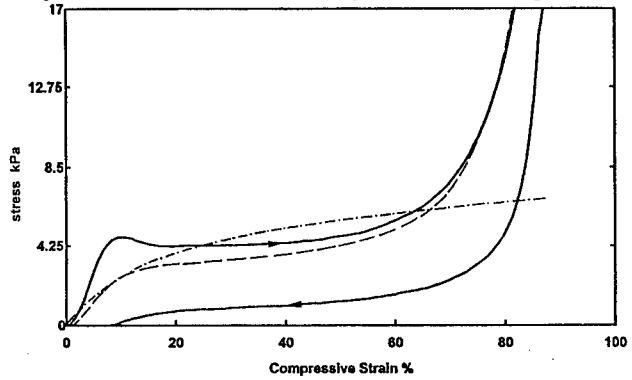

Figure 4. Stress-strain curves for PU foam compressed along — and across ---- the rise direction, c.f. the prediction, for the same density and modulus, for [111] compression -·-·

DISCUSSION

The model analysed is the most isotropic of any proposed for foams. Nevertheless it becomes anisotropic at high strains, since the deformation mechanisms differ with loading direction. The quantitative predictions of the foam stress-strain curve are an advance on Gibson and Ashby's(4) dimensional analysis, which assumed that the edges buckled elastically under axial compression, a deformation mechanism not found in open-cell foams. Use of Euler's buckling analysis, which gives a single collapse load, cannot predict the progressive deformation of edges. In low-density open-cell foams, the rigid vertices apply complex loads to the ends of the edges, which bend and twist. A full analysis of the edge shape then allows the calculation of the foam stress-strain curve, and shows how this is related to a progressive change in the cell geometry. If realistic edge cross-sectional shapes and the measured polymer modulus are used, the prediction can be checked quantitatively against experiment. Buckling is predicted to develop slowly if the polymer remains linearly-elastic, so a 'plateau stress' when a foam is compressed 5% is likely to be due to non-linear material response. The high-strain upturn in the compressive stress-strain curves cannot be predicted by a model which ignores edge interactions.

References

1. Kelvin (1887), Phil. Mag., **24**, 503.
2. Dement'ev A.G. and Tarakanova O.G, (1970), Mekh. Polim. **6**, 859-865, translated as Polymer Mechanics, **6**, 744-749
3. Zhu HX, Knott JF and Mills NJ, J. Mech. Phys. Solids, 1997, to appear
4. Gibson, L.J and Ashby, M.F, (1988), *Cellular Solids*, Pergamon, Oxford.
5. Timoshenko, S. P., and Gere, J. M., (1961), *Theory of Elastic Stability*, McGraw-Hill, NY.
6. Zhu HX, Mills NJ and Knott JF, J. Mech. Phys. Solids, submitted.

A COMPARISON OF THE DEFORMATION AND FRACTURE MECHANISMS IN RUBBER TOUGHENED PMMA AND IN PU/PMMA INTERPENETRATING POLYMER NETWORKS.

Ph.Béguelin, H. H. Kausch*

The tensile and fracture properties of rubber toughened poly(methylmethacrylate) (rtPMMA) modified by spherical core-shell particles, and poly(urethane)/poly(methyl methacrylate) (PU/PMMA) interpenetrating polymer networks (IPN) are investigated at different strain rates. The deformation and fracture mechanisms are studied by transmission electron microscopy (TEM). The results of the tensile tests show that deformation in both rtPMMA and IPN involves cavitation. The amount of cavitation increases with the strain rate in both kinds of material. This leads to similar mechanical properties in each case, and shows that a spherical particle morphology is not prerequisite for cavitation. A phenomenological model of the micromechanisms of deformation in core-shell particle modified PMMA is proposed.

MATERIALS

The two core-shell particle modified PMMAs investigated here are industrially produced materials. The particles are prepared by emulsion polymerisation and consist of an inner glassy core of PMMA, surrounded by a rubbery shell based on Poly(*n Butyl Acrylate-co-Styrene*). An outer layer of PMMA grafted to the shell ensures good adhesion between the particles and the matrix. The grades are refered to here as 3L20 and 3L30, containing particle volume fraction of 20 and 30 % respectively. The molecular weight of the matrix is close to 130'000 g/mol.

An interpenetrating polymer network PU/PMMA is also studied. This material, referred to as IPN, is the same as one of those studied by Heim et al. [1]. It is a co-continuous network containing 5% of rubbery PU in a crosslinked matrix of PMMA and the particle size is comparable (180-200 nm for the core, and 230-250 nm for the shell diameter).

EXPERIMENTS

In order to distinguish the different processes contributing to the overall tensile deformation, low rate experiments (2 to 200 mm/min) have been performed at room temperature on 3L30 and IPN. The volume change during the deformation process has been measured, using simultaneous longitudinal and lateral extensometry, following the approach proposed by Frank and Lehmann in 1986 [2]. The elastic strain, ε_{elast}, has been calculated assuming that the overall elastic modulus, E, does not change significantly during the deformation process. Using the same assumption, the permanent cavitational strain, ε_{cav}, was calculated by the following relation:

$$\varepsilon_{cav} = (1+\varepsilon)(1+\varepsilon_{lat})^2 - 1 - \varepsilon_{elast}(1-2\nu_{elast}) \qquad (1)$$

where ε is the longitudinal strain, ε_{lat}, the lateral strain and, ν_{elast}, the Poisson's ratio measured in the elastic region.

The shear strain, ε_{shear}, was taken to be the non-elastic and non-cavitational strain, such that:

$$\varepsilon_{shear} = \varepsilon - \varepsilon_{elast} - \varepsilon_{cav} \qquad (2)$$

Fracture mechanics experiments on these three materials, at testing speeds between 10^{-4} and 10 m/s were conducted on compact tension (CT) specimens, using the experimental approach

* EPFL Laboratoire de Polymères, MX-D, CH 1015 Lausanne, Switzerland

developed in our laboratory [3]. The critical stress intensity factors, K_{IC}, have been calculated from the maximum of force. The energy used to calculate the critical energy release rate at initiation, G_{IC}, was obtained by integrating the force-displacement curves up to the maximum of force.

RESULTS

It is well known that stress whitening occurs when rtPMMA modified by spherical particles is strained. It is more surprising that the same effect is observed in PU/PMMA interpenetrating polymer networks. It has been clearly established by in-situ optical measurements of this phenomenon that stress whitening can be detected at very low strains (about 1%), but increases drastically near the yield point of the stress-strain curve [3] in both materials.

Our volume strain measurements during tensile experiments (see Figure 1) show that, for both type of materials, the permanent cavitational strain detectable using this approach, occurs at the apparent yield strain of the materials. Thus, cavitation is closely related to the overall yielding of the material. Therefore, dilatational deformation mechanisms occur with both types of morphologies of the modifying phase, and one can conclude that a spherical morphology of the rubbery phase is not necessary to induce cavitational strain in the material.

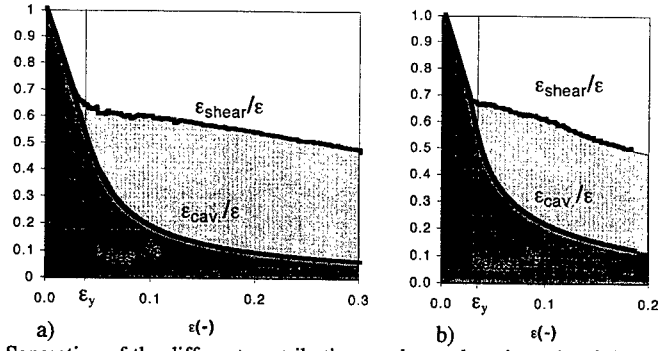

Figure 1: Separation of the different contributions to the total strain: ratio of the elastic strain, $\varepsilon_{elast}/\varepsilon$, of the cavitational strain, $\varepsilon_{cav}/\varepsilon$, and of the shear strain $\varepsilon_{shear}/\varepsilon$, to the the total strain, plotted versus the total strain, ε. a) 3L30 at $\dot{\varepsilon} = 3.5 \times 10^{-2}\ s^{-1}$, b) IPN at $\dot{\varepsilon} = 4.3 \times 10^{-2}\ s^{-1}$

Compared with approaches in which only one or two testing speeds are used, the use of a wide range of testing velocities, v, in fracture experiments gives a more complete picture of the fracture behaviour of the materials. The results are shown in figure 2. Although no tough to brittle transitions are found at high loading rates, dK/dt, for the IPN and the matrix modified with 30% of core-shell particles (3L30), a brittle transition is reached at 10 m/s for the material modified with 20% of core-shell particles (3L20). This transition is clearly seen when considering the critical stress intensity factor, K_{IC}, shown in Figure 2 a. The initial increase in K_{IC} with the testing speed is attributed to the increase of the elastic modulus with the strain rate which has been observed in tension [3].

The critical strain energy release rates measured at the initiation of fracture, G_{IC}, plotted in Figure 2 b, show a constant value over the whole range of testing speeds for the IPN, but decrease above 1m/s in both materials modified by core shell particles.

From a fractographic point of view, it is relevant to mention that the stabilisation of K_{IC} and the decrease of G_{IC} found at high loading rates in the 3L30 and 3L20 occurs when partially unstable fracture is observed, whereas in the IPN, the crack propagation is stable over the whole range of testing speeds. Furthermore, the brittle transition of the 3L20 is associated with the unstable fracture over the entire ligament [4].

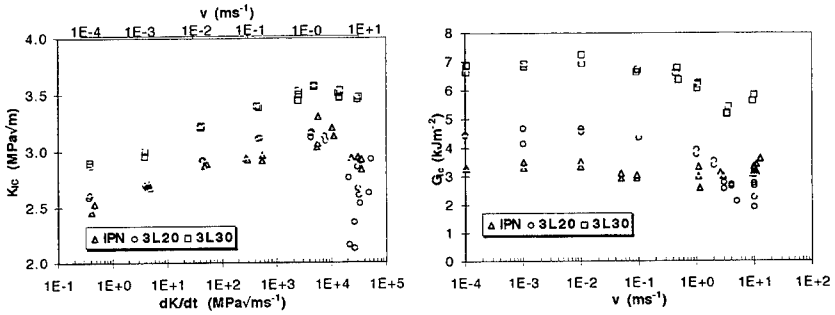

Figure 2: a) Critical stress intensity factor, K_{IC}, plotted versus the log of the crack tip loading rate, dK/dt, for PMMA modified with 20% and 30% vol. of core-shell particles (3L20, 3L30) and for the IPN. The upper scale indicates the testing speed, v. b) Critical strain energy release rate, G_{IC} plotted against the log of the testing speed, v.

TEM OBSERVATIONS OF THE DEFORMATION MECHANISMS

Microtomed sections of 100 nm thick were cut from the bulk of 2L20 and IPN specimens. The sections were removed from the crack front arrested after propagation in a stable manner at the testing speed of 10^{-3} m/s. They were observed by transmission electron microscopy (TEM) using a Philips EM 300.

The 3L20 was chosen because the low concentration of particles gives a relatively large interparticle distance, facilitating the observation of the deformation mechanisms in the matrix. Since the surroundings of a crack front offer a complete picture of the strain gradient, it is possible to observe the whole sequence of deformation mechanisms involved in fracture. As an example, Figure 3 a shows the portion of the crack the closest to the crack tip. TEM picture of the crack front in IPN is shown in Figure 3 b for comparison.

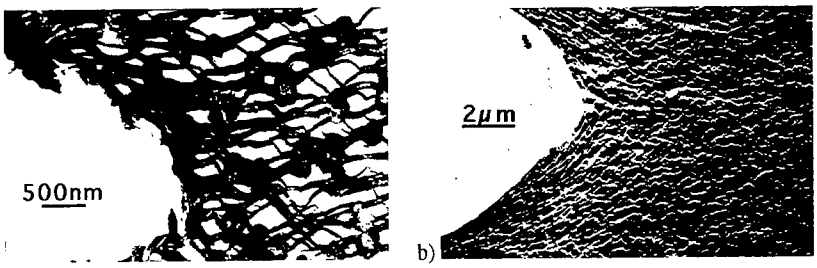

Figure 3: Deformation mechanisms in front of a crack tip in a) a PMMA modified with 20% vol. core-shell particles (3L20), b) an IPN.

DISCUSSION AND PHENOMELOGICAL MODEL

Based on the TEM observations performed on 3L20, we propose a phenomelogical model for the deformation mechanisms in core-shell type modified materials. This model explains the damage developpement by three different mechanisms. It is shown schematically in Figure 4.

The initial damage is initiated by the negative hydrostatic pressure applied to the particles by the remote stress, and cavities of small size begin to grow in the poles of the rubbery shells of the particles. The sudden increase of stress in the matrix surrounding the particles, triggered by

the shell cavitation, results in the initiation of crazes at the particle equators. These crazes then propagate in the matrix regions between the particles by a mechanisms of growth at constant stress in the craze fibrils, as in unmodified PMMA. Once the crazes penetrate in regions mechanically influenced by neighbouring particles, they deviate from their initial plane of propagation. In the highly strained region of the crack tip, most of the craze tips split into two new crazes which deviate towards the poles of neighbouring particles. The crack then propagates by a mechanisms of flow of the matrix. Matrix yielding occurs locally, since triaxiality of stress can no longer exist in such small isolated regions of the matrix, linked only by the surrounding craze fibrils.

Evidently the material is progressively embrittled as the strain rates increase, because the time available for the above mechanisms becomes too short to permit their full development.

It is not clear yet whether the mechanism of *craze splitting* is related specifically to the presence of core-shell type particles (as opposed to rubbery core type particles), which appear to remain active in terms of stress concentration well after their cavitation. Nevertheless, craze splitting should be considered as being very efficient in terms of energy dissipation, because it significantly increases the area of fracture.

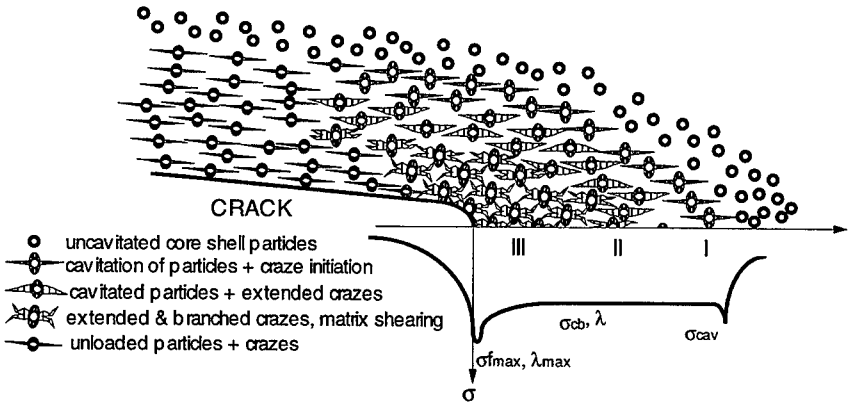

Figure 4: Schematic representation of the deformation mechanisms and the related stress state ahead of the crack tip in a PMMA modified by core-shell type particles.

In the PU/PMMA interpenetrating polymer networks, no craze formation is observed. High magnification TEM observations show that cavitation exists, but is initiated in star-shaped regions of the PU rubbery phase. The volume of the matrix elements isolated by the rubbery ligaments is in the same order of magnitude as that observed in the crazed rtPMMA. Thus, despite its slightly crosslinked structure, similar mechanisms of crack growth by matrix flow can occur. Since the micromechanisms responsible for toughening are governed only by the glass transition temperature of the rubbery phase, it is therefore not surprising that the brittle transition is shifted towards higher strain rates, which were not attained in this study. Furthermore, the lower activation energy of the rubbery phase responsible for toughening in the IPN, compared with that required by craze formation in the glassy matrix of particle modified PMMA, explains the lower fracture energy of the IPN.

References

1 Heim Ph., Wrotecki C., Avenel M, Gaillard P., Polymer 34 (1993)
2 Frank O., Lehmann J., Colloid and Polymer Science 264 (1986)
3 Béguelin Ph., PhD thesis No 1572, EPFL, Lausanne (1996)
4 Julien, O., Béguelin Ph., Monnerie L., Kausch H.H., in 'Toughened Plastics II', Advances in Chemistry Series 252, Riew C.K. & Kinloch A.J. ed., ACS Washington DC, (1997).

THE EFFECT OF MOLECULAR STRUCTURE AND PROCESSING VARIABLES ON THE FATIGUE PERFORMANCE OF MEDICAL GRADE POLYETHYLENES

L. Bailey, D. Baker, D. Crane, M. Goldman*, and L. Pruitt

Department of Mechanical Engineering, University of California
Berkeley, CA 94720, USA

*Department of Materials Science and Engineering, University of California
Berkeley, CA 94720, USA

INTRODUCTION

Structural properties such as molecular weight, crystallinity, density and morphology have been shown to have a pronounced effect on the fatigue fracture response of many polyolefins (1). In addition, it has been shown that differences in polymer processing can dictate the critical stress intensity range or fatigue threshold necessary for the inception of fatigue cracks from stress concentrations (2). An important application in which fatigue loading of polymers occurs is found in the orthopedics industry where sterile medical grade ultra high molecular weight polyethylene (UHMWPE) is used as the articulating surface in total joint replacements and is routinely subjected to cyclic loading conditions with principal stresses ranging from 10 MPa of tension to 40 MPa of compression (3). The growth of fatigue cracks in UHMWPE under cyclic compressive and tensile loading plays an important role in wear damage and ultimately limits the life of these orthopedic components. In this work, we have investigated the role of resin molecular weight, processing conditions, and sterilization method on the fatigue resistance of medical grade polyethylene.

MATERIALS AND EXPERIMENTAL METHODS

Three different medical grade polyethylenes were used in this study: GUR 1020, GUR 1050, and GUR 415. The structural properties of these compression molded UHMWPE resins are given in Table 1. The first two resins, GUR 1020 and GUR 1050, were chosen to investigate the role of molecular weight on the fatigue properties of UHMWPE. The last resin, GUR 415, was chosen to study the effect of calcium stearate (Ca St) addition in the processing. For relevance to orthopedic applications, two current medical sterilization methods were employed: gamma radiation and gas plasma sterilization. Non-sterile material was used as a control for the GUR 1050 resin. The fatigue performance of all material samples was evaluated using compact tension specimens. Fatigue tests were performed using a servohydraulic closed loop testing machine. The loading frequency was chosen to be 5 Hz, to avoid hysteretic heating effects, with a sinusoidal waveform and a load ratio of 0.1 All mechanical tests were performed in ambient air conditions at a temperature of about 23°C. Fatigue cracks were monitored using an optical microscope with a resolution of 0.2 μm. At the completion of the tests, fractography was performed using scanning electron microscopy (SEM). Transmission electron microscopy (TEM) was used to correlate the near-tip structure with the fatigue response of the polymer. A density gradient column and differential scanning calorimeter were used to measure the density and crystallinity of the UHMWPE both at the crack tip and in the bulk polymer.

RESULTS AND DISCUSSION

As shown in Figures 1(a-b), the molecular weight of the UHMWPE is found to have little effect on the fatigue threshold and fatigue crack growth resistance in both the (a) gamma radiated and (b) plasma sterilized GUR 1020 and GUR 1050. While increasing molecular weight has been shown to play a major role in improving the fatigue properties

of high density polyethylenes (1), it appears that the increase in molecular weight from 3 million g/mol to 5 million g/mol does not provide additional resistance to crack propagation. This result may be due to an insignificant increase in the tie molecule density for these two resins. Figure 2 shows the crack propagation rate as a function of stress intensity range for the GUR 1050 in the plasma and gamma sterilized condition. It is found in this study that the plasma sterilized material offers improved resistance to fatigue crack inception. Further, the addition of calcium stearate appears to play an important role in the fatigue crack resistance of medical grade UHMWPE. Figure 3 compares the fatigue behavior of compression molded GUR 415 (with Ca St) and GUR 1050 (without Ca St). It is clear from this data that the UHMWPE with calcium stearate provides a higher fatigue threshold indicating better resistance to fatigue crack growth. This finding is corroborated by SEM analysis which indicates that the GUR 1050 processed without calcium stearate has significantly more consolidation defects than the GUR 415. Fractography confirms no major differences in fracture surfaces for the two different molecular weight resins but reveals that gamma radiation results in a transition from a ductile to brittle mode of fracture. Table 1 shows the results of near-tip and bulk analysis of crystallinity and density as well as the fatigue threshold values for the resins used in this study. This study provides evidence that the density and crystallinity in the near-tip process zone decrease slightly in comparison to the bulk properties. It was thought that TEM would reveal the formation of fibrils or voids due to the decreasing density in the near-tip region, but instead only subtle morphology changes are observed in the near crack-tip studies.

TABLE 1. Properties of the compression molded polyethylenes used in this study.

GUR Resin type	Steriliz. Process	Mol. Wt. (g/mol)	Density (g/cm^3) Bulk	Density (g/cm^3) Tip	Crystall (%) Bulk	Crystall (%) Tip	$\Delta K_{threshold}$ (MPa$\sqrt{m}$)
1020 no Ca St	Gamma	$3x10^6$	0.941	0.941	52 %	51 %	1.31
1020 no Ca St	Plasma	$3x10^6$	0.937	0.936	48%	47 %	1.35
1050 no Ca St	Gamma	$5x10^6$	0.946	0.941	53 %	46 %	1.31
1050 no Ca St	Plasma	$5x10^6$	0.939	0.932	48 %	46 %	1.36
1050 (no Ca St	None	$5x10^6$	0.939	0.938	49 %	46 %	1.36
415 w/ Ca St	None	$5x10^6$	0.935	N/A	48 %	N/A	1.7

ACKNOWLEDGMENTS

This work is supported by NSF. Mr. Chuan Lee, Mr. Guy Ng, Mr. Ed Park, and Ms. Neha Parekh are gratefully acknowledged for their assistance.

REFERENCES

1. Hertzberg, R.W., and Manson, J.A., 1980, 'Fatigue of Engineering Plastics', Academic press.
2. Pruitt, L. and Bailey, L., 1997, Polymer, in rev.
3. Bartel, D.L. Bicknell, V.L., Wright, T.M., 1986, J. Bone Joint Surg. 68, 1041.

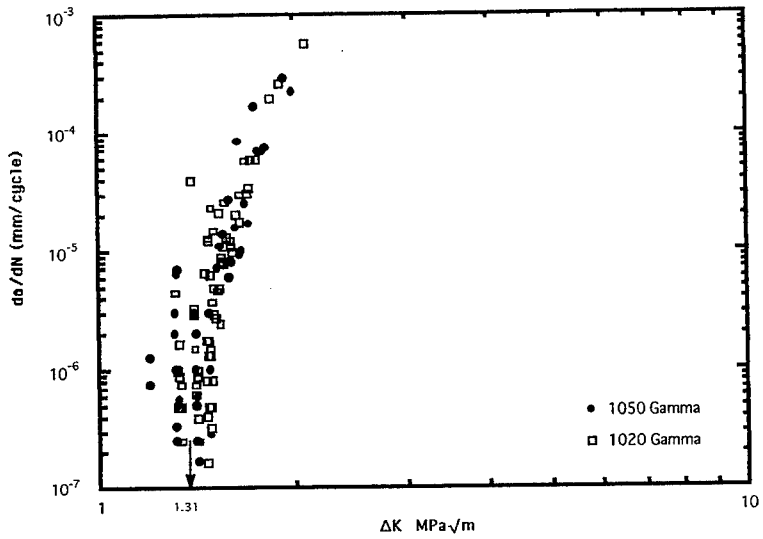

Figure 1(a) The effect of molecular weight on fatigue behavior of gamma sterilized UHMWPE.

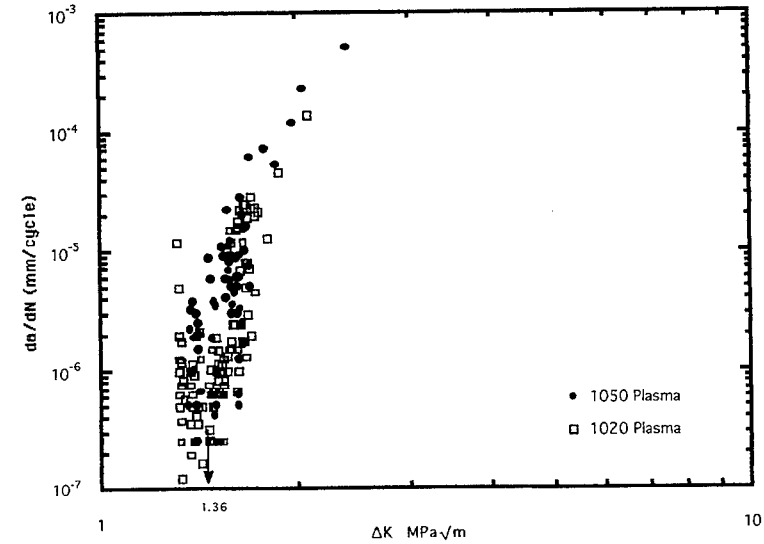

Figure 1(b) The effect of molecular weight on fatigue behavior of plasma sterilized UHMWPE.

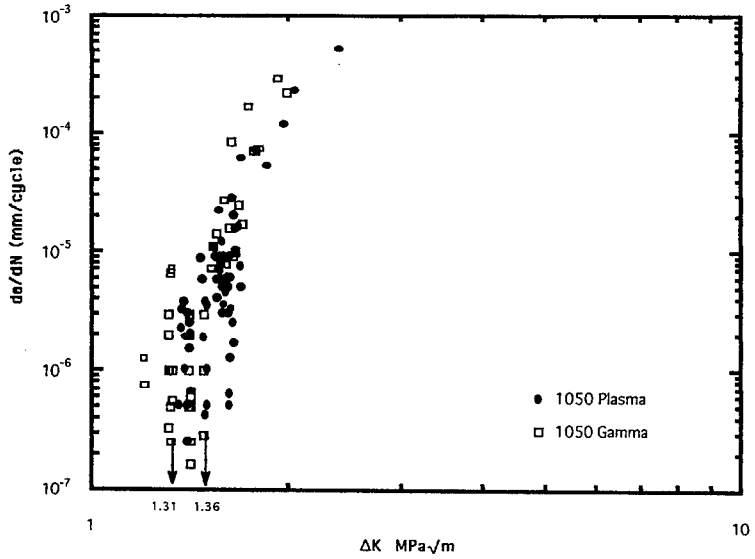

Figure 2. The effect of sterilization method on GUR 1050.

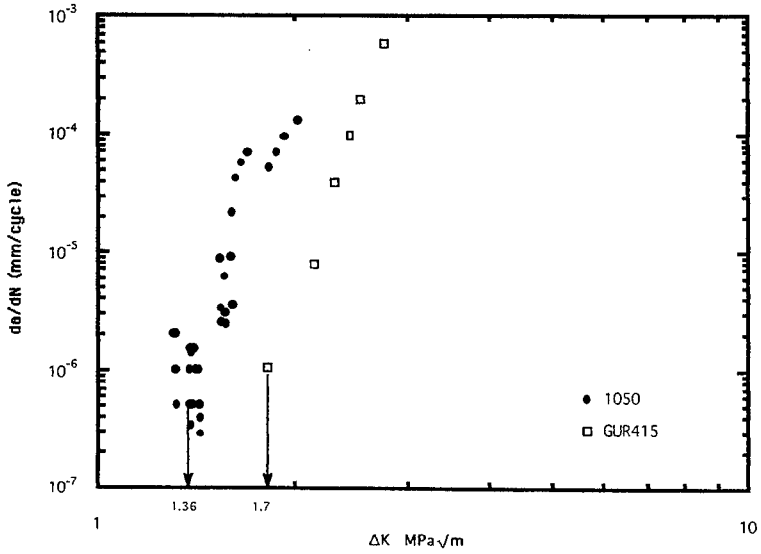

Figure 3 The effect of calcium stearate on fatigue behavior of UHMWPE.

THE ESC INITIATION BEHAVIOUR OF POLYCARBONATE IN MIXED ENVIRONMENT SYSTEMS

J.C. Arnold* and J.E. Taylor†

INTRODUCTION

Environmental stress cracking (ESC) remains one of the most common forms of failure of polymeric components, and although it is a much studied area, a reliable method of predicting this phenomenon has yet to be formulated. The most succesful predictive methods are those based on the use of solubility parameters [1,2], or more particularly, three-dimensional solubility parameters [3,4]. For single environments, these provide a reasonable guide to ESC behaviour, but are by no means conclusive.

When the environment comprises more than one solvent, the use of a linear law of mixtures of solubility parameters has been postulated. This would suggest that a mixture of two environments with solubility parameters either side of that of the polymer would, as concentration varied, produce a better stress cracking agent than either of the single environments. This effect has only rarely been shown to be true, and yet no alternative method of dealing with mixed environments has been produced to date. This work examines the non-linear stress cracking behaviour of polycarbonate in mixed environments (predominantly alcohols), relates the results to a law of mixtures prediction and proposes an alternative method for predicting ESC.

EXPERIMENTAL DETAILS

The material used was Lexan Polycarbonate, chosen as a typical amorphous thermoplastic that shows clear ESC crazes. Strip samples of 13 mm width and 55 mm length were cut from annealed 1 mm thick sheet. The edges of these were then ground with abrasive papers to remove excessive stress concentrations. The samples were then placed in three point bend testers, of a similar design to those used by Vincent and Raha [4], a pre-determined strain was imparted and the sample was immediately immersed in the test liquid. After a test period of two hours, which was shown to be long enough to ensure that no further crazes would form, the samples were removed and the width of the band of crazing was measured using an optical microscope. Where no crazing was observed a width value of zero was recorded. Several tests at different values of applied strain were performed for each mixture. The critical strain was determined as the strain required to just form crazes, as this has been shown to be the most reliable measure [5].

The environments used were all alcohols apart from water. They were : water, ethanol, benzyl alcohol, ethyl hexanol and 1,3,3 trimethyl hexanol (TMH). Binary mixtures of these environments were prepared to cover all possible combinations, apart from water, which was only mixed with ethanol. Mixtures were produced to give a reasonable spread of volume percentages in

* Department of Materials Engineering, University of Walea Swansea, Singleton Park, Swansea
† Rapra Technology Ltd, Shawbury, Shrewsbury, Shropshire.

each case. The solubility parameters and molar volumes of all the environments used are listed below in Table 1 [6]. Also included are the solubility parameters for polycarbonate, which are determined as the average values from published data, but it should be stressed that these are open to considerable debate as there is no reliable method of measuring such parameters.

Table 1 : The solubility parameters and molar volumes of the environments used.

Environment	Hildebrand Solubility Parameter $MPa^{1/2}$	Hansen (partial) $MPa^{1/2}$			Molar Volume (cm^3 / mol)
		Dispersive	Polar	Hydrogen	
Water	48.0	15.5	16	42.2	18
Ethanol	26.6	15.8	8.8	19.4	59
Benzyl alc.	23.7	18.4	6.3	13.7	104
Ethyl Hex.	20.1	16.0	3.3	10.9	157
TMH	18.5	15.4	3.0	10.0	174
Polycarbonate	22.7	18.5	8.2	10.2	-

RESULTS AND ANALYSIS

The values of craze width against applied strain are shown in Figure 1 for the Benzyl alcohol / TMH system. It can be seen that for each environment, the craze width decreases as the applied strain decreases, until it reaches a critical value, below which no crazes are seen. It can also be seen that this critical strain value increases as the proportion of TMH increases. Similar graphs were produced for all the combinations tested. From these, the values of critical strain were plotted against volume concentration, an example of which can be seen in Figure 2 for Benzyl alcohol / TMH. This shows that the Benzyl alcohol is a much stronger ESC agent than TMH, with a much lower value of critical strain. For intermediate concentrations, there is a gradual, but decidedly non-linear variation, with values of critical strain for mixtures being significantly lower than would be predicted from a simple linear variation between the end-members.

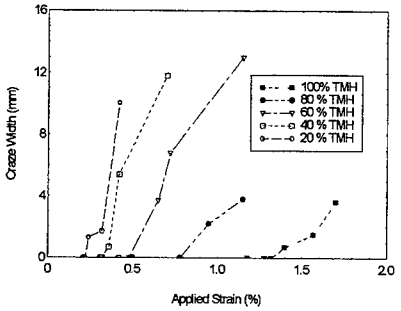

Figure 1. The craze width versus applied strain for Benzyl Alcohol / TMH mixtures.

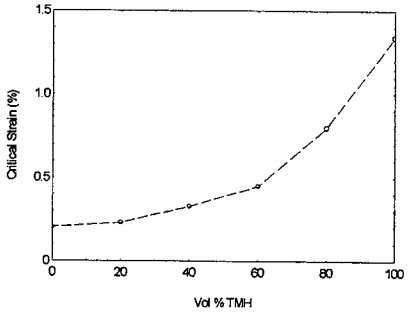

Figure 2. The critical strain to crazing versus concentration for Benzyl Alcohol / TMH mixtures.

For each of the mixtures, a solubility parameter was calculated on the basis of a law of mixtures, using volume fractions and the Hildebrand parameters. The critical strains for crazing were then plotted against these solubility parameters and are shown in Figure 3. Examining the position of the end-points, it can be seen that there is a reasonable correlation with single environments. The critical strain dips to a minimum in the region where the solubility parameters of liquid and polymer match, and rises to either side of this. For the mixtures however, the correlation does not hold. Firstly there is a decided degree of non-linearity between the end members with most combinations. Secondly, for liquids with solubility parameters either side of that for polycarbonate, a law-of-mixtures would predict a minimum critical strain for intermediate mixtures. Examination of the results for Ethanol / TMH and Ethanol / Ethyl Hexanol shows that this is plainly not the case.

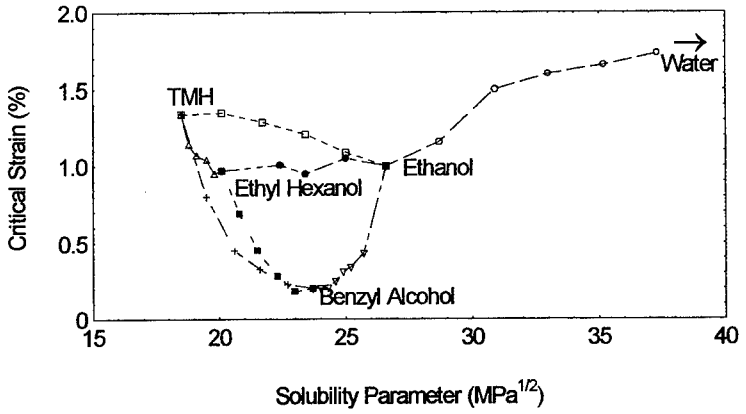

Figure 3. The critical strain to crazing versus law-of-mixtures solubility parameter for all the mixtures investigated.

There are several reasons why this very simplistic approach breaks down. Firstly, there may be significant interactions between the two liquids, which would cause the non-linear varitions seen. Secondly, the solubility parameter approach deals with the enthalpy of mixing, and so rather than taking an average value as above, a more realistic method would be to add proportionately the enthalpy of mixing for the two components. Thirdly, it has been demonstrated that a three-dimensional approach to solubility parameters, separating contributions from dispersive, polar and hydrogen bonding forces is more likely to be successful than the single value used above.

To accomodate the latter two of these points, a new correlation was tried, where the critical strain to crazing was plotted against the enthalpic contribution to mixing, including a separation of the solubility parameter into three components. This enthalpic term, χ_h is expressed as :

$$\chi_h = \phi_2 V_2 \left\{ (\partial_{d1} - \partial_{d2})^2 + (\partial_{p1} - \partial_{p2})^2 + (\partial_{h1} - \partial_{h2})^2 \right\} + \phi_3 V_3 \left\{ (\partial_{d1} - \partial_{d3})^2 + (\partial_{p1} - \partial_{p3})^2 + (\partial_{h1} - \partial_{h3})^2 \right.$$

The subscripts 1,2,3 refer to the polymer and the two environments respectively; ϕ is the volume fraction, V is the molar volume, ∂_d is the dispersive parameter, ∂_p is the polar parameter and ∂_h is the hydrogen bonding parameter.

Values of critical strain to crazing are plotted against this enthalpic term in Figure 4. It can be seen that although there are still some non-linear effects, the overall correlation is much better. Given the fact that this is still a relatively crude model, taking no account of the synergistic interaction between the two liquids and the polymer, it nevertheless shows that this approach is certainly worth pursuing and may well lead to an acceptable way of dealing with mixed environments.

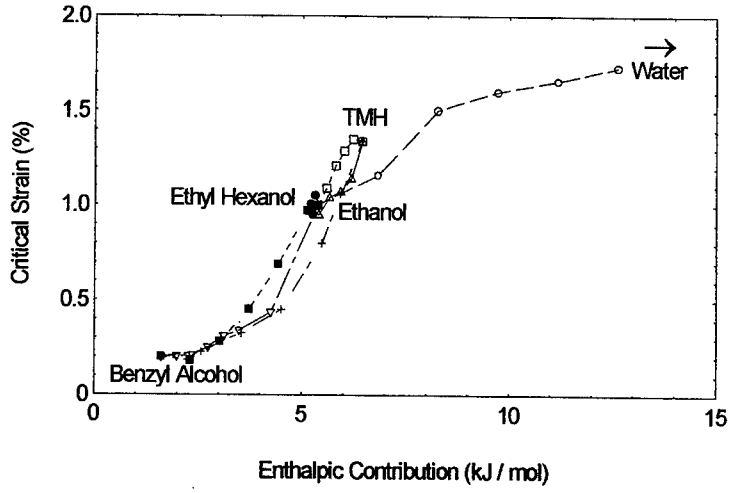

Figure 4. The critical strain to crazing versus enthalpic contribution for all the mixtures investigated.

REFERENCES

1. Bernier, G.A. and Kambour, R.P. *Macromolecules*, **1**, (1968) 393.
2. Jacques, C.H.M. and Wyzgoski, M.G. *J. Appl. Polym. Sci.*, **23**, (1979), 1153.
3. Mai, Y.W., *J. Mater. Sci.*, **21**, (1986), 904.
4. Vincent, P.I. and Raha, S., *Polymer*, **13**, (1972), 283.
5. Arnold, J.C., *Polym. Eng. Sci.*, **34** (1994), 665.
6. Barton, A.F.M., *CRC Handbook of Solubility Parameters*, CRC Press, Florida, (1983), 8.

STRENGTH PROPERTIES OF ELASTOMERS IN HIGH PRESSURE CO_2

J.C.ARNOLD*, O.M. DAVIES† and S.SULLEY††

INTRODUCTION

Decompression damage can be an operational problem for elastomer seals used to contain high pressure gases. The industries for which this has particular relevance are the oil / natural gas industry (methane and sour gas) and parts of the nuclear power generating industry (high pressure CO_2 coolant). At present, theoretically-based models of this process are not sufficiently developed to underwrite seal integrity. Therefore where specific assurances are required, plant simulation tests are typically carried out.

There have been many studies of the mechanisms and degree of decompression damage seen with elastomers. Of the controlling factors, the solubility and diffusion behaviour have received considerable attention [1-10], with the general conclusions that high solubilities and low diffusion rates (seen with low chain mobility) increase the severity of decompression damage. After solubility and diffusion rate, which are difficult to influence for given applications, the most important material parameter would seem to be the stiffness of the elastomer[3]. There have been several attempts at modelling decompression damage, following on from work on cavitation [3-5,8-10]. The one major problem with such predictive models is that the material properties of interest (stiffness, strength, tearing energy) are typically assumed to be those measured in the absence of the high pressure gas. From the limited work published on the mechanical properties of elastomers in high pressure gases [11] and by comparison to swelling by liquids, it is likely that the properties are considerably altered in swelling gases such as CO_2. Until the mechanical properties of elastomers in high pressure gases are known, the use of predictive models of decompression damage will be highly questionable. The main purpose of this work is to address this point by directly measuring the mechanical properties of a range of elastomers when saturated in high pressure CO_2 as well as studies in high pressure nitrogen, a non-swelling gas intended as a control.

EXPERIMENTAL METHODS

In order to overcome the problems of testing in high pressure gases, a specially designed tensometer pressure vessel was constructed. This is shown diagramatically in Figure 1. A major feature of the tensometer was an internal load cell, comprising a strain gauged beam at the base of the pressure vessel. The arrangement with the load cell inside the vessel eliminated concerns

*: Department of Materials Engineering, University of Wales Swansea, Singleton Park, Swansea.
†: Seals Group, BHR Ltd, Cranfield, Beds.
††: Nuclear Electric Ltd, Barnwood, Gloucester.

over force errors arising from the drag of the dynamic seals on the pull rod or the correction required for the gas pressure-induced loading of the pull rod. The load cell was calibrated in ambient air against a traceable standard and was found to be both accurate and linear to within 1% over the range of interest. The accuracy of the load cell when testing in high pressure gases was checked by measuring the force / displacement characteristics of a calibrated spring in ambient air and with the tensometer pressurised with 4 MPa nitrogen and CO_2. No significant differences were seen. The effect of long-term exposure of the load cell to high pressure CO_2 was also investigated and shown to be negligible. The tests were carried out in a modified proprietary tensile testing machine.

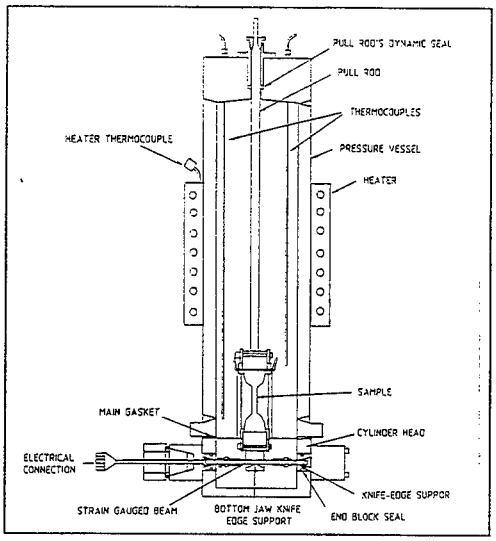

Figure 1 A schematic of the rubber tensometer.

Standard dumb-bell samples (BS903) were placed in the tensometer, which was then pressurised with the test gas and allowed to equilibrate for 24 hours. At the end of the soak time, the tensometer was clamped to the base of the tensile testing machine and the sample was extended at a constant rate of 500 mm / min. The extension was measured from the cross-head displacement. Calibration marks were put on the sample by the grips to ensure that if slippage occurred, the test result could be discounted. A range of elastomers were tested in ambient air and in 4 MPa nitrogen. A fluorocarbon (80 Shore; F80), nitrile (80 Shore; N80) and a silicone (65 Shore; S65) were then tested in ambient air and in 4 MPa CO_2. For each combination, three tests were performed at about 23°C.

RESULTS AND DISCUSSION

Individual tensile test results in air and in 4 MPa nitrogen are shown in Figure 2 for a 60 Shore fluorocarbon. It can be seen that there is very little difference in the observed modulus between the samples tested in air and those tested in high pressure nitrogen. Although there is some degree of scatter in the values of ultimate tensile strength (UTS), there is not a large difference between the two environments. Indeed, average values show that the strength is slightly higher in nitrogen, probably due to compression of surface flaws. The other elastomers tested showed no significant differences between air and nitrogen. Examination of the fracture surfaces of all materials did not show a marked change in morphology between samples tested in air and high pressure nitrogen.

The tensile test results in 4 MPa CO_2 show significant differences to the results in air. These are plotted individually in Fig 3 for F80, with average values of UTS for all the materials shown in Figure 4. In all cases, the samples tested in CO_2 had a lower initial modulus, a significantly lower strength and a lower elongation at break. These effects were most noticeable for the F80, and least so for the N80. The S65, although exhibiting the least difference in modulus, has a UTS 50% lower in CO_2 than in air. Examination of the fracture surfaces showed consistently smoother fracture surfaces in CO_2 than the equivalent tests in air.

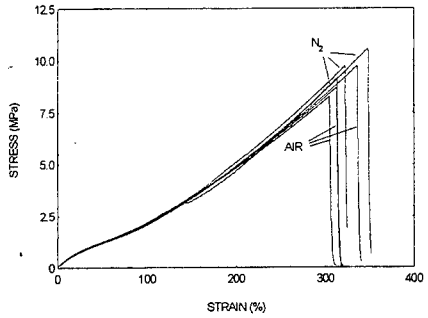

Figure 2. Stress/strain curves for F60 tested in air and 4 MPa nitrogen

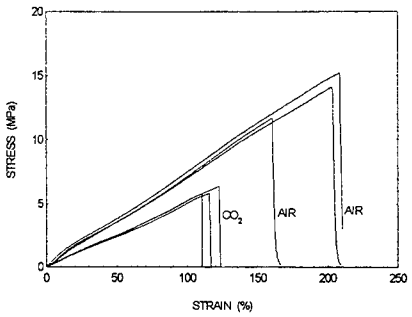

Figure 3. Stress/strain curves for F80 tested in air and 4 MPa CO_2

Apart from the change in fracture surface morphology, there is another indicator as to the reasons for the substantially different behaviour in high pressure CO_2. For the samples tested in air, the stress/strain curves rise most steeply over the first 20% strain. This effect is well known (Mullins effect) and is due to the interaction between the rubber and the filler particles and due to load sharing between the shortest chains. This effect is completely absent for the samples tested in high pressure CO_2. These effects point to a mechanism of plasticisation by the high pressure CO_2. By analogy with the effects that occur in elastomers swollen by liquid organic solvents, the plasticisation by high pressure CO_2 could lead to the disruption of filler - polymer bonds, as well as the polymer - polymer entanglements. This in turn will result in reduced load sharing, leading to a lower strength, lower modulus without an observed Mullins effect, lower elongation at break and a smoother fracture surface.

CONCLUSIONS

From the tests and analysis performed, it has been established that :
a) Elastomer seal materials (fluorocarbon, nitrile and silicone) are substantially weakened when saturated with high pressure (4 MPa) CO_2. The modulus also falls slightly.
b) Fluorocarbons are very slightly strengthened in high pressure (4 MPa) nitrogen; nitriles and silicones are unaffected.
It is concluded that high pressure CO_2 has a plasticisation effect on the elastomers and has important implications to the understanding of depressurisation damage. The effects of variations in pressure and in temperature will be presented in future publications.

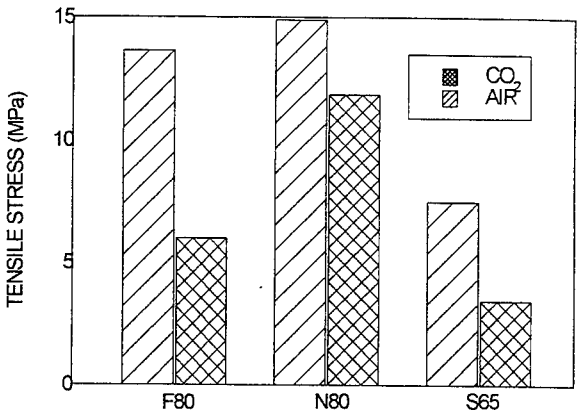

Figure 4. The average UTS for samples tested in air and 4 MPa CO_2

Acknowledgement

This paper is published by permission of Nuclear Electric Ltd. No liability can be accepted by Nuclear Electric for the views expressed or the application of data presented in this document.

REFERENCES

1. George A. F., "The effect of high pressure CO_2 on fluorocarbon and silicone seal materials", Proceedings 10th International Conference on Fluid Sealing, Innsbruck, paper D2 (BHRA 1984)
2. Eudes M, Langlois M, Narcy P, Dejeux M.A and Moret D.N, *Nuc. Eng.* 7 (1968) 586.
3. Gent A. N and Lindley P. B, *Proc. Roy. Soc. Lond.* **A249** (1958) 195.
4. Williams M. L and Schapery R. A, *Int. J. Fract. Mech.* **1** (1965) 64.
5. Oberth A. E and Bruenner R. S, *Trans Roy. Rheol.* **9(2)** (1965) 165
6. Briscoe B. J and Zakaria S, *J. Mater. Sci.* **25** (1990) 3017
7. Gent A. N and Wang C, *J. Mater. Sci.* **26** (1991) 3329
8. Gent A. N and Tompkins D. A, *J. Appl. Phys.* **40** (1969) 2520
9. Briscoe B. J and Zakaria S, *J. Polym. Sci. Polym. Phys.* **30** (1992) 959
10. Briscoe B. J and Liatsis D, *Rubber Chem. and Tech.* **65(2)** (1992) 350
11. Briscoe B. J and Zakaria S, *J. Polym. Sci. Polym. Phys.* **29** (1991) 196

DEFORMATION BEHAVIOUR OF PA/PPO BLENDS IN RELATION TO PROCESSING CONDITIONS

M. Quehen, J.M. Gloaguen, J.M. Lefebvre

The deformation behaviour of PA/PPO blends has been investigated in relation to key processing parameters in injection moulding.
Tensile tests at constant strain-rate have been performed at room temperature, and video extensometry is used to monitor volume variations during drawing. Two linear cavitational regimes are evidenced along the stress-strain curve. The most discriminating mechanical parameter with respect to processing conditions is the cavitation rate, i.e. $d(\Delta V/V)/d\varepsilon$. Linear correlations are established between cavitation rate and injection pressure. In the deformed state, morphological informations obtained using both SEM and TEM in combination with contrasting techniques indicate that cavitation predominantly occurs within the PPO particles. Moreover it is shown that internal morphology of the PPO phase plays a key role in the observed behaviours.

INTRODUCTION

The use of thermoplastics for structural applications has led to the development of specific blends offering high rigidity over a broad temperature range while displaying efficient energy absorbing mechanisms under impact conditions. Noryl GTX grades from General Electric Plastics are an example of such high performance engineering plastic alloys used in the automotive industry for body panel applications. In this respect, it is of great matter to understand how processing conditions influence the end-use mechanical properties.

EXPERIMENTAL

Two Noryl GTX grades, namely 914 and 964 have been provided by General Electric Plastics. They both consist of a Polyamide (PA6.6) matrix and dispersed Polyphenylenoxide (PPO) phase with a roughly 50/50% composition. Reactive extrusion enables to monitor particle size of the dispersed phase, promote adhesion and stabilize microstructure in view of the further processing steps. The PPO phase is modified by an undisclosed amount of elastomer material, presumably in the form of a block copolymer as mentioned in the literature (1, 2). Internal microstructure of the PPO particles is rather complex, with the elastomer phase appearing as tortuous domains. GTX 914 and 964 grades mainly differ by the nature of the elastomer phase.
In order to simulate the injection moulding of thin body panels, 2mm thick plates, 175x175mm2, have been prepared at constant injection speed and mould temperature. The processing parameters considered in this study are melt temperature T_m, holding pressure P_m and residence time ts. Injection pressure P_{inj} is also recorded. Residence time is held at either 3 or 8 minutes, and melt temperature is varied between 295 and 315 °C in the case of 914, and between 295 and 325°C in the case of 964. Holding pressure is in the range $20<P_m<85$ bar. The latter parameter may strongly influence crystallization and frozen-in stress relaxation upon cooling, while temperature will show in the viscosity effects on shear gradients in the blends, and also in terms of potential thermal degradation, in which case it should be coupled to residence time.

Laboratoire "Structure et Propriétés de l'Etat Solide", UST Lille/CNRS, Bat. C6,
59655 Villeneuve d'Ascq Cedex, France.

Tensile testing is performed on an Instron machine at constant strain-rate. Volume strain is recorded upon drawing with video extensometry (3, 4). A special profile of the tensile specimen, with a large radius of curvature enables to monitor strains in all three directions in the region of maximum stress. True stress and volume strain are thus recorded as a function of longitudinal strain.

RESULTS AND DISCUSSION

In order to illustrate the drawing behaviour, typical data are presented in figure 1 in the case of GTX 964 . Yielding is characterized by a plateau value at roughly 4% strain, followed by a slight hardening. The latter phenomenon is more pronounced and the yield stress is higher in GTX 914 under similar processing conditions (T_m=296, P_m=50, ts=3). Volume strain exhibits two quasi linear regimes as a function of longitudinal strain, with a higher slope in the first regime. Cavitation is much less pronounced in GTX 914.

The cavitation rate, i.e.$d(\Delta V/V)/d\varepsilon$, taken in the first cavitation regime has been retained to probe the influence of processing conditions on the deformation behaviour of these blends.

No particular correlation is obtained with either residence time or holding pressure, whereas melt temperature enables some discrimination of the processing conditions. However the most striking result is shown in figure 2 and 3, which relate the cavitation rate to the injection pressure. This parameter is not a controlled variable and is a complex function of temperature and shear gradients. Noryl GTX 964 exhibits a linear variation of the cavitation rate as a function of injection pressure, the lower is the latter, the higher is the cavitation rate. Surprisingly, a reverse trend of evolution is observed in the case of GTX 914. It is therefore crucial to elucidate how the microstructure of the blends is responding to draw.

Morphological studies have been undertaken, using both SEM and TEM techniques. First of all, blend characteristics have been derived in relation to the various processing conditions. Neither particle size nor particle size distribution appear significantly altered, even under somewhat abusive conditions.

SEM investigations on cryofractured surfaces after tensile drawing reveal a distinct behaviour of the two blends. GTX 914 fracture surfaces offer a rather compact morphology, with a cavitational process essentially linked to particle-matrix interface rupture. No drastic evolution as a function of processing conditions may be deduced from the SEM pictures. On the contrary, GTX 964 shows a complex fibrillated structure associated with elastomer cavitation and intense drawing of the inner particle PPO ligaments. Profuse fibrillation of the PPO particles is thus the key to the observed deformation behaviour of this blend. Comparison of deformed samples issued from mild and abusive processing conditions (mainly refering to temperature and residence time) clearly corroborate the mechanical data. After withstanding the high temperature, low injection pressure situation, drawing of the sample results in a far more cavitated particle substructure and the matrix-particle interface also seems disrupted.

The key role played by the elastomer phase is emphasized in the comparison made in figure 4 of the typical drawing behaviour of a PA/PPO blend without rubber with that of GTX 914. The drop in yield stress accompanied by a raise in cavitation in GTX 914 underlines the essential contribution of the elastomer phase to trigger the plasticity of the PPO phase.

Even more convincing are the data gathered in figure 5 in which shear versus cavitational components of deformation have been derived following Heikens et al (5). Going from the pure PA/PPO blend to GTX 914 and 964 results in an increased cavitational component, responsible for the decrease in yield stress and for enhanced plasticity in the form of PPO fibrillation in the case of GTX 964.

Returning to the original question of end-use properties, and more specifically to impact behaviour, it is worth addressing the problem in terms of active energy dissipating mechanisms. The inner particle cavitational capability of Noryl GTX 964 is certainly a key to extensive fibrillation and thus high energy dissipation. As pointed out by Yee and coworkers (1, 6), multiple crazing and particle bridging ought to be operative at high deformation rates. One may add that unlike the present experimental situation, the state of stress in the impact

testing of a body panel is highly triaxial, which means that crazing/fibrillation will be favored by the intraparticle cavitational processes at the PPO-elastomer interface in this blend.

CONCLUSION

By analyzing the plastic deformation behaviour of PA/PPO engineering blends, it has been possible to relate the extent of intraparticle cavitation to a rather complex parameter of the injection process, the injection pressure. Depending on the nature of the elastomer phase in these blends, a reverse trend of evolution is observed when going from standard to severe processing conditions.

Inner PPO particle microstructure thus appears as a key element for achieving toughness, as long as the PPO-matrix interface remains coherent. The higher capability of Noryl GTX 964 as compared to GTX 914 regarding intraparticle fibrillation is in favor of a higher toughness.

The financial support of Renault, Direction des Recherches, Rueil-malmaison and General Electric Plastics, Bergen op Zoom is gratefully acknowledged.

REFERENCES

1 Sue H.J., Yee A.F., *J. Mater. Sci.* **1989**, *24* , 1447.
2 Laverty J.H., Ellis T., O'Gara J., Kim S., *Polym. Eng. Sci.* **1996**,*36* ,347.
3 G'Sell C., Hiver J.M., Dahoun A., Souahi A., *J. Mater. Sci.* **1992**, *27*, 1.
4 François P., Gloaguen J.M., Hue B., Lefebvre J.M., *J. Phys.III* **1994**, *4*, 321.
5 Heikens D., Sjoerdsma S., Coumans W.J., *J. Mater. Sci.* **1981**, *16*, 429.
6 Sue H.J., Yee A.F., *J. Mater. Sci* **1991**, *26*, 3449.

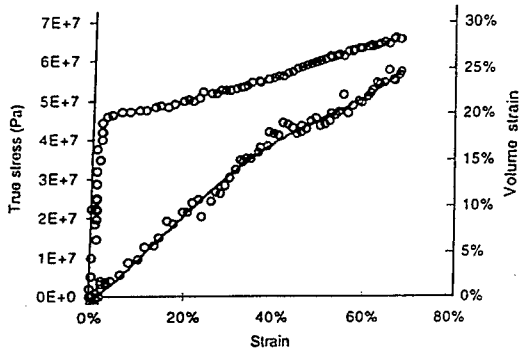

Fig.1: Typical evolutions of stress and volume strain as a function of strain, GTX 964.

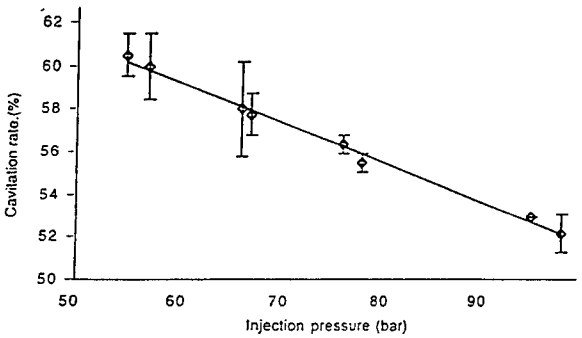

Fig.2: Cavitation rate versus injection pressure GTX 964.

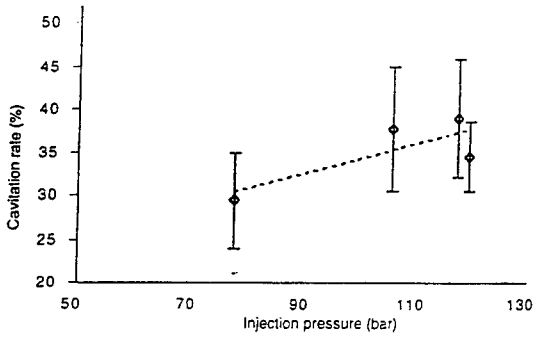

Fig.3: Cavitation rate versus injection pressure, GTX 914.

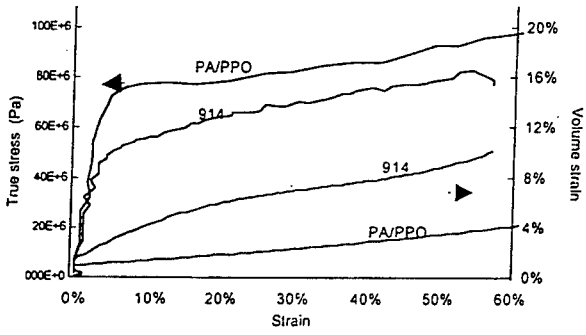

Fig.4: Comparison of stress and volume strain behaviours for PA/PPO and GTX 914.

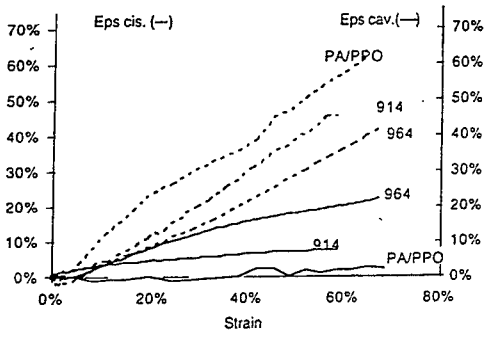

Fig.5: Shear and cavitational components of strain.

INSTRUMENTED ULTRAMICROTOMY – A METHOD TO STUDY NANO-SCALE CRACK GROWTH

ML Ericson* and H Lindberg+

Ultramicrotomes are generally used for preparation of very thin sections for transmission electron microscopy (TEM). Earlier we showed that instrumented ultramicrotomes can be used for measurement of fracture energy of polymers. Our instrumentation is a sample holder which uses two piezo-electric force transducers measuring two force components simultaneously. The fracture energy was almost in the same order of magnitude as theoretical predictions from chemical bond fracture only (approximately 10 J/m^2) as the section thickness is decreased to around 50 nm. Since the energy for chain scission showed to be such a large part of the fracture energy we suggest that instrumented ultramicrotomy is useful when information on covalent bond density is of interest. Therefore, the method has potential to quantify nano-scale crack growth in polymers and other materials. Effects of chemical structure and cross-links are presented and discussed. The chemical structure and cross-links had as expected very little effect on fracture energy at small section thickness.

INTRODUCTION

Material scientists are concerned with quantitative mechanisms of toughening of most engineering materials, especially polymers and polymer based composites. This endeavour should enable chemists to develop new polymers or tailor existing polymers to meet new requirements. Today we see results from decades of polymer developments and indeed many components are manufactured in new tougher materials. Examples are toughened epoxies in high performance fibre reinforced composites, adhesives and toughened thermoplastic polymers formed by injection moulding. Is it possible to further improve these materials and if so, how should we find more fundamental knowledge on how to optimise the microstructure of the materials? One draw-back with traditional measurements of toughness (e.g. compact-tension tests or double cantilever beam tests) is that the activated volume in front of the crack tip is relatively large, several micrometers. It is therefore difficult to correlate the information from the fracture mechanics test to microstructural details, such as morphology and/or size of a second toughening phase. In order to develop a method to characterise the energy dissipation at a true microscopic level, we earlier developed an instrumented ultramicrotome [1, 2].

An ultramicrotome is used for sample preparation for transmission electron microscopy (TEM). By use of a very sharp knife (diamond or glass), extremely thin sections or "chips" of polymers or biological materials are prepared. The chip thickness is typically between 30 nm and 150 nm and in order to get good sectioning results the sample needs to be in the solid or preferably the glassy state. Since microtome sectioning create two new surfaces one may look at the sectioning as a crack propagation process. Ericson and Lindberg [1, 2] showed that if the ultramicrotome is instrumented in order to measure sectioning forces it is possible to calculate the work to section during the crack propagation. Since the thickness of the sections are very small this might give us some insight in very local fracture energy dissipation mechanisms. The objective of the present work is to show the principle of instrumented ultramicrotomy and to discuss some potential applications.

* Division of Polymer Engineering, Luleå University of Technology, S-971 87 Luleå, Sweden
+ Department of Wood Technology, Luleå University of Technology, SKERIA 3, S-931 87 Skellefteå, Sweden

EXPERIMENTAL

A special instrumented sample holder was designed and built. Two piezo-electric load cells (Model PCB® M209A12 from PCB® Piezoelectronics, Inc., USA) with battery-powered signal conditioner (Model 480E09 from PCB®) were mounted between a sample clamping unit and the connection for the ultramicrotome specimen arm and pre-stressed. See Figure 1. The analogue signal from the signal conditioner were sampled by a computer for further analysis.

For demonstration of the method, two polymers, polymethylmethacrylate (PMMA) and an epoxy, diglycidyl ether of bisphenol A with curing agent diethylene triamine (DGEBA/DETA), were sectioned with the instrumented sample holder. PMMA is a thermoplastic polymer whereas DGEBA/DETA is a thermoset (cross-linked). Both materials are amorphous and in the glassy state at room temperature. For more details about the materials, see ref. [2].

The ultramicrotome used was a LKB 2088 Ultrotome® V. The knife was a diamond knife (from Juniper Ultra Micro, Sweden). The radius of the knife edge is, according to the manufacturer, between 5 nm and 7 nm. Specimens were first cut from sheets and then trimmed in the ultramicrotome in order to get an appropriate sectioning block, a so called "mesa", of about 1 mm^2. The chip thickness, h, was determined from the interference colour created in the sections on the water surface in the water. The sectioning speed during measurements was 1 mm/s and h was varied between 60 to 250 nm at four discreet levels. For each h, sectioning forces for at least ten sections were recorded. The total work to section per created surface area, W_S, was determined as:

$$W_S = F_S/b \qquad (1)$$

where F_S is the sectioning force component in the sectioning direction (see Figure 2), and b is the chip width.

RESULTS AND DISCUSSION

Although the load cells were pre-stressed, the large difference in stiffness between the load cells and the prestress rods (approximately 350 N/mm and 5 N/mm respectively) made it possible to fully use the very high sensitivity of the load cells. Since the load cells are positioned symmetrically in the sample holder, it is possible to simultaneously detect both the sectional force, F_S, and the transverse force, F_t (see Figure 2). F_t is proportional to the sum of the forces in the two load cells whereas F_S is proportional to the difference. The smallest possible load to detect for each load cell is 0.22 mN. Due to the built-in lever mechanism, the smallest possible detectable F_S and F_t is as low as 0.05 mN and 0.4 mN respectively. Since the smallest sectioning force per section width for amorphous polymers was found to be about 10 mN/mm [1, 2], the sensitivity of the sample holder is more than sufficient for the desired purposes. Since the maximum allowable load is ± 200 N the sample holder is believed to be very robust. After calibration the sample holder showed very good agreement with simulated loads.

The sectioning force per unit width, F_S/b,, which is equal to the work to section (W_S), and transverse force, F_t/b, as function of section thickness h is presented in Figure 2 for PMMA and DGEBA/DETA. As observed previously [1, 2], W_S, decreases down to less than 30 J/m^2 for the two materials. Keeping in mind that the macroscopically determined fracture energy, G_{IC}, for PMMA and DGEBA/DETA is 500 J/m^2 and 130 J/m^2, respectively, it is remarkable that W_S for the two polymers do not differ more. The theoretically determined minimum fracture energy, the so called intrinsic fracture energy, G_0, is about 1 J/m^2 for PMMA. G_0 is the energy required to cut the chemical bonds at the fracture plane and is believed not to differ significantly for DGEBA/DETA. Since W_S for very thin sections and G_0 are in the same order of magnitude we believe that the total energy dissipated during sectioning is dominated by chain scission. Other possible energy dissipation mechanisms include chain stretching prior to scis-

sion and chain pull-out after bond rupture [3, 4]. However F_t/b, differ significantly between PMMA and DGEBA/DETA. We believe that differences in other energy dissipation mechanisms, such as friction, may cause this. In order to estimate the effect of other energy dissipation mechanisms, one needs to model the chip formation process and the frictional forces.

Results from instrumented ultramicrotome studies are encouraging. We strongly believe that instrumented ultramicrotomy opens room for several new applications for ultramicrotomes, for material properties characterisation (nano-scale crack growth) as well as sectioning optimisation (sectioning parameters or the equipment). Another interesting application is characterisation of molecular anisotropy for which only preliminary data exists but the results are promising.

CONCLUSIONS

By use of two piezo-electric load cells in the sample holder it was possible to measure two force components simultaneously during sectioning. The smallest load possible to detect was less than 0.1 mN. The method was successfully demonstrated by sectioning of PMMA and an epoxy (DGEBA/DETA). Very small levels of work to section was measured (less than 30 J/m^2) for both materials. It is suggested that the method of instrumented ultramicrotomy may be useful whenever information on chemical bond density in a material is of interest. For instance, fracture energies at the molecular level and molecular anisotropy can be studied with the method.

REFERENCES

1. M.L. Ericson and H. Lindberg, Design and potential of instrumented ultramicrotomy, Accepted for publication in Polymer.
2. M.L. Ericson and H. Lindberg, A method to measure energy dissipation during crack propagation in polymers with an instrumented ultramicrotome, Journal of Materials Science, 31 (1996) pp. 655-662.
3. L.H. Sperling, Introduction to physical polymer science (2nd edition), John Wiley & Sons, Inc. (New York) 1992, pp. 537-538.
4. M. Sambasivam, A. Klein, and L.H. Speling, Energy-consuming micromechanisms in the fracture of glassy polymers. 2. Effect of molecular weight on the fracture of polystyrene, Macromolecules,28 (1995) 152-159.

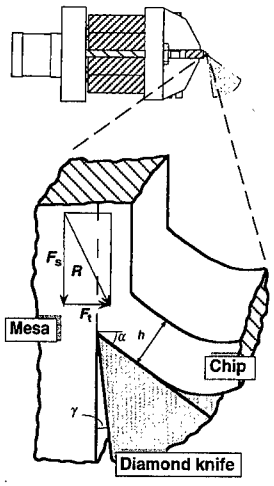

Figure 1 Schematic figure of instrumented sample holder for the intrumented ultramicrotome.

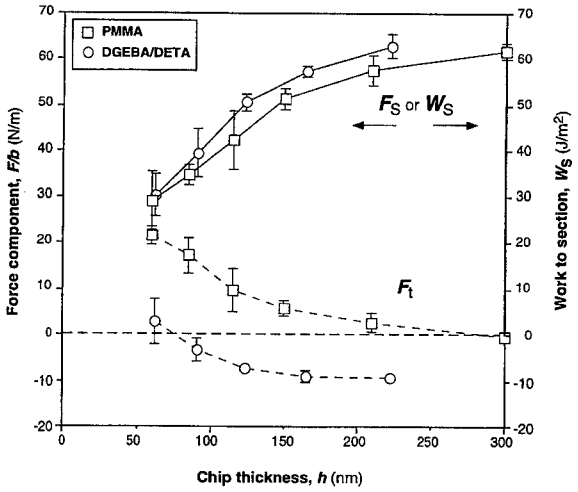

Figure 2 Sectional forces and work to section, W_S, for two amorphous polymers, PMMA and DGEBA/DETA.

KINETICS OF CRAZE TIP ADVANCE IN AMORPHOUS GLASSY POLYMERS IN THE PRESENCE OF LIQUID ENVIRONMENTS

L.M. Yarysheva*, L.Yu. Kabal'nova*, O.V. Arzhakova*, A.A. Mironova*, A.L. Volynskii*, and N.F. Bakeev*

The effect of the nature of liquid environment on the craze density and linear rates of craze tip advance in PET was studied. The effect of liquid environment on the stage of craze nucleation may be classified as surface-active, whereas the effect of the liquid environment on the kinetics of craze tip advance may be described as adsorption+plasticization.

For classical solvent crazing in amorphous glassy polymers in the presence of various liquid environments, linear rates of craze tip advance, structure and kinetics of craze tip advance were studied as a function of loading conditions. A principal problem of solvent crazing of polymers is associated with the effect of liquid environment on the mechanism of solvent crazing. Usually, this effect is provided by a decrease in surface energy of polymer or is associated with local plasticization of polymer in the active deformation zone (1, 2, 3).

Solvent crazing is accompanied by a simultaneous development of numerous crazes in polymers. This work is devoted to studying the mechanism of the effect of liquid environment on structure and individual stages of the development of solvent crazes accounting for the behavior of the whole ensemble of growing crazes. The principal results were obtained for amorphous unoriented PET, and solvent crazing was performed by tensile drawing polymers films under creep conditions. As active liquid environment, the liquid which, under normal conditions, are able to wet but not swell polymer, and assist the development of solvent crazing. These liquids were referred to as surface-active liquids (SALs). For PET, as surface-active liquids, alcohols, hydrocarbons, aqueous solutions of various alcohols were used.

The mechanism of the effect of SAL on the craze nucleation was examined by studying craze density for the PET samples prepared by solvent crazing in the presence of different liquid environments. Craze density was shown to change according to the decrease in surface energy of polymer in the presence of liquids, and for aqueous

*Polymer Department, Faculty of Chemistry, Lomonosov Moscow State University, Moscow, Russia

solutions of alcohols, a certain critical concentration of alcohol exists. Below this concentration, no crazing is observed (4). On the basis of this evidence, for solvent crazing of polymers, a local-critical approach was advanced, and the effect of liquid environments was described as surface-active.

As the next step, the kinetics of craze tip advance was studied. Different rates of craze tip advance of individual craze suggest that the description of the whole ensemble of crazes, a statistical treatment of experimental data was performed, and the corresponding distributions of the rates of craze tip advance were obtained. The nature of these distributions was described in (3) and was explained by the presence of a set of microdefects in initial polymer, which serve as stress-concentrating sites for local plastic deformation. From these distributions, the most probable rates of craze tip advance were obtained, and the effect of the nature of liquid environment on the stage of craze tip advance was analyzed studying the variations in this parameter.

The first attempts were focused on finding a correlation between the rates of craze tip advance and surface energy at the polymer--liquid environment interface. However, no evident correlation was obtained. It seems reasonable to assume that the rate of craze tip advance is controlled by flow of liquids to the craze tip. In connection with this, the rates of craze tip advance were compared with the flow of liquids through the fibrillar--porous structure of solvent crazes. Even for the liquids with high viscosity (*n*-hexanol), linear rate of liquid flow through the fibrillar--porous structure of crazes appears to be much higher (by several orders of magnitude) than the most probable rate of craze tip advance. This evidence allows one to conclude that, under the conditions studied, craze growth is not limited by liquid flow to the craze tip.

To estimate the activity of the above SALs from the viewpoint of the local stress-induced plasticization of polymer, we studied the sorption of these liquids at elevated temperatures, taking into account the similar effect of temperature and stress. Sorption of the liquids was studied at 65°C (this temperature is lower than glass transition temperature of PET, which is equal to ~70°C). Sorption of liquids in PET is known to be accompanied by Case II diffusion. In this case, glass transition temperature decreases, and solvent-induced crystallization takes place. Even at temperatures close to glass transition temperature, sorption of the above SALs in PET is rather small (several percent). The changes in the most probable rates of craze tip advance were compared with the degrees of swelling of PET in the above SALs at 65°C for 2 h. We found that changes in the most probable rates of craze tip advance are proportional to changes in the degrees of swelling of PET in different solvents. This evidence allowed one to conclude that, under the loading conditions studied, diffusion of liquids in PET is a limiting stage for the craze tip advance. Hence, in addition to the meniscus instability theory, the description of the kinetics of craze tip advance should account for the possible local plastcicization of polymer in the active deformation zone.

REFERENCES

1. Kramer, E.J., 1973, Developments in Polymer Fracture, 1.
2. Brown, H.R., 1989, J.Polym.Sci., B27,. 1273.
3. Volynskii, A.L., and Bakeev, N.F.,. 1995, Solvent Crazing of Polymers, Elsevier. Amsterdam.
4. Yarysheva, L.M., Chernov, I.V., Kabal'nova, L.Yu., Volynskii, A.L., Kozlov, P.V., and Bakeev, N.F., 1989, Vysokomol. Soedin., B31, 1544.

STRUCTURAL AND MECHANICAL BEHAVIOR OF POLYAMIDES WITH OXYAROMATIC COMPOUNDS

M.S. Arzhakov*, A.V. Volkov*, A.L. Volynskii*, and N.F. Bakeev*

The distribution of oxyaromatic compound in PA-6 amorphous regions between two structural forms was studied. Physical and mechanical properties (glass transition temperature, water sorption, elastic modulus) of PA-6 containing oxyaromatic compound were shown to be controlled not only by the net content of oxyaromatic compound in polymer, but by the above distribution. The experimental evidence obtained was discussed with the account for structural heterogeneity of the amorphous regions of semicrystalline PA-6.

Improvement of physical and mechanical properties of polymer materials may be achieved by their physical modification via introduction of compatible low-molecular-mass compounds (LMs) into polymers. Generally, for these polymer/LM systems, compatibility of the components is controlled by complexation between polymer macrochains and molecules of LM. As was shown by Lewin et al (1), Zaikov et al (2), and authors (3), in some cases, LMs, which were introduced into the polymer from the swelling solutions, appear to be distributed within polymer matrix between two different forms, reversibly (RB) and irreversibly bound (IB) with polymer. As compared with IB form, RB form may be easily removed from polymer by keeping polymer/LM samples in a pure solvent. Mechanism of the distribution observed was discussed in terms of structural inhomogeneity of amorphous polymers or amorphous phase in semicrystalline polymers - existence of, at least, two different noncrystalline regions (sublevels) with different packing densities and ordering. According to this mechanism, development of IB form of LM in polymer is associated with the formation of a stable complex between LM molecules and polymer macrochains in densely packed structural regions of polymer. Complexation of LM molecules with polymer macrochains in loosely packed structural regions is accompanied by development of RB form of LM with lowered energy of interaction as compared with IB form. This approach allows controlled occupation of different structural regions of polymer with LM molecules, i.e., separate modification of the above structural regions.

In this paper, for model systems based on PA-6 modified with oxyaromatic compound (OAC), the effect of distribution of modifying agent between loosely and densely packed structural regions within amorphous phase of polymer on physical and mechanical behavior of as-modified polymer material was studied.

*Polymer Department, Faculty of Chemistry, Moscow State University, Moscow, Russia

In this work, as OAC the product of condensation of sulfonated β-naphthol and dioxydiphenylsulfone with formaldehyde was used. As was shown by authors (4, 5), the treatment of isotropic PA-6 films in OAC aqueous solutions is associated with the development of both IB and RB forms of OAC in amorphous phase of polymer. In other words, occupation (modification) of both loosely and densely packed structural sublevels with OAC molecules takes place (hereinafter, Samples I). The removal of RB form from the loosely packed structural sublevels after treatment of PA-6/OAC samples in pure water implies that only densely packed structural regions appears to be modified (hereinafter, Samples II).

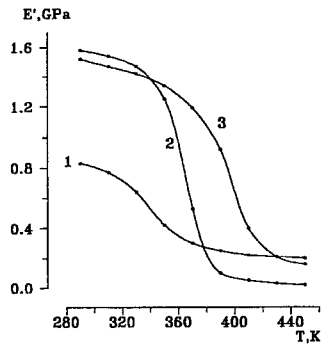

Figure 1. Temperature dependences of storage modulus of initial PA-6 (1), Sample I (2), and Sample II (3).

For initial PA-6, Samples I and II, Fig. 1 shows the temperature dependences of storage modulus E'. As is visible, for PA-6/OAC samples, the temperature dependences of E' have an inversion point, T_I. That is, at temperatures below T_I, OAC shows reinforcing (antiplasticizing) action on the polymer elastic properties, whereas at temperatures above T_I this action is weakening (plasticizing). Note, that the removal of RB form from polymer (transition from curve 2 to curve 3) is accompanied by shifting of T_I towards higher temperatures. Let us analyze the behavior of the elastic properties of PA6/OAC samples in the temperature range from ≈380 to ≈430 K.

In this temperature range, the values of E' for Sample I (curve 2), which contains both IB and RB forms of OAC, are lower than those for the initial polymer (curve 1). In the case of Sample II (curve 3), which contains only IB form of OAC, the values of E' are still higher than those for the initial polymer. This means, that in the samples studied, the same modifying agent may have opposite effect on the elastic properties of the polymer, depending on its form in the polymer matrix.

With increasing temperature, the mobility of OAC molecules in PA-6 increases. Increasing mobility of OAC molecules is responsible for decreasing the energy of intermolecular interaction between polymer macromolecules. As a result, reinforcing action of OAC on PA-6 is replaced by weakening action. For the PA-6/OAC samples, this mechanism may be invoked to explain the existence of the inversion point T_I in the temperature dependences of storage moduli. The peculiarities of the mechanical behavior of the PA-6/OAC samples are related to their complicated molecular organization, i.e., to the existence of two different forms (IB and RB) of OAC in polymer matrix. In a certain temperature range, mobility of RB form of OAC is likely to be higher than that of IB form. This difference in mobility of IB and RB forms can be explained

by the fact, that IB form of OAC is localized within the densely packed structural regions of amorphous phase of PA-6, which are characterized by a high level of intermolecular interaction. The RB form of OAC occupies loosely packed structural regions of amorphous phase with lower energetics of intermolecular interaction. From this standpoint, IB form of OAC exhibit an antiplasticizing action on PA-6 whereas RB exhibit a plasticizing action on polymer. Hence, the mechanical behavior of PA-6/OAC samples is likely to be associated with the difference in temperature-induced molecular mobility of IB and RB forms of OAC because of their localization within different structural regions in polymer amorphous phase. For detailed discussion of this phenomenon, let us consider the glass transition temperatures T_g and E' of PA-6/OAC samples (Table I).

TABLE I - Physical and Mechanical Properties of Dry PA-6/OAC Samples

Sample	Content of OAC, mol/kg	T_g, K	E', GPa at 360 K
Initial PA-6	0	353	0.38
Sample I	0.15	383	0.48
Sample I	0.37	388	0.53
Sample II	0.12	403	0.75
Sample I	0.5	393	0.67
Sample II	0.17	406	0.8

The comparison of Samples I and II evidences that removal of RB form from polymer samples results in a growth in both T_g and E'. Let us emphasize that, at the same net OAC content, for Samples II, the above parameters exceed those for Samples I. As was mentioned above, this phenomenon may be attributed to the interplay between plasticizing action of RB form of OAC on mechanical properties of PA-6 and antiplasticizing action of IB form in this temperature range. To gain a deeper insight into the influence of distribution of OAC between IB and RB forms on physical and mechanical behavior of PA-6/OAC samples, let us discuss the data on water sorption by the samples of the initial PA-6 and PA-6 containing OAC.

For initial PA-6 and Samples II containing only RB form of OAC, in the whole range of humidities the values of water sorption quantitatively coincide. However, for Sample I with the same net content of OAC a marked decrease in water content is observed. In other words, the sorptional properties of PA-6/OAC samples are controlled by the fractional content of IB form of OAC in the polymer. Note, that the studies of elastic properties of PA-6/OAC samples in a humid atmosphere also support a complicated pattern of influence of OAC on the mechanical properties of the polymer (Table II). As compared with initial PA-6, for Samples I, increasing OAC content leads to decreasing water sorption, and, as a result, to increasing elastic modulus. Desorption of RB form of OAC from polymer (transition from Samples I to Samples II) results

in an abrupt increase in water sorption which is comparable to that for initial polymer. However, no decrease in elastic modulus is observed. In other words, distribution of OAC between RB and IB forms is associated with peculiar "division of labor": RB fraction of modifying agent occupies loosely packed structural levels of polymer amorphous phase and is responsible for water sorption, whereas macroscopic elastic properties in humid atmosphere are controlled by IB fraction localized in the densely packed regions.

TABLE II - Elastic properties of PA-6/OAC Samples at $p/p_0 = 0.47$.

Sample	Content of OAC, mol/kg	Water Content, mol/kg	E_0, GPa
Initial PA-6	0	2.1	1.3
Sample I	0.15	1.4	1.8
Sample I	0.37	0.6	2.5
Sample II	0.12	2.0	2.4
Sample I	0.5	0.9	3.0
Sample II	0.17	1.9	2.8

Hence, the complicated character of interaction of OAC with PA-6 (distribution of OAC between RB and IB forms within polymer amorphous phase) is responsible for a complicated molecular dynamics of PA-6/OAC samples, and, as a result, for specific features of mechanical behavior of the material. This experimental evidence may be interpreted as the scientific approaches for controlled modification of polymer materials via controlled occupation of different structural sublevels with molecules of modifying agents.

REFERENCES

1. Lewin, M., Guttman, H., and Naor, Y., 1988, J. Macromol. Sci., A, 1367.
2. Polishchuk, A.Ya., Zimina, L.A., Madyuskin, N.N., and Zaikov, G.E., 1993, Polym.Sci., A, 35, 80.
3. Arzhakov, M.S., Volkov, A.V., Volynskii, A.L., and Bakeev, N.F., 1991, Makromol. Chem., Macromol. Symp., 44, 165.
4. Arzhakov, M.S., Red'ko, N.V., Volkov, A.V., Volynskii, A.L., and Bakeev, N.F., 1994, Polym. Sci., A, 36, 929.
5. Arzhakov, M.S., Nechaeva, E.V., Red'ko, N.V., Volkov, A.V., Volynskii, A.L., and Bakeev, N.F., Polym. Sci., A, 35, 62.

SPECIFIC FEATURES OF FINE STRUCTURE OF SOLVENT CRAZES

O.V. Arzhakova*, A.A. Mironova*, L.M. Yarysheva*, A.L. Volynskii*, and N.F. Bakeev*

Specific features of fine structure of solvent crazes in various amorphous and semicrystalline polymers were studied. This evidence allowed one to describe a fine structure of solvent crazes as a typical colloidal system with high free surface energy. According to this approach, a real structure of solvent crazes is controlled not only by the conditions of craze nucleation and growth but also by dramatic structural rearrangements within the craze matter. The intensity of structural rearrangements is provided by the flexibility of asymmetric craze fibrils, which, in turn, depends on the length and diameter of fibrils as well as on their ability to interact with neighboring fibrils.

Solvent crazing is known to be a specific mode of plastic deformation in polymers, which is accompanied by polymer fibrillation into fine aggregates of oriented polymer (craze fibrils) and development of microporous structure (1, 2). Usually, a fine structure in solvent crazes is shown to be controlled by the conditions of craze nucleation and is described within the fundamentals of the meniscus instability theory (2, 3). According to this classical approach, a whole system is modeled as a forest of rigid rods of non-interacting craze fibrils. However, in many cases, this model fails to describe a real behavior of solvent-crazed polymers. As known, craze fibrils are characterized by colloidal dimensions and, hence, the whole system may be treated as a typical colloidal system, where craze fibrils are treated as specific asymmetric colloidal particles, whose ends are tightly fixed in the craze walls by bulk polymer.

The objective of the present work was to characterize the structure and structural rearrangements in solvent-crazed polymers and to reveal the factors responsible for them. In this work, fine structure of solvent crazes in amorphous glassy (PET, PVC, *etc.*) and semicrystalline polymers (HDPE, PP, polyamides, *etc.*) was studied.

*Polymer Department, Faculty of Chemistry, Lomonosov Moscow State University, Russia

RESULTS AND DISCUSSION

Fuller details concerning the preparation of materials, experimental work, and treatment of experimental data can be found in reference (5).

In this work, time dependences of liquid flow through the porous structure of solvent-crazed PET films (with a tensile strain of 50%) were studied. All measurements were performed for the test samples under isometric conditions when the shrinkage of the solvent-crazed samples was completely prevented. We found that the liquid flow markedly decreases with time and most pronounced changes take place within the first 24 hours. This evidence suggests the craze matter is able to experience dramatic structural rearrangements. Under isometric conditions, these structural rearrangements are likely to be provided only by reorganization within the solvent crazes via the interaction and coagulation of neighboring craze fibrils, and the intensity of this interaction is controlled by the flexibility of craze fibrils. To prove this conclusion, let us suppress the flexibility of fibrils, for example, by decreasing their length. At one and the same tensile strain of solvent-crazed polymer, this idea may be accomplished by increasing the number of crazes. The experiments showed that when the number of crazes (craze density) was increased from 330 to 450 mm^{-1}, the changes in liquid flow are still observed but they are far less pronounced. Let us go further and nucleate maximum crazes in the sample. To do this, the samples were pre-crazed in air to a strain of 3--5%, and the as-drawn samples were drawn in the presence of surface-active liquid. In this case, craze density was about 800 mm^{-1}. In this case, that almost no drop in the liquid flow is observed. This evidence suggests that the final structure of solvent crazes is controlled by the structural rearrangements, which are likely to occur even during tensile drawing of polymer in the presence of active liquid environment. In connection with this, a correct description of the fine structure of solvent crazes necessitates the development of a new approach taking into account the specific features of the colloidal structure of solvent-crazed polymers.

In whole, the network of fibrils may be treated as a highly disperse colloidal system, which possesses a high level of free surface energy. According to this approach, fine structure of solvent crazes is specified not only by the conditions of craze nucleation, craze tip advance, and craze thickening (loading conditions, surface energy, temperature, *etc.*) but this fibrillar structure is shown to be able to reduce its high free surface energy via dramatic structural rearrangements and coagulation. This structural evolution is provided by interaction and coagulation between the neighboring craze fibrils. In connection with this, an important problem concerns the effect of liquid environment on the structure of relaxed solvent-crazed samples. In these experiments, the test samples were prepared by tensile drawing in the presence of one liquid environment and were allowed to stay in this solvent under isometric conditions until a certain equilibrium state was attained. After that, in crazes, this liquid environment was substituted by another liquid environment with different surface activity. The structure of the as-prepared samples was characterized. The experiments showed that, independently of initial conditions of solvent crazing, the resultant diameter of craze fibrils is completely

controlled by the surface activity of the liquid environment in crazes. This evidence agrees well with the behavior of typical colloidal systems when the level of dispersion solely depends on surface activity of liquid environment. The validity of this colloidal approach is demonstrated both for classical solvent crazing in amorphous glassy polymers and delocalized solvent crazing in semicrystalline polymers. Coagulation processes in solvent crazes are shown to be primarily controlled by flexibility of crazes fibrils (their length and diameter, elastic modulus of polymer) and their ability to interact with neighboring fibrils (nature of liquid environment, tensile strain, applied stress, *etc.*).

REFERENCES

1. Volynskii, A.L., and Bakeev, N.F.,. 1995, Solvent Crazing of Polymers, Elsevier. Amsterdam.
2. Kramer, E.J.,. 1983, Microscopic and Molecular Fundamentals of Crazing.
3. Paredes, E., and Fischer, E.W., 1979, Makromol.Chem, 180, 2707.
4. Brown, H.R., 1989, J.Polym.Sci., B27,. 1273.
5. Arzhakova, O.V., Yarysheva, L.M., Gal'perina, N.B., Volynskii, A.L., Bakeev, N.F., and Kozlov, P.V. 1989, Vysokomol. Soedin., B 31, 211.

STRAIN RATE DEPENDENCE OF THE TENSILE PROPERTIES OF INJECTION MOULDED PROPYLENE-ETHYLENE COPOLYMER FOR DIFFERENT PROCESSING CONDITIONS

J.C. Viana*, A.M. Cunha* and N. Billon+

ABSTRACT

The tensile-impact behaviour of axisymetrical samples injection moulded under different processing conditions was studied for several test velocities (1, 3 and 5 m/s). The thermomechanical conditions were evaluated by two indexes that can be associated to the microstructure developed under processing. The results show the relation between the impact properties and these indexes, evidencing the importance of the skin-core microstructure on the performance of the mouldings. Within the range of conditions used, the high deformation properties (energy and strain at break) present always the same type of dependence of the test velocity.

INTRODUCTION

The mechanical properties of polymeric materials are very sensitive to the strain rate. They also vary in a small but still significant extent with the local thermomechanical conditions imposed during the processing stages, as a result of the complex microstructure developed [1,2]. In semicrystalline injection moulded thermoplastics, a characteristic anisotropic layer-up structure is formed, which can be divided in three layers: two external highly oriented skins and a central spherulitic core. The relative dimensions and morphology of these layers leads to distinct deformation behaviours, that are enhanced for high strain rates [3].

The skin thickness, its degree of molecular orientation and the core microstructure are the main parameters controlling the material properties, being determinated by the thermomechanical history imposed under processing. In a previous study, this history was evaluated by two thermomechanical indexes calculated from computational simulations of the filling stage. The cooling index, Y, evaluates the time allowed for skin relaxation and, simultaneously, the crystallisation process of the core, being defined as:

$$Y = \frac{\text{overheating temperature difference}}{\text{cooling rate}} = \frac{T_b - T_c}{T_b - T_m} \qquad (1)$$

where T_b is the velocity weighted temperature through the thickness, T_c is the crystallisation temperature and T_m the mould temperature. An high Y value reflects an high thermal level of the core (e.g., higher spherulite dimensions and crystallinity). The degree of orientation of the skin is evaluated by a thermomechanical index, τ_Y, defined as:

$$\tau_Y = \frac{\text{flow induced orientation}}{\text{time allowed for relaxation}} = \frac{\tau_w}{Y} \qquad (2)$$

where τ_W is the maximum wall shear-stress. An high value of τ_Y reveals an higher degree of molecular orientation. T_b and τ_Y are easily obtained from simulations of the mould filling process using commercial finite elements based packages (e.g., C-MOLD).

*Polymer Engineering Department, University of Minho, 4810 Guimarães, PORTUGAL
+Centre de Mise en Forme des Matériaux, U.R.A. CNRS 1374, École des Mines de Paris, BP207 06904, Sophia-Antipolis, FRANCE

EXPERIMENTAL

The material used was a commercial grade of a propylene-ethylene sequential copolymer, APPRYL 3120 MR5. Axisymmetrical dumbbell-like samples (1.5 mm of diameter and 20 mm of reference length) were injection moulded under different moulding conditions, in order to obtain a wide variation of the two thermomechanical indexes (table 1). These were locally calculated by C-MOLD filling analysis. The tensile tests were carried out at constant velocities of 1, 3 and 5 m/s (corresponding to strain rates from 25 to 125 s^{-1}), in a ZWICK-rel 1842 hydraulic machine at room temperature (at least 7 samples per condition were tested). From the homogeneous stress versus homogeneous strain curves, the Young modulus, E, the energy and strain at break were (U_r and ε_r, respectively) calculated. The fracture surfaces were observed by scanning electron microscopy.

RESULTS AND DISCUSSION

The table 1 presents the values of the thermomechanical indexes for each moulding condition. As in injection moulding the thermal and mechanical effects are coupled, it is impossible to separate the contributions of the two selected indexes, Y and τ_Y. For all samples, E increases with the test velocity (figure 1), as well as the differences between moulding conditions. These are also reflected in the variations of U_r (figure 2) and ε_r. with the test speed, evidencing the distinct contributions of the microstructure to the sample capability to absorb energy. The dependence of U_r and ε_r is similar, indicating that the variations of the stress level are not significant.

The figure 3 and 4 show the fracture surfaces of the samples moulded with the extreme values of the thermomechanical indexes, for the two limit test velocities. It is clear a decrease in ductility of the mouldings with the test velocity, cases a) and b) of both figures. It is also evident the distinct behaviour of both samples: the one in figure 3 (where Y is maximum and τ_Y minimum) is more deformed; for the moulding in figure 4, (corresponding to the minimum Y and maximum τ_Y) the skin-core structure is clearly visible, being the core more deformed. This suggests that a thicker and more oriented skin inibites the deformation capabilities of the samples.

In the figure 5 are presented the variations of E with the thermomechanical indexes, for the three test velocities. There is no clear dependence with both indexes, indicating that both the skin and core properties determine the initial behaviour of the samples. There are also different variations with the test velocity, revealing different microstructure sensitivities. The evolutions of U_r and ε_r with the thermomechanical indexes are presented in the figure 6, showing a more clear dependence. For low values of Y and τ_Y, U_r decreases, but for high values of both is the opposite. It suggests that the behaviour of sample is controlled by the core properties for high values of Y and low τ_Y, and by the orientation and thickness of the skin for the opposite condition. This is corroborated by the micrographs shown in the figures 3 and 4, as discussed above. In fact, it is expected an increasing of the ductility of the samples for low spherulite dimensions [4], and a decreasing with the degree of orientation, for samples highly oriented [5]. The factor controlling the sample response depends on the relative importance of these two opposite effects. The sample present almost the same dependence on the test velocity, in the range of variation considered.

CONCLUSIONS

From this work, it can be concluded that:

- The thermomechanical history imposed during processing controls differently the mechanical behaviour of the material.
- The high deformation properties have a similar evolution with the test velocity for all the processing conditions considered.
- The material properties are dependent on the skin-core structure. The Young modulus is affected by both, independently of their properties; on the other hand, the energy and strain at break are controlled by the core morphology for high values of Y and low τ_Y, and by the skin properties for the inverse thermomechanical conditions.

REFERENCES

[1] Phillips, R, et. al., Poly. Eng. Sci., **34**, 23, (1994), p. 1731-1743

[2] Cunha, A.M., Pouzada, A.S., in "Impact and Dynamic Fracture of polymers and composites", ESIS19, ed. J.G. Williams and A. Pavan, Mech. Eng. Publ. (London), 1995, p.315-325

[3] Viana, J.C., Cunha, A.M., Billon, N., Polymer Int. (accepted for publication in 1997)

[4] Ouederni M, Phillips, P.J., Proced. ANTEC'96, Indiannapolis, 1996

[5] Cunha, A.M., Pouzada, A.S., Crawford, R.J., Plast. Rubb. Comp. Proc. Appl., **18**, 2, (1992), p.79-90

TABLES AND FIGURES

Table 1. Processing and thermomechanical conditions used.

T_{inj} (°C)	T_m (°C)	Q_{inj} (cm^3/s)/t_i (s)	Y	τ_Y (MPa)
230	30	5/4	0.2321	0.861
230	30	10/2	0.2861	0.586
230	30	20/1	0.3176	0.337
280	80	5/4	0.4286	0.211
280	30	20/1	0.4512	0.173

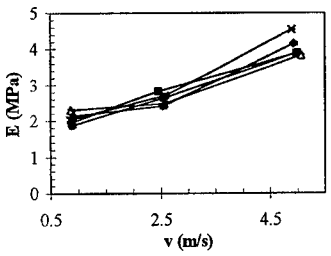

Figure 1. Modulus, E, vs. test velocity.

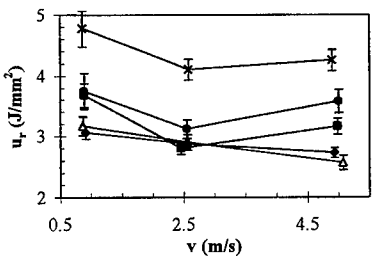

T_{inj} (°C)/T_m (°C)/Q_{inj} (cm^3/s): ■ 230/30/5 ◆ 230/30/10 ▲ 230/30/20 ● 280/80/5 * 280/30/20

Figure 2. Energy at break, U_r, vs. test velocity.

a) v = 1 m/s **b) v = 5 m/s**

Figure 3. SEM micrographs of the fracture surface (T_{inj}=280 °C, T_m = 30 °C, Q_{inj} = 20 cm^3/s).

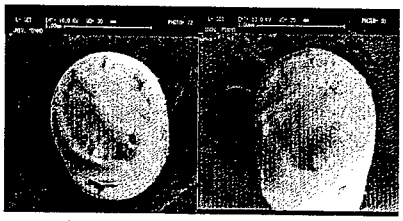

a) v = 1 m/s **b) v = 5 m/s**

Figure 4. SEM micrographs of the fracture surface (T_{inj}=230 °C, T_m = 30 °C, Q_{inj} =10cm^3/s).

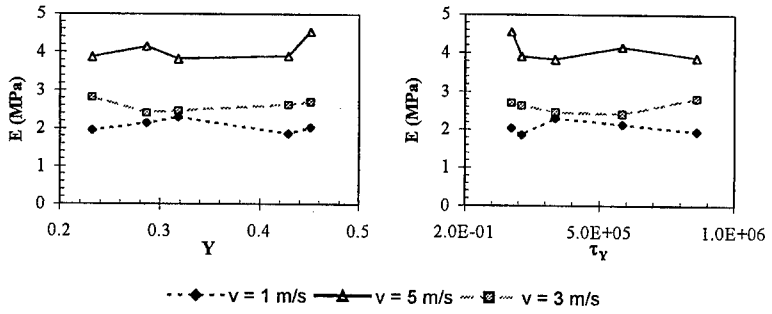

Figure 5. Variation of the modulus, E, with the thermomechanical indexes.

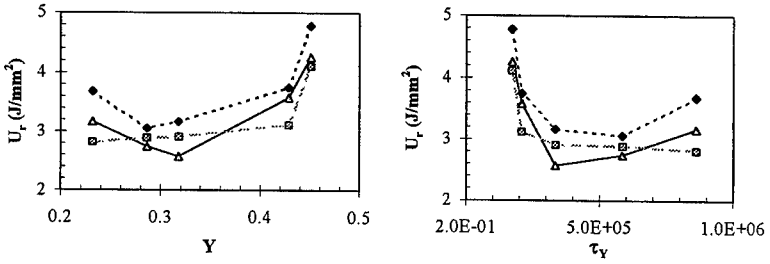

Figure 6. Variation of the energy at break, u_r, with the thermomechanical indexes (legend in figure 5).

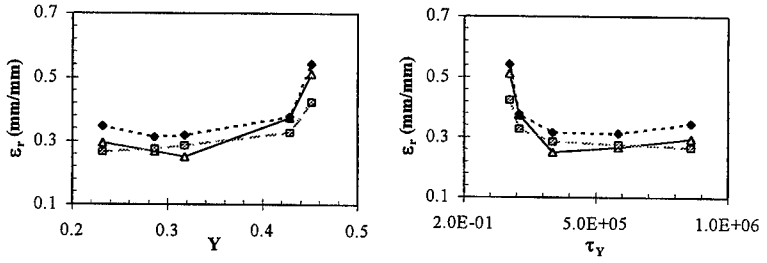

Figure 7. Variation of the strain at break, ε_r, with the thermomechanical indexes (legend in figure 5).

PLASTIC DEFORMATION OF ALIPHATIC POLYESTER : EFFECT OF ROLLING ON THE MECHANICAL PROPERTIES OF POLY (ε - CAPROLACTONE) SHEETS

K Nakayama*, AAJ Ketelaars*

Poly (ε - caprolactone) [PCL] is one of the biodegradable aliphatic polyesters. Isotropic PCL sheets were rolled at temperatures below the melting point. The successful rolling gave a large deformation to the PCL sheets. Dynamic storage modulus at lower temperatures increased with increasing rolling ratio. The anisotropy of the modulus for rolled sheets showed interesting results. The molecular orientation of rolled PCL sheets was evaluated by use of X-ray diffraction. Highly deformed specimens showed the uniplanar-axial orientation.

INTRODUCTION

Plastic deformation can be applied to the processing or forming of semi-crystalline polymers. There has been a great interest in the effect of molecular orientation on the mechanical properties of semi-crystalline polymers. Poly (ε - caprolactone) [PCL] is one of the biodegradable aliphatic polyesters. It is expected that the deformation of PCL influences the degradation process due to an increase in the amount and orientation of the crystalline phase in the polymer. The melting temperature of PCL is about 60℃ and it can easily be deformed in the solid-state at ambient temperatures. This work was conducted in order to know the advantages of rolling of PCL sheets.

EXPERIMENTAL

PCL sheets were obtained by melt-extrusion of commercial PCL (Tone, UCC) by use of a single-screw extruder and T-die. Melt-extruded sheets were quenched in a water bath. Isotropic PCL sheets (74 x 0.8 mm) were rolled at temperatures below the melting point of PCL. A pair of rollers with a diameter of 120 mm and a length of 150 mm were heated with internal cartridge heaters. A rolling mill was equipped with an apparatus for applying tension forces to the sheet during rolling (Figure 1). The successful rolling gave a large deformation to the PCL sheets.

The molecular orientation of rolled PCL sheets was evaluated by use of X-ray diffraction. Stress-strain curves were obtained on a tensile testing machine. To know the thermo-mechanical properties, measurements of temperature dependence of dynamic mechanical properties were conducted by use of a non-resonant forced vibration method.

* National Institute of Materials and Chemical Research,
1-1 Higashi , Tsukuba, Ibaraki 305, JAPAN

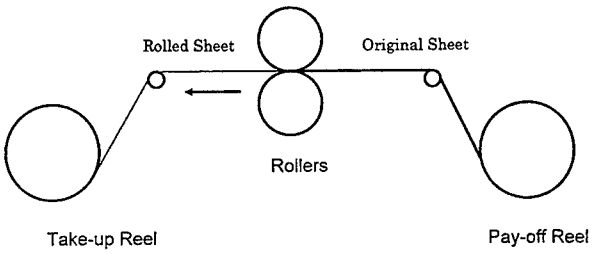

Figure 1 Schematic drawing of rolling apparatus.

RESULTS AND DISCUSSION

Cold rolling The effects of rolling process and rolling conditions on the deformation of PCL sheets have been investigated. Deformation ratio (rolling ratio, λ) of up to 5 could be obtained for these sheets by cold rolling at 30℃. Due to friction of the polymer sheet to the rollers, the width of the sheet is nearly constant during this type of processing. Stable rolling of PCL and higher rolling ratios were achieved by applying a tensile force after the roll to prevent recovery. Transparency of PCL sheets was improved by the rolling (Figure2). Density of rolled sheets increased with the increase of rolling ratio.

Dynamic mechanical properties The dynamic mechanical behaviors of PCL were sensitive to the structures (Figure 3). The main dispersion peak observed at -47℃ corresponds to the glass transition of PCL. The glass transition temperature Tg of rolled PCL was determined from the maximum in tan δ at 35Hz. With increasing rolling ratio, the glass transition temperature increases from -47℃ to about -20℃. This increase is due to an increase in orientation of the amorphous phase of the polymer as a result of rolling, thus limiting the molecular mobility in the amorphous phase. Also, increase of the amount of crystalline PCL could inhibit mobility in the amorphous phase.

The dynamic moduli E' at lower temperatures increase considerably with the increase of rolling ratio. There is a considerable drop in E' on passing the glass transition temperature. For the transverse direction of rolling (=90°), on the other hand, there seems to be a small decrease in E' at low temperatures and hardly any decrease on passing the glass transition temperature. This leads to the well known 'crossing' of these two curves at temperatures above the glass transition temperature of PCL, as can described by the well known models of Takayanagi.[1]

Mechanical properties The breaking stress increased with the increase of rolling ratio. To know the anisotropy of mechanical behavior of rolled PCL sheets, the stress-strain curves were measured as a function of angle with the rolling direction (Figure 4). For increasing rolling ratio, the anisotropy of Young's modulus clearly indicates an increase in preferential orientation. The breaking stress increased with the increase of rolling ratio. This is most likely due to the fact that the strain in the dynamic mechanical measurements is very small (in the order of 0.05%) compared to the tensile

tester (~ 2 % for Young's modulus). Apparently, all deformation along the rolling direction in the dynamic measurements is taken up by the amorphous phase at room temperature and the orientation of the crystalline phase can not be assessed. Therefore, the results of the Young's modulus at room temperature as determined from the stress-strain curves are believed to more accurately indicate the actual orientation of the crystalline phase as a result of rolling.

WAXD analysis of the crystalline orientation The crystalline orientation at room temperature can be studied using WAXD. The unit cell of PCL is orthorombic[2]. Both the equatorial (110) and (200) reflections are strong at 2 θ values of 21.5° and 24°, respectively. WAXD patterns showed that the c-axis (molecular chain axis) aligns to the rolling direction. It is possible to conclude that the crystalline orientation in rolled PCL sheets is a (100)<001> uniplanar axial orientation.

CONCLUSION

Isotropic PCL sheets were rolled at temperatures below the melting point. The successful rolling gave a large deformation to the PCL sheets. The molecular orientation of rolled PCL sheets was evaluated by use of X-ray diffraction. Highly deformed specimens showed the (100)<001> uniplanar-axial orientation. Based on the dynamic mechanical moduli E' at -150℃, it is concluded that the average orientation in crystalline and amorphous phases is easily achieved during processing at ambient temperatures and that molecular chains align in the rolling direction (RD). The dynamic modulus at 23℃ do not provide any information with respect to the crystalline orientation. At 23 ℃, $E'(\perp) > E'(\parallel)$. This phenomenon can be explain in terms of a simple model. Crystalline and amorphous phases are in series in the rolling direction. Based on the stress-strain curves at room temperature it can be concluded that crystalline orientation does occur during processing.

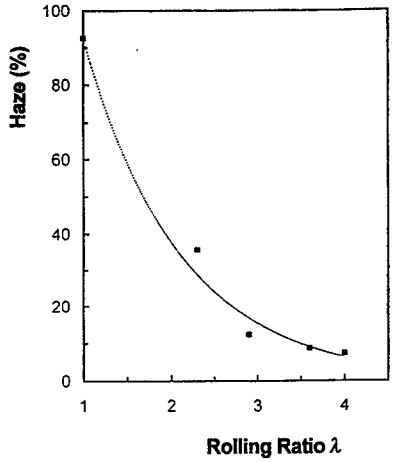

Figure 2 Change of transparency of PCL sheets with rolling.

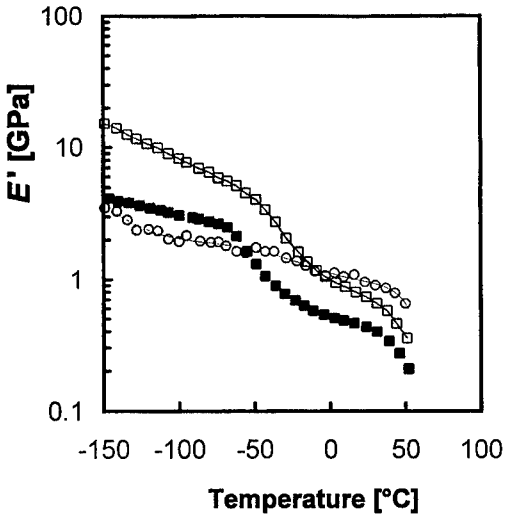

Figure 3 Temperature dependency of the dynamic modulus E' for unoriented and rolled PCL sheets.

■ : unoriented PCL,
□ : $\lambda=5$ $\phi=0^{\circ}$ (rolling direction)
○ : $\lambda=5$ $\phi=90^{\circ}$ (transverse direction)

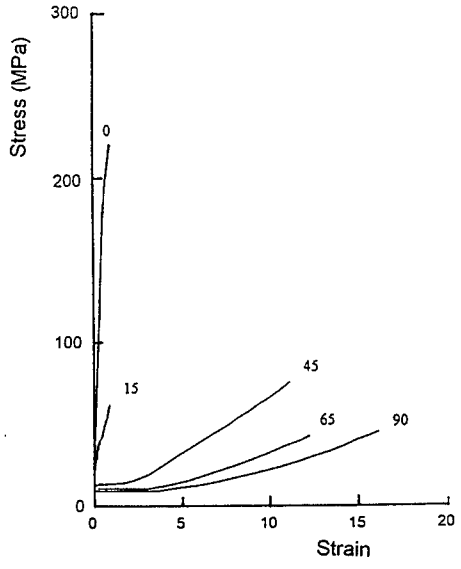

Figure 4 Stress-strain curves at room temperature as a function of the angle with rolling direction for $\lambda=5$.

References 1) M. Takayanagi, I. Imada and T. Kajiyama, *J. Polymer Sci.*, **15**, 263 (1966).
2) Y. Chatani, Y. Okita, H. Tadokoro and Y. Yamashita, *Polymer J.*, **1**, 555 (1970)

Phase separation behaviour at Weld Line in PC/ABS Injection Moldings

Hiroyuki HAMADA
Faculty of Textile Science
Kyoto Institute of Technology
Matsugasaki, Sakyo-ku 606 Kyoto Japan
Tel +81-75-724-7844
Fax +81-75-724-7800
e-mail hhamada@ipc.kit.ac.jp

Abstract
PC/ABS is very common immiscible polymer blends because their high rigidity and high processability. Internal structure such as distribution of each consistent would be changed by processing parameters in injection molding. According to observation of cross section in short-shot moldings in which ABS had been etched out, the surface of moldings were covered by PC. This phenomenon must be phase separation and was understood through finite element flow analysis by minimum kinetic energy theory.

Weld line is formed by meeting two melt flows which were injected through multigate or were splitted by pin or core. Internal structure at weld region would be very complex form because of phase separation flow. Etching out method was also used to observe distribution state at weld region. Below of V notch which is located at the surface of weld region PC rich region was observed and thickness of PC rich region varied through thickness direction. When tensile load was applied perpendicular to the weld line the fracture initiated from the interface between PC rich region and ABS region which was just behind the PC rich region. The final fracture occurred along this interface. This phenomenon means that fracture did not occur below the V notch. Usually the fracture at weld region initiated from V notch, so that the phenomenon observed in PC/ABS was considered unique characteristic of immiscible polymer blends.

Fracture and deformation of LCP reinforced polymers

Hiroyuki HAMADA
Faculty of Textile Science
Kyoto Institute of Technology
Matsugasaki, Sakyo-ku 606 Kyoto Japan
Tel +81-75-724-7844
Fax +81-75-724-7800
e-mail hhamada@ipc.kit.ac.jp

Toshihiko OKUMURA
Technology Research Institute of Osaka Prefecture
Ayumino,Izumi city 590-02 Osaka Japan

Abstract
LCP is very useful reinforcement in polymers because of high strength and high rigidity to the longitudinal direction. However in actual injection moldings LCP distribution state are greatly changed by processing parameters such as resin temperature, injection speed and so on. In this paper we used three different base polymers; PC, PA and PPS. LCP contents were changed from 0 to 100% without any compatibilizer in order to understand basic deformation and fracture behaviour of LCP reinforced polymers. Dumbbell type tensile specimens and bar type bending specimens were fabricated under various processing conditions. Deformation behaviour was measured by changing environmental temperature and further time-temperature superposition was used , so that activation energy was obtained. Skin/core structure is very important in the specimens. Therefore bending tests were performed by using removed skin specimen in which skin was cut out from specimen and the difference between normal specimen and skin removed specimen in activation energy was discussed. Fracture surface of static tensile specimen and impact bending specimen were observed and reinforcing mechanism was discussed. Moreover the differences of PC, PA and PPS were discussed.

MOLECULAR MODELING OF SILOXANE BASED SIDE CHAIN LIQUID CRYSTALLINE POLYMERS

B. L. Farmer*, G. M. Podojil*, R. Pachter[+] and W. W. Adams[+]

Molecular dynamics simulations have been used to examine the development of liquid crystalline order in a series of polysiloxanes having biphenyl, cholesteryl and methoxynitrostilbene (MONS) substituents tethered to the siloxane backbone by two different spacer groups. The simulations demonstrate that ordering between mesogens develops quite rapidly, giving order parameters comparable to experimental values seen in similar systems. Strong interactions between cholesteryl groups tend to give the longest-lived pair-wise associations. Biphenyl and MONS also show orientation in these systems, in part arising from their associations with cholesteryl mesogens, but also from their own homo-associations. Both the overall order parameter as well as that determined for just the cholesteryl mesogens is typically enhanced by the incorporation of biphenyl or MONS, which tend to relieve the crowding between cholesteryl groups. Highest order parameters have been seen for molecules having about 50% cholesteryl mesogens. The deformation behavior of these materials at the molecular level has also been examined by molecular modeling simulations. The deformation of the unsubstituted siloxane chain has been compared with that shown by the siloxane chains having cholesteryl substiutents.

Side chain liquid crystalline polymers (LCPs) are of interest for possible applications in a variety of optical applications. In particular, LCPs may provide a means both to optimize and to stabilize the orientation of substituents having the desired optical properties (e.g., chromophores). Above the glass transition of the polymer, the liquid crystalline character of the material can induce preferred orientation of the chromophore. That orientation can then be preserved by reducing the temperature to bring the material into its glassy state. Notably, even low molecular weight cyclic siloxanes having cholesteryl {C} and biphenyl {B} substituents demonstrate this temporal stability of the order induced between the glass and clearing temperatures [1,2]. Previous simulations have [3,4] have examined the behavior of cyclic and polymeric siloxanes having {C} and {B} substituents. Results indicate that mesogen ordering occurs quite rapidly and the order parameter is similar to that observed experimentally for related materials. Characterizing the influence that a chromophore (specifically, MONS {M}) has on the LC properties and the ability of the LC to induce orientation of the chromophore are the objectives of this modeling study. The general structure of the polymer is shown in Fig. 1. It should be noted that, of these substituents, only the {C} is mesogenic in the absence of connection to a polymer backbone.

METHOD

The calculations were made for a single polymer chain *in vacuo*. The number of substituents

*Department of Materials Science and Engineering, University of Virginia
[+]Materials Directorate, Wright Laboratory, Wright-Patterson Air Force Base

was 15 or 16, depending on the particular set of substituents under consideration. A variety of molecules were studied: homopolymers having each substituent individually, alternating copolymers, various block copolymers, and terpolymers in various arrangements. (The terms copolymer and terpolymer are used in the sense that the substituents on the repeating units were different - the polymer backbone itself was always the same.)

Molecular mechanics and molecular dynamics (MD) simulations were carried out using SYBYL [5] and a modified Tripos Force Field [6]. The simulations were carried out for a simulated temperature of 300 K and for a duration of 200 ps, using a time step of 0.001 ps. MD trajectories were saved for analysis every 5 ps. All atoms were considered explicitly. Electrostatic interactions were ignored. (Their role in systems containing MONS is currently under investigation.)

The order parameter, S, is defined as $\frac{1}{2} \langle 3\cos^2 \theta - 1 \rangle$, where the brackets denote averaging over the substituents and over the duration of the simulation. The average lifetimes of associations between mesogens were computed as follows: Any two mesogens whose orientation vectors gave a minimum dot product of 0.75 for at least 10 ps were considered "associated". The longevity of each association was determined and the second moment of the distribution of these lifetimes taken over all mesogen pairs and over the duration of the simulation is reported below as the average lifetime.

RESULTS

Table 1 presents the average order parameters calculated for the polymers considered. The order parameter was calculated for all the substituents ({C}, {B}, and {M}), for just the {C} substituents and for the {B} and MONS substituents taken together. (M* denotes that MONS was attached using a short spacer; i.e. without the benzoate group bracketed in Fig.1.) The average lifetimes of the various types of associations were also computed. Fig. 2a shows a molecule having a repeated substituent sequence of cholesteryl-biphenyl-cholesteryl-MONS (designated C/B/C/M in Table 1) and 2b shows the molecule having alternating MONS in alternation with cholesteryl substituents (designated M/C). These showed average order parameters of 0.36 and 0.05, respectively. Their average association lifetimes were 105 and 77 ps, respectively. The depictions in Fig. 2 show the backbone and spacers as segmented rods and the mesogens as straight rods. This representation highlights the alignment present in the conformation rather than the atomic detail actually used for the MD simulations.

There are several general observations that can be made. First, the order parameter is not directly related to the fraction of cholesteryl mesogens present. Fig. 3 shows a plot of overall order parameter *vs.* percent cholesteryl substituent. The largest order parameters are seen in systems having about 50% {C} groups. Greater amounts of {C} seems to hinder higher degrees of orientation. Note also that when tethered to a polymer backbone, both all-biphenyl and all-MONS substituted polymers achieve order parameters of the same order as the all-{C} chain. Second, inspection of the MD trajectories shows that in polymers having mixed substituents, the {B} and {M} groups associate for long times with the cholesteryl groups, resulting in their own fluid alignment with the {C} groups and by reducing local density, help facilitate increased orientation of {C}-{C} pairs. Third, the association lifetimes are not simply related to order parameter, as shown in Fig. 4. Higher order parameter does not correlate with longer association times. {C}-{C} associations tend to be the longest, forming early in the simulation and frequently lasting for the duration of the simulation. {M}-{M}associations tend to be shortest. Mixed associations of {C} with {B}or {M} are of intermediate duration.

It is also interesting to examine the deformation behavior of such polymers. For a preliminary exploration of how MM and MD tools might be used in this regard, the behavior of an all

{C}-substituted polysiloxane chain comprised of ten repeat units has been studied. A "random" conformation having an end-to-end distance of about 18 Å (taken from the end of an MD simulation) was used as a starting point. The energy was minimized under the constraint that the end-to-end distance not change. The energy of the molecule was then minimized as the end-to-end distance was successively increased, in 1 Å increments, from 18 to 27 Å. Using the same starting siloxane chain conformation but with the substituents removed and replaced by hydrogen atoms, the same procedure was carried out for the unsubstituted polysiloxane chain. (Interestingly, initial minimization of this molecule did not result in significantly shortening the end-to-end distance.) The plot of relative energy *vs.* end-to-end distance is shown in Fig. 5. (There are two anomalous points at small deformations wherein the minimization algorithm was unable to overcome some unfavorable interaction in order to achieve a reasonably low energy structure). As expected, the unsubstituted siloxane chain can be extended more easily than the substituted chain. The energy curve for the unsubstituted chain is rather flat and only increases substantially when the chain approaches full extension. It would be expected that this plateau region would increase as longer (more coiled) molecules are considered. Of course, for the substituted chain, extension from the starting conformation results in an immediate increase in energy. Extension by about 3 Å increases the energy by about 10 kcal/mol while the unsubstituted chain lengthens by about twice this amount for a comparable increase in energy. Clearly, dragging the cholesteryl substituents past one another has the effect of dramatically stiffening the molecule. The modulus of the substituted siloxane (as determined from the second derivative of the least-squares polynomial fit to the data) is about 75% greater than that of the unsubstituted polysiloxane chain.

Molecular modeling techniques are able to provide insight into the optical and mechanical properties of side chain LCPs. Future studies will further elucidate the influence of the chromophores on the LC behavior of the polymer and, conversely, the influence of the LC environment on the chromophores.

REFERENCES

1 Patnaik, S. S., Pachter, R., Bunning, T. J., Crane, R. L., and Adams, W. W., *Liq. Cryst.*, **16**, 911 (1994)

2 McNamee, S. G., Bunning, T. J., McHugh, C. M., Ober, C. K., and Adams, W. W. *Liq. Cryst.*, **17**, 179 (1994).

3 Socci, E. P., Farmer, B. L., Bunning, T. J., Pachter, R., and Adams, W. W. *Liq. Cryst.*, **31**, 811 (1993).

4 Podojil, G. M., Farmer, B. L., and Adams, W. W. *Polymer*, **37**, 1825 (1996).

5 SYBYL, Version 6.01, Tripos Associates, Inc., St. Louis, MO,1992

6 Clark, M., Cramer III, R. D., and Van Opdenbosch, N. *J. Comp. Chem.*, **10**, 982 (1989)

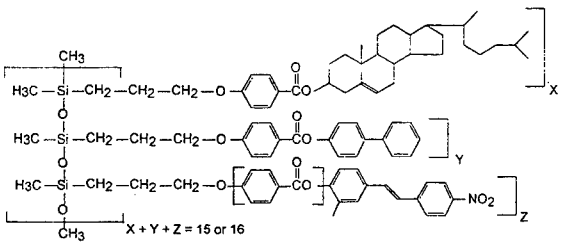

Fig.1 General structure of the polysiloxane

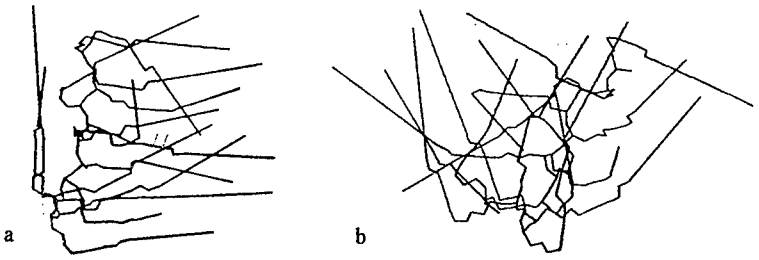

Fig. 2 Conformations of (a) C/B/C/M, and (b) M/C after 200 ps.

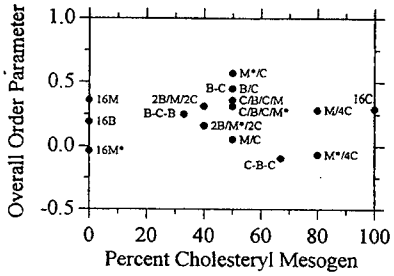

Fig. 3 Overall order parameter *vs.* percent cholesteryl substituent.

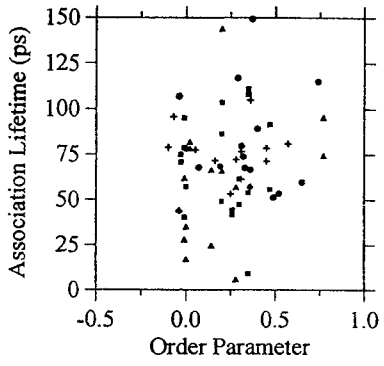

Fig. 4 Average association lifetimes *vs.* overall order parameter. +, overall; •, {C}; ■, {B}/mixed; Δ, {M}/mixed

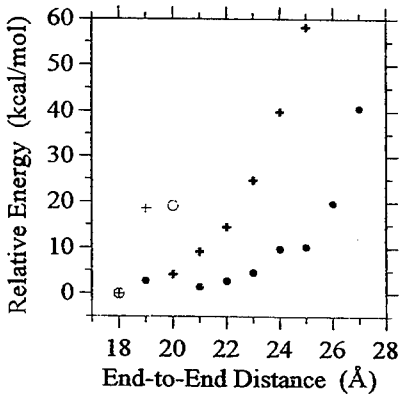

Fig. 5 Relative energy vs. end-to-end distance for siloxane deformation +, all-{C}; •, unsubstituted

Table 1	Order Parameter		
Molecule	Overall	{C}	{B,M}
16B	0.19		0.19
16C	0.29	0.29	
16M	0.36		0.36
16M*	-0.04		-0.04
B/C	0.45	0.36	0.47
8B/8C	0.45	0.74	0.26
5C/6B/5C	-0.10	0.4	-0.03
5B/6C/5B	0.25	0.49	0.30
M/C	0.05	0.07	0.02
M*/C	0.57	0.32	0.77
M/4C	0.28	0.31	0.28
M*/4C	-0.07	-0.04	0.14
C/B/C/M	0.36	0.37	0.35
C/B/C/M*	0.31	0.65	0
2B/M/2C	0.31	0.52	0.20
2B/M*/2C	0.16	0.33	-0.01

ENVIRONMENTAL INFLUENCES ON THE MECHANICAL PROPERTIES OF SPIDER SILKS AND WEBS

Lorraine H. Lin* † and Donald T. Edmonds*

The mechanical properties of major ampullate spider silk (species: *Araneus diadematus*) are significantly affected by the moisture content of the surrounding air. Threads exposed to a rise in relative humidity exhibit a reduction in stiffness and an increase in ultimate tensile strain. Thus, a sudden variation in RH has the potential to alter whether an orb-web is an effective trap for prey. However, extrapolation to 100% RH does not approach the mechanical behaviour known as "supercontraction" which could be due to a hydrophobic skin-core microstructure for silk.

When found in nature, spider silk is a semi-crystalline, non-linear viscoelastic biopolymer that functions in a region well above its glass transition temperature, T_g= -75°C, and remains stable up to a temperature of ~200°C without showing signs of melting (1,2). Under normal working conditions, this high performance fibre demonstrates toughness, a high ultimate tensile strain, ε_b ~ 25%, and an ultimate strength of $1x10^9$ N/m^2 (3). It is also known that the mechanical properties of silk are greatly influenced by water (4,5). In the extreme case, when submerged in water, silk exhibits supercontraction with a reduction in material stiffness by orders of magnitude (6,7).

Our study of silk produced naturally by the garden cross spider show that environmental changes affect its mechanical properties. *Araneus* builds webs in all humidities and in temperatures between slightly above 0° to 40°C (8). Thus, radial, frame, and dragline threads were tested in conditions likely to be experienced in nature (2°C<T<40°C, 0%<RH<100%). These results from the silk were analysed to show their subsequent effect on the structural design for which silk has evolved, orb-webs. Finite-element analysis in real time allows us to model accurately the effects of temperature and humidity on the stresses and deformations of complete webs.

MATERIALS AND METHODS

Juvenile spiders (25 specimens) were kept in PVC frames (30x30x5cm) under laboratory conditions (T=22±3° C, RH<25%, 18 hrs light per day). Spiders were watered once a day and fed *Drosophila* (fruit flies) twice a week. Webs were destroyed daily, so that spiders would build fresh ones. As spider silk is known to degrade over time (9), all samples were tested within three days of "manufacture". Long samples of silk were removed from fresh webs using callipers and a hot wire to prevent unwanted straining. Each thread was divided into a number of sub-samples (gauge length ~1 cm) assumed of constant diameter (in accordance with observations). Sub-samples were transferred unstressed into a microbalance (C.I.Electronics), secured with cyanacrylate glue then allowed to equilibrate for at least an hour. Due to the small diameters (~1μm), this time interval proved adequate for the threads to reach equilibrium giving virtually identical results as those left for 14 hours. Sub-samples were tested only once, either to rupture or cyclically. To regulate ambient conditions, the microbalance (response time 30 ms) was enclosed in an incubator. The relative humidity was controlled using phosphorus pentoxide and trays of water of

*Clarendon Laboratory, Parks Road, Oxford OX1 3PU
†Department of Zoology, South Parks Road, Oxford OX1 3PS

varying surface area. The temperature was measured to an accuracy of ± 2 °C and relative humidity, ± 7%. The microbalance with a stepping motor (0.27 mm per step) was controlled using LABVIEW software by National Instruments on a MacIntosh IICX. Samples were tested over a range of strain rates. However, for comparison of the mechanical properties shown in Figures 2 to 4, a slow average strain rate of 1mm/min (1step per 16s) was selected to reduce artefacts from sampling. For Scanning Electron Microscopy, an untested sub-sample from each strand was gold-sputtered (4 minutes, 1 kV, 30-40mA; rate of coating 15nm per min.), then its diameter measured (error ±7%). The area of our naturally produced silk, assuming a circular cross-section (10), appeared uniform over the length of a thread. Because of the highly non-linear nature of an orb-web, the FE computer program OASYS Dyna3d was employed for real-time dynamic analysis. This included the introduction of a special spring element to simulate silk behaviour. The topography of the model, as shown in **Figure 1**, was constructed from a digitised photograph of an orb web with air-resistance of the threads incorporated into the analysis (11).

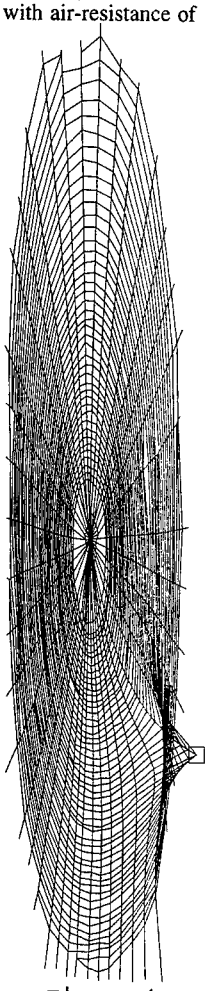

Figure 1

RESULTS

It is believed from observing spiders spin webs that radial and frame threads are the same type of silk extruded from major ampullate spinnerets with a different number of fibres; dragline threads, on which much of the recent research has focused, is reported to consist of silk produced by both major and minor ampullate glands (12, 13). The radial and frame threads we examined were typically composed of 2 to 4 and 4 to 6 strands of silk, respectively. Our data confirm this result: mechanical properties of frame and radial threads are similar - they are almost certainly both major ampullate silk (MAS). Dragline threads, however, displayed markedly different properties.

Unlike synthetic polymers, there is considerable variation in the mechanical properties of biomaterials. In spite of the scatter due to differences between individual spiders, our data show that within the working range, humidity has a far greater effect than temperature. When the environment is dry, MAS is stiffer and more brittle. An increase in the ambient humidity can reduce the silk's initial modulus (error ±15%) by a factor of ~10 (**Figure 2**) and almost double the breaking strain (error ±3%) (**Figure 3**). The domination of the mechanical properties of MAS by humidity is probably the result of water molecules diffusing into the polymer breaking hydrogen bonds between protein chains, thus reducing stiffness and increasing elasticity. However, unlike some other biopolymers (14), the ultimate tensile strength is not well-correlated with either T or RH (data not shown). With cyclic loading, this viscoelastic material dissipates the greater part (over 90%) of its total absorbed energy within the first cycle. In subsequent cycles, MAS demonstrates virtually elastic behaviour. In **Figure 4**, an increase of moisture in the air can reduce the first cycle of a thread's hysteretic capacity by 50%. From previous studies with DMA (dynamic mechanical analysis) of *Nephlia Clavipes* dragline threads (1), the average Young's modulus over a much greater temperature range is known to decrease with rising T. However, within the working range of *Araneus diadematus*, our data show that the mechanical properties of MAS and temperature are not well correlated - with the possible exception of when the air is very dry.

In contrast to radial and frame threads, changes in relative humidity do not significantly affect the stiffness of dragline threads and, in general, they show a longer relaxation time (data not shown). This is presumably the result of the minor ampullate silk.

Data from representative samples of radial threads in moist and dry environments at T=25 °C were incorporated into our computer model of a complete web. Viscid capture spirals were not tested, as it was previously reported that the shape of their stress-strain curve does not vary with relative humidity (13). **Figure 5** shows the applied force on a mass of 20 mg with an initial velocity of 1.0m/s as it is flung into the web (a reasonable estimate of an impacting insect). In order to prevent potential prey from escaping and avoid the "trampoline effect", the adhesive glue on the viscid spirals must exert a force greater than the product of the mass and acceleration of an insect. The upper limit of the force required to separate a mass from the sticky spirals has been measured to be ~60 mg weight (15). In our example, a sharp drop in relative humidity increases the rebound force by about 15%. Thus, a change in humidity could make all of the difference when at the threshold of prey entrapment. It is not yet known whether spiders modify their webs in the event of a change in humidity.

Supercontraction of spider silk is a well-studied phenomena. When an unrestrained strand of MAS is wetted with water at room temperature, the sample spontaneously supercontracts with a reduction in initial modulus by two orders of magnitude and an increase in breaking strain (6). The turning point of supercontraction of MAS in water occurs slightly below zero strain (7), thus can be prevented by tension in the threads. Extrapolation of our data (Figure 2) to 100% RH does not approach the behaviour of supercontraction. Our MAS threads, although typically secured in the microbalance slightly slack, invariably failed to supercontract in high humidities. Additional samples did not always supercontract (~85% RH) when released from restraint by moving together the glued ends of a thread by 25% of the initial length. This failure to supercontract could be the result of a hydrophobic coating or skin which inhibits the diffusion of water into the silk. Only when this layer is punctured, such in the case of a surface defect or at the cut ends of a short sample submerged in water, does supercontraction occur. The existence of a hydrophobic outer layer could explain the lack of correlation with temperature at the intermediate range of humidities we tested, as hydrophobic biomaterials are known to expel water with rising temperature. Thus, the predicted reduction in stiffness with increasing temperature is not present in our data (Figure 2) - possibly negated by a reduction in "free water" molecules in the silk due to greater hydrophobicity of an outer skin. Although there are currently differing views on the microstructure of MAS, the skin-core model has been directly observed before (16,17).

REFERENCES

1. Cunniff PM et al., Polymers for Advanced Technologies 5 (1994) 401-410
2. Osaka S, ACTA Arachnol. 37 (1989) 69-75
3. Gosline JM et al., Endeavor 10 (1986) 37-43
4. Vollrath F & Edmonds DT, Nature 340 (1989) 305-307
5. Bonthrone KM et al., Proc. R. Soc. Lond. B 248 (1992) 141-144
6. Work RW, J. exp. Biol. 118 (1985) 379-404
7. Shao Z & Vollrath F, 'Proceedings from the 10th International Conference on Deformation, Yield and Fracture of Polymer' (Cambridge, UK), 1997
8. Vollrath, in prep.
9. Jackson C and O'Brien JP, Macromolecules 28 (1995) 5975-5977
10. Dunaway DL et al., Journal of Material Science 30 (1997) 4161-4170
11. Lin LH et al., Nature 373 (1995) 146-148
12. Ed. by Kaplan D et al., 'Silk Polymers: Materials Science and Biotechnology', ACS Symposium Series 544, (Washington DC), 1994
13. Denny M, J. exp. Biol. 65 (1976) 483-506
14. Thwaites JJ and Mendelson NH, Proc. Natl. Acad. Sci. USA 82 (1985) 2163-2167
15. Edmonds DT and Vollrath F, Proc. R. Soc. B 248 (1992) 145-148
16. Li SFY et al., Biophysical Journal 66 (1994) 1209-1212
17. Vollrath F et al., (1996) Proc. R. Soc. B 263 (1996) 147-151

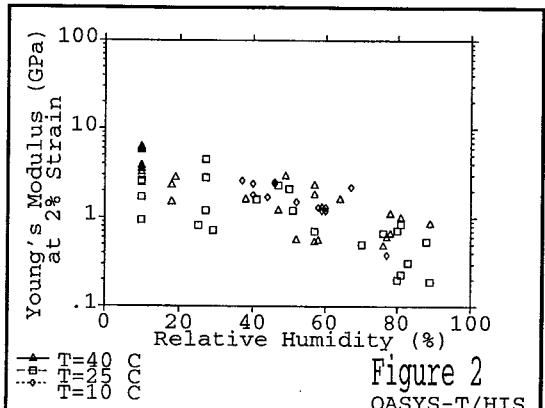

Figure 2
OASYS-T/HIS

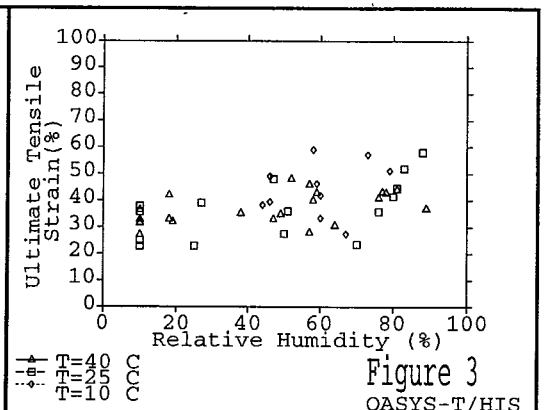

Figure 3
OASYS-T/HIS

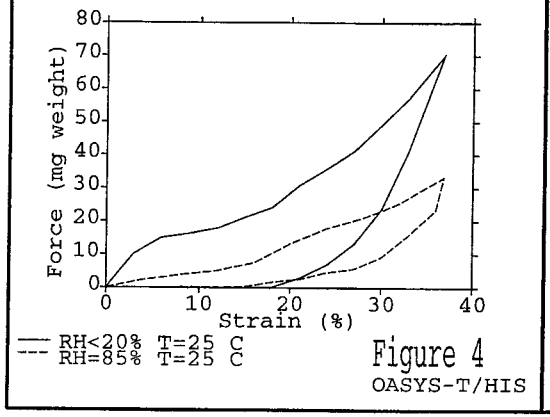

Figure 4
OASYS-T/HIS

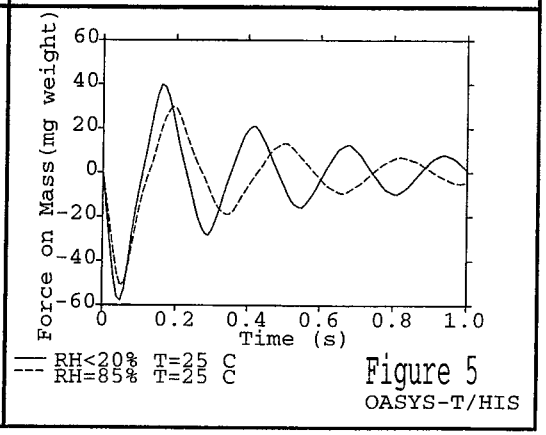

Figure 5
OASYS-T/HIS

THE HOT COMPACTION OF SPECTRA GEL-SPUN POLYETHYLENE FIBRES

R.J.Yan*, P.J.Hine*, I.M.Ward*, R.H.Olley#, D.C.Bassett#

The hot compaction of gel spun high molecular weight polyethylene fibre (SPECTRA 1000) has been investigated for a range of compaction temperatures between 142 and 155°C. Differential scanning calorimetry, scanning electron microscopy and broad-line nuclear magnetic resonance have been used to examine the structure of the compacted samples. DSC and SEM studies show that the mechanisms of compaction , for processing below 154°C, are a combination of localised fibre welding and interlocking with little apparent fibre surface melting. NMR studies show, however, that the rigid crystalline fraction of the compacted materials is significantly lower than the original fibre for all compaction temperatures, due to the annealing effect of the compaction process.

INTRODUCTION

The hot compaction of high modulus thermoplastic fibres has been studied extensively in these laboratories over the last few years [1-5]. The essence of the process is to take an arrangement of highly drawn fibres, and compact them at a temperature which is just sufficient to cause selective surface melting of each fibre to occur, such that on cooling the molten material recrystallises to bind the fibres together. This process is a route to high volume fraction, single type materials, and offers a method for transferring the properties of highly drawn fibres into solid homogeneous products.

The previous studies have concentrated on melt spun fibres, namely melt spun polyethylene [1,2], polypropylene [3] and polyethylene terephthalate [4]. In this paper we will describe an investigation into the compaction of gel-spun high molecular weight polyethylene (PE) fibre, SPECTRA 1000, for a range of compaction temperatures between 142°C and 155°C. Flexural tests have been made to examine the relationship between the retention of fibre mechanical properties, the development of fibre to fibre bonding and the compaction temperature. Differential scanning calorimetry (DSC), and broad-line nuclear magnetic resonance (NMR) have been used to obtain insight into the structural changes ocurring during compaction, while more definitive information on the morphological changes has been obtained using scanning electron microscopy of etched sections taken from the compacted samples.

* IRC in Polymer Science and Technology, University of Leeds, Leeds, LS2 9JT, UK
# J.J.Thompson Physical Laboratory, Whiteknights, Reading, RG6 6AF, UK

EXPERIMENTAL

The fibres used in these experiments were SPECTRA 1000, gel spun polyethylene fibres, manufactured by Allied Signal, USA. The fibres were unidirectionally wound around a frame, and arranged in a matched metal mould which was placed into a hot press set to the compaction temperature. A pressure of 2.8 MPa (400psi) was applied to the sample and once the assembly reached the compaction temperature, it was left for further 10 minutes. This initial contact pressure was significantly higher than that employed in previous work on melt spun polyethylene (0.7 MPa/100psi) and was required to prevent the gel spun fibres from shrinking during compaction. After the dwell time of 10 minutes, a higher pressure of 12.1 MPa (1700psi) was applied for 1 minute, after which the assembly was cooled to 100°C and the sample then removed from the hot press.

The melting behaviour of the original fibre and the compacted samples was investigated using a Perkin Elmer DSC-7 series differential scanning calorimeter: the heating rate for all the tests was 10°C/min. An important aspect of the melting behaviour was the effect of constraint. Constrained melting behaviour was measured by winding fibres around a small I-shaped frame of aluminium, which was then placed into the DSC pan. The mechanical properties of the compacted materials were measured using a three point bend flexural test. For measuring the longitudinal modulus (a measure of the retention of the fibre structure) samples were cut parallel to the fibre direction, while for measuring the transverse strength (a measure of the development of fibre to fibre bonding) samples were cut perpendicular to the main fibre direction. For morphological analysis, samples were cut at 45° to the main fibre direction using a glass knife, with the sample cooled with liquid nitrogen. The sample surfaces were then etched for 2 hours in a 1% solution of potassium permanganate in a mixture of 2 volumes of concentrated sulphuric acid a 1 volume dry orthophosphoric acid [5]. The broad-line NMR tests were performed using a Varian DP60 Spectrometer operated at 60 MHz. For examining the original fibres, they were wound around a thin rod, then taken off the rod and pressed into a strip. This allowed the fibres to be arranged either parallel or perpendicular to the magnetic field: results will only be presented here for the fibres arranged parallel to the magnetic field. The modulation amplitude was 0.39 Gauss and the average field interval at which the signal was recorded was about 0.05 Gauss.

RESULTS

Figure 1 shows the measured mechanical properties of samples compacted between 142 and 155°C. The filled squares refer to the values of the longitudinal flexural modulus (parallel to the fibre direction), while the open circles refer to values of the transverse strength (perpendicular to the fibre direction). The measurement of these two properties for a unidirectional arrangement of fibres, allows the trade-off between retention of the original fibre structure (longitudinal modulus) and the development of fibre to fibre bonding to be explored. Over the temperature range 142 to 150°C both remain relatively constant. The value of the longitudinal modulus measured over this range (of the order of 50GPa) is significantly less than that for the original fibre (78GPa at an equivalent strain rate) suggesting that for all temperatures there has been a significant change in the fibre structure due to the compaction process. However one consequence of this is the development of a reasonable transverse strength (15MPa).

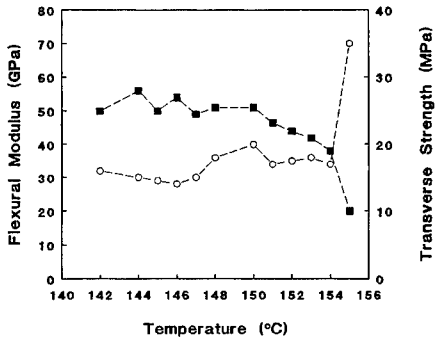

Figure 1: Flexural properties of compacted SPECTRA 1000

Above 150°C the longitudinal modulus falls more rapidly until at 155°C there is a dramatic fall. This sudden change is reflected in a sudden rise in the transverse strength, suggesting major changes in the fibre structure are occurring at this temperature.

The results of DSC and morphological investigations are consistent with the above mechanical results. Etched sections taken from the samples compacted between 142 and 154° C have broadly similar morphologies. The irregular polygons of the SPECTRA 1000 fibre are seen to have been crushed together during the compaction process, so that they deform to fill most of the available space. There is no evidence of intervening melted and recrystallised material, as seen with previous studies on the compaction of melt spun polyethylene. As the compaction temperature increases, the tendency is for any remaining gaps between the fibres to become closed, and for there to be a greater percentage of fibre to fibre 'welds'. The most dramatic morphological changes occur between 154 and 155°C. At 155°C the fibres appear to have greatly softened, and the boundaries between the fibres are much less distinct.

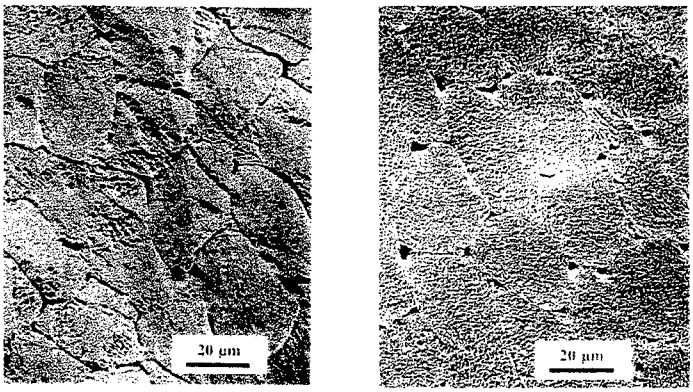

Figure 2: Typical etched surfaces at for samples compacted at 148 and 155°C

DSC measurements confirm these conclusions, with the compacted materials between 142 and 154°C all showing similar melting behaviour: a single melting peak which corresponds to the original fibre with only the suggestion of a lower temperature melting peak, which would be indicative of any selective melting of the fibre surfaces. At 155°C a different thermogram was measured, showing two melting peaks and a much reduced heat of fusion (reduced crystallinity and hence the destruction of the original fibre structure). While DSC and morphological studies are instructive in looking at change over the compaction range, broadline NMR measurements proved particularly useful in comparing the structure of the compacted materials with the structure of the original fibre. As a result of the complicated melting behaviour of these gel spun polyethylene fibres, DSC proved less useful in this respect. Figure 3 shows a comparison of the absorption spectra of the original fibre (a) and a sample compacted at 148°C (b).

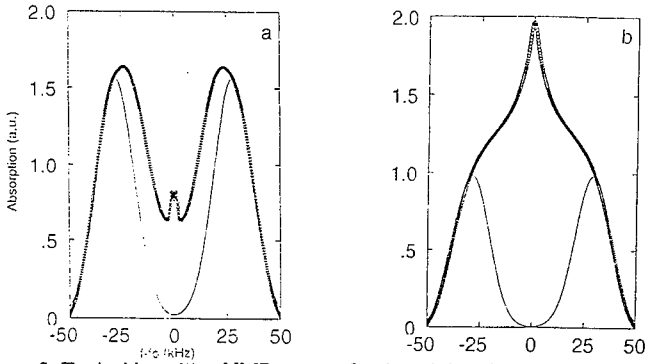

Figure 3: Typical broadline NMR spectra for the original fibre and a compacted sample.

The spectra for the original fibre shows a clear gaussian doublet, with a small peak at the centre due to a machine artifact. The NMR proton signal from polyethylene can usually be considered as the superposition of two components [6]: a gaussian doublet associated with the rigid crystalline regions, and a narrow single component associated with the more mobile materials. Although on first sight, Figure 3a would appear to be only a gaussian doublet, the best fit to the data was found using a combination of a rigid component (70%) and a mobile component. The spectra for a sample compacted at 148°C, more typical of that usually seen with polyethylene, shows a large increase in the mobile component and an associated reduction in the rigid component down to 41%. The changes in the longitudinal modulus due to compaction were found to correlate much better with the NMR rigid crystalline fraction, than the crystallinity determined by DSC measurements.

REFERENCES

1. P.J.Hine, I.M.Ward, R.H.Olley and D.C.Bassett, J.Mat. Sci., **28**, (1993) 316.
2. R.H.Olley, D.C.Bassett, P.J.Hine and I.M.Ward, J. Mat. Sci., **28** (1993) 1107.
3. J.Rasburn, P.J.Hine, I.M.Ward, R.H.Olley, D.C.Bassett and M.A.Kabeel, J. Mat. Sci. **30** (1995) 615.
4. M.I.Abo El-Maaty, D.C.Bassett, R.H.Olley, P.J.Hine, and I.M.Ward, J.Mat.Sci., **31** (1996) 1157.
5. R.H.Olley and D.C.Bassett, Polymer, **26** (1982) 1707.
6. H.Pranadi and A.J.Manuel, Polymer, **21** (1950) 1707.

EFFECTS OF CHEMICAL ENVIRONMENT ON LONG TERM STRENGTH OF POLYMERS

Dale Edwards
L.J. Broutman
L. J. Broutman & Associates, Ltd.
Chicago, IL 60616

Polyacetal and polyester (PBT) polymers have been subjected to aqueous environments containing various concentrations of free chlorine while under constant tensile load. The time to failure is determined at various loads, temperatures and chlorine concentrations. Micro tensile specimens have been developed to minimize the loads required for testing and specialized equipment has been designed to allow testing of multiple specimens in a single bath maintained at fixed temperatures and chlorine concentrations. The chlorine content is adjusted continuously in order to maintain constant concentrations. The ph of the environment is also maintained constant.

Chlorine concentrations have been varied from 1 ppm to 100 ppm. Testing has been conducted at both room temperature and at elevated temperatures up to 80°C. Also, 2 different flow grades (molecular weights) have been tested for both the polyacetals and the polyesters.

In the case of the polyacetals, the effect of chlorine concentration on failure time was studied at one elevated temperature. An equation is presented to predict the effect of chlorine concentration on failure time. Equations are also presented to predict the effect of temperature at fixed chlorine concentrations. The mechanism of failure will also be discussed for both the polyacetal and polyester resins with regard to surface embrittlement, hydrolysis and/or oxidation.

NEW DEFORMATION MECHANISMS IN POLY(STYRENE-b-BUTADIENE-b-METHYLMETHACRYLATE) TRIBLOCK COPOLYMERS

R.Weidisch*, S.Goerlitz*, G.H.Michler*, R.Stadler**

It has been shown that the microphase separation in ABC-triblock copolymers consisted of three chemically different components is much more complicated than in diblock copolymers (1-3). The morphology in ABC-triblock copolymers depends not only on the temperature, the overall molecular weight and the volume fraction of the components but also on the sequence of the blocks and on the interaction between the three components. The types of morphology in these copolymers will be determined by the balance of surface tensions. The interface tension between PS and PB is higher than between PB and PMMA. The morphologies are caused by consequence of minimization of the unfavorable A/B and B/C contacts. In a recent paper (4) the morphologies of symmetric PS-b-PB-b-PMMA triblock copolymers was presented: triblock copolymer with 38% PB shows a lamellar morphology, the decrease of the PB content up to 17% leads to a morphology consisting of PB-cylinders, which are placed at the interface of PS and PMMA lamellae. Triblock copolymer with 6% PB shows that PB-phase as spheres are located at the interface of PS and PMMA lamellae („ball at the wall"). There is a few studies on the deformation mechanisms in ABC triblock copolymers. The aim of this work is to investigate the deformation mechanisms and mechanical behaviors of symmetric and unsymmetric PS-b-PB-b-PMMA triblock copolymers.

EXPERIMENTAL

In this study two types of triblock copolymers have been investigated: symmetrical and unsymmetrical triblock copolymers. Symetrical triblock copolymers possess three different types of morphologies, including lamellar morphology (ll), PB-rods at the interface of PS and PMMA-lamellae (lc), PB-spheres at the interface of PS and PMMA lamellae (ls). In the unsymmetrical triblock copolymers there are two types of morphologies, PB-cylinders at PMMA-cylinders in the polystyrene matrix (cc) and core-shell structure of PB and PMMA in a PS-matrix (cic) (5).

„Dog-bone" shaped specimens for tensile tests were prepared from cast films with an average thickness of 0.5 mm and then annealed 3 days long at 120°C. Tensile tests (Zwick 1425) were performed with a cross head speed of 1.5 mm/min. To analyse the deformation of the individual components the deformed specimens in tensile tests were stained with osmium tetroxide and microtomed for TEM (Jeol, 200 kV).

* Institute of Material Science, Martin-Luther-University Halle-Wittenberg, D-06217 Merseburg, Germany

** Institute of Organical Chemistry, Johannes-Gutenberg-University, D-55099 Mainz, Germany

TABLE I - The molecular weights and compositions of triblock copolymers

morphology	overall molecular weight 10^{-3} M_n	weight fraction [%] w_{PS}	w_{PB}	w_{PMMA}
lamellar (ll)	245	24	38	38
PB-cylinders at the interface of PS/PMMA-Lamellae (lc)	238	48	17	35
PB-spheres at the interface of PS/PMMA-Lamellae (ls)	225	45	6	49
PB-cylinders at PMMA-cylinders in a PS-matrix (cc)	235	65	16	19
core-shell-cylinders of PMMA und PB in a PS-matrix (cic)	94	64	21	15

RESULTS

The tensile strength and the tensile modulus of symmetrical triblock copolymers decrease with increasing rubber volume fraction. A relatively sharp transition from brittle to tough takes place at 17% PB.

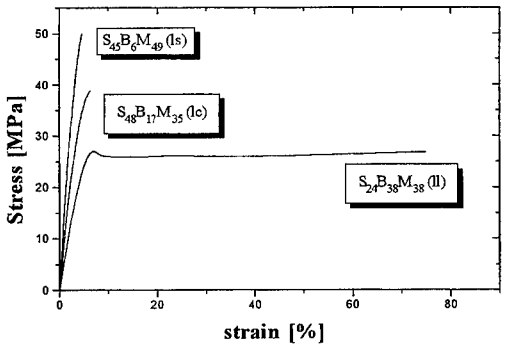

Fig. 1: Stress-strain curves for symmetrical poly(styrene-b-butadiene-b-methylmethacrylate) triblock copolymers

In general, the tensile strength in rubber modified polystyrene and PS-b-PB diblock copolymers with a comparable PB-content is lower than that of neat PS. It is surprising in the case of unsymmetrical triblock copolymers with core-shell structures (cic), that their tensile strength is higher than that of neat PS. In compare with PS-b-PB diblock copolymers with about 20% PB (7), it is occurred a remarkable reduction in the ultimate strain for the core-shell structures (cic).

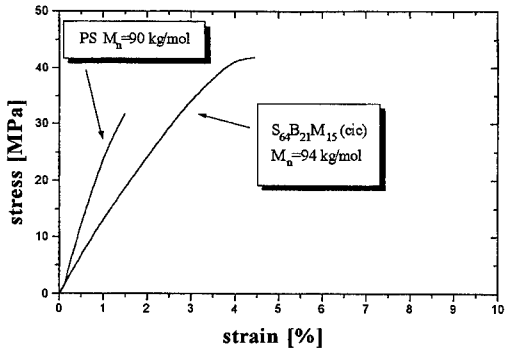

Fig. 2: Stress-strain curves for polystyrene and a unsymmetrical triblock copolymer with core-chell structure (cic)

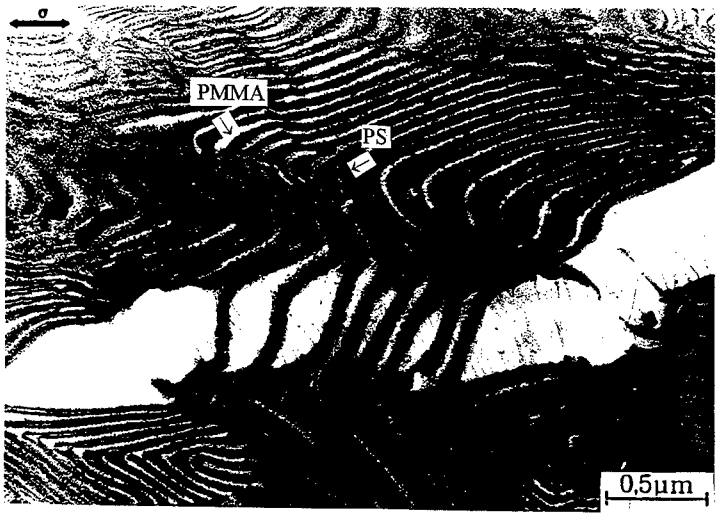

Fig. 3: Deformation structures in a lamellar triblock copolymer (ll); the cavitation in the PMMA-phase is clearly shown

Argon (6) has found that in the lamellar block copolymers consisting of PS and PB cavitation occurs in the PB phase. In contrast to these block copolymers, for the lamellar triblock copolymers (ll) the failure occurs in the PMMA-phase. In other types of symmetrical triblock copolymers the plastic deformation takes place also in the PMMA-lamellae. For the lamellar structure (ll) the large deformation zones with delocalised cavitation reveal in the deformed specimen. In the morphology types of (lc) and (ls) it is appeared a more localised cavitation.
In contrast to the symmetrical triblock copolymers (ll, lc, ls), in the unsymmetrical triblock copolymers, i.e. (cc) and (cic), the most of the plastic deformation occurs in the PS-matrix.

It has been found that the PS-b-PB diblock copolymers with cylindrical PB domains are deformed by a two step cavitation mechanism (7). In the core-shell cylindrical structure consisting of a glassy PMMA core surrounded by rubbery PB shell, these cylinders act as the same as the fibers in the polymer composites. As a consequence the yield stress is increased in contrast to the PS-b-PB diblock copolymers.

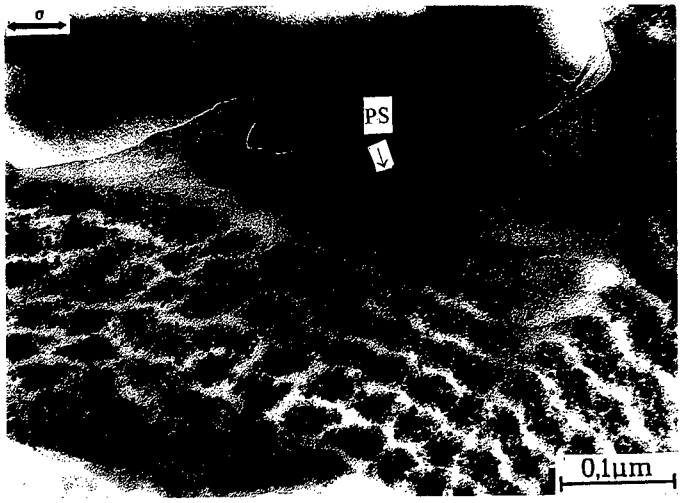

Fig. 4: Deformation structures in a unsymmetrical triblock copolymer with core-shell structure (cic) with a large deformation in the PS-matrix

The differences between the deformation mechanisms of PS-b-PB diblock copolymers and PS-b-PB-b-PMMA triblock copolymers are caused by their different molecular structure. Because the chain ends from PB phase reduce the critical cavitational stress, the cavitation cannot occur in the PB-phase in the case of the triblock copolymers presented here. This is an agreement with the observation of Koltisko et. al (8). They have found that in PS-b-PB-b-PS triblock copolymers the cavitation occurs in the PS-phase.

REFERENCES

(1) Mogi, Y; Mori, K; Kotsuji, H; Matushita, Y; Noda, I; Han, C: Macromolecules (1993), 26:5169
(2) Gido, S. P; Schwark, D. W; Thomas, E. L; Goncales, MC; Macromolecules (1993), 26:2636
(3) Auschra, C; Stadler, R.: Macromol. Rapid Commun., 15, (1994), 67
(4) Auschra, C; Stadler, R: Macromolecules, 26, (1993), 2171
(5) Krappe, U.: Doctoral Dissertation, Johannes Gutenberg University, Mainz, 1995
(6) Argon, A. S.; Cohen,R. E.; Jang, B. Z.; Vander Sande, J. B.: J. Polym. Sci.: Polym. Phys. Ed., vol. 19, (1981), 253
(7) Schwier, C. E., Argon, A. S., Cohen, R. E.: Polymer 26 (1985), 1985
(8) Koltisko, B; Hiltner, A; Baer, E.; J. Polym. Sci. Polym. Phys., 24 (1986), 2167

THE MICRO-HARDNESS OF CRAZED POLYMERS

M. Ensslen[1], G.H. Michler[1], F.I. Baltá-Calleja[2], L. Könczöl[3], W. Döll[3]

One can clearly distinguish between the microhardness of the cracked region, the craze zone and the bulky polymer. The elastic modulus can be calculated from the microhardness measurement.
Craze length detected by microhardness are in good agreement with the vlues calculated from interference optical pattern.

INTRODUCTION

Crazing is a wide occuring phenomenon in polymeric materials. There are a lot of publications concerning shape and microstructure of crazes. Crazes are zones of highly plastically deformed polymer and consist mostly of fibrils along the direction of applied stress. As far as we know there is no publication dealing with the micro-hardness (MH) of craze fibrils and the correlation of craze shape and MH. The aim of this paper is to answer these open questions.
In addition the elastic moduli of the crazed material is calculated.

EXPERIMENTAL

The measurements were done at commercially available poly-styrene (PS), styrene-acrylonitril-copolymers (SAN) and two types of both poly-vinylchloride (PVC) and poly-methyl-methacrylate (PMMA).
The experiments were done at a Shimadzu Dynamic Ultra Micro Hardness Tester DUH 202 with a square pyramidal diamond indenter (136° Vickers) at room temperature. The MH value was calculated from the penetration depth. The load rate was 1.4mN/s and the final load was 10mN. The penetration depth were about 1.5µm. MH was taken after holding the final load for 6s in every case then the sample was reloaded. For each sample the bulk MH was measured separately. Elastic moduli (EM) were calculated according to the procedure established by Doerner and Nix (1).
The MH was measured along the direction of crack propagation. To look for the craze it is necessary to measure first the cracked region, than the crazed and finally the non deformed bulk material. The arrangement of the diagonal of the indenter was along the crack/craze propagation direction. The craze width at the area of indentation was measured by optical microscopy.

[1]Institut für Werkstoffwissenschaft, Martin-Luther-Universität Halle-Wittenberg, Germany
[2]Instituto de Estructura de la Materia, CSIC, Madrid, Spain
[3]Fraunhofer-Institut für Werkstoffmechanik, Freiburg, Germany

Results and Discussion

The MH values of all the investigated samples can be divided into three parts:

1) the MH of the cracked region
2) the MH of the crazed zone and
3) the MH of ther bulk material.

This is illustrated in Figure 1. The MH of the cracked region is considerably lower than the MH of the bulk polymer. And the MH of the crazed zone is much bigger than the MH of the bulk.

To evaluate the MH of the cracked region a very simple geometrical assumption was taken: The diagonal of indentation was reduced by the crack width. Then with the known load and the reduced indentation depth a MH was calculated. This may called reduced MH. The reduced MH was then compared with the bulk MH. It was shown that the deviation of rMH from bulk MH for crack width smaller than 2μm is less than 20%. This deviation is possibly due to surface energies. That means also that this simple procedure is applicable to the calculation of the craze MH neglecting surface energies.

Assuming this, the craze MH was calculated. Figure 4 shows that the craze MH (squares) is at least 20% bigger than the bulk MH (crosses). Furthermore one can assume a fibril volume content of about 50%. That means that the MH of craze fibrils is double the value of the craze MH. This underlines the consideration of highly oriented/highly packed polymer chains in craze fibrils.

An another interesting aspect has to be mentioned: The MH values near the craze tip are smaller than the MH of the bulk polymer. Figure 2 shows a detailed view of Figure 1. The broken lines indicate the accuracy of the bulk MH. It is known from electron microscopic investigations that the crazes fibrils very close to the sample surface are destroyed. The used very small loads cause indentations nearby the sample surface. So it is assumed that crazes with very small craze opening acting under the choosen experimental conditions as cracks.

According to Doerner and Nix [1] the elastic moduli were calculated. To devide bulk modulus from craze modulus a serial model was applied. The results are shown in Figure 5. The squares symbolize the modulus of the entire craze and the crosses the bulk modulus. The moduli of the crazes are at least 10 % bigger than the bulk moduli. An assumed fibril volume content of 50% would double the difference between bulk and craze moduli.

The craze shape was investigated by interference optics. Both craze length and craze opening are detectable. By MH was tried to identify the craze length. The shape of a craze in PS revealed by interference optics is shown. in Figure 3. The corresponding plot of MH vs distance from edge is shown in Figure 2. Accepting the missing values due to distortions at the sample surface one can get the idea of a craze length of about 150μm. This value is comparable to 180μm calculated from the optical interference pattern.

CONCLUSIONS

It is shown that very small craze zones are detectable by means of MH indentation. The MH of crazed material is bigger than the MH of the bulk polymer which is due to the orientation of the polymer chains in the craze fibrils. Also the elastic modulus in the craze is bigger than the modulus of the bulk. The determination of craze length by MH is possible, but less acurate than by other techniques.

ACKNOWLEDGEMENTS

The financial support of Deutsche Forschungsgemeinschaft and Deutscher Akademischer Auslandsdienst is gratefully acknowledged. We acknowledge F. Ania for the helpful discussions.

REFERENCES

1. M.F. Doerner and W.D. Nix, J. Mater. Res. 1 (1986), 601

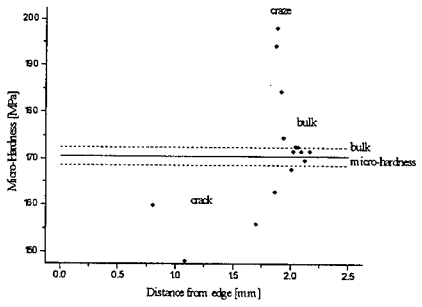

Figure 1: Micro-Hardness in the cracked, crazed and bulky material (PS)

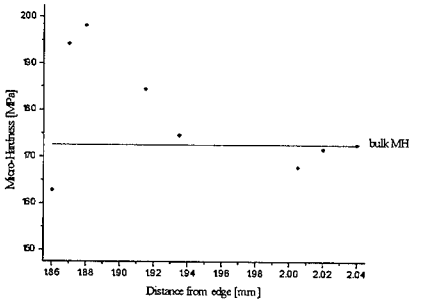

Figure 2: Detailed view on the micro-hardness of different places of a craze in PS along the direction of craze propagation

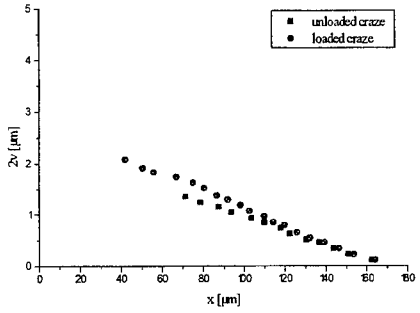

Figure 3: Craze opening and length of a craze in PS measured by interference optics

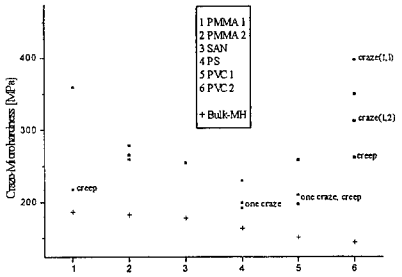

Figure 4: Micro-hardness of crazes (fatigue and creep) of different polymers and the bulk micro-hardness

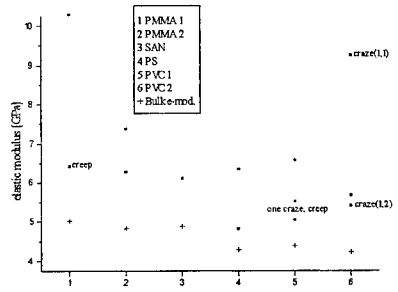

Figure 5: Elastic moduli measured by micro-hardness of crazes (fatigue and creep) of different polymers and the elastic modulus of the bulk

CRACK TIP CRAZES CREATED IN BULK SAMPLES INVESTIGATED BY INTERFERENCE MICROSCOPY AND TRANSMISSION ELECTRON MICROSCOPY

M. Ensslen[1], G. Schulze[1], G. H. Michler[1], L. Könczöl[2], W. Döll[2]

Identical crazes were investigated by high voltage electron microscopy and interference optics. The craze contours are comparable. The microstructure of crazes created under plain strain conditions is similar to the structure of crazes produced in thin films or sections. The accuracy of the determination of the craze structure was proofed by small angle X-ray scattering.

INTRODUCTION

The importance of crazing in polymers was recognized more than 20 years ago, which prompted the beginning of systematic investigations of the structure of crazes in polymers by transmission electron microscopy (TEM) [1-3]. The majority of the experimental observations has been devoted to determing the morphological parameters of large `mature´ crazes introduced by creep and monotonic loading in various homopolymers, copolymers, blends and composites. These studies have established that a typical craze formed under uniaxial deformation is characterized by a network of almost cylindrical fibrils, oriented nearly perpendicular to the craze-bulk interface and parallel to ther external stress [4-9]. The fibrils are composed of highly drawn (oriented) polymeric material, and are often interconnected by `cross-ties´ [10]. The craze morphology and fibril diameter may change depending on the type of the polymer (e.g. entanglement density, molecular weight, crosslinks), and external variables such as temperature, rate of deformation, crazing agents, specimen thickness and other factors [4, 5, 11, 12]. Craze initiation in thin polystyrene (PS) films [13] and thick PS sections [12] has been studied under monotonic loading conditions. It has been found that the formation of localized surface deformation zones or precraze `furrows´ leads to the generation of small voids, which coalesce and grow into large, mature crazes. The existance of such nuclei whose dimensions are significantly larger than the size of the `frozen-in´ density fluctuations was proposed by Argon et. al. [14]. Studies by small angle X-ray scattering (SAXS) showed also the fibrillar structure [15] of the craze and a voided structure [16] of the precraze. Optical microscopy, especially interference optical microscopy (IOM), is the most frequently used method for studying the

[1]Institut für Werkstoffwissenschaft, Martin-Luther-Universität Halle-Wittenberg, D-06217 Merseburg, Germany
[2]Fraunhofer-Institut für Werkstoffmechanik Freiburg, D-79101 Freiburg, Germany

contour of a craze [17, 18].

It should be noted that a combination of several structural methods is frequently employed to study craze structures in polymers (TEM and SAXS can be regarded as complementary in this respect) [8, 9,15]. In a more recent work the size of precrazes were compared by means of TEM and SAXS [16,19] at the same set of samples. But despite of the abundance of microscopic data and scattering pattern, investigations of the same craze by different methods has not been reported. In this paper , we want to report the investigation of the same craze by two independend methods. First we measure the craze contour by IOM and we observe craze contour and structure by TEM.

EXPERIMENTAL

The samples investigated in this work were commercially available products. It were used PMMA, PVC, PS and PC.

Optical interference measurements were made on single crack tip crazes in small compact tensile (CT) specimens (4 x 8 x 10 mm^3). The IOM arrangement and analysis were described previously [20,21]. The samples were loaded at room temperature. Loading conditions were cyclic and static load, slow crack propagation and creep.

After measuring the contour of the single crack tip craze the sample was prepared for TEM investigations. The direction of cutting was perpendicular to the direction of applied stress and parallel to the direction of craze propagation from craze tip to crack tip. The microtomed slices, with thicknesses from 0.5 to 1µm, were lifted off the knife on an adhesive foil.

The specimen were examined in a JEOL High Voltage TEM (HVEM) at an accelerating voltage of 1MV. The HVEM allows a minimal beam damage and also the use of X-ray films to achieve very short exposure times [22].

The comparison of SAXS experiments and electron microscopy was used to distinguish clearly between artifact and true structure in the TEM micrographs.

RESULTS AND DISCUSSION

In this work we want to compare only that crazes which show the same craze length determined by IOM and TEM and IOM investigations.

The accuracy of the structural parameters investigated by TEM was proofed by SAXS

PMMA: The contour of a craze in PMMA is close to a Dugdale shape. But a more detailed view on the craze tip by TEM shows distinct changes in curvature. Especially, a circular shape

of the craze tip was found. The radius of curvature is about 50nm. No regular craze structures as well as fibrils in single crack tip crazes can be reported. The homogeneous structure of a craze is impossible in the case of craze growth under plain strain conditions. The loss of any information on craze structure by TEM investigations of PMMA is due to the very high sensitivity to electron damage of this material. By TEM investigations on thin section no fibrillar structure was found [12]. The sharp interference peak in SAXS measurements is discussed as a scattering of hexagonal packed fibrils [23]. Our SAXS experiments show the validity of both the hexagonal arrangement and the face centred cubic (fcc) packing.

PVC: TEM observations show roughly fibrillated craze structures as well as network like structures. IOM results show on principle a different shape of curvature of the craze contours of PVC1 and PVC2. It was not possible to proof this fact by TEM.

PS: By TEM fibrillated crazes were found. Fibril diameters and fibril thicknesses are similar to the values observed at thin films or sections(5,12).

PC: PC samples were used to study the craze microstructure by SAXS and TEM. Both fibril diameter as well as fibril distance coincide well. The SAXS pattern were extrapolated to zero and infinity. Then fcc or hexagonal packing was assumed and the parameters of the craze-structure were calculated. No value from other experiments (for instance: fibril extension ratio) was necessary.

CONCLUSIONS

The results described above show that the comparision of craze contours in different polymeric materials by means of IOM and TEM is possible. The main point for the coincidence is the craze length. Differences in the craze opening are due to the stress relaxation during the transition from plain strain in the bulk material to the plain stress in the semi thick section. The linear extrapolation of the craze contour derived from IOM towards the craze tip is now our best knowledge.

In PMMA no craze structure was resolvable. At this stage we can not decide whether this is an open or a closed cell structure.

The craze structure of all the PVC samples was an open cell structure near the crack tip. Near the craze tip no structural details were resolvable. We assume that under plain strain conditions void generation is the starting point for craze initiation. The consequence is that craze growth is first the growth of the voids. The craze has a closed cell structure in this initial state. The closed cell structure changes into the open cell structure if the voids grow further.

ACKNOWLEDGEMENTS

This work is supported by the Deutsche Forschungsgemeinschaft under grant no. Mi 358/1 and Do 214/10. We acknowlegde the support of the Max-Planck-Institut für Mikrostrukturphysik using the HVEM.

REFERENCES

1. Kambour, R. P. and Holik, A. S. *J. Polym. Sci. A2* 1969, **7**, 1393
2. Kambour, R. P. and Russel, R. R. *Polymer* 1971, **12**, 237
3. Beahan, P., Bevis, M. and Hull, D. *Phil. Mag.* 1971, **12**, 1267
4. Kambour, R. P. *Macromol. Rev.* 1973, **7**, 1
5. Kramer, E. J. *Adv. Polym. Sci.* 1983, **52/53**, 1
6. Argon, A. S.. Cohen, R. E., Gebizioglu, O. S. and Schwier, C. E. *Adv. Polym. Sci.* 1983, **52/53**, 275
7. Kausch, H.-H. in `Polymer Fracture', Springer, Berlin, 1987, Ch. 9, p. 332
8. Kramer, E. J. and Berger, L. L. *Adv. Polym. Sci.* 1990, **91/92**, 1
9. Argon, A. S., and Cohen, R. E. *Adv. Polym. Sci.* 1990, **91/92**, 301
10. Yang, A. C.-M. and Kramer, E. J. *J. Mater. Sci.* 1986, **21**, 3601
11. Donald, A. M. and Kramer, E. J. *J. Polym. Sci., Polym. Phys. Edn.* 1982, **20**, 899
12. Michler, G. H. in `Kunststoff- Mikromechanik', Carl Hanser, Munchen, 1992
13. Wellinghoff, S. and Baer, E. *J. Macromol. Sci.-Phys.* 1975, **B11(3)**, 367
14. Argon, A. S. and Hanoosh, J. G. *Phil. Mag.* 1977, **36**, 1195
15. Brown, H. R. *Mater. Sci. Rep.* 1987, **2**, 315
16. Hristov, H. A., Yee, A. F., Xie, L. and Gidley, D. W. *Polymer* 1994, **35**, 4287
17. Döll, W. *Adv. Polym. Sci.* 1983, **52/53**, 105
18. Döll, W and Könczöl, L. *Adv. Polym. Sci.* 1990, **91/92**, 137
19. Hristov, H. A., Yee, A. F., and Gidley, D. W. *Polymer* 1994, **35**, 3604
20. Döll, W., Könczöl, L. and Bevan, L. in `Encyclopedia of Polymer Science and Engeneering', John Wiley & Sons, 1987,vol. 9, 745
21. Könczöl, L., Döll, W. and Bevan, L. *Coll. & Polym. Sci.* 1990, **268**, 814
22. Michler, G. H. and Dietzsch, Ch. *Cryst. Res. & Technol.* 1982, **17**, 1241
23. Paredes, E. and Fischer, E.W. *Makromol. Chem.* 1979, **180**, 2707

THE BIAXIAL DRAWING BEHAVIOUR OF POLYETHYLENE TEREPHTHALATE

R.G. Matthews, R.A. Duckett, I.M. Ward*
and D.P. Jones+.

It is shown that the biaxial drawing of poly(ethylene terephthalate) at temperatures above the glass transition temperature T_g can be satisfactorily described by the Ball, Doi, Edwards and Warner model of rubber elasticity, providing that the chain entanglement density is assumed to be a linear function of the logarithmic shear strain rate. With this assumption the behaviour for uniaxial, constant width and equi-biaxial drawing can be fitted by a single set of model parameters.

INTRODUCTION

Much previous research has shown that the uniaxial deformation of poly(ethylene terephthalate) (PET) fibres and films can be described in terms of stretching a molecular network. In this project it was shown that this concept can be extended to the biaxial stretching of PET. This work follows closely that of Sweeney and Ward (ref. 1, 2) where the biaxial drawing of PVC was also modelled by a network model. It was found that the true stress-strain curves for a wide range of shear strain rates could be reproduced by this model, providing the number of chain entanglements was made a function of the shear strain rate. It was considered particularly satisfactory that the same network parameters then produced good predictions for the three drawing modes.

The network model used in this work was that of Ball, Doi, Edwards and Warner (ref. 3 henceforth referred to as the Ball model) as summarised in equation 1, where the free energy, F, for a molecular network at a given state of strain is defined by the principal draw ratios λ_1 , λ_2 and λ_3.

$$\frac{F}{kT} = \frac{1}{2} N_c \sum_i \lambda_i^2 + \frac{1}{2} N_s \sum_i \left(\frac{(1+\eta)\lambda_i^2}{1+\eta\lambda_i^2} + \ln\left(1+\eta\lambda_i^2\right) \right) \qquad 1$$

where N_c= cross link density, N_s= chain entanglement density and η describes the freedom of the entanglements. The principal stresses, σ_{ii}, corresponding to the state of strain of the rubber can be calculated using equation 2 where p is a hydrostatic pressure term.

$$\sigma_{ii} = \lambda_i \frac{\partial F}{\partial \lambda_i} + p \qquad 2$$

EXPERIMENTAL

The 700μm thick isotropic and amorphous PET film examined in this work, supplied by ICI plc, had an initial density of 1337kg/m^3, an initial birefringence of 0.0010 and an intrinsic viscosity of 0.6. The film was drawn at 85°C at a constant true strain rate in three modes at constant width, equi-biaxially and uniaxially on a rig, designed and built in-house (ref. 1, 2).

For a given deformation mode the level of stress can usually be related to any one of the principal strain rates but in comparing drawing modes this is no longer adequate. In

* IRC In Polymer Science And Technology, The University of Leeds, Leeds LS2 9JT, UK
+ ICI Polyester, PO Box 90, Wilton, Middlesborough, Cleveland TS90 8JE, UK

describing the general deformation of polymers with a rubber network model the concept of equivalent deformations has therefore to be introduced. A more general measure of the total deformation rate is needed that combines the effects of all the applied principal strain rates. Following Sweeney and Ward (ref. 1, 2) it is assumed that the octahedral shear strain rate is the appropriate measure of deformation rate i.e. by performing different drawing modes at the same octahedral shear strain rates, results from all drawing modes can be described by the same set of model parameters. The relationship between the octahedral shear strain rate $\dot{\gamma}$ and the principal strain rates, $\dot{e}_{ii}$ for i=1, 2 and 3 is given as (ref. 1, 2)

$$\dot{\gamma} = \frac{-1}{9\tau_{oct}}\left((\sigma_{33} - 2\sigma_{11})\dot{e}_{11} + (\sigma_{33} + \sigma_{11})\dot{e}_{22} + (\sigma_{11} - 2\sigma_{33})\dot{e}_{33}\right)$$

where τ_0 is the octahedral shear stress σ_{11} and σ_{33} are the principal stresses in the 1 and 3 axes respectively and σ_{22}=0. Therefore when the principal draw direction is in the 3-axis we get:

Uniaxial Shear Strain Rate $$\dot{\gamma} = \frac{\sqrt{2}\dot{\lambda}_3}{3}\left(1 + \frac{1}{2}\lambda_3^{-3/2}\right) = \frac{\sqrt{2}}{3}\frac{d}{dt}\left(\lambda_3 - \lambda_3^{-1/2}\right)$$

Equi-biaxial Shear Strain Rate $$\dot{\gamma} = \frac{\sqrt{2}\dot{\lambda}_3}{3}\left(1 + 2\lambda_3^{-3}\right) = \frac{\sqrt{2}}{3}\frac{d}{dt}\left(\lambda_3 - \lambda_3^{-2}\right)$$

Constant Width Shear Strain Rate $$\dot{\gamma} = \frac{\sqrt{2}\dot{\lambda}_3}{3\sqrt{a^2 - a + 1}}\left(1 - \frac{a}{2} + \frac{1+a}{2}\lambda_3^{-2}\right).$$

The situation of drawing at constant width is more complicated because it involves less symmetry so the shear strain rate is dependent on the ratio of the principal stresses, $a = \frac{\sigma_1}{\sigma_3}$, as shown above.

The most important feature of the curve fitting process is that the values for the parameters in the network model are obtained by fitting the true stress-strain curves for constant width drawing where there are two different principal stresses to be fitted to the same model parameters. This has been shown by previous work (ref. 1, 2) to be a much more effective procedure than either fitting to uniaxial or equi-biaxial drawing where one principal stress is measured.

The photo-elastic behaviour of the PET film was also examined to gain evidence to support the presence of a rubber-like network. The birefringence of an extended Gaussian rubber-like network has been shown to have a linear dependence on the true stress. Samples of the isotropic PET film were drawn uniaxially at 85°C to draw ratios between 1.7 and 3.3 to produce a range of orientations and true stresses. Folowing drawing the samples were held at constant length, at 85°C, allowing the stress to relax until they were all at the same true stress before rapid cooling to below T_g. If the behaviour were rubber-like they should all have the same level of birefringence.

RESULTS AND DISCUSSION

From the curve fitting to the constant width data the value of N_c was found to be zero, which is consistent with the absence of chemical cross linking in PET. η was also found to be a constant at 0.083. Only N_s was found to be a rate dependent parameter with

$$N_s kT = 0.398\ln(\dot{\gamma}/\dot{\gamma}_0) + 3.252$$

for shear strain rates in the range $5\times10^{-3}s^{-1}$ to $0.5s^{-1}$, where $\dot{\gamma}_0=1$. An example of the fit obtained to the constant width data is shown in figure 1(a).

The fitting to uniaxial and equi-biaxial data is less accurate than for the constant width drawing so assumptions were made to simplify the situation. It was proposed that the values of the rate independent parameters N_C and η obtained from the constant width experiments should be used in the curve fitting to the data from the other drawing modes.

Examples of the excellent fits obtained to the experimental data when only N_S is allowed to vary with the shear strain rate are shown in figures 1(b) and 1(c). In figure 2 comparison is made of the rate dependence of N_S for all three drawing modes and it shows that they exhibit the same dependence. This result confirms the suggestion that different drawing modes can be performed equivalently by drawing at equivalent shear strain rates.

These results give rise to a value for the number of monomers per chain increasing from 7 to 17 as the shear strain rate is reduced from $0.135s^{-1}$ to $0.0067s^{-1}$ because the entanglement density is a function of the shear strain rate. Previous research has suggested a value of 15 (ref. 4).

In figure 3 the birefringence of the drawn PET samples, before and after relaxation is plotted against the applied draw ratio. It shows that at draw ratios below 2.2, the birefringence, of the samples relaxed to a fixed stress, is independent of the final draw ratios which is a feature of rubber-like behaviour. At draw ratios higher than 2.2 the birefringence of the relaxed samples increases with increasing draw ratio, probably due to strain crystallisation locking-in the network extension. At draw ratios above 3 the sample birefringence actually increases during the stress relaxation test because annealing probably increases the crystallinity and the orientation for these samples. These results suggest that at draw ratios above 2.2 the rubber-like behaviour of the PET is perturbed by strain induced crystallisation rather than the stress optical law breaking down due to the high stress level (ref. 5).

AKNOWLEDGEMENTS

We would like to thank EPSRC and ICI plc for their financial support for this project.

REFERENCES

1. J. Sweeney, I.M. Ward, Polymer, Polym., **36**, (1995), 299.
2. J. Sweeney, I.M. Ward, Trans. Inst. Chem. Eng., **5**, (1989), 593.
3. R.C. Ball, M. Doi, S.F. Edwards, M. Warner, Polymer, **22**, (1981), 1010.
4. S.D. Long, I.M. Ward, J. Appl. Poly. Sci., **42**, (1991), 1921-1929.
5. M. Doi, S.F. Edwards, The Theory Of Polymer Dynamics, 1986, Clarendon Press, Oxford.

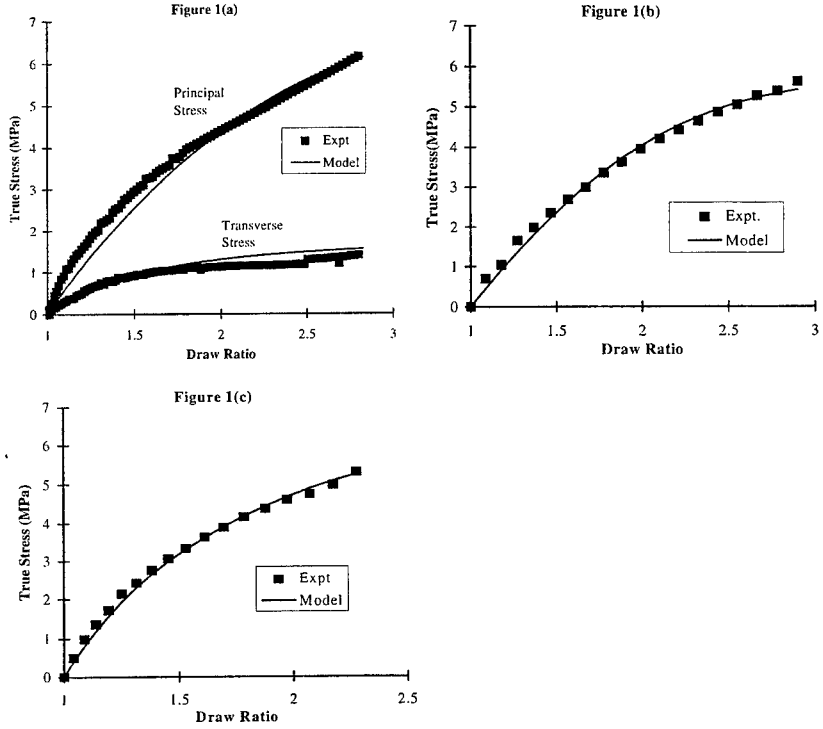

Fig 1. Fitting the Ball model to the constant width drawing of PET at 85°C at a constant shear strain rate Of $0.025s^{-1}$ where N_c =0 and η=0.0833 and N_s is left free a) Constant width, b) Equi-biaxial and c) uniaxial.

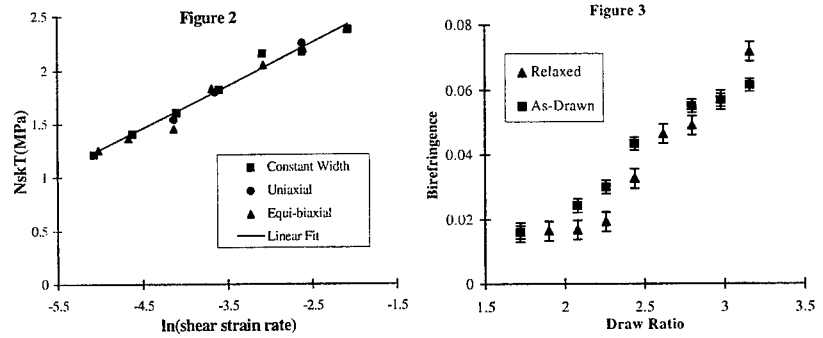

Fig 2. Comparing the N_skT values obtained from curve fitting to the true stress strain curves for PET drawn at 85°C assuming N_c=0 and η=0.083.

Fig 3. The effect on the birefringence of allowing PET samples drawn uniaxially at 85°C at a shear strain rate of $0.04s^{-1}$ to relax at 85°C to the same true stress.

MICROSCOPIC IN-SITU CHARACTERIZATION OF THE CONSTRAINED PLASTIC DEFORMATION OF A POLYMERIC MATRIX IN A COMPOSITE

C. Briançon*, S. Chambaudet*, P. Sigety*, C. G'Sell+

The attempts to improve the resistance of transverse plies in carbon fibre laminated composites through the substitution of brittle matrices (epoxies) by much tougher polymers, gave unsatisfactory results. In order to give a relevant explanation to this failure, experimental work has been carried out on both a brittle thermoset and a more ductile thermoplastic, each as a neat resin and as the matrix of a transversally loaded unidirectional composite. Although tensile and compression tests on plain resins reveal major behavioural differences, a mode-I crack propagating in the associated composites displays similar large-strain yielding and fracture processes. Moreover, the dissipation zone remains strictly limited by the surrounding fibres, inducing a globally brittle behaviour.

INTRODUCTION

Carbon/resin laminates always include plies oriented off the axes of the external loading in order to improve the transverse strength of a composite structure. As they are subjected to the same strain as the longitudinal plies, multiple transverse cracking occurs at low global deformation causing a decrease of overall stiffness and initiating other types of damage such as local delamination and fibre fracture[1]. This critical problem in composite materials technology has led to extensive studies on the effects of the matrix on transverse failure. While impact tolerance and interlaminar fracture toughness were significantly improved through the development of tougher matrices, no equivalent result was achieved on transverse cracking which remains a major concern for designers and engineers. The aim of this paper is to present experimental results on strain mechanisms inside a composite material. First, tension and compression tests were performed on unreinforced resins in order to study their features in terms of strain capability: a brittle epoxy thermoset (STRUCTIL DA508) and a ductile amorphous PolyPhenylSulfone thermoplastic (AMOCO Radel8320). Then, these results were related to those from the same polymers used as matrices of unidirectional composites (T300J/DA508, T650-42K/Radel8320) subjected to transverse loading. These tests are performed inside the chamber of a Scanning Electron Microscope (SEM), and consist in propagating a single crack on CT-shaped specimens. A microlithographic technique to reveal local matrix strains inside the composite on the fibre scale was elaborated through the use of microgrids settled on specimen surfaces.

PLASTIC BEHAVIOUR OF NEAT RESINS

Mechanical properties were characterized through tension and compression tests for both polymers. For this study, we applied a video-controlled materials testing system which was described elsewhere[2]. In contrast with conventional tests, these procedures are based on the local control of strain, strain-rate and stress in a specific zone of the specimen, instead of the overall values of these variables.

* Direction Scientifique des Matériaux, ONERA, 29 avenue de la Division Leclerc, BP 72, 92322 Châtillon, France
+ Ecole des Mines-INPL, LMPSM (CNRS 155), Parc de Saurupt, 54042 Nancy, France

The specimens are axisymetric: hour-glass-shaped in tension, and cylindrical in compression. True strain is measured at the mid-plane in real time through the analysis of the video image of the deforming specimen acquired by a digital interface (Figure1). This real-time process offers major advantages in terms of constitutive law and representative volume element approaches: (i) true strain, $\varepsilon = 2\ln(D_0 / D)$, is representative of the local strain across the mid-plane; (ii) the displacement of the servo-hydraulic testing machine is controlled by a digital closed-loop system in such a way that the local strain-rate $\dot{\varepsilon}$ is maintained constant; (iii) local stress is given by $\sigma = F_T(4F / \pi D^2)$, where F_T represents the Bridgman triaxiality factor which converts the complex measured stress due to the sample necking or bulging into its uniaxial equivalent. Results obtained for both tension and compression until rupture at a strain rate of 5.10^{-4} s^{-1} are presented in Figure 2, and the values of yield stress and of strain at rupture are displayed in table 1.

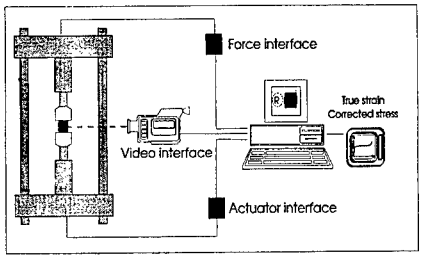

Figure 1. Video-controlled testing system

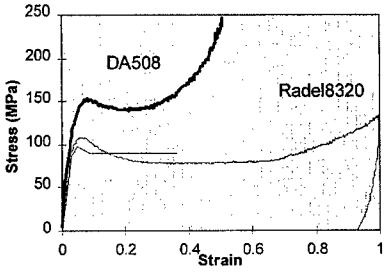

Figure 2. Stress-strain curves

Table 1. Mechanical properties of the unreinforced resins under tension and compression

	Tension		Compression	
	σ_{Yield} (MPa)	$\varepsilon_{Rupture}$	σ_{Yield} (MPa)	$\varepsilon_{Rupture}$
DA508	94 (Rupture)	0.024	153	0.50
Radel8320	98	0.36	108	1.11

The above results show that the thermoplastic resin undergoes large plastic deformation while the epoxy resin fractures much earlier. Optical and SEM fractography studies reveal no significant damage prior to rupture inside those polymers. Additionally, compression tests performed on samples with various initial height-to-diameter ratios, show that specimen geometry has no significant influence on the stress-strain response. Furthermore, compression tests performed at different strain-rates ranging from $5.10^{-5}s^{-1}$ to $5.10^{-3}s^{-1}$, lead to a strain-rate sensitivity coefficient, $m = (\partial \ln\sigma / \partial \ln\dot{\varepsilon})_{\varepsilon}$, equal to 0.027 and 0.020 for DA508 and Radel8320 respectively; this indicates the somewhat viscous nature of their mechanical behaviour.

IN-SITU OBSERVATION OF THE MATRICES DEFORMATION

It was previously shown[3] that the large modification of plastic deformation capability only leads to minor improvements in terms of ultimate strain of the associated composites subjected to transverse tension. Since no relative macroscopic parameter could explain this

lack of properties improvement, a miniature testing machine (Figure 3) was designed to study strain mechanisms, on the fibre scale, of an unidirectional composite inside a SEM.

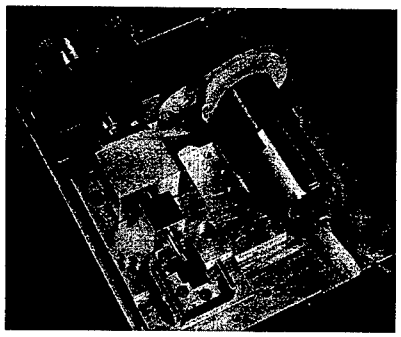

Figure 3. SEM testing machine

The testing procedure consists in the very slow opening of the notch of a CT-shaped specimen, due to the motorized introduction of a low-angle wedge. The fibre direction is perpendicular to the faces of the specimen in order to observe strains in the transverse plane. The formation and propagation speed of a single crack is monitored through the real-time observation of strain rates ahead of its tip (Figure 4).

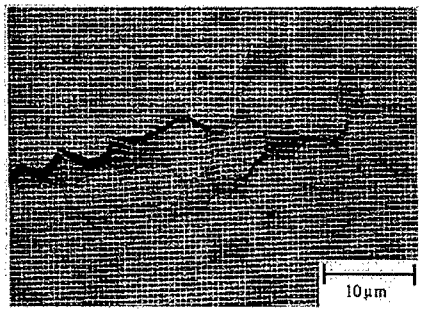

Figure 4. Propagating crack in the composite

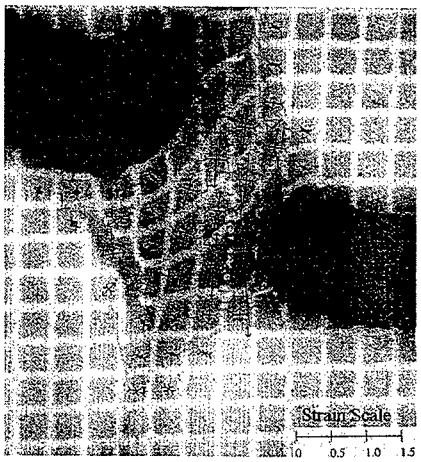

Figure 5. Local strain gradients

Since observed interfibre spacing ranges from 0.5 to 5µm in these composites, the average local strains in the matrix can be revealed by the comparison of distorted gold microgrids with their appropriate initial square dimensions of 0.6µm x 0.6µm. A microlithographic technique using the SEM-controlled irradiation of a thin coating of PMMA, previously spread on the sample, was used to obtain the microgrids. With the same standard fibre volume fraction of

0.6, both types of composites unexpectedly display similar crack propagation mechanisms and localized high-strain gradients up to nearly 50-100% (Figure 5): (i) competition occurs between matrix failure and interfacial debounding around the fibres neighbouring the crack tip. (ii) microcracks are bridged by plastically deformed matrix ligaments whose final rupture depends upon the initial ductility of the polymers. It is remarkable in Figure 4 that the plastic strain on the resin remains constrained by the nearest fibres. Moreover, on this scale, the strain heterogeneities are diffuse and no shear band is observed.

DISCUSSION AND CONCLUSION

Constitutive laws of resins are derived from tension and compression tests carried out on neat resin specimens. The recorded differences do not entail such contrasted behaviour on the associated composites. Quite unexpectedly for such a triaxial state of stress, both matrices display a very high local strain level. Crack propagation corresponds to a competition between interfacial debounding and matrix failure, which both occur prior to large-strain yielding. Their relative contribution to failure initiation can be modified by a change in the interfacial strength[3]. In no case, a spreading of the plasticized zone beyond the nearest fibres seems possible. Qualitatively, this study shows that extensive plastification is not an effective process for energy dissipation inside composites and other mechanisms should be explored like rubber micro-spheres addition inside the matrices. Current work concerns numerical simulation of constrained plasticity with a Finite Element code. This will take two parameters into account: (i) fibres volume fraction and distribution, and (ii) matrix constitutive law.

REFERENCES

1. Garrett, K.J. & Bailey, J.E., 1977, The effect of resin failure strain on the tensile properties of glass fibre-reinforced polyester cross-ply laminates, J. Mater. Sci., 12, 2189.
2. G'Sell, C., Hiver, J.M., Dahoun, A. & Souahi, A., 1992, Video-controlled tensile testing of polymers and metals beyond the necking point, J. Mater. Sci., 27.
3. Briançon, C., Sigety, P. & G'Sell, C., 1996, In-situ study of matrix strain in carbon-resin composite materials, Comp. Sci. Technol., 56, 835.

PLANE-STRAIN TENSILE BEHAVIOUR OF BIAXIALLY DRAWN POLY(ETHYLENE TEREPHTALATE) SHEETS

A. Aubert*, C. G'Sell*, J.M. Hiver* and M. Aboulfaraj**

Bi-oriented plates of polyethylene terephtalate were stretched under plane-strain tension at different draw temperatures and strain rates by means of an original video-controlled testing system which gives direct access to the intrinsic strain-stress behaviour of flat samples. Analysis and calculation based on tensile experiments and a general plasticity theory show that the experimental set up with a very short calibrated length can be adopted as a valuable plane-strain test.

INTRODUCTION

For several years, emergence of polyethylene terephtalate (PET for short) has been successful in packaging, specially in bottles for soft drink. In the same time, an important effort was performed by scientists to study PET mechanical behaviour in relation with its structure (orientation and induced crystallization).

Regarding our work, we want to analyse mechanical behaviour of PET during its processing and its use for a packaging application, which implies the determination of constitutive equations. For this, we have used the video-controlled tensile testing technique developed at the Ecole des Mines de Nancy for several years (1) by adapting this technique to the case of plane strain tension of PET sheets.

The main objective of the present work is to present this novel technique and its application to our samples.

MATERIAL AND METHODS

Bi-oriented plates of PET, about 0.8 mm thick, were obtained by equi-biaxial stretching at a draw ratio of 1.8 x 1.8. Square test pieces, 25 x 25 mm^2, are carefully cut from these plates and notched on the vertical sides in order to define a very short calibrated length and thus to confine the deformation in the middle plane of samples (figure 1). The upper and lower parts serve to be clamped in the grips of the servo-hydraulic tensile testing machine.

Plane geometry of the samples allows them to be subjected to subsequent stretching experiments under plane-strain tension by means of a new variant of the original video-controlled testing system (VideoTraction©) (figure 2) especially developed for determining the intrinsic stress-strain behaviour of flat samples (films, sheets and plates) at various temperatures and strain rates.

* Laboratoire de Métallurgie Physique & Science des Matériaux (CNRS 155)
Ecole des Mines de Nancy - INPL, Parc de Saurupt, 54042 Nancy, France
** Pechiney, Centre de Recherche de Voreppe, BP 27, 38340 Voreppe, France

The deformation of the material is assessed from the current distortion of a close array of four fluorescent ink dots initially printed onto the samples prior to deformation. These markers (of a diameter less to one millimetre) are revealed by an ultraviolet illuminator and monitored by a video camera interfaced with a fast image processor which analyses in real time the extension ratio, λ_1, between the two particular dots aligned vertically along the stretching axis. The axial true strain is thus $\varepsilon_1 = \ln\lambda_1$. Also, the in-plane transverse strain, $\varepsilon_2 = \ln\lambda_2$, is determined from the contraction, λ_2, between the two markers aligned along the horizontal axis. The axial true stress, σ_1, is defined as the current load applied to the specimen divided by the actual cross section of the sheet at the location of the analysed markers. This cross section is calculated from the initial cross section and the current true strain, within the assumption of isochoric deformation. Furthermore, a digital closed loop system controls the ram speed of the hydraulic tensile machine in such a way that the true strain rate, $\dot{\varepsilon}_1 = d\varepsilon_1 / dt$, is maintained at a constant value during the whole test.

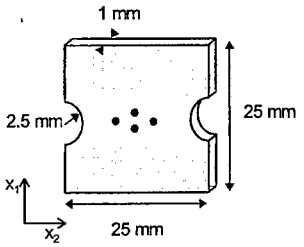

figure 1 :
plane geometry used for plane strain tension

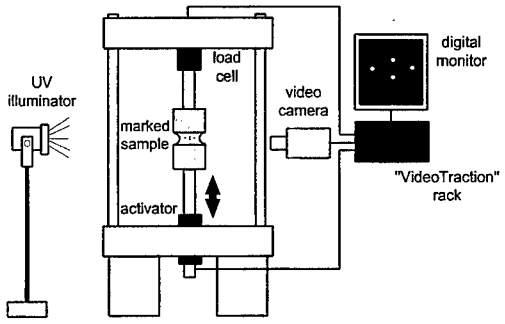

figure 2 :
general diagram of video-controlled tensile testing system

RESULTS AND DISCUSSION

For tests performed at temperatures ranging from 30°C to 70°C, the curves in figures 3 and 4 show an initial viscoelastic stage, followed by a yield transient marked by a small but significant stress drop whose amplitude increases with $\dot{\varepsilon}_1$. At the sub-T_g temperatures under investigation, the experiments show the onset of a neck at yield, perpendicularly to the tensile direction. Nevertheless, thanks to local strain control, this plastic instability does not impede data acquisition. Subsequently, strain hardening develops until rupture occurs at $\varepsilon_1 \approx 0.5$ (*i.e.* $\lambda_1 \approx 1.65$).

The respective influence of strain rate and temperature on the plastic behaviour of the PET sheets is analysed. As it is observed in figures 3 and 4, increasing strain rate or reducing draw temperature result in an increase of plastic flow stress. This is due, in part, to the decrease of the enthalpic component of the flow stress in the glassy structure (2) and, in part, to the decrease of the induced orientation of the macromolecular network (3). The fact that $\sigma(\varepsilon)$ are nearly parallel for different conditions promotes the former contribution.

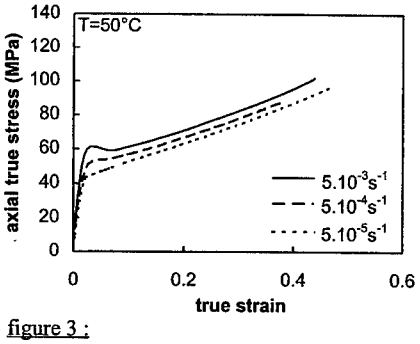

figure 3 :
strain rate influence on tensile behaviour

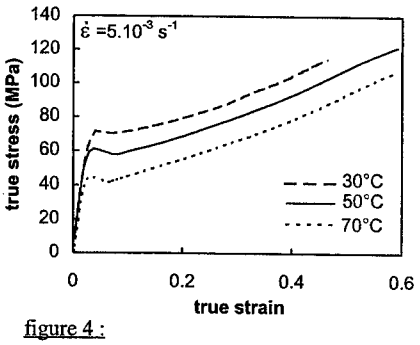

figure 4 :
temperature influence on tensile behaviour

Although the sample geometry was designed to generate a plane strain path (ideally $\varepsilon_2 = 0$), it is observed in our tests that a definite strain occurs in the transverse direction, about 10% of the axial strain ε_1 (figure 5). Therefore, it is important to analyse the influence of this offset of strain path on the recorded stress-strain behaviour. In a first approximation, we choose to tackle this point within the frame of : i) isotropic, ii) isochoric and, iii) strain rate dependant J_2 associated law (Norton-Hoff formalism). The effective stress-strain-strain rate relationship is supposedly identical in each strain path :

$$\bar{\bar{s}} = \frac{2}{3}\frac{\sigma_{eff}(\varepsilon_{eff},\dot{\varepsilon}_{eff})}{\dot{\varepsilon}_{eff}}\bar{\bar{\dot{\varepsilon}}} \qquad [1]$$

In the case of PET, considering that the stress drop at yield is quite limited, it is not illegitimate to adopt the G'Sell-Jonas constitutive equation (4) to represent the intrinsic behaviour.

$$\sigma_{eff}(\varepsilon_{eff},\dot{\varepsilon}_{eff}) = K\left(1-\exp(-w\varepsilon_{eff})\right)\exp\left(h\varepsilon_{eff}^2\right)\dot{\varepsilon}_{eff}^m \qquad [2]$$

This equation where the 'effective' variables are defined in the sense of von Mises, and originally introduced for highly crystalline polymers, was already utilised for modelling the strain hardening of PET by Marquez-Lucero (5). This formalism rewrites under explicit expressions according to the specific strain path considered :

- for uniaxial tension, the stress-strain relation along the tensile axis, $\sigma(\varepsilon,\dot{\varepsilon})$, has a form identical to the effective stress-strain equation [2] :

$$\sigma(\varepsilon,\dot{\varepsilon}) = K\left(1-\exp(-w\varepsilon)\right)\exp\left(h\varepsilon^2\right)\dot{\varepsilon}^m \qquad [3]$$

- for plane-strain tension ($\varepsilon_2 = 0$), the required axial stress is higher than the effective stress, because of the transverse stress induced by the transverse constraint :

$$\sigma_1(\varepsilon_1,\dot{\varepsilon}_1) = 1.155K\left(1-\exp(-1.155w\varepsilon_1)\right)\exp\left(1.133h\varepsilon_1^2\right)\left(1.155\dot{\varepsilon}_1\right)^m \qquad [4]$$

- for 'quasi plane' tension with a transverse strain ε_2 about 10% of axial strain ε_1 :

$$\sigma_1(\varepsilon_1,\dot{\varepsilon}_1) = 1.149K\left(1-\exp(-1.102w\varepsilon_1)\right)\exp\left(1.213h\varepsilon_1^2\right)\left(1.102\dot{\varepsilon}_1\right)^m \qquad [5]$$

Following the above correction procedure, the parameters of the constitutive equation are readily obtained : for instance, at 50°C, K=35 MPa, w=75, h=1.42, m=0.04. As it is shown in figure 6, the intrinsic behaviour related to the 'quasi plane-strain' path corresponds to an

intermediate state between uniaxial and plane-strain tensile behaviour. However, in the practical case under investigation ($\varepsilon_2 = 10\%\ \varepsilon_1$), the stress-strain curve is quite close to the ideal plane-strain response, within the range of experimental errors.

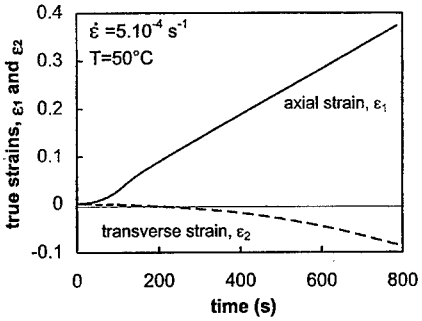

figure 5 :
comparison of transverse and axial strain during tensile experiments

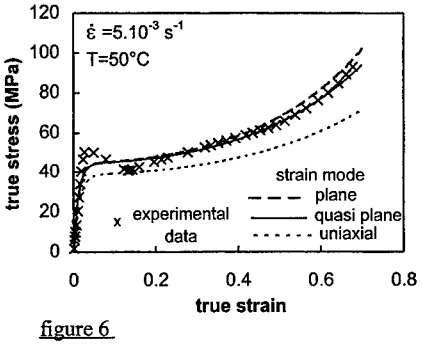

figure 6
comparison of three strain paths

CONCLUSIONS

A novel tensile testing was developed for the determination of the plastic behaviour of flat polymer samples tested under nominally plane-strain conditions. It is based on real-time image processing of fluorescent ink markers and on the automatic control of the local strain rate in order to obtain the intrinsic true strain-stress behaviour of the material.

By means of this technique, tensile tests were performed with sheets PET at different temperatures and strain rates within the sub-T_g range. The respective influence of strain rate and temperature on the constitutive behaviour of the PET sheets was analysed.

On the basis of reasonable assumptions (Norton-Hoff plastic flow formalism and G'Sell-Jonas constitutive law), it was shown that the discrepancy observed with respect to the ideal plane-strain condition ($\varepsilon_2 \approx 0.1\varepsilon_1$ instead of $\varepsilon_2 = 0$) causes practically negligible errors in the parameters of the effective stress-strain relation.

REFERENCES

1. G'Sell C., Hiver J.M., Dahoun A., Souahi A., J. Mater. Sci. 27 (1992) 5031
2. Argon A.S., Phil. Mag. 28 (1973) 839
3. LeBourvellec G., Monnerie L., Jarry J.P., Polymer 28 (1987) 1712
4. G'sell C., Jonas J.J., J. Mater. Sci. 14 (1979) 583
5. A.Marquez-Lucero, C.G'Sell, Polymer 34 (1993) 2740

APPLICATION OF RELAXATION THERMODYNAMICS TO THE MODELLING OF POLYMERS CREEP

B Paysant-Le Roux [*], Z Ayadi [**], P Marceron [**], C G'Sell [*], C Cunat [**]

An application of the Distribution of Non Linear Relaxations (DNLR) theory based on nonequilibrium thermodynamics of continuous media is proposed to predict the creep for two industrial polymers : polycarbonate (PC) and polyvinylidene fluoride (PVDF) whose experimental data are available at various stresses for a fixed temperature. The results are discussed in terms of the influence of each parameter on i) the different creep stages, ii) the relaxation times and, iii) the evolution of free energy in deformation and restoration.

MODEL

According to thermodynamic approach of relaxation, a previous work was developed by Cunat (1-2) to predict the behaviour of materials subjected to complex loading histories. Constitutive laws from this approach can be summarised by a set of two general relationships, one concerning the evolution of the state variables and the other concerning the evolution of dissipative variables such as affinities *i.e.* thermodynamic forces. State variables are either observable variables or experimentally controlled variables. Dissipative variables determine the advancement degree of internal reorganisation modes.

This model is formulated by assuming two fundamental assumptions at material point scale : i) whatever the time, the continuous medium is considered as an homogenised medium which is characterised by a Representative Elementary Volume (VER) without gradient for state variables, ii) the internal thermodynamic equilibrium is not reached, the VER is in local nonequilibrium state. Consequently, it tends to move spontaneously towards internal equilibrium by relaxation processes.

Gibbs' generalisation, according to De Donder, is the starting point of the present thermodynamic formulation. A couple of dissipative variables $(\bar{z}, \bar{A})$ is introduced to characterise the internal reorganisation ; the vector $\bar{z}$ is a set of order parameters and the vector $\bar{A}$ is the associated set of affinities. Thus, the variation of the generalised potential is given by :

$$\dot{\psi} = \underline{\beta}\,\underline{\dot{\gamma}} - \bar{A}\,\dot{\bar{z}} \qquad (1)$$

where $\underline{\beta}, \underline{\gamma}$ are state variable vectors and $\bar{A}, \bar{z}$ dissipative variables. The constitutive laws which link the couples of dual state variables $(\underline{\beta}, \underline{\gamma})$ and dissipative variables $(\bar{A}, \bar{z})$ derive directly from the potential ψ :

$$\underline{\dot{\beta}} = \underline{\underline{a}}^{u}\,\underline{\dot{\gamma}} + \bar{\underline{b}}\,\dot{\bar{z}} \quad ; \quad \bar{A} = -\bar{\underline{b}}^{t}\,\underline{\dot{\gamma}} - \bar{\bar{g}}\,\dot{\bar{z}} \qquad (2\text{-}3)$$

$\underline{\underline{a}}^{u}$, $\bar{\underline{b}}$, $\bar{\underline{b}}^{t}$, and $\bar{\bar{g}}$ are matrixes build by second derivatives of ψ ($\bar{\underline{b}}^{t}$ transposed of $\bar{\underline{b}}$).

[*] LMPSM (CNRS 155), Ecole des Mines, Parc de Saurupt 54042 Nancy Cedex, France.
[**] LEMTA (CNRS 875), ENSEM, BP 3, 54501 Vandoeuvre, France

In the case of unidirectional creep, $\varepsilon(t)$ was obtained by Ayadi (4) from the above formalism

$$\dot{\varepsilon}(t)=\sum_{j}^{r}\dot{\varepsilon}_j(t)=\underbrace{-\sum_j\frac{\varepsilon_j^{tr}-\varepsilon_j^{r}}{\tau_j^{u\to r}}-\sum_j\frac{\varepsilon_j^{tr}-\varepsilon_j^{u}}{\tau_j^{u\leftarrow r}}-\sum_j\frac{\varepsilon_j^{u}-\varepsilon_j^{r}}{\tau_j^{u\leftarrow r}}}_{\text{dissipative part}} \tag{4}$$

where $\tau_j^{u\to r}=\frac{h}{kT}\exp\frac{\left(\Delta G^{+*\,u\to r}+K\left(\varepsilon-\varepsilon^{r}\right)\right)}{RT}$; $\tau_j^{u\leftarrow r}=\frac{h}{kT}\exp\frac{\left(\Delta G^{+*\,u\leftarrow r}+K\left(\varepsilon-\varepsilon^{u}\right)\right)}{RT}$ (5–6)

with $\Delta G^{+u\to r}=\Delta G^{+*\,u\to r}+K\left(\varepsilon-\varepsilon^{r}\right)$; $\Delta G^{+u\leftarrow r}=\Delta G^{+*\,u\leftarrow r}+K\left(\varepsilon-\varepsilon^{u}\right)$ (7–8)

The delayed dissipative response is described by a set of internal reorganisation modes associated with relaxation times deduced from the Prigogine's fluctuation theory (3). It is analysed as resulting of the competition between deformation and restoration processes, each one being governed by a kinetic law. The application of an incremental scheme made possible to model different testing conditions such as yield, relaxation and creep (4-5). The summation on j can be performed by using the initial relaxation spectrum deduced from the analysis of the fluctuations near the equilibrium :

$$\frac{\varepsilon_j^{u}-\varepsilon_j^{r}}{\sum_j(\varepsilon_j-\varepsilon_j^{r})}=B\sqrt{\tau_j^{*}} \tag{9}$$

true for $u\to r$ and $r\leftarrow u$ processes. (B : constant for relaxation spectrum)

COMPARISON BETWEEN SIMULATIONS AND EXPERIMENTAL DATA

In order to assess the capability of the theoretical model to reproduce typical creep data, we analysed the experimental response of two industrial polymers namely polycarbonate (PC) and polyvinylidene fluoride (PVDF) for which strain vs. time curves, obtained at fixed temperatures for different stresses, were kindly provided by General Electric and Solvay, respectively.

In the case of polycarbonate (figure 1), a very good agreement is obtained under a simple linear approximation by setting K = 0. The whole creep process is described through four parameters E^{u}, E^{r}, $\Delta G^{*\,u\to r}_{max}$, $\Delta G^{*\,u\leftarrow r}_{max}$ determined either from the method of Marceron (6), adapted from an empirical approach by Garofalo (7), or by the Newton-Gauss method.

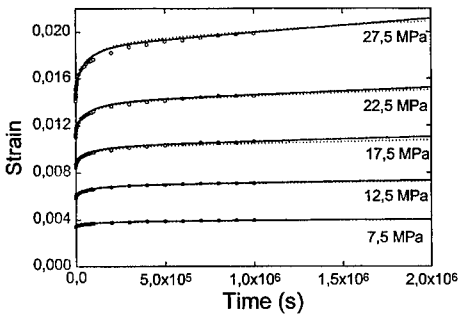

figure 1 : *Comparison of experimental creep data and simulated curves for PC at 60°C for various stresses*

°°°° experimental data
— simulated curves (Marceron method)
..... simulated curves (Newton-Gauss method)

In the case of PVDF, the above approximation fails and modelling requires a more sophisticated, non linear treatment involving $K \neq 0$. In other words, that means that the activation free enthalpy varies under creep with the actual microstructural state, similarly as observed by Cunat (8) for ageing behaviour of glasses. The simulation requires now five adjustable parameters. A correct set of parameters can be found to reproduce transient, secondary and tertiary creep stages in the experimental range. The results are presented in figure 2. The upturn of the curve is ascribed to tertiary creep induced by damage. Figure 3 represents time evolution during the creep test of the two activation free enthalpies involved in the model.

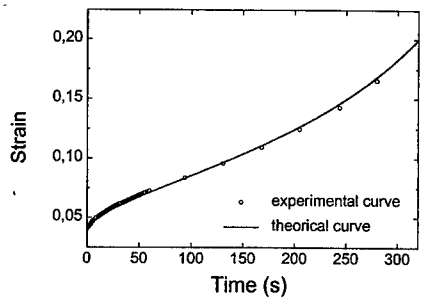

figure 2 : *Comparison between experimental data and creep model for PVDF at 95°C for σ =22 MPa*

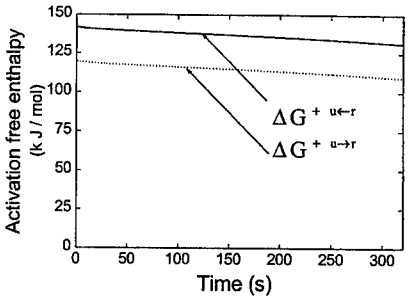

figure 3 : *Evolution of the activation free enthalpy versus time for PVDF during the creep test presented in figure 2*

DISCUSSION

We will examine here two specific aspects of the model. The first point concerns the role of the four parameters (when K = 0) on the shape of the creep curves (figure 4). The bold curve corresponds to the best fit for polycarbonate under σ = 12,5 MPa and T = 60°C

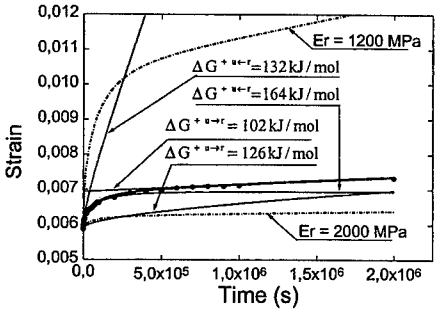

figure 4 : *Effect of model parameters on the creep deformation calculated by varying each time only one of the 4 parameters determined by the minimisation*

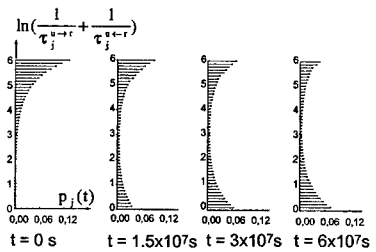

figure 5 : *Evolution of the 50-process fluctuation distribution spectrum versus time during creep*

with the reference parameters, $E^u = 2119\,MPa$, $E^r = 1801\,MPa$, $\Delta G^{+u\to r} = 116\,kJ/mol$ and $\Delta G^{+u\to r} = 144\,kJ/mol$. The other curves are obtained by changing one parameter only as indicated on figure 4. The second point deals with the prediction of the induced change in relaxation spectrum by the equation :

$$p_j(t) = \frac{\varepsilon_j(t)}{\sum_j \varepsilon_j(t)} = f(\ln \tau_j) \qquad (10)$$

It is presented on figure 5 for the creep behaviour of polycarbonate. With increasing time, it appears that initially negligible short processes play an increasingly important role on creep, this result being based on the assumption that secondary creep takes place without tertiary creep.

CONCLUSIONS

The DNLR model was applied to the prediction of creep in polymers. Under the linear approximation, it gives a good representation of the transient and secondary creep stage only. Additionally, if the free enthalpy is let to vary with time, the model takes into account the tertiary creep induced by damage as well.

SYMBOLS USED

$\underline{\underline{a}}^u$ = square matrix linkink state variables (Tiszas matrix)

$\underline{\underline{b}}$ = rectangular matrix coupling state and dissipative variables

$\underline{\underline{g}}$ = square matrix coupling the set of internal reorganisations one each other

ε_j^x = strain of the process j, for unrelaxed or relaxed state respectively for x = u, x = r

τ_j^y = relaxation time of the process j, respectively for deformation ($y = u \to r$), and for restoration ($y = u \leftarrow r$)

E^x = unrelaxed or relaxed modulus of elasticity respectively for x = u, x = r

ΔG^{*+} = activation free enthalpy in the relaxed state (J / mol)

R = gas constant (J / mol / K)

h = Plank's constant (J . s)

k = Boltzmann's constant (J / K)

REFERENCES

1 Cunat C., J. of Non-Cristalline Solids, 131/133, (1991), 196-198

2 Cunat C., J. of Non-Cristalline Solids, 131/133, (1991), 812-815

3 Prigogine I., "Introduction à la thermodynamique des processus irreversibles", Dunod, Paris (1968)

4 Ayadi Z., Thesis, INPL, Nancy, (1995)

5 Loukil M., Thesis, INPL, Nancy, (1996)

6 Marceron P., *in* "Deformation, yied and fracture of polymers", Inst. Of Mat., London, (1997), this book p13

7 Garofalo F., "Fundamentals of creep and creep-rupture in metals", Macmillan Series in Material Science, (1965), 46-55

8 Cunat C., Thesis, Nancy, (1985)

FRACTURE BEHAVIOUR OF POLYMERIC COATINGS ON STEEL SHEETS

G Robert[*], C G'Sell[*], S Etienne[*], R Hellouin[**] and C Bonnebat[**]

This study deals with the industrial films of paint deposited on steel sheets by coil coating. Paints are studied both as free films, to characterise intrinsic mechanical behaviour and as coatings to characterise damage when sheet undergoes a high deformation level. Films are made in laboratory, coated sheets come from industrial products. Mechanical behaviour is determined by plane strain loading experiments, using a novel technique developed in the laboratory. Damage is characterised in each layer and interface. In pigmented coatings, the flaws develop within the thickness of the polymer, without emerging at the external surface nor at the metal interface.

INTRODUCTION

Coil coating is a process of increasing importance for European steelmakers, whose aim is to sell pre-primed or prepainted galvanised steel for applications in buildings, electric appliances and cars. Many papers have been published on this subject, for instance by Waggoner and Blum (1) and Mitchell (2). Paints used in such cases exhibit two apparently opposite properties : i) high toughness to allow cold forming and ii) high modulus to promote resistance to scratches and high gloss. The best industrial systems undergo large strains without losing their protective efficiency, although they are intrinsically brittle. The purpose of this study is to make a link between the mechanical properties of the polymeric layers, their damage mechanisms, and their performances as coatings.

MATERIALS

The paints used in this study are thermosetting systems. The precursors we chose are polyester resins whose molecular weights are in the top range of polymeric paint formulations usually processed in similar industrial applications, because concentration of polymers in solvent for such weights is small. The crosslinking agent is melamine. These paints are used either as protective layers (primers), mixed with a small quantity of corrosion inhibitors and pigments, either as top coat layers, mixed with a higher quantity of pigments. After curing, the glass transition temperatures range from 35°C to 80° C. The main properties of the cured paints we used are listed in Table I. These coatings present a great porosity which depends on the kind of paint used, and is inherent in the industrial process. Free films of paint are prepared with the following technique : the substrate is first coated

[*] LMPSM (CNRS 155), Ecole des Mines, Parc de Saurupt 54042 Nancy, France.
[**] CED, SOLLAC, BP109, 60761 Montataire, France.

with a silicone film that prevents adhesion of the paint ; then paint is applied using a wire bar according a procedure described by Kerchiss (3) and cured as an industrial coating. With this method we prepared both monolayered and bilayered films with precisely calibrated thicknesses, ranging from 5 to 15 μm.

Table I : *Properties of the studied coatings*

Resin	Function	T_g (°C)	$\overline{M_n}$ (g/mol)	$\overline{M_w}$ (g/mol)	Pigment rate (% Vol.)
A	primer	35	17090	36742	19
B	primer	80	9690	19240	15
C	top coat	80	9690	19240	19

EXPERIMENTAL

Free films are tested using a variant of the video-controlled tensile testing technique developed in the laboratory (VideoTraction©) by G'Sell *et al.* (4). The samples, marked with an array of ink markers are deformed under plane strain loading. The video system allows the automatic analysis of the distortion of the marker set, and, subsequently provides in real time the true stress- strain behaviour of the film material at constant true strain rate. The galvanised steel sheets are also tested using the video-controlled tensile system.

As for the coated steel sheets, they are strained with another method. The central area of each sample is covered with a grid. Then, it is deformed under plane strain loading. The grid allows to determine strain precisely in a given area. The samples are observed by reflection optical microscopy to characterise strain inhomogeneities, and Scanning Electron Microscopy (SEM) to analyse cracks.

PLANE TENSION EXPERIMENTS ON FILMS

The graph in figure 1 shows the response to plane strain of the materials under investigation, different free films and the plain steel sheet, for a temperature of 25°C. The films C and B show very similar behaviour. Both having a high T_g, they exhibit a very small ultimate strain. The films A have a lower T_g, and are much more ductile. Bilayered films made of one layer of A and one layer of C have an intermediate behaviour : they undergo a maximum strain intermediate between the rupture strain of both components. On other words, the failure is not controlled by the most brittle layer alone. By the way, the steel sheet has a maximum strain intermediate between the ones of the films A and the one films C (or B). Also it is important to study the films behaviour at temperatures reached during bending or cold forming operations, because of steel self heating. Figure 2 shows experiments of plane strain tension on films made of paint A, at temperatures ranging from 25°C to 40°C. The flow stress decreases strongly as temperature rises. The oscillations on the curves are caused by the temperature control, and the low thermal inertia of the samples. The experiments made on paints whose T_g is about 80°C or higher show that they have a very brittle behaviour at the temperatures of a cold forming. Complementary experiments not shown here on films C and B in the same temperature range as above exhibit brittle fracture in all instances.

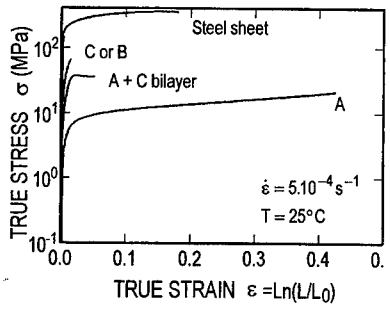

Figure 1 : *mechanical behaviour of free films of paint and their substrate*

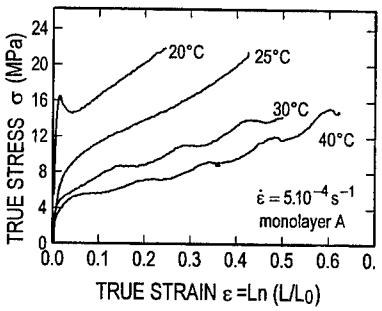

Figure 2 : *temperature dependence of primer A free films*

DAMAGE BEHAVIOUR OF COATINGS

In the sheet coatings under investigation, two different damage processes have been identified, each of them appearing at a given strain threshold. The first mechanism is initiated at very low strains, in the form of hollows appearing on the originally smooth surface, and developing when strain increases. Figure 3 shows this for two different paints, strained in two different directions. Both have the same characteristics : a development of hollows for strains larger than 0.02, a quick growth until ε=0.1, and then saturation. These hollows are attributed to localised plastic deformation occurring at the surface of the coating. Paint B presents more of these instabilities because of its higher fragility. It is interesting to notice that monolayered coatings of paint B resist to intensive plastic deformation, although free films of B have a very brittle behaviour.

The second mechanism refers to cracking. Figure 4 shows the shape of these cracks for a sample highly strained in plane tension. Primer A remains uncracked until the steel sheet failure. Conversely, in primer B cracks appear when strain becomes higher than ε=0.06. The cracks formed are embedded in the coating : they are covered by a fine superficial layer, and so they do not emerge at the surface. From $0.06 < \varepsilon < 0.1$, SEM observations show that the number of cracks and their mean width increase, but experimental problems caused by the fine layer covering the cracks make impossible really reliable countings. The contrast between a crack and its surroundings is very weak, so the cracks are only partially detected. For strains higher than 0.1, this problem disappear as shows Figure 4. The contrast of SEM observations improves, and it is now possible to identify two different behaviours : narrow and wide cracks. Narrow cracks remain covered by the same tough superficial layer until the steel breaks. An example of this is the crack on the left of Figure 4. On wider cracks, small holes appear in this layer, as shown by the crack on the right of Figure 4. For the widest ones, the tough superficial layer can even disappear. and it is possible to see the inner structure of the cracks : some *pseudo*-fibrils of about 100 nm join each edge, and faces of the crack have a shape which shows that strong plastic deformation has occurred. As contrast improves, it is also possible to realise precise countings. They show that crack density slowly increases and reaches 80 cracks per mm for the most strained samples, at ε=0.18. A very important point is that even at the highest strains reached, the crack propagation does not reach the interface. This means that the coating keeps its protective efficiency.

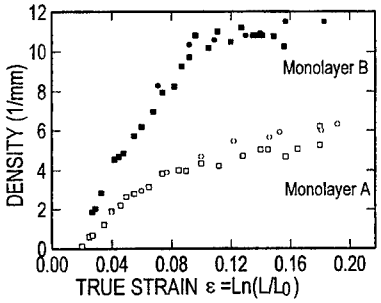

Figure 3 : *development of plastic instabilities on monolayered coatings.*
■ □ : *rolling direction,* ● ○ : *transverse direction.*

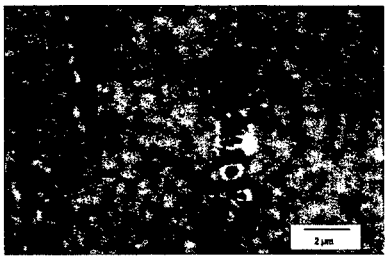

Figure 4 : *cracks on a highly strained sample of primer B.*

DISCUSSION

The concepts of fracture mechanics developed recently by Hutchinson and Suo (5), and Beuth (6) do constitute valuable tools for crack modelling in thin coatings. These concepts are based on Linear Elastic Fracture Mechanics. The analysis of the energy release rate of a crack either propagating toward the substrate-coating interface, either channelling within the coating, leads to the determination of two damage criteria associated with each extension mode. For a given thickness of the coating, cracking is possible when the toughness/stress ratio (K_{Ic}/σ) is smaller than a determined limit. However the application of these concepts requires a good evaluation of the depth of the cracks, and also of the constitutive law of the films for strains which are not reached in tension experiments on free films : the paint B cracks at strains reached on plane tension of a steel sheet, but at a strain that a free film can not reach, and the steel sheet fails before the cracking of paint A. However some points can be understood with a simple analysis of the theoretical concepts developed by Beuth and the experimental data available. The effect of the substrate on the coating is simple : the modulus of steel is much higher than the coating's one, and moreover it imposes strain at the interface, assuming perfect adhesion. The coating, which shows early cracking as a free film is now much more resistant to damaging since the energy involved in cracking is higher, because of the influence of the substrate on the stress field near the crack tip. On other words, the substrate imposes its ductility to the coating. Furthermore, stresses in paint A are much smaller than stresses in paint B. Since cracking depends on stress in the coating, it is a first explanation to the best properties of paint A.

REFERENCES

1. Waggoner, RA, and Blum FD, J. Coat. Technol. 61, (1989) 51.
2. Mitchell, PJ, Sheet Met. Ind. 64 (1987) 74.
3. Kerchiss, TR, Polymers Paint Colour Journal 6, (1993) 75.
4. G'Sell, C, Hiver, JM, Dahoun, A, and Souahi, A, J. Mater. Sci. 27, (1992) 5031.
5. Hutchinson, JW, Suo, Z; Advances in applied mechanics 29, (1992) 63.
6. Beuth, JL, Int. J. Solids Structures 29 , (1992) 1657.

A MONTE CARLO INVESTIGATION OF AMORPHOUS POLYMER DEFORMATION

Clarence Chui* and Mary Boyce*

A poly-bead model of amorphous polymer networks is constructed and deformed via Monte Carlo simulation techniques. The onset and development of deformation localization, as measured through the aggregate motion of discrete particles, is correlated to the computed macroscopic stress-strain response in both the rubbery and glassy states.

INTRODUCTION

Although the evolution of the material state for amorphous polymers is generally acknowledged to be sensitive to factors such as temperature, pressure, deformation rate, and thermo-mechanical history, a complete understanding of the fundamental mechanisms responsible for these dependencies has not yet been reached. Previous attempts to simulate the behavior of these materials have covered various length scales ranging from the atomic level(1,2), where molecular dynamics methods attempt to explicitly model all of the complex particle interactions through the use of realistic force fields and masses, to the continuum(3), where constitutive models attempt to embody the aggregate behavior of the material structure through either mechanistically or phenomenologically motivated arguments.

In this investigation, a three-dimensional mesoscopic model of amorphous networks is evolved via Monte Carlo techniques in an attempt to quantify the relationship between the initial material state and reduced system parameters such as crosslinking density, bond length, excluded volume radius, temperature, and pressure. Using this characterization, the networks are then deformed at various temperatures, strain rates, and strain states in order to correlate the evolution of relevant structural quantities to the initial material state and macroscopic network response. Of particular interest is the nucleation and degree of spatial correlation of localized deformation which provides insight as to how the characteristic stress-strain responses of both the rubbery and glassy states develop.

METHODOLOGY

The model consists of beads connected by springs with bond lengths and bond angles being governed by harmonic potentials. The bond torsion angles are controlled by a three-fold cosine function while the intermolecular(i.e. non-bonded) interactions are described by a hard sphere potential, a form which is sufficient for investigating the qualitative effects of "excluded" volume on mechanical behavior. The links and beads in the network are not meant to explicitly represent actual bonds present in polymer chains

* Department of Mechanical Engineering, Massachusetts Institute of Technology, Cambridge, MA 02139, USA

but are instead viewed as larger scale entities possibly representing groups of bonds or other aggregate molecular structures.

Networks are generated by discretizing the desired domain into evenly spaced cubic regions. Each cube contains a chain segment generation seed. A chain segment is constructed by emanating a chain link from one of the generation seeds and continuing to grow it in a biased random walk fashion up to a prescribed number of links which can vary from segment to segment. In order to form a well connected network, the ends of the chain segments are attached to the nearest generation seed that is within a specified tolerance distance. Periodic boundary conditions are also enforced in order to minimize size effects.

The initially generated networks are annealed using the classic Metropolis algorithm(4) and isothermal-isostress ensemble. A variation of the dynamic Monte Carlo method(5) is used to evolve cooled systems, allowing simulation of constant strain rate(with stress-free side surfaces) conditions. By partitioning the domain into many control volumes and using position "density" as a transport variable, the relative motion of the control-volume-averaged center of positions is computed by time integrating Reynolds' Transport Theorem(6). From these locally averaged particle positions, the deformation gradient is calculated via a difference scheme. Further details of the methodology are provided in (7).

DISCUSSION OF RESULTS

One important measure of the initial material state is the reduced density which quantifies the packing ability of the system and roughly characterizes the ease with which the system accommodates local particle motions. The simulations indicate that changes which reduce the overall mobility of the particles such as decreasing the temperature or increasing the pressure, hard sphere radius, or crosslinking density tend to increase the system density. These basic parametric dependencies are essentially independent of system size for networks composed of more than 1500 particles. Also, by scaling the Boltzmann temperature, kT(where k is Boltzmann's constant and T is the absolute temperature), with the bond rotation energy barrier, E_{rot}, the temperatures corresponding to the different regimes of behavior(i.e. rubbery, glassy, etc.) are estimated.

The accompanying figures correspond to constant strain rate uniaxial tension simulations performed on single chain systems composed of 4000 particles. Figure 1 displays a snapshot of a typical annealed system's morphology while figure 2 shows the stress-strain response of the system at two temperatures. The qualitative characteristics of these curves are quite representative of systems in the rubbery(high temperature) and glassy(low temperature) states. In the rubbery state, the stress-strain response indicates that throughout the simulated strain range, the system is quite compliant, behavior representative of rubbery materials deformed up to relatively small strains. That the stress is due mainly to bond orientation is indicated by the constancy of all global internal energy measures(7) as also observed in related simulations by Weiner and Gao(8). This effect is normally attributed to thermodynamic configurational entropy through statistical/probability arguments but instead has a very mechanistic cause. Since stress is essentially computed by counting the number and orientation of lines of force which pass through the fictitious plane cuts in the domain, alignment effects tend to increase the

number density of bonds which contribute to the force in the direction of tension. Also, the high characteristic temperature also suggests that the local particle motions are dominated not by externally applied forces but instead by large thermal fluctuations, creating rather randomly distributed peaks in deformation throughout the entire simulation. Figure 3 depicts regions where the norm of the local deformation gradient is at least 8% larger than that of the macroscopic deformation gradient.

The above described response can be contrasted to that of systems deformed in the glassy state. The initially stiff response, corresponding to macroscopic linear elastic behavior, becomes non-linear near a strain of .1, signaling the onset of macroscopic yield. The initial yield point, occurring at the first peak in the stress-strain curve, is followed by a region of strain softening leading to the steady-state flow behavior characteristic of glassy polymers. Although the bond orientation distribution evolves in a manner quite similar to that of the rubbery state simulations, thus producing a comparable entropic state, the data indicates that thermal relaxation does not initially occur rapidly enough to liberate energy stored as a result of the externally applied deformation. However, at larger strains, the non-linear portion of the stress-strain response leading up to initial yield is indicative of the nucleation and development of clustered regions of cooperatively moving particles as shown by the grouping of highly deformed control volumes in figure 4. These intensely deforming pockets appear to offer a way for the system to accommodate large deformations and maintain relatively constant macroscopic stress levels by allowing the competing effects of orientation strain hardening and localization softening to cancel.

CONCLUDING REMARKS

Currently, much larger systems are being simulated in order to observe the formation and interaction of organized flow structures such as shear bands and estimate the sensitivity of these structures to crosslinking density and other relevant model parameters. Identification of specific mechanisms responsible for these cooperative processes remains difficult, which a detailed study of particle kinematics in highly deforming regions requires, but a qualitative understanding is guiding efforts to develop more accurate physically based constitutive models.

ACKNOWLEDGEMENTS

Support for this work was provided by the Kodak Foundation and the National Science Foundation grant no. DDM-9157899

REFERENCES

(1) Brown and Clarke, *Macromolecules* Vol 24, pp 2075- , 1991
(2) Argon et al., "Plastic Deformation in Glassy Polymers by Atomistic and Mesoscopic Simulations", *J. Rheol.* Vol 39(2), pp 377-399, 1995
(3) Boyce et al., "Large Inelastic Deformation of Glassy Polymers, Part I: Rate Dependent Constitutive Model", *Mechanics of Materials* Vol 7, pp 15-33, 1988
(4) Metropolis et al., "Equation of State Calculations by Fast Computing Machines", *J. Chem. Phys* Vol 21, pp 1087-1092, 1953
(5) Binder, K Ed., *Monte Carlo and Molecular Dynamics Simulations in Polymer Science*, Oxford University Press, New York, 1995

(6) Gurtin, M., *An Introduction to Continuum Mechanics*, Academic Press, Inc., 1981
(7) Chui, C., Ph.D. Thesis, MIT, Cambridge 1997, in preparation
(8) Gao, J. and Weiner, J. H., "Excluded-Volume Effects in Rubber Elasticity. 1. Virial Stress Formulation", *Macromolecules* Vol 20, pp 2525-2531, 1987

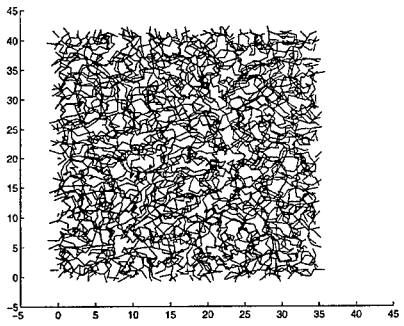

figure 1

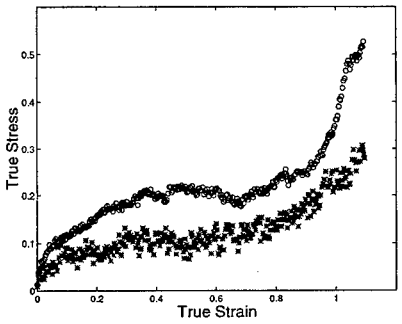

figure 2

figure 1 - Plane view of a typical annealed system's bonds
figure 2 - Stress-Strain response at two temperatures(* $kT/E_{rot} = 0.5$; o $kT/E_{rot} = 0.02$)

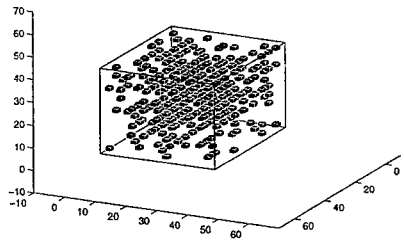

figure 3

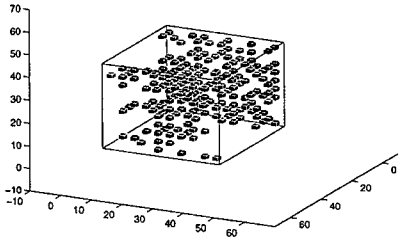

figure 4

figure 3 - Plot of control volumes with deformation gradient norms exceeding set tolerance levels for $kT/E_{rot} = 0.5$ at a macroscopic true strain of 0.25: At high temperatures, large fluctuations pervade the system in rather random patterns.

figure 4 - Plot of control volumes with deformation gradient norms exceeding set tolerance levels for $kT/E_{rot} = 0.02$ at a macroscopic true strain of 0.25: At lower temperatures, regions of localized deformation, which occupy a smaller percentage of the system's volume than at high temperatures, appear to form in clusters.

TIME-DEPENDENCE OF ELASTOMERIC MATERIALS: EXPERIMENTS AND MODELING

J. S. Bergström*, M. C. Boyce*

In this paper a new constitutive law for the time-dependent behavior of elastomeric materials is presented. The model is found to capture the rate dependence of the true stress-strain behavior, stress relaxation, and hysteresis. By performing a careful experimental investigation, it has been possible to probe the material response to different strain histories and to find the influence of different microstructural parameters such as concentration of filler particles and number density of crosslinking sites. From the experimental data a constitutive model based on reptational relaxational motion of chain molecules has been developed. In the model, the macroscopic mechanical behavior is determined by the dynamic interaction between two networks acting in parallel: a perfect network giving the equilibrium response and an elastically 'inactive' network that deforms with the perfect network during fast macroscopic deformations but, when given sufficient time, relaxes towards a lower energy state.

1. Introduction

The modeling and prediction of the stress-strain behavior of elastomers has been an area of interest for many years. The aim of this work was to develop a consistent model that allows for predictions of the time-dependent behavior of elastomeric materials over a wide range of loading conditions. With this in mind, a detailed experimental investigation was undertaken in an effort to probe the mechanical behavior of Chloroprene rubber under different loading conditions as discussed in Section 2. The experimental data provided a foundation for the constitutive model presented in Section 3.

2. Experiments

In the experiments, specimens with three different levels of carbon black particles and with two different levels of crosslink densities were used. The tests were performed both in uniaxial compression of ASTM compression set buttons, and in plane strain compression. Prior to testing for rate effects all virgin samples were conditioned to remove the Mullins effect, where we note that there is a clear distinction between softening from Mullins effect versus hysteresis loops. Fig. 1a shows the stress-strain behavior during one load cycle under uniaxial compression to different final strains. To investigate the time dependence of the material, tests were run with strain rate jumps and with stress relaxation segments. Fig. 1b shows the result from a constant strain-rate uniaxial compression test in which the strain was held constant for 120 seconds at strain levels of -0.3 and -0.6 during both the compression and the unloading phases. The graph clearly illustrates that the stress relaxes towards an equilibrium state when the strain is held constant. Repeating the experiment at a different strain rate furthermore shows that the equilibrium state is independent of the applied strain rate [1].

3. Constitutive Modeling

The foundation of the constitutive model is the assumption that the mechanical behavior of the material can be modeled by one equilibrium network acting in parallel with one time dependent network and where the micromechanism responsible for the time-dependence is the reptation

*Department of Mechanical Engineering, Massachusetts Institute of Technology, Cambridge, USA

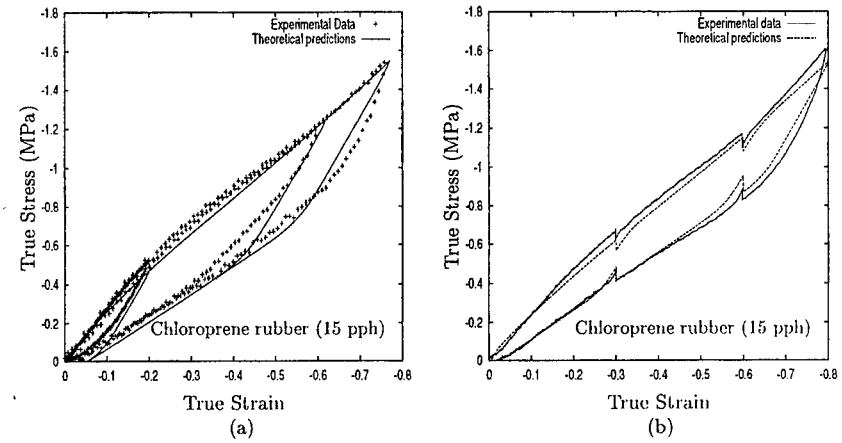

Figure 1: (a) Stress-strain curves to different final strain levels. $\dot{\epsilon} = -0.01$ s^{-1}. (b) Stress relaxation behavior, 120 seconds relaxation time. Strain rate used $\dot{\epsilon} = -0.002$ s^{-1}.

of macromolecules that are elastically 'inactive' (*ie* molecules that carry less load and have the capability to significantly change conformation during creep loading.) To illustrate this view consider the model with a free chain-end located in a network of chains as illustrated in Fig. 2 (bottom left). If the network is deformed fast enough then the chain with a free end will also deform more or less affinely with the network, giving an additional deformation resistance. If the applied strain is then held constant in the deformed state the free chain will slowly, by Brownian motion, return to a more relaxed configuration. Another chain topology that could give rise to the same qualitative behavior is shown in Fig. 2 (right).

The loop ABC in Fig. 2 (right) undergoes Brownian motion and has an equilibrium position at a finite distance from the constraining chain DD'. Hence, DD' behaves as an obstacle which imposes an energy barrier to the relaxation process. The total deformation resistance of the material can be modeled as two networks acting in parallel as illustrated in Fig. 2 (top left). One network gives the equilibrium response and the other network the time-dependent behavior. The second network, by itself, consists of a 'perfect' network in series with a time-dependent element. The stress-strain relation for the two perfect networks are modeled by a compressible[†] version of the 8-chain model [2]

$$\sigma_i = C_R\sqrt{n}\,\frac{\lambda_i^2 - \lambda_{chain}^2}{\lambda_{chain}}\,\mathcal{L}^{-1}\left(\frac{\lambda_{chain}}{\sqrt{n}}\right) + B\ln\left(\sqrt{I_3}\right) \tag{1}$$

where

$$C_R = \frac{NkT}{3}, \qquad \lambda_{chain} = \sqrt{\frac{\lambda_1^2 + \lambda_2^2 + \lambda_3^2}{3}}, \tag{2}$$

B is the bulk modulus, and both σ_i and λ_i are located in principal space. To develop the constitutive equation of the time-dependent element consider a free chain-end of the type illustrated in Fig. 2 (bottom left), but keep in mind that the presented arguments should also hold for

[†]A very small amount of compressibility is added to the perfect networks for numerical convenience.

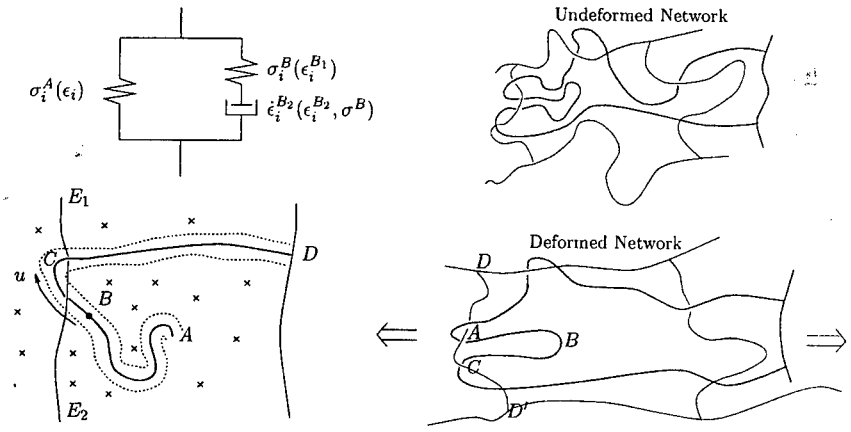

Figure 2: Top Left: Rheological representation of the constitutive model. $\boldsymbol{\sigma} = \boldsymbol{\sigma}^A + \boldsymbol{\sigma}^B$, $\boldsymbol{\epsilon}^B = \boldsymbol{\epsilon}^{B_1} + \boldsymbol{\epsilon}^{B_2}$; Bottom Left: Relaxation of a chain-end in a perfect network; Right: Relaxation of inactive chain segments in a perfect network.

the more general situation in Fig. 2 (right). The chain segment at B is constrained to move back and forth along the constraining tube by Brownian motion in a combination of reptation motion and contour length fluctuations. The average displacement of B can be approximated by $C_3\sqrt{\phi(t)}$, where the scaling law $\phi(t) \propto C_1 t^{C_2}$ is given from reptation dynamics [3]. The effective chain stretch in the time-dependent element can therefore be written

$$\lambda_{chain}^{B_2}(t) = 1 + C_4 t^{C_5} \tag{3}$$

where $C_4 > 0$ and $C_5 \in [0.5, 1.0]$. The effective macroscopic creep rate is obtained by eliminating t in Eq. (3) and incorporating a stress dependence due to the energy activated nature of the relaxation process giving

$$\dot{\epsilon}_i^{B_2} = \frac{C_1}{\lambda_{chain}^{B_2}} \left[\lambda_{chain}^{B_2} - 1\right]^{C_2} \left[\frac{s^B}{\hat{\tau}}\right]^m \frac{\mathsf{S}^B}{||\mathsf{S}^B||} \tag{4}$$

where s is an effective stress measure and S is the deviatoric stress tensor. Equation (4) captures the rate dependence of the stress-strain response as well as stress relaxation. For loading under a given fixed strain, the time-dependent element B_2 will creep, thus increasing the stretch in B_1 which relaxes the overall stress to the equilibrium state.

4. Comparison with Experimental Data

The constitutive model presented in the previous section can now be compared with experimental data. Even though the constitutive model was derived for an unfilled rubber we have in this section applied it to a Chloroprene rubber with the filler content of 15 pph carbon black, see Fig. 1. The argument for doing this is that this material has so low filler content that the fillers can be considered to only affect the mean chain lengths and crosslink density. A different approach to carbon black filled elastomers is discussed in the next section.

5. Finite Element Simulation of Filled Elastomers

It is of interest to see how well the proposed model works for elastomers with higher levels of carbon black. To evaluate this we have run finite element simulations of simple FEM meshes of the type illustrated in the inset in Fig. 3. In the inset the dark elements are the carbon black

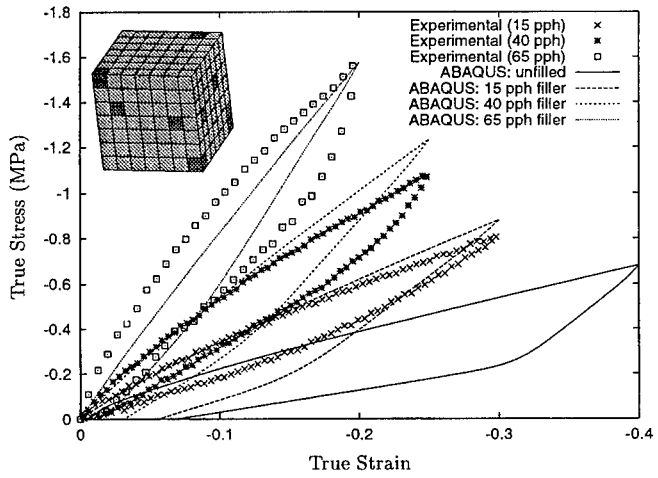

Figure 3: Comparison between FEM predictions and experimental data. $\dot{\epsilon} = -0.01\ s^{-1}$.

particles which are modeled as stiff linear elastic material and the behavior of the surrounding matrix is given by the model presented in Section 3. By varying the number of filler elements it is possible to simulate different particle concentrations allowing a comparison with experimental data. The results of this comparison with Chloroprene rubber is shown in Fig. 3 indicating a good agreement between theory and experiments. These results appear promising at providing the underlying effects of filler on the various aspects of rubber behavior as well as providing an accurate and predictive constitutive representation of the behavior.

Acknowledgment

The research has been founded by the U.S. National Science Foundation grant no. DMM-9157899. We also gratefully acknowledge Alan Dickey of the Caterpillar Corporation for supplying the rubber material.

References

[1] Bergström J.S., Boyce M.C., Paper in preparation for publication.

[2] Arruda E.M., Boyce M.C., *J. Mech. Phys. Solids.*, Vol. 41, pp. 389-412, 1993

[3] Doi M., Edwards S.F, The Theory of Polymer Dynamics, Oxford University Press, 1986.

MODELLING THE COMPRESSION OF LOW DENSITY FLEXIBLE CELLULAR POLYMERS (FOAMS).

S M Thorpe and A H Windle *

A computer model has been devised to simulate the behaviour of foams in compression. This paper describes the model and presents results obtained for simple two and three dimensional systems.

INTRODUCTION

One major application of low density flexible foams is as a cushioning material, where they find widespread use. There is consequently a considerable commercial benefit in understanding the relationship between their structure and deformation behaviour during compression. Such foams may be classified according to their density, and whether their structure is open or closed celled. The density is typically expressed as a volume fraction of polymer, given by (all unexplained symbols are listed at the end):

$$\phi = \rho_f / \rho_s \qquad (1)$$

This study is concerned with foams which are of a low density ($\phi < 0.1$) and have an open celled structure, so that the foam compartments are all interconnected and the passage of air through the material is unrestricted. Stress-strain responses for such a foam, of volume fraction 0.04 are shown in Fig. 1. [1]. This curve may be identified with a region of linear elasticity at low strains, followed by a long collapse plateau and finally a steep rise in the gradient in the high-strain densification region [2]. A computer model has been devised with the aim of predicting such behaviour for simulated foam structures.

THE COMPUTER MODEL

The model consists of a network of elastic struts which are uniform along their length and which meet at junctions to simulate the structure of an open celled foam. During the simulation, a compressive strain increment is applied to the model and the junctions are allowed to move under the guidance of a Metropolis [3] algorithm (see later) so that the system energy is minimised under the imposed strain. By a process of repeated application of strain increments, an energy-strain profile is built up for the model system. Stress-strain information is obtained by calculating the gradient of the energy-strain curve.

Relatively recent studies [2,4] have indicated that strut element bending is favoured over deformation of the struts parallel to the force vector, as was assumed in earlier work, such as [5]. Observation of compressed foam samples under Scanning Electron Microscopy provides support for this conjecture, and also reveals that little deformation appears to occur in the proximity of the strut junctions where the polymer material is concentrated. On the basis of these findings, the first implementation of the model considers only strut bending as the deformation mode in the struts, and treats the junctions as being unable to deform, through a fixing of the strut connection angles at their starting values. From an initial configuration of the struts, set up to resemble a foam structure, a strain is applied to

* Department of Materials Science and Metallurgy, University of Cambridge.

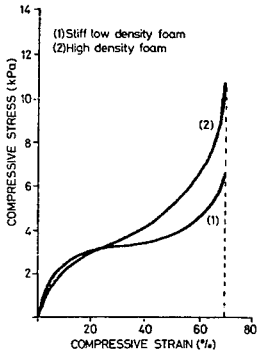

Figure 1: Stress-strain curves for a flexible open celled foam, showing the effect of density. Taken from [1].

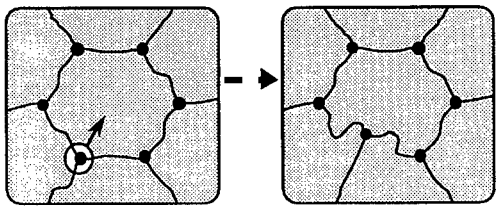

Figure 2 : A trial translation for one of the junctions is attempted in a Metropolis step. Note that the angles which the struts make relative to each other at the junctions must remain constant in all trial changes.

the model by moving all the strut junctions a scaled distance along the strain axis, as a first step. The Metropolis algorithm is then initiated, and involves picking junctions at random and subjecting each to a small translation or rotation (Fig. 2) within a certain range. After each trial change, the system energy is recalculated and compared to that which existed prior to the selection. The trial configuration is accepted or rejected according to the Metropolis test as follows: If the energy of the trial state is lower than the old one, the new configuration is accepted. If, however, the energy of the trial state is higher than previous, the new state is only accepted with probability:

$$P = e^{-\beta(E_{new}-E_{old})} \qquad (2)$$

where β is a variable parameter and may be considered as a reciprocal temperature, but only for the purposes of comparing the algorithm with simulated annealing techniques. For efficient running of the algorithm, β should be started very low and gradually increased as the procedure of selecting trial junctions is repeated. Note that the use of such terms does not imply that we are running the simulation at any particular physical temperature. The energy reassessment following a trial change consists of recalculating only the bending energies of the struts which are connected to the junction under selection, since all others are held fixed. The form of the bending energy for a deformed strut is given by:

$$\text{Bending Energy} = B/2 \int_0^L (\text{curvature}(s))^2 \, ds \qquad (3)$$

where the curvature is a function of the distance along the strut (s). This bending energy is constrained by the distance between the junctions, the strut length, and the connection angles made at the junction (Fig. 2).

RESULTS

The model was implemented first in two, and then in three dimensions. Figs. 3 - 6 display results obtained from very simple model structures of each type. Fig. 3 shows the appearance of a two dimensional model consisting of twenty four interconnected identical struts at both zero and 30% compressive strain. The resulting energy prediction with engineering strain given by the model is shown in Fig. 4, along with the derived engineering stress profile. The units displayed may be regarded as arbitrary, and not representative of a quantitative prediction at this stage, but are consistent between the two model types presented, since the elemental struts are identical in size in each. It should be noted that two dimensional cellular structures, or honeycombs, are found experimentally to produce a stress-strain response similar in form to that of foams [2]. Fig. 5 shows the appearance of the simple three dimensional cell model at zero and 30% compression. The model is a regular tetrakaidecahedron cell which is composed of six square and eight hexagonal faces. This type of cell is space-filling when placed on a body-centred cubic lattice, and is often taken as a basis for an idealized open-celled foam structure, for example in [6]. Fig. 6 illustrates provisional energy-strain and stress-strain results obtained from a first implementation of the three dimensional model.

CONCLUSIONS

A computer model based around a Metropolis algorithm has been used to obtain stress-strain predictions for simple two and three dimensional models. The two dimensional prediction exhibits a sigmoidal shape characteristic of cellular systems under compression, and reminiscent of observed responses of honeycombs. The three dimensional model is in an early stage of development, however, and displays a shift along the energy axis, thought to be attributable to 'thermal energy' left over by the failure of the Metropolis algorithm to reach the absolute minimum energy states in the running time allocated. The stress-strain prediction for the three dimensional tetrakaidecahedron cell is thus presented as a preliminary result only, and further refinement of the model is currently underway.

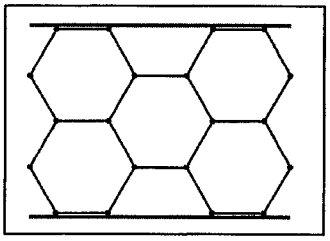

Strain on model = 0.0
System energy = 0.0

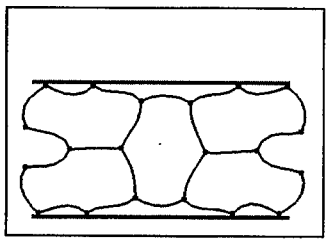

Strain on model = –0.30
System energy = 686.6

Figures 3 (above) and 4 (below) : Two dimensional model shown at zero and 30% compressive strain, with the corresponding energy–strain and stress–strain predictions.

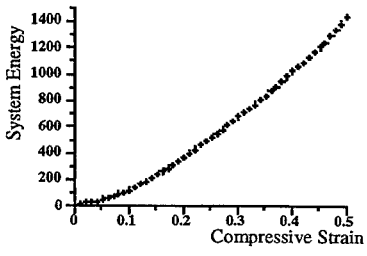

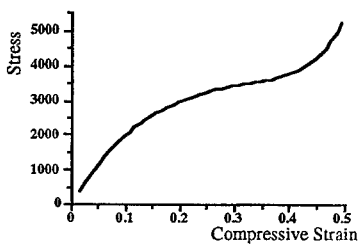

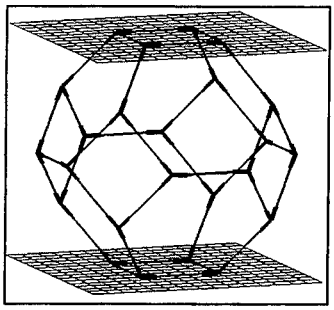

Strain on model = 0.0
System energy = 0.0

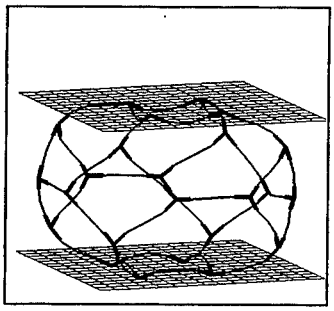

Strain on model = –0.30
System energy = 492.0

Figures 5 (above) and 6 (below) : Three dimensional tetrakaidecahedron cell model shown at both zero and 30% compressive strain states. The energy–strain and stress–strain results are also presented.

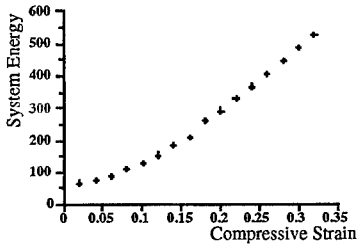

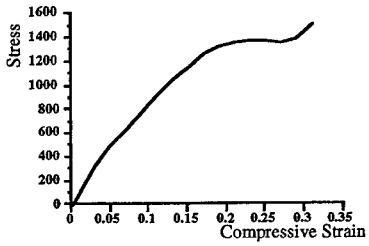

SYMBOLS USED

ρ_f	density of foam sample (kg/m^3).
ρ_s	density of solid polymer comprising cellular matrix (kg/m^3).
E_{new}	energy of model system following trial Metropolis step (J).
E_{old}	energy of model system prior to trial Metropolis step (J).
B	flexural rigidity of strut (Nm^2). (equivalent to the product of the Young's modulus and the second moment of area of the strut).
L	strut length (m).

REFERENCES

[1] Woods, G., 1982, 'Flexible Polyurethane Foams', Applied Science Publishers.
[2] Gibson, L.J. and Ashby, M.F., 1988, 'Cellular Solids-Structure and Properties', Pergamon Press.
[3] Metropolis, N., Rosenbluth, A.W., Rosenbluth, M.N., Teller, A.H. and Teller, E., 1953, J. Chem. Phys 21 1087
[4] Warren, W.E. and Kraynik, A.M., 1988, J. Appl. Mech 55 341
[5] Gent, A.N. and Thomas, A.G., 1963, Rubber Chem. Tech. 36 597
[6] Renz, R. and Ehrenstein, G.W., 1982, Cellular Polymers 1 5

POSTER SESSION TWO

NON-LINEAR RESPONSE OF AMORPHOUS POLYMERS : ANELASTIC/VISCOPLASTIC COMPONENTS THROUGH T_g AND THERMOSTIMULATED STRAIN RECOVERY

J. Perez and C. Gauthier
G.E.M.P.P.M.-umr CNRS 5510-INSA, Villeurbanne 69621 France

During the last years, a new theory for non-linear response of amorphous polymers was derived from the following basis [1] : (i) the deformation is supposed to result from thermomechanical nucleation of shear-microdomains (smd) with a kinetic depending on the disorder described in terms of quasi-point defects (qpd); (ii) those smd can expand but the elastic energy stored all allong lines boardering them provokes their recovery when the stress is released (**anelastic response**); (iii) for stress high enough or applied for a long time or at high temperature, smd coalesce and the elastic energy is lost (**visco-plastic response**); (iv) the mechanical response induces the creation of disorder i.e. the formation of new qpd but structural relaxation implies a decreasing concentration of qpd ; the visco-plastic flow could then correspond to a stationary regime with a constant qpd concentration. All events presented above are controlled by molecular mobility previously described in terms of hierarchically constrained movements.

Such an approach was shown to be also satisfactorily used in the description of α mechanical relaxation. Then both small (linear domain) and high (non-linear) stress-strain experiments were analysed in a self-consistent unic frame [2].

New results obtained with PVC [3], PET [4], PS, PMMA and PC [5], epoxy resins [6], have helped us to develop further the theory summarized above Thus several unexplained features could be clarified ; in particular :
- the strain hardening observed during the flow regime, is shown to result only partly from entropic forces due to chain extension ;
- the ratio between anelastic/visco-plastic components decreases and becomes zero when the temperature increases up to T_g ; moreover, only anelasticity appears to be responsible of changes in the microstructure and, consequently, in the physical properties ;
- the role of entropy and of stored energy in thermostimulated strain recovery, is specified.

References :
[1] J. Perez, L. Ladouce and R. Quinson, "Yield and fracture of polymers", Cambridge 1994.
[2] N. Ouali, M. Mangion and J. Perez, Phil. Mag., 67 (1993) 827.
[3] R. Florès-Florès, Thesis INSA-Lyon, 1994.
[4] L. Ladouce, R. Vassoille and J. Perez, J. Phys., 6 (1996)35.
[5] R. Quinnson, J. Perez, M. Rink and A. Pavan, to be published in J. Mat. Sci. (1996).
[6] O. Sindt, J. Perez and J.F. Gérard, Polymer, 37 (1996) 2989.

MACROPOROUS THERMOSETS SYNTHESIZED VIA CHEMICALLY INDUCED PHASE SEPARATION: A NEW APPROACH TOWARDS VOID TOUGHENING?

*J. Kiefer,** *J.G. Hilborn**

INTRODUCTION

The major inconvenient of thermosets is the inherent brittleness which is a direct consequence of the highly crosslinked network structure. The toughness can be increased through the incorporation of second phase particles (1-4). Even though this strategy is a well established method since more than two decades, there exists still a controversal discussion concerning the morphological features for most effective toughening. The nature of the dispersed phase does not play the predominant role for toughening, and a wide variety of thermoplastic or rubbery particles, that are generated via a phase separation process have been used for these purposes. Alternatively a considerable improvement in toughness can be achieved by blending with core shell particles. Conversely to previous strategies to achieve a maximum dispersion of core-shell particles, very recent investigations show better toughenability in materials displaying agglomerated particles (5). The higher toughness is attributed to a larger plastic zone size, which was observed in their systems clearly showing interconnected particles. In contrast to its nature, the size and distribution of the second phase particles seems to be crucial for effective toughening. Several research groups observed, that no toughening occurs, if the second phase particles are smaller than 150 - 200 nm (6). Theoretical considerations predict, that this is a lower critical size to induce cavitation of rubber particles in a polymeric matrix (7). Furthermore it could be proven with scattering techniques, that the cavitation preceeds the onset of shear band formation (8), which is recognized as the most important toughening mechanism in toughened thermosets. Hence cavitation can be regarded as a prerequest for toughening. Additionally, the contribution of the plastic void growth, succeeding cavitation, to the total toughness can become as important as shear banding, especially at elevated temperatures (9). The cavitation process is equal to the generation of a series of voids. Indeed, such a morphology has been simulated by using either a non reactive rubber (10) or hollow latex spheres (11, 12) as the dispersed phase. In the first study no insight was given in the removal of the liquid rubber and only one single composition has been studied. In the second studies, hollow particles were used, thus creating an additional interface. Using such pseudo-porous systems, both groups indicated the ability of voids to toughen epoxies in the same manner and in the same magnitude as rubber particles. In parallel to the experimental studies, the stress distributions of spherical inclusions, being either rubber or voids, in an isotropic epoxy matrix have been calculated based on a finite element model (13-15). It was concluded, that the effect of voids or a rubbery phase is very similar. These inclusions can release the degree of triaxial stresses at the crack tip. Even though, this model allowed to predict the possibility of void toughening, the finite element approach does not allow to take into account the multiple interactions between voids. Therefore we have developed a refined model, which is based on a zero order approximation and allows to visualize the stress distributions in porous epoxies (16). This model predicts the buildup of internal stresses. We assume, that this might initiate multiple shear banding, thus leading to effective toughening. However,

* Swiss Federal Institute of Technology, Polymers Laboratory, CH-1015 Lausanne

Bucknall and coworkers report that the mechanical behaviour of well-bonded cavitated rubber particles differs fundamentally from simple voids (17).

The experimental verification of the above theoretical predictions of void toughening requires a technique which yields porous thermosets having closed pores with sizes and distributions in the μm-range similar to those commonly used for toughening with rubber or thermoplastic particles. Therefore, we have developed a new technology, termed Chemically Induced Phase Separation (CIPS) (18-21), for the generation of the desired morphology which is governed by a phase separation process resulting from a chemical quench (22). This new type of macroporous thermosets is characterised by a very narrow size distribution in the μm-range, a significant lower density and dielectric constant without any loss in thermal stability.

It is the purpose of this paper to present the major results of our experimental studies concerning the evaluation of the fracture toughness of epoxies which were prepared via the CIPS technique. These investigations are intended to throw some light on the ongoing discussion on the role of cavitation for the toughening of thermosets.

EXPERIMENTAL PROCEDURE

Macroporous epoxy networks were prepared according to the CIPS technique as described in (23). The precursors to build the epoxy network were diglycidylether of bisphenol-A (DER 332 from Fluka) and 2,2'-bis(4-amino-cyclohexyl) propane (HY2954 from Ciba-Geigy). Cyclohexane, purchased in analysis grade, was used as the low molecular weight liquid. The critical stress intensity factor K_{Ic} and the fracture energy G_{Ic} were determined with single edge notch bending specimens strictly following the guidelines in (24).

RESULTS

In the strategy of the CIPS technique, the epoxy precursor and curing agent are reacted in the presence of a low molecular weight liquid, which turns into a non-solvent upon curing, thus initiating a phase separation proceeding via a nucleation and growth mechanism. After the curing, the system consists of liquid droplets which are randomly dispersed in the solid epoxy network. Such materials will be called solvent-modified epoxies in the following. We have investigated the role of the reaction parameters such as the chemical nature of the solvent, its concentration and the curing temperature, thus allowing to control the morphology (19). The generation of a porous morphology is subsequently achieved by holding the samples for 5 days 20 K above the ultimate T_g, thus allowing for diffusion of the liquid through the crosslinked matrix without significant alteration in the size and distribution of the dispersed phase. The size and the distance between the dispersed droplets, respectively voids depends strongly on its volume fraction as shown in figure 1. This figure also reflects a typical characteristic of two phase materials, where the second phase is generated in situ via a phase separation process. The size of the domains increases almost lineary with the volume fraction, whereas the distance between the domains decreases continously. This ripening process is also accompagnied by a decrease in the concentration of the dispersed droplets. Thus the CIPS technique does not allow to change the radius independently of the inter pore distance.

Our experimental results indicate, that the toughness depends strongly on the degree of drying. Shown in figure 2 are the fracture energies of solvent-modified and porous epoxies prepared via the CIPS technique. In the solvent-modified system, the increase in fracture energy from around 0,25 kJ/m^2 to around 0,4 kJ/m^2 can be attributed to a plastification effect resulting from the cyclohexane remaining in the matrix. The additional, considerable increase in fracture energy is caused by the generation of liquid droplets in the crosslinked matrix. A maximum is observed in the solvent-modified systems, which is in perfect agreement with results obtained with hollow particles as modifiers (11). The maximum value in fracture energy is around 4 times higher than the unmodified epoxy network. However, as the solvent is removed to leave voids a substantial decrease in fracture energy is observed. Due to there extreme brittleness, no measurements could be undertaken with samples having a porosity lower than 10%.

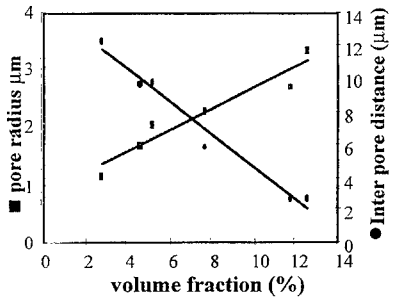

Fig.1: Morphological characteristics of macroporous epoxies prepared via CIPS

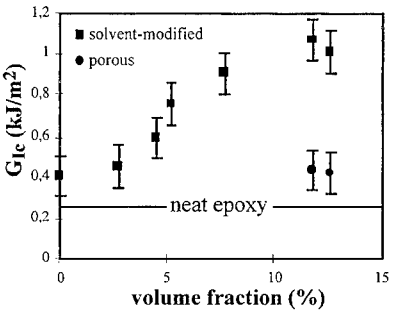

Fig.2: Fracture toughness of solvent-modified and porous epoxies prepared via CIPS

The question arises, whether this embrittlement results from the generation of voids, or if it might be a consequence of the drying procedure accompagnied with the buildup of internal stresses. Therefore, we have carried out a second serie of experiments with an additional heat treatment, wherein the samples were heated for only 1 hour above the ultimate T_g. The density measurements (Fig. 3) clearly reveal that a semi-porous morphology is obtained.

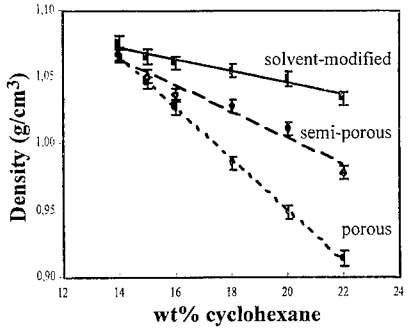

Fig.3: Density values of epoxies prepared via CIPS after various stages of drying

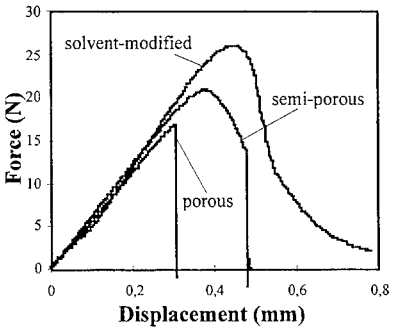

Fig.4: Deformation behaviour of epoxies prepared via CIPS after various stagesof drying

In perfect agreement with the previous results, we also observe in this serie a substantial lowering in the fracture toughness as the liquid is removed. This is qualitatively reflected in figure 4, where the load displacement curves recorded with SENB test geometry are shown for epoxies which are prepared with identical compositions after various drying steps. We have confirmed with image analysis, that the size and distributions are not affected by the different drying procedures. Furthermore the crack lengths were nearly identical for the experiments shown in figure 4. Thus the decrease in the maximum force is proportionnel to the decrease in K_{Ic}. One can clearly see, that the deformation behaviour changes drastically upon drying. The solvent-modified epoxies display a stable crack growth behaviour, equivalent with a high amount of energy absorption. In the semi-porous systems a semi-ductile behaviour is observed, whereas the sample breaks in a completely brittle manner, without any plastic deformation after the generation of a porous morphology.

CONCLUSIONS

The fracture toughness of epoxies, which are prepared via the CIPS technique by using a low molecular weight liquid, depends not only on the size and distribution of the dispersed domains, but also on the degree of drying. A high toughness is observed in solvent-modified systems, whereas the drying process leads to a considerable embrittlement. Even though the drying results in the generation of voids without affecting the morphology, it has to be verified, that the embrittlement does not result from the creation of internal stresses as a consequence of the drying procedure.

REFERENCES

1. Riew C.K., Gillham J.K. 'Rubber-modified thermoset resins', Adv. Chem. Ser. 208 (1984)
2. Riew C.K. 'Rubber toughened plastics', Adv. Chem. Ser. 222 (1989)
3. Riew C.K., Kinloch A.J. 'Toughened Plastics', Adv. Chem. Ser. 233 (1993)
4. Riew C.K., Kinloch A.J. 'Toughened Plastics II', Adv. Chem. Ser. 252 (1996)
5. Bagheri R., Pearson R.A., J. Mat. Sci. 31 (1996) 3945
6. Dompas D., Groeninckx G. et al., Polymer 35 (1994) 4743, 4750, 4760
7. Lazzeri A., Bucknall C.B., J. Mat. Sci. 28 (1993) 6799
8. Bubeck R.A., Buckley D.J., Kramer E.J., Brown H.R., J. Mat. Sci. 26 (1991) 6249
9. Huang Y., Kinloch A.J., J. Mat. Sci. Lett. 11 (1992) 484
10. Huang Y., Kinloch A.J., Polymer 33 (1992) 1330
11. Bagheri R., Pearson R.A., Polymer 37 (1996) 4529
12. Bagheri R., Pearson R.A., Polymer 36 (1995) 4883
13. Huang Y., Kinloch A.J., J. Mat. Sci. 27 (1992) 2763
14. Guild F.J., Kinloch A.J., J. Mat. Sci. 30 (1995) 1689
15. Bucknall C.B., Karpodinis A., Zhang X.C., J. Mat. Sci. 29 (1994) 3377
16. Fond C., Kiefer J., Kausch H.H., Hilborn J.G., J. Mat. Sci. to appear
17. Bucknall C.B., Soares V.L.P., Yang H.H., Zhang X.C., Macromol. Symp. 101 (1996) 265
18. Kiefer J., Hilborn J.G., Manson J.A.E., Leterrier Y., Hedrick J.L., Macromolecules 29 (1996) 4158
19. Kiefer J., Hilborn J.G., Hedrick J.L., Polymer 37 (1996) 5715
20. Kiefer J., Porouchani R., Mendels D., Ferrer J.B., Fond C., Hedrick J.L., Kausch H.H., Hilborn J.G., MRS Symp. Proc. 431 (1996) 527
21. Kiefer J., Hilborn J.G., Hedrick J.L., Cha H.J., Yoon D.Y., Hedrick J.C., Macromolecules 29 (1996) 8546
22. Pascault J.P., Macromol. Symp. 93 (1995) 43
23. Kiefer J., Kausch H.H., Hilborn J.G., Polym. Bull. 38 (1997) in press
24. 'Testing protocol LEFM Standard, ESIS, Polymer & Composites Task group', (1990)

The effect of molecular weight on mechanical properties of polyimide

Mitsuo NOTOMI*, Hisashi INABA*, Kikuo KISHIMOTO*, Toshikazu SHIBUYA*,
Atsushi MORITA†, Yasunori YOSHIDA†

The effects of molecular weight on mechanical properties of the thermoplastic polyimide are investigated. The specimens which have 4 different molecular weights (M_w) ranging from $2.5x10^4$ g/mol to $3.8x10^4$ g/mol were prepared. Young's modulus, tensile strength and Poisson's ratio were determined by the tensile tests. To obtain the fracture toughness, J_{IC} the multiple specimen method was applied since the crack propagation occurs in a stable manner. Although Young's modulus, tensile strength and Poisson's ratio are almost constant over the range of M_w tested, the J_{IC} increases with the increase of molecular weight. The rib-like pattern and the river-like pattern are observed on the fracture surfaces of lower and higher M_w specimen, respectively. These observations indicate that the crazes significantly grow for the specimens with higher M_w. This is considered to be the reason for the increase of fracture toughness. The relationship between the fracture toughness and molecular weight are obtained based on Kusy and Turner.

INTRODUCTION

New type of polyimide resin which shows high heat resistance and mechanical properties is being developed. Although this resin has a high glass transition temperature, T_g (=250°C), it is thermoplastic, neither thermoset nor semi-thermoplastic, so that the processability of injection and extrusion molding is improved. Since mechanical properties, especially fracture toughness, depend on the molecular weight (M_w) in general(1-5), it is important to understand the relationship between the mechanical properties and M_w for future improvement of material characteristic.

Therefore, we have investigated the effects of M_w on tensile properties and fracture toughness of this thermoplastic polyimide (PI). The fibril formation during fracture has been characterized by fractography. Moreover, we have discussed the dependence of M_w on fracture toughness.

Kusy and Turner(3) derived a relationship between fracture energy and M_w theoretically based on the assumption that only molecules exceeding a critical M_w can contribute to the work of plastic deformation and showed that a good correlation was attained for the experimental results of PMMA. This relationship can be employed to estimate the fracture toughness of PI over wide rage of M_w. We have applied the theory to our experimental results.

EXPERIMENTAL PROCEDURES

The material studied is PI with four kinds of M_w as shown in Table 1. Type D contains10 wt% of plasticizer to decrease the viscosity during molding. A dumbbell type, single-edge-notch bending (SENB) and compact tension (CT) were prepared by injection molding. Thickness of all specimens is 3.3 mm.

The tensile tests using a dumbbell type specimen were conducted with a crosshead speed of 3

*Department of Mechanical & Intelligent Systems Engineering, Tokyo Institute of Technology
†Plastics & Processing Research Laboratory, Mitsui Toatsu Chemicals, Inc.

mm/min at room temperature. The stress-strain relations and Poisson's ratio were obtained. A notch was machined for SENB and CT specimens and a natural crack was introduced using by sliding a razor blade at the notch root. Fracture tests were conducted with a crosshead speed of 1 mm/min at room temperature. The multiple specimen method was applied to determine the fracture toughness according to 'Standard Test Method for J_{IC}' (ASTM E813). The fracture surfaces were observed by a scanning electron microscope (SEM).

TENSILE PROPERTIES AND FRACTURE TOUGHNESS

Young's modulus (E), tensile strength (σ_B) and Poisson's ratio (υ) obtained are shown in Table 2. E, σ_B and υ normalized by those of Type A are shown in Figure 1. E, σ_B and υ are almost constant over the range of M_W tested. The slight increase of E and σ_B of Type D would be caused by the plasticizer.

Table 1 Molecular weight of specimens.

Type	Molecular weight [g/mol]
A	2.5×10^4
B	2.8×10^4
C	3.0×10^4
D	3.8×10^4

Table 2 Tensile properties of specimens.

	A	B	C	D
E [GPa]	3.18	2.98	3.14	3.68
σ_B [MPa]	88.3	88.3	86.6	110
υ	0.395	0.399	0.390	0.382

Table 3 Fracture toughness of specimens.

J_{IC} [kN/m]	A	B	C	D
SENB	3.0	5.7	6.8	**
CT	3.6	5.7	6.6	7.8

Figure 2 shows a typical J_R curve and 0.2 mm offset line. A similar results are obtained for another type specimens. J_{IC} values determined by SENB and CT specimens are shown in Table 3. Both values are in good agreement with each other. Figure 3 shows the normalized fracture toughness, $J_{IC}/J_{IC\,(SENB\ Type\ A)}$ as a function of M_W. In contrast to the

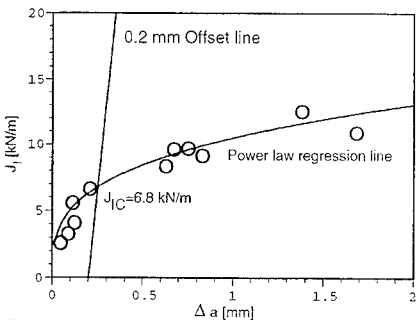

Figure 2 Typical J_R curve of specimens. This shows J_{IC} for SENB of Type C equal to 6.8 kN/m.

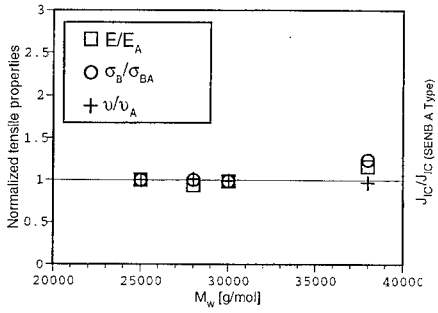

Figure 1 Normalized tensile properties against molecular weight.

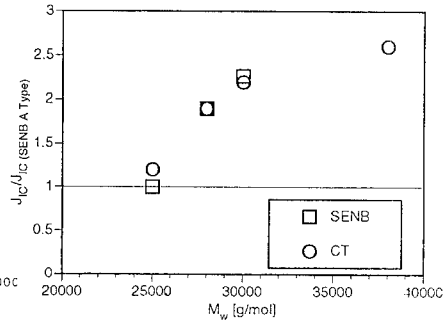

Figure 3 Normalized fracture toughness of SENB and CT specimens agasint molecular weight.

tensile properties, J_{IC} increase with the increase of M_W.

OBSERVATION OF FRACTURE SURFACE

Figure 4 shows the fracture surfaces of Type A, B and C near the inital crack tip. The direction of crack growth is orientated from a bottom to a top of the figures. A rob-like pattern is visible on the surface of Type A. This is the characteristic surface of the material with low fracture toughness, e.g. similar pattern reported on PC broken in a brittle manner on an impact test reported by R. Greco and et al(6). However, the fracture surfaces of Type B and C show a river-like pattern which is characterized by a series of fibril lines. Similar fracture surfaces are obtained for Type D. A three dimensional representation of rib and river-like patterns are schmatically shown in Figure 5 . For lower M_W resin (Type A), the molecular chain is short so that the fibrils are easily formed at the various points of the crack front as shown in Figure 5(a). However, the fibrils do not fully developed due to pulling out of the molecule.

On the other hand, for higher M_W resin (Type B to D), the formation of fibrils is restricted. However, the fibrils can grow higer as shown in Figure 5(b) once the craze initiate. It is well known that molecule ends cause the fibril failure(4). Increase of M_W reduces the number of molecule ends which are found in fibrils.

The main energy consumption would arise from the plastic work during fibril development. Therfore, the specimen showing the river-like pattern has higher fracture toughness than the specimen showing the rib-like pattern.

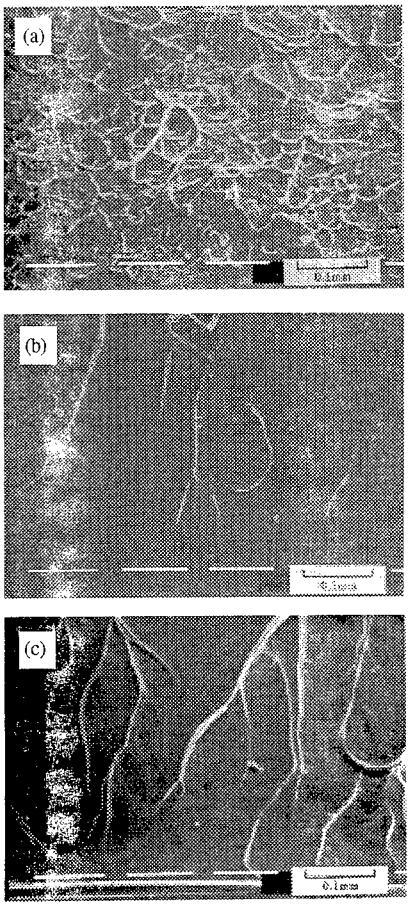

Figure 4 SEM photographs of fracture surface of (a) Type A showing a rib-like pattern (b) Type B and (c) Type C showing a river-like pattern.

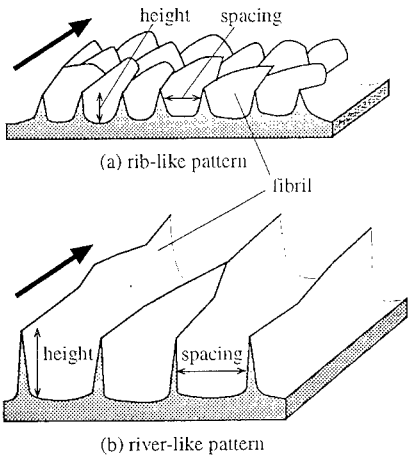

Figure 5 Schematic representation of fracture surfaces is obtained the rib-like pattern for Type A and the river-like pattern for Type B to D. Arrows indicate the direction of crack growth.

RELATIONSHIP BETWEEN FRACTURE TOUGHNESS AND MOLECULAR WEIGHT

Kusy and Turner(3) proposed that the fracture surface energy, γ of polymer is represented by the following equation based on the assumption that only molecules exceeding a critical degree of polymerization, p_c can contribute to the work of plastic deformation.

$$\gamma = \gamma_1 + \gamma_2 \quad (1)$$

where γ_1 and γ_2 is the total fracture energy required to rupture a monolayer of covalent bonds and the viscus flow term, respectively. γ_2 may be expressed as the product of the volume fraction of molecular, v_2 and a constant energy term, γ_c. Equation (1) becomes

$$\gamma \cong \gamma_1 + v_2\gamma_c = \gamma_1 + (1 - w_1)\gamma_c \quad (2)$$

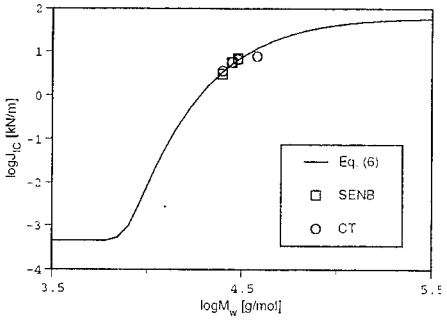

Figure 6 Fracture surface energy as a function of molecular weight.

where w_1 represents the weight fraction of all molecules with up to p_c. If we assume the molecular weight distribution of a material according to most probable distribution, i.e. the exponent in the Schulz distribution equals to 1, The weight fraction, $w(p)$ at the degree of polymerization, p results

$$w(p) = p / p_n^2 \exp(-p / p_n) \quad (3)$$

where p_n is the number-average degree of polymerization and $p_n = M_n/M_0$ with number-average molecular weight, M_n and molecular weight of the monomer, M_0. w_1 is obtained by integrating $w(p)$ from 0 to p_c.

$$w_1 = \int_0^{p_c} (r / p_n^2) \exp(-r / p_n) dr \quad (4)$$

Substitution of w_1 to equation (2) yields equation (5)

$$\gamma = \gamma_1 + \gamma_c(1 + p_c / p_n)\exp(-p_c / p_n) \quad (5)$$

For the present case, $M_w \cong M_v = 1.89M_n = 1.89p_nM_0$ and molecular weight of polyimide monomer, $M_0 = 450$, so that equation (5) yields

$$\gamma = \gamma_1 + \gamma_c(1 + 850p_c / M_w)\exp(-850p_c / M_w) \quad (6)$$

where M_v and M_n is viscosity average and number average molecular weight, respectively. The above equation could be interpreted as the relationship between J_{IC} and M_W for PI. By employing the value of $\gamma_1 = 4.5 \times 10^{-4}$ kN/m reported by Berry(7), γ_c and p_c were determined by using the experimental data except for Type D because the plasticizer might affect the results. Consequently, $\gamma_c = 60$ kN/m and $p_c = 135$ were obtained. The solid curve as shown in Figure 6 represents equation (6) with these constants. It is shown that equation (6) well fit the experimental data. In general it is difficult to prepare the variations of specimen over the wide range of M_W. Thus, if we could determine the value of γ_1 from another experimental data, equation (6) is utilized as to estimate the value of fracture toughness for wide range of M_W.

REFERENCES

1. Flory, P. J., 1945, J. Am. Chem. Soc., 67, 2049
2. Berry, J. P., 1964, Polym. Sci. (A), 2, 4069
3. Kusy, R. P., Turner, D. T., 1976, Polymer, 17, 161
4. Kramer, D. J., 1978, J. Mater. Sci., 14, 1381
5. Pitman, G. L., Ward, I. M., 1979, Polymer, 20, 895
6. Greco, R., Astarita, M. F., Dong, L., and Sorrentino A., 1994, Adv. Polym. Tech., 13, 259
7. Berry, J. P., 1961, J. Polym. Sci., 50, 107

Characterization of the Large Strain Deformation Response of Polypropylene at Low Temperatures and High Strain Rates

Ellen M. Arruda
The Department of Mechanical Engineering and Applied Mechanics
The University of Michigan
Ann Arbor, Michigan 48109-2125

Abstract

Polypropylene is an attractive material for automobile interior trim panels. It has good toughness and is easily molded. The addition of fillers such as talc reduces both the cost and anisotropic shrinkage of injection molded polypropylene panels. During side impact collisions, interior panels are subjected to high strain rate loadings. Accurate constitutive models of polypropylene at low temperatures and high strain rates are needed to assess the crashworthiness of trim panels in side impact collisions.

The strain rate and temperature dependent responses of polypropylene near room temperature are examined through constant strain rate compression tests to large deformations ($\epsilon = -2.0$). Tests included constant strain rate loading/unloading cycles and constant strain rate loading tests followed by stress relaxation. Observations of the strain rate and temperature dependent strain hardening and the amount of stress relaxation are used to examine the activation energies associated with various amorphous and crystalline deformation mechanisms. Additional studies including density measurements and differential scanning calorimetry (DSC) on deformed polypropylene provide further information about the relative amounts of crystal slip and amorphous orientation that occurred in any given test. For the range of conditions examined in this study, the large deformation responses includes cases for which crystallographic slip occurs and others for which amorphous deformation mechanisms dominate. The relationship of these mechanisms to features of the large deformation response such as rate dependent yielding and strain hardening is discussed.

A constitutive model for the rate and temperature dependent large strain response of polypropylene is introduced. This viscoplastic model takes into account crystalline and amorphous deformation processes but doesn't attempt to predict texturing effects other than amorphous alignment effects. The ability of the model to predict strain rate and temperature dependent behavior of polypropylene over the range of conditions tested is discussed.

TIME DEPENDENCE IN THE STRESS OPTIC RESPONSE OF CROSSLINKED ELASTOMERS

Paris R. von Lockette*
Ellen M. Arruda+

Polarized light intensity experiments were used to examine the time dependent stress and birefringence responses of two samples of polydimethylsiloxane (PDMS). Measurements were taken in real time via computer controlled data acquisition equipment. The material was deformed in compression at strain rates ranging from quasi-static measurements to step response tests. Differing time dependence in the birefringence and stress responses of the material are shown to lead to hysteresis in the stress and birefringence curves. A search for an analytical model for the time dependent behavior of PDMS leads to the incorporation of the slip-link model (1,2) concept into the eight-chain model (3,4) for rubber elasticity.

INTRODUCTION

Elastomeric materials contain long-chain molecules linked together in an amorphous network. The mechanical response of the network is influenced heavily by the amount of orientation in the molecules. This orientation, for uniaxial tests, is proportional to the birefringence. One of the authors has successfully developed a model which predicts the birefringence (orientation) and stress responses of elastomers under quasi-static loading conditions. Many elastomers, however, exhibit viscoelastic effects under loading at constant strain-rates. Recent work using molecular dynamics modeling has also shown time dependence in birefringence response (5). The purpose of this work is to experimentally capture the time-dependence of both the stress and birefringence responses in two samples of PDMS. The concept of slip-links proposed by Edwards and Vilgis (1) in conjunction with the eight-chain model of Arruda and Boyce (2) will be utilized as a means to characterize the time dependence analytically.

EXPERIMENTS

Materials: Cubic test specimens, roughly 6mm per side, were cut from sheets of PDMS provided by G. T. Burns at Dow, Bay City, MI. Two types of sample were studied: sample type (A) Mc=62,000 g/mol; and sample type (B) Mc=11,500 g/mol.

Equipment: An MTS servohydraulic frame was used to compress the specimens. LabTech Notebook data acquisition software was used to interface with the data acquisition card in order to drive the MTS actuators and read in voltage signals from the displacement transducers of the MTS, the load cell , and a photo diode. All data were read into the computer's RAM to avoid the delay in writing to the disk during a test.

*Ph.D. Candidate, Department of Mechanical Engineering, University of Michigan
+Assistant Professor, Department of Mechanical Engineering, University of Michigan

Setup: The upper platen of the MTS was affixed to the load cell which was attached to the upper actuator. Specimens were placed between the platens of the MTS. The contact surfaces were lubricated to provide friction free surfaces to reduce barreling. A 10 mW He-Ne laser (λ =632.8 nm) was directed through the center of the specimen, through a polarized lens crossed with the axis of polarization of the laser, and into the photo diode. The actuators produced symmetric displacement about the midplane of the specimen keeping the laser centered.

Kinematics: Several experiments were run at different strain rates for each specimen. A sample of type A was tested under quasi-static conditions in which it was allowed to rest five minutes between each step in strain to a maximum of ε=-.69. Samples of type A were also tested at constant strain rates of $\dot{\varepsilon}$ =-.01, $\dot{\varepsilon}$ =-.1, $\dot{\varepsilon}$ =-.5, and $\dot{\varepsilon}$ =-1.0 per second to a maximum strain of ε =-.69. Finally, a sample of type A was given a step of ε =-.69. Samples of type B were tested at constant strain rates of $\dot{\varepsilon}$ =-.01 and $\dot{\varepsilon}$ =-.1 per second to a maximum strain of ε =-.45. A sample of type B was also given a step of ε =-.45. The maximum strain values are so chosen to avoid barreling effects.

Calculations: The data acquisition card read voltages from the diode, load cell, and actuators. These signals were converted into physical birefringence, load, and displacement values, respectively. Voltage signals from the load cell and the actuators scaled linearly with physical load and displacement values. Voltage signals from the photo diode were related to birefringence, $\Delta\eta$ by the following equation:

$$I = Io \sin^2\left(\frac{\pi \Delta\eta\, d}{\Gamma}\right) \qquad [1]$$

where I is the measured intensity, Io is a scale factor dependent on the experimental setup, Γ is the wavelength of light used, and d is the current length of the path the light takes through the specimen. By normalizing the light intensity curve the birefringence can be found by use of inverse trigonometric functions. The incompressibility constraint was used to calculate d.

RESULTS:

Both samples of type A and B showed signs of time dependence in their response to step inputs in strain, see figures 1a and 1b. Figure 1a shows the stress response of sample A taking less time to reach its equilibrium value than the birefringence response. Figure 1b shows the reverse trend in sample B. Consequently the stress-optic coefficient, C (the slope of the birefringence-stress curve), increases in sample A and decreases in Sample B with time in response to a step strain input.

Figure 2a shows the loading stress-birefringence response of sample A for various strain rates. Though the data show some scatter due to the sensitivity of the load cell to electronic noise, it can be seen that the initial slopes of the curves increase with strain rate. These data also show nonlinear stress-optic behavior.

Figures 3 shows the hysteresis in the stress and birefringence curves for sample B during a constant strain rate test at ε=-0.1 . In each case the lower portion of the curve represents the loading path, the upper portion the unloading path. The figures show a shift in the stress and optic responses of the material upon unloading at a constant strain rate.

CONCLUSIONS:

This work shows that both the birefringence and stress responses of the PDMS samples tested have an innate time or strain rate dependence. Rate dependence of the stress optic coefficient has also been shown by Kröger *et al* (5) using molecular dynamics simulations.

It is proposed that the slip link mechanism be used to develop an analytical expression for capturing the time dependence of the stress optic response shown in figure 2a. The proposed analytical model for uniaxial stress incorporates the eight-chain stress function and the effects due to slip links to yield

$$\sigma = \frac{nk\Theta}{3}\sqrt{N}L^{-1}\left\{\frac{\sqrt{\lambda^2+2/\lambda}}{\sqrt{N}}\right\}\frac{\lambda^2-\frac{1}{\lambda}}{\sqrt{\lambda^2+2/\lambda}} + n_s k\Theta\left(b'(\lambda)-\lambda^{-3/2}b'(\lambda^{-1/2})\right) \qquad [2]$$

where b' is the derivative of the slip link function, b, detailed in Sweeney and Ward (2), and L^{-1} is the inverse Langevin function described in Arruda and Boyce (3). Incorporating slip link effects into the eight-chain model for birefringence, following the work of Sweeney and Ward (2), yields

$$\Delta\eta = \frac{QnN}{3(\lambda^2+2/\lambda)}\left(1-\frac{3}{\lambda^2+2/\lambda}\Big/L^{-1}\left\{\frac{3}{\lambda^2+2/\lambda}\right\}\right)+Qn_s(\lambda_{eff}^2-\lambda_{eff}^{-1}) \qquad [3]$$

The effective stretch, λ_{eff}, depends on the value of the slip link function, b. Derivation of λ_{eff} is given in Sweeney and Ward (2). The slip link function itself depends upon a 'slipperiness' factor. Assuming the slipperiness of the links, and possibly the number of affected slip links, is rate dependent, equations [2] and [3] can be used to fit the experimental data showing rate dependence in the stress optic response.

SYMBOLS USED

I - light intensity
Io - light intensity amplitude
$\Delta\eta$ – birefringence
n_s – slip link density
n - chain density
Q - optical constant of material
k - Boltzman's constant
d - light path length
λ – applied stretch
Γ – light wavelength
N - number of links per chain
π – Pi
Θ - Temperature

REFERENCES

1. Edwards S, Vilgis T, Polymer (1986) 483
2. Sweeney J, Ward I M, Journal of the Mechanics and Physics of Solids (1996) 1033
3. Arruda E M, Boyce M C, Journal of the Mechanics and Physics of Solids (1993) 389
4. Arruda E M, Przybylo P, Polymer Engineering (1995) 395
5. Kröger M, Lump C, Muller R, Macromolecules (1996)

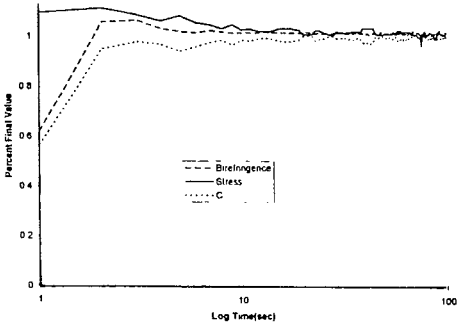

Figure 1a: Response to Step in Strain, ε=-.69, Mc=62,000

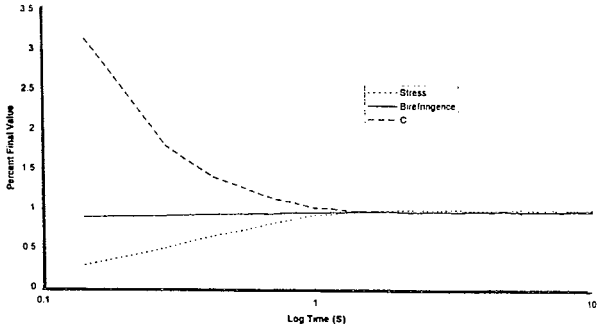

Figure 1b: Response to Step in Strain, ε=-.45, Mc=11,500

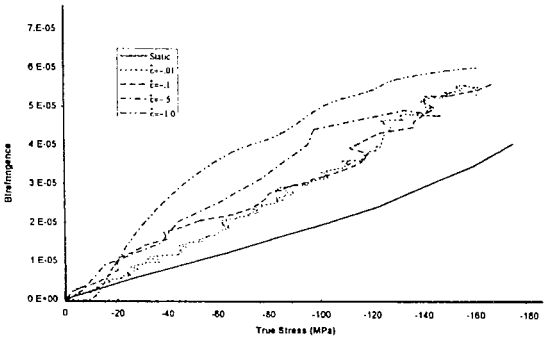

Figure 2a: Stress-optic response of Mc=62,000 for various strain rates

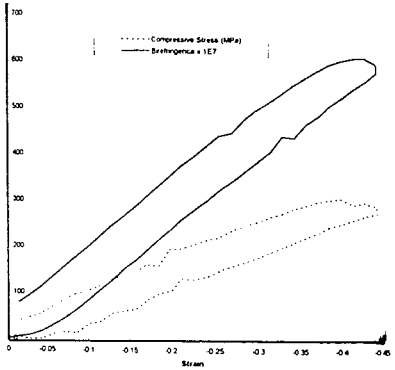

Figure 3: Hysteresis in Stress and Birefringence Responses, Mc=11500, Strain Rate=-0.1

TENSILE BEHAVIOUR OF GLASSY POLYMERS : DESCRIPTION BY A NON-LINEAR VISCOELASTIC MODEL

Nicole Heymans*

A Zener model including a viscoelastic β element has been shown to describe adequately linear viscoelastic behaviour using a single characteristic time. In the non-linear range, the characteristic time becomes stress and strain dependent, and also depends on the structural temperature which increases on straining. The model is combined here with a Davies-Jones annealing equation to simulate a network of stress-strain curves. General features are adequately described, but finer details require a distribution of characteristic times.

INTRODUCTION

A hierarchical viscoelastic model has been given previously by Heymans and Bauwens (1), leading to a fractional differential equation describing viscoelastic behaviour. In its simplest form, the model is a Zener model in which the viscous element is replaced by a generalized viscoelastic element whose behaviour is described by the fractional differential equation :

$$\sigma = E_0 \tau^{\beta} \frac{\partial^{\beta} \varepsilon}{\partial t^{\beta}} \qquad (1)$$

Heymans (2) has shown that the model correctly decribes dynamic mechanical behaviour in the linear range of viscoelasticity, over a wide range of frequencies, using a restricted number of fitting parameters; the complex modulus obtained from the model is an explicit function of reduced frequency. The behaviour of the element can be described by an equivalent ordinary differential equation in special situations such as creep; in this case it is found that the creep compliance of the model follows a power law (1) in agreement with experimental behaviour observed by Hellinckx et al (3). In more general situations numerical integration of the fractional differential equation is required. Hellinckx et al (4) have successfully modelled non-linearity and ageing during creep by introducing time and stress dependence of the characteristic time.

It is attempted here to generalize the model to the case of constant strain rate loading (i.e. a tensile test). It is well known that both the yield stress and yield drop are sensitive to the structural state of the sample, i.e. to the « structural temperature », and also that the structural temperature increases during plastic deformation (rejuvenation). The generalized Zener model is combined here with an annealing equation to account for this modification of structural temperature during a tensile test.

* Physique des Matériaux de Synthèse 194/8, U.L.B., B-1050 Brussels, Belgium

MODEL

The model is fundamentally a Zener model, (figure 1) in which the initial modulus E_0 represents local high modulus elasticity of the monomer, the viscoelastic element is characterized by front factor $E_0\tau^{\beta}$ and exponent β, and spring E_1 in parallel represents rubbery elasticity of an entangled length, controlling strain hardening beyond yield, and governed by the following equation :

$$\sigma = \frac{E_1 \lambda_M}{9}\left\{\mathcal{L}^{-1}\left(\frac{\lambda}{\lambda_M}\right) - \frac{1}{\lambda^{3/2}}\mathcal{L}^{-1}\left(\frac{1}{\lambda_M \lambda^{1/2}}\right)\right\} \tag{2}$$

where λ is the draw ratio, λ_M is the maximum draw ratio and $\mathcal{L}^{-1}$ is the inverse Langevin function. The structural temperature increases during deformation (rejuvenation process) but can also decrease due to annealing. The annealing process is insensitive to stress, thus the characteristic time appropriate for annealing is :

$$\tau_\vartheta = \tau_0 \exp\left(-k_\vartheta\left(\vartheta - \vartheta_0\right)\right) \tag{3}$$

and the annealing equation is therefore :

$$d\vartheta = k_\varepsilon d\varepsilon + \left(T - \vartheta\right)\frac{dt}{\tau_\vartheta} \tag{4}$$

The characteristic time τ of the viscoelastic element is both stress dependent, via an Eyring type equation expressing stress-activation; and also depends on structural temperature :

$$\tau = \tau_\vartheta \frac{\sigma / \sigma_0}{\sinh\left(\sigma / \sigma_0\right)} \tag{5}$$

Stress-strain curves were computed by numerical integration of the constitutive equation of the viscoelastic element, iterating the procedure to ensure compatibility of stress and strain with the elastic elements. Parameters were $E_0 = 2400$ MPa, $E_1 = 16$ MPa, $\lambda_M = 2.1$, $\sigma_0 = 1.28$ MPa, $k_\theta = 0.7$, $\theta_0 = 403$K (corresponding to a well-annealed sample), or 418K (corresponding to a slowly cooled sample), $\beta = 0.3$, and $k_\varepsilon = 200$ K. Except for the last two parameters which were arbitrary, parameters are obtained independently from the litterature and correspond to polycarbonate at room temperature.

RESULTS

The model correctly describes the main features of stress-strain behaviour : strain-rate dependence of the yield stress, yield drop, strain hardening beyond yield. It predicts an increase in structural temperature at yield, followed by a stabilization beyond yield; it is this stabilization that allows strain hardening due to restraint by the entanglement network to set in. Very little deviation from linearity is found below yield; this is consistent with the observation that ageing, which affects the extent of the linear region, is linked not to any variation of the structural temperature but to its distribution.

DISCUSSION

The calculated stress-strain curves display a far more extended low-strain linear region than experimental curves. Thus, this region can only be described adequately by applying the annealing equation to a distribution of structural temperatures. The requirement of a distribution of structural temperatures appears in other manifestations of polymer behaviour,

e.g. in the small endotherm preceding the sub-T_g exothermal plateau in a DSC scan on rejuvenated samples such as observed by Bauwens-Crowet and Bauwens (6). The present model, which ignores any such distribution, corresponds to an extremely well-aged sample (geologically aged !!).

The lower yield stress (or rather, the minimum of the stress-strain curve) is less sensitive to prior history than the upper yield stress, in agreement with experimental observations : by the time the minimum is reached, the structural temperature has reached its maximum value, and the residual dependence of stress on initial conditions is merely due to the lower draw ratio at which saturation is reached in the quenched sample.

The calculated yield drop is much larger than is observed experimentally, even when a low value of k_ε is used (200K instead of the value of 2650K found by Othmezouri-Decerf (7) by fitting loss tangent data obtained on rejuvenated samples). (All other parameters were given values from the litterature). This disagreement could be attributed to inadequacy of the linear relationship between entropy and retarded strain over a large strain range, or again to a distribution of structural temperatures : accounting for a distribution would spread the retarde deformation, leading both to an increase in anelastic deformation before yield and to a more gentle drop after yield. Also, since a yield drop causes strain localization, an increase in strain rate occurs in the yielded zone; this would lead to an increase in the stress required for further deformation, attenuating the yield drop.

The computed increase of structural temperature (reaching 478K beyond yield) is compatible with the value of structural temperature (460K) inferred from yield stress measurements obtained on rejuvenated samples by Bauwens-Crowet and Bauwens (5). The model predicts that the value obtained during drawing is insensitive to the draw ratio; however, this is difficult to check experimentally as the structural temperature will settle rapidly after unloading to a temperature-dependent value independent of prior history.

CONCLUSIONS

The model presented here is a first attempt to describe the complete stress-strain behaviour of a glassy polymer using a modified 4 parameter Zener model in combination with an annealing equation. The description is qualitatively correct if stress activation, rejuvenation and annealing are accounted for; remarkably so in view of the low number of parameters required, most of which can be determined independently and experimentally. Quantitative agreement will require accounting for a range of structural temperatures, and also for strain localization leading to an inhomogeneous strain rate.

REFERENCES

1. Heymans N., Bauwens J.-C. *Rheol Acta* **33** (1994) 210
2. Heymans N., *Rheol Acta* **35** (1996) 508
3. Hellinckx S., Heymans N., Bauwens J.-C. *J Non-Cryst Solids* **172-174** (1994) 1058
4. Hellinckx S., Heymans N., Bauwens J.-C. *9th Internat Conf on Deformation, Yield and Fracture* Cambridge UK, 1994, P81
5. Bauwens-Crowet C., Bauwens J.-C. *Polymer* **29** (1988) 1985
6. Bauwens-Crowet C., Bauwens J.-C. *Polymer* **28** (1987) 1863
7. Othmezouri-Decerf J. *Polymer* **35** (1994) 4734

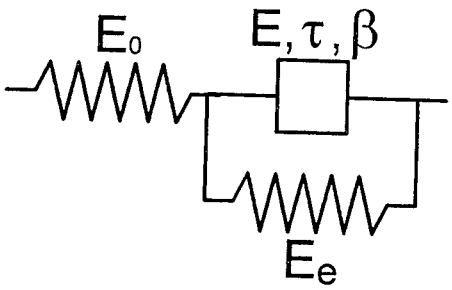

Figure 1
Generalized Zener model for viscoelastic behaviour

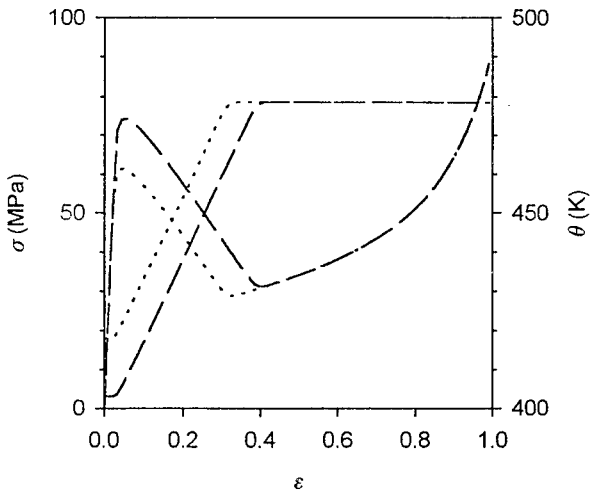

Figure 2
Stress-strain curves and increase in structural temperature resulting from the model.
Dashed lines : $\theta_0 = 403K$
Dotted lines : $\theta_0 = 418K$

AN INVESTIGATION OF YIELDING BEHAVIOUR IN DRAWN LDPE

N Thavarungkul* and IR Harrison*

Extruded low density polyethylene (LDPE) has been drawn under different conditions. Data from mechanical tests along with characterization results from small angle x-ray scattering (SAXS), differential scanning calorimetry (DSC), shrinkage, and birefringence suggest that the morphology in drawn LDPE is row nucleated. Yield stress and modulus in the transverse direction are controlled by crystal lamellae functioning as short aspect ratio reinforcing fibers in an amorphous matrix. Mechanical properties in the machine direction are dominated by orientation.

Studies of plastic deformation mechanisms (1-4) as well as structure/yield stress relationships in polymers (5-11) have been undertaken by many researchers in order to understand and improve mechanical properties. Oriented polymers are known to have excellent mechanical properties in the orientation direction (12,13) , however , an underlying molecular mechanism that justifies a particular yield stress is not known. To obtain information that can lead to some explanation for yield behavior in polymers, low density polyethylene (LDPE) 526I from Dow Chemical has been studied.

The purpose of this study was to understand the influence of crystalline/amorphous phase structure and orientation on yield stress.

Experimental Procedure

LDPE 526I was extruded as sheet (300-350 μm thick) and then "cold drawn". Selected samples were subsequently annealed; drawing and annealing conditions are shown in Table I. Mechanical properties and characterization information are shown in the following section.

Results and Discussion

Modulus in the machine direction is greater than that in the transverse direction for the samples which were not annealed after cold drawing (Figure 1). In contrast, modulus in the machine direction is less than that in the transverse direction when samples were annealed. "As extruded" samples are a special case that behaved as if they had experienced "annealing".

In addition, the annealed samples set has a smaller full-width at half maximum intensity (FWHM) along the width of the SAXS diffraction spot compared to those of the unannealed set as shown in Figure 2. Lateral dimensions of crystals are inversely proportional to FWHM. This data suggests that when a sample is annealed, crystals grow larger laterally compared to their original sizes without thermal treatment. The crystals, then, function as short reinforcing fibers as stated in the composite model by Simpson (14) and a row nucleated morphology can be applied as shown in Figure 3.

* Polymer science Program, Department of Materials Science and Engineering, The Pennsylvania State University.

Table I Preparation conditions for drawn LDPE

Sample	Draw Rate %	Draw Temperature (°C)	Annealing Temperature (°C)	Annealing time (min)	Relaxation time (hrs)	Separation Distance (mm)
a	-	-	-	-	-	-
b	500	RT	-	-	-	-
c	500	RT	80	200	-	305.8
d	500	RT	80	500	-	305.8
e	500	RT	95	200	-	305.8
f	1000	RT	-	-	-	-
g	1	RT	-	-	-	-
h	500	RT	-	-	48	305.8
i	500	RT	80	200	-	210
j	500	RT	95	200	-	210
k	1	RT	80	200	-	190
l	500	80	-	-	-	-
m	500	80	80	200	-	305.8

Yield stress increases linearly with modulus tested in the transverse direction, as shown in Figure 4. This suggests that yield stress in the transverse direction is also controlled by the short fiber-like crystals.

Unlike previous findings by other researchers that, for unoriented polymer, yield stress increases proportionally to modulus (15), or crystallinity (5, 6); Figures 5, and 6 show that the yield stress of drawn polyethylenes is more dependent on draw ratio, or degree of orientation.

References

1. Peterlin A., 1971, J. Mat. Sci., 6, 490
2. Gent A.N., and Jeong J., 1986, Polym. Eng. Sci., 26, 285
3. Juska T.D., 1984, Ph.D. Dissertation, The Pennsylvania State University
4. Kestenbach H.K., and Petermann J., 1994, Polymer, 24, 5217
5. Nunes R.W., Martin J.R. and Johnson J.F., 1982, Polym. Eng. Sci., 22, 205
6. Popli R., and Mandelkern L., 1987, J. Polym. Sci.: Polym. Phys. Ed., 25, 441
7. Darras C., and Seguela R.,1993, J. Polym. Sci.: Polym. Phys. Ed., 31, 759
8. Starkweather H.W., Jr., and Brooks R.E., 1959, J. Appl. Polym. Sci., 2, 236
9. Hanrahan B., 1984, Master Thesis, The Pennsylvania State University
10. Capaccio C., and Ward I.M., 1975, Polymer, 16, 239
11. Micher G.H., 1992, Coll. Polym. Sci., 270, 627
12. Starkweather H.W., Jr., Jordan T.F., and Dunnington G.B., 1992, Polym. Eng. Sci., 14, 674
13. Seguela R., and Rietsch F., 1990, Polymer, 27, 532
14. Simpson D.M., 1993, Ph.D. Dissertation, The Pennsylvania State University
15. Bicerano J., 'Prediction of Polymer Properties', Marcel Dekker, Inc., New York, 1993

Figure 1. Modulus of LDPE in Machine and Transverse Direction

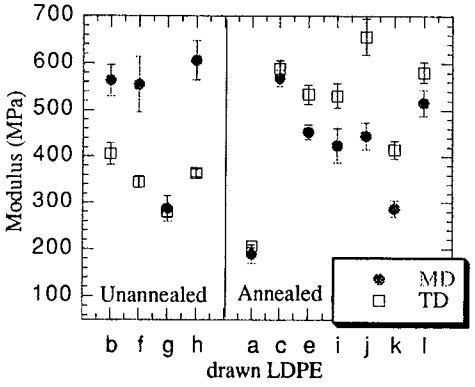

Figure 2. FWHM of Drawn LDPE prepared under different conditions

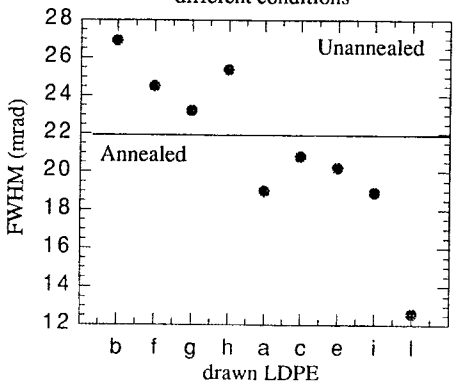

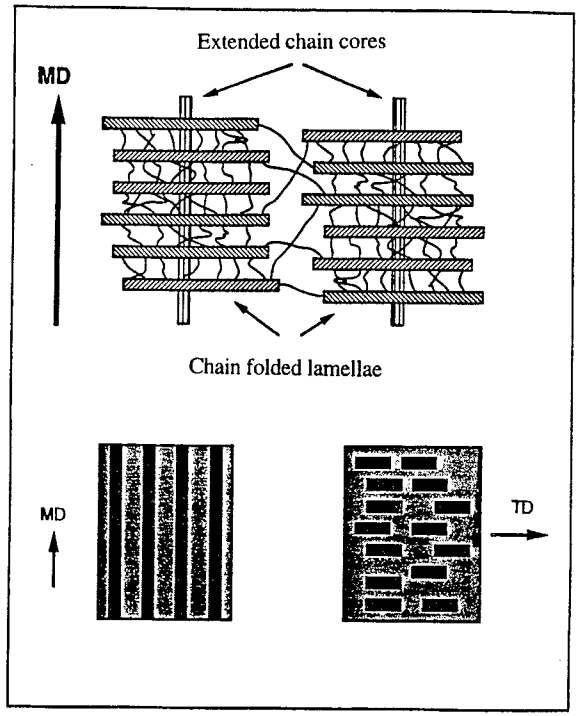

Figure 3. Composite analogies for PE crystalline morphology

Figure 4. Modulus vs Yield Stress of drawn LDPE in both machine and transverse direction

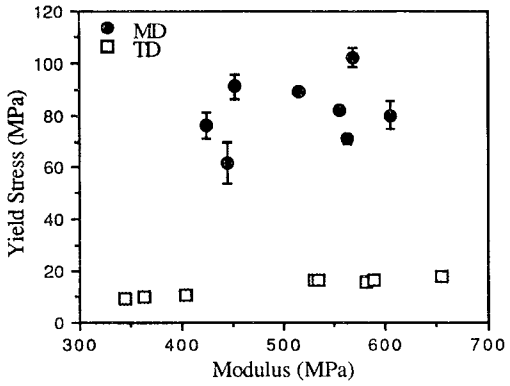

Figure 5. Yield Stress vs Crystallinity

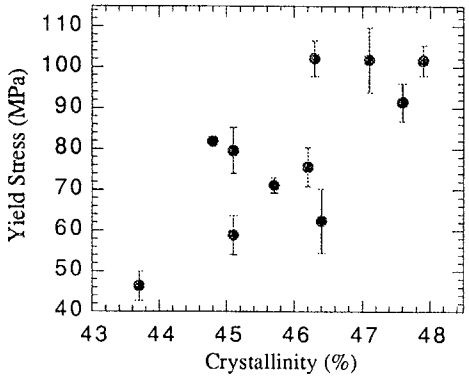

Figure 6. Yield Stress vs Contraction Ratio

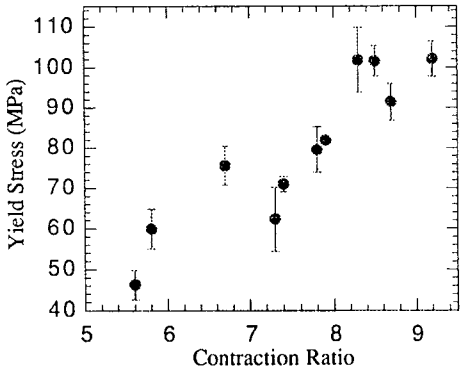

MEASUREMENT OF AN ISOCHORIC GLASS TRANSITION

Dina M. Colucci and Gregory B. McKenna*

INTRODUCTION

In the work presented here, we describe recent measurements[1] in which a polycarbonate melt is pressurized at a fixed specific volume and then cooled slowly while the specific volume is maintained constant. We address several questions with the results: (i) does one observe and isochoric glass transition, (ii) if one does observe an isochoric glass transition, how do the glass formation points compare with those observed isobarically, and (iii) how do the isobaric and isochoric transition strengths compare?

EXPERIMENTAL

The material used in the studies was a Lexan LS-2, medium viscosity, UV stabilized, commercial grade poly(carbonate) from the General Electric Company[2]. It was machined into cylindrical rods with a diameter of 12 mm and a length of 16 mm. Before placement into the PVT apparatus, the sample was dried for 5 days at 150 °C. Periodically, the sample was removed and weighed and after 72 hours no further weight loss was detected. The sample was then stored in a sealed test tube with standard desiccant until placed in the PVT apparatus.

In this work, we used a reference specific volume of the poly(carbonate) at 10 MPa and 30 °C of 0.8350 cm^3/g[3,4]. This was measured using method ASTM D 792 on a Sartorious R160D balance with hydrostatic weighing device[1]. The value of 0.8350 cm^3/g is the average of the two referenced sources, corrected to account for the fact that the reference state in the PVT apparatus is set at 30 °C and 10 MPa not atmospheric pressure which was used to determine the density.

The results reported here are for PVT measurements and were performed using a commercial Gnomix dilatometer that operates over ranges of 30-400 °C and 10-200 MPa while measuring volume changes to within ± 0.0001 cm^3/g. A detailed description of the Gnomix apparatus, operation, and calibration can be found in the Gnomix PVT manual[5]. Isobaric studies were performed as follows: (i) the material was heated to a temperature of 75-100 °C above T_g at the desired testing pressure and allowed to stabilize (ii) the sample was cooled at 1 °C/min while maintaining a constant pressure and simultaneously monitoring the volume. Isochoric experiments were performed using a similar procedure: (i) the material was heated to a temperature of 75-100 °C above T_g and the pressure was increased until the desired constant volume conditions were obtained (ii) after stabilization, the polymer was cooled at 1 °C/min with the isochoric conditions maintained by adjusting the pressure while simultaneously

*Polymers Division, National Institute of Standards and Technology, Gaithersburg, MD 20899, USA

monitoring the pressure versus temperature behavior. Importantly, corrections were made for the PVT behavior of the mercury and apparatus so that the system could be controlled to keep the sample volume constant unlike the other work described earlier in which the total volume of sample and mercury was kept constant.

RESULTS

Figure 1 depicts the specific volume versus temperature isobars for the PC at pressures ranging from 10 to 160 MPa. The isochoric results for specific volume isochores ranging from 0.8275 to 0.8550 cm^3/g are shown in Figure 2. In order to determine the formation pressure, volume and temperature P_{gf}, V_{gf}, and T_{gf} points, linear regression was performed on the data at temperatures above and below where the glass transition seems to occur. The solid lines in Figures 1 and 2 result from the regression analysis. (The isochoric responses at the largest volume values of 0.8550 and 0.8500 cm^3/g were not analyzed using linear regression since insufficient glassy data exist to make an accurate determination of the formation points.) Clearly a glass transition exists in both the isochoric and isobaric cases. It is readily seen that the change in behavior in going from the rubber to the glass is much greater for the isobaric case; hence, the "strength" of the isobaric transition appears to be significantly stronger than that of the isochoric transition.

It is of interest to ask whether or not the glass formation points for the isobaric and isochoric formation paths are the same. The appropriate comparison of the T_{gf} versus P_{gf} values is shown in Figure 3. The data of V_{gf} versus P_{gf} are shown in Figure 4. These plots show that both the isobaric and isochoric results have approximately the same glass formation values. The error bars associated with the determination of P_{gf}, V_{gf}, and T_{gf} are also contained in Figures 3 and 4 and were obtained by performing the bootstrap error analysis[6]. The isochoric result with a P_{gf} of approximately 60 MPa is the only potential outlier in the set. The discrepancy is attributed to the fact that only a small amount of glassy data are available to perform the regression analysis for this isochore.

Even though the rubbery surfaces and glass formation points are the same in the isobaric and isochoric PVT results, the glassy responses differ significantly. The isobaric and isochoric rubbery and glassy surfaces were analyzed numerically such that an equation was derived for the relationship of the volume to the pressure and temperature with the results shown three-dimensionally in Figure 5. The differences in the glassy responses for the isochoric and isobaric cases become quite evident, where the isochoric glassy surface lies beneath the isobaric surface.

SUMMARY

PVT experiments were performed over the glass transition range for poly(carbonate) in both isochoric and isobaric conditions. A glass transition was identified in both isochoric and isobaric experiments and the pressure, volume, temperature formation points were found to be the same for both glass formation paths. The isobaric and isochoric PVT data were the same in the equilibrium rubbery state and differed in the non-equilibrium glassy states. In particular, the isochoric glass transition was not as pronounced as was the isobaric transition.

REFERENCES

1. Colucci D.M., McKenna G.B., Filliben J.J., Lee A., Curliss D.B., Bowman K.B., and Russell J.D., *J. Poly. Sci.: Part B, Poly. Phys.*, accepted

2. Certain commercial materials and equipment are identified in this paper to specify adequately the experimental procedure. In no case does such identification imply recommendation or endorsement by the National Institute of Standards and Technology, nor does it imply necessarily that the product is the best available for the purpose.

3. General Electric Database, http://www.ge.com/datasheets/LEXANLS2.html

4. AC Technology Polymer Laboratories, Ithaca, NY, personal communication.

5. Gnomix PVT Manual, Gnomix Inc., Boulder, CO, 1990

6. Efron B. and Tibshirani R., *Stat. Science*, 1, 1, 54, 1996

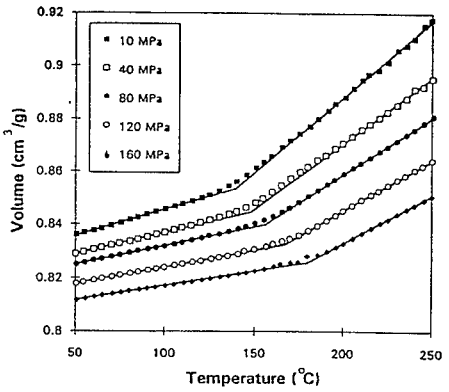

Figure 1: Isobaric PVT Results. The symbols are the experimental data while the solid lines are the linear regression results.

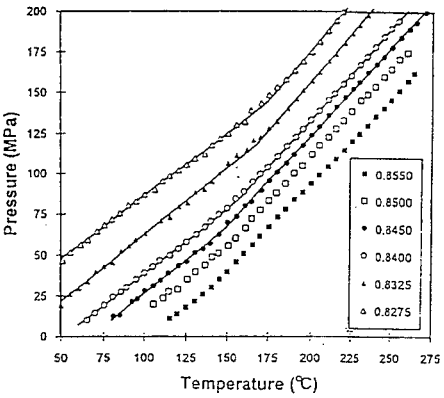

Figure 2: Isochoric PVT Results. The symbols are the experimental data while the solid lines are the linear regression results.

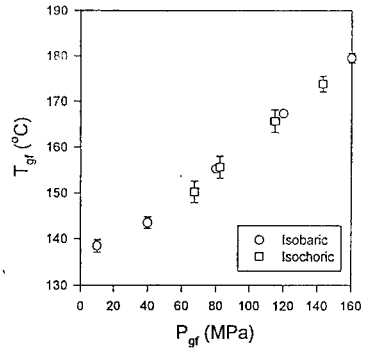

Figure 3: Glass Formation Temperature Versus Formation Pressure for the Isobaric and Isochoric PVT Data.

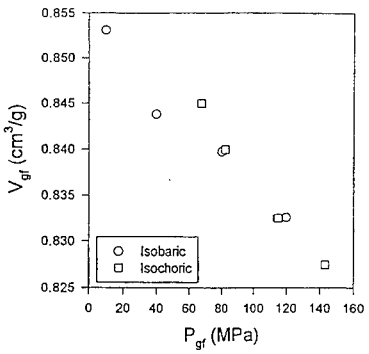

Figure 4: Glass Formation Volume Versus Formation Pressure for the Isobaric and Isochoric PVT Data.

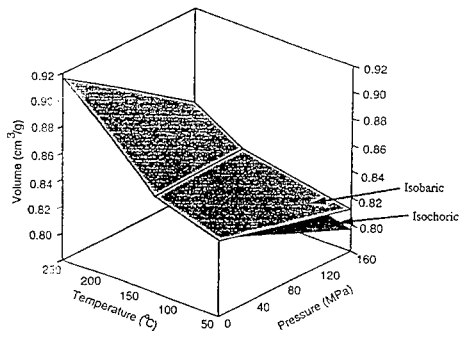

Figure 5: Three Dimensional Plot of Both the Isobaric and Isochoric PVT Data. The plot shows that the rubbery surfaces and glass formation points are the same, but the glassy surfaces are different.

REDUCED TIME CONCEPTS AND THE SUB-T_g RESPONSE OF A POLYCARBONATE GLASS

Paul A. O'Connell* and Gregory B. McKenna

INTRODUCTION

Ongoing work in this laboratory (1,2) has been aimed at buuilding a comprehensive material database for glassy polymer behavior. As part of this work a systematic study of one industrially important polymer (polycarbonate (Lexan LS)) supplied by the General Electric Company (3) has been carried out under a range of loading conditions and geometries. Here we examine time - temperature, time - aging time and time - strain superposition behaviors of this polycarbonate in torsion. These are three procedures which are commonly used to estimate the long term material performance from relatively short-term tests.

Data are presented from tests of the stress relaxation response of the polycarbonate under torsional deformations. Tests were performed on samples over a range of strains from 0.0025 to 0.08, temperatures from 30 to 135 °C and aging times from 1800 to 64800 s. Individual data sets at each strain, temperature and aging time could be described using a stretched exponential form relaxation function and time - aging time superposition was found to be applicable to the data under all test conditions. The double logarithmic aging time shift rate, μ, was found to vary significantly with both temperature and strain. Over the range of temperatures studied the data could be superimposed using conventional time-temperature superposition. However, the master curve could not be described by a stretched exponential function. For strains up to 0.07 the data at each temperature could also be superimposed to form a master curve following the principle of time-strain superposition. Interestingly, the master curves found from time-strain and time-temperature superposition did not have the same form.

TIME - TEMPERATURE SUPERPOSITION

Time - temperature superposition is widely used in the description of polymer behavior at temperatures above the glass transition temperature T_g (5). One representation for the response function in stress relaxation experiments is the stretched exponential of Kohlrausch-Williams-Watts (KWW) (6,7)

$$M(t) = M_o \, e^{-(t/\tau_o)^{\beta}} \qquad (1)$$

where M(t) is the torque response at time t, τ_o a characteristic time, β a shape parameter related to the breadth of the relaxation curve, and M_o is the zero time torque response. A change in temperature from T_o to T results in a change in the characteristic relaxation time

*Polymers Division, National Institute of Standards and Technology, Gaithersburg, MD 20899 USA

leading to a temperature shift factor $a_T = \tau_{T_o} / \tau_T$. Vertical shifts are seen as a temperature dependent zero time torque response M_o ; $b_T = M_{o,T_o} / M_{o,T}$.

TIME - STRAIN SUPERPOSITION

The principle of time - strain superposition is essentially the same as that for time - temperature superposition, though now there is a strain induced shift (acceleration) in the time scale of the material response (8). Again, within the context of the KWW function one can write the time-strain shift function as $a_\gamma = \tau_{o,\gamma o} / \tau_{o,\gamma}$ where the γ_o and γ subscripts represent the reference and current strains, respectively. Similarly, the vertical strain shifts are $b_\gamma = M_{o,\gamma o} / M_{o,\gamma}$.

TIME - AGING TIME SUPERPOSITION

Again, within the context of the KWW function one can write the time-aging time shift function as $a_{te} = \tau_{o,te o} / \tau_{o,te}$ where the t_{eo} and t_e subscripts represent the reference and current aging times, respectively. Similarly, the vertical aging time shifts are $b_{te} = M_{o,te o} / M_{o,te}$.

EXPERIMENTAL

Cylindrical samples with a gauge section of 30mm length and 4mm diameter were machined in order to grip the samples in a special fixture for the torsion of solid samples (9). To remove the effects of previous thermal and/or mechanical history, the samples were heated to 145 °C for 1 hour prior to testing. This is approximately 4 °C above the measured T_g, as determined from DSC measurements at a heating rate of 10 °C/ min after slow cooling of the sample (4).

The torque relaxations measurements were made at nominal strains $\gamma = R \phi / L = R \Psi$ from 0.0025 to 0.08 where ϕ = angle of twist, R the cylinder radius, L the length of the gauge section and Ψ the angle of twist per unit length. The accuracy of measurements in the sample radius and length lead to a final error in the torque reading (i.e. sample to sample variation) of approximately ±1%. In addition to this error, noise on the data acquisition system gives an error on individual torque force readings of ±0.001 N.m which, depending on the applied strain and temperature, translates to an error of up to ±1 %.

A classical sequence of loading following Struik's (10) procedure was used for the aging time tests.

RESULTS

Application of the appropriate shift factor, a_{te}, to the relaxation data results in a superposition of the data to form the time-ageing time 'master curve'. A plot of the $\log(a_{te})$ vs $\log(t_e)$ values show good linearity, the slope of which is the double logarithmic shift rate, μ. Fig 1 illustrates the effect of both temperature and strain on the shift rate, μ, for temperatures up to 110 °C and strains up to 0.07. The error bars shown are the root mean square deviation from the average value. At low strains (<0.02) the shift rate is approximately constant at any given temperature. The small strain shift rate can be seen to increase slightly as the temperature increases. There is a systematic decrease in the shift rate with increasing strain.

This strain dependence of the shift rate is seen to become smaller as temperatures increases. The temperature dependence of the shift rate then increases at higher strains. Significantly, the decreasing dependence of the shift rate on strain continues to such an extent that the shift rate is independent of strain at 110 °C.

The time - temperature superposition data presented here are for 0.02 strain and an ageing time of 64800 seconds. The master curve is shown in Fig 2. The corresponding temperature shift factors are shown in Fig 3. Similar data obtained previously (2) from dynamic tests are also shown. At temperatures just below T_g the temperature shift factor rises rapidly [WLF-like (4)] with decreasing temperature, until about 20 °C below T_g where the rate begins to decrease. The rate then continues to decrease as the temperature is further reduced.

Referring again to Fig 2 the KWW fit to the master curve data is shown. It is clear that the KWW equation is only an approximate representation to the relaxation behavior when oned considers the whole range of data. This is surprising since the individual data sets at each temperature did appear to be described very well by KWW equations. So, although the KWW expression can fit the data over a short time scale (approximately 4 decades), the deviation in the fits seems to show up when a larger time range is used (~ 7 decades).

For study of time - strain superposition strains from 0.0025 to 0.07 were examined, and the resulting master curve, for 30 °C and referenced to 0.0025 strain, is included in Fig 2. The relevant time shift factors are shown in Fig 4. The master curve covers approximately 8 decades of time, which is comparable to the range covered with time-temperature superposition. The shift factors are approximately constant at low strain (< 0.015). They then rise monotonically with increasing strain.

The two master curves obtained above [time-temperature superposition and one from time - strain superposition (30 °C; 0.02 strain)] are shown in Fig 2. At short times (low temperatures or small strains), the data coincide. At longer times (>4 decades) the two data sets begin to diverge, with the time - temperature data showing a significantly greater relaxation rate compared to the time - strain data. The implication is that temperature and strain affect the relaxation response in different ways.

REFERENCES

1. Pesce J.J. and McKenna G.B. Society of Plastic Engineers ANTEC (1995) 1932
2. Niemiec J., Schultheisz C., Schutte C. and McKenna G.B., Society of Plastic Engineers ANTEC (1995) 2402
3. Certain commercial materials and equipment are identified in this paper to specify adequately the experimental procedure. In no case does such identification imply recommendation or endorsement by the National Institute of Standards and Technology, nor does it imply necessarily that the product is the best available for the purpose.
4. Ferry J.D. 'Viscoelastic Properties of Polymers', J. Wiley and Son (New York) 1980
6. Kohlrausch F. Pogg. Ann. Phys. 12 (1847) 393
7. Williams G. and Watts D.C. Trans. Faraday Soc. 66 (1970) 80
8. Shapery R.A. Poly. Eng. Sci. 9 (1969) 4
9. McKenna G.B. and Kovacs A. Poly. Eng. Sci. 24, 1138 (1984)
10. Struik L.C.E 'Physical Ageing in Amorphous Polymers', Elsevier, (Amsterdam) 1978

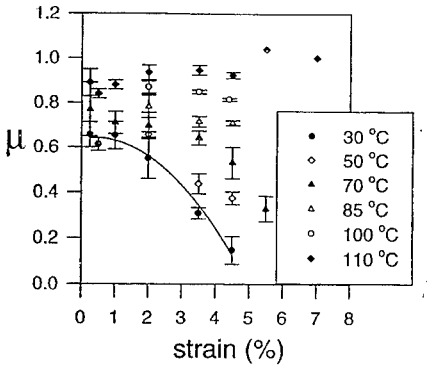

Fig 1 Average μ values as a function of temperature and strain.

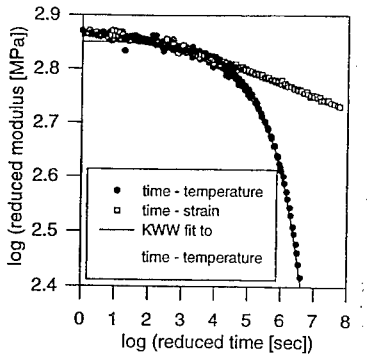

Fig 2. Master curves for time-temperature and time-strain superposition, with the KWW fit to the time-temperature master curve.

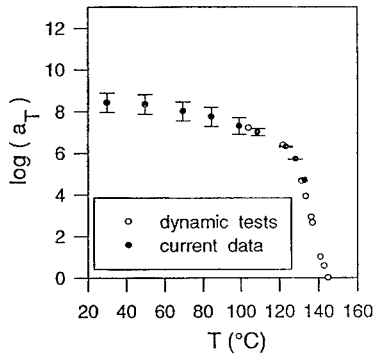

Fig 3. Temperature shift factors ,a_T, as a function of temperature.

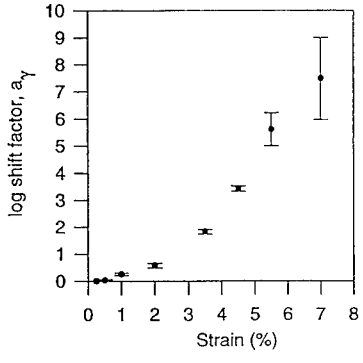

Fig 4. Strain shift factors ,a_γ, as a function of strain.

VOLUME RECOVERY AND PHYSICAL AGING IN POLYCARBONATE FOLLOWING TEMPERATURE JUMPS

CR Schultheisz* and GB McKenna*

When subjected to temperature changes in the neighborhood of the glass transition (T_g), amorphous polymers exhibit evolution of both structure (as characterized by the volume or enthalpy) and mechanical response (physical aging). We have performed dilatometric experiments on polycarbonate using temperature-jump histories, and modeled the results using a nonlinear volume response incorporating a material time clock that depends on the current volume. In down-jumps close to T_g, a direct comparison between the evolution of the volume and the mechanical responses (measured in separate torsion experiments) indicates that the mechanical properties cease evolving (reach equilibrium) before the volume. These results are similar to behavior seen previously in this laboratory with epoxy glasses near to the glass transition. We interpret the results to imply that each material process has a different fictive temperature.

The nonequilibrium response of polymer glasses is a subject of considerable interest. There are two aspects to the subject that we address here. First, the nonequilibrium structure (volume or enthalpy) of the glassy material undergoes recovery which has important kinetics [1-7]. Second, along with the structural changes, the mechanical properties also change in a process labeled physical aging [8-10]. Recently, there have been several studies [11-15] reporting that the time scales of the evolution of the properties towards equilibrium can be different. Our results indicate that the mechanical response in down-jump experiments achieves equilibrium before the volume [13-15]. However, this behavior is not universal [16] and we suggest that the apparent conflict may be due to differences in materials.

Physical Aging - Torsion Experiments

The material employed in these investigations was a commercial Bisphenol-A polycarbonate, a UV stabilized, medium viscosity grade for applications with high optical requirements. T_g was measured as 141.3 °C using differential scanning calorimetry heating at 10 °C/min [9].

In prior work [9] dynamic mechanical experiments were performed to investigate the

*National Institute of Standards and Technology, Gaithersburg, MD, 20899, USA

physical aging behavior of the polycarbonate. Samples were conditioned at 145 °C before cooling to the testing temperature. Time-aging time superposition [8] was employed to evaluate aging time shift factors, a_{te}, as shown in Figure 1 for four different test temperatures. The figure shows that at 122 °C aging continues beyond the time of the experiments. At higher temperatures, the aging time shift factor ceases to change after some time, indicating that the mechanical properties have achieved equilibrium. In contrast with the dilatometric results described below, note that the flat response at 137 °C demonstrates that, at this temperature, the mechanical response equilibrates in less than 1800 s, the shortest aging time tested.

Phenomenological Description of the Volume Recovery

Common descriptions of the kinetics of structural recovery are the Tool-Narayanaswamy-Moynihan-KAHR models [1-5]. We have employed a hybrid model [17] to obtain relevant phenomenological fits to temperature jump experiments. The volume departure from equilibrium, δ, is related to the thermal history and material properties as:

$$\delta(z) = (V(z)-V_\infty)/V_\infty = -\Delta\alpha\int_0^z R(z-z')\frac{dT}{dz'}dz' \qquad (1)$$

where $V(z)$ is the current volume and V_∞ is the volume of the equilibrium liquid. T is the temperature, and $\Delta\alpha$ is the difference between the liquid and glassy coefficients of thermal expansion. $R(z)$ is a retardation function written in terms of the reduced time of the material denoted by z, which is calculated from the experimental time t through shift factors a_T and a_δ that depend on temperature T and structure δ, respectively:

$$z = \int_0^t \frac{d\xi}{a_T(T(\xi))a_\delta(\delta(\xi))} \qquad (2)$$

If we assume that the temperature history is a step function in temperature from T_1 to T_0 at $t = z = 0$, the convolution integral in equation (1) reduces to $\delta(z) = -\Delta\alpha\, R(z)\,(T_0 - T_1)$. The volume response function $R(z)$ is expressed as a stretched exponential (as used in [5]),

$$R(z) = \exp\left[-(z/\tau_r)^\beta\right] \qquad (3)$$

where τ_r is a characteristic time. The shift factors are exponentials as suggested in [4],

$$a_T = \exp\left[-\Theta(T-T_r)\right], \qquad a_\delta = \exp\left[-(1-x)\Theta\delta/\Delta\alpha\right] \qquad (4)$$

where T_r is a reference temperature. Θ is a constant, and x is a partitioning parameter ($0 \le x \le 1$) that weights the relative contributions of the temperature and the structure to the shift factor. The parameters $\Delta\alpha$, τ_r, β, Θ and x were then evaluated from the experimental data by adapting a Levenberg-Marquardt nonlinear curve-fitting algorithm [18] as detailed in [17].

Volume Recovery Experiments

The volume behavior of the polycarbonate was measured using an automated mercury dilatometer similar in conception to those used by Kovacs [3]. The sample consisted of approximately 3.38 g of polycarbonate pellets with a volume of approximately 2.85 cm^3 at

room temperature. The uncertainty in the relative volume measurements (expressed as one standard deviation) is estimated as 5×10^{-5} cm^3. The glassy and liquid coefficients of thermal expansion were measured as $\alpha_G = 2.15 \times 10^{-4}$ cm^3/(cm^3 °C) and $\alpha_L = 5.94 \times 10^{-4}$ cm^3/(cm^3 °C), respectively. The uncertainty (expressed as one standard deviation) is estimated to be 10^{-5} cm^3/(cm^3 °C). The difference between the coefficients of thermal expansion is $\Delta\alpha = \alpha_L - \alpha_G = 3.79 \times 10^{-4}$ cm^3/(cm^3 °C).

In order to study the nonequilibrium volume recovery, asymmetry of approach experiments were performed. Up and down-jumps of 5 °C were performed to a final temperature of T_0 = 140 °C, and up and down-jumps of 2 °C were performed to a final temperature of T_0 = 138 °C. Thermal equilibration took 100 to 200 s.

Results and Discussion

The results of the curve fit to the temperature jump data are shown in Figure 2. The points used in the curve fit are indicated by symbols in the figure, and the lines show the prediction of the model using the calculated parameters given in Table 1. Hodge [7] obtained similar parameters of β = 0.46, Θ = 0.87 K^{-1} and x = 0.19 from enthalpy recovery measurements on a Bisphenol-A polycarbonate.

For this limited set of data, the model represents the experiments reasonably well. Obviously, experiments using larger jumps at lower temperatures should provide better data for the curve fit to compare with direct measurements. Simulations using the model indicate that the approximation of the temperature history as a jump is acceptable, because the volume recovery resulting from a finite rate temperature change quickly approaches the volume recovery from a jump once the final temperature has been reached.

Parameter	T_r = 140 °C
$\Delta\alpha$ (10^{-3} K^{-1})	4.41
τ_r (s)	138
β	0.398
Θ (K^{-1})	0.876
x	0.177

Table 1. Hybrid model parameters determined from volume recovery data in Figures 2 and 3.

Although the temperatures used in the different tests were not identical, one can readily see that the volume requires more than 10^4 s to equilibrate at 138 °C while the mechanical properties have reached equilibrium in less than 1800 s at a lower temperature (137 °C). This result is consistent with observations from this laboratory in experiments with a model epoxy [13-15] using the NIST torsional dilatometer.

References

1. Tool AQ, J. Res. NBS 37 (1946) 73; J. Am. Ceram. Soc. 29 (1946) 240.
2. Narayanaswamy OS, J. Am. Ceram. Soc. 54 (1971) 491.
3. Kovacs AJ, Fortschr. Hochpolym.-Forsch. 3 (1963) 394.
4. Kovacs AJ, Aklonis JJ, Hutchinson JM, Ramos AR, J. Polym. Sci. Polym. Phys. Ed. 17 (1979) 1097.
5. Moynihan CT, Macedo PB, Montrose CJ, Gupta PK, DeBolt MA, Dill JF, Dom BE, Drake PW, Esteal AJ, Elterman PB, Moeller RP, Sasabe H, Wilder JA, Ann. N.Y.

Acad. Sci. 279 (1976) 15.
6. McKenna GB, Comprehensive Polym. Sci., Vol. 2: Polymer Properties, pp. 311, C Booth and C Price, eds, Pergamon Press (Oxford) 1989.
7. Hodge IM, J. Non-Crystalline Solids 169 (1994) 211.
8. Struik LCE, 'Physical Aging in Amorphous Polymers and Other Materials', Elsevier (Amsterdam) 1978.
9. Pesce J-J, Niemiec JM, Chiang MY, Schutte CL, Schultheisz CR, McKenna GB, Current Research in the Thermo-Mechanics of Polymers in the Rubbery-Glassy Range AMD-203, pp. 77, M Negahban, ed, ASME (New York) 1995.
10. Hutchinson JM, Prog. Polym. Sci. 20 (1995) 703.
11. Scherer GW, 'Relaxation in Glass and Composites', Wiley (New York) 1986.
12. Roe R-J, Millman GM, Polym. Eng. Sci. 23 (1983) 318.
13. McKenna GB, Leterrier Y, Schultheisz CR, Polym. Eng. Sci. 35 (1995) 403.
14. McKenna GB, Schultheisz CR, Leterrier Y, Deformation, Yield and Fracture of Polymers, Proc. 9th Int. Conf., Cambridge, UK (1994) 31/1.
15. Schultheisz CR, Colucci DM, McKenna GB, and Caruthers JM, Mechanics of Plastics and Plastic Composites MD-68/AMD-215, MC Boyce, ed, ASME (1995) 251.
16. Echeverria I, Su PC, Simon SL, Plazek DJ, J. Polym. Sci., Polym. Phys. Ed. 33 (1995) 2457.
17. Schultheisz CR, McKenna GB, Leterrier Y, Stefanis E, Proc. Soc. Exp. Mech., Spring Conference, Grand Rapids, MI, June (1995) 329.
18. Press WH, Flannery BP, Teukolsky SA, Vetterling WT, Numerical Recipes, Cambridge University Press (Cambridge) 1986.

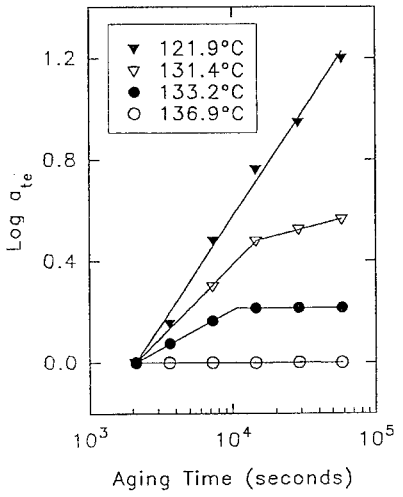

Figure 1. Aging time shift factors (a_{te}) versus aging time for dynamic torsion experiments at four measurement temperatures.

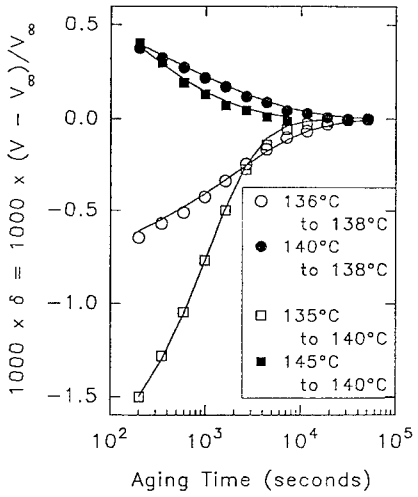

Figure 2. Experimental structural recovery (symbols) and fit to model (lines) for ± 5 °C jumps to 140 °C and ± 2 °C jumps to 138 °C.

TEMPERATURE AND MOLECULAR-WEIGHT DEPENDENCE OF THE STRAIN HARDENING BEHAVIOUR OF POLYCARBONATE

L. E. Govaert*, C.A.C. van Aert* and J. Boekholt*

In this study the temperature dependence of the post yield behaviour of two commercial grades of polycarbonate were investigated. The strain hardening modulus is found to decrease substantially with increasing temperature. A decrease in molecular weight only appears to have a small influence on the strain hardening behaviour, whereas it leads to a dramatic decrease in the failure strain of the material.

Introduction

When subjected to a tensile test, a glassy polymer displays an initial elastic region followed by rate depended yielding, due to stress-activated segmental motion. The post-yield behavior of glassy polymers is governed by two phenomena; firstly intrinsic strain softening, that leads to a decrease in the stress level with increasing deformation, and secondly strain hardening, that leads to a subsequent increase of the stress level. This investigation will focuss on the latter.

It seems generally accepted that the strain-hardening response in (glassy) polymers originates from the rubber elastic response of the entanglement network [1-3], the prime indication being the complete recovery of plastic deformation if the polymer is heated above the glass-transition temperature. However, a quantitative agreement between the strain-hardening modulus observed in the post-yield behaviour below T_g, and the rubber-plateau modulus that is observed above T_g, still seems to be lacking [3]. In this study it is attempted to clarify this disagreement by investigating the temperature dependence of the strain hardening modulus of two grades of polycarbonate with different molecular weights.

Experimental

The materials investigated were two commercial grades of polycarbonate, Lexan 101 from General Electric and Macrolon CD2000 from Bayer. The Lexan 101-grade had a weight-average molecular weight M_w of 33500 g/mol, whereas the CD2000 grade had a M_w of approximately 13000 g/mol (estimated from shear viscosity).

The most straightforward way to study the post-yield behaviour experimentally is to apply large homogeneous deformations. However, most polymer systems, and especially polycarbonate, are prone to inhomogeneous deformation (necking). In polymer glasses, this tendency to strain

* Centre for Polymers and Composites, Eindhoven University of Technology

localisation is especially influenced by intrinsic-strain softening. A possible way to enable large homogeneous plastic deformations is therefore to eliminate strain softening by mechanical conditioning. For this purpose axis-symmetrical tensile bars were subjected to large strain torsion at room temperature. The torsion was applied manually, by clamping the sample in a universal lathe and turning one side over 720~degrees, with a line on the sample as a reference. Subsequently the sample was returned to its undeformed state by rotating in the opposite direction, again using the line on the sample as a reference. On these pre-conditioned samples tensile tests were performed at a strain rate of 10^{-2} s^{-1} at various temperatures below T_g.

Torsional dynamic mechanical analysis was performed on a Rheometrics RDS II in a plate-plate geometry at a frequency of 1 Hz and temperatures of 170 to 240 °C, well above the glass transition temperature. The samples were compression moulded disks with a thickness of 2 mm and a diameter of 25 mm.

Results

In Figure 1 the results of the tensile experiments are presented in a plot of true stress versus the strain measure (λ^2-λ^{-1}). After this mechanical treatment, the strain softening behaviour has disappeared and the samples deform homogeneously in a standard tensile test. Due to the mechanical treatment the strain softening effect has almost totally disappeared and the bars are observed to deform homogeneously. From Figure 1 it is clear for both materials that the post yield behaviour at all temperatures can be represented by a neo-hookean strain hardening response visualised by a linear relationship between the true stress and (λ^2-λ^{-1}), or :

$$\sigma(T) = \sigma_y(T) + G_R(T)(\lambda^2 - \lambda^{-1}) \qquad (1)$$

where σ_y is the yield stress, λ is the draw ratio and G_R represents the strain hardening modulus. According to the Gaussian network approximation the shear modulus of a cross-linked network can be expressed as:

$$G_R = nkT \qquad (2)$$

where n is the number of elastically active chains and k is Boltzmann's constant. In this classical rubber-elastic approach an increase of temperature will typically lead to an increase of the strain hardening modulus. However, in contrast to the chemical network that is assumed in the Gaussian network approach, the molecular network in a thermoplastic material is of a physical nature, Viz. entanglements. It is therefore not surprising that the values of the strain-hardening moduli determined from the experimental data in Fig. 1, represented in Table I, clearly *decrease* with increasing temperature. According to Arruda [4] this decrease is related to a decrease of the number of elastically active chains n, which is equivalent to an increase in the number of monomer units between entanglements. In other words, the network relaxes (dis-entangles) with increasing temperature.

Temperature (°C)	G_R [MPa], Lexan 101	G_R [MPa], CD2000
25	23.7	23
50	21.3	20.6
75	18.7	17
100	15	13.5

Table I: *Temperature dependence of the strain hardening modulus of Lexan 101 and Macrolon CD2000*

In the polymer rheology field, it is well established that relaxation of the entanglement network results from reptation [5]. With this process in mind, it seems instructive to compare the temperature dependence of the strain hardening modulus, shown in Table I, to that of the dynamic shear modulus G_D measured (1Hz) in the melt (Figure 2).

In the case of both materials, the temperature dependence of the strain-hardening modulus appears to correlate well with the relaxation behaviour of the entanglement network in the melt. This observation supports the view that strain hardening originates from a rubber-elastic response of the entanglement network, which becomes operable when segmental motion is allowed.

At low temperatures, the strain hardening modulus is only slightly influenced by a reduction in molecular weight. This could be expected, since the molecular weight between entanglements is not influenced by chain length. However, as the number of entanglement per chain decreases, the relaxation of the network will occur faster, which leads to the differences that are observed between the two grades at higher temperatures (Fig.2). A more dramatic effect of a decrease in molecular weight is its strong influence on the strain to break, as can be observed in Fig.1.

References

1. Thackray, G and Haward, RN, Proc. Roy. Soc. London, A302, (1968), 453.
2. Arruda, EM, and Boyce, MC, Int. J. Plast., 9, (1993) 697
3. Haward, RN, Macromolecules, 26, (1993), 5860
4. Arruda, EM, 'Characterization of the strain hardening response of amorphous polymers', Ph.D thesis, Massachusetts Institute of Technology (1992)
5. de Gennes, PG, J. Chem. Phys., 55 , (1971), 572

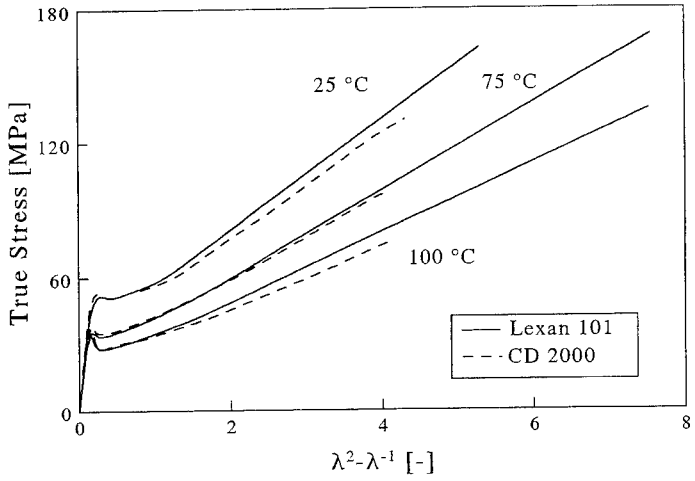

Figure 1. True stress-strain curves of mechanically pre-conditioned samples of Lexan 101 (solid line) and Macrolon CD2000 (dashed line) at various temperatures

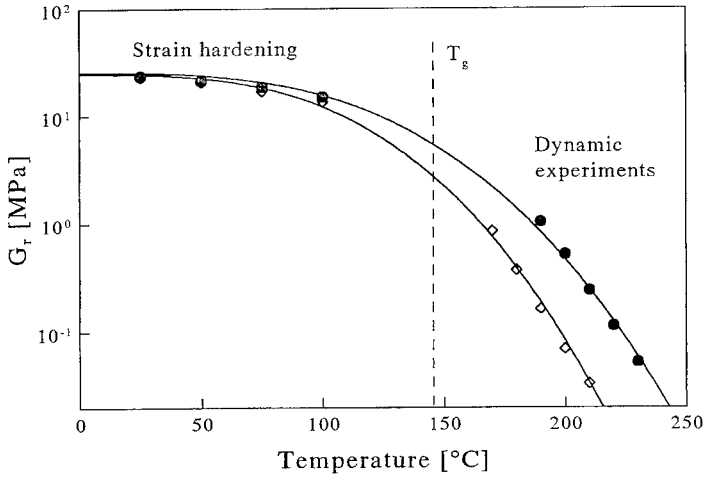

Figure 2 Strain hardening modulus and dynamic shear modulus vs. temperature for Lexan 101 (solid symbols) and CD2000 (open symbols)

MICROMECHANICAL MODELLING OF TIME -DEPENDENT FAILURE IN TRANSVERSELY LOADED COMPOSITES

L.E. Govaert*, R.J.M. Smit* and T. Peijs*

In this study the time-dependent fracture behaviour of transversely loaded E-glass/epoxy laminates is investigated using a 3-D micromechanical finite element approach in combination with a constitutive equation, that is able to capture the yield behaviour of the epoxy matrix. It is shown that this approach, in combination with a strain criterion for matrix failure, can be used successfully for the prediction of the rate dependent tensile strength and the creep life-time of transversely loaded E-glass/epoxy composites.

Introduction

Models for the prediction of strength of composite materials are generally directed to short-term failure using laminate analysis based on classical mechanics, coupled with a common failure theory such as maximum stress or maximum strain concepts. Since almost all engineering components are subjected to load and environmental histories which differ strongly over the service time of the component, it is clear that there is a need for the development of new approaches for the prediction of failure of composites which enable us to include time-variable circumstances. In case of matrix dominated failure-modes, such as transverse and shear failure, it seems therefore obvious to investigate the time- and stress-dependent failure of the polymer matrix.

With recent developments in three-dimensional constitutive modelling of large strain plasticity in amorphous polymers [1-3], the numerical simulation of the behaviour of the polymer matrix under complex loading conditions is well within reach. In this research this technique was employed, in combination with micromechanics, to evaluate short-term and long-term transverse failure of unidirectional glass/epoxy laminates.

Experimental

A rather brittle epoxy system of Ciba Geigy (Araldite LY556/HY917/DY070) was used as matrix system in this study. This epoxy system is based on diglycidyl ether of bisphenol-A with an anhydride curing agent. E-glass fibres (Silenka 0.84-M28) were used as reinforcement material.

* Centre for Polymers and Composites, Eindhoven University of Technology

In order to characterize the yielding behaviour of the matrix five different (multi-axial) tests were performed on the pure matrix material at strain rates varying over several decades, viz. uniaxial extension, uniaxial compression, planar extension, planar compression and simple shear tests. The testing of the unidirectional composites consisted of transverse three-point bending experiments at different strain rates. The composites were also tested under (constant load) creep conditions in three-point bending.

Characterization of matrix material

In this research, a three-dimensional yield expression, usually referred to as pressure modified Eyring flow, is employed to describe the multi-axial yield behaviour of the epoxy matrix. This approach was initially proposed by Ward and Duckett [4] and expresses the stress state and deformation rate at the yield point in terms of the octahedral shear stress τ_{oct} and the octahedral shear rate γ_{oct}, respectively:

$$\dot{\gamma}_{oct} = \dot{\gamma}_0 \sinh \left[\frac{\tau_{oct}\, \upsilon}{k\, T} \right] \exp\left[- \frac{p\, \Omega}{k\, T} \right] \qquad (1)$$

where T is the absolute temperature, k is Boltzmann's constant, υ is the shear activation volume, P is the hydrostatic pressure, Ω is the pressure activation volume and γ_0 is, in isothermal conditions, a material constant. The results of the uniaxial extension, planar extension, uniaxial compression, planar compression and simple shear test are presented in Fig. 1, where the octahedral shear stress is plotted versus the octahedral shear rate for all loading geometries. All experiments were performed at room temperature (295 Kelvin). The drawn lines are predicted by Eq. 1, using: $\gamma_0 = 1.5\ 10^{-21}\ s^{-1}$, $\Omega = 0.441\ nm^3$ and $\upsilon = 3.5\ nm^3$, showing clearly that all experiments are in good agreement with this modified Eyring equation.

Micromechanical analysis of composite materials

To account for the complex stress and strain situation in a composite, micromechanical simulations are performed with the Finite Element Method (FEM). The micromechanical simulations are based on a hexagonal fibre array, from which the finite element mesh, representing a fibre volume fraction of 50% is shown in Fig. 2. To facilitate finite element analysis a three-dimensional constitutive model is required. In this study the compressible Leonov model was used, which is described in detail elsewhere [3]. In this model the matrix material is regarded as a linear elastic, compressible solid up to the yield point, with a modulus of 3200 MPa and a Poisson's ratio of 0.37. The yield behaviour of the material is described as a generalised Newtonian fluid with a flow characteristic according to the data presented in Fig. 1. The strain hardening behaviour was also modelled as a Gaussian, rubber elastic spring. The rubber modulus was estimated at 31.5 MPa, as determined experimentally with dynamic mechanical thermal analysis.

Since there is no limit to the deformation in the constitutive model an additional failure criterion is needed. In this study a limiting value of 15% for the octahedral shear strain was chosen. This value

was estimated from a numerical simulation of a tensile experiment at a global strain rate of 10^{-4} s^{-1} by evaluating the local strain state in the composite at an externally applied stress equal to the experimentally observed tensile strength. For the prediction of failure at other strain rates or under the influence of a statically applied stress (creep), a micromechanical simulation of the desired test was performed up to a global state of deformation where the local maximum of the octahedral shear strain equals the critical value of 15%.

Validation

The results of maximum stress versus strain rate of the composites in three-point bending are presented in Fig. 3. The error bars are the standard deviation of the experimental outcome. The predicted strain rate dependence of the transverse strength is represented by the solid line and shows that the experimental results are well described by the strain criterion. Similar to the constant strain rate tests, the numerical predictions for creep failure were compared with experimental results. Again the local strain criterion is used to predict the creep time to failure for the different applied engineering stresses. The results of the experiments and the numerical simulations are shown in Fig.4. It can be seen that the micromechanical model in combination with this failure criterion is able to describe time to fracture of the transversely loaded E-glass/epoxy composites.

Conclusions

In this study it is demonstrated that the modified Eyring equation can be satisfactory used for the description of the yield behaviour of the epoxy system under multi-axial loading conditions. The various multi-axial experiments also showed that the epoxy system clearly exhibits a pressure dependent yield behaviour. By introducing these parameters into the compressible Leonov model, numerical (FEM) simulations of the mechanical behaviour of the epoxy system could be performed. Micromechanical simulations of rate dependent transverse strength of unidirectional composites, showed the validity of a failure criterion based on a maximum local strain. Moreover, this failure criterion could be used for the prediction of creep time to failure.

References

1) Boyce MC, Parks DM and Argon AS, Mech. Mater. 7., (1988) 15
2) Wu PD, van der Giessen E, J.Mech. Phys. Solids 41, (1993) 427
3) Tervoort, TA, Klompen, ETJ and Govaert, LE, J. Rheol. 40., (1996) 779
4) Ward, IM, 'Mechanical properties of solid polymers',
John Wiley and sons, Chichester, second edition (1990)

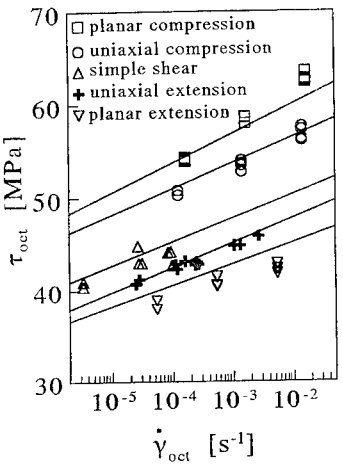

Figure 1. Octahedral shear stress at the yield point versus octahedral strain rate for the epoxy matrix. Solid lines: fitted with Eq. 1.

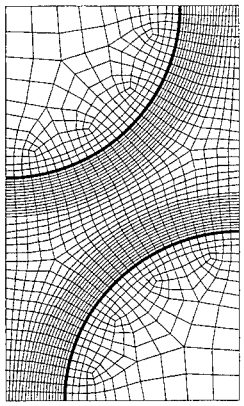

Figure 2. Mesh used for the micromechanical analysis, representing a hexagonal stacking of fibres in the composite (50 vol%).

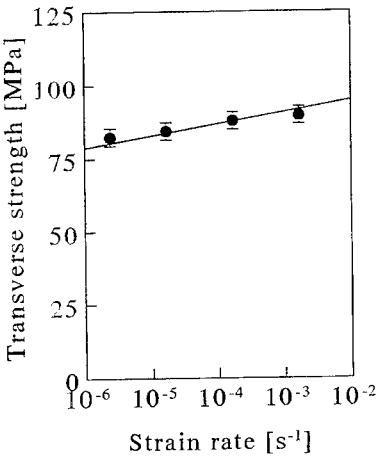

Figure 3. Strain-rate dependence of the transverse strength of the composite material compared to model prediction (solid line).

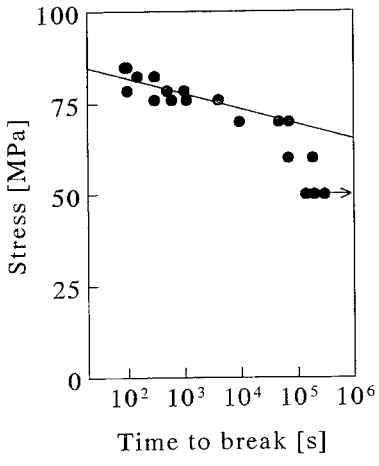

Figure 4. Applied stress versus time to break of the composite material compared to model prediction (solid line).

FATIGUE FRACTURE AND MORPHOLOGY IN INJECTION MOLDED POLYACETAL

Wataru MIZUNO*, Makoto KAWAGOE†, Jianhui QIU†, and Mikio MORITA†

Variations in viscoelastic properties and morphology during fatigue of injection-molded polyacetal were examined. Under low maximum stress and at low ambient temperature, fracture behavior was brittle. When the maximum stress and the ambient temperature were increased, fracture behavior became more ductile. In brittle fracture, the crack propagated along one fracture surface. In ductile fracture, the specimen was stretched and the crystals were largely deformed. The crystallinity in a local region near the fracture surface of the specimen was decreased by the fatigue. When the ductile fracture, the crystallinity all over the specimen was increased by self-heating during the fatigue process.

INTRODUCTION

The fatigue behavior of polymeric engineering materials has received growing attention in recent years. This may result from that the elucidation of fatigue mechanism is one of the most important problem with respect to the reliability of engineering materials. In this study, the effects of test conditions on the fatigue behavior of injection-molded polyacetal are discussed with particular reference to the variation in dynamic viscoelasticity during the fatigue process. Also, the changes of morphology by fracture are discussed.

EXPERIMENTAL

The dumbbell-shaped specimens of polyacetal were molded by injection molding machine. Only their rectangular gauge region was used in the experiment. Figure 1 shows the block diagram of the measuring system of the fatigue tester [1,2]. In this tester, E', $\tan\delta$, specimen elongation and surface temperature simultaneously and continuously measured until fracture. Influences of the maximum stress and the ambient temperature on the dynamic viscoelasticity and surface temperature of specimen during fatigue process were evaluated by this type of fatigue tester at a stress ratio of 0.04 and applied frequency 10Hz. The fracture surface and inner the morphology of the specimen were investigated by scanning electron microscopy. optical microscopy, infrared spectroscopy and differential scanning calorimetry(DSC) studies.

RESULTS AND DISCUSSION

Figure 2 shows the effect of maximum stress on the fatigue property. In the case of low maximum stress of 21MPa, E' remains almost constant, $\tan\delta$ clearly decrease. Just before fracture, E' and $\tan\delta$ drastically decrease and increase, respectively. Specimen elongation and surface temperature remains almost constant until fracture. In the cases of high maximum stress

* Central Research Institute, Toyama Industrial Technology Center (150 Futagami, Takaoka, Toyama 933, Japan)

† Department of Mechanical Systems Engineering, Faculty of Engineering, Toyama Prefectural University (5180 Kurokawa, Kosugi, Toyama 939-03, Japan)

of 23MPa and 24MPa, E' and tan δ monotonically decreased and increase, respectively, until fracture. Specimen elongation and surface temperature continuously increase to fracture. It may be because of self-heating and melt of resin. Fracture behavior are changed from brittle to ductile with increases of maximum stress. The fatigue life time was greatly reduced with increases in the maximum stress. In the case of low ambient temperature of 40℃ and 50℃, E' remains almost constant, and tan δ decrease. The specimen elongation and surface temperature remains almost constant . In this case, fracture behavior are brittle like the case of lower maximum stress. In the case of higher ambient temperatures of 60℃ and 70℃, E' and tan δ monotonically decrease and increases, respectively. The specimen elongation and surface temperature drastically increase to fracture. In this case, fracture behavior are ductile like the case of higher maximum stress.

Figure 3 shows fracture surfaces of fatigued specimens at various stress levels. (a) 21MPa (starting region); (b) 21MPa (propagation region in skin); (c) 24MPa. In the case of brittle fracture under maximum stress of 21MPa, the fractures of spherulites and radial arrangement of lamellar are observed at fracture starting region (a). The picture (b) is a propagation region of crack in the skin. The crack propagates to upper-side in the picture. (The surface of the specimen is left-side in the picture.) The direction of crack are different between the skin and the core of specimen. In the case of ductile fracture at maximum stress of 24MPa, the resin is highly softened and stretched in during fatigue. Figure 4 shows polarized micrographs of cross section of fracture surface. It shows variation of morphology with the maximum stresses. (a) 21MPa and (b) 24MPa. The crystals are not deformed near the fracture surface under maximum stress of 21MPa. On the other hand, the resin is stretched and the crystals are deformed under 24MPa. The skin is more stretched than core. In brittle fracture under low maximum stress and at low ambient temperature, the crack propagated along one fracture surface to the destruction of crystals. In ductile fracture under higher maximum stress and at higher ambient temperature, the specimen was stretched and the crystals were largely deformed by self-heating during fatigue.

Table I shows the fatigue properties measured under various test conditions. In the cases of low maximum stress and low ambient temperature, the entharpy Δ H obtained by DSC studies is relatively low value compared with before the test. With increases of maximum stress and ambient temperature, the value of Δ H increases. The result of crystallinity by infrared spectroscopy studies shows the same tendency as DSC studies. The DSC studies also show that the crystals are fractured by fatigue. This fracture occur in micro region of inter- or intra-crystals, therefore the fracture of crystals can not be observed in the polarized micrographs of fracture surface(Figure 4, (a)). On the other hand, when the ductile fracture takes place, self-heating of the specimen occur during the fatigue process. This process also results in the increase in the crystallinity of the specimen.

CONCLUSIONS

Under low maximum stress and at low ambient temperature, fatigue fracture behavior was fundamentally brittle. In this case, the crack propagated along only one fracture surface. When the maximum stress and the ambient temperature were increased, fracture behavior became more ductile. The specimen was stretched and the crystals were largely deformed. As the fatigue behavior was changed from brittle to ductile mode, the fatigue life time was greatly reduced. When the ductile fracture took place, the crystallinity of the fracture surface was increased by self-heating during the fatigue process.

REFERENCES

1. Takahara, A., Yamada, K., Kajiyama, T. and Takayanagi, M., J. Appl. Polym. Sci., **26**, 1085(1981).
2. Kaiya, N., Takahara, A. and Kajiyama, T., Polymer J., **22**, 859(1990).

Table I Fatigue properties measured under various test conditions.

Run No.	Maximum Stress (MPa)	Ambient temperature (°C)	Life-time (sec)	DSC Melting temperature (°C)	DSC ΔH (J/g)
1	21	24	140000	159.0	143.7
2	22	24	4500	158.7	144.1
3	23	24	320	158.5	144.8
4	24	24	250	158.2	145.1
5	20	40	64000	159.1	142.8
6	20	50	43000	158.4	143.8
7	20	60	1100	159.4	144.7
8	20	70	140	158.8	148.7
Before test				159.1	145.1

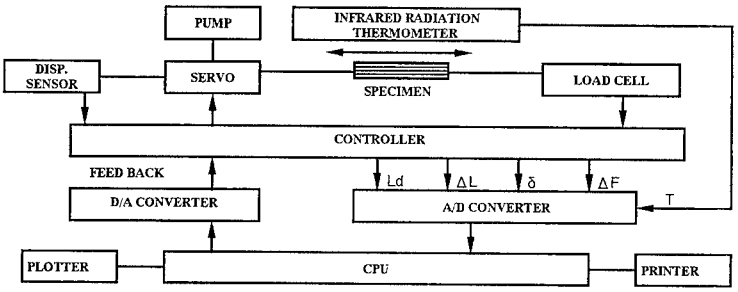

Figure 1 Block diagram of the measuring system of the fatigue tester .

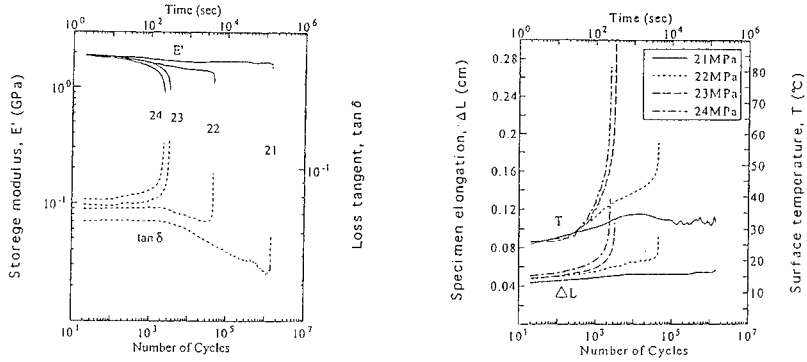

Figure 2 Effects of maximum stress on the dynamic viscoelastic properties during fatigue.

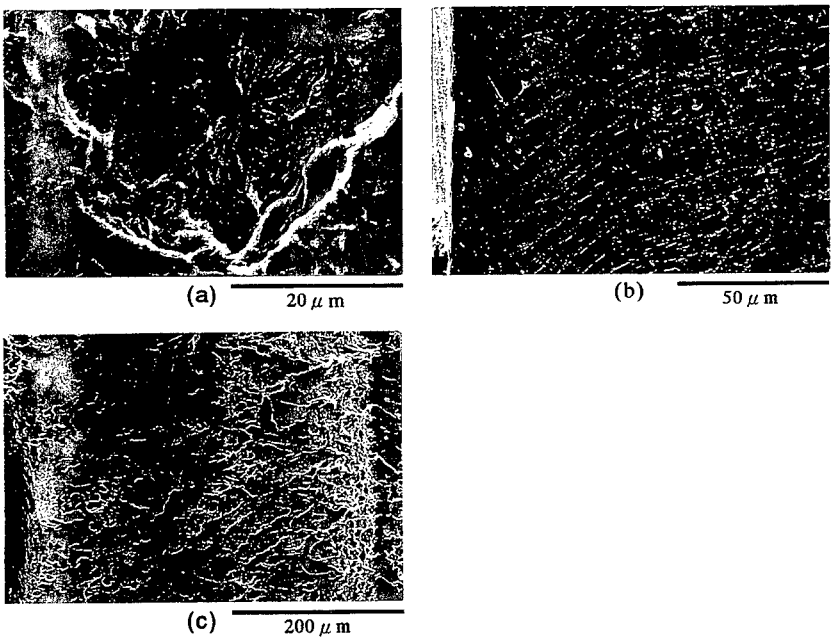

Figure 3 Fracture surfaces of fatigued specimens under various stress levels;
(a) 21MPa (starting region); (b) 21MPa (propagation region in skin); (c) 24MPa.

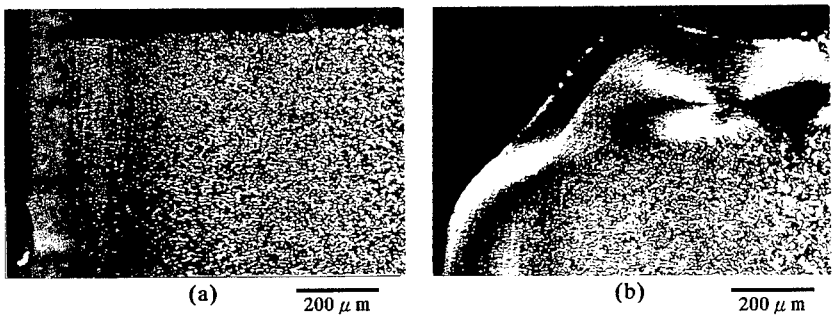

Figure 4 Polarized micrographs of cross section of fracture surface;
(a) 21MPa; (b) 24MPa.

THE ROLE OF MOLECULAR WEIGHT IN THE HOT BIAXIAL DRAWING OF AMORPHOUS POLY(ETHYLENE TEREPHTHALATE).

J.Shirodkar*, C.P.Buckley*, J.L.Harvie+

The effect of molecular weight during the biaxial drawing of amorphous, isotropic poly(ethylene terephthalate) (PET) film at temperatures immediately above the glass transition has been investigated by comparing the responses of two grades of PET with significantly different molecular weights. The results showed that strain stiffening was initiated at lower strains and occurred more rapidly in the higher molecular weight PET. Analysing the results in terms of the hybrid glass-rubber constitutive model for PET showed that the portion of the stretch associated with entanglement slippage was much greater for the lower molecular weight PET, and as temperature increased the difference between the slippage stretches for the two grades increased. The difference is explained by the dependence of melt viscosity on molecular weight.

INTRODUCTION.

Poly(ethylene terephthalate) (PET) has become a very important polymer in many industrial applications, not least in the food packaging industry where the use of PET for production of such items as carbonated drinks bottles has increased dramatically in recent years. The production of PET bottles involves deformation of the material at temperatures just above the glass transition, thereby introducing substantial molecular orientation into the end product and enhancing the mechanical properties of the bottles. Although a large body of literature already exists on the hot drawing of PET, there is at present only a limited understanding of how to model it. Moreover, very little data has actually been produced under conditions comparable with those experienced in such processes as industrial bottle blowing i.e, biaxial deformation at high rates of strain, this is primarily due to the limitations of conventional testing machines.

In view of this, we have conducted laboratory-based drawing experiments on a novel Flexible Biaxial Film Tester (FBFT), which can achieve biaxial drawing conditions similar to those of the manufacturing process. Previous work by Buckley et al (1,2) has shown that the data obtained from testing PET with the FBFT can be fitted using a large strain, glass-rubber constitutive model for amorphous polymers near the glass transition. The model is based on several physically based theories which describe polymer deformation. It is founded on the idea that there are two completely separate constituents to the free energy (the "bond stretching" and "conformation" or entropic components) which combine additively during deformation of the polymer. The present study examines the effect of variation in molecular weight on the hot drawing of PET under biaxial conditions.

EXPERIMENTAL DETAILS

The FBFT achieves flexibility in testing by means of computer control of the two orthogonal axes and the heating system. Both axes can be driven independently of each other, such that the final strain and the strain-rate on both axes can be varied according to requirements.

The test procedure involves mounting of a test piece in the 24 pneumatic grips of the testing machine, before rapidly bringing it up to temperature and maintaining it there for five minutes

*Department of Engineering Science, University of Oxford, Parks Road, Oxford, OX1 3PJ.
+ICI Chemicals & Polymers, PO Box 90, Wilton Centre, Middlesbrough, Cleveland, TS90 8JE.

before straining of the sample. After the cessation of the straining sequence the sample is rapidly quenched back to room temperature. All the tests were conducted under isothermal conditions and at constant rates of extension to predetermined stretches on both axes. Here we report results of drawing under constant width (CW) and equal biaxial (EB) conditions. The nominal rate of strain used in all the tests was $1s^{-1}$, whilst the film temperatures ranged between 80 - 102°C. The stress on each axis was measured by a load cell attached to the central grip of each axis.

Two different grades of PET were studied, both of which were in the form of amorphous film with a nominal thickness of 260μm. The film was produced by melt extrusion onto a water cooled casting drum so as to achieve an essentially isotropic film. The number average molecular weights of the films were determined from the intrinsic viscosity to be $M_n = 1.9 \times 10^4$, and $M_n = 2.8 \times 10^4$.

RESULTS AND DISCUSSION

Typical CW and EB true stress verses nominal strain curves for the two molecular weights at various film temperatures are shown in figures 1-4. It can be seen that there is a profound difference in the drawing behaviour of the two grades, this is primarily seen in the strain stiffening region of the curves. For a given film temperature strain stiffening intervenes at lower strains and occurs more rapidly in the higher molecular weight PET, and stresses are higher throughout the tests. Additionally, drawing the film in an EB rather than a CW manner produces a greater degree of strain stiffening, with its occurrence also coinciding with lower strains.

PET is often thought of as a network of molecules which are coupled together by entanglements. The constitutive model which was initially proposed (1) was based on this concept, however at high temperatures it was found that the model was unable to predict the deferral of strain stiffening to higher strains with increasing film temperature (as shown in the experimental data). This phenomenon is thought to arise due to the extra contribution to the strain from slippage of the entanglements, the rate of which increases with temperature.

Entanglement slippage can be thought of as a viscous flow process. In relation to the above results, the difference in the drawing behaviour can be interpreted in terms of the difference in the viscosity of the two different PET grades. It is well known that the viscosity of PET increases with molecular weight (weight average) in line with the relation $\mu \propto M_w^{3.4}$, when the molecular weight is at least twice the average molecular weight between entanglements (M_e): M_e was taken as having a value of 3200 (1). The higher viscosity of the high molecular weight PET results from the increases in the number of entanglements per chain with increasing molecular weight, consequently each chain becomes more constrained in the network, thus strain stiffening occurs sooner and more rapidly. It was calculated that for a given temperature the viscosity of the high molecular weight PET would be 3.41 times greater than that of the low molecular weight PET. This is equivalent in terms of stress-strain response to drawing the higher molecular weight PET at a temperature 9°C above that of the lower molecular weight PET so as to reduce its viscosity to the same level as the lower molecular weight material.

By conducting the following analysis it was possible to quantify the differences in the drawing behaviour of the two materials by isolating the relative amounts of entanglement slippage which occurs in the two grades. According to the model the Cauchy stress is composed of both a bond stretching and conformational component.

$$\sigma_i = \Delta\sigma_i^b + \Delta\sigma_i^c \qquad i = 1,2,3 \qquad (1)$$

By examining the low strain results of drawing experiments as isometric plots of true stress versus temperature it was found that a rubber-like plateau exists in the region of 96 - 108°C (the

stress remains constant with increasing temperature). On the plateau the deviatoric bond-stretching contribution to stress is zero, thereby leaving only the conformational component as a contributor to the overall stress. It was found that the stress level on the plateau is lower for the lower molecular weight PET, as expected because of the higher density of ineffective "dangling ends". At higher strains and temperatures the deformation is composed of two contributions: the reversible network stretch (λ^N); and the irreversible stretch due to entanglement slippage (λ^S). The two components are assumed to combine multiplicatively ($\lambda = \lambda^N \lambda^S$). According to the theory of rubber elasticity:

$$\sigma_i = N_e k_B T F_i\left(\lambda_1^N, \lambda_2^N, \lambda_3^N\right) \qquad (2)$$

Where F_i depends on the choice of the conformational entropy function and where:

$$N_e = N_e^{\infty}\left(1 - \frac{2M_e}{M_n}\right) \qquad (3)$$

It can be shown that λ_1^N uniquely determines λ_2^N, λ_3^N. As a result of the two materials having different stress values on the plateau they can only be compared at any given temperature if the true stress is divided by the Flory correction factor to eliminate the effect of dangling ends.

$$\sigma_i' = \left(\frac{\sigma_i}{1 - \frac{2M_e}{M_n}}\right) = g\left(\lambda^N\right) \qquad (4)$$

Since the network stretch is the same in both cases at any given value of σ' we see that:

$$\left(\frac{\lambda}{\lambda^s}\right)_H = \left(\frac{\lambda}{\lambda^s}\right)_L \therefore \frac{\lambda_L}{\lambda_H} = \frac{\lambda_L^s}{\lambda_H^s} \qquad (5)$$

Where H and L refer to higher and lower molecular weight respectively.

The results obtained by plotting the ratio of the slippage stretches versus σ' for the low and high molecular weight materials (at temperatures on or above the plateau), and for both CW and EB tests are shown in figures 5 and 6 respectively. These show that for any given temperature and value of σ' the strain associated with entanglement slippage is much greater for the lower molecular weight PET. As the temperature increases the difference in the slippage values between the two materials becomes even more pronounced. The EB results show that the difference between the slippage values for the two PET grades levels off, thereby indicating that the slippage process does not continue indefinitely but is arrested at a certain point. This is believed to reflect the development of crystallinity which is known to occur during hot drawing of PET and is in line with previous findings (2).

REFERENCES

1. Buckley, C.P., Jones, D.C., and Jones, D.P., Polymer 37 (1996) 2403
2. Adams, A.M., D.Phil. Thesis University of Oxford (1995)

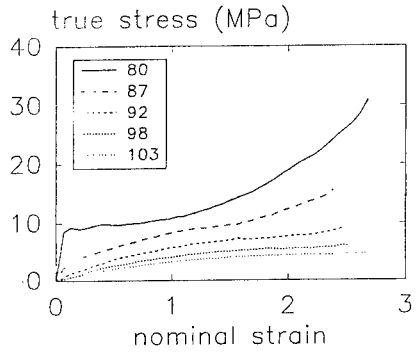

Figure 1: CW drawing of low molecular weight PET at temperature (°C) shown.

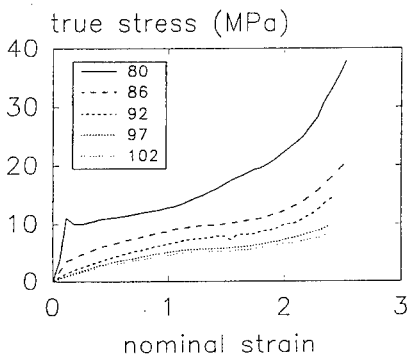

Figure 2: CW drawing of high molecular weight PET at temperature (°C) shown.

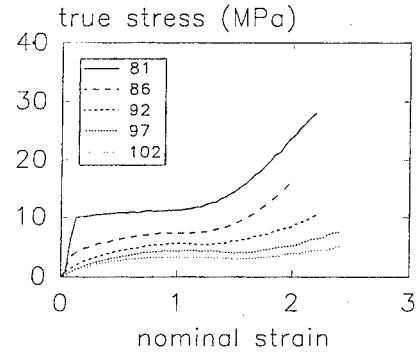

Figure 3: EB drawing of low molecular weight PET at temperature (°C) shown.

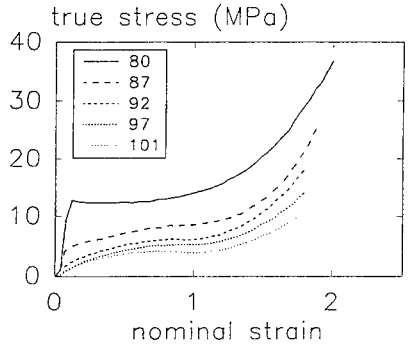

Figure 4: EB drawing of high molecular weight PET at temperature (°C) shown.

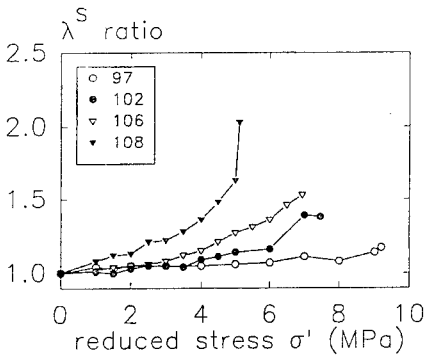

Figure 5: Slippage stretch ratio $\lambda_L^s / \lambda_H^s$: CW drawing of PET at temperature (°C) shown.

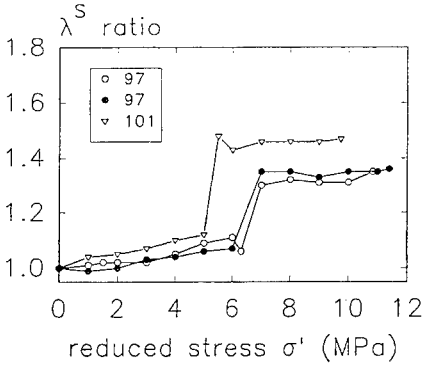

Figure 6: Slippage stretch ratio $\lambda_L^s / \lambda_H^s$: EB drawing of PET at temperature (°C) shown.

Evolution of the Crystalline Texture of High-Density Polyethylene under Uniaxial Drawing Studied by Video-Controlled Tensile -Testing and WAXD

R. Hiss and G. Strobl
Fakultät für Physik der Albert-Ludwigs-Universität
Hermann-Herder-Str. 3 , 79104 Freiburg Germany

The morphological changes associated with the necking of semicrystalline polymers like polyethylene are mostly studied under engineering conditions, where the nominal values of the strain, the strain rate and the total force are registered. We have constructed and used a video-controlled tensile tester similar to Gsell's device. Fig.1 shows a schematic drawing of the set-up. It allows to draw samples with a constant local strain rate and to measure the true local strain and stress; the (Hencky-)strain rate can be varied over two decades, $\dot{e}_H = 10^{-4} - 10^{-2} s^{-1}$. Samples of polyethylene and ethylene-vinylacetate copolymers were investigated. One observes a systematic change in the true stress-strain curves between the rubbery copolymer and PE. Fig.2 collects some results obtained at a strain rate $\dot{e}_H = 10^{-2} s^{-1}$. The behavior indicates that the drawing behavior of PE at large elongations is mostly controlled by the entanglement network; the reorientation, destruction and reformation of the crystallites acts like an effective strong viscous force. In order to investigate the structural background, samples were deformed to different Hencky-strains and then investigated by WAXD. Analysis can be based on the the intensity distributions of the (110)- and (200)-reflections of the orthorhombic phase. Fig.3 depicts a typical example. Curves are indicative for the occurrence of three different textural phases; their volume fractions can be determined by a numerical decomposition. Our experiments confirm reports in the literature that structure evolution during drawing takes place in two steps. First there is a transition from the isotropic to a tilted crystallite orientation, and then, in a second step a change from the tilted to the fibrillar structure. Fig.4 shows how the volume fractions of the three phases vary during drawing. Characteristic points of the stress-strain curves can be related to the two-step structure evolution. The plateau observed directly after the onset of plastic flow can be associated with the first step, and strain hardening sets in with the second step, i.e. the occurrence of the fibrillar phase. This is demonstrated by the results shown in Fig.5. At the yield points indicated by the circles the tilted phase begins to appear. The triangles give the strains, where the isotropic phase has just disappeared, being completely replaced by the tilted phase, and the fibrillar phase emerges for the first time. The transition from the tilted into the fibrillar phase is completed at the positions of the squares. As can be seen, the ranges of existence of the tree phases vary with the strain rate in a characteristic way, thus explaining the variations in the stress strain curves. The influence of the texture on the sample shrinkage on heating can also be studied. Fig.6 shows one example. There is a small spontaneous length reduction on removing the load, which is then followed by an extensive shrinkage during heating. In this case there remains only a small irreversible part. Fig.7 gives the dependance of the spontaneous and the irreversible part on the strain imposed by the cold-drawing. Again we find a relation to the texture evolution. It turns out that throughout the first step the original shape of the sample is completely recovered; an irreversible part arises with the occurrence of the fibrillar phase.

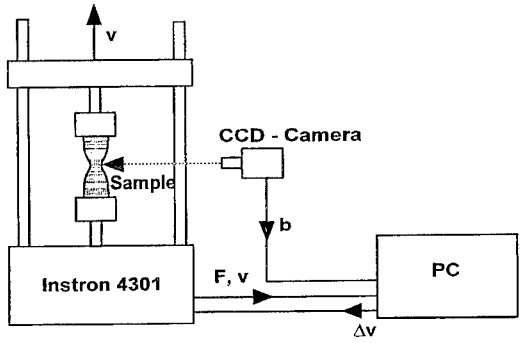

Fig.1 Device for measurements with constant local strain rate

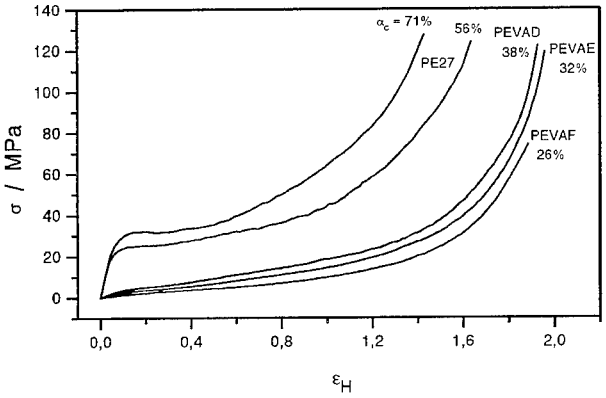

Fig.2 True stress/ true strain curves under a constant strain rate, measured for linear PE and E/Vac-rubbers of different crystallinity

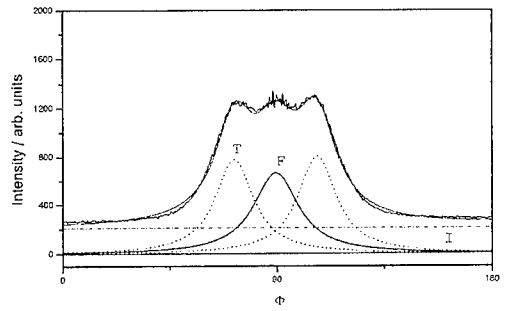

Fig.3: 110-reflexion with contributions of a tilted and a fibrillar phase

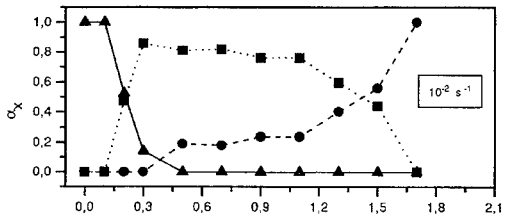

Fig.4 Fractions of the three orientational phases in dependence on strain

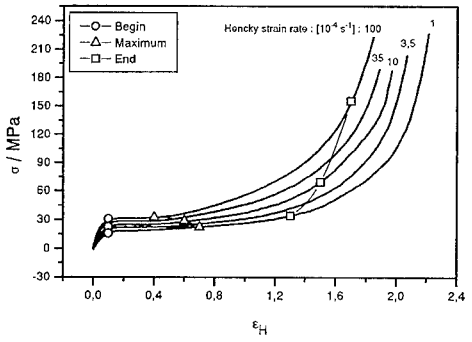

Fig.5 Existence ranges of the three orientational phases in dependence of the strain rate

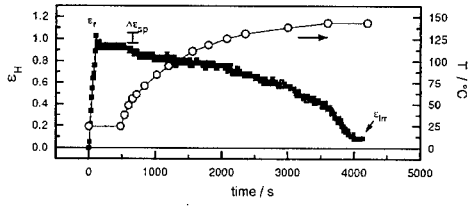

Fig.6 Shrinkage on heating a sample

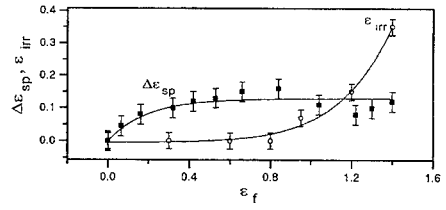

Fig.7 Spontaneous shrinkage and irreversible part of the deformation

THE KINETICS OF DILATATIONAL BANDS AND THE INTERPARTICLE DISTANCE EFFECT IN RUBBER TOUGHENED POLYMERS

A Lazzeri*

The stress field at the tip of a dilatational band is calculated as well as the strain energy ahead of the band. The volume strain energy density is inversely related to the distance to the tip of the band. Cavitation, therefore, will occur preferentially in rubber particles located near the tips of the band. The rate of band growth is also considered, as well the stability of band propagation. This concept will be discussed in relation to the interparticle distance effect observed previously in some rubber toughened polymers.

INTRODUCTION

Rubber toughening of polymers has been a very active research field for a long time, but some experimental aspects need a clear understanding, the main perhaps being the so called critical interparticle distance proposed by Wu (1). Moreover some authors still investigate the role of rubber cavitation compared to hole toughening (2).

In recent publications (3-4) it has been proposed that, in a first stage, cavitation initiates randomly within the biggest rubber particles, and that subsequently criteria for the onset of a shear instability within a porous polymer are met. This leads to the nucleation of planar yielded regions with a high concentration of cavitated particles, called *dilatational bands,* which subsequently grow via a mechanism of repeated cavitation of the rubbery phase (4). More recently other studies by Baer et al. have confirmed the evidence of the formation of this type of bands (5). The purpose of this paper is to investigate the conditions of propagation of these bands. In particular, the Argon equation for the kinetics of crazing by repeated cavitation will be modified to model the kinetics of dilatational bands.

STRESS FIELD AND VOLUME STRAIN ENERGY AT A DILATATIONAL BAND TIP

The stress field in proximity of a dilatational band can be analysed by considering that it is similar to that of a crack subjected to a uniform far field stress superposed to uniform normal and tangential closing stresses acting on the crack surfaces. These stresses originate from the resistance, σ_L, to flow in the matrix ligament between two cavitating particles and from the resistance to stretching in the rubber shell surrounding the ligament.

Consider a dilatational band of length $2l$ in a infinite body subjected to a far field biaxial tension stress σ_o and a shear stress τ_o. The origin of both coordinate systems (x,y) and (r,θ) is located at the band tip. The elastic near tip stress field for a general mixed mode crack is given by (6):

$$\sigma_{ij}=\frac{K_I}{\sqrt{2\pi r}} f_{ij}(\theta)+\frac{K_{II}}{\sqrt{2\pi r}} g_{ij}(\theta), \quad (i,j=1,2) \tag{1}$$

where K_I and K_{II} are the stress intensity factors for mode I and mode II respectively; $f_{ij}(\theta)$ and $g_{ij}(\theta)$ are dimensioless parameters depending on the geometry and are given in reference (6). The volume strain energy density ahead of the band tip is given by:

* Centre for Materials Engineering, University of Pisa, Via Diotisalvi 2, 56125 Pisa, Italy

$$\left(\frac{dW}{dV}\right)=\frac{1-2\nu}{6E}(\sigma_{xx}+\sigma_{yy}+\sigma_{zz})^2=\frac{1-2\nu}{6E}I_1^2 \tag{2}$$

where I_1 is the first invariant of the stress field.

The stress intensity factors, for a band normal inclined of an angle ψ respect to the ligament axis, with a far field stresses superposed to the closing stress, σ_L, due to the resisting forces in the ligament,can be written as (7):

$$K_I=(\sigma_o-\sigma_L\cos^2\psi)\sqrt{\pi l} \qquad K_{II}=(\tau_o-\frac{1}{2}\sigma_L\sin 2\psi)\sqrt{\pi l} \tag{3}$$

where ψ is angle between the normal to the band and the interparticle ligament axis. Now defining:

$$\overline{K}=\sqrt{K_I^2+K_{II}^2}=\overline{\sigma}\sqrt{\pi l} \tag{4}$$

with

$$\overline{\sigma}=\sqrt{(\sigma_0-\sigma_L\cos^2\psi)^2+(\tau_0-\frac{1}{2}\sigma_L\sin 2\psi)^2} \tag{5}$$

and

$$I_1=\frac{\overline{K}}{\sqrt{2\pi r}}\overline{I}_1, \qquad \overline{I}_1=(1+\nu)\left\{k_1[f_{xx}(\theta)+f_{yy}(\theta)]+k_2[g_{xx}(\theta)+g_{yy}(\theta)]\right\} \tag{6}$$

with

$$k_1=\frac{K_I}{\overline{K}} \qquad \text{and} \qquad k_2=\frac{K_{II}}{\overline{K}} \tag{7}$$

The stress field at the tip of the band, therefore is:

$$\sigma_{i,j}=\frac{\overline{K}}{\sqrt{2\pi r}}\,\overline{\sigma}_{i,j}=\frac{\overline{\sigma}\sqrt{\pi l}}{\sqrt{2\pi r}}\,[k_1 f_{i,j}(\theta)+k_2 g_{i,j}(\theta)] \qquad (i,j=1,2) \tag{8}$$

Eqn. (2) becomes:

$$\left(\frac{dW}{dV}\right)=\frac{1-2\nu}{12E}\,\frac{l}{r}\,\overline{\sigma}^2\overline{I}_1^2 \tag{9}$$

Eqn. (9) shows that the strain energy enhancement is proportional to the length of the band (that is, the number of particles cavitated in the array), is inversely proportional to the distance from the band and it is also related to the closing stress in the ligament between cavitating particles, σ_L.

BAND PROPAGATION

The distance from the band tip at which cavitation occurs, Δ can be obtain by Eqn. (9):

$$\Delta=\frac{1-2\nu}{12E}\,\frac{l}{w_c}\,\overline{\sigma}^2\overline{I}_1^2 \tag{10}$$

where $w_C=(dW/dV)_C$ is the critical strain energy density for rubber cavitation. Following Argon's approach for the velocity of craze growth by repeated cavitation (8), it is possible to calcolate the rate of propagation of a dilatational band, d*l*/d*t*:

$$\frac{dl}{dt}=\frac{\Delta}{\varepsilon_d}\,\dot{\varepsilon} \tag{11}$$

where ε_d is the maximum strain reached by the fibrillating ligaments in the mature part of the dilatational band and $\dot{\varepsilon}$ is the shear rate. As shown above, Δ is a function of the length of the band. From Eqn. 10 we obtain:

$$\frac{dl}{dt}=\frac{(1-2\nu)}{12}\,\overline{I}_1^2\,\frac{\overline{\sigma}^2\dot{\varepsilon}l}{\varepsilon_d w_c E} \tag{12}$$

Eqn. (12) means that the process is controlled by the initial phase of random cavitation within the

bigger rubber particles. Upon increasing the stress level, more cavitation occurs in particles with a diameter a little smaller than the previous ones. At some stage, small clumps of cavitated particles form. The stress field near these clumps is enhanced, and the critical strain energy density for rubber particle cavitation may be overcome at a distance from the clump where other (smaller) particles are present. Therefore, other particles cavitate. Far from the clumps of cavitated rubber particles, the stress intensity is still too small for the particles to cavitate. So, only the particles at the tip of the clumps are likely to cavitate. Planar arrays (dilatation bands) containing several cavitated particles now form. While the external load is increased the number of bands increases as their length. The rate of band propagation also increases as they extend.

Temperature is a main variable affecting the rate of propagation, through its effect on the rubber shear modulus, and hence on w_C, and on the matrix elastic modulus E and resistance to flow. An increase in temperature, brings to an increase in both $\bar{\sigma}$ (via a reduction of σ_L) and $\dot{\varepsilon}$. The rubber shear modulus also increases linearly with T, although this is not enough to balance the exponential increase in $\dot{\varepsilon}$. The total effect is a raise in the rate of propagation of dilatational bands.

DILATATION BAND STABILIZATION

It has been shown (9-10) that in impact tests adiabatic heating at the crack tip can occur leading to melt fracture. Adiabatic heating can also occur in the plastic zone surrounding the crack tip. This region has the important role of shielding the crack tip by drawing of the ligaments between cavitated rubber particles in the dilatational bands, thus dissipating the external energy into plastic work and heat. When the ligaments become too hot, the flow resistance drops and so the energy adsorbed. More energy becomes available at the crack tip as kinetic energy and the crack accelerates. The deformation process is more and more localised at the crack tip leading to a brittle fracture.

In conditions of adiabatic heating the stretching of the rubber shell around the ligament requires an extra amount of energy to be dissipated. It should be noted that, for rubbers, the elastic modulus increases with T. Rubber stretching contributes more and more to the band stability as the ligament becomes hotter.

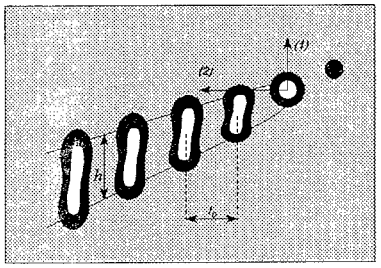

Fig. 1 - Schematic of a dilatational band tip zone showing the stretching of rubber particles behind the band tip.

The stress in the rubber, σ_R is given by:

$$\sigma_R = G_R(\lambda - \frac{1}{\lambda^2}) \tag{13}$$

where G_R is the rubber shear modulus and λ is the extension ratio of the particle, which can be expressed in terms of the strain ε, as:

$$\lambda = 1 + \varepsilon \tag{14}$$

and ε can be defined as: $$\varepsilon \approx \frac{h}{d} \tag{15}$$

where d is the particle diameter and h is the length of the stretched portion of the particle which can be considered to be equal to (11):

$$h_n = \frac{4(1-\nu^2)\bar{K}}{E}\sqrt{\frac{2nI_D}{\pi}} \tag{16}$$

where n is the number of particles from the band tip and I_D is the interparticle distance (Fig. 1). The strain energy in the n-th particle is:

$$W_n = \frac{\pi}{12} G_R d^3 (\lambda - \frac{1}{\lambda^2})(\lambda - 1) \approx \frac{8}{3}\frac{G_R(1-\nu^2)^2}{E^2} d\bar{K}^2 n I_D \tag{17}$$

The total strain energy in the rubber particle of a band, W_p, is:

$$W_p = W_1 + W_2 + W_3 + \ldots + W_n \approx \frac{4}{3}\frac{G_R(1-\nu^2)^2}{E^2} d\bar{K}^2 \frac{l^2}{I_D} \tag{18}$$

Finally the rubber stretching energy rate (per unit surface), $\dot{w}_p$, is given by:

$$\dot{w}_p = \frac{4}{3}\frac{G_R(1-\nu^2)}{E}\,\frac{\bar{K}^2(1-\nu^2)}{E}\,\frac{1}{I_D}\frac{dl}{dt} = \frac{4}{3}\frac{G_R(1-\nu^2)}{E}\,\bar{G}\,\frac{dn}{dt} \tag{19}$$

The stretching energy accumulation rate is, thus, a function of the rate of particle cavitation. The interparticle distance dependence is a consequence of the fact that smaller particles have a higher strain energy density and are more effective in band stabilization.

THE INTERPARTICLE DISTANCE EFFECT

It is known that a rubber toughened polymer will show brittle fracture in impact if the interparticle distance is larger than a critical value (1). Eqn. (19) provides the basis for discussing the role of the interparticle distance in rubber toughening. In fact, by writing:

$$I_D = \frac{4}{3}\frac{G_R(1-\nu^2)}{E}\,\frac{\bar{G}}{\dot{w}_p}\frac{dl}{dt} \tag{20}$$

it is possible to understand that I_D is mainly related to the ratio between $\bar{G}$ and $\dot{w}_p$, as the length of the dilatational band increases. A critical value of this ratio may exist above which the excess $\bar{G}$ will result in overheating the ligaments, leading to an insufficient shielding effect of the plastic zone. When the rate of band propagation is too low (low temperatures), a smaller particle size and, hence a smaller I_D, is needed to accumulate enough rubber elastic energy in the plastic zone and prevent a brittle failure. In this sense, the interparticle distance effect may be considered, more correctly, a particle size effect. I_D is also dependent upon G_R, although this relation is more complex, since the rubber shear modulus influences both d*l*/d*t* (through w_c in Eqn. 12) and $\bar{G}$ (through its influence on σ_L).

At slow tests speeds a band propagates under isothermal conditions, and the rate of propagation is governed by Eqn. (12). Since bigger particles cavitates more easily (larger Δ), an inverse particle size effect should be expected under these conditions.

ACKNOLEDGEMENT

The author wishes to thank Prof. C.B. Bucknall for his helpful discussions and comments.

REFERENCES

1. Wu S, Polymer, **26** (1985) 1855.
2. Sue H-J, Yee AF, Polym. Eng. Sci., **36** (1996) 2320.
3. Lazzeri A, Bucknall CB, J. Mat. Sci., **28** (1993) 6799.
4. Lazzeri A, Bucknall CB, Polymer, **36** (1995) 2895.
5. Cheng C, Hiltner A, Baer E, Soskey PR, Mylonakis SG, J. Mater. Sci., **30** (1995) 587.
6. Chen WF, Zhang H, 'Structural Plasticity', Springer Verlag (New York), 1991.
7. Williams JG, 'Fracture Mechanics of Polymers', Ellis Horwood Ltd (Chichester), 1984.
8. Argon AS, Cohen RE. Gebizlioglu OS, Schwier CE, pag. 275-334 in 'Advances in Polymer Science', (Kausch H. H., ed), Springer Verlag (Berlin) 1983.
9. Dijkstra K, ter Laak J, Gaymans RJ, Polymer, **35** (1994) 315.
10. Leevers PS, Int. J. Fracture, *73* (1995) 109.
11. Ahmad ZB, Ashby MF, Beaumont PWR, Scripta Metallurgica, **20** (1986) 843.

YIELDING KINETICS IN RUBBER TOUGHENED POLYMERS

A Lazzeri*, D Giuliani*

Stress relaxation tests were carried out in tension and compression on a series of rubber toughened materials. The stress concentration factor in tension and compression (at constant rubber volume fraction) is equal for the non cavitating rubber modified blends. When the rubber is able to cavitate, the stress concentration factor in tension is about 30% higher than the corresponding value in compression. The results are discussed in terms of a dilatational yielding model using a modified Gurson equation to construct cavitation diagrams.

INTRODUCTION

One of the most important property of rubber toughened polymers is their capacity of reaching very high elongations before breaking. In a tensile test, these materials absorb much more energy because of their higher elongation at break. These characteristics are the result of matrix yielding.

The role of the rubber particles in the toughening mechanism is generally associated to:

- increase in the rate of yielding due to their action as stress raisers, thus promoting plastic deformation within the matrix;
- cavitation with subsequent increase in volume, enabling matrix flow;
- stabilization of the yielded polymer by stretching after cavitation.

All these functions seem to be necessary in order to obtain an effective toughening, even if their relative importance can vary with the type of material. Some other type of additives, including voids, can act as stress raisers, but only rubber particles can stretch with the matrix and redistribute the stress in the yielded regions [1]. This aspect can have a critical importance during impact and is discussed elsewhere [2]. Despite the amount of efforts spent in clarifying the role of rubber particles in toughening, some authors still question the fact that rubber cavitation promotes yielding in the matrix [3]. In a previous paper [4], it was shown that the rate of yielding in rubber toughened nylon is accelerated considerably at stresses above the cavitation resistance of the rubber. The purpose of this paper is to further investigate the role of rubber cavitation in the yielding kinetics of toughened polymers.

YIELDING KINETICS

The rate of plastic deformation is dependent upon temperature according to an Eyring type equation:

$$\dot{\varepsilon}_p = \dot{\varepsilon}_0 \exp(-\Delta G_a/kT) \quad (1)$$

where

$$\Delta G_a = \Delta G_0 - (\sigma_a - \sigma_i)V_a \quad (2)$$

is the activation free energy [5], $\sigma^* = \sigma_a - \sigma_i = \gamma\sigma_a$ is the effective stress and V_a is the thermodynamic activation volume:

$$V_a = \left(\frac{\partial \Delta G_a}{\partial \sigma_a} \right)_{P,T,(structure)} \quad (3)$$

The presence of rubber particles raises the effective stress in the matrix, and γ, thus affecting the kinetics of yielding. By substituting Eqn. (2) into Eqn. (1) we get:

$$\dot{\varepsilon}_p = \dot{\varepsilon}_0 \exp - \frac{(\Delta G_0 - \gamma\sigma_a V_a)}{kT} \quad (4)$$

* Centre for Materials Engineering, University of Pisa, Via Diotisalvi 2, 56126 Pisa, Italy

The operational (apparent) activation volume has been defined as the stress sensitivity of the strain rate, $\dot{\varepsilon}_p$ [5]:

$$V_0 = kT\left(\frac{\partial \log \dot{\varepsilon}_p}{\partial \sigma_a}\right)_{T,\sigma_t} = \gamma V_a + kT\left(\frac{\partial \log \dot{\varepsilon}_0}{\partial \sigma_a}\right)_{T,\sigma_t} \quad (5)$$

and coincides with γV_a when $\dot{\varepsilon}_o$ is not stress dependent. The apparent activation volume can be determined by measuring the slope of σ_y versus $\log\dot{\varepsilon}_p$ (Eyring plot). This technique can give rise to experimental errors since the range of strain rates available on a tensometer is generally limited to a few decades. The stress relaxation technique is a better alternative. In this type of test the total strain rate $\dot{\varepsilon}_t = 0$, therefore,

$$\dot{\varepsilon}_p = -\frac{1}{E}\frac{\partial \sigma_a}{\partial t} \quad (6)$$

Eqn. (1) can be expanded in Taylor-Maclaurin's series in terms of stress to give:

$$\dot{\varepsilon}_p(t) = \dot{\varepsilon}_p(0)\exp\frac{V_0 \Delta\sigma}{kT} \quad (7)$$

which substituting into Eqn. (6) leads to the time evolution of stress during a stress relaxation experiment:

$$\Delta\sigma = -\frac{kT}{V_0}\log\left(1 + \frac{t}{c}\right) \quad (8)$$

from which the experimental chart $\Delta\sigma(t)$ yields a measurement of $V_0 = \gamma V_a$. By assuming $\gamma = 1$ for the pure matrix, measurements of V_0, as a function of rubber content, in tension and compression relaxation tests, will determine the dependence of the stress concentration factor upon rubber volume fraction and also the effect of cavitation.

EXPERIMENTAL

Three system were studied. The first system was based on an Epon 828 epoxy resin from Shell Co. flexibilized with Jeffamine D-200 from Huntsman Co.. Aminoethylpiperazine (AEP) was added as a catalyzer. For this system a core shell rubber modifier, KM334 from Rohm & Haas, was used. The second system was based on the same epoxy resin, crosslinked with piperidine. The rubber used was a CTBN from BF Goodrich. The third system was a commercial nylon 66 blend, containing 0, 5, 10, 15 and 20% by weight of a maleanised ethylene-propylene (EPR) rubber. Mechanical tests were conducted on a Instron tensometer model 4302.

RESULTS AND DISCUSSION

In order to separate the effects of cavitation, on the kinetics of yielding, from those related to the stress concentration around low modulus inclusions, three systems were investigated:

- a high yield stress glassy matrix toughened with rubber particles with relatively low cavitation resistance (CTBN/epoxy blends);
- a lower yield stress glassy matrix toughened with rubber particles with relatively high cavitation resistance (KM334/flexibilized epoxy blends);
- a semicrystalline polymer toughened with relatively low cavitation resistance rubber particles (EPR/nylon 66 blends).

The first system has been very well examined in the literature on toughened epoxies, and it is known that the rubber particles cavitate in tension. Also in this study, volume measurements and scanning electron microscopy (SEM) have shown cavitation within the rubber particles in tension. In the second system, the behaviour of the materials in both compression and tension is similar. The Young's modulus is very little affected by rubber content, while the yield stress is progressively reduced upon increasing rubber volume fraction. The compression stress-strain behaviour shows evidence of intrinsic strain softening which is less evident when the rubber content increases. The flexibilized epoxy matrix shows a low yield stress of about 30 MPa in tension, which is much lower than the cavitation stress of the rubber (equal to 55 MPa). In the third system, also well known in the literature on toughening, the rubber particles cavitate in tension above 30 MPa.

Figure 1 shows the decrease of the apparent activation volume with strain for the system epoxy/10 phr CTBN rubber. At the yield point a plateau value is reached and this is taken as the experimental activation volume, V_0. Similar graphs were obtained for all materials in both tension and compression stress relaxation tests. Fig. 2 shows the activation volume in tension and compression for the flexibilized epoxy- KM334 system. The activation volume of the matrix is different in tension and compression due to the effect of the mean stress on the molecular mobility. Since no cavitation takes place in the rubber particles, the activation volume increases, and also γ, with rubber content in the same way in both tension and compression, and the two corresponding lines are parallel. A different behaviour is shown in Figs. 3 and 4. In this case, the rubber particles cavitate in tension, and the activation volume increases more rapidly in tension than in compression. As a consequence, γ is about 30% larger in tension. This clearly shows that cavitation allows the blends to deform at much higher rates than in the case of solid rubber particles.

The effects of cavitation on the yield behaviour can be modelled using a modified version of the Gurson's equation [6], which can be further modified to take into account the corrections suggested by numerical analysis [7-8] to take into account the interactions between voids and also the effect of the rubber shell surrounding the void:

$$\frac{\sigma_e^2}{\sigma_o^2}+2fq_1\cosh\left(\frac{3}{2}q_2\frac{\sigma_m-\sigma_R}{\sigma_o}\right)-\left(1-\frac{\mu\sigma_m}{\sigma_o}\right)^2-q_1^2f^2=0 \qquad (9)$$

The cavitation diagram [9] sketched out in Fig. 5 provides a convenient method of discussing this behavior. For the matrix containing no rubber particles or voids, the yield envelope is represented by a straight line (a). For the corresponding rubber modified blend, in absence of cavitation, the yield line will be shifted to lower values, line (b) in Fig. 5. When rubber cavitation occurs, yielding will take place at lower stresses, as predicted by Eqn. 9, which corresponds to point Y on curve (c). It is interesting to note that point Y also belongs to curve (d) which corresponds to the yielding curve of a non cavitating rubber modified polymer with a higher rubber content. The effect of cavitation is equivalent in an increase in the effective rubber content, thus explaining the measured increase of the stress concentration factor.

SYMBOLS

ΔG_a	activation free energy	$\dot{\varepsilon}_0$	preexponential constant
ΔG_0	athermal free energy	c	integration constant
γ	stress concentration factor	E	Young's modulus
μ	Coulomb's coefficient	f	rubber volume fraction
σ_a	applied stress	k	Boltzmann's constant
σ_e	effective (von Mises) stress	q_1, q_2	Tvergaard's constants
σ_i	internal stress	R	gas constant
σ_o	effective stress at $\sigma_m = f = 0$	t	time
σ_R	stress in the rubber shell	T	temperature
$\dot{\varepsilon}_p$	plastic strain rate	V_a	activation volume
$\dot{\varepsilon}_t$	total strain rate		

REFERENCES

1. Sue H-S, Yee, AF, Polym. Eng. Sci., **36** (1996) 2320.
2. Lazzeri A, Paper P75, this conference.
3. Havriliak S, Cruz CA, Slavin SE, Polym. Eng. Sci., 36 (1996) 2327.
4. Bucknall CB, Heather PS, Lazzeri A, J.Mat. Sci., 16 (1989) 2255.
5. Escaig B, Plastic Deformation of Amorphous and Semicrystalline Materials, Escaig B and G'Sell C Eds., Les Editions de Physique Publ., (Les Ulis) 1982, p. 187.
6. Gurson AL, J. Engng. Mater. Technol., **99** (1977) 2.
7. Jeong H-J, Pan J, Int. J. Solids Structures, **32** (1995) 3669.
8. Steenbrink AC, van der Giessen E, Proc. European Symposium on Polymer Blends, Maastricht, May 12-15, 1996, p. 254.
9. Lazzeri A, Bucknall CB, Polymer, **36** (1995) 2895.

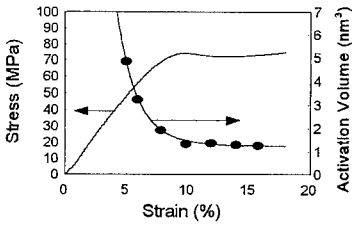

Figure 1 Activation volume versus strain for epoxy / 10 phr CTBN blend, during compression tests.

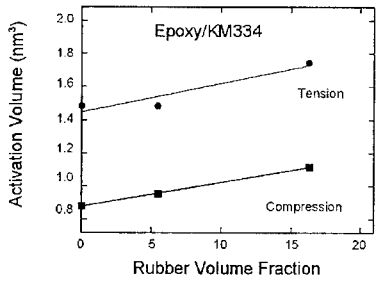

Figure 2 Tension and Compression activation volume as a function of rubber content KM334/Epoxy blends.

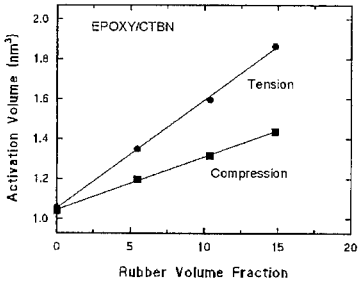

Figure 3 Tension and Compression Activation Volume as a function of rubber content in CTBN/Epoxy blends.

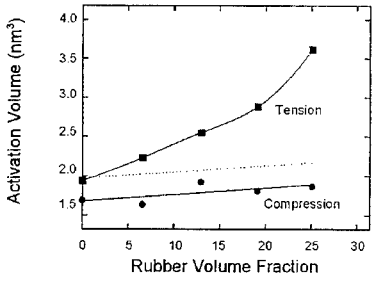

Figure 4 Tension and Compression Activation Volume as a function of rubber content in EPR/Nylon 66 blends.

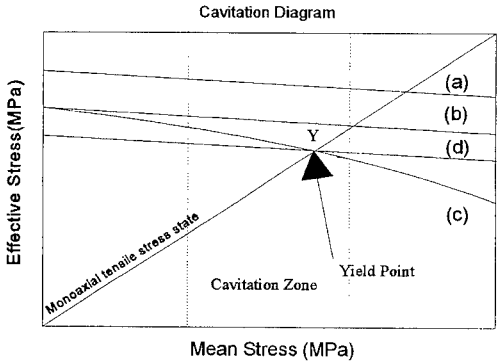

Figure 5 Schematic representation of a cavitation diagram.

FATIGUE AND FRACTURE IN POLYACETAL RESINS

A Lazzeri*, A Marchetti*, I Anguillesi*

In polyacetal resins, cyclic stressing determines phenomena of bond breaking within the polymeric chains. The process includes the formation of reactive radicals which subsequently give rise to microvoids, in presence of repeated stresses. This paper discusses the kinetics of molecular degradation and the consequent decrease in fracture resistance during fatigue stressing. The results are analized in terms of the Zhurkov-Bueche fracture theory.

INTRODUCTION

Polyacetal resins (also known as polyoxymethylene - POM - copolymers) play an important role among engineering polymers as competitors of nylons, which show some deficiencies, particularly in presence of humidity. Moreover, for their excellent mouldability, polyacetal resins are particularly appreciated when it is needed to produce complex forms or mechanical components with reduced dimensions. Despite the relatively large usage of polyacetal resins in engineering applications very limited work (1-4) has yet been published about the resistance to cyclic stressing. The fatigue behaviour is quite a relevant issue in applications such as silent gears and self-lubricating precision mechanics. Lesser (3), comparing the fatigue behaviour of polyacetals and nylons, pointed out that although POM is more crystalline and shows better resistance to fatigue crack growth than nylons (1), the overall fatigue life is shorter. This means that the resistance to crack initiation time is lower in polyacetals (3). A recent paper (5) has shown that in POM cyclic stressing determines phenomena of bond breaking within the polymeric chains. The process is likely to be associated to the formation of reactive radicals which subsequently give rise to microvoids in the amorphous phase, in presence of high or repeated stresses. It was also shown (5), that low molecular mass polyacetal resins undergo brittle fracture with no substantial subcritical crack growth during fatigue crack propagation (FCP) tests.

The purpose of the work reported here, was to determine the kinetics of molecular mass degradation and the consequent decrease in fracture resistance. This will enable the comprehension of the molecular processes occuring at the crack tip during FCP experiments. The results are then analysed in terms of the Zhurkov-Bueche fracture theory.

EXPERIMENTAL

Three types of commercial polyoxymethylene copolymers, classified on the basis of their relative molecular mass (RMM) as low (LM), medium (MM) and high (HM) molar mass, were used in this work. A fourth material, a medium molecular mass POM (MM-st) containing a free radicals stabilizer was also used. Unnotched samples of size 115 x 50 x 6 mm were fatigued for

* Centre for Materials Engineering, University of Pisa, Via Diotisalvi 2, 56126 Pisa, Italy

4000 to 60000 cycles at different values of maximum stress amplitude, σ_{max}, and subsequently were cut into three samples of size 73 x 15 x 6 mm. After razor notching, the samples were tested in three point bending. A minimum of 9 specimens have been used for K_{IC} determination. Fuller details of specimen preparation and sizes are given in reference (5).

The weight-average molar mass, $\overline{M}_w$, was determined with the dilute solution viscosimetric analysis. The inherent viscosity η_{inh} of the materials was measured with a Ubbelhode suspended-level viscosimeter at a temperature of 60°C. About 50 mg of the polymer was dissolved in 50 ml of a mixture of para-chlorophenol and α-pinene (weight ratio 98/2). The measurement of the flow times has been performed by means of a AVS 310 automatic viscosity measurement system. The weight-average molar mass, $\overline{M}_w$, was determined according to the semiempirical correlation of Wagner and Wissbrun (6):

$$\eta_{inh}=4.13\cdot10^{-4}\cdot\overline{M}_w^{0.724} \qquad (1)$$

RESULTS AND DISCUSSION

Figure 1 shows the effect of fatigue on RMM of POM-LM. The variation of the weight-average molar mass as a function of the number of cycles, N, follows an exponential pattern. $\overline{M}_w$ first decreases very rapidly and then decreases more and more slowly until is reached an asyntotic value, indicated as $\overline{M}_{w,Lim}$, which is a function of the maximum stress. This behaviour can be associated to mechano-chemical degradation of the polymer caused by chain scissions. For this type of reactions, the rate of bond scission is proportional to the difference between the RMM at time t and the limiting molar mass, $\overline{M}_{w,Lim}$. Therefore, we can write:

$$-\frac{d\overline{M}_w}{dN}=k_M(\overline{M}_w-\overline{M}_{w,Lim}) \qquad (2)$$

where k_M is the RMM degradation constant. Upon integration of Eqn. (2) we get:

$$\overline{M}_w=\overline{M}_{w,Lim}+(\overline{M}_w^{\,o}-\overline{M}_{w,Lim})\exp(-k_M N) \qquad (3)$$

Eqn. 3 is plotted in Fig. 1 as a continuous line. The agreement with the experimental data is excellent. The RMM degradation constant, k_M, as well as the limiting molar mass, $\overline{M}_{w,Lim}$, are a function of the maximum stress, σ_{max}, as shown in Fig. 2. Similar results were found for the other materials.

Since fracture toughness depends upon molecular mass with a relationship of the type $K_{IC}=a-b/\overline{M}_w$, which, in the particular range of molar masses used in this work, is approximately linear with $\overline{M}_w$, it is foreseen that K_{IC} will decrease with the number of cycles according to the following equation:

$$K_{IC}=K_{IC,Lim}+(K_{IC}^{\,o}-K_{IC,Lim})\exp(-k_F N) \qquad (4)$$

Figure 3 shows results of fracture mechanics tests on fatigued POM - LM at different stress levels and different number of cycles. Eqn. 4 is plotted as a continuous line. Again, the agreement between the theoretical curve and the experimental points is very good. The fracture toughness degradation constant, k_F, has similar values to k_M, although not coincident, and also varies with σ_{max} in an exponential way, as shown in Fig. 4. For both constants, this is consistent with a Zhurkov-Bueche relationship (7):

$$k=k^{\,o}\exp-\frac{(U_o-\gamma\sigma_{max})}{RT} \qquad (5)$$

The limiting fracture toughness, as well as $M_{w,Lim}$, also depends upon σ_{max}.

It is known that, during fatigue, ellipsoidal shape microvoids are formed in POM (8), which also cause a volume change measurable by fatigue dilatometry (4). Microvoids appear preferentially in the amorphous phase at interlamellar boundaries (8). The molecular degradation

process, observed in this work, is probably associated with microvoid formation. In general, microvoids relax the degree of constraint at plane strain crack tips, resulting in a much higher rate of shear deformation. Crack blunting can occur, leading to a higher fracture toughness. In the case of POM, however, microvoids nucleation may be associated with entanglement loss due to chain scission of the tie molecules interconnecting crystalline regions leading to molecular mass degradation. This may bring to a decrease in the density of tie molecules and, therefore, in the load carrying capacity of the material, as measured by the decrease in K_{IC}. These findings can bring some light in the understanding of the molecular processes occurring during fatigue in POM. Nucleation of microvoids is a stress activated process due to chain scission of the least favorable oriented chains. The rate of chain scission increases with the maximum applied stress and so the volume fraction of microvoids. Nucleation of microvoids is very rapid in the early stages of fatigue life and, later, only expansion of microvoids occurs. This is consistent with the observed dependence of the fatigue volume change with stress (4).

These observations also apply to the material at the crack tip in Fatigue Crack Propagation (FCP) tests. In the early stages of the FCP life, chain scission and molecular degradation occur at the crack tip. The local fracture resistance of the material decreases progressively and falls below the applied K_I. For the lower molecular mass materials, a catastrophic fracture will occur. In the case of higher molecular mass materials, the crack may advance very rapidly for a few cycles and then stop for a considerable number of cycles (stick-slip behaviour).

This work has shown that molecular degradation is a precursor of fatigue fracture in POM. More research is necessary to determine whether these chain scission fenomena are limited to polyacetals or are present in other polymers.

SYMBOLS USED

γ	= activation volume for bond scission
η_{inh}	= inherent viscosity
σ_{max}	= maximum stress in cycle
K_{IC}	= fracture toughness
K_{IC}^{o}	= initial fracture toughness
$K_{IC,Lim}$	= limiting fracture toughness
k_m	= RMM degradation constant
k_F	= fracture toughness degradation constant
N	= number of cycles
$\overline{M}_w$	= weight-average molar mass
$\overline{M}_w^o$	= initial weight-average molar mass
$\overline{M}_{w,Lim}$	= limiting weight-average molar mass
T_g	= glass transition temperature
U_o	= activation energy for bond scission

REFERENCES

1. Hertzberg RW, Manson JA, "Fatigue of Engineering Plastics", Academic Press (New York), 1980.
2. Runt J, Gallagher KP, J. Mat. Sci., **26** (1991) 792.
3. Lesser AJ, J. Appl. Polym. Sci. **58** (1995) 869.
4. Lesser, AJ, Polym. Eng. and Sci. **18** (1996) 2366.
5. Lazzeri A, Marchetti A, Levita G, accepted for publication in Fatigue & Fracture of Engng Materials & Structures
6. Wagner HL, Wissbrun KF, Makromol. Chem. **81** (1965) 14.
7. Kausch H.-H., "Polymer Fracture", 2nd ed. Springer-Verlag (New York), 1987.
8. Wendorff JH, Progr. Coll. Polym. Sci. **66** (1979) 135.

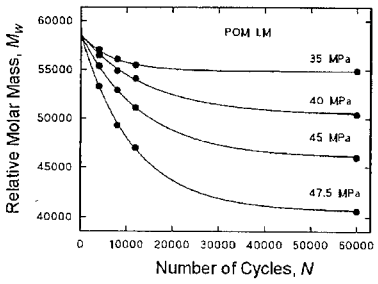

Figure 1 - Relative Molar Mass as a function of the number of cycles, at different maximum stresses for POM - LM.

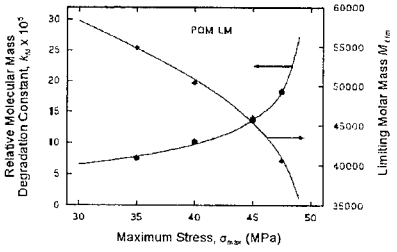

Figure 2 - Dependence of RMM degradation constant, k_M, and of M_{Lim} from maximum stress, σ_{max}.

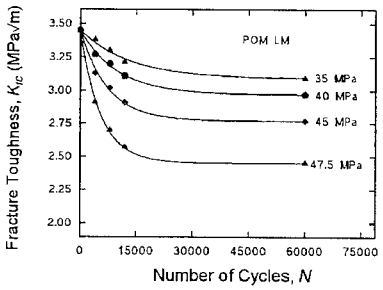

Figura 3 - Fracture toughness as a function of the number of cycles, at different maximum σ_{max}, for POM - LM.

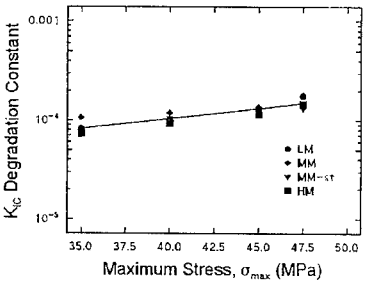

Figure 4 - Fracture toughness degradation constant, k_F, as a function of the maximum stress, σ_{max}.

The Impact Toughness and Morphological Characteristics of Modified PVC Polymers

E. J. Ingham and G. P. Marshall[†]

Instrumented impact tests have been conducted on unplasticised poly (vinyl) chloride (uPVC) and blends of uPVC containing a chlorinated polyethylene (CPE) impact modifier. An elastic plastic fracture mechanics approach was used to evaluate the essential and inessential work of fracture associated with the particular mode of failure of each blend. With blends containing low concentrations of CPE although the toughness was enhanced, failure proceeded by brittle cracking. However blends incorporating sufficient CPE exhibited exceptional impact toughness, when compared to HDPE and ABS. Examination of the two phase morphology of blends using Transmission Electron Microscopy (TEM), showed that the onset of highly ductile failure occurs when a CPE network structure starts to form. It is however proposed that high toughness is not consistent with the formation of a CPE network, but the CPE phase achieving critical particle sizes, which are capable of cavitation in impact, as observed with other rubber toughened polymer systems.

Introduction

With polymers which exhibit brittle cracking under conditions of impact, it is possible to alter the failure mechanism of the parent material by the use of a rubbery impact modifier. In brittle polymers such as High Impact Polystyrene (HIPS), the toughening effect of the rubber particles is to promote crazing of the polymer matrix. However in some polymers where the structure of the matrix is such that crazing is prevented, the toughening mechanism which operates is cavitation of the rubber particles, followed by ductile shear yielding of the matrix. For rubber cavitation to occur requires that the rubber particles are of a critical size, which is dependent on the particular polymer blend.

Experimental

Charpy impact specimens were produced from modified PVC (mPVC) pipes, containing different concentrations of CPE. Impact testing was performed on an Rosand instrumented falling weight impact machine. The morphology of selected blends were examined using Transmission Electron Microscopy (TEM). Ultrathin sections (80nm) of each blend were prepared at room temperature, after selectively staining the CPE phase using a technique referred to by Kanig (1).

Results and Discussion

Elastic Plastic Fracture Mechanics

All the impact data obtained were analysed by adopting an elastic plastic fracture mechanics approach, which was first proposed by Mai (2), using the following equation;

$$W_f = W_e + \beta l W_p \qquad (1)$$

Using this analysis it is possible to partition the work of fracture associated with brittle cracking (essential work of fracture (W_e)) and the work dissipated in the formation of a plastic zone at the tip of an advancing crack (inessential work of fracture βW_p).

[†]Pipeline Developments, Manchester, England.

Impact data analysed in this way for the uPVC and uPVC blends containing CPE are shown as figure 1. With the uPVC and uPVC blends containing low concentrations of CPE the failure mode was exclusively brittle. In these cases there is no plastic work dissipated remote from the fracture process zone and the total work of fracture is equal to the essential work of fracture (W_e). On the work of fracture plot, the data for uPVC and the 6phr CPE blend are shown as a lines with no gradient, the intercept of which are the Gc_1 values for each material.

Increasing the concentration of CPE to 15phr results in a substantial increase in the inessential work of fracture term, with the sample exhibiting a ductile failure mechanism. Further increasing the CPE concentration (18phr) produces blends which show exceptional toughness, exhibiting approximately a two fold increase in the inessential work of fracture term, when compared to the 15phr version. Interestingly all the blends containing 15phr CPE and above are tougher than both HDPE and ABS.

Blend Morphology

Transmission electron micrographs of the 15phr CPE and 18phr CPE blends are shown as plate 1 and plate 2 respectively. In the blend containing 15phr of modifier the CPE exists as discrete particles, however in the 18phr blend, the CPE appears to be developing into a network structure enveloping the PVC particles. As with other work with PVC blends (3,4) it was first apparent that the large enhancement in toughness observed between 15phr and 18phr CPE, was consistent with the change in morphology from discrete particles to a CPE network.

1μm
Plate 1. TEM showing
15phr CPE/PVC Blend x25

1μm
Plate 2. TEM showing
18phr CPE/PVC Blend x25

Net Section Yielding

With the blends that fail in a ductile manner, plastic deformation dominates the fracture process and it is possible to reanalyse the data using a net section yield criterion (5). For all the highly modified blends the data overplot precisely as shown in figure 2, indicting that at the strain rate adopted for the impact tests ($45s^{-1}$) all the materials exhibit the same yield stress. The value of the net section stress at the peak condition is (σn = 116 MPa). Since the impact tests were performed in bending this value must be divided by a factor of 1.5, to compensate for the collapse condition, to give an equivalent tensile yield stress value of 75 MPa. The fact that these materials exhibit the same yield stress in impact is therefore extremely unusual, especially since uniaxial tensile test data shown in figure 3, indicate that all the materials exhibit different values of yield stress and there is no convergence of the fitted lines at $45s^{-1}$.

Under impact conditions, with PVC containing low modifier levels the particles are too small to undergo internal cavitation or initiate crazing. As a result, the volume strain in the matrix material increases to a critical value, at which the material breaks open into crazes, which act as crack extensions and cause brittle failure. As more modifier is added, the rubber particles agglomerate and essentially act as larger single particles. In the case where enough modifier is added to achieve a critical particle size, the volume strain in the matrix causes the particles to

cavitate internally. The triaxial stress state generated in the central region of the crack is relieved and a state of uniaxial tension exists on the ligaments of the PVC matrix. The uniaxial stress state allows ductile shear yielding throughout the matrix material. It is hence proposed that the net section yield stress observed with all these mPVC materials is actually the yield stress of the PVC matrix material. This explanation would in fact resolve the issue of why PVC materials incorporating high levels of impact modifier exhibit the same yield stress, under conditions of impact loading.

It may therefore be possible that in CPE modified PVC the enhancement of the toughness at a given extent of CPE, may not be due to the formation of network structure, but the attainment of a critical particle size. The elongated structures of CPE (plate 2) must be due to agglomeration of individual particles, which is consistent with the achievement of a critical particle size. The actual agglomeration of MBS particles has been experimentally used to produce particles, which are large enough to undergo cavitation (6). In the highly ductile CPE blend the diameter of portions of the network are approximately 500nm, which suggests that in this system larger particles are required to achieve cavitation in impact, compared to MBS mPVC where the critical rubber particle size is in the order of 150nm (7).

Conclusions

(1) The work of fracture technique used was extremely effective in differentiating between modified PVC polymers of very high toughness and tough polymers such as ABS and HDPE.

(2) The use of a net section stress analysis appears to provide additional evidence that rubber cavitation is a precursor to yielding of the PVC matrix, resulting in a high degree of ductility.

Symbols Used

W_f = total work of fracture;	W_e = essential work of fracture
W_p = inessential work of fracture	l = ligament length
β = geometric shape factor	D = sample depth
B = sample thickness	a = notch depth
Ut = total impact energy	Gc_1 = plane strain impact toughness

References

(1) Kanig, G., Kunstoffe, (1974), 64, 470.
(2) Mai Y.W, Polymer Communications, 1989, 30, 330.
(3) Siegmann A, Hiltner, Polymer Engineering and Science (1984), 24, 11, 876.
(4) Mc Gill W.J., Wittstock T, Plastics and Rubber Processing and Applications 3, (1983),77.
(5) Morley K, Criteria of Failure for Polymer Blends, PhD Thesis, (1992).
(6) Dompass D, Groeninckx G, Isogawa, M, Polymer, (1994), 35, 22.
(7) Dompass D, Groeninckx G, Isogawa, Hasegawa T, Kadokura, Polymer (1994),35,22.

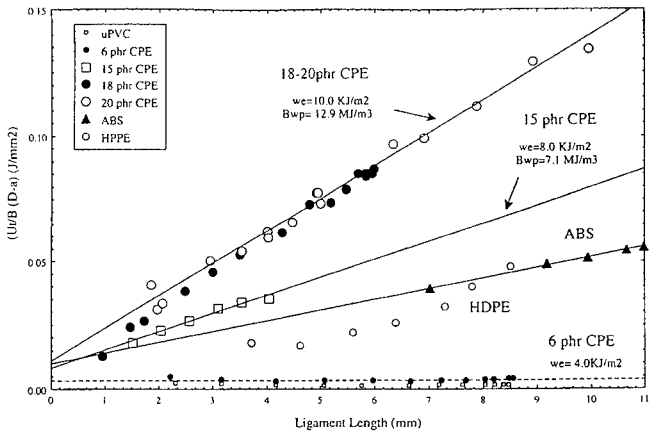

Figure 1 Total Work of Fracture Versus Ligament Length

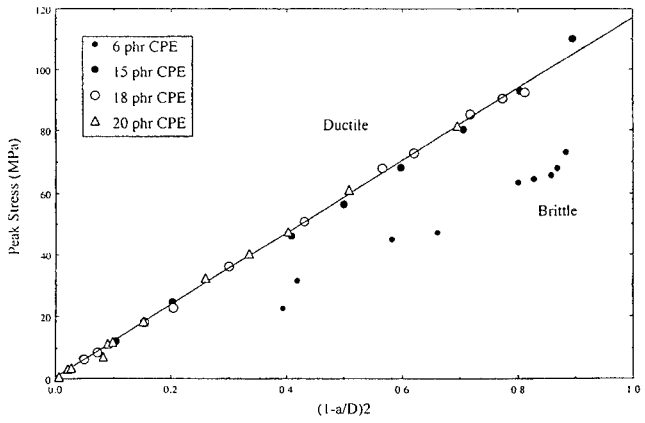

Figure 2. Net Section Yield Stress data for PVC/CPE Blends

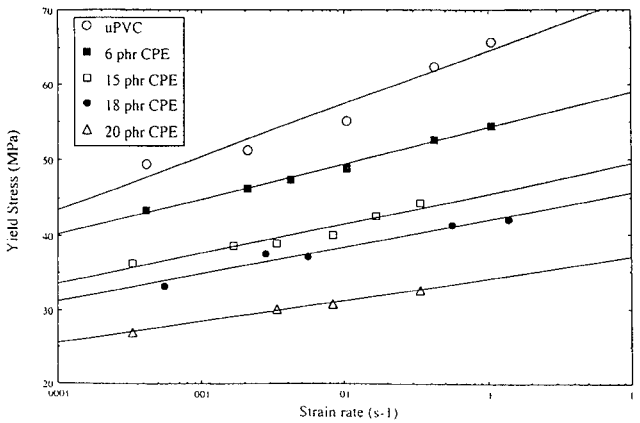

Figure 3 Variation of Tensile Yield Stress with Strain Rate for mPVC

EVIDENCE FOR PARTICLE CAVITATION AS THE PRECURSOR TO CRAZING IN HIGH IMPACT POLYSTYRENE

H H Yang and C B Bucknall

Uniaxial tensile and creep tests on pre-strained and annealed HIPS specimens have been used to determine whether rubber particle cavitation is responsible for craze initiation, or vice versa. Annealing of specimens taken beyond a critical tensile strain (of order 0.2%) consistently results in a drop in yield stress σ_y (load maximum) but not in flow stress σ_{flow} (load minimum). The critical pre-strain is a function of rubber content and temperature. Comparable effects are seen in creep tests. Small levels of pre-straining have little effect if the specimen is not annealed before reloading. It is concluded that rubber particle cavitation is a necessary precursor to multiple crazing in rubber toughened plastics.

INTRODUCTION

It has long been assumed (1-3) that craze initiation occurs at points of maximum stress concentration in the polystyrene matrix, and that cavitation (or debonding) of the rubber phase is an inevitable consequence of the increasing volume strain in the surrounding matrix. However, this view must now be questioned in the light of current developments. Studies by Buckley (4) concerning the mechanisms of energy absorption in HIPS have shown that rubber particle cavitation is responsible for over half of the total post-yield strain, and that the onset of cavitation occurs simultaneously with, or slightly earlier than, the beginning of craze formation. These observations, combined with the cavitation model developed by Bucknall (5), suggest that cavitation of the rubber phase is the cause and not the consequence of craze initiation.

Under γ-irradiation, the rubber phase of HIPS becomes highly cross-linked (6). This not only raises the shear modulus of the rubber and makes it more resistant to cavitation, but also increases the stress carried by the rubber phase when the matrix begins to craze. These experiments confirm that rubber particles are load-bearing elements during deformation, and are consistent with Buckley's results, which show that particle cavitation is responsible for over half of the total post-yield strain in HIPS subjected to tensile impact.

According to the energy balance model, rubber particles cavitate when the available volumetric strain energy associated with the particle exceeds the energy needed to form new surface and to stretch the rubber immediately surrounding the void (5, 7). For a cross-linked rubber, chain scission is an inevitable result of cavitation. If a cavitated rubber particle is unloaded (allowing the voids to close up) and then reloaded, the triaxial stress required for the second cavitation will be lower than that needed in the first place. The difference between the two stresses will increase if the voids in the cavitated particle are allowed to expand and cause further bond scission.

* Cranfield University, Bedford MK43 OAL, UK

This effect of strain history upon the properties of rubber particles is the basis of the present study. If crazes can initiate only from cavitated rubber particles, then rates of crazing should be increased when the rubber particles have previously been cavitated, provided that all other factors are equal. The aim of the study has therefore been to develop and apply techniques to determine whether prior cavitation of the rubber particles affects yielding of HIPS by the multiple crazing mechanism.

EXPERIMENTAL

The HIPS used was a commercial grade, BP-4300, which contained 9 vol% polybutadiene rubber dispersed as 'salami' particles with an average diameter of 1.0 μm (range 0.1 to 5 μm). The polystyrene matrix had a weight-average molecular weight of 200,000. The $T_g s$ of PS and rubber were 98.5°C and -87.5°C respectively. The original HIPS was melt-compounded with PS to produce a series of blends with HIPS/PS ratios of 1/0, 3/1, 1/1 and 1/3. Test pieces were saw cut from compression moulded plaques and machined into ASTM D638 dumb-bell specimens. An Instron Model 6025 test machine was used for all mechanical tests. Tensile tests, including pre-straining, were performed at 23°C with a cross-head speed of 0.1 mm/min. Creep specimens were loaded at an initial cross-head speed of 2 mm/min, followed by a constant stress of 13 MPa. Strains in both tests were measured using an Instron extensometer.

Tensile specimens were pre-strained to chosen strain levels, which were held constant for 3 minutes before unloading. The strained specimens were then conditioned for 48 hours at 23°C prior to annealing. It is well known that crazes can be healed by heating the thermoplastic above its T_g. At the annealing stage, it is important to eliminate all traces of crazing in the polystyrene matrix, without causing distortion or thermal degradation of the material. After extensive trials, an annealing temperature of 113°C was chosen for BP-4300 HIPS. Annealing was then carried out in a vacuum oven controlled at 113±5°C. Specimens were loaded into a metal jig to prevent distortion, and annealed for 3 hours. The oven was then switched off and allowed to cool slowly to room temperature to ensure uniform thermal history. Unless otherwise stated, annealed specimens were tested to failure at 23°C.

RESULTS

In the absence of an intermediate annealing stage, yield and flow stresses are unaffected by prestraining at $0 > \varepsilon > 0.85\%$. By contrast, pre-straining followed by annealing has a marked effect upon yield behaviour, as illustrated in Fig. 1. The principal effect, up to an initial strain of 25 %, is to depress the load maximum, which defines σ_y. However, pre-straining has little effect upon either the flow stress σ_{flow}, or the remainder of the stress-strain curve up to the failure stress σ_f. These results show that pre-straining HIPS beyond its yield strain, which is ~0.85 %, causes damage in the material that is not reversed by annealing. Further detailed examination shows that the first evidence of a depression in σ_y appears at very small pre-strains (~ 0.2 % at 23°C). This means that tensile stresses of about 1.5 - 3 MPa applied during the pre-straining process begin to cause significant damage to the particles. However, it must be borne in mind that differential thermal contraction generates substantial internal stress within the rubber particle even before load is applied.

Lowering the volume fraction of rubber particles means that fewer crazes are initiated under given loading conditions, thus causing an increase in yield stress (see Fig. 2) and yield strain (up from 0.85 to 1.4%), and earlier failure (down from 45 to 7 %). The threshold strain for damage is shifted from 0.2% to 0.7 % (dashed line in Fig. 2). The higher yield stresses in the blends means that a higher proportion of particles cavitates and initiate crazes, but this is not enough to compensate for the reduction in the number of rubber particles.

Creep tests show similar effects (Fig. 3). Pre-straining up to certain level (typically between 0.1 and 0.3 %) has no effect. Creep rates increase rapidly with prestrains above this threshold, but become independent of pre-strain when the pre-treatment exceeds σ_y. Examination in the TEM shows that when the pre-strain goes beyond yield at ε_y ~1%, most large particles ($\geq$ 2μm) are already either cavitated or have initiated crazes at the particle-matrix interface. Recent work on HIPS with larger particle sizes has shown that the increased particle size causes a decrease in the critical level of pre-strain needed to produce a depression in σ_y after annealing, as predicted by the energy balance model for cavitation (2).

DISCUSSION

These results are consistent with the theory that yielding is preceeded by cavitation of the larger rubber particles, involving chain rupture within the rubber phase, and that initiation of crazing in the surrounding polystyrene is dependent upon this cavitation process in the rubber particle. Annealing repairs most of the damage associated with crazing in the matrix, so that pre-strain has little effect upon the flow stress and subsequent deformation, but annealing cannot completely eliminate the damage within the cavitated and fibrillated rubber phase. The voids may close up, and the fibrils may recover, but chemical bonds remain broken. On reloading, energy is required to form new void surface in the rubber and to stretch the resulting rubber fibrils, but (unlike the prestraining stage) not to break chemical bonds. These effects can be easily understood using the Takayanagi model in Fig. 4. The large cavitated particles will initiate crazing at lower strains than undamaged particles. Thus pre-straining has the opposite effect to γ-irradiation, which forms new bonds that have to be broken during cavitation, and therefore delays the onset of crazing. It is clear from these experiments that the main changes induced in the material occur during either pre-strain or annealing. Specimens that have first been annealed, then pre-strained, and then annealed for a second time, show a consistent trend: pre-straining affects σ_y but not σ_{flow}. Repeated pre-straining and annealing causes a progressive decrease in both yield and flow stresses, indicating a thermal fatigue effect.

This work supports the view that cavitation of the rubber particles is the rate-determining step in the yielding of HIPS by the multiple-crazing mechanism. If craze initiation is determined entirely by the levels of stress concentration in the polystyrene matrix, as has previously been suggested, it is difficult to understand why subjecting the material to a pre-strain of 0.25 to 25% should cause a substantial reduction in yield stress, but leave the flow stress unaffected, i.e. reduce the craze initiation stress and not the propagation stress. If pre-straining caused sufficient bond rupture in the polystyrene to make crazing intrinsically easier, then both initiation and propagation would occur at reduced stresses. The present study has shown that breaking chemical bonds, through pre-straining followed by annealing, has the effect of reducing resistance to cavitation and hence to craze initiation. Clearly, cavitation is the initial step in the process.

Acknowledgements

The authors thank the National Defence Department of Taiwan, ROC for financial support of this progamme.

References

1. S Kunz-Douglass, P W R Beaumont and M F Ashby, J. Mater. Sci., **15** (1980) 1109.
2. F J Guild and R J Young, ibid. **24** (1989) 298 (part 1), 2454 (part 2).
3. Y Huang and A J Kinloch, Polymer, **33** (1992) 1330.
4. R A Bubeck, D J Buckley, E J Kramer and H R Brown, J. Mater. Sci. **26** (1991) 6249.
5. C B Bucknall, A Karpodinis and X C Zhang, ibid., **29** (1994) 3377.
6. C B Bucknall, H H Yang and X C Zhang, "POLYMAT '94 International", Imperial College, London, 19-22 Sept. 1994, 673.
7. A Lazzeri, C B Bucknall, J. Mater. Sci. **28** (1993) 6799.

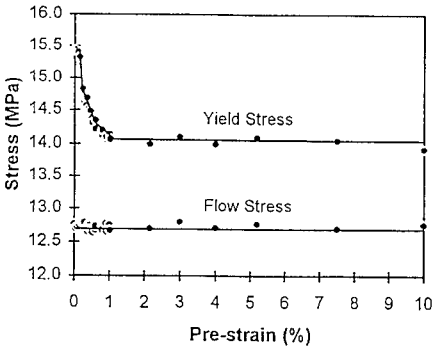

Fig.1. Effects of pre-straining on yield and flow behaviour of HIPS.

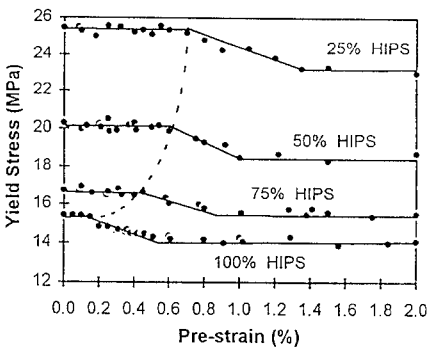

Fig.2. Effects of pre-straining on HIPS/PS blends.

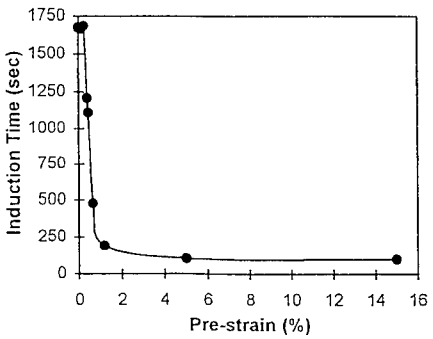

Fig.3. Effects of pre-straining on creep test induction time.

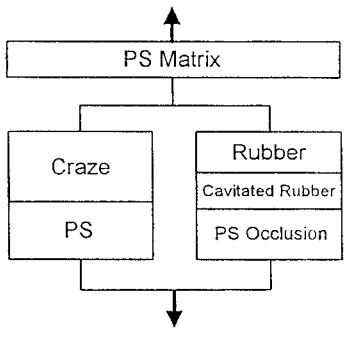

Fig.4. Takayanagi model of craze in parallel with rubber particle.

CRITERIA FOR CAVITATION IN TOUGHENED PLASTICS CONTAINING RUBBER PARTICLES WITH RIGID CORES

D. S. Ayre and C. B. Bucknall*

Criteria for cavitation of complex rubber particles containing glassy sub-inclusions are developed from an earlier model by incorporating expressions to represent thermomechanical interactions between the complex rubber particles and the surrounding matrix. The model is tested using tension, compression and three point bending experiments over a range of temperatures on a transparent rubber toughened polymer. Cavitation is detected by visual observation and by monitoring tensile yield behaviour with respect to compressive yield behaviour: cavitation causes a depression of the tensile yield stress.

INTRODUCTION

A recent model for rubber particle cavitation [1,2] has shown that growth of a void within a rubber particle of defined size and physical properties is energetically possible above a critical volume strain. Before we can compare the model with experimental results we need to measure volume strain in the rubber particle, or calculate it from known variables.

This paper relates the volume strain in a rubber particle to two independent dilatational stresses: a thermal stress due to the significant difference in thermal contraction strain between matrix and rubber particle when the temperature falls below the matrix T_g, and the applied external stress on the specimen .

MODEL

The model compares the energy of the system before and after cavitation. Volume strain energy is released as the void grows, but is required in order to form new surface and to stretch the rubber surrounding the void. When cavitation occurs at a fixed particle volume strain ΔV_{pR}, so that the energy changes are restricted to those occurring within the boundary of the rubber particle, the energy is given by [1,2]:

$$U(r) = \frac{2}{3}\pi R^3 K_p\left(\Delta V_{pR} - \frac{r^3}{R^3}\right)^2 + 4\pi r^2\Gamma + 2\pi r^3 G_p F(\lambda_f) \qquad (1)$$

total = term 1 + term 2 + term 3 (see Fig. 1)

where R = radius, K_p = bulk modulus, Γ = surface energy, G_p = shear modulus, r = cavity radius, $F(\lambda_f)$ is a function of the extension ratio of the rubber at failure in equi-biaxial tension, and subscripts m and p denote matrix and particle. From eq. 1, it can be seen that increasing the volume strain ΔV_{pR} eventually takes the rubber particle to a state where the formation of a cavity results in a decrease in energy of the system, Fig. 2.

In a rubber toughened material, dilatational volume strains will be imposed on the rubber particles at all temperatures T lower than the matrix T_g (T_{gm}) because of the significant difference between the volumetric coefficients of thermal expansion β_m, β_p [3]. Application of an external stress to the material will increase the volume strain of the rubber particle in

* Advanced Materials Department, Cranfield University, Bedford MK43 0AL

accordance with the standard elastic equations for a spherical element consisting of a rigid outer shell of radius Q and a rubbery inner core [2,4], Fig. 3. Assuming that the matrix/rubber particle interface remains intact, we obtain the following expression:

$$(T_{gm}-T)\ (\beta_m-\beta_p) = \frac{P_R}{K_p} - \left[P_Q\left(\frac{4G_m+3K_m}{4G_mK_m(1-\phi)}\right) - P_R\left(\frac{4G_m\phi+3K_m}{4G_mK_m(1-\phi)}\right)\right] \quad (2)$$

where ϕ = volume fraction of rubber particles, P_Q and P_R ($\equiv K_p\Delta V_{pR}$) are mean stresses at radius Q and R in the element.

EXPERIMENTAL RESULTS

Tension, compression and three-point bending experiments were carried out on compression moulded bars of a transparent toughened PMMA. At low strain rates, this material whitens at the tensile yield point, provided the temperature is below 55°C. Above this temperature specimens remain transparent and tensile(T) and compressive(C) yield stresses converge, Fig. 4. In three-point bend tests, monitoring of the neutral plane position at total plastic collapse shows an obvious change in the C/T ratio between 50°C and 60°C , Fig. 5.

DISCUSSION

The rubber particles toughening the PMMA have a core/shell morphology with a soft shell of butyl acrylate copolymer rubber surrounding a PMMA core. This complex rubber particle morphology is treated by calculating an effective K_p and β_p [3,5].

$$K_p = \frac{K_cK_s}{K_sV_c - K_c(1-V_c)} \quad (3)$$

$$\beta_p = \beta_cV_c + \beta_s(1-V_c) \quad (4)$$

where subscripts c and s indicate rigid core and rubbery shell, and V_c is the volume fraction of the rubber particle occupied by the core.

Previous work [2] concentrated on energy changes occurring within the rubber particle during cavitation, acknowledging that energy changes in the matrix would make a significant contribution, inducing rubber particle cavitation at lower rubber volume strains. In order to improve the model, the three-layer element shown in Fig. 3 has been analysed: the rubber particle of radius R is surrounded by a pure matrix shell of outer radius Q, which in turn is surrounded by a composite (rubber toughened) thick shell of outer radius Z, where Z » Q. A limiting condition of constant mean stress (one third of the tensile stress) at the external surface of the system is applied and it is assumed that overall changes in volume are negligible during cavitation of one particle. Using the experimental tensile yield stress data, we obtain the energy/cavity radius diagrams shown in Fig. 6. Cavitation is possible below the yield stress at all test temperatures because it results in a net decrease in energy. This result indicates that another more restrictive criterion governs rubber particle cavitation.

Equation 1 necessarily produces an 'energy barrier' during the initial stages of cavity growth. As the test temperature increases, yield stresses decrease, and the height of the energy barrier at the yield point increases. The experimental results suggest that cavitation can proceed at an observable rate only if the energy barrier is sufficiently low, i.e. the applied mean stress is relatively high.

CONCLUDING REMARKS

The original energy-balance model for rubber particle cavitation [1,2] has been refined by considering thermal and energy contributions from the matrix. When the new model is

compared with experiment, it is apparent that a net energy loss is a necessary but not sufficient condition for cavitation, and that rates of cavitation are limited by another factor, probably an 'activation energy' which is dependent upon the applied stress (see Fig. 6b).

ACKNOWLEDGEMENTS

The authors thank the Engineering and Physical Science Research Council (GR/K24703) for financial support of this project, and Rohm and Haas for providing the toughened material.

REFERENCES

1. A. Lazzeri and C. B. Bucknall, J. Mater. Sci. 28 (1993) 6799.
2. C. B. Bucknall, A. Karpodinis and X. C. Zhang, J. Mater. Sci. 29 (1994) 337.
3. M. E. Boyce, A. S. Argon and D. M. Parks, Polymer 28 (1987) 1680.
4. H. Reismann and P. S. Pawlik, "Elasticity:Theory & Applications", Wiley, NY 1980.
5. C. Fond, A. Lobbrecht and R. Schirrer, Int.J. Fract. 77(1996) 141.

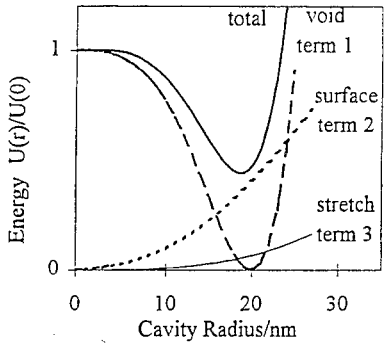

Figure 1 Energy contributions

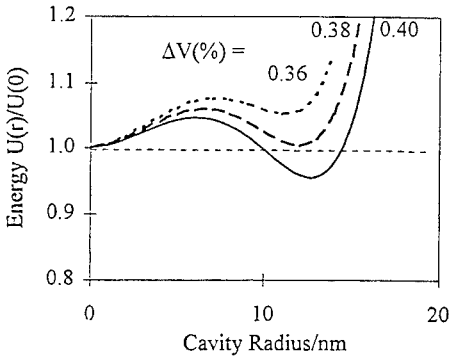

Figure 2 Cavitational energy diagram

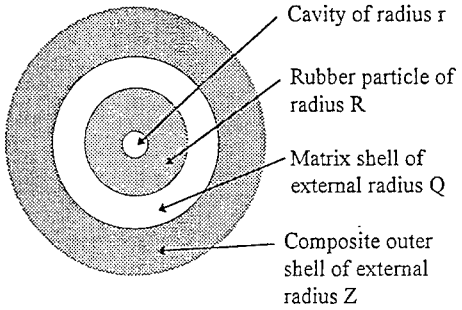

Figure 3 Representation of material for modelling energy changes as a cavity grows at the centre

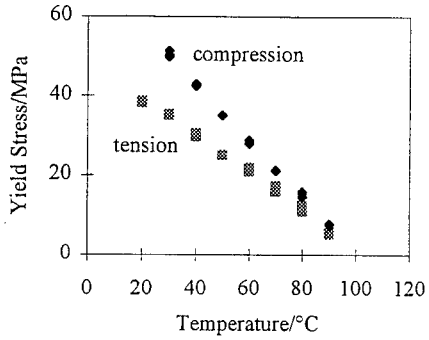

Figure 4 Experimental yield data

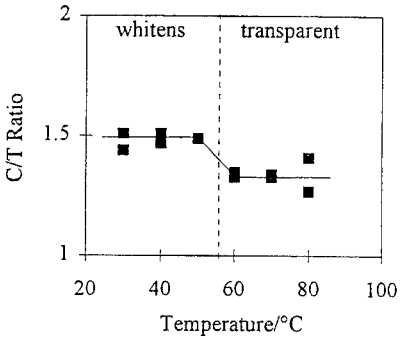

Figure 5 Neutral plane displacement effect with cavitation

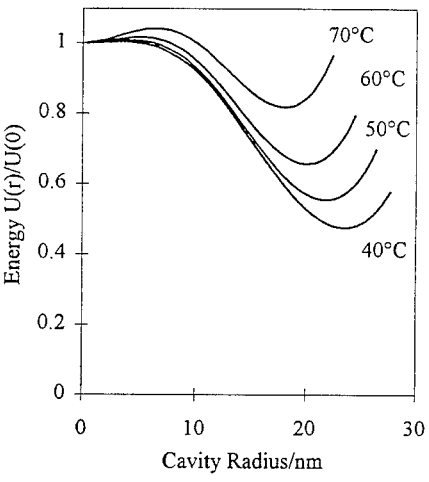

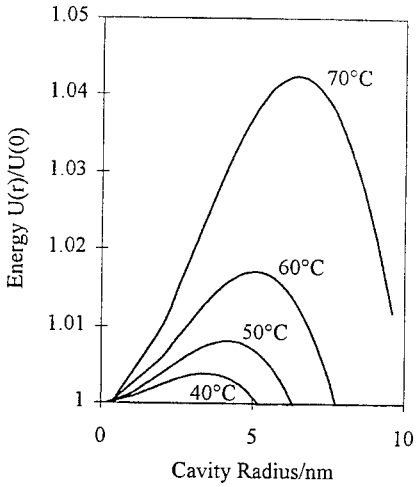

Figure 6 Changes in energy, U(r), in element of radius Q

(a) minimum energy

(b) maximum energy

CRITERIA FOR FRACTURE OF HIGH-IMPACT POLYSTYRENE UNDER UNIAXIAL TENSION

B. O'Connor*, C.B. Bucknall* and J.L. Hahnfeld**

The fracture of High-Impact Polystyrene (HIPS) in tension was investigated following a procedure described in an earlier paper by Sjoerdsma and Boyens[1]. The present study has revealed that fracture of HIPS is initiated not by the coalescence of crazes, as proposed by those authors, but by rubber particle breakdown, which occurs when the fibrillated rubber is stretched past its maximum extension ratio λ_{max}. Criteria for the failure of HIPS materials having a range of rubber cross-link densities and rubber volume fractions are outlined and discussed. Weibull statistics were found to describe reasonably well the probability of fracture of HIPS.

INTRODUCTION

The influence of rubber content, rubber particle morphology and rubber cross-link density on the toughness and failure of HIPS is still not fully understood. Cross-linking in the rubber phase is partly responsible for the familiar effects of outdoor ageing on the failure of rubber toughened materials, an area of primary importance to the industry. The aim of this study is to identify the dominating factors responsible for fracture of HIPS and obtain further insights into the high strain deformation of this material.

To date, the most promising analysis of final rupture in HIPS has been made by Sjoerdsma and Boyens[1], who postulated that HIPS fractures when crazes impinge upon each other, owing to the inevitable misalignment of the craze fibrils. Sjoerdsma and Boyens' model leads to Eq. 1, where the cumulative probability of fracture, P_f, is a function of the square of the craze strain, ε_{cr}, taken by these authors as being the total plastic dilatation of the material, and of A, a parameter dependent on the specimen geometry and on the craze geometry.

$$P_f = 1 - \exp(-A\varepsilon_{cr}^2) \qquad \text{(Eq. 1)}^1$$

For the one HIPS material Sjoerdsma and Boyens investigated, they found that $\ln(P_{sv})$ was linear with ε_{cr}^2, where P_{sv}, the probability of survival, is defined as $(1 - P_f)$.

MATERIALS

The materials investigated in this study were all based on HIPS A, a commercial grade HIPS with approximately 8 wt. % polybutadiene. HIPS B and C were produced by melt blending HIPS A with 0.28 and 0.56 wt. % pure sulfur respectively. HIPS D-F were produced by melt blending 75, 50 and 25 vol. % HIPS A with General Purpose Polystyrene of a similar molecular weight. Compounding was carried out in a double screw co-rotational Werner Pfleiderer

* Cranfield University, Bedford MK43 OAL, UK
** Dow Chemical Company, Midland, Michigan 48667, USA

extruder with a medium shear screw profile and a processing barrel temperature of 200°C. Following the procedure described in the Sjoerdsma and Boyens[1] paper, batches of between 20 and 70 identical creep specimens were tested for each set of test conditions.

The testing was carried out at 23°C on either an Instron screw machine or a custom built creep testing rig. Strains were recorded on the Instron using a clip-on 25mm. gauge length extensometer, and extensions were recorded on the creep rig using linear voltage displacement transducers. A correction factor was applied to the creep rig results to allow for specimen shoulder effects.

Results and Discussion

The constant stress (creep) behaviour of HIPS blended with sulfur is shown in figure 1. Sulfur has the effect of increasing the cross-link density of rubber, decreasing its compliancy and extension at break. With increasing ratio of sulfur/HIPS, the induction time[2] (defined as the time preceding rapid dilatation of the material) increases significantly and the strain rate decreases. HIPS strain-hardens at high strain, the limiting strain decreasing with increasing sulfur content. These results demonstate the influence of rubber cross-link density on strain-hardening in HIPS. The mean strain at fracture is also indicated, showing that the highest probability of fracture coincides with the onset of strain-hardening.

Weibull[3] statistics were used to correlate the fracture strain data for HIPS, which were found to fit Eq. 2.

$$1 - P_f = P_{sv} = e^{-\alpha(\varepsilon_f)^{\beta}} \qquad \text{(Eq. 2)}$$

where α and β are Weibull fitting parameters and ε_f is the strain at failure of the material. Figure 2 shows $\ln(P_{sv})$ plotted against (fracture strain)$^{\beta}$ for HIPS B, where $\alpha = 337$ and $\beta = 6.4$. From this it can be seen that Weibull statistics describes reasonably well the failure probability of HIPS.

The proposed mechanism for fracture of HIPS under tensile creep conditions is as follows. Crazes are initiated from cavitated rubber particles[4] and extend laterally until they meet another craze or rubber particle. As the craze thickens (mainly through surface drawing[5] rather than craze fibril creep) it will stretch the adjoining rubber particles with it, causing further cavitation and fibrillation of the rubber phase. Widespread craze extension and thickening, rubber cavitation and fibril extension results in a sharp increase in the strain rate, beyond the percolation threshold. As each craze thickens and 'draws' the associated rubber particle, the rubber fibrils strain-harden and become increasingly load bearing. (See figure 3).

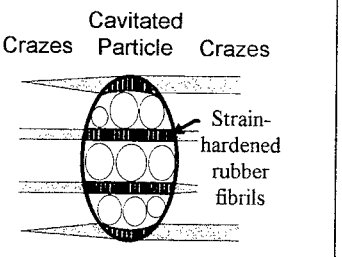

Figure 3: High strain deformation of HIPS.

This causes the observed decrease in strain rate at high strains. Macroscopic strain-hardening occurs in neat HIPS A at $\varepsilon \sim 20$ %. However local strain-hardening almost certainly begins at much lower strains, immediately following the induction period ($\varepsilon > \sim 2$ %). Wherever the rubber fibrils are

fully stretched, fracture is possible. However the probability of fracture increases with the volume of rubber that has fibrillated and stretched.

This explains why the maximum probability of failure of HIPS in tensile creep, as indicated by the open circles in figure 1, occurs not when the mean stress on the crazes is highest (at the point of inflexion in ε vs. t), as would be presumed if the crazes were responsible for final failure, but when the mean stress on the rubber fibrils has increased significantly.

Figure 4 shows the creep behaviour of HIPS A and HIPS D. Reducing the rubber content has similar effects to increasing the rubber cross-link density, i.e. increased induction time, decreased strain rate and limiting deformation. The fractional contribution of the rubber phase to the total volume changes can be represented by:

$$\Delta v_r = \Delta v_t \delta_r = \Delta v_t . (1-\delta_c) = (\varepsilon_t - \varepsilon_{el}).(1-\delta_c) \qquad \text{(Eq. 3)}$$

and $$\Delta v_r = \phi_r(\lambda_r - 1) \qquad \text{(Eq. 4)}$$

where Δv_t is the total volume change, ε_{el} is the elastic strain, ϕ_r is the rubber content, δ_c and δ_r are, respectively, the fractional contributions of the crazing and rubber fibrillation to the post-yield dilatation of the material (=0.5 after Bubeck et al.[6]). Combining Eqs 3 and 4 gives Eq. 5:

$$\varepsilon_{max} = \varepsilon_{el} + \frac{\phi_r(\lambda_{max} - 1)}{1-\delta_c} \qquad \text{(Eq. 5)}$$

where ε_{max}, λ_{max} are, respectively, the maximum possible strain and rubber extension ratio. Shear yielding is assumed to be negligible. Figure 5 shows the relationship between the rubber content ϕ_r, λ_{max} and the maximum fracture strains for test batches of HIPS A and HIPS D-F. Linear regression was used to find a value of $\lambda_{max} = 4.3$ for the data in figure 5.

CONCLUSIONS

- Both increasing rubber cross-link density and decreasing rubber volume fraction caused an increase in the induction time, while decreasing, (a) the strain rate, (b) the strain at which strain-hardening takes place, and (c) the fracture strain.
- The probability of failure of HIPS is highest when the material begins to strain harden.
- The two dominant factors controlling fracture in HIPS appear to be the volume of fibrillated rubber and the mean stress on the rubber fibrils.

ACKNOWLEDGEMENTS

We thank the Dow Chemical Company for permission to publish this work.

REFERENCES

1. Sjoerdsma, S.D., Boyens, J.P.H., *Polym. Eng. Sci.*, **34** (1994) 89
2. Bucknall, C.B., Clayton, D., J. *Mater. Sci* , **7** (1972) 202
3. Weibull, W. J., *J. Appl. Mech.*, **18** (1951) 293
4. Yang, H. H., Bucknall, C. B., Poster 79, this conference
5. Lauterwasser, B. D., Kramer, E. J., *Phil. Mag.*, **39A** (1979) 469
6. Bubeck, R. A., Buckley, D. J., Kramer, E. J., Brown, H. R., *J. Mater. Sci.*, **26** (1991) 6249

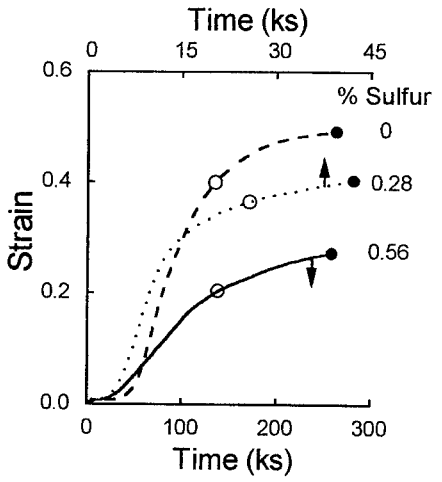

Fig. 1: Creep of HIPS with 0 % S at 14 MPa, 0.28 % S at 13.7 MPa and 0.56 % S at 13.7 MPa. (•), failure strain ε_f for specimen; (O), **mean** failure strain ε_m for **batch**. (See figure 4 for time scale of 100 % HIPS A, 0 % sulfur).

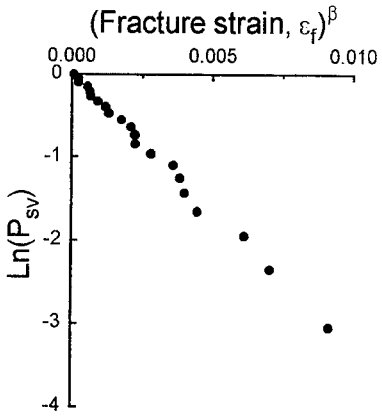

Fig. 2: Survival probability P_{sv} of HIPS B containing 0.28 % sulfur, plotted according to Eq. 2.

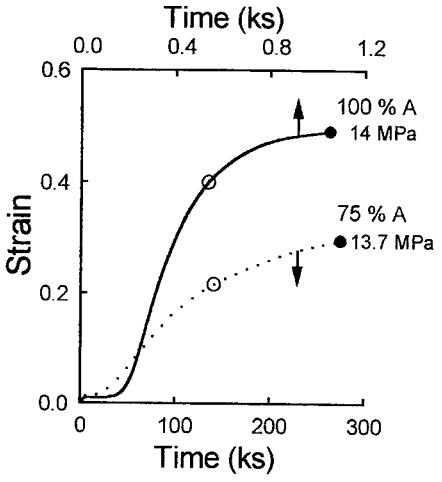

Fig. 4: Effect of rubber content on creep behaviour of HIPS. (•), failure strain ε_f for specimen; (O), **mean** failure strain ε_m for **batch**.

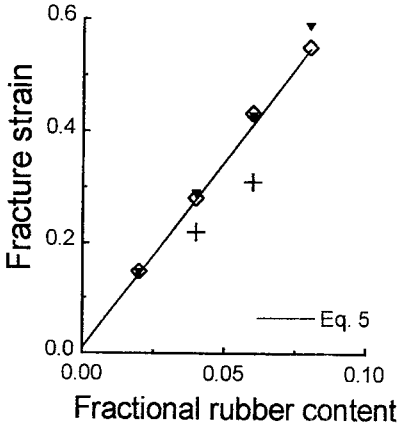

Fig. 5: Effect of rubber content, on maximum fracture strain from batches of HIPS A and HIPS D - F. For each blend $\sigma_{app}(\blacktriangledown) > \sigma_{app}(\Diamond) > \sigma_{app}(+)$.

Computer simulation of crack propagation in rubber toughened polymers

A. Sauron* C.M. Care* D.J. Cleaver* R. Ettelaie†

Abstract

We present results from a computer modelling study of crack formation in rubber toughened polymer. Using a simple lattice model comprising two bond types (e.g one for the rubber, one for the polymer matrix), and a stochastic breaking mechanism [1] simulations have been performed on both 2- and 3-dimensional systems.

The model allows the measurement of the total damage before failure and the stress distribution during the crack evolution. These are measured as a function of the loading of the matrix with rubber-toughening particles.

1 Introduction

Glassy polymers are frequently toughened by the addition of rubber particles [4]. Such two-phase polymers are indeed experimentally found to be more impact resistant than the unmodified ones. Fracture initiation, crack growth and toughening mechanisms in this kind of composite materials are still to be fully understood. Analytical approachs have difficulties which may be overcome by computer models [1-3].

2 The model

In the model used in this work, the material is represented by a simple cubic lattice of nodes. Each bond has a set of parameters which characterize the nature of the material (e.g. polymer or rubber). The bonds are randomly distributed according to their desired concentration. A fixed external stress is applied in the x direction on the x surfaces. The other surfaces are free. Under this stress, bonds elongate. In this preliminary study the stress-strain relation for each bond is assumed to be governed by a Hookean law.

Bonds are allowed to break according to a stress-dependent stochastic rule. When a bond is broken, it is removed from the lattice. Following [1] and [5], we set the breakage probability of an elongated polymeric bond to :

$$p_i \propto e^{k_i \Delta x_i - f_a}$$

*Materials Research Institute, Sheffield Hallam University
†Colloid and Rheology Unit, ICI Wilton

where k_i, Δx_i and f_a are defined at the end of this document.

At each step of the simulation a single bond is to be broken. Because the model is static, after each step, the system is allowed to return to a complete equilibrium state expressed in a matrix form as follows :

$$\mathbf{k}.\mathbf{x} = \mathbf{F}$$

where $\mathbf{k}$, $\mathbf{x}$ and $\mathbf{F}$ are defined at the end of this document. The above set of equations is just the usual condition that sum of all the forces (external + internal) on each node should be zero at equilibrium.

Among all the different numerical methods tested to solve this set of linear equations, the most efficient was found to be the *conjugate gradient* (CG) method.

3 Damage results

The effects of the rubber loading Φ are shown in Fig 1. They can be divided in three regions :

- $\Phi < 15\%$, *weakening region* : When there are just a few rubber particles, these are not numerous enough to terminate neighbouring cracks but will nonetheless be crack initiation sites themselves. Therefore, once cracks initiate very easily around these sites, the only remaining way for the system to dissipate energy will be at these cracks tips, leading to an acceleration in the main crack development.

- $15\% \leq \Phi < 40\%$, *toughening region* : The role of the rubber particles is to initiate localised energy absorbing mechanisms, such as, in this bond model, bond breakage. When the number of rubber particles is large enough, numerous small local crack initiations occur. These act as energy dissipators, and so prevent neighbouring small cracks from developing into a main crack. Widespread damage occurs throughout the whole volume of the material and its failure is delayed by the presence of rubber bonds pinning the crack surfaces.

  Note that the toughness increases rapidly around $\Phi = 25\%$ which is the percolation surface limit in such a lattice network.

- $40\% \leq \Phi \leq 60\%$, *plateau region* : Saturation of rubber toughening effect. The addition of more rubber does not improve the material toughness any further.

4 Stress results

We present in Fig 2 typical maximum stress evolutions (i.e. local load on the most stressed bond) in the lattice during the whole beaking process. The stress field goes through 4 regimes as the crack develops :

- Steady increase : As the polymer bonds break, mainly around the rubber bonds, the stress builds up in the vicinity of the voids so created.

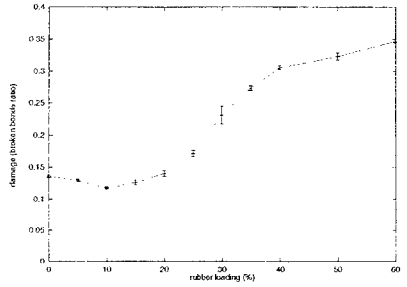

Figure 1: Damage in 20x20x20 sytems

- Noisy regime : The stress gets suddenly greater, the stress average in the system increases, the stress distribution becomes totally inhomogenous, some bonds see a great increase of their sustained stress and break, moving the maximun stress bond about the whole system. During this regime crazes develop throught out the whole bulk of the material.
- New steady increase : The onset of this regime corresponds to a stabilisation in the breaking of the polymer bonds which are parallel to the applied force. Small perpendicular crack surfaces which were created previously connect as a result of the breaking of perpendicular bonds. At this point the unzipping of microcracks is over, some microcracks join, become dominant and so develop into major cracks.
- Failure regime : On big rubber loadings, the onset of this regime corresponds to the stabilisation of polymer bond breaking. The maximum stress is located on the few remaining rubber bonds which are now sustaining the whole stress.

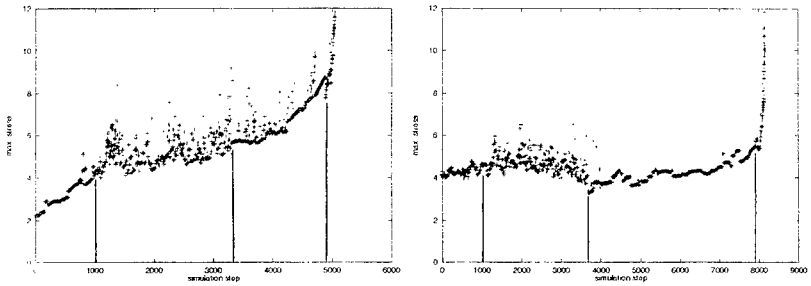

Figure 2: Stress evolution in a 20x20x20 system with $\Phi = 30\%$ (left) and 60% (right)

5 Conclusion

The results from this computer modelling study of crack growth in rubber toughened polymer give damage versus loading curves which show three distinct regions: *small rubber loading* - slightly reduced material toughness, probably as a result of enhanced crack initiation; *moderate rubber loading* - increase in toughness as particle density becomes sufficient to inhibit crack growth; *high rubber loading* - saturation of rubber toughening effect.

These observations are consistent with experimental work on polymer composites, although the data are unable to resolve the first region unambiguously.

Stress fields are also measured and the mode of failure is found to change as the cracks develops.

The simulations offer insight into the mesoscopic mechanisms which underlie rubber toughening. In particular, it appears that *crazing* and *crack pinning* are both significant factors in limiting catastrophic crack growth.

6 Symbols used

f_a : material dependent constant corresponding to an activation force

k_i : elastic coefficient of bond i

Δx_i : bond elongation in the x direction

$\mathbf{k}$: matrix of elastic coefficients

$\mathbf{x}$: vector of nodes displacements

$\mathbf{F}$: vector of applied forces

Φ : concentration of rubber bonds

References

[1] Meakin, P. (1991), *Science*, **252**, p226

[2] Hassold, G.N., & Srolovitz (1989), *Phys. Rewiew B*, **39**, p9273

[3] Jogota, A. & Bennison, S.J. (1995), *Model. Simul. Mater. Sci. Eng.*, **3**, p485

[4] Kinloch, A.J. & Young, R.J. (1983), *Fracture Behavior of Polymers*, Elsevier Applied Science, London

[5] Kausch, H.H. (1987), *Polymer Fracture*, Spring-Verlag, Berlin

CHARACTERISATION OF THE SURFACE DEFORMATION, YIELD AND FRACTURE OF POLYMERS DURING SCRATCHING

B.J. Briscoe*, E. Pelillo* and S. K. Sinha*

This paper presents results obtained from the scratching of two polymeric systems; a poly(methyl methacrylate) (PMMA) and a poly(carbonate) (PC). Scratches are produced by drawing a rigid conical indenter along the surface of the polymers under a specified normal load and at a certain velocity. The results show that this technique provides a convenient means of characterising the surface mechanical responses of these polymers in terms of the scratch deformation mechanisms, the scratch hardness -which primarily is a plastic yield property of most polymers- and the fracture of such materials under a range of imposed contact conditions. Scratch hardness and deformation mechanism maps for both dry polymers (poly(carbonate) and poly(methyl methacrylate)) are presented and the data considered in terms of the established bulk mechanical properties of these materials.

INTRODUCTION

The mechanical response of polymeric surfaces depends upon the imposed contact conditions and the mechanical properties of the system. In general, scratching deformations on polymeric surfaces occur when an external mechanical stress is generated by a relatively sharp and hard body contacting the polymer at a certain velocity and under a fixed load. Some practical examples of such damage situations may be found in a number of applications such as automotive, home appliances, industrial components and optical applications.

The techniques which have been applied for such studies were normal and scratch indentation hardness (1,2) surface topography (3,4) and spectroscopy (5,6). A range of responses such as elastic, elastic-visco-plastic and fracture deformations have been encountered (1-4,6,7). In general, the surface deformation responses are similar in character to the familiar bulk responses and depend upon the general mechanical properties of the materials such as the elasticity (Young's modulus), the yield strength, the fracture toughness, the ductility and the ductile to brittle transition. The main contact deformation parameters are defined by the imposed strain (the geometry of the deformation), the apparent load at the interface and the velocity of the deformation, i.e. the strain rate (time dependence). The severity of contact is primarily defined by the experimental combination of the imposed strain (contact angle, θ; see Figure 1), the contact pressure (load) and the state of lubrication (environment). In this paper the effect of the environmental conditions will not be addressed. Here, we present an account of the scratch hardness for two polymers (PC and PMMA) to demonstrate the usefulness of the scratching technique for the characterisation of the surface deformation, yield and fracture behaviours of polymers.

RESPONSES OF POLYMERS TO SURFACE MECHANICAL DAMAGE

As was mentioned above, polymers intrinsically show three main responses during scratch

*Imperial College, Chemical Engineering Department, London SW7 2BY, UK.

deformation and these are elastic, elastic-visco-plastic (yield) and fracture deformations, according to their intrinsic mechanical properties and the contact conditions.

Elastic response. In general, a fully elastic response to scratching is encountered when polymeric surfaces are in contact with lightly loaded blunt asperities (spheres and blunt cones, (3,8)). In this case, the material supports the load in an elastic fashion; the mean pressure at the contact, pm, is low and the material is assumed to recover entirely when the imposed strain is removed. The theory of plasticity considers the ratio E/Y(tanθ), where E is the Young's modulus and Y is the yield stress of the material, and θ is attack angle (the angle between the slope of the indenter and the material free surface; see Figure 1) as a criterion to predict the limit of contact strain beyond which the material cannot fully recover from the imposed deformation (8,9).

Elastic-visco-plastic response. The material yields permanently and most of the imposed strain is, therefore, retained. In incompressible systems, the deformation involves material displacement or removal. As was mentioned earlier, the theory of plasticity sets the criteria to evaluate the yield conditions (as a combination of material properties and contact geometry; see for example references (8,9)) but, due to the semi-static nature of the approach, it cannot include the strain rate or time dependence.

The scratch hardness in an elastic-visco-plastic regime of deformation may be evaluated , by analogy with the normal indentation hardness, H, as (3,4);

$$H_s = \frac{8W}{\pi d^2} \qquad (1)$$

where W is the normal load and d is the average scratch width. As a first order analysis, it may be estimated that $H_S \cong CY$, where C is a material constant (2,10), dependent only to a certain extent upon the geometry of the indenter. This is demonstrated by a previous work (1); $H_s \cong H$ under lubricated contact and $H_s \cong (1.2 \div 1.5)H$ with no lubrication.

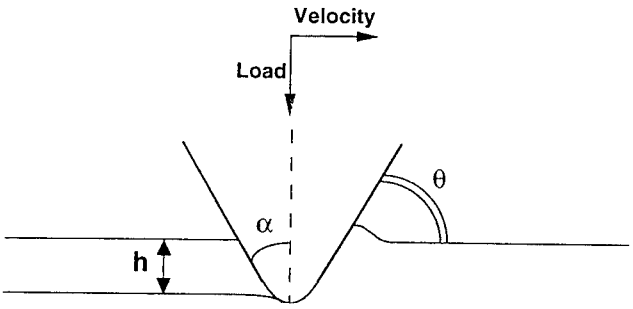

Fig.1 - Geometry of scratching (α=cone semi-angle; h= depth of penetration; θ=attack angle)

Similar relations may be found for any polymeric surface. The viscous, or time dependent, features of the scratch deformations of polymers may be conveniently analysed during scratching of polymers under different scratch velocities (see for example references (4,6)). In general, the scratch velocity affects the strain rate of the deformation; in fact, the effective strain rate, $\dot{\varepsilon}$, may be defined as (3); $\dot{\varepsilon} = v / d$ where v is the scratching velocity and d is the width of the scratch.

Fracture deformations. When an amorphous polymer, intrinsically brittle in its nature, such as PMMA, is deformed by scratching under severe contact conditions (i.e. $2\alpha<100°$, W>0.5 N), surface or near surface crack systems and fractures may occur. The relatively high elasticity of the material (E=3.1 GPa), combined with its hardness (Rockwell R_M= 95) and low toughness (K_I=2.5 MPa $m^{0.5}$; Izod impact strength (un-notched)= 12 kJm^2) and its poor elongation at break (ca. 5%) do not allow a ductile and homogeneous displacement of the material ("dynamic yield") around the indenter during its motion and any elastic recovery is negligible. The evaluation of the penetration depth and, therefore, of the scratch hardness, is strongly affected by the fragmented nature of the deformation and the occurrence of material loss, i.e. debris, is sometimes observed. Some authors have studied the plastic-brittle transition (9,11), and a few criteria have been developed as functions of certain material properties (usually normal hardness and fracture toughness) and the contact geometry (attack angle).

This paper presents results from scratching of two different polymeric systems, PMMA and PC, in an attempt to demonstrate the convenience and versatility of the scratch method to characterise the scratch deformation of these systems, which have different material properties (PC: E=2.5 GPa; Rockwell R_M=75; Izod impact strength (notched)=30 kJm^2; tensile elongation at break=110%).

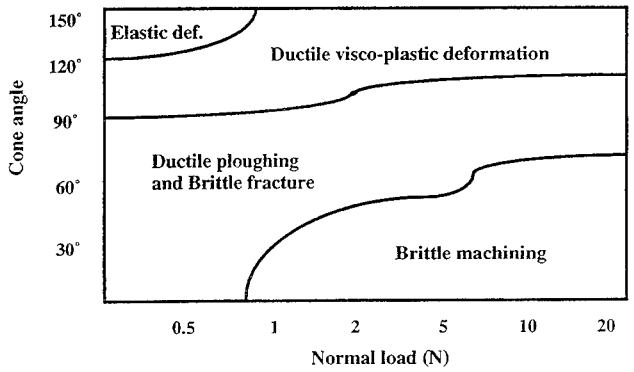

Fig.2 - Deformation map for PMMA (T=21°C; v=0.02 mm/s).

RESULTS AND DISCUSSION

Deformation maps for PMMA and PC. Figure 2 shows a deformation map generated from the SEM observation of scratches produced on a PMMA surface under different loads and for different cone angles. The map shows the dependence of the deformation modes upon the contact conditions and the observed transitional regions. PMMA undergoes a transition from ductile deformation, or "ploughing", to brittle fracture for scratches produced under the higher loads and the sharper cones. A critical penetration depth has been identified in previous works (7). Figure 3 shows a deformation map for PC, constructed for various loads and different cone angles (strains). PC seems relatively more resistant to fracture, probably due to its higher toughness and elasticity. Subsequently, its scratch hardness has been found to be more pronounced than that of PMMA for any angle and similar contact conditions (4,7).

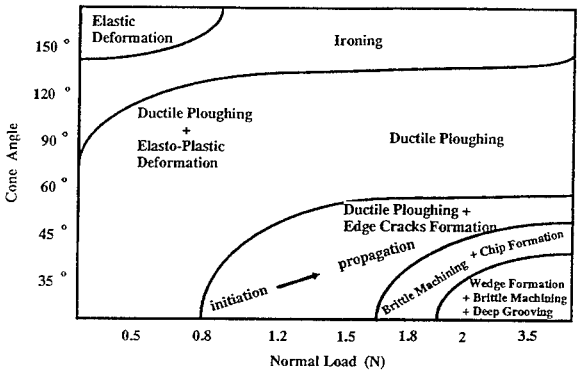

Fig.3 - Deformation map for PC (T=21°C; v=2.6 mm/s).

CONCLUSIONS

The deformation response to scratching observed for poly(carbonate) and poly(methyl methacrylate) show that the deformation mechanisms of these polymers is very much dependent upon the imposed contact conditions as well as upon their intrinsic mechanical properties. A slight change in these conditions alters the deformation mechanism and hence any response measured during deformation changes accordingly (e.g. the scratch hardness).

ACKNOWLEDGMENTS

The authors thank The Dow Chemical Co. (USA) for their financial support for this project.

LIST OF SYMBOLS

Hs Scratch hardness
W Normal load
d Scratch width

REFERENCES

1. B.J.Briscoe, P.D.Evans, S.W.Biswas and S.K.Sinha, Trib.Int., 29 2 (1996) 93-104.
2. B.J.Briscoe and S.Sebastian, Proc. Roy. Soc. Lond. A, 452 (1006) 439-457.
3. B.J.Briscoe, P.D.Evans, E.Pelillo and S.K.Sinha, Wear, vol. 200, n. 1-2 (1996) 183-193.
4. B.J.Briscoe, E.Pelillo and S.K.Sinha, Poly.Eng.Sci., vol. 36, n.24, Dec. 1996.
5. B.J.Briscoe and B.H.Stuart, Spectrochimica Acta, 50A, n. 11, (1994) 2005-2009.
6. B.J.Briscoe, E.Pelillo and S.K.Sinha, Proc. 11th European Conf. on Fracture, 3-6 Sep. 1996, Poitiers, Futuroscope (France).
7. B.J.Briscoe, E.Pelillo and S.K.Sinha, Proc.1997 Jubilee Event - IChemE, 7-9 April 97, Universities of Loughborough and Nottingham, UK.
8. K.L.Johnson, "Contact Mechanics", Cambridge University Press, England, 1985.
9. J.A.Williams, Trib.Int., vol. 29, n.8 (1996) 675-694.
10. P.D.Evans, PhD Thesis, Imperial College, London, 1987.
11. B.R.Lawn and E.R.Fuller, J.Mater.Sci., 10 (1975) 2016-2024.

AMORPHOUS POLYMERS TOUGHENED WITH SPHERICAL RUBBER PARTICLES: A METHOD TO COMPUTE THE MECHANICAL INTERACTION BETWEEN PARTICLES.

C. Fond and R. Schirrer
Institut Charles Sadron, 6, rue Boussingault F67083 Strasbourg

A numerical method has been implemented to calculate the stress interactions in an amorphous brittle polymeric matrix with rubber particles. The method assumes linear elastic behaviour but nevertheless predicts qualitatively the organisation of micro-damages and micro-shear bands. A simulation of the interactions in a random distribution of spherical particles leads to a three dimensional heterogeneous stress field at the level of the particles.

INTRODUCTION

The mechanical interactions between inhomogeneities influence the properties of most two (or more) phases materials. The volume fraction of the reinforcing phase is generally high and therefore the equations neglecting interactions valid at low volume fraction are inaccurate. Moreover, the random character of the spatial distribution of the inhomogeneities can be a key-point of the toughening mechanisms and hence the analysis via a unit cell of an equivalent organised material is not relevant. In the most general case, the complexity of the analysis of the interactions between inclusions takes its origin from the morphology, especially in three dimensions and from the non linear behaviour of the material. Fortunately, in the case of the impact loading, rubber toughened polymers behave elastically up to the first step of the damage process and visco-platicity can be introduced in the elastic moduli and in the yield stress [1,2].

Using the works done by N. M. Ferrers [3] and F. W. Dyson [4] to calculate potentials for ellipsoids, at the end of the nineteenth, J. D. Eshelby [5] found the exact solution for an ellipsoidal inhomogeneity embedded in an infinite matrix, in the case of linear elasticity. Z. A. Moschovidis and T. Mura [6] went further by proposing to use Taylor's series to describe the stresses in the inhomogeneities and so computet approximate solutions for interacting inhomogeneities. Recently, W. Hort and W. C. Jonhson [7], successfully used this equivalent inclusion method (EIM) in the case of spherical metallic precipitates for which elastic constants are slightly different from those of the matrix. They showed that the number of effective interacting neighbouring spheres was finite. As far as the authors know, the EIM has never been used forto study polymers blends.

The EIM method leads to a reduced number of unknowns depending on the order of the Taylor's series. Indeed, once integrals are analytically computed for an inclusion, the latter can be considered as a three dimensional element for which no discretization of volume or surface is necessary. This is the fundamental difference between EIM and finite element or boundary element methods. However, the analytical solution involves a huge number of terms of the Taylor's series and can only be treated by means of large recent computers. This is one reason why this method has been rarely used for the case of random distributions of inclusions and Taylor's series above the second order. The EIM appears to be a good compromise between

accuracy, computer capacity and a realistic model of the spatial distribution of inclusions in blend materials.

BRIEF REVIEW OF THE EIM TECHNIQUE

An eigenstrain or stress free strain is a thermal dilatation or transformation phase like strain which does not induce any stress in the isolated inclusion. For instance, a uniform eigenstrain ε_{xx} transforms a sphere into an ellipsoid of axis x. Uniform eigenstrains constitute the basis of the exact Eshelby's solution [5]. Figure 1(b) shows a stress free state induced by an non uniform eigenstrain of density $\varepsilon_{xx} = xz^2$, the origin of the co-ordinates being the centre of the sphere of Fig. 1(a). Since one considers a perfect cohesion at the interface inclusion/matrix, stresses arise from the constrains at the inclusion boundary. The stressed state shown in Fig. 1(c) is known analytically [3,4,5,6]. The EIM technique has been described in detail in [6,7,8]. The eigenstrains are denoted $\beta_{mn}^{n_{q1}\, n_{q2}\, n_{q3}}$, the subscript mn refers to the components of the strain tensor and the upper scripts n_{qi} to the exponent of x_i, in Cartesian co-ordinates. The value of β_{mn} at the location $\mathbf{x} = (x_1,x_2,x_3)$ in the q^{th} inclusion is then $\beta_{mn}^{n_{q1}\, n_{q2}\, n_{q3}}\, x_1^{n_{q1}}\, x_2^{n_{q2}}\, x_3^{n_{q3}}$. The effect of $\beta_{mn}^{n_{q1}\, n_{q2}\, n_{q3}}$ on the strains in the medium is analytically known and can be expressed in a Taylor's series. The derivatives $\frac{1}{n_{p1}!\, n_{p2}!\, n_{p3}!}\frac{\partial^{n_{p1}}\partial^{n_{p2}}}{\partial x_1\, \partial x_2}\frac{\partial^{n_{p3}}}{\partial x_3}$ of the strain function corresponding to the effect of $\beta_{mn}^{n_{q1}\, n_{q2}\, n_{q3}}$ on the component kl of the strain tensor at the point $\mathbf{x}$, is denoted $D_{klmn}^{n_{p1}\, n_{p2}\, n_{p3}\, n_{q1}\, n_{q2}\, n_{q3}}(\mathbf{x})$. The equivalency equation expresses the equality between the stress state inside the inhomogeneity and the corresponding equivalent inclusion which undergoes an eigenstrain

$$C_{ijkl}^{p}\left(\varepsilon_{kl}^{\infty\, n_{p1}\, n_{p2}\, n_{p3}}(\mathbf{x}_p) + D_{klmn}^{n_{p1}\, n_{p2}\, n_{p3}\, n_{q1}\, n_{q2}\, n_{q3}}(\mathbf{x}_p)\,\beta_{mn}^{n_{q1}\, n_{q2}\, n_{q3}}\right) =$$

$$C_{ijkl}\left(\varepsilon_{kl}^{\infty\, n_{p1}\, n_{p2}\, n_{p3}}(\mathbf{x}_p) + D_{klmn}^{n_{p1}\, n_{p2}\, n_{p3}\, n_{q1}\, n_{q2}\, n_{q3}}(\mathbf{x}_p)\,\beta_{mn}^{n_{q1}\, n_{q2}\, n_{q3}} - \beta_{kl}^{n_{p1}\, n_{p2}\, n_{p3}}(\mathbf{x}_p)\right) \quad \text{.....(1)}$$

with summation over the repeated indices, where C_{ijkl}^{p} and C_{ijkl} denote respectively the compliance tensors of the p^{th} inhomogeneity and the matrix. $\mathbf{x}_p$ is the position vector of the centre of the p^{th} inhomogeneity and $\varepsilon_{kl}^{\infty\, n_{p1}\, n_{p2}\, n_{p3}}(\mathbf{x}_p)$ is the component kl of the strain tensor applied at infinity, expanded around $\mathbf{x}_p$ in a Taylor's series. The strain field applied at infinity is not necessarily uniform. The $\beta_{mn}^{n_{q1}\, n_{q2}\, n_{q3}}$ unknowns are the solution of the linear system obtained by identifying the same order terms in (1). As one has to truncate the Taylor's series, (1) gives an approximate solution with an accuracy increasing with the order of the terms. As we consider here isotropic materials, the compliance C_{ijkl} is entirely defined by the bulk modulus k and the shear modulus G.

APPLICATION TO RUBBER TOUGHENED POLYMERS

The aim of this work was to analyse the stress distribution in rubber toughened polymers to predict qualitatively the organisation of the micro damages or the localisation of deformation at the microscopic level. Obviously, the stress level at which non linear behaviour takes place corresponds to the limit of validity of the computations. In the case of rubber particles and impact loading, it can be shown that plasticity appears in the matrix after cavitation in the rubber and that a damaged rubber particle behaves nearly like a void [2]. Therefore, the particles breakage may be described by a step by step process within the hypothesis of linear elasticity and the organisation of the generated "croids" may be compared to experimental observations. By means of large computers simulations with 10^4 or more particles can be done.

Fig. 1 and Fig. 2 give an illustration of the ability of the EIM. A pseudo random spatial distribution of approximately 2000 identical spheres is created with a computer. The spheres represent 23% in volume of the concerned domain. The computation is focused at the centre of the domain containing 106 spherical particles. Each particle of radius r interacts with all the particles contained in a surrounding spherical domain of radius 4*r. The Poisson's ratio $\nu = (3\,k - 2\,G) / (3\,k + 2\,G)$, is about 0.4 for the matrix. For the rubber ν is nearly 0.5, $k = 2$ GPa and $G = 0.333$ MPa leading to $\nu = 0.499917$. The ratio between the Young's moduli of the matrix and the rubber is 10^3. All the particles have same elastic moduli and the Taylor's series are at the first order . A uniform stress field corresponding to uniaxial tension along the z axis is applied at infinity. Once the eigenstrains β_{ij} are known, stresses and strain can be computed anywhere in the media.

The Fig. 1 (left) shows the von Mises stresses in an arbitrary plane perpendicular to the z axis. The interaction between particles appear in dark. If the behaviour of the polymeric matrix conforms to a von Mises criteria for plasticity, plasticity is expected in the black regions. Fig. 1 (right) indicates the level of hydrostatic stresses inside the particles, which is known to be responsible for cavitation [2,9,10]. Fig. 3 shows the statistical distribution of von Mises stress concentrations and where the maxima are located in the space. The overall effect of the interactions increases the mean stress values. Shear stresses between particles seem to be oriented at about 45°.

CONCLUSION

The EIM technique seem to be an efficient tool to predict the mechanical interactions between rubber particles in an amorphous polymeric matrix. Nevertheless, as the original method does not include non linear stress-strain behaviour, only the first steps of damage or plasticity are predictable with the numerical simulations.

REFERENCES

[1] R. Schirrer, C. Fond and A. Lobbrecht, J. Mat. Sc., 1996, **31**(24), pp. 6409-6422.

[2] C. Fond, A. Lobbrecht and R. Schirrer, Int. J. Fract., 1996, 77, pp. 141-159.

[3] Ferrers, N. M., Quarterly J. of Pure and Appl. Math., **XIV**, (1877), pp. 1-22.

[4] Dyson, F. W., Quarterly J. of Pure and Appl. Math., **XXV**, 1891, pp. 259-288.

[5] Eshelby, J. D., Proc. Roy. Soc. Lond. A, **241**, 1957, pp. 376-396.

[6] Moschovidis, Z. A. and Mura, T., J. Appl. Mech., Trans. ASME, 1975, pp. 847-852.

[7] Hort, W. and Johnson, W. C., Metal. and Mat. Trans. A, 1994, **25**, pp. 2695-2703.

[8] Mura, T., *Micromechanics of Defects in Solids*, Kluwer Academic Publishers, Dordrecht/Boston/London, 1993, second, revised edition, reprinted.

[9] Bucknall, C. B., Karpodinis, A., Zhang, X. C., J. Mat. Sci., **29**, 1994, pp. 3377-3383.

[10] Dompas, D., Groeninckx, G., Pol. **35**, 1994, pp. 4743-4749.

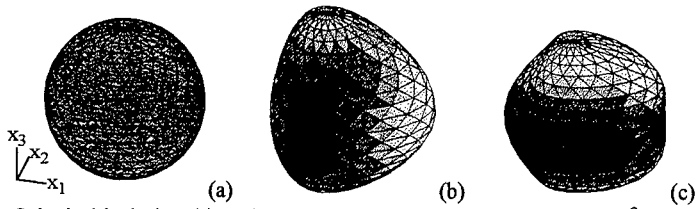

Figure 1. Spherical inclusion (a) undergoing an eigenstrain of density $\varepsilon_{xx} = xz^2$. (b) deformed stress free state (displacements magnified 0.5 time) "outside of the matrix" for $\nu = 0.3$ - the grey level corresponds to the amplitude of the displacement vector at the interface. (c) deformed state (displacements magnified 5 times) - the grey level corresponds to the amplitude of the von Mises equivalent stress at the interface.

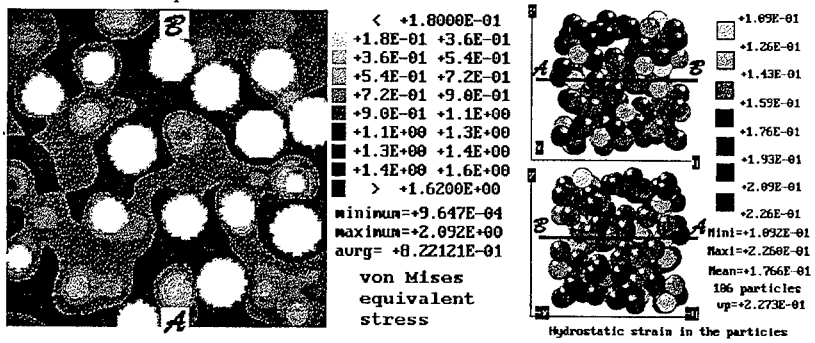

Figure 2. Left: Von Mises equivalent stress map in a plane perpendicular to the axe of uniaxial tension $\sigma_{zz} = 1$ at infinity. As there is not significant shear stress in the rubber particles, they appear in white. Right: Distribution of the particles in the region of the map $\mathcal{A}$-$\mathcal{B}$. The grey level of each sphere indicates the intensity of the hydrostatic stress. The volume fraction of particles is 22.7%.

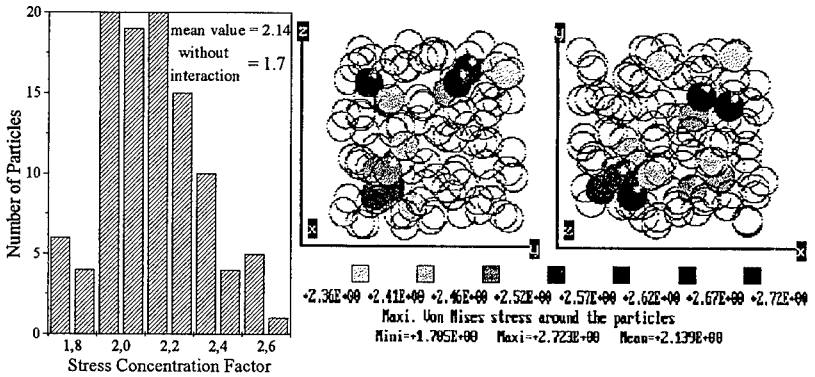

Figure 3. left: Same computation as in Fig. 2 for 106 particles. Distribution of the von Mises' stress concentration factors $\sigma_{eq.\ max.}$ Right: Particles generating $\sigma_{eq.\ max} > 2.4\ \sigma_{zz}$, the other particles are drawn "transparent".

ANALYTICAL MODELLING OF THE DEFORMATION OF AUXETIC POLYMERS

A Alderson[*], K Sasaki[*+] and KE Evans[*++]

Two analytical models (Node-Fibril model and Helical model) are presented for the design of materials having a negative Poisson's ratio. Both models employ multiple deformation mechanisms acting concurrently. The 2D Node-Fibril model is found to be in good agreement with the experimental data for auxetic microporous polymers. The 3D Helical model has potential application in a variety of helical structures, such as Liquid Crystalline Polymers.

INTRODUCTION

Auxetic materials [Evans *et al.* (1)] are materials which exhibit a negative Poisson's ratio, i.e. they expand laterally when stretched in a longitudinal direction. Materials possessing this novel property include microporous polymers such as expanded forms of polytetrafluoroethylene (PTFE) [Caddock & Evans (2)] and ultra-high molecular-weight polyethylene (UHMWPE) [Alderson & Evans (3), Neale *et al.* (4)]. The range of materials being discovered, fabricated or designed to have auxetic functionality is increasing and recently, for example, the concept of auxetic Liquid Crystalline Polymers (LCPs) has been advanced to the stage where attempts are being made at synthesis of model compounds to demonstrate the effect [Baker *et al.* (5)].

Simple analytical models have been developed for auxetic behaviour, where the deformation of a structure is considered due to a single mode of deformation [e.g. the deformation of honeycombs via flexure of the honeycomb arms - Gibson *et al.* (6)]. Recently analytical models have been developed where multiple deformation mechanisms act concurrently [Evans *et al.* (7)], giving a better approximation to the deformation of real materials.

The elastic constants for auxetic microporous polymers have been modelled using a 2D array of nodules interconnected by fibrils, where deformation of the node-fibril (NF) network is assumed to be due to either fibril hinging, stretching or flexure [Evans (8), Alderson & Evans (9)]. In this paper we present results from a more realistic NF model where fibril hinging and stretching act concurrently [Alderson & Evans (10)].

We also present a new 3D model for auxetic behaviour in helical structures in which multiple deformation mechanisms act concurrently. The dependency of Poisson's ratio on the various model parameters is discussed. This generic model has potential application to main chain LCPs, and indeed to any helical (or helix-based) structure, irrespective of length scale.

* BNFL, Company Research Laboratory
*+ Department of Materials, Imperial College of Science, Technology and Medicine
*++ School of Engineering, University of Exeter

CONCURRENT NODE-FIBRIL MODEL

The NF network and geometrical parameters are defined in Fig. 1. Application of a stress in either of the x or y directions leads to variations in fibril length and angle. Full derivations of the elastic moduli associated with the NF network illustrated in Fig. 1 are given in reference (10). Examples of the Poisson's ratio (ν_{xy}) and Young's modulus (E_x) expressions are:

$$\nu_{xy} = \frac{\left[1 - K_s / K_h^{eff}\right]\sin\alpha\cos\alpha}{\left[\left(K_s / K_h^{eff}\right)\sin^2\alpha + \cos^2\alpha\right]} \frac{a + l\cos\alpha}{b - l\sin\alpha} \tag{1}$$

$$E_x = \frac{a + l\cos\alpha}{(b - l\sin\alpha)\left[\left(\sin^2\alpha / K_h^{eff}\right) + \left(\cos^2\alpha / K_s\right)\right]} \tag{2}$$

where K_s and K_h^{eff} are stretching and hinging force coefficients, respectively, governing the strength of each mode of deformation. K_s and K_h^{eff} can be related to the intrinsic material properties making up the NF network. It is clear from equations 1 and 2 that the elastic moduli are now determined by the geometry and strengths of the deformation mechanisms acting, giving much greater flexibility than the simpler single-mode models.

Reference (10) contains a detailed analysis of the dependence of the elastic moduli on each of the geometrical and force coefficient parameters within the model, as well as strain-history calculations. This enables comparison between the concurrent model and the experimental strain-dependent data for auxetic PTFE and UHMWPE. Good agreement is found for both polymers when realistic nodule and fibril parameters are employed in the NF model. For example, the concurrent NF model and experimental data for the Poisson's ratio and engineering Young's modulus of PTFE are compared in Figs. 2(i) and 2(ii), respectively. Of particular note is the plastic region of deformation (region III in Figs. 2(i) and 2(ii)) at the highest strains in the experimental data. The flexibility of the concurrent model allows this to be modelled by lowering the K_s/K_h^{eff} ratio at the onset of plastic deformation (the value being assumed to remain constant otherwise). Discrepancies between the concurrent NF model and experiment are attributed to the assumptions of (i) a constant K_s/K_h^{eff} ratio, (ii) rigid and regular rectangular nodules, and (iii) a 2D model being used to represent a 3D network.

CONCURRENT HELICAL MODEL (HM)

Fig. 3 shows the repeat unit-cell for a helix, used to develop expressions for the elastic constants in the HM model where helical pitch angle and arc length variations are assumed to act concurrently. For loading in either of the x or y directions we have also considered cross sectional shape changes in the helix (i.e deformation of a circular cross-section helix to one with an elliptical cross-section). The procedure used to develop the expressions for the elastic constants is directly analogous to that used in references (7) and (10). An example of the expressions thus obtained is given below for the Poisson's ratio ν_{zx}

$$\nu_{zx} = \frac{-\left(K_\theta / K_r\right)\cos^3\theta\left(\pi^2 + 4\tan^2\theta\right)^{\frac{3}{2}} + 4r^2}{\left(K_\theta / K_r\right)\sin^2\theta\cos\theta\left(\pi^2 + 4\tan^2\theta\right)^{\frac{3}{2}} + r^2\pi^2}\tan^2\theta \tag{3}$$

where θ is defined in Fig. 3, r is the arc length of one full turn of the helix, and K_θ and K_r are the force coefficients governing the angle and arc length variation deformation mechanisms.

The variation of ν_{zx} with θ is shown in Fig. 4 for r = 1m and K_θ/K_r = 1, 0.31, 0.1 and -1 m^2/radian. In all cases $\nu_{zx} = 0$ at $\theta = 0°$, and $\nu_{zx} = [r^2/(2K_\theta/K_r) - 1]$ at $\theta = 90°$. For any one value of K_θ/K_r the Poisson's ratio can be tailored to a specific value by a suitable choice of θ. However, the range of values the Poisson's ratio can adopt depends crucially on the value of K_θ/K_r. For example, for the parameters used in Fig. 4, $K_\theta/K_r > 0.5$ yields $\nu_{zx} \leq 0$ (see curve for $K_\theta/K_r = 1$), whereas when $0.129 < K_\theta/K_r < 0.5$ positive and negative values of ν_{zx} can be realised, with a solution also existing for $\nu_{zx} = 0$ when $\theta > 0°$ (K_θ/K_r = 0.31 curve). For $0 < K_\theta/K_r < 0.129$, $\nu_{zx} \geq 0$ (K_θ/K_r = 0.1 curve). It is clear from equation 3 and Fig. 4 that there is a finite range of ν_{zx} possible when $K_\theta/K_r > 0$. However, for negative values of K_θ/K_r then $-\infty \leq \nu_{zx} \leq -1.5$ and $0 \leq \nu_{zx} \leq +\infty$ (see $K_\theta/K_r = -1$ curve).

SYMBOLS USED

a = major nodule axis length (m)
b = minor nodule axis length (m)
K_s = fibril stretching coefficient (N m^{-1})
K_h^{eff} = fibril hinging coefficient (N m^{-1} radian^{-1})
K_θ = helix angle variation coefficient (N m radian^{-1})
K_r = helix arc length stretching coefficient (N m^{-1})
l = fibril length (m)
r = arc length of one turn of a helix (m)
x = Cartesian axis
y = Cartesian axis
z = Cartesian axis
α = fibril angle (radians)
θ = helix angle (radians)
ν_{ij} = Poisson's ratio due to loading along the i axis ($i = x, y$ or z; $j = x, y$, or z; $j \neq I$)
ε_x = Total true strain along the x axis
E_x = Young's modulus due to loading along the x axis (GPa)
E_x^e = Engineering Young's modulus due to loading along the x axis (GPa)

REFERENCES

1. Evans KE, Nkansah MA, Hutchinson IJ, Rogers SC, Nature (1991) 353 124
2. Caddock BD, Evans KE, J. Phys. D: Appl. Phys. (1989) 22 1877
3. Alderson KL, Evans KE, Polymer (1992) 33 4435
4. Neale PJ, Alderson KL, Pickles AP, Evans KE, J. Mat. Sci. Lett. (1993) 12 1529
5. Baker JB, Douglass AG, Griffin AC, ACS Polym. Preprints (1995) 36(2) 346
6. Gibson LJ, Ashby MF, Schajer GS, Robertson CI, Proc. R. Soc. Lond. (1982) A382 25
7. Evans KE, Alderson A, Christian FR, J. Chem Soc. Faraday Trans. (1995) 91(16) 2671
8. Evans KE, J. Phys. D: Appl. Phys. (1989) 22 1870
9. Alderson A, Evans KE, J. Mat. Sci. (1995) 30 3319
10. Alderson A, Evans KE, J. Mat. Sci. (1997) In press

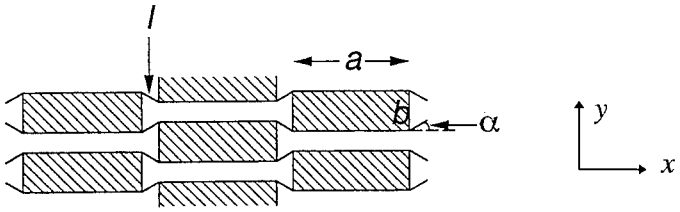

Figure 1. Node-Fibril network illustrating geometrical parameters and coordinate system employed in NF model

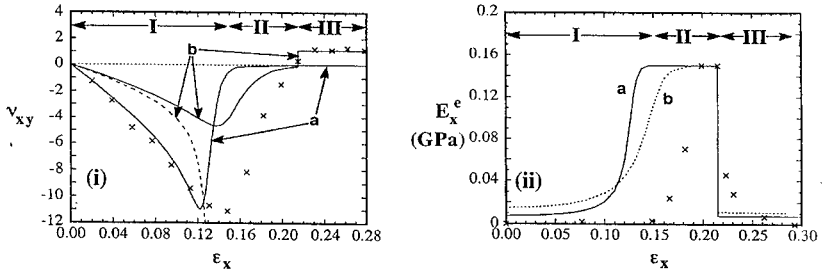

Figure 2. (i) ν_{xy} vs ε_x for the concurrent NF model employing: (a) $b = 0.25a$, initial value of $l = 0.125a$, $K_s/K_h^{eff} = 20$ (regions I and II), $K_s/K_h^{eff} = 1$ (region III); (b) $b = 0.40a$, initial value of $l = 0.14a$, $K_s/K_h^{eff} = 10$ (regions I and II), $K_s/K_h^{eff} = 0.65$ (region III) - dashed curve corresponds to deformation due to hinging only. Initial value of $\alpha = 90°$. Experimental data shown as crosses. (ii) E_x^e vs ε_x for the concurrent NF model employing same parameters as for 2(i); experimental data are shown as crosses. (From reference (10))

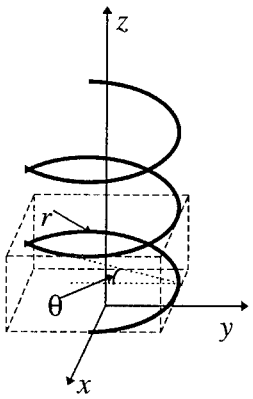

Figure 3. Unit-cell for helix illustrating geometrical parameters and coordinate system employed in HM model

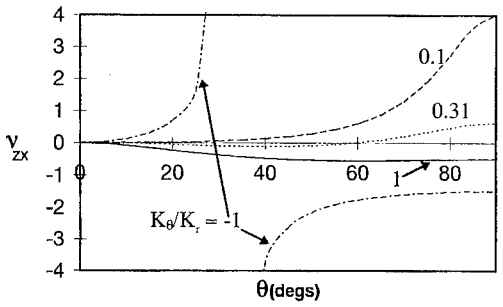

Figure 4. ν_{zx} vs θ for the HM model employing $r = 1$m and $K_\theta/K_r = 1$, 0.31, 0.1 and -1

CHARACTERIZATION OF TOUGHENING MECHANISMS IN VARIOUS IMPACT MODIFIED SEMICRYSTALLINE POLYMER SYSTEMS

G.-M. Kim and G. H. Michler*

Relationships between morphology and micromechanical deformation processes in various toughened semicrystaline polymers with various different types of modifier particles have been investigated by several electron microscopy, including transmission (TEM), scanning (SEM), and high voltage electron microscopy (HVEM), using in situ tensile techniques. From the study of phase structure of modifier particles two morphological standard types are classified for the analysis of toughening mechanisms: the binary system (homogeneous modifier particles dispersed in the matrix), and the ternary system (heterogeneous modifier particles dispersed in the matrix) Taking into account these categories and the phase adhesion between the modifier particles and the matrix, micromechanical deformation processes have been characterized and different schematic models for micromechanical deformation processes are proposed.

INTRODUCTION

The current understanding of the toughening mechanisms of modified polymeric materials is highly advanced in individual blend system. Toughening mechanism found from a system is limited to apply in other system, because it is extremely influenced by many morphological and micromechanical parameters. The highly heterogeneous structure of toughened material leads to specific micromechanical deformation processes that occur mainly at the particle-matrix interface or inside particles [1]. Therefore, for the development of polymer systems it is necessary to investigate the relationship between the morphology and micromechanical deformation process and to characterize the fundamental toughening mechanisms depending on the type, the phase structure of modifier particles. In the present work, the influence of the morphology of various modifier particles in toughened semicrystalline polymers on the deformation structure and in particular on the micromechanical deformation processes has been studied.

EXPERIMENTAL

Toughened thermoplastics studied were

I) PP / EPR block copolymers,
II) PP / PA / SEBS-g-MA blends,
III) PP / EPDM blends,
IV) PP / $Al(OH)_3$ composites,
V) PA / butyl acrylate mechanical blends

The phase morphology of the blend systems has been investigated in a transmission electron microscope (TEM), and the particle size, the particles size distribution, the interparticle distance and interparticle distance distribution were quantitatively determined using scanning electron micrographs (SEM) from the low temperature fractured surfaces. The micromechanical deformation processes have been investigated in various electron microscopes (HVEM, TEM, SEM) using in situ techniques.

* Department of Materials Science, Martin-Luther University Halle-Wittenberg, D-06217 Merseburg, Germany

RESULTS AND DISCUSSION

From the TEM study of morphology of modifier particles two morphological standard types are classified for the analysis of toughening mechanisms:

- the ternary system (heterogeneous modifier particles dispersed in the matrix);

In the PP/EPR block copolymer (I) and PP/PA/SEBS-g-MA (II) blend systems, the phase structure of modifier particles shows the one of core-shell particles, including the semicrystalline matrix, the shell consisted of amorphous rubbery phase and the semicrystalline inclusion. These phase structures of modifier particles will be defined in the present work as manduparticles [2], in contrast to the salami-particles in HIPS [3].

- the binary system (homogeneous modifier particles dispersed in the matrix);

In the other blend systems and polymer composites (III, IV, V), the modifier particles consisted of only one phase without shell are dispersed relatively finely in the matrix.

The results of the electron microscopic investigation for micromechanical deformation processes have been described in form of Three-Stage-Mechanism [4, 5];

- Stage 1: Stress concentration
- Stage 2: Void and shear band formation
- Stage 3: Induced shear yielding

In the present work it will be more appropriately modified for the models describing of the micromechanical deformation processes of individual blend systems [6].

a) Single cavitation process in ternary blend systems

Figure 1 shows a schematic model of micromechanical deformation process in ternary blend systems (PP/EPR block copolymer, PP/PA/SEBS-g-MA blend). In these blends the modifier particles possess only one inclusion and are relatively fine dispersed in the matrix. At first stress concentration takes place around the modifier particles. In the next stage the modifier particles deform together with the matrix, and void formation appears in form singular cavitation with or without fibrils at the interface between the modifier particles and the matrix. This process depends essentially upon the inherent properties of rubbery shell. Simultaneously with the growth of voids, the shear bands form in the matrix between the modifier particles. In the third stage, when the polymer specimen will be further strained, the shear yielding will be induced in the matrix. As a result plastic deformation of matrix will be significantly enhanced. In the case of PP/PER block copolymer the voids grow gradually with the straining of specimen, whereas in the case of PP/PA-SEBS-g-MA blend the fibrils break down at the interface.

b) Single cavitation process in binary blend systems.

In the case of PA/butyl acrylate blend, in which the modifier particles consist of only one rubbery phase, the micromechanical deformation process can be followed in the form of single cavitation process (Figure 2). In the first stage the stress concentration occurs around the modifier particles the same as in other blends systems. In the second stage, the modifier particles can be slightly stretched, and microvoids are formed in the plastically stretched modifier particles. With the void formation inside particles, shear bands form in the matrix between the modifier particles. With further straining of specimen, the voids will be more elongated, and the matrix will be further deformed through the shear yielding.

c) Single debonding process

Figure 3 shows the schematic micromechanical deformation process of single debonding process. This process takes place in the blend systems, in which the phase adhesion between the

modifier particles and matrix is poor as in the cases of particulate polymer composites or PP/EPR mechanical blend systems. In the first stage, stress is concentrated around the particles. In the case of particulate polymer composite (PP/$Al(OH)_3$) its maximum lies in the polar regions of particles. Due to the poor phase adhesion debonding can easily take place on the both polar regions of filler particles in the perpendicular external stress direction. Additionally, simultaneous shear bands form in the matrix (in the second stage). In the next stage, with combination of debonding process the matrix strands between the filler particles deform thorough the shear flow process.

d) Fibrillized debonding process at the interface

This process is schematically shown in Figure 4. When a certain phase adhesion between the modifier particle and the matrix exists, the deformation occurs through a debonding process with fibrillation at the interface between modifier particles and matrix. In the first stage stress concentration occurs around the particles. The modifier particles will be slightly stretched due to the stress concentration. Due to the existence of a certain amount of phase adhesion, fibrils form at the interface between modifier particles and matrix and simultaneously shear bands form in the matrix. With increasing the strain of the specimen the fibrils break down at the polar regions of particles; only a few fibrils remain in the area of equator regions of particles (in the direction of external stress). In the third stage, the further shear flow of matrix is considerably enhanced.

CONCLUSIONS

It has shown that the mechanical deformation processes and its deformation structures of impact modified heterogeneous thermoplastics will be decisively influenced by the morphology of modifier particles. From the analysis of different toughening mechanisms, a few morphological standard types are derived for the toughening models, namely binary and ternary systems.

In the ternary blend systems, according the specific inherent properties of the interface, cavitation processes occur with or without fibrils in the plastically deformed rubbery shell. In the binary blends modified with rubber or inorganic filler particles, the phase adhesion has a great significance for the courses of events in micromechanical deformation processes. When the phase adhesion between the modifier particles and the matrix is good, the plastic deformation occurs via single cavitation processes inside modifier particles, whereas when there is no or poor phase adhesion, the micromechanical deformation processes are followed by debonding.

According to the phase structure of modifier particles, the phase adhesion between modifier particles and matrix and the void formation processes, different schematic models for micromechanical deformation processes are proposed. The individual toughening mechanisms in the impact modified semicrystalline polymers could be described in form of three-stage-mechanism. In the all blend systems studied, the considerable enhancement of impact strength results from the flow processes of matrix material followed by microvoid formation. The results from the present work allow a reduction in the generalizible standard model types for the micromechanical deformation processes proposed above, which can be considered as a model atlas for modified semicrystalline polymers.

REFERENCES

[1] G. H. Michler, Kunststoff-Mikromechanik: Morphologie, Deformations- und Bruchmechanismen, Carl Hanser Verlag, München, Wien, 1992.

[2] G.-M. Kim, G. H. Michler, Proc. IUPAC MACRO Seoul'96, 36th IUPAC International Symposium on Macromolecules, Seoul, Korea, Aug. 1996.

[3] C. B. Bucknall, F. F. Cote and I.K. Partridge, J. Mater. Sci. 1981, **16**, 3141.

[4] G. H. Michler, Acta Polymerica 1993, 44, 699.
[5] G.-M. Kim, G. H. Michler, M. Gahleitner and J. Fiebig, J. Appl. Polym. Sci. 1996, 60, 1391.
[6] G.-M. Kim, PhD Thesis, Martin-Luther-University Halle-Wittenberg, Germany, 1996.

Schematic model of micromecahnical deformation processes

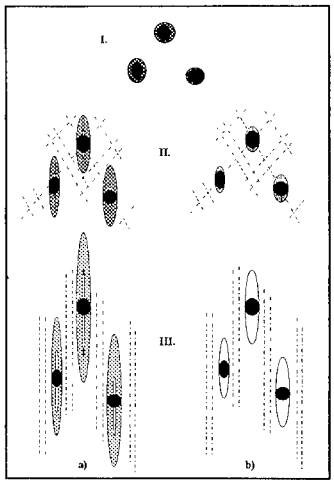

Fig. 1 Single cavitation process in ternary systems; a) by I), b) by II)

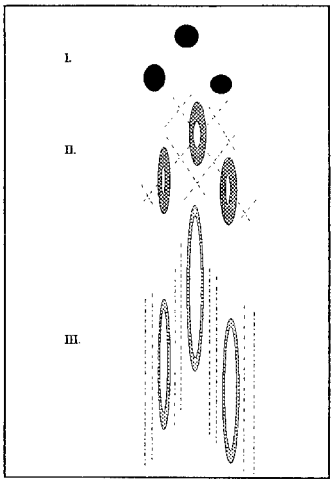

Fig. 2. Single cavitation processes in binary blend systems

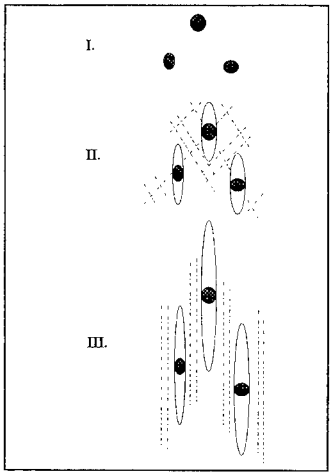

Fig. 3. Single debonding process

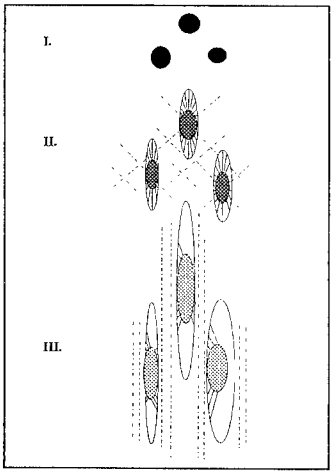

Fig. 4. Fibrillized debonding processes at the interface

Correlation between Toughness and Molecular Relaxation Behaviour in Amorphous Polymers

W.Grellmann and R.Lach

Martin-Luther-University Halle-Wittenberg, Department of Materials Science,
D-06099 Halle/S., Germany

Summary

The instrumented Charpy impact tests were done in a wide range of temperatures from -200°C to 100°C, to determine quantitatively toughness behaviour of amorphous polymers (PC, PS and PMMA) by using the concepts of the elastic-plastic fracture mechanics. The combined application of the J-integral and COD-concepts contribute to better understanding of the fracture behaviour. The J-integral shows significant maxima in its dependence on temperature except that in PS. The toughness increase at -60°C in PC as well as at 50°C in PMMA correlates with the secondary (β) relaxation. Results of the dynamic-mechanical analysis (DMA) were used to plot an Arrhenius graph with the lines of maxima of the mechanical loss factor, tan δ and a frequency estimated from the time to fracture. The intersection points between these lines and the frequency of fracture confirm the correlation between the maxima of J-integral and the β-relaxation. The local maximum of stable fracture surface at -40°C for PC shows the importance of molecular relaxation phenomena for fracture processes, because stable crack propagation indicates non-linear viscoelastic-plastic material behaviour. The maximum J-value in the temperature dependence at 60°C and the COD-value maximum are caused by a stress induced shear flow process. This process is explicable by the pressure dependence of the flow temperature, i.e. by the temperature dependence of the dynamic yield stress σ_{yd}. The comparison between the experimentally obtained σ_{yd}-T-dependence and the theory on describing the flow transition by means of a pressure-temperature phase diagram based on the Williams-Landel-Ferry equation delivers a good agreement. There occurs a relationship between the height of the β-relaxation peak, the deformation behaviour at high loading rate and the value of the β-stimulated toughness. In the case of β-relaxation, the energy dissipation is mainly due to the stimulation of shear deformation mechanisms.

Introduction

Fracture is the mostly observed failure due to from materials. Therefore, in addition with enhancing of stiffness, strength and other mechanical properties optimization of toughness behaviour has become to be one of the central purposes of materials developing. Fracture mechanics parameters have been proven to be appropriate to investigate toughness behaviour. They separate the various fractions of energy dissipated during fracture processes and hence, can evaluate adequately the toughness level of materials with different crack growth behaviour. Polymeric materials, are characteristic of viscoelasticity, show strongly temperature and loading rate dependent material properties. These can be attributed to polymer-specific stress relaxation phenomena, which influence the elastic as well as plastic deformation behaviour of polymeric materials. Therefore, they play an important role on fracture processes.

Experimental investigations

For the present investigations three-point-bending specimens with length L=80mm, width W=10mm and thickness B=4mm from the amorphous polymeric materials: polycarbonate (PC), polystyrene (PS) and polymethylmethacrylate (PMMA), were used. Some of them were provided with a 2mm deep sharp notch. Fracture mechanics tests were conducted in a temperature range from -200°C to 100°C by means of an instrumented Charpy impact tester at a pendulum hammer speed of 1.5 m/s, where the force and deflection were registrated. The observed elastic-plastic material behaviour with a non-negligible energy-dissipative zone requires the application of elastic-plastic fracture mechanics concepts. The J-integral values were determined according to the approximation method from Sumpter and Turner, and the COD values were calculated based on the plastic hinge model. Additionally, optical and scanning electron microscopic investigations of fracture surface as well as the dynamic-mechanical analysis (DMA) were performed, which should contribute interpreting the temperature-dependent fracture behaviour.

Results

In the temperature dependence of resistance against unstable crack growth in terms of critical J-integral, J_{Id}^{ST} and critical COD, δ_{Id} predominant athermical fracture behaviour is observed at low temperatures (Figs. 1 and 2). It was shown, that in this temperature range the J_{Id}^{ST}- and δ_{Id}-values are very small and nearly independent of temperature. However, there occurred pronounced maxima in the temperature dependence of the energy-determined J-integral except for PS. Through DMA (Fig. 3), it can be concluded that the toughness increasing at -60°C in PC and at 50°C in PMMA correlate with the secondary (β) relaxation. In an Arrhenius graph, the lines of maxima of mechanical loss tan δ and a frequency, estimated from the time to fracture are plotted. As can been seen from the intersection points between these lines and the frequency of fracture, the maxima of J-integral is in correlation with the β-relaxation (Fig. 4). The local maximum of stable fracture surface at -40°C in PC shows the importance of molecular relaxation phenomena in fracture processes, because stable crack propagation indicates non-linear viscoelastic-plastic material behaviour (Fig. 5).

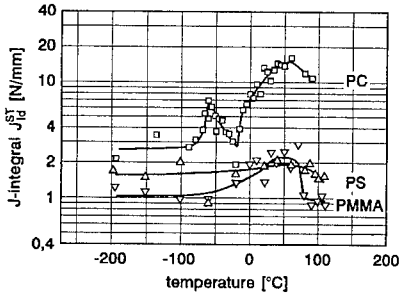

Figure 1
Temperature dependence of critical J-integral values J_{Id}^{ST} (ST: evaluation method from Sumpter and Turner)

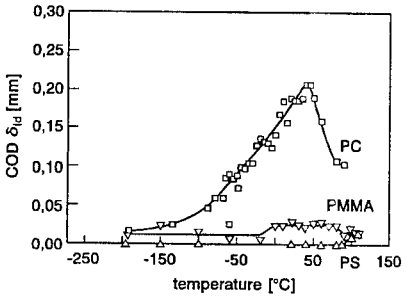

Figure 2
Temperature dependence of critical COD values δ_{Id}

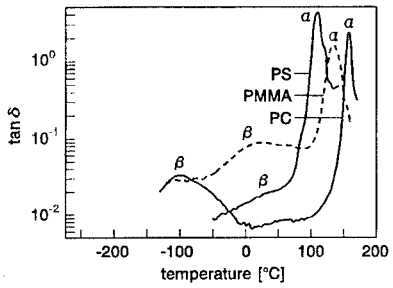

Figure 3
Mechanical loss factor tan δ at a frequency of 1 Hz (α: α-relaxation, β: β-relaxation)

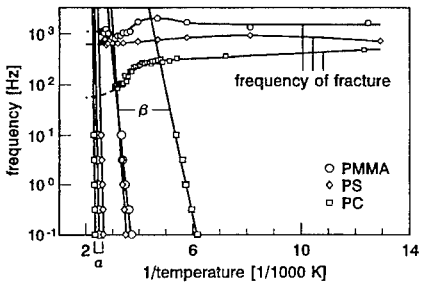

Figure 4
Arrhenius plot with the lines of tan δ maxima and the frequency of fracture (α: α-relaxation, β: β-relaxation)

In polycarbonate, the J-value maximum in the temperature dependence at 60°C and the δ-value maximum are caused by a stress induced shear flow process. This process is explicable by the pressure dependence of the flow temperature, i.e. by the temperature dependence of the dynamic yield stress σ_{yd}. The flow transition is described by the Williams-Landel-Ferry equation (WLF-equation). The WLF-equation is formulated analogically for various intensive values as pressure and temperature. From the validity of the WLF-equation in its temperature as well as in its pressure formulation isochrones (lines of constant mean correlation or relaxation time) of the flow transition in a pressure-temperature phase diagram (p-T-diagram) are also hyperbolical with frequency-independent pressure and temperature asymptotes [1]. The comparision between the experimentally obtained σ_{yd}-T-dependence and the theory on describing the flow transition by means of a p-T-diagram based on the WLF-equation delivers a good agreement (Fig. 6). For polycarbonate, the temperature dependencies of the stretch zone width and the stretch zone height are qualitatively comparable to that of δ_{1d} and have the same causes as the COD based on the geometrical interpretation of the COD (Fig. 5).

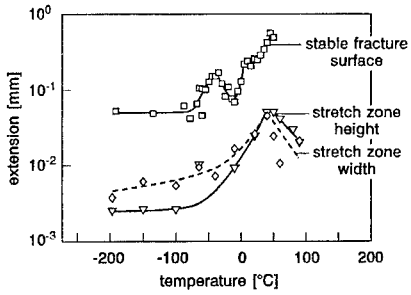

Figure 5
Stable fracture surface, stretch zone width and height for polycarbonate

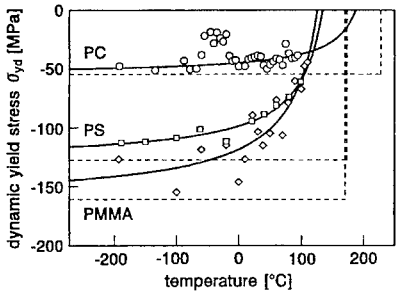

Figure 6
Dynamic yield stress σ_{yd} in a pressure-temperature phase diagram, full lines: theory from Donth [1]

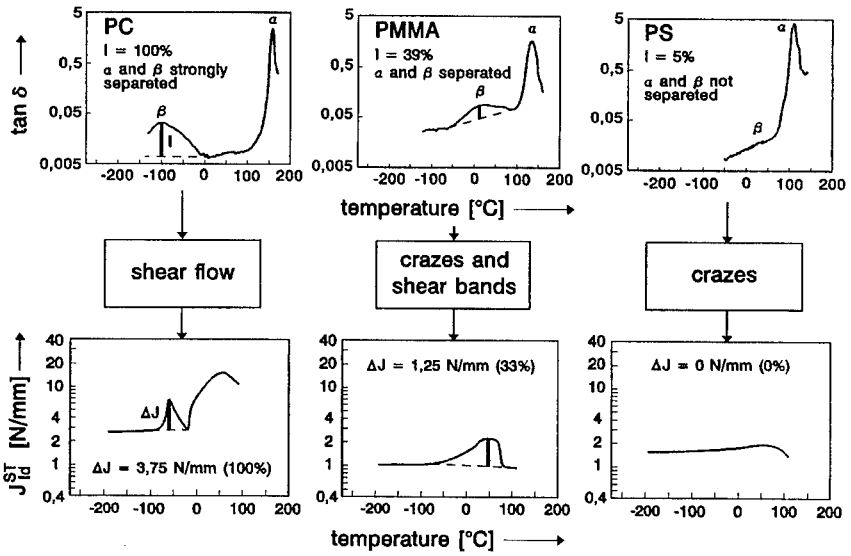

Figure 7
Relationship between the height of the β-relaxation peak, the deformation behaviour at high loading rate, and the value of the β-stimulated toughness

There occurs a relationship between the height of the β-relaxation peak, the deformation behaviour at high loading rate, and the value of the β-stimulated toughness (Fig. 7). In the case of β-relaxation, the energy dissipation is due to the stimulation of shear deformation mechanisms. The shear deformation, extending a much greater volume than crazing, has contributed to the increasing toughness. The greatest relative intensity of the β-relaxation and the very good separability of α- and β-relaxation phenomena are found in PC. A shear flow process, that extends a relatively great volume of specimen, and a great β-stimulated toughness increasing are observed. In comparision to PC, shear and tension deformation mechanisms are operative in PMMA during deformation. The cause of the resulted co-existence of shear bands and crazes is the relative low intensity of the β-relaxation peak and separability of the α- and β-relaxations which are quite difficult to be separated each other. In PS the discernible β-peak can be hardly separated from the α-peak, and correspondingly, only crazing is observed. As a result, only athermical fracture mechanisms are active in the whole range of temperature, so that no maximum of toughness comes into occurrence in the J-integral temperature dependence.

References

[1] E.Donth, Relaxation and Thermodynamics in Polymers. Akademie Verlag, Berlin, 1992.
[2] W.Grellmann and R.Lach, Angew.Makromol.Chem. 237 (1996) 191.

PREDICTION OF THE MECHANICAL BEHAVIOUR OF HETEROGENEOUS POLYMER SYSTEMS, BASED ON THEIR MICROSTRUCTURE

R.J.M. Smit*, W.A.M. Brekelmans*, H.E.H. Meijer* and L.E. Govaert*

The overall mechanical behaviour of heterogeneous hour-glass-shaped polycarbonate tensile bars was predicted from the microstructural properties by using a multi-level finite element method (MLFEM). The multi-level method, providing an objective relationship between the deformation and stresses at macro level (FE model of tensile bar) and micro level (FE model of matrix material with inclusions), is introduced briefly. The simulations indicate that the addition of a fine dispersion of non-adhering low-modulus rubbery particles seems to result in toughening of the sample: the deformation spreads out over the whole specimen. The basic mechanism for this toughness enhancement is explained.

INTRODUCTION

Microstructural adaptations in polymer systems are often used for mechanical property enhancement. In particular the toughness and impact resistance of glassy and semi-crystalline polymers are strongly improved by the addition of a fine dispersion of a low modulus phase (1,2). Accurate predictions of these property enhancements are of major importance for polymer blend development and applications. These property predictions are often inaccurate or impossible by (i) complicated constitutive behaviour of the microstructure (e.g. large deformations, visco-elastic behaviour, crazing) and (ii) the unclear relationship between the properties on user scale (typical length scale $10^{-3} - 10^{-1}$ m) and morphological scale (typical length scale $10^{-8} - 10^{-6}$ m).

This paper presents a novel approach to simulate the large strain time-dependent mechanical behaviour of heterogeneous polymeric solids based on the microstructure. A recently developed large-strain elasto-viscoplastic constitutive equation (3,4) for the modelling of pre-failure mechanical behaviour of polymer glasses, is combined with a novel accurate objective homogenisation method that has recently been developed (5). The method is used to study the influence of the microstructure on shear band formation in plane strain hour-glass-shaped polycarbonate specimen with a fine dispersion of non-adhering low-modulus rubbery particles.

HOMOGENISATION OF HETEROGENEOUS SYSTEMS

The homogenisation method originates from the classical assumption of local spatial periodicity of the morphology (6), allowing a macroscopic structure with different microstructures at different points. The microstructure is identified by a representative volume element (RVE, e.g. a cube with irregularly distributed spherical inclusions) with periodic boundary conditions. The macro-micro relationship is obtained by the assumption that

*Faculty of Mechanical Engineering, Eindhoven University of Technology, P.O. Box 513, 5600 MB Eindhoven, The Netherlands

the local macroscopic deformation and stress tensors are equal to the RVE averaged deformation and stress tensors. Consequently, the macroscopic displacement field is decoupled from the microscopic displacement field: to each macroscopic point (in fact an integration point in the macroscopic mesh) a periodic RVE is assigned that relates the macroscopic deformation tensor to the macroscopic stress tensor. This decoupling has severe implications for the finite element formulation of this homogenisation method. The macroscopic structure is considered as a homogeneous solid and is discretised accordingly. In each macroscopic integration point the local deformation tensor is applied to the associated discretised RVE, such that the RVE averaged deformation tensor equals the local macroscopic deformation tensor. The resulting inhomogeneous RVE stress field is averaged and returned to the macroscopic integration point as the local macroscopic stress. This procedure is repeated for each macroscopic integration point in order to obtain an estimation of the macroscopic stress field. Multi-level (macro-micro) finite element procedures are applied to converge iteratively to a deformed macroscopic equilibrium state.

CONSTITUTIVE MODELLING OF GLASSY POLYMERS

For the constitutive modelling of the large-strain time-dependent mechanical behaviour of the individual polymeric components, a constitutive model has been adopted from Tervoort *et al.* (3) and Timmermans (4). It concerns a so-called "Leonov model with hardening", a Maxwell model with an Eyring viscosity describing the typical visco-elastic polymeric behaviour combined with a neo-Hookean model describing strain hardening behaviour due to molecular orientation. The resulting elasto-viscoplastic constitutive model is assumed to predict the strain rate, temperature and history dependent yield, intrinsic strain softening and subsequent strain hardening of glassy polymers.

RESULTS AND DISCUSSION

Numerical simulations of shear band formation in heterogeneous plane strain hour-glass-shaped tensile specimen have been performed, using the aforementioned homogenisation method and Leonov model. The systems considered are pure polycarbonate and polycarbonate with 30 vol.% dispersed non-adhering low-modulus rubbery particles.

The initial geometry and mesh of the macroscopic plane-strain tensile specimen is shown in Fig. 1a. The specimen is chosen to be asymmetrical in order to obtain a preferred and thus controlled shear direction (the curved edges, with identical radii, are shifted with respect to each other). The geometries and meshes of the plane strain periodic RVEs, representing the microstructures at the macroscopic integration points, are visualised in Fig. 1b,c. The rubbery inclusions are considered as being voids, since the properties of the non-adhering low-modulus particles are expected not to influence the mechanical behaviour of the unit cells under the expected positive hydrostatic stress states. The time-dependent mechanical behaviour of the glassy polycarbonate is modelled by the Leonov model with hardening, using material parameters adopted from Timmermans (4).

The predicted averaged stress-strain responses of the RVEs under isothermal uniaxial plane strain extension (strain rate 0.01 s^{-1}) are depicted in Fig. 2. The homogeneous polycarbonate shows the typical mechanical behaviour that is representative for a range of glassy polymers: an initial elastic response, followed by intrinsic strain softening and

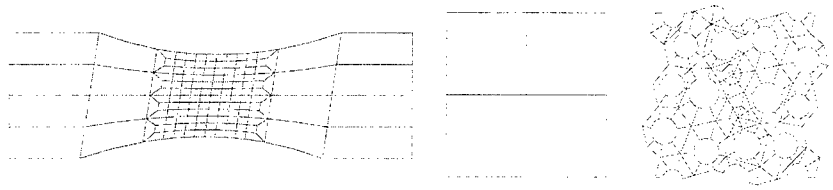

a b c

Figure 1: Geometry and mesh of (a) the undeformed plane strain hour-glass-shaped tensile specimen, and the spatially periodic RVEs that represent the local microstructure: (b) homogeneous polycarbonate, (c) polycarbonate with 30 vol.% voids.

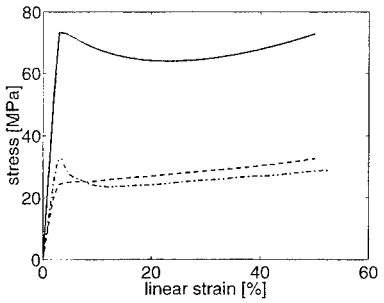

Figure 2: Volume averaged stress-strain responses for polycarbonate RVEs containing no voids (solid), and 30 vol.% voids in an irregular stack (dashed) and a regular cubic stack (dash-dot).

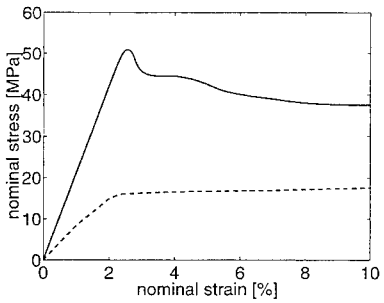

Figure 3: Predicted mechanical response of the macroscopic polycarbonate specimen with no voids (solid) and 30 vol.% voids (dashed).

subsequent strain hardening. The introduction of voids has a pronounced influence on the deformation behaviour: stiffness and yield stress are reduced considerably and the stress drop by intrinsic strain softening is diminished. Evidently the reduction of stiffness and yield stress is caused by the decrease of load-bearing material by the presence of voids. The reduction of strain softening originates from the irregular distribution of the voids. Due to this irregular distribution, the shear bands are formed between the holes in an arbitrary order and subsequently stabilised by strain hardening, before they coalesce into large shear bands that dominate the RVE deformation behaviour. This is in contrast with the behaviour of RVEs with regularly stacked inclusions: a cubic stack causes a simultaneous formation of shear bands between all the holes, and the overall material behaviour is dominated by the shear band formation, which is accompanied by intrinsic softening (compare the stress-strain responses of the RVEs with regular and irregular distributed voids in Fig. 2). Since intrinsic strain softening is known to be the main cause of unstable material behaviour, often resulting in shear band formation, the decrease of softening will evolve in a more stable overall material behaviour.

The macroscopic specimen is stretched with a constant strain rate of 0.01 s^{-1} to a

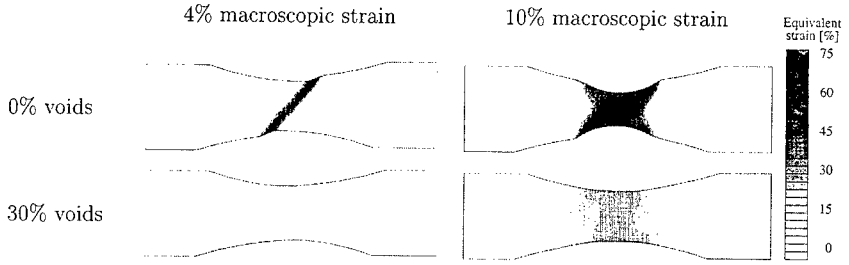

Figure 4: Contours of equivalent strain in the deformed polycarbonate sample with 0 and 30 vol.% voids at a nominal macroscopic strain of 4 and 10%.

total nominal strain of 10%. The predicted macroscopic nominal stress responses are shown in Fig. 3. The equivalent strain in the macroscopic samples at 4 and 10% strain is plotted in Fig. 4. Pure polycarbonate shows a characteristic deformation behaviour: at a nominal strain of 0-2%, initial stiff overall elastic response; 2-3%, load fall by shear band formation; 3-4.5%, some stabilisation and growth of the first shear band; 4.5-5.5%, load fall by a second shear band formation; 5.5-10%, formation and growth of the neck. Hence, the behaviour of the pure polycarbonate is dominated by a strong concentration of deformation in the shear bands (up to 75% local strain); neck formation and a large unstable post-yield stress drop occur. The addition of voids results in a broader shear band almost perpendicular to the load direction. Instead of a neck, a broad dilatation zone is formed and the deformation is distributed over a large part of the sample. As a result, the maximum equivalent strain at 10% nominal strain decreases with a factor 3. A decrease in stiffness and yield stress results, and the post-yield stress drop disappears.

Many experimental evidence is available indicating that toughness is enhanced by the addition of easily cavitating and/or non-adhering rubbery particles (1,2). However, the basic mechanism of this toughness enhancement was not really understood yet. The results of the multi-scale analyses indicate that the random stack of easily cavitating rubbery particles has a pronounced influence on the toughness enhancement of heterogeneous polymeric systems by the removal of the intrinsic softening behaviour.

REFERENCES

1. van der Sanden, M.C.M., De Kok, J.M.M., Meijer, H.E.H., *Polymer* **35** (1994) 2995.
2. Magelhães, A.M.L., Borggreve, R.J.M., *Macromolecules* **28** (1995) 5841.
3. Tervoort, T.A., Klompen, E.T.J., Govaert, L.E., *J. Rheol.* **40** (1996) 779.
4. Timmermans, P.H.M., 'Evaluation of a constitutive model for solid polymeric materials'. Ph.D. thesis, Eindhoven University of Technology, Eindhoven, The Netherlands (1997).
5. Smit, R.J.M., Brekelmans, W.A.M., Meijer, H.E.H., *Comp. Meth. Appl. Mech. Engng.*, submitted (1996).
6. Bensoussan, A., Lions, J.L., Papanicolaou, G., 'Asymptotic Analysis for Periodic Structures'. North-Holland, Amsterdam (1978).

EFFECTS OF WATER ABSORPTION AND DESORPTION ON THE STRENGTH OF POLYMER / GLASS INTERFACE

M. Kawagoe*, N. Fuwa*, Y. Doi†, T. Yasuda†,
K. Takada†, J. Qiu*, and M. Morita*

The effects of water absorption and desorption on the interfacial strength of a bilayer specimen made of unsaturated polyester and a glass plate were evaluated by measuring a crack extension force under inserting a razor blade into the interface. The specimes were subjected to cyclic absorption-desorption treatments, of which an elemental process was done by soaking the specimen in distilled water at 30°C for 24h and subsequently by drying in air at 20°C for 24h. It was demonstrated that the interfacial strength is markedly lowered only by one time of treatment, then recovered by subsequent cycles, and again reduced by 7-9 cycles of treatment. Such behaviour may be explained by relaxation of residual tensile stress in the polymer and a mechano-chemical fracture mechanism at the interface.

INTRODUCTION

The degradation of glass fibre reinforced polymers (GFRP) is mainly caused by a reduction of fracture resistance at the interface of the polymer matrix and the glass fibre, which is strongly influenced by absorbed water. Several testing methods applied for GFRP unfortunately are not always adequate to evaluate only the resistance to interfacial facture.

In this study bilayer specimens consisting of unsaturated polyester and a glass plate are prepared to imitate a situation of the interface, and their interfacial fracture resistances are relatively evaluated by measuring a crack extension force under inserting a razor blade into the interface. The effects of cyclic treatment of water absorption and subsequent desorption on the interfacial strength are examined by this testing mothod.

EXPERIMENTAL

The polymer used is commercially avalable unsaturated polyester (PS-2202PT, Hitachi Chemical Co. Ltd). It was mixed with a curing agent of methylethylketoneperoxide (PERMEC-N, Nihon Yushi Co. Ltd) by 1wt%, and then applied onto a glass plate of 13 x 38mm^2 cut from the standard laboratory microscope slides, of which the surface was preliminarily treated with γ - methacryloxypropyltrimethoxysilane (A-174, Nippon Unicar Co. Ltd). The silane coupling agent dissolved in methanol (1:4 in vol.) was coated on the glass surface, and dried in air at 100°C for 1h. The polymer on the glass was flattened by covering with another glass plate treated by a non-shift type release agent (CHEMLEASE/40, Chemlease Co.Ltd). The thickness was adjusted to 1.0mm by insertng a spacer of metal plate. The specimen was left at 60°C for 15h in a forced-air oven for curing the polymer, and offered to the tests mentioned below about 200h later after mixing the polymer with the curing agent.

The mechanical resistance to interfacial fracture was evaluated by a blade insert testing (BIT) method, designed by making reference to the method developed by Smith and coworkers [1]. The razor blade was mounted on a holder of our own making, and inserted into the polymer-glass interface of the bilayer specimen at an angle of 55° to

* Dept. of Mechanical Systems Engineering, Toyama Prefectural University
5180 Kurokawa, Kosugi, Toyama 939-03, Japan
† Hitachi Kasei Unit Co. Ltd, 1010 Ippongi, Toyama 930, Japan

the glass surface at a moving speed of 5mm/min by means of a hydraulic servo-controlled testing machine (EHF FBKN 10LA, Shimadzu Co. Ltd). The preliminary experiments demonstrated that the dynamic resistance for advancing the razor blade is abruptly lowered when an interfacial crack rapidly propagates along the glass surface. The measurements by micro-FT infrared spectroscopy also revealed that no vestiges of the applied polymer exists on the glass surface which is newly formed under inserting the razor blade. This result means that the present BIT method using the bilayer specimen may actualize a real interfcial fracture. Therefore it may be possible to evaluate the relative interfacial strength by comparing with each peak load corresponding to rapid crack extension.

The bilayer specimens were subjected to cyclic absorption-desorption treatments, of which the elemental process was done by soaking the specimen in distilled water at 30°C for 24h and subsequently drying in air at 20°C for 24h. It was noted that only the upper side of polymer opposite to the interface is always in contact with water. After several times of treatment, the interfacial strength was measured by the BIT method.

The residual stress generated both by the shrinkage of polymer during the curing process and by thermal shrinkage under colling was calculated by means of the finite element method (FEM). Three-dimensional analyses were performed by use of a program for thermal stress anaysis (ANSYS 5.0A, Swanson Analysis Systems Inc.). Only the elastic stresses were estimated, approximating the deformation behaviour of the unsaturated polyester to be elastic until fracture.

RESULTS AND DISCUSSION

Figure 1 represents the typical examples of the load-displacement relation for advancing the razor blade along the interface of the specimens subjected to several cycles of water absorption and desorption. The numbers in the figure denote the number of repeating cycles. For the as-cured specimen the load is lenearly increased with increasing displacement, and abruptly reduced showing a sharp peak, which corresponds to unstable crack propagation along the interface. By one cycle of treatment both the load and the displacement at the peak are much lowered, although the linear relation between them is maintained. It is noted that the peak load and displacement are somewhat increased by 3-5 cycles of treatment, indicating lower inclination probably due to plasticization effect of water absorbed in the polymer. For the specimens subjected to 7 cycles of treatment the peak load is again lowered, and finally both the load and the displacement at the peak are greatly reduced by 9 cycles of treatment.

Figure 2 shows a schematic representation of the maximum principal stress σ_1 remaining in the polymer at the interface. This result was obtaned by the FEM for the as-cured specimen. σ_1 is always tensile and takes larger value at each edge. The mean value of σ_1 along the line A-A in the figure is calculated to take 84.2MPa. Since the stress due to thermal shrinkage under colling is only 2.3MPa (2.7%), the residual stress may almost all be generated by shrinkage of the polymer during curing process at 60°C. According to the preliminary measurements, the volume shrinkage was about 12%. In addition, σ_1 is oriented at an angle of 56° to the glass surface at the center of the line A-A, and therefore may assist the crack propagation caused by the razor blade inserted into the interface at 55°. Since the calculation shows the residual stress to strongly be affected by the value of elastic modulus, water absorption will influence on the interfacial strength by a plasticization effect of water.

A relative concentration, C/C_0, of water existing in the polymer at the interface during the cyclic absorption and desorption was estimated by assuming the movement of water to obey the Fick's 2nd law. The calculaton was conducted using the coefficients of absorption and desorption obtained from the another measurements of weight gain of the rectangular specimens. The calculated result is shown in Figure 3. It is noted that water remains at the interface after drying for 24h and takes C/C_0 of 3% by the first cycle, and then is accumulated holding the constant value of 3% for subsequent

treatments, as shown by a dotted line in the figure, although the actual amount of water accumulated at the interface may be much larger.

From the above calculations a possible explanation for Figure 1 may be as follows. The first cycle of treatment causes scission of hydrogen bonding between the unsaturated polyester and the glass, and thus provides much reduction in the interfacial strength. For subsequent 3-5 cycles, a decrease in the elastic modulus and slight swelling of the polymer may be brought about by water accumulated at the interface, and somewhat relax the residual stress in the polymer adhering to the glass surface. This may recover the interfacial strength. By many times of aborption-desorption treatment, however, the accumulated water may hydrolyze polyester, and further break a siloxane bond to make a pair of silanol under the action of residual tensile stress at the interface. Such chemical and mechanochemical effects will again reduce the interfacial strength.

COCLUSIONS

The interfacial strength of unsaturated polyester and glass was evaluated by measuring the crack extension force under inserting a razor blade into the interface of the bilayer specimen. By the cyclic treatments of absorption and desorption of water, the interfacial strength was once lowered, then more or less recovered, and finally again reduced. Such behaviour may result from the relaxation of tensile residual stress in the polymer and chemical and mechanochemical degradation mechanisms at the interface, which are caused by water accumulated during cyclic process of soaking and drying.

REFERENCES

1. Smith, J.W., Kramer, E.J., Xiao, F., Hui, C., Reichert, W., and Brown, H.R., *J. Mater. Sci.*, **28**, 4234 (1993)

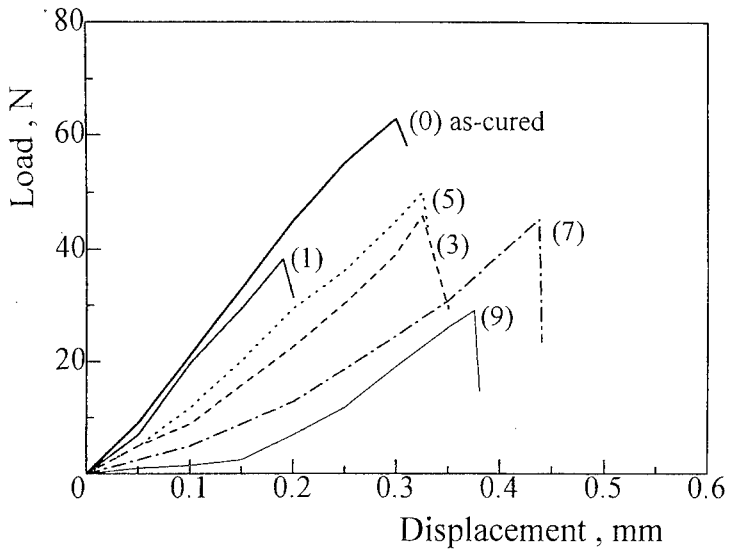

Fig. 1 Effects of water absorption-desorption cycles on the load-displacement relation for advancing the razor blade along the polymer-glass interface

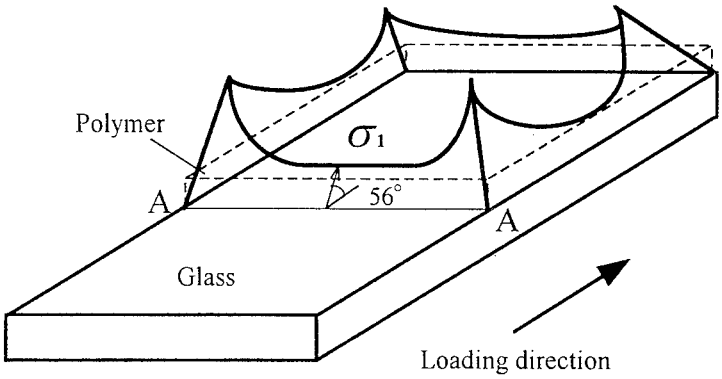

Fig. 2 Schematic representation of the residual maximum principal stress in the polymer at the interface for the as-cured specimen

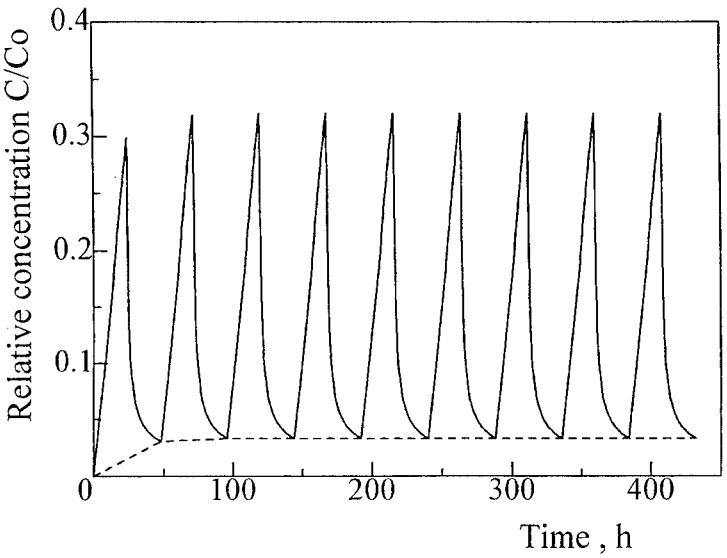

Fig. 3 Estimated relative concentration of water in the polymer at the interface under cyclic process of water absorption and desorption

TOUGHENING OF HIGHLY FILLED POLYPROPYLENE : ROLE OF PARTICLE SIZE AND SURFACE TREATMENT.

G. Orange*

Fracture toughness of PP/$CaCO_3$ composites were investigated in terms of J-Δa curve : initiation and propagation fracture criteria. The crack initiation is mainly determined by the matrix, i.e. by the polymeric phase itself which is modified in terms of cristallinity or spherulite size by the $CaCO_3$ dispersed particles. The crack propagation is controlled by the ability to develop local deformation along particle/matrix interface : the cavitation development is shown to be the main toughening mechanism in these filled materials.
The cavitation process is controlled by the matrix/particle bonding strength which is a function of the size of the particle and the adhesion energy.

INTRODUCTION

Particulate-filled polymers are of increasing interest in industry, and specially for the development of high performance low-cost composites for structural applications. Stiffness and impact behaviour compromises are often crucial for the applicability of these materials in a given structural part [1,2].

Rigid fillers with controlled interfacial adhesion are usually used to enhance the elastic modulus of polymeric materials. It is possible also to develop a reinforcing effect via local relaxation mechanisms : improvement of the fracture behaviour of polymers. But up to now the role of filler characteristics on the fracture toughness of composites has remained unclear.
One of the most practically useful criteria for quasi-brittle fracture of polymers relies upon the linear elastic fracture mechanics. In the case of plasticity, post-yield fracture mechanics such as the J-integral method must be used for a quantitative characterization of fracture toughness of filled polymers [3,4].

In this paper, some of the properties of mineral-filled polypropylene (PP) were studied. A special interest was devoted to the measuring of toughness via the J-integral method : initiation and propagation energy.

EXPERIMENTAL PROCEDURE

1.- Materials and Preparation

A commercially available polypropylene homopolymer, ELTEX P HV 001 P (SOLVAY) having a melting point of about 160°C and a density of 0.902 was used as matrix material. The resin was supplied in powder form to facilitate uniform dispersion when compounded with minerals.

Basically, four different $CaCO_3$ minerals (Calcite) were used as filler : 2 µm natural $CaCO_3$ (Omyalite 90 and 95T : OMYA), and 0.1 µm precipitated $CaCO_3$ (Calofort U and Calofort S : RHONE POULENC CHIMIE).

* RHONE POULENC, Centre de Recherche d'Aubervilliers F-93308 Aubervilliers, France.

A stearic acid treatment was used (Omyalite 95T, and Calofort S) to improve dispersion of the fillers into the matrix.
Compounds with 10% (vol.) filler and an antioxizing additive (Irganox) were prepared with a twin screw extruder (ZSK), at a temperature of 190°C.
4 mm thick plates were fabricated from compounds by hot pressing (180°C, 350 bars). Specimens were cut out from the plates.

2.- Characterization techniques
Elastic modulus and yield stress were measured by compression tests on 10 x 10 x 4 mm^3.
The J-integral measurements (J-Δa curve) were made from tensile test on CT specimens of 48 x 40 x 4 mm^3 size, with the single specimen technique to determine the value of the energy J versus crack growth Δa (ASTM E813-89). The starting crack was made using a razor blade (notch radius < 50 μm) up to a depth a_o of 10 mm.

Two fracture criteria are determined : critical energy $J_{0.2}$, and the slope dJ/d(Δa) at Δa = 0.2 mm (ESIS procedure P1-92). The tearing modulus is calculated from the elastic modulus E, the yield stress σ_y and the slope of the J resistance curve : $T_m = \frac{E}{\sigma_y^2} \frac{dJ}{d(\Delta a)}$ [5].

RESULTS AND DISCUSSION

The increase of elastic modulus with fine fillers (< 0.1 μm) as precipitated $CaCO_3$ (Calofort U) is due to both the good filler - matrix adhesion and the increase of cristallinity rate. Similar effect is observed on the yield stress.

TABLE 1 : Experimental results

Incorporated filler (10% vol.) in PP	Young modulus (MPa)	Yield stress (MPa)	$J_{0.2}$ (kJ/m^2)	$(dJ/d\Delta a)_{0.2}$ (10^3 kJ/m^3)	$T_{0.2}$
No filler : PP	1300	26.5	16.5*	30*	56*
Calofort U	2000	37	8.5	2.7	1
Omyalite 90	1700	28	18	40	86
Calofort S	1600	27.5	19.5	22	25
Omyalite 95T	1700	29	18	40	86

(*) Under test conditions (23°C, quasi-static), polypropylene has a semi-brittle behaviour, to a crack extent of 1 mm, and is brittle at larger crack growth.

Small size precipitated $CaCO_3$ (0.1 μm), without surface treatment, induces a brittle behaviour of the filled polymer. At the opposite, a ductile behaviour is observed with large size natural $CaCO_3$ (> 1 μm) : increase of initiation and propagation energy levels,.and also the tearing modulus T_m (> 85). This ductile behaviour is due to the formation of a large whitened damage zone in front of the main crack which is considerably larger than the plastic zone : *'process zone'*. This process zone dissipates a large amount of energy and so induces a toughening effect of the material [6].

The different J-R curves (J - Δa) are plotted on the Fig. 1. The size effect seems to be a major parameter in the control of the $CaCO_3$/PP composite toughness.
Surface treatment, which contributes to a better particle dispersion and lower particle - matrix interaction is more effective as the particle size is decreased.

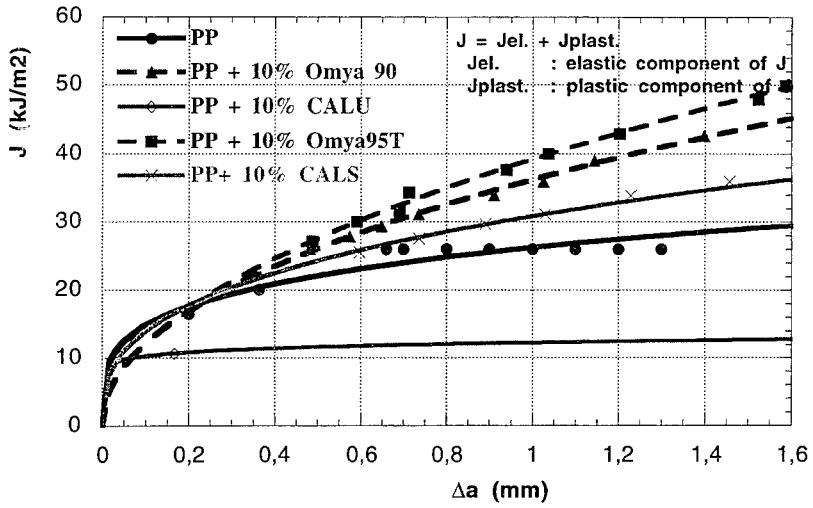

Fig. 1 : J as a function of crack growth for $CaCO_3$ filled Polypropylene (23°C)

The fracture energy increase is due to the contribution of non reversible dissipated energy (plastic component : $J_{plast.}$) as the crack propagates through the material : it is the dissipated energy which determines the damage tolerence and so the toughness of the filled polymer.

Microstructural observations show that the damage which is developing in the process zone as the crack propagates through the material corresponds to the formation of a large density of cavities localized around dispersed mineral particles. The crazing process doesn't induce important energy dissipation : that is the cavitation process which is the main toughening mechanism in $CaCO_3$ filled Polypropylene.

It is possible to explain the J energetical parameter as :

$J = J_0 + \Delta J$, where J_0 is the contribution of the matrix, and ΔJ is a function of the main toughening parameters as to the process zone size, the filler content, the critical cavitation stress, and the associated deformation.

The basic micromechanical mechanisms depend on the material properties and loading conditions. The stress distribution analysis shows that maximum stress concentration develops in the radial direction at the pole of the particle, and shear yielding is initiated at around 45° on the surface of rigid particles. Debonding occurs at the pole of the particle, and extent to a critical angle [7].
Cavitation is controlled by the debonding stress at the particle/matrix interface : it only occurs when the local debonding stress is lower than the rupture stress of the matrix itself. For debonding, no accepted criteria exist. If we consider that the energy necessary to create new surfaces during debonding corresponds to the change in elastic energy, we can write the debonding stress σ_D as follows :

$\sigma_D = Cte \left(\frac{G.E}{d}\right)^{1/2}$, where G is correlated to the interface energy , E is the local elastic modulus, and d is the particle size [8, 9].

G is the local toughness at the interface : it is dependent on the particle/matrix adhesion energy.

The dependence of the debonding stress on adhesion and particle size have been used to explain the yield and fracture stress [9]. It can also explain the Charpy impact strength of $CaCO_3$/PP materials [10].
In the case of not treated precipitated $CaCO_3$ (Calofort U), the adhesion energy is high : G >>, and d << => the debonding stress is at a high level (σ_D : about 20 MPa, from [9]). Elastic modulus is also increased with these precipitated $CaCO_3$ particles (nucleating effect) which contributes to an increase of the debonding stress.
With surface treatment (Calofort S), the decrease of the surface free energy results in lower matrix/filler interaction and as a consequence the debonding stress is reduced. This effect is more effective with small particle size fillers (precipited $CaCO_3$).
With large size $CaCO_3$ (natural $CaCO_3$), the particle size is the main parameter : d >> , and the debonding stress is reduced, even for not surface treated particles (σ_D < 10 MPa).

The debonding stress is maximum in case of Calofort U, and minimum with Omyalite 95T. effect.

We have compared the experimental values as a function of size and surface energy. The modifications of the polymeric matrix also have to be considered, and specially the α/β ratio.

CONCLUSIONS

Experimental fracture toughness values were determined (J-Δa curves) on $CaCO_3$/PP composite. If the reversible energy (elastic component : $J_{el.}$) is slightly reduced with addition of mineral particle, the dissipated energy (plastic component : $J_{plast.}$) can be considerably increased with surface-treated or large size $CaCO_3$ fillers.

The dissipation of energy as the crack propagates through the material is due to a cavitation process, localized within the process zone in front of the main crack.
A criterion for debonding, which assumes that the debonding stress is proportional to the strength of adhesion and depends on the particle size of the filler, might explain the experimental observations on toughness.

From this analysis, it seems possible to optimize the toughness of filled polymers by an appropriate design of the mineral particles.

REFERENCES

1. Nielsen L.E., "Mechanical Properties of Polymers and Composites", M.Dekker (N.Y.), 1974.
2. Bucknall C.B., "Toughened Plastics", Applied Science Publ. (London), 1977.
3. Broek D., "Elementary Engineering Fracture Mechanics", 4th ed. Kluwer Academic (Dordrecht), 1991.
4. Hashimi S., Williams J.G., Polym. Eng. Sci. 27 (1986) 38
5. Grellman W., Seidler S., J. of Polym. Eng. 11(1992) 71-101.
6. Donming L., Wenge Z., Zongneng Q, J. Mater. Sci. 29 (1994) 3754-3758.
7. GoodierJ.N., J. Appl. Mech. (Trans ASME) 55 (1933) 39-44.
8. Gent A.N., J. Mater. Sci. 15 (1980), 2884-2888.
9. Pukansky B., Voros G., Composite Interfaces 1 (1993) 411-427.
10. Jancar J., Dibenedetto A.T., Dianselmo A., Polym. Eng. Sci. 33 (1993), 559-563.

Experimental study of deformation and fracture mechanisms of expanded polystyrene under bending loading conditions

J-P. Yvrard [*], A. Imad [*], M. Nait Abdelaziz [**], G. Mesmacque [**], B. Beghin [***], R. Daffara [***].

The mechanical properties, such as the elastic modulus and the stress threshold σ_p, of an expanded polystyrene (E.P.S.) material issued from bending tests have been found to vary linearly according to the material density. Concerning the fracture mechanisms, the fracture mode is essentially intergranular. Globally, the E.P.S. mechanical strength is depending on the grains cohesion.

INTRODUCTION

Expanded polystyrene (E.P.S.) is a cellular thermoplastic polymer exhibiting a complex heterogeneous structure (1) (2). This structure depends on the observation level (3) :

1) agglomerate of beads (macroscopic level),
2) beads containing cells (mesoscopic level),
3) polystyrene cells containing air (microscopic level).

Macroscopic level Mesoscopic level Microscopic level

Our purpose is to examine the mechanical response as well as the fracture mechanisms of expanded polystyrene under bending loading conditions.

[*] Laboratoire d'Etudes des Structures, Hautes Etudes Industrielles, 59046 Lille, France.
[**] Laboratoire de Mécanique de Lille, 59653 Villeneuve d'Ascq, France.
[***] Huntsman Chemical Company France, 60772 Ribécourt Cedex, France.

MATERIALS - SPECIMEN - EXPERIMENTS

Three points bending tests are performed under a constant cross head speed of 4 mm/mn on variety of E.P.S. covering density from 13 to 37 kg/m^3. The specimens are parallelepipedic with dimensions 240 x 50 x 40 mm^3. Each test is carried out on 5 specimens in order to assure its reproductibility.

The E.P.S. behaviour, which can be described by the « load - deflection » response, is characterized by (figure 1.) :

- a non linear elastic zone defined by an initial tangent modulus E (Kpa),
- a stress threshold σ_p beyond which strains become inelastic.

RESULTS - DISCUSSIONS

The σ_p value can be determined using two methods :

- conventionally, σ_p is the stress value given by the intersection of two straight lines (the first tangent to the origin and the second to the point of fracture) (4),
- more precisely, it can be determined from « loading - unloading » tests. The σ_p value is the stress beyond which residual displacement occurs.

Our results indicate that conventional σ_p is 10 % higher than the value issued from « loading - unloading » tests.

Given the manufacture process as well as the structure of the material (arrangement of grains in a volume), the isotropic behaviour can be assumed as clearly shown in figure 3 where results for three directions (figure 2a.)of specimen prelevement are compared (5).

The mechanical properties of E.P.S. are dependant on the material density as illustrated in figures 4a. and 4b. Indeed, the σ_p threshold and the initial tangent modulus E increase linearly according to the density. These results are confirmed by anterior tests in simple compression (6).

Concerning the fracture mechanisms, the rupture take place in the inferior fiber where the normal stress is maximal (figure 2b.). This rupture is influenced by the complex structure of E.P.S. and more particularly by the size of grains. Indeed, the observation of the fracture surfaces shows that the percentage of transgranular ruptures increases up to 30 % approximately when the radius of grains increases. Moreover, since the higher the density is the smaller the grain size is, preferential intergranular mode of fracture is therefore observed of high density specimens. It may be concluded that E.P.S. strength is essentially governed by the grain cohesion.

REFERENCES

1. C.J. Benning, ''Plastic foams'', Wiley-Interscience, Tome 1 & 2, 1969.
2. B. Béghin, ''Polystyrène expansé'', Techniques de l'Ingénieur, AM.1., pp. 3341, pp. 1-12.
3. L.J. Gibson, M.F. Ashby, ''Cellular solids : Structure & properties'', Pergamon Press, 1988.
4. I.M. Ward, D.W. Hadley, ''An introduction to the mechanical properties of solid polymers'', Wiley-Interscience, 1993.
5. T. Daneels, L. Gautier, 'Caractérisation mécanique d'un P.S.E. sollicité en flexion simple'', Travail d'Etude et Recherche, H.E.I., Lille, Juin 1996.
6. A. Imad, A. Lefebvre, C. Fornallaz, B. Beghin, 'Etude du comportement mécanique du polystyrène expansé (P.S.E.)', Colloque International Francophone sur le Génie Mécanique des Caoutchoucs et des Elastomères Thermoplastiques, Nancy, Octobre 1994.

FIGURES

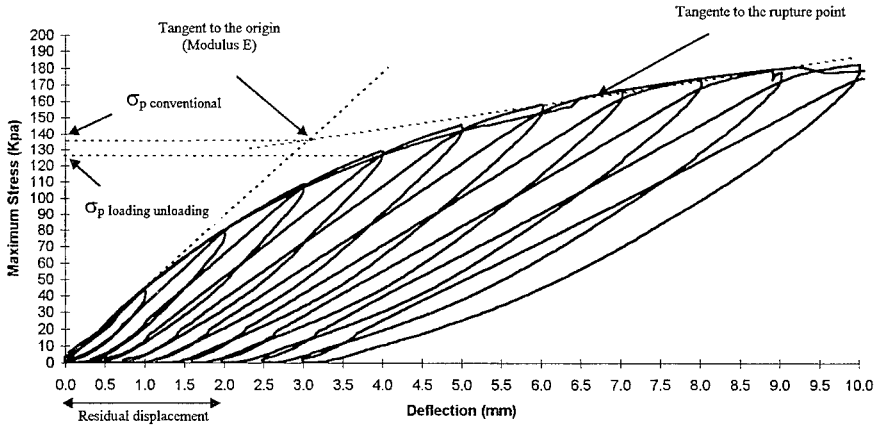

Figure 1. E and σ_p determination.

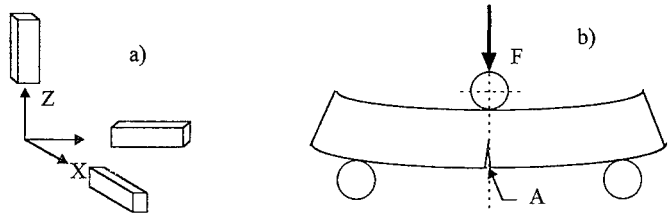

Figure 2a. Specimens directions, 2b. Specimens fracture.

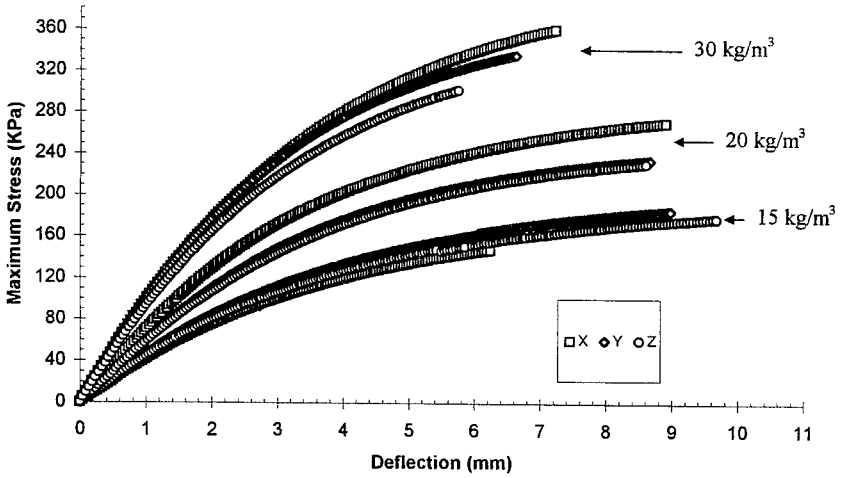

Figure 3. Mechanical behaviour for 3 specimens directions.

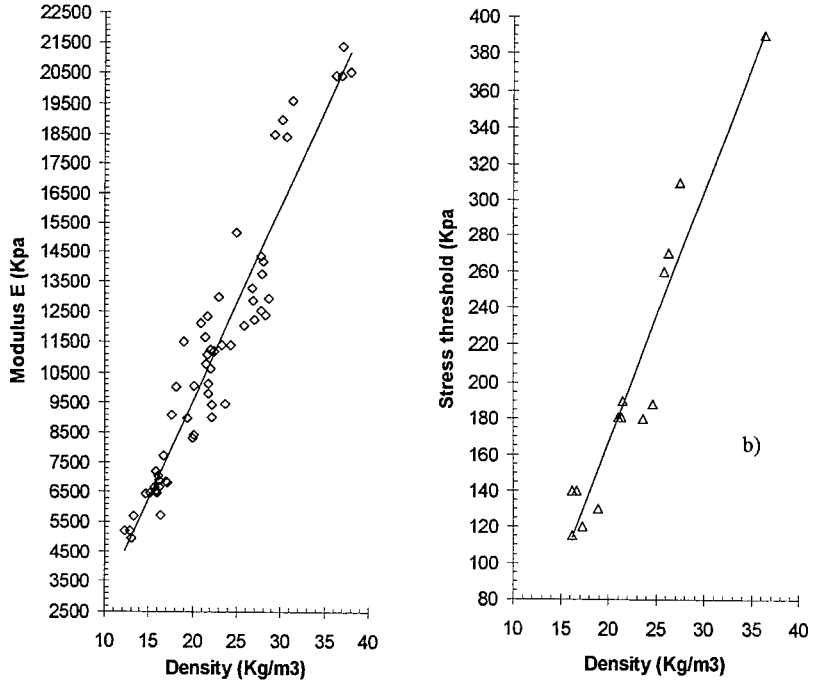

Figure 4a. 4b. E and σ_p evolution according to density.

STUDY ON THE FRACTURE STRENGTH AND PROPERTIES OF POLYMERIC MATERIALS V. LINEAR FRACTAL DEMENSIONS OF ENTANGLED NETWORKS AND ITS DEPENDENCE OF STRAIN ENERGY RELEASE RATE

MS Song* GX Hu*

By a method combining the fracture mechanic and the constrainted topology of entangled networks, this paper found a new relation between linear fractal dimension (D_f) and fracture properties for both polymer matriax and reinforced composites. The experimental data of polyarylether sulfone and its composite with carbon fiber were introduced to testify the theory. It shows a good agreement between the theoretical and experiment results.

In recent years, one of the new research fields of metals lies in the characterization of metallic microscopic structure. Most works focused on the relation between the fractal dimension D_f of fractured surface and the fracture properties. The physical mechanism of the relationship between D_f and material fracture properties remains unclear yet. In the light of fractal concept and crack extension theory, some researchers attempted to explain the reason why D_f was inversely proportinal to both K_{IC} and crack extention force G_{IC}.

Since there have been little information availiable with respect to the fractal characterization of non—metallic fractured surfaces, in the authors' present paper a new relation of linear fractal dimension to fracture properties for polymer matriax and reinforced composites was derived by a combining method of fracture mechanics (1,2) and the constrained topology of entangled networks (3).

Dependence of Linear Fractal Dimension on Fracture Properties

Relation of K_{IC} to Linear Fractal Dimension According to Griffth theory (1), K_{IC} may be expressed as:

$$K_{IC} = \left(\frac{2\Gamma^m E^m}{\Pi}\right)^{1/2} \qquad \cdots\cdots (1)$$

* Research Institute of Polymer Materials, Beijing University of Chemical Technology

After introducing the dependence (2) of Γ^m and E^m on the primary molecular weight of polymers, and combining the topology entangled networks (3), then we have:

$$K_{1C} = \left(\frac{2\Gamma^m E^m}{H}\right)^{1/2} \cdot \frac{\nu^m_{3eff}(\infty)}{\nu^m_{3ef}} exp\left[-\frac{3}{\sqrt{2}}D_f{}^m + \frac{3}{\sqrt{2}}\right] \quad \cdots\cdots\cdots (2)$$

Dependence of G_{1C} on Linear Fractal Dimensions According fracture mechanics (1), G_{1C} may be expressed as:

$$G_{1C} = \frac{K^2_{1C}}{E} \cdots\cdots\cdots (3)$$

Introducing Eq. (2) into Eq. (3), we have :

For polymer matriax

$$G^m_{1C} = 2\left(\frac{\Gamma^m_0}{\pi}\right)\frac{E^m_f}{E^m_0}\left(\frac{\nu^m_{3eff}(\infty)}{\nu^m_{3ef}}\right)exp\left(-\frac{3}{\sqrt{2}}D^m_f + \frac{3}{\sqrt{2}}\right)$$
$$= 2\left(\frac{\Gamma^m_0}{\pi}\right)\left(\frac{\nu^m_{3eff}(\infty)}{\nu^m_{3ef}}\right)exp\left(-\frac{3}{\sqrt{2}}D^m_f + \frac{3}{\sqrt{2}}\right) \cdots\cdots\cdots (4)$$

When the failure of reinforced composite specimens mainly occurs in polymer matriax, then Eq. (4) may be reduced to Eq. (5):

For reinforced composites:

$$G^R_{1c} = 2\left(\frac{\Gamma^m_0}{\pi}\right)\frac{E^R_f}{E^R_0}\left(\frac{\nu^R_{3eff}(\infty)}{\nu^R_{3ef}}\right)exp\left(-\frac{3}{\sqrt{2}}D^R_f + \frac{3}{\sqrt{2}}\right)$$
$$= 2\left(\frac{\Gamma^m_0}{\pi}\right)\left(\frac{\nu^R_{3eff}(\infty)}{\nu^R_{3ef}}\right)exp\left(-\frac{3}{\sqrt{2}}D^R_f + \frac{3}{\sqrt{2}}\right) \cdots\cdots\cdots (5)$$

When the testing of specimens is prepared with a same kind of polymers and is tested at a same condition, then the parameters of Γ^m_0, $\nu^m_{3eff}(\infty)$, $\nu^R_{3eff}(\infty)$, ν^m_{3ef} and ν^R_{3ef} are all constants, so Eqs. (4) and (5) may be rewritten as:

$$G_{1c} = Bexp\left(-\frac{3}{\sqrt{2}}D_f + \frac{3}{\sqrt{2}}\right) \cdots\cdots\cdots (6)$$

where $B = 2\left(\frac{\Gamma^m_0}{\pi}\right)\left(\frac{\nu_{3eff}(\infty)}{\nu_{3ef}}\right)$, taking logarithm on both side of Eq. (6), we have:

$$ln(G_{1c}) = ln(B) - \frac{3}{\sqrt{2}}D_f + \frac{3}{\sqrt{2}} \quad \cdots\cdots\cdots\cdots\cdots\cdots \quad (7)$$

Eq. (4) shows that there is a linear relation between $\ln(G_{1c})$ and D_f.

Comparision of the Theory with Experiments

The relation of G_{1c} to D_f for the polyarylether sulfone and the resin — based composite consisting of carbon fiber reinforced polyarylether sulfone was experimentally studied by Guangming Lin(4). The result is given in Fig. 1. It shows that Eq. (7) is in a good agreement with the experiments.

SYMBOLS USED

D_f= linear fractal dimension of polymers

D_f^m=linear fractal dimension of polymer matriax

D_f^R=linear fractal dimension of reinforced composites

E^m=extension modulus for polymers

E_0^m=extension modulus at initial time for polymer matriax

E_f^m=extension modulus at fracture time for polymer matrix

E_0^R=extension modulus at initial time for reinforced composites

E_f^R=extension modulus at fracture time for reinforced composites

G_{1C}=energy release rate

G_{1c}^m=energy release rate for polymer matriax

G_{1c}^R=energy release rate for reinforced composites

K_{1C}=fracture toughness

Γ^m=surface energy for polymers

Γ_0^m =surface energy for polymer matriax

ν_{3ef}^m =the number of elastically active extended polymer chains with a given molecular weight(M) in polymer matriax

$\nu_{3eff}^m(\infty)$ =the number of elastically active extended polymer chains with infinitive molecular weight($M_n=\infty$) in polymer matriax

ν_{3ef}^R =the number of elastically active extended polymer chains with a given molecular weight(M) in reinforced composites

$\nu_{3eff}^R(\infty)$ =the number of elastically active extended polymer chains with infinitive molecular weight($M_n=\infty$) in reinforced composites

REFERENCES

1. Willams, J. G., "Fracture Mechanics of Polymer", John Wiley & Sons (New York), 1984

2. Song, M. S. and Hu, G. X., 1993, Polymer Testing, 12(4), 311

3. Song, M. S. and Yang, J. C., 1995, J. Mater. Sci. Technol., 11(13), 197

4. Lin, G. M., etal, 1992, "Fractal Characterization of Fractured surfaces in a Resin—Based Composite", Proceeding of the International Symposium on Polymer Alloys and Composites, HongKong, 372.

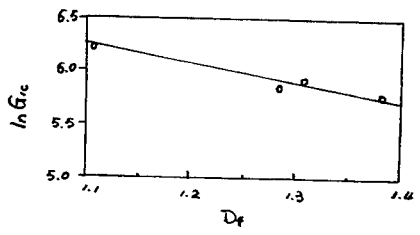

Fig. 1. Dependence of $\ln G_{1c}$ on D_f.

THE HIGH SPEED FRACTURE OF POLYMER COMPOUND MATERIAL WITH DISPERSAL CONTACT LAYER

A.D. ZJUZKOV ♦* , P.N. BOGDANOVICH, B.V. GRUNKIN.

It is shown that the fracture of dispersal contact layer (DCL) of material which made from phenolic compound filled by graphite is caused by thermodestruction of the binding in conditions of intensive frictional heating. As a result a quinoid structure having a lesser strength than the compound is formed. It lead to the fracture of part of a contact surface where the maximal temperature is observed. The wear intensity is proportional to contact area with maximal temperature and depend on the regularities of the heat transfer in contact zone. The deformations of contact layer have influence on a friction coefficient and on a heat discharge consequently.

The materials having a set of sphere particles as the contact layer are widly used in friction pairs characterized high sliding speed (15-25 m/s). A polymer matrix of spheres is usially filled by graphite to decrease the friction coefficient. In spite of frictional heating decreasing the fracture of polymer compound is dued to high temperature effects in this case.

The purpose of the work reported here, was to establish an influence of deformations and heating on the wear of compound.

The model investigation of temperature fields arising on contact spots of material with DCL were carried out previoslly (1). The pyrometry of contact region has allowed mesure the temperature and its distribution on contact spot. The results achieved are showing the existance of three varios heating

*Metal-Polymer Research Institute named after V.A. Belyi of Belarussian Academy of Sciences (MPRI BAS). Gomel, Belarus

regimes in dependence on sliding speed. The first regime is observed at relative low speed (in dependence of surface geometry from 0 to 10 - 15 m/s). The second and third regimes are specific high speed ones. They are characterized by the stability or the insignificant growth of maximal temperature on contact spots during speed increasing. This temperature is equal to the thermodestruction temperature of sphere material. The friction coefficient is decreasing with growth of speed during second regime. During third regime the friction coefficient is constant.

The wearing tests of polymer material with DCL were carried out at sliding speed 15-25 m/s (Fig. 1a,b). It was founded that the behavior of friction coefficient is analogous its behavior in the model experiment (see Figure 1a).

The analysis of wear debris of polymer material has allowed establish that the temperature exeeds the destruction temperature of polymer matrix during the debris formation (2). The frictional heating causes the fracture of polymer binding on the part of contact spot where the maximal temperature is observed. The process of fracture consists in the oxidation of methilen bind in the binding moleculas. Therefore the wear rate of polymer compound depends on the area of contact spot where the temperature exeeds the thermodestruction temperature of polymer matrix. For the determinating of this value we consider the temperature distribution on contact spot and its dependence on the deformations of contact layer.

The culculation of deformations has allowed establish that the deformations are increasing when the size of the contact layer particles is increasing. At the same time the depth of location of maximal deformation is increasing (see Figure 2). The culculation was made in accordance with the solution of the second principal task of elasticity for an infinite strip (3).

The comparation of the dependences drawn on Fig. 1b , 2 is showed the different modifying of the wear rate and the deformation with modifying of particle's size. If we'll consider the behavior of friction coefficient with modifying of particle's size, the correlation between its dependence and dependance of deformation has been drawn. Therefore we shall conclude that the deformations directly influence on the friction coefficient. At the same time the deformation influence on the wear rate is indirect.

We'll consider the temperature distribution on contact spot for the different size particles (see Fig. 3). For second and third regimes mentioned above the maximal temperature is almost constant. The increase of the friction coefficient occured with the increase of particle causes the lifting of the temperature distribution. At the same time the heat transfer intensifys from contact spot. It finds expression in the narrowing of the distribution curve. As a result the growth of area with maximal temperature is only occuring when the size of particle exeeds the some value.

Therefore the wear may be explane as a result of co-operation action of deformation and heating. The frictional heating cause the fracture of polymer binding on the part of contact spot. Than the deformation cause the formation and separation of wear debris.

REFERENCES

1. Zjuzkov A.D., and Bogdanovich P.N., 1996, "Modeling and Experimental Studies of Temperature Fields Arising on Intrerface of Three-Layer Polymer Material with Disresal Contact Layer Rubbed against Solid Plane", ICPSI-2 Proceedings, Namur, Belgium.

2. Zjuzkov A.D., Bogdanovich P.N., and Prushak V.J., 1996, "The Influence of Frictional Heating on Wear of Composite Materials with Dispersal Contact Layer", PICh 12th Conference Proceedings, Chenstohowa, Poland.

3. Kuznetzov E.A., 1982 " Dependence of Contact Characteristics from Modifying of Poisson ratio of Contacting Bodies", Problems of Friction and Wear V. 9, 12, 43-47.

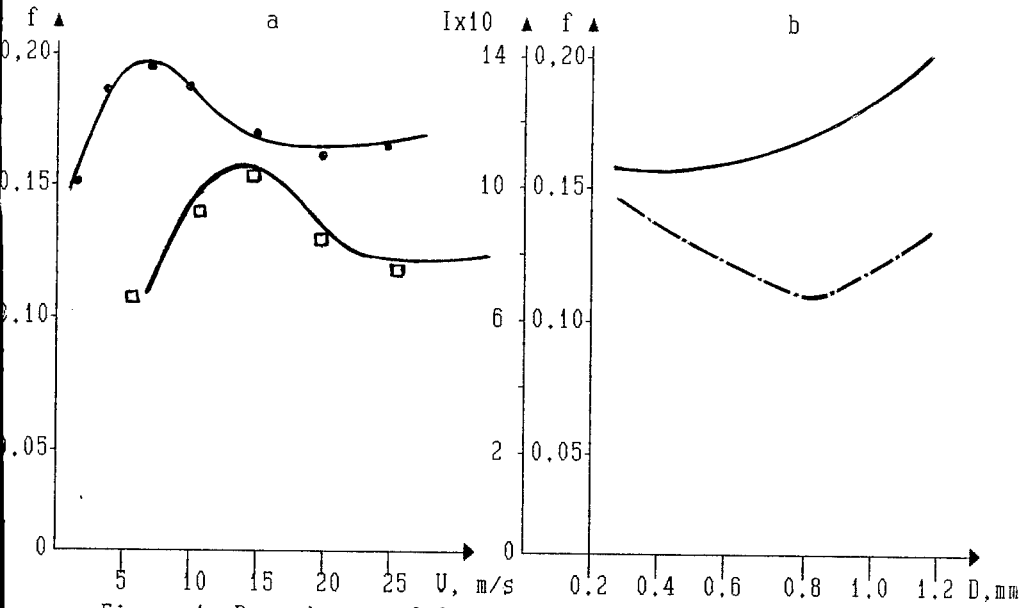

Figure 1. Dependences of friction coefficient(—) and ear rate (-.-) on sliding speed (a), on particles size (b) in omparasion with the model experiment (a)(□).

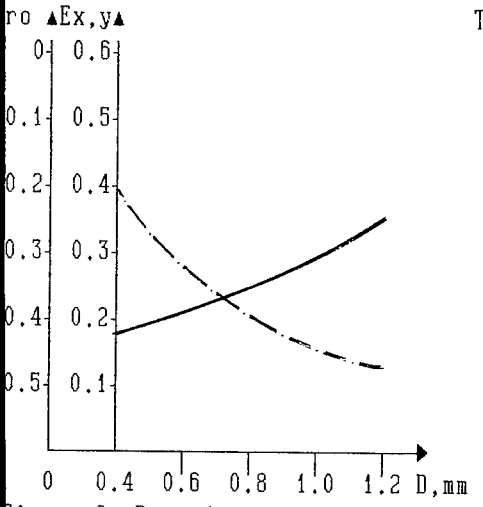

Figure 2. Dependences of deformations - -) and localisation of their maximum --) on particles size

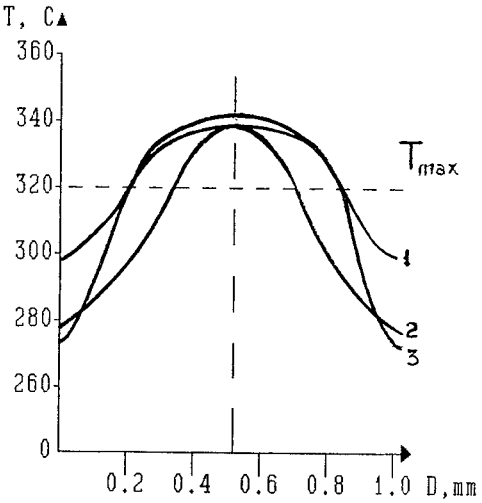

Figure 3. The temperature distribution on contact spot: 1-D=1.0; 2-D=0.6; 3-D=0.2 mm

The Effect of Chlorine on the Long-Term Durability of Crosslinked Polyethylene Pipe

Steven W. Bradley and Walter L. Bradley, Texas A&M University, College Station, Texas 77843-3123

The use of plastic pipe in infrastructure requires satisfactory service for 30-50 years. There is a great need to be able to predict long-term durability of plastic pipe with short term tests. Most work to date predicts the time to failure as a function of hoop stress for macroscopically ductile and brittle fracture but does not consider the effect of chlorine. This paper addresses new work in which the effect of chlorine on polyethylene is considered.

INTRODUCTION

Despite the poor experience with polybutylene plastic pipe in residual housing in the United States, there is still keen interest in the possibility of using plastic pipe in this enormous market. The biggest challenge is to be able to predict the long-term durability of plastic pipe with short-term tests. The basic approach which is used today is to pressurize the pipe to various levels and measure the time to failure as a function of the pressure, or associated hoops stress. Acceleration is provided by testing at higher temperatures than the anticipated service temperature. Typical test data is shown in schematically in Fig. 1. The so-called ductile rupture in Stage I begins with a local bulging of the pipe leading to splitting. Here the failure is ductile macroscopically and microscopically. Stage II "brittle" fracture shows only a pinhole leak or a small slit, which is the result of time dependent crack growth from some incipient flaw in the pipe. Stage III failure is due to environmental stress cracking leading to the initiation of a very large number of cracks, with failure resulting when there is local coalescence of these cracks. In hot water piping, chlorine is the primary cause of environmental attack.

SEM fractographs of the inside surface of crosslinked polyethylene pipe tested to failure at elevated temperatures are presented in Figures 2-4. The Stage III damage due to continuous flow of water with 3ppm chlorine at a pH of ~8.1 is seen in Fig. 2 at 50X, but can easily be seen with the naked eye. When tap water with an initial chlorine content of ~1ppm is used in a recirculating system (such as one would have in a floor heating system), only very fine cracking is noted, as seen in Fig. 3 at 800X. In the absence of any chlorine at all, Stage II failures are observed, as seen in Fig. 4, with only one large crack. The scale on the surface seen in Figs. 3 and 4 is cuprous oxide from the fitting used in the system and did not seem to degrade the plastic pipe. Removal of the cuprous oxide showed the same or lesser density of cracks than in regions which were bare.

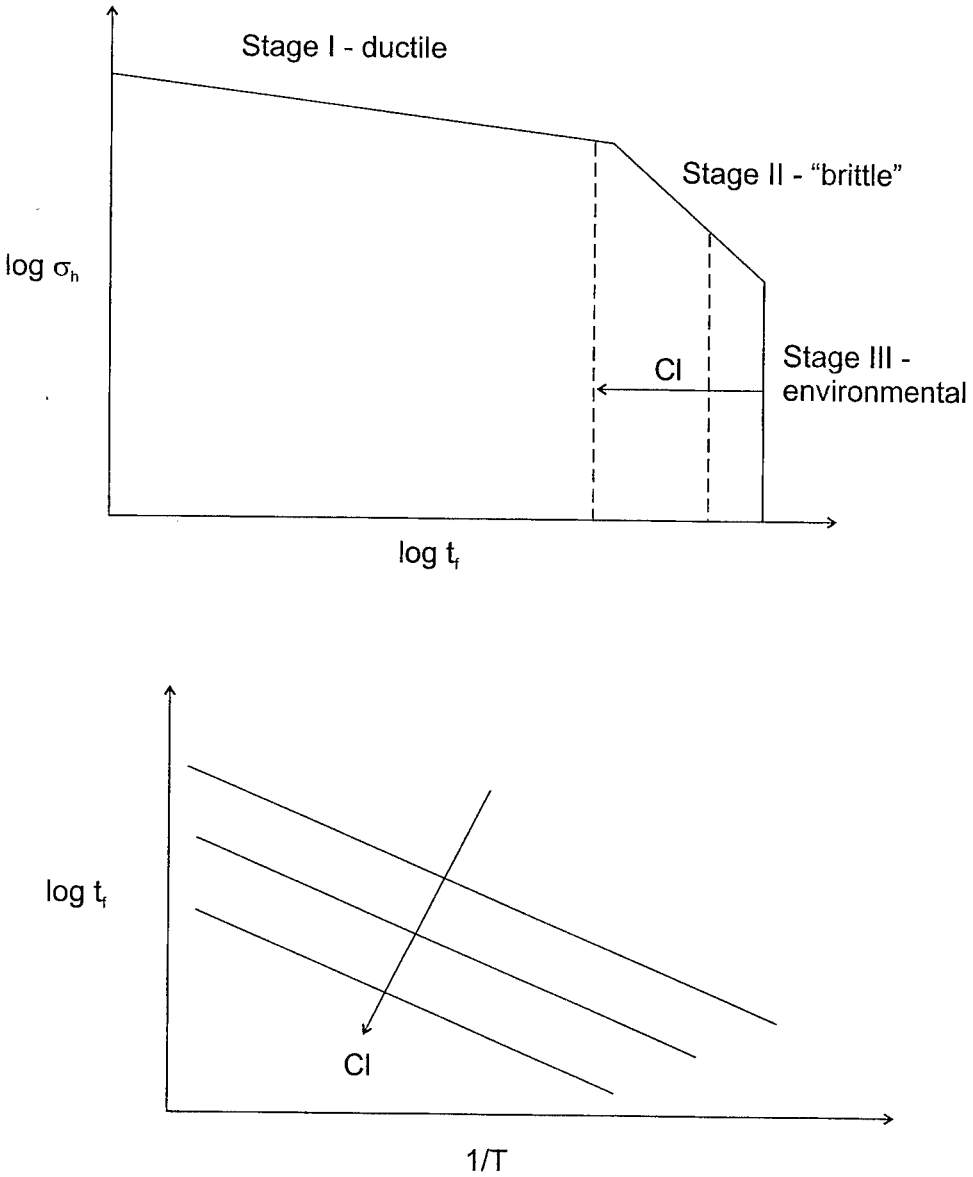

Fig. 1. Schematic of long term durability testing of plastic pipe.

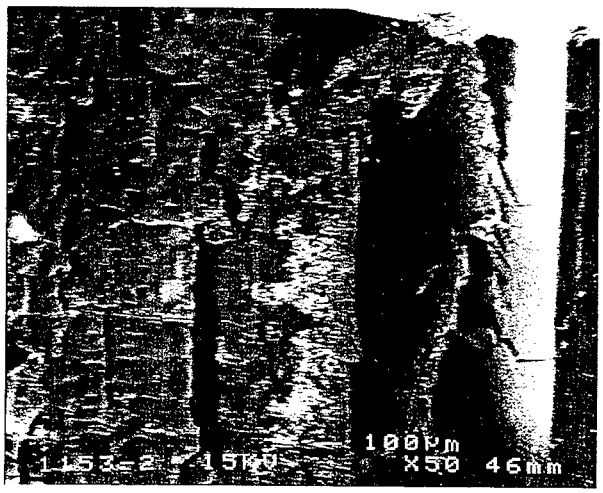

Fig. 2. SEM fractographs of inside diameter of crosslinked polyethylene pipe, 115°C, 3 ppm chlorine, t_f~3 weeks, 50X.

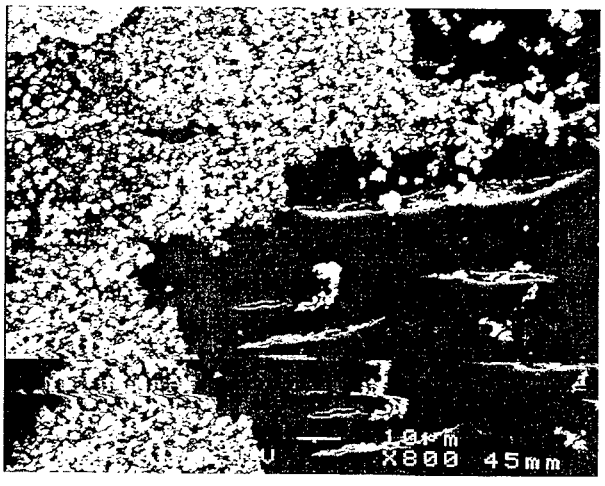

Fig. 3. SEM fractograph of inside diameter of crosslinked polyethylene pipe, 105°C, tap water recirculated, t_f~5 months, 800X.

Fig. 4. SEM fractograph of inside diameter of crosslinked polyethylene pipe, 120°C, 0 ppm chlorine, t_f~5 months, 50X.

Chlorine is added as a very aggressive oxidizing agent to purify the water. However, it can also oxidize the polymer, leading to chain scission, reduction in molecular weight, and loss of strength and ductility. Chlorine is generally present as HClO in water, with dissociation to H^+ and ClO^-. It is the ClO^- radical that appears to be responsible for chain scission. The concentration of ClO^- depends on both the chlorine concentration in the water (usually 0.5-5ppm) and the pH (usually 6.5-8.5). Since the chlorine content in water and the pH vary widely in the USA, it is desirable to monitor the oxidation reduction potential which depends on both the chlorine content of the water and the pH. Different water with widely varying chlorine content (and possible metal ion contents as well) but similar oxidation reduction potential (due principally to differences in pH) should give similar rates of environmental degradation. When the chlorine content is sufficiently large, Stage II "brittle" fracture may not be observed at all. The usual relationships for shifting failure time by elevating temperature will most likely not be valid for Stage III environmental attack, as the rate limiting processes may be different or the same processes may have a different activation energy in the presence of chlorine. Determining the failure time as a function of temperature at several temperatures for various chlorine contents will be necessary to determine the activation energy needed to predict long-term service. A further (but beneficial) complication is that the stabilization package will postpone this degradation process. Thus, the consumption of the stabilization package by oxidation (from inside or outside) by leaching at the inside diameter or diffusion controlled oxidation is a key issue. Significant degradation such as that seen in Fig. 2 begins only after the OIT time is essentially zero.

EFFECTIVE YOUNG'S MODULUS OF A POLYMER COMPOSITE

R Wojnar*

Using an analogy between a polymer chain configuration and random walk situation we derive a formula for the elastic modulus of a nonhomogeneous polymer chain arranged in series. This formula together with corresponding result for a polymer chain arranged parallely, lead to an effective elastic modulus formula for a general three-dimensional Gaussian polymer net. In a particular case of series-parallel arrangements of polymer chains, a mean geometric formula for the effective elastic modulus is obtained.

Introduction

The tension of an elastic solid can be expressed as the change of Helmholtz free energy per unit extension

$$f = \left(\frac{\partial A}{\partial \lambda}\right)_T$$

Here

$$A = E - TS$$

where E denotes internal energy, T - temperature and S - entropy. Experimental evidence indicates that in a large class of rubber-like polymers there is no change in the internal energy of the system on deformation. If ΔA and ΔS denote the change of free energy and entropy respectively, for such class of polymers, we obtain

$$\Delta A = - T \Delta S$$

This implies that the stress in a rubber-like polymer is represented by the entropy derivative w.r. to the extension multiplied by a negative function.

The entropy of a polymer network is generally computed from the number of configurations of the system of polymer chains composing the whole system. It is shown in [2, 3] that a problem of random walk described by the probablility $P_v(r)$ is equivalent to that of a chain polymer molecule shape.

*Polish Academy of Sciences, IPPT Institute of Fundamental Technological Research, Świętokrzyska 21, 00-049 Warszawa, Poland, rwojnar@ippt.gov.pl

Random walk

At first we are going to investigate the probability

$$P_\nu(r ; l_1, l_2, ..., l_\nu)$$

that after ν stretches $l_1, l_2, ..., l_\nu$ taken in directions at random the distance from the starting point $\mathcal{O}$, shall be less than an assigned magnitude r. As was pointed out by Lord Rayleigh [1] such probability can be expressed by the formula

$$P_\nu(r ; l_1, l_2, ..., l_\nu) = \frac{2}{\pi} \int_0^\infty dx \, \frac{\sin rx - r x \cos rx}{x} \, \frac{\sin l_1 x}{l_1 x} \, \frac{\sin l_2 x}{l_2 x} \, ... \, \frac{\sin l_\nu x}{l_\nu x}$$

If we assume that the l's are mutually equal in two groups, one counting m, and the second n elements, *i.e.*

$$l_1 = l_2 = ... = l_m = l, \qquad l_{m+1}, l_{m+2}, ..., l_{m+n} = L$$

where $m + n = \nu$, we get

$$P_\nu(r ; l, L) = \frac{2}{\pi} \int_0^\infty dx \, \frac{\sin rx - r x \cos rx}{x} \left(\frac{\sin lx}{l x} \right)^m \left(\frac{\sin Lx}{L x} \right)^n$$

This is the chance that the distance is less than r. For the chance that the distance lies between r and r+dr, we have as the coefficient of dr

$$\frac{dP_\nu}{dr} = \frac{2}{\pi} r \int_0^\infty dx \; x \; \sin rx \left(\frac{\sin lx}{l x} \right)^m \left(\frac{\sin Lx}{L x} \right)^n$$

So

$$\frac{1}{r} \frac{dP_\nu}{dr} = \frac{2}{\pi} r \int_0^\infty dx \; x \; \sin rx \; \exp \left[- (m l^2 + n L^2) x^2/6 \right] \times \{ 1 + m h_4 (l x)^4 + m h_6 (l x)^6 + ... \} \times \{ 1 + n h_4 (L x)^4 + n h_6 (L x)^6 + ... \}$$

where

$$h_4 = -1/180, \quad h_6 = -1/2835, ...$$

The expression for the principal term is

$$\frac{dP_v}{dr} = \frac{4\ b^3}{\sqrt{\pi}}\ r^2\ e^{-b_s^2 r^2}$$

where

$$b_s^2 = \frac{3}{2}\ \frac{1}{m\ l^2 + n\ L^2}$$

Hence the probability density

$$p(r) = \frac{1}{4\pi r^2}\frac{dP_v}{dr} = \frac{b^3}{\pi^{3/2}}\ e^{-b^2 r^2}$$

and for n=0 we obtain the known case of a walk with constant stretch, [1,4]. If we let

$$b^2 = \frac{3}{2}\ \frac{1}{m\ l^2} \qquad B^2 = \frac{3}{2}\ \frac{1}{n\ L^2}$$

we have

$$\frac{1}{b_s^2} = \frac{1}{b^2} + \frac{1}{B^2}$$

Entropy of a nonhomogeneous chain

The case of a random walk with variable stretches corresponds to that of a non-homogeneous polymer chain made of different chains arranged in a series. For the entropy of a polymer made of two different chains we obtain

$$s_s = -\ k_B\ T\ \ln\ p(r)\ = c_s\ +\ k_B\ T\ \ b_s^2$$

where k_B is the Boltzmann constant and c_s is a constant.

On the other hand, for two chains connected parallely (i.e. with identically placed ends), the probability density is given by, [2-4]

$$p(r) = \frac{b_p^3}{\pi^{3/2}}\ e^{-b_p^2 r^2}$$

where $b_p^2 = b^2 + B^2$ and the entropy of two chains is

$$s_p = -\ k_B\ T\ \ln\ p(r)\ = c_p\ +\ k_B\ T\ \ b_p^2$$

where c_p is a new constant.

In general, the polymer chains form a three dimensional net and the two described cases are only the limit cases of a three dimensional net.

If we note that for any two positive different numbers a and b

$$a + b > \sqrt{ab} > \frac{ab}{a + b}$$

by virtue of the probability density formula

$$p(r) = \frac{b_g^3}{\pi^{3/2}} e^{-b_g^2 r^2}$$

we obtain

$$b_p > b_g > b_s$$

In a special case, when the system of chains has a symmetry

$$b_g = \sqrt{b_p\, b_s} \qquad (1)$$

Elastic moduli

The elastic Young's modulus G of a polymer chain is proportional to the square of constant b and the result (1) gives

$$G_g = \sqrt{G_p\, G_s} \qquad (2)$$

Clearly, the result (2) is obtained for a three dimensional Gaussian net. For a two dimensional elastic composite the mean geometric formula (2) was obtained in by Berdichevskiy in [5] and by the author in [6]. The mean geometric electric conductivity formula was derived by Keller [7].

REFERENCES

1. Lord Rayleigh, Phil. Mag. 37, 321 (1919)

2. M.V. Volkenstein, Configurational statistics of polymeric chains, Interscience, New York 1963

3. P. J. Flory, Statistical mechanics of chain molecules, Interscience Publishers - John Wiley, New York-London 1969

4. L.R.G. Treloar, The physics of rubber elasticity, Clarendon Press, Oxford 1958

5. V. L. Berdichevskiy, Variational principles for mechanics of continuous media, Izd. Nauka, Moskva 1983

6. R. Wojnar, "On elastic moduli of a two-dimensional two-phase system", Minisymposium on homogenization, GAMM Conference, Prague 1996

7. J. B. Keller, J. Math. Phys. 5, 548 (1964)

MODELLING OF RAPID CRACK PROPAGATION ALONG PRESSURISED PLASTIC PIPES

G.P. Venizelos, A. Ivankovic and P.S. Leevers*

The most dangerous failure mode of a pressurised pipeline is rapid crack propagation (RCP). In our effort to establish a design procedure against RCP we have been developing a finite volume (FV) numerical model. The aim is to predict safe service conditions for a plastic pipeline, based on the results of our small-scale (S4) laboratory pipe test. This paper presents in brief the implementation of the FV model in this design procedure. Simulations of S4 tests yield values of fracture resistance that compare favourably with other fracture tests and a recently developed analytical fracture model. Matching fracture resistance to crack driving force (again obtained via FV simulations) we predict critical conditions for both the S4 and the full-scale test.

INTRODUCTION

The widespread use of plastic pipes for gas and water distribution, under ever increasing performance demands, makes safeguarding against RCP imperative. Most buried distribution pipelines are now made from advanced grades of polyethylene which although extremely tough, can fail in RCP under certain conditions. A fast-running crack, if initiated by impact or otherwise, can continue to 'unzip' a pipeline at speeds of 100-300 m/s for an indefinite distance, under stresses much lower than the material's ultimate strength.

New standards for pipe systems, specify a *critical pressure*, above which sustained RCP becomes possible, using the Small-Scale Steady-State (S4) test [1,2]. However, S4 results have to be correlated with 'full-scale' results. The full-scale test is extremely expensive and time consuming and in addition, a glut of data might tend to confuse rather than clarify the situation. Appropriate modelling has to be included in the analysis. The critical pressure is determined from a balance between the crack driving force, G, exerted by the loaded structure, and the dynamic fracture resistance of the material, G_D.

We are implementing the following procedure: • Perform S4 tests on a particular pipe grade. • Simulate the S4 tests to obtain the dynamic fracture resistance of the pipe. • Compare fracture resistance to crack driving force (again obtained via FV simulations) to predict critical pressure for both the S4 and the full-scale test. Computationally, this problem is extremely demanding as RCP is a complex phenomenon, involving dynamic structural deformation and fracture, as well as fluid and soil dynamics, all closely coupled together.

THE FINITE VOLUME MODEL FOR RAPID CRACK PROPAGATION IN PLASTIC PIPE

The work presented here is an initial stage in developing a unified computational model, based on FV discretisation, for coupled fluid-structure analysis of RCP in plastic pipelines. This is an extremely demanding computational problem, involving the dynamic interaction of a non-linear elastic pipe with a contained (in)compressible fluid and a surrounding quasi-fluid backfill.

Literature on the FV method includes: • A detailed description of a model for structural analysis of complex domains employing unstructured meshes with cells of arbitrary topology [3,4]. • Application of the method to non-linear solids [5,6]. • Analysis of coupled fluid flow, heat transfer and stress analysis [7]. • FV modelling of fracture problems including dynamic fracture [8-10]. Here, only a brief outline of the method is given.

The formulation employed in this work is restricted to small strains. Material behaviour is represented by incremental Hooke's law. The starting point is the momentum equation in integral form, and its discrete counterparts are obtained as follows: • Vector and Tensor components related to a global Cartesian system are generally preferred, as they lead to a strong conservation form of the momentum equation. For pipe problems however, a cylindrical

* Mechanical Engineering Department, Imperial College, London SW7 2BX

co-ordinate system is chosen because this produces a structured mesh. • The solution domain is divided into a number of contiguous cylindrical control volumes (cells) with six cell-faces. • The time domain is subdivided into an arbitrary number of time-steps. • The computational nodes are placed at the centres of the cells where displacement and stress increments are stored. Boundary nodes required for the specification of boundary conditions reside at the centres of the boundary cell-faces. • Both surface and volume integrals are calculated employing the mid-point rule. A piece-wise linear spatial distribution of displacement increments is employed, guaranteeing a second order accurate spatial discretisation. • A fully implicit time discretisation is adopted in the temporal variation of dependent variables for its unconditional stability. The magnitude of the time step is restricted only by the temporal accuracy requirement .

FV discretisation results in three mutually coupled sets of N linear algebraic equations with three unknown components of displacement increments (N is the number of control volumes). A segregated solution procedure [3] is employed to solve these equations. The sets of equations for each dependent variable are temporarily decoupled by assuming that coefficients and source terms are known, i.e. these coefficients and source terms are calculated using the values of the dependent variables from the previous iteration or the previous time step. As a consequence, a system of linear algebraic equations is obtained for each component of displacement increment, in the form:

$$A\delta\boldsymbol{u} = \boldsymbol{b}, \qquad (1)$$

where: A is a seven diagonal / diagonally dominant / positive definite / symmetric sparse $N \times N$ matrix, vector $\delta\boldsymbol{u}$ contains the vector component values of current displacement increments, and $\boldsymbol{b}$ accommodates the sources at N nodes. The segregated solution approach allows reuse of the same storage for A, $\boldsymbol{b}$ and $\delta\boldsymbol{u}$ components, resulting in very small requirements in computer memory (only $8N$ storage locations are required). Eqn. 1 is solved sequentially for each $\delta\boldsymbol{u}$ component in turn, using a line-by-line TDMA iterative solver which takes advantage of the structured mesh employed in this study. There is no need to solve Eqn. 1 to a tight tolerance since A and $\boldsymbol{b}$ are only approximations (based on the solution from a previous iteration). A reduction of residuals by one order of magnitude is sufficient. After solving Eqn. 1 for all three components of displacement increments, the elements of coefficient matrix A and source vector $\boldsymbol{b}$ are updated. The procedure is repeated until overall convergence is reached, i.e. until the sum of absolute residuals for all equations is below a prescribed tolerance (typically 10^{-3}).

Having computed the displacement increments, stress increments are obtained from the constitutive relations, and the total displacements and stresses in the current time step are calculated. The solution is then advanced to the next time step and the whole procedure is repeated.

In our current FV model of pipe RCP, crack length history is prescribed and the contained fluid is represented by a pattern of pressure forces which are uniform ahead of the crack front ($p = p_t$) and decay linearly behind it over the decompression length, L, (Fig. 1). Neither crack speed or decompression length need to be constant with time. A fixed-mesh, cell-release technique is employed for the analysis of an axial crack with a straight front, propagating rapidly along a pipe. Backfill effects are not accounted for at this stage. Due to symmetry, only half of the pipe is modelled.

The initial conditions for the transient calculation are obtained by solving for the quasi-static loading of the uncracked pipe under uniform pressure p_t. The crack is initiated from zero length and propagated by releasing the row of cells along the straight through-thickness front, according to the specified crack length history (generation mode analysis). Surface forces on the released cell faces are decayed linearly from their maximum values at the instant of release, to zero as crack traverses the cell face. This is the *holding back force* procedure, well known in RCP modelling. The energy absorbed by the propagating crack is calculated either from the local work done by these forces or from the global energy balance. The two approaches give matching results, demonstrating the accuracy of the FV model [11].

Crack driving force vs. crack length and crack driving force vs. crack speed

In the FV model of the full-scale test, axial displacements at the opposite end from crack

initiation and circumferential displacements (of the uncracked pipe) at the symmetry plane are set to zero. Additional displacement constraints imposed on the pipe by the test apparatus [2] are implemented in the model of the S4 test. From each transient simulation we obtain the variation of crack driving force with crack length.

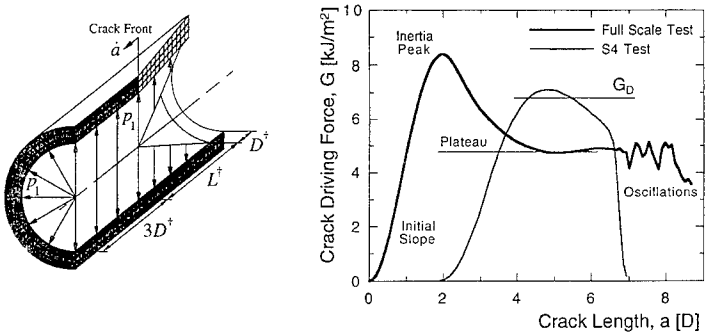

FIGURE 1: (a) Schematic of the finite volume model for rapid crack propagation in pipe; (b) Computed curves of crack driving force as a function of crack length
(PE80, 160SDR11, FS: p_o=7.13 bar, $\dot{a}$=100 m/s, L=1.5 D, S4: p_o=3 bar, $\dot{a}$=100 m/s, L=2.5 D).

A typical G vs. a curve of the full-scale test exhibits the following features (Fig. 1b): • An initial slope which depends on the inertia of the system: the higher the crack speed the smaller the slope. • An inertia peak which corresponds to a profile of maximum crack opening [11]. This inertia peak is absent at high crack speeds. • A plateau which corresponds to a profile of constant crack opening translating along the pipe [11]. • Oscillations, over the last diameters of crack growth, due to contact between the crack flaps [11].

A typical G vs. a curve of the S4 test exhibits the following features (Fig. 1b): • An initial slope which depends on the inertia of the system: the higher the crack speed the smaller the slope. • An absence of inertia peak, as the ends of the pipe are constrained to zero radial displacement due to the end caps [2]. • Zero crack driving force over the first two diameters of crack growth, as the gas is displaced by the initiation anvil [2]. Zero crack driving force at a crack length of 7 diameters (7D is the standard length of an S4 test pipe) again due to the end cap constraint. • When the FV inputs of crack speed and decompression length are from experimental records, the computed G is a measure of the pipe fracture resistance because $G = G_D$ at propagation (Fig. 1b).

By conducting simulations at various combinations of crack speed and decompression length we obtain a family of G vs. $\dot{a}$ curves (Fig. 2). The G we extract from each simulation is either the plateau value – full-scale test – or the average over a crack length of 4-6 diameters – S4 test (Fig. 1b). For a given pipe size, we only need to compute the G vs. $\dot{a}$ curves at one value of pressure, as we have established that G is proportional to the square of the pressure.

Obtaining fracture resistance and predicting critical pressure

By simulating a series of S4 experiments – at and above critical pressure – we obtain the characteristic curve of fracture resistance as a function of crack speed, G_D vs. $\dot{a}$ (Fig. 2a). Again, the value of G_D (and $\dot{a}$) that we extract from each simulation is the average over a crack length of 4-6 diameters. It is obvious from the shape of the curve that there exists a minimum G_D and a limiting $\dot{a}$. In Fig. 2b we compare the S4 fracture resistance curve against data from other tests and the recently proposed thermal decohesion fracture model [12]. There is excellent agreement between the values of $G_{D,min}$ as determined by the three fracture tests (High Speed Double Torsion, Hydrostatic S4, S4) and the model. There is however a discrepancy between the value of limiting crack speed as predicted by the model and as observed in the S4 test. We believe this is due to the parabolic shape of the crack front which is not currently (but can be) accounted for in the thermal decohesion model.

In order to predict critical conditions, we choose the most representative of experimental evidence from the G vs. $\dot{a}$ curves in Fig. 2. These are the curves of 3D and 4D decompression length, for the S4 and the full-scale test respectively (bold lines in Fig. 2). The predicted critical pressure is the pressure that satisfies critical conditions, i.e. $G_{max} = G_{D,min}$, and the predicted crack speed is the speed at $G = G_{max}$ (Fig. 4). Predictions and measurements are summarised in the table below.

	Crack Speed [m/s]		Critical Pressure [bar]	
	Predicted	Measured	Predicted	Measured
S4 test	140	175	1.72	1.75
full-scale test	220	260	1.80	9.00

CONCLUSIONS

The finite volume method is a powerful tool for modelling rapid crack propagation in the S4 and full-scale pipe tests. We have obtained values of fracture resistance that compare favourably with other fracture tests and a recently developed analytical fracture model. We have achieved good prediction of critical conditions in the S4 test but have not yet obtained satisfactory prediction of critical conditions in the full-scale test. This is partly due to backfill effects in the full-scale test which had not, up to now, been accounted for in the model. Evidence from an approximate backfill model suggests a considerable improvement in the predicted critical pressure. Another area of uncertainty is the relationship between pressure, crack speed and decompression length. A coupled model of fluid/structure interaction – currently under development – will resolve this issue. Last but not least, crack path/front shape effects are as yet unquantified and may also prove important.

REFERENCES

[1] Yayla, P. & Leevers, P.S. *Eng. Fract. Mech.* **42** (1992) 675-682.
[2] ISO DIS 13477, "Thermoplastics pipes for the conveyance of fluids - Determination of the resistance to Rapid Crack Propagation (RCP) - Small-Scale-Steady-State (S4) Test".
[3] Demirdzic, I. & Muzaferija, S. *Int. J. Num. Meth. Eng.* **37** (1994) 3751-3766.
[4] Demirdzic, I. & Ivankovic, A., *Finite Volume Stress Analysis*, Lecture Notes, Imperial College, 1996.
[5] Demirdzic, I., Martinovic, D. *Comp. Meth. App. Mech. Eng.* **109** (1993) 331.
[6] Dioh, N.N., Ivankovic, A., Leevers, P.S. & Williams, J.G. *Proc. R. Soc.*, London A **449** (1995) 187-204.
[7] Demirdzic, I. & Muzaferija, S. *Comp. Meth. App. Mech. Eng.* **125** (1995) 235-255.
[8] Ivankovic, A., Demirdzic, I., Williams, J.G. & Leevers, P.S. *Int. J. Fracture* **66** (1994) 357-371.
[9] Ivankovic, A. & Williams, J.G. in *Dynamic Fracture Mechanics*, ed. M.H. Aliabadi, Computational Mechanics Publications, Southampton, 1995, 101-135.
[10] Ivankovic, A., Muzaferija, S. & Demirdzic, I. *Proceedings IUTAM Symposium on Innovative Computational Methods for Fracture and Damage*, Spring 1997.
[11] Ivankovic, A. & Venizelos, G.P. *J. Mech. Phys. Solids* (submitted).
[12] Leevers, P.S., *Int. J. Fracture* **73** (1995) 2, 109-127.

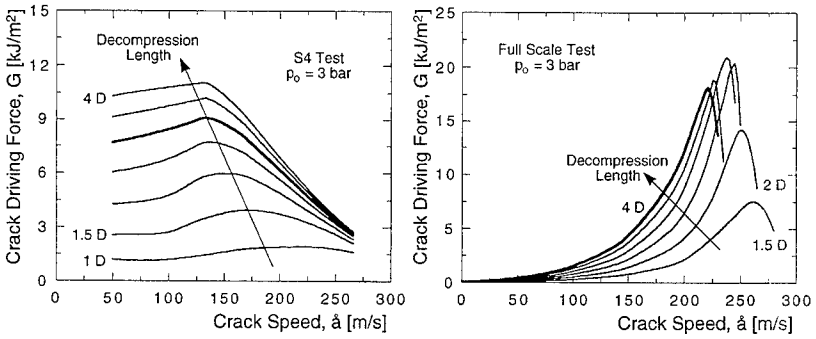

FIGURE 2: Computed crack driving force as a function of crack speed, PE80, p_o = 3 bar; (a) S4, 160SDR11 (b) FS, 250SDR11.

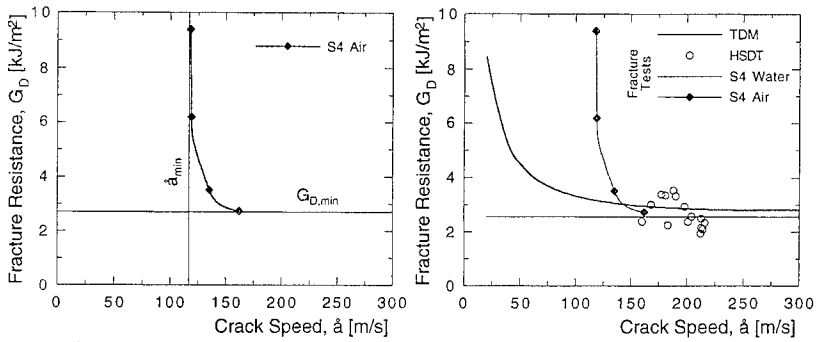

FIGURE 3: Fracture resistance as a function of crack speed, PE80; (a) Obtained via finite volume simulation of S4 experiments, 160SDR11; (b) Comparison of data from three fracture tests and the thermal decohesion model.

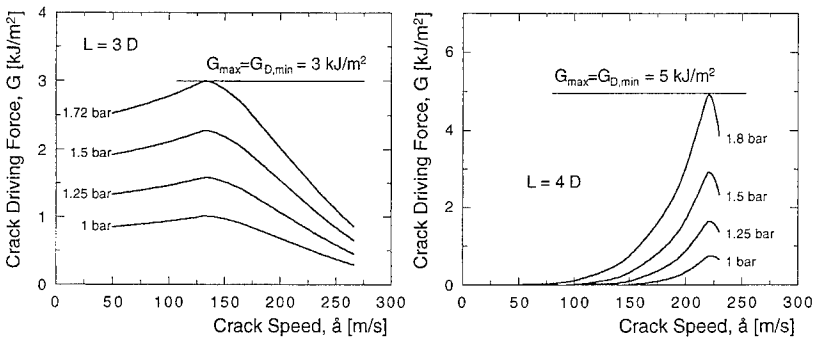

FIGURE 4: Schematic representation of the method for predicting critical pressure; (a) S4, 160SDR11; (b) FS, 250SDR11.

THE MEASUREMENT AND MODELLING OF THE STRAIN DEPENDENT POISSON'S RATIO IN MICROPOROUS POLYETHYLENE

R.S. Webber*, K.L. Alderson and K.E. Evans+**

Techniques have been developed to enable continuous monitoring of the strain dependency of the Poisson's ratio of three forms of ultra high molecular weight polyethylene (UHMWPE). In conjunction with simple geometric modelling based on the UHMWPE microstructure, a full analysis has been performed of the interdependence of microstructure and properties. It is now possible to predict the microstructural form required to obtain a specific Poisson's ratio and to relate this to initial processing conditions.

INTRODUCTION

Ultra high molecular weight polyethylene (UHMWPE) can be readily processed via the powder processing techniques of compaction, sintering and extrusion (1) to produce a structural material with an anisotropic strain dependent Poisson's ratio. The Poisson's ratio that can be achieved is dependent on the microstructure generated in the material, which consists of nodules interconnected by fibrils. This interconnectivity is crucial in determining the magnitude and sign of the range of Poisson's ratios displayed by the material since both highly positive and highly negative values are equally possible. A schematic of the microstructure required for each of these two scenarios is shown in fig. 1.

Initial attempts at studying the Poisson's ratio and its relationship with the microstructure were necessarily very simple due to the nature of the first specimens obtained which tended to be both too small and irregular to undergo conventional testing techniques successfully. Single values of Poisson's ratio were obtained from simple compression testing, with very many tests needed to construct an approximate strain-history map. This was related to the microstructure of the material by a simple geometrical model (2) based on nodule translation which requires knowledge of nodule shape and size, fibril length and the angle between the fibril and nodule.

* Department of Materials Science and Engineering, University of Liverpool, UK
** Faculty of Technology, Bolton Institute, UK
\+ School of Engineering, University of Exeter, UK.

These parameters were measured using micrographs obtained from a scanning electron microscope (SEM).

This approach, however, is very limited. In particular, it requires that any sample produced be destructively analysed to provide information and it gives rise to single values of Poisson's ratio for each compression test performed instead of providing the ideal situation of a continuous strain history which would completely characterise the material.

Production of larger specimens with a greater structural integrity (i.e. a modulus of 0.2GPa (3)) provided a spring board for work to begin to develop new measuring techniques to enable continuous monitoring at both microstructural and macrostructural levels to be carried out.

TECHNIQUES FOR MEASURING THE STRAIN DEPENDENT POISSON'S RATIO

On a macrostructural level, the specimens underwent compression testing as previously, but the tests were monitored using video extensometry. This has allowed the complete strain history of a single sample to be recorded and, by manipulation of the experimental data, it is now possible to study changes in both Poisson's ratio and modulus with applied strain. An example of a Poisson's ratio against strain plot is shown in fig. 2.

Changes to the microstructure of the specimens have also now been observed by use of an in-built SEM straining stage. The importance of this is that the actual mechanism that leads to the strain dependent effect can now be identified for the first time, allowing the simple geometrical model (based solely on nodule translation) which has been used effectively to be experimentally verified.

APPLICATION OF MEASUREMENT AND MODELLING TECHNIQUES TO OTHER FORMS OF UHMWPE

Once the measurement and modelling techniques had been established and found to apply successfully to the base microporous material, two further forms of microporous UHMWPE were fabricated by modifying the processing route (4) and tested. One of these was produced by omitting the compaction stage of the processing route, resulting in an extrudate lacking in structural integrity. The other produced a structural form of the material by replacing the extrusion stage of the processing route by multiple sintering of the UHMWPE compacts.

Continuous monitoring of the strain dependency of the Poisson's ratio for both these forms of UHMWPE using video extensometry techniques revealed that they were very different. The first form was found to be highly strain dependent while the second found to still display strain dependent behaviour but to be more isotropic. The microstructural variations were also studied using the SEM straining stage and the parameters measured and compared between the 3 forms of the UHMWPE. This allowed all the forms to be modelled successfully.

Thus, it is now possible to both predict the microstructure of the material from the strain-history of the specimens or to predict the strain dependent Poisson's ratio, or indeed modulus, from the microstructure. This can be related to initial processing conditions, allowing tailoring of the processing route to the required Poisson's ratio to be undertaken.

CONCLUSION

By a combination of continuous monitoring of the strain dependency of the Poisson's ratio macrostructurally and microstructurally and simple geometrical modelling, it is now possible to predict the microstructural form required to obtain a specific Poisson's ratio and stiffness and hence to relate this to initial processing conditions.

ACKNOWLEDGEMENT

RSW would like to acknowledge the support of EPSRC through a studentship.

REFERENCES

1. Alderson, K.L. and Evans, K.E., Polymer 33 (1992) 4435.
2. Evans, K.E., J. Phys. D: Appl. Phys. 22 (1989) 1870.
3. Evans, K.E. and Alderson, K.L., J. Mat. Sci. Lett. 11(24) (1992) 1721.
4. Webber, R.S., PhD Thesis, University of Liverpool (1997).

FIGURE 1. Schematic representation of the microstructure which produces (a) highly negative and (b) highly positive Poisson's ratios.

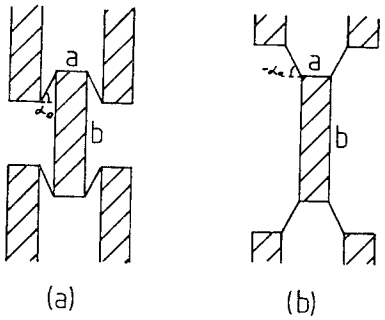

FIGURE 2. An example of a Poisson's ratio against strain plot generated by video extensometry.

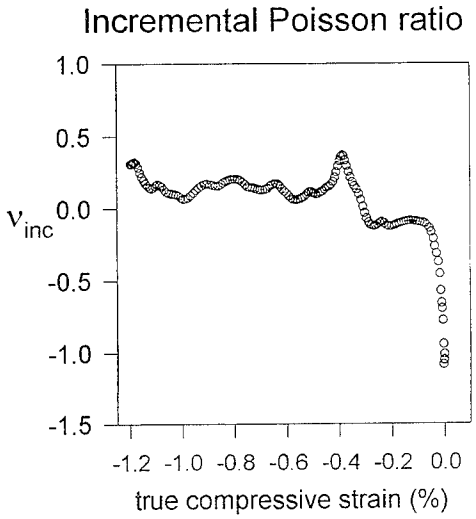

CAVITATIONAL DAMAGE IN PVDF STRAINED AT ROOM TEMPERATURE

S. Castagnet * , J.L Gacougnolle * , P. Dang **

Uniaxial tensile and tensile cyclic tests were performed on apolar poly(vinylidene fluoride) (PVDF) at room temperature. By means of measurements of both axial and transverse strains, the volume strain of the sample can be deduced. Results of this mechanical approach give the evidence of a cavitational damage in this polymer. The strain rate dependance of this damage is studied.

INTRODUCTION

Non-piezoelectric Poly(vinylidene fluoride) (PVDF) is a cristalline polymer known to exhibit a double glass-transition (Tg1 = -40°C ; Tg2 = 60°C). Below Tg1, the whole amorphous phase is glassy and the fracture is brittle. Between Tg1 and Tg2, only free amorphous phase is relaxed ; during elongation, a whitening occurs in the sample which breaks in the striction area. Above Tg2, the whole amorphous phase is relaxed and the striction propagates. Whitening is the macroscopic appearance of micro-voids created in the strained material. This damage looks very similar to this occuring in Polypropylene (1)(2). The purpose of this paper is to study the damage of strained PVDF at room temperature through a global mechanical approach based on uniaxial creep and tensile tests.

EXPERIMENTAL

The studied PVDF form α was supplied by ELF-ATOCHEM (Kynar 1000 HD®) as extruded sheets 4 mm thick. This polymer is characterized by the following molecular weight distribution, measured by gel permeation chromatography : $M_w \approx 150000$ g.mol^{-1} and $M_n \approx 80000$ g.mol^{-1}, meaning that, on average, a molecular chain is made up of 2350 [CH_2-CF_2] monomers and is 0,35 µm long. The cristallinity of this material, deduced from WAXS measurements, is 55%. Dumbbell samples were machined from the extruded sheets in the extrusion direction with specifications ISO R527.After machining, sections were grained and edges smoothed with fine emery papers. Local variations of the cross-section width resulting from this specimen preparation are about 2%.

Tensile (continuous loading) and tensile cyclic (following loading / unloading steps) tests were performed at room temperature in an Instron Testing Machine. Measurements were made at three different crosshead speeds of 1, 10 and 100 mm/min, implying strain rates from 0,00025 to 0,025 s^{-1}. Creep tests were performed using the same machine. The applied stress varied from 40 to 45 Mpa.

* Laboratoire de Mécanique et Physique des Matériaux ENSMA Site du Futuroscope BP109 86960 Futuroscope Cédex FRANCE

** Centre d'Etudes de Recherche et de Développement ELF-ATOCHEM 27470 Serquigny FRANCE

To estimate the cavitational damage occuring in strained PVDF, volume strain was measured using the double extensometric system illustrated Figure 1. Axial strains were measured using a classical strain gage extensometer and transverse strains using a laser scan micrometer. As the hypothesis of transverse strains isotropy $\varepsilon_x = \varepsilon_y$ was experimentaly checked, true stresses can be calculated:

$$\sigma = \frac{F}{l_x l_y} \qquad (1)$$

True volume strains are given by : $\varepsilon_{vol} = \varepsilon_x + \varepsilon_y + \varepsilon_z = \varepsilon_z + 2\,\varepsilon_y$ (2)

The scatter of these experiments is ± 2% on stresses and axial strains and ± 10% on volume strains.

RESULTS

Nature of the damage

All along the tensile test, volume variations confirm the hypothesis of damage by micro-voids nucleation and growth. As shown Figure 2, between 0 and 2% the volume of the strained sample slightly increases. The Poisson's ratio is 0,45. For axial strains higher than 5%, the volume strain clearly raises. This critical strain corresponds to the whitening of the sample. Beyond 15% of axial strain, the cross-section area of the sample nearly keeps a constant value : the growth of voids in the direction of tension is responsible for 90% of the elongation of the sample.

The damage occuring in strained PVDF is confirmed by the loss of secant modulus during the tensile cyclic test illustrated in Figure 3. It decreases from 2400 MPa for the first cycle down to 638 MPa for the last one. Successive unloadings and loadings constitute increasing hysteresis area : the mechanism results more and more dissipative.

Volume strain is due to elastic, plastic and cavitational contributions. During the first cycle drawn in bold line on Figure 3 (axial strain value is 4% at the end of the load), unloading clearly points out that , below 5%, volume strain is elastic one. Beyond 5%, plastic flow and cavitational damage begin. Since the former is assumed to occur at constant volume (3), cavitational strain is responsible for the total volume strain increase. Unloading brings additionnal information about plastic contribution. On the second cycle drawn in bold line on Figure 3 (axial strain value is 19% at the end of the load), it can be noted that volume strain keeps a high value after unloading. It implies that the plastic flow seated around voids prevents them from closing totally. To know whether crystallites or constrained amorphous phase is involved, the temperature should be raised up to 80°C.

Strain rate dependance of the microscopic damage

Figure 4 shows tensile tests performed at three crosshead speeds. On a macroscopic scale, the damage is the same whatever the strain rate. First, voids are nucleated beyond the same axial strain value (about 4-5%). Then, for the same value of axial strain, the total amount of created voids is equal. On a microscopic scale, the size, morphology and density of voids cannot be evaluated with such experiments. Nevertheless, the local damage mechanism is expected to be thermally activated.

Results from tensile cyclic tests performed at the same crosshead speeds lead to the same conclusions. The evolution of transverse and volume strains are identical whatever the strain rate. The voids closing and opening mechanism is similar to this described in the previous paragraph. The loss of secant modulus shown Figure 5 is the same as well. From these results,

it can be pointed out that PVDF damage is macroscopically strain rate independant at room temperature in this rate range.

On Figure 6 are compared the volume strain in tensile and creep tests. It clearly appears that plastic flow is more important in the strain rate range (about 10^{-5} s^{-1}) involved in creep tests. It probably can be linked to an increasing contribution of the constrained part of amorphous phase. Then, plastic strain is expected to increase at higher temperatures, near Tg2.

CONCLUSIONS

It results from this global mechanical study that the nucleation and growth of voids is the main phenomenon occuring in PVDF plastically strained at room temperature. In the strain rate rage involved in tensile tests, cavitational damage prevails over plastic flow. At lower strain rates, the contribution of strained amorphous phase increases.

As all these tests were performed at room temperature, between Tg1 and Tg2, only the free part of amorphous phase was relaxed. The influence of strain rate on the cavitational damage of PVDF is to be completed performing similar tests at higher temperatures, in particular greater than Tg2.

REFERENCES

1. Aboulfaraj M., G'Sell C., Ulrich B. and Dahoun A. ; « In situ observation of the plastic deformation of polypropylene spherulites under uniaxial tension and simple shear in the SEM », 1995, Polymer, 36 (4)
2. Friedrich K. ; « Crazes and shear bands in semi-cristalline thermoplastics », 1983, Advances in Polymer Science, 52/53
3. Kausch H.H., Plummer C.J.G. and Scaramuzzino P. ; « Damage development in time-dependent polymeric materials », 1995, ICMTDM First Congress Proceedings, Ljubljana, Slovenia

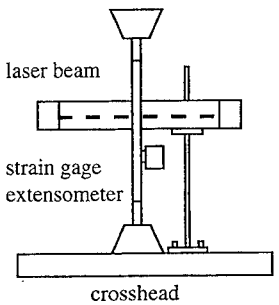

Figure 1. Experimental device

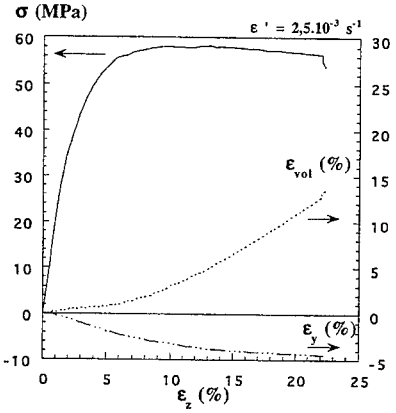

Figure 2. Tensile test (T=21°C)

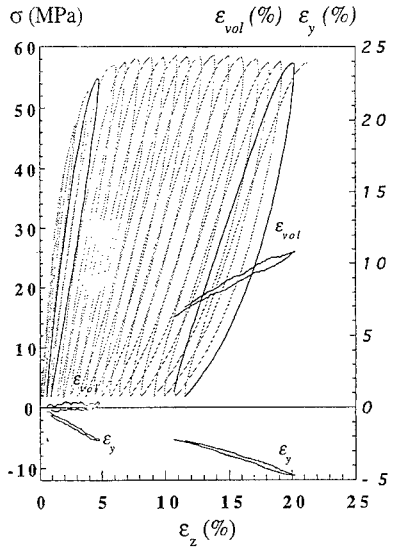

Figure 3. Tensile cyclic test (T = 21°C)

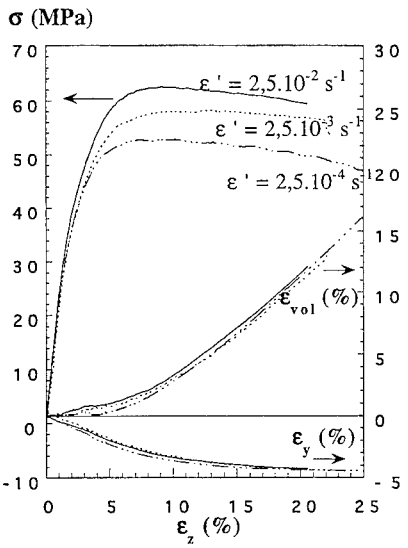

Figure 4. Strain rate dependance of macroscopic damage (T = 21°C)

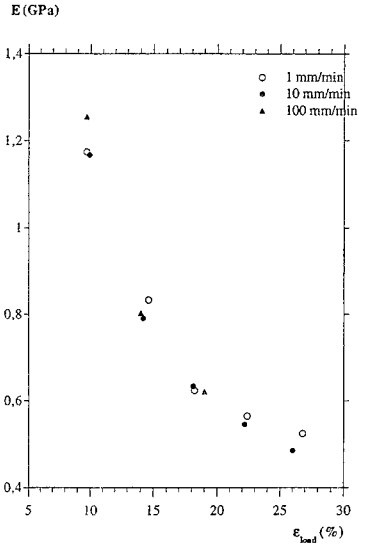

Figure 5. Strain rate influence on secant modulus (T=21°C)

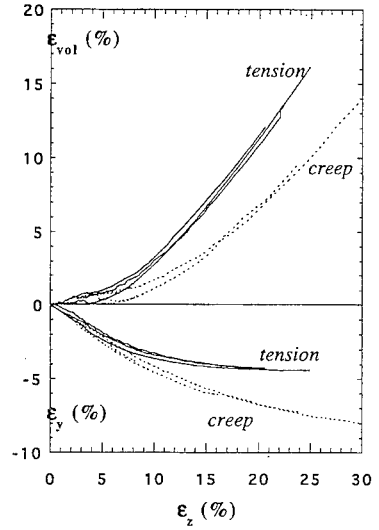

Figure 6. Comparison between tensile and creep tests (T=21°C)

IR and Raman Spectroscopic Study Deformation of Chemical Bonds under Stress and Temperature in Volume and Surface Layers of Polymer Specimens

V.I. Vettegren

A.F. Ioffe Physical - Technical Institute Russian Academy of Science, 194021, Polytecnical Str. 26, Saint-Petersburg, Russia.

It was studied the shift of the regularity bands in IR and Raman spectra more than 50 Polymers (Polyolefines, Polyamides, Polyimides and so on) under stress and temperature in volume, surface layers and interfaces of films, fibers and polymer composites.

1. It was calculated the values of Grunaizen parameters from the shift under stresses for more than 100 bands in spectra of studied polymers. It was measured the local stresses near to macroscopic concentrators, as crack or open in thin loaded film by the shift of the bands.
2. It was shown that shift of the bands under temperature is caused by expansion of the axis's polymer molecules under thermal and zero vibrations. It was studied the values of the expansion of axis's for other polymer molecules from 80 K to near melt temperatures.
3. On free surface of polymer specimens the frequencies of the regularity bands decreases but on interfaces of composites polymer-metal increases. These effects show that in the surface layers of specimens the axis's of molecules are stretched but in the interfaces with metals they are compressed. Deformation of molecular axis's was explained by scattering of atomic vibrations in surface or interfaces.

Characterising Fracture behaviour in Rubber Toughened Polymers using the Essential Work of Fracture.

David Taylor,
Trinity College Dublin, Ireland.
Paul Blackie,
Regional Technical College, Athlone, Co. Westmeath, Ireland
Finbar Dolan,
Trinity College Dublin, Ireland.

Synopsis

The fracture behaviour of plastics materials has been conventionally characterised in terms of linear elastic fracture mechanics or in terms of the J Integral. Protocols have been developed for their use with plastics. However the inherent mechanisms of deformation associated with crack propagation in the materials conflict with the theoretical assumptions of both LEFM and J integral approaches.

Further it is the general experience for the majority of plastics materials, providing the necessary geometrical constraint required for plane strain conditions is impractical to manufacture. Moreover the resultant data from such tests are found to be difficult to apply in the design of parts and in assessing performance in service. Compliance with the necessary assumptions breaks down most dramatically for the case of rubber toughened materials and characterising their fracture toughness has been particularly problematic, with conflict in the results from different sources.

The results of the work presented suggest the work of fracture approach as the most appropriate means of characterising fracture in plastics materials. This both from a theoretical and practical perspective.

In it the essential work of plane strain and plane stress fracture in HIPS resins in parts of varying thicknesses using materials of varying effective rubber phase volume (ERPV), vis. inherent constraint, are compared.

The findings of the work show it is possible to determine concurrent values for the limiting values of material toughness and to model the variation in performance in terms of geometry as well as secondary phase morphology.

Thus it is the conclusion of this work that the work of fracture approach provides a theoretically 'sound' and practical method for the characterisation of the fracture behaviour of rubber toughened materials in customary wall thicknesses as well as providing a means of evaluating the limiting values of conventional toughness parameters, i.e., G_{IC}, J_{IC} and K_{IC}

The implication of the work is that it should be possible to apply Fracture Mechanics (work of fracture data) to designing parts in polymeric systems with greater confidence than previously possible.

ON THE THICKNESS DEPENDENCE OF TOUGHNESS IN SHORT FIBRE REINFORCED POLYMERS

F Lumini*, M Puricelli*, A Pavan*

The influence of specimen thickness on fracture toughness in short fibre reinforced polymers was investigated to ascertain if a minimum thickness is needed to obtain valid linear elastic fracture mechanics data.
Two sheet moulding samples of a short fibre reinforced polymer having quite a different microstructural arrangement were used: one substantially unidirectional and one of the skin/core/skin type. Fracture tests on both materials were performed at sections (crack plane) showing a uniform through-thickness fibre orientation. For each specific microstructure and crack plane orientation, toughness turned out to be independent of thickness over the entire range of practical interest. The size requirement established in conventional fracture mechanics testing standards for homogeneous materials appears to be dispensable for these materials.

INTRODUCTION

One of the requirements for the validity of linear elastic fracture mechanics tests is that specimen thickness should be large enough to assure sufficient constraint at the crack tip, so that a condition of plain strain prevails. Under such a condition, the measured fracture toughness value should be a true material property, independent of thickness. For metals, the following criterion

$$B > B_{min} = 2.5\,(K_{Ic}/\sigma_y)^2 \qquad (1)$$

(in which B is the specimen thickness, K_{Ic} is the mode I fracture toughness under plane-strain conditions and σ_y is the tensile yield strength of the material) was set forth early [1] and the same limit was proposed and adopted for plain polymers [2-4].

In this paper two samples of a polyamide 6.6 reinforced with short glass fibres having two quite different microstructural arrangements, i.e. one substantially unidirectional and one of the more common skin/core/skin type which is normally obtained by injection moulding, were examined to assess fracture toughness dependence on thickness and to check the fitness of the above-said criterion (eq. 1) to validate toughness measurements.

EXPERIMENTAL

Material and moulding - Side-gated injection moulded disks of Latamid 66 H2 G30 (nominal fibre content: 30 wt%) were kindly supplied by LATI SpA, Vedano Olona, Italy in four thicknesses in the range from 1 to 5 mm.

Thin extruded rods (about 3 mm in diameter) of Radilon ARV 300 (nominal fibre content: 30 wt%) were kindly provided by RADICI NOVACIPS, Villa D'Ogna, Italy. After kiln-drying the rods were accurately aligned side by side in a rectangular mould cavity and compression moulded. Sheets of five different thicknesses in the range from 1.2 to 7.2 mm were produced.

Microstructural characterisation - Fibre content and dimensions were measured after burn-off of the polymeric matrix at 700°C. The naked fibres were then poached in acetone to ease their disentanglement and measured under an optical microscope equipped with image analysis facilities.

To determine fibre orientation the method proposed by Advani and Tucker [5] was used. It consists in sectioning the moulding and measuring the length of the axes of the elliptical cross-

*Dipartimento di Chimica Industriale e Ingegneria Chimica, Politecnico di Milano, Italy

sections of the fibres exposed on the section plane. The section surface was prepared for light microscope observation by using metallographic techniques and dyeing with an aqueous Iod solution to gain contrast.

Fibre orientation was described by Advani-Tucker's tensor. The tensor components a_{ij}^{α} are referred to the coordinate axes systems specified in Fig. 1 with α denoting an in-plane rotation of a frame of reference with respect to the primitive one. The tensor components in a new frame of reference can of course be calculated from the old ones via the transformation matrix.

From the symmetry of the injection moulded disks and of the unidirectional plates it follows that $a_{12}=0$. As a consequence, for a section at $\alpha=45°$ to the principal moulding direction (see Fig. 1) the following relationship should hold:

$$a_{11}^{45} = a_{22}^{45} = (a_{11}^{0}+a_{22}^{0})/2 \qquad (2)$$

If fibre distribution is planar, then $a_{33}^{\alpha} = 0$ and a_{11}^{45} and a_{22}^{45} should be 0.5 across the whole thickness.

Mechanical testing - Stress-strain tests were carried out on the unidirectional material in uniaxial compression, taking special care to get rid of friction effects arising at the contact between test specimen and dies. The injection-moulded material was tested in both uniaxial compression and tension. Because of the anisotropy of these materials, the yield stress to be used in eq. (1) is to be determined by tests carried out in the same direction as the applied stress in the fracture tests, i.e. normal to the predicted crack plane (mode I fracture). The uni-directional material was thus tested at varying orientations, and the injection moulded material was tested at 45° to the mould-fill direction.

Though yielding is not a well defined phenomenon in these kind of materials, a conventional yield stress value was determined by assuming, quite arbitrarily, that either a maximum in the load or a more or less well defined knee in the stress-strain curve were indicative of the yield point.

Mode I fracture tests were performed in three-point bending following the lines drawn in ESIS testing protocol for plastics [3]. The following specimen dimensions were generally used: specimen width W=2B, span S=4W, initial notch depth a_0=0.5W, and the specimen thickness B was the plaque thickness. For the thinnest plaques, i.e. B=1mm for the injection moulded discs and B=1.2mm for the unidirectional plates, W=4B and S=6.5W were used. A notch with a root radius of about 13 μm was introduced by sliding a truncated razor blade scalpel-wise.

All specimens were kiln dried just before testing. Cross-head speeds were such as to obtain a time-to-yielding approximately equal to the average time-to-fracture, as recommended in [3].

RESULTS

Microstructure - Fibre content and size are given in Table I. Fibre orientation across thickness is shown in Fig.s 2a and 2b for the two materials investigated. The injection moulded discs (Fig. 2a) show a fibre distribution which is typical of the skin/core/skin type of structure, although the three layers are not clear-cut. By contrast, in the plates prepared by compaction of extruded rods (Fig. 2b) fibre orientation resulted in being effectively unidirectional and quite uniform, with orientation factor values higher than in the skin layers of the injection moulded samples, irrespective of plate thickness. This material was therefore fit for the present study. In the injection moulded samples a through-thickness uniform fibre orientation, with an orientation factor's value of 0.5, was found on sections at 45° to the mould-fill direction, as expected.

Table I - Average fibre content and dimensions

Material	Weight percentage	Volume fraction	Average length (μm)	Diameter (μm)	Average aspect ratio
Latamid HE G30	31.0	0.167	130	8	16.2
Radilon ARV 300	30.4	0.164	300	6	50.0

Yield stress - Fig. 3 shows the yield stress values measured on sheets of the unidirectional material with three different thicknesses loaded in uniaxial compression at varying angle α to the fibre direction, plotted versus the fibre orientation factor a_{11}^{α}. There appear to be two different branches: in the low range of the orientation factor, the yield stress is almost independent of fibre orientation, whereas at angles α smaller than 45° (fibre orientation factor larger than 0.5) the yield stress increases steeply with orientation.

For the tensile and compressive yield stresses measured on the injection moulded material at 45° to the mould-fill direction we obtained $\sigma_{yt} = 102$ and $\sigma_{yc} = 120$ MPa respectively, resulting in a ratio $\sigma_{yt}/\sigma_{yc} = 0.85$ comparable with values normally observed in the unreinforced matrix polymer. This value was used to convert the yield stress values measured in compression on the unidirectional material, to tensile values to be used in eq. (1) for determining B_{min}. Use of a compressive yield stress, σ_{yc}, would result in underestimating B_{min}, although prudentially.

Fracture toughness - The dependence of fracture toughness on fibre characteristics (content, length, aspect ratio and orientation) forms the subject of a communication presented elsewhere [6]. Here we consider its possible dependence on the overall state of stress (a combination of plane stress and plane strain) which usually shows up in a variation of fracture toughness with plate thickness in homogeneous materials.

The results obtained are displayed separately in Fig.s 4a and 4b for the two types of sheet moulding materials investigated in the present work. The horizontal lines represent average values over the thickness range covered for each orientation of the crack plane (expressed by the orientation factor a_{11}^{α}). The thick vertical dash drawn on each line indicates the minimum thickness, B_{min}, evaluated according to eq. (1) for each material and orientation.

It is seen that fracture toughness is independent of specimen thickness over the entire range explored, which largely covers the range of practical interest for the applications of these materials in the sheet form. The range examined extends substantially beyond (i.e. below) the value of B_{min} estimated by eq. (1) according to the fracture mechanics testing standards established for homogeneous materials.

The independence of fracture toughness from thickness can be explained by considering the failure micromechanisms which operate in these materials: fibre debonding and pull-out, fibre breaking, matrix microcracking. They are determined by the highly localized stress concentration produced by the fibre inclusions at the "micro" scale, which may be scarcely influenced by the overall state of stress imposed at the "macro" scale, as demonstrated for the case of spherical inclusions previously [7].

CONCLUSION

Fracture toughness in short glass fibre reinforced polyamide 6.6, measured on sheet mouldings with different microstructure and varying orientation, was found to be independent (for a given microstructure and crack plan orientation) of sheet thickness over the range of practical interest. The limitation in thickness required by existing fracture mechanics testing standards for determining a thickness independent (plane strain) toughness value of homogeneous materials appears to be dispensable for this type of materials.

REFERENCES

[1] ASTM E 399 - 72, Annual Book of ASTM Standards, ASTM, Philadelphia, PA (1972)
[2] Hashemi S and Williams J G , J. Mater. Sci. 19 (1984) 3746-3759
[3] ESIS Document "A linear elastic fracture mechanics standard for determining K_c and G_c for plastics", Testing protocol prepared for ESIS TC4 by J G Williams, March 1990
[4] ASTM D 5045 - 93, Annual Book of ASTM Standards, ASTM, Philadelphia, PA (1993)
[5] Advani S G and Tucker C L, J. Rheol. 31 (1987) 751-784
[6] Pavan A, Lumini F and Puricelli M, "Relationship between fibre orientation and toughness in short fibre composite materials", 4th Int.l Conf. on "Deformation and Fracture of Composites", Manchester, UK, 24-26 March 1997 (preprint)
[7] Pavan A and Mercante L , Makromol.Chem., Macromol.Symp. 48/49 (1991) 211-221

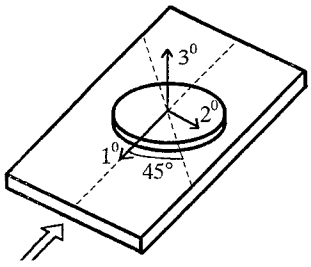

Fig. 1 - Coordinate axes

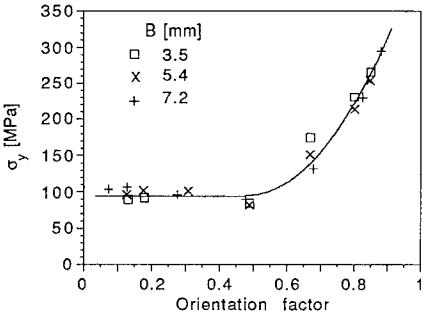

Fig. 3 - Compressive yield stress vs. orientation factor a^{α}_{11}. in the unidirectional material. Line drawn by guesswork.

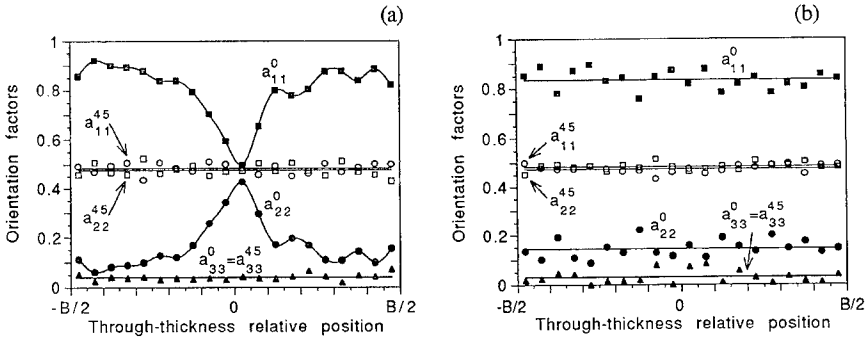

Fig. 2 - Through-thickness fibre orientation in injection-moulded disks (B=1mm) (a) and unidirectional plates (B=2.3mm) (b)

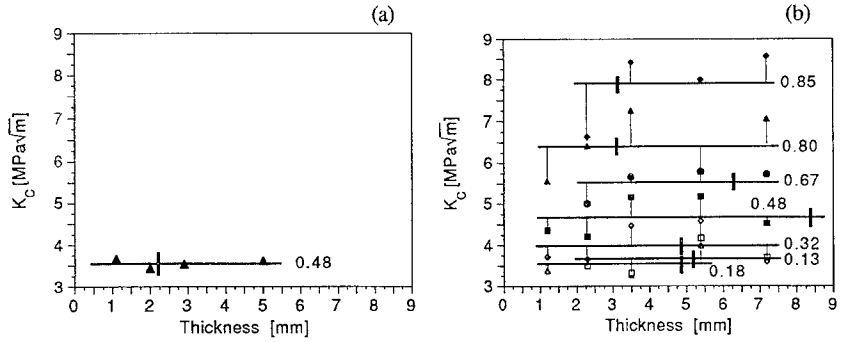

Fig. 4 - Critical stress intensity factor vs. thickness in injection-moulded disks (a) and unidirectional plates (b). Labels: orientation factor a^{α}_{11}.

INFLUENCE OF THE ENVIRONMENT ON TIME DEPENDENCE OF CRACK PROPAGATION IN POLYESTER RESINS

A.ROY, X. NENNIG, J.L. GACOUGNOLLE
Laboratoire de Mécanique et Physique des Matériaux, ENSMA, Site du Futuroscope, B.P. 109, 86960 Futuroscope Cedex

This paper deals with environmental effects on a time dependence of mechanical properties of polyester resins. Those resins are widely used as matrix of glass reinforced composites for marine applications. It has been shown that crack initiation of roving/unidirectional laminates depends mainly on the mechanical behaviour of the resin while the propagation is located at the fibre/resin interface. Furthermore, the cracking is strongly time dependent both in the composite and in the resine alone. Then, fracture tests have been made in mode I , on DCN samples for the composite and on CT specimen for the bulk resin.

First, the time dependence of the cracking has been studied in room conditions (T=23°C ; Hr=50%). Fracture tests have been made on a wide range of crosshead speeds and two types of cracking appear depending on the velocity. Between 0.5 and 50 mm/mn, the crack propagates in an unstable manner with a stick-slip phenomenon which its magnitude decreases as thevelocity increases. For crosshead speeds higher than 100 mm/mn the cracking becomes stable and brittle. For both the composite and the bulk resin, the transition from stable to unstable propagation occurs for a crack velocity of about $3\ 10^{-3}$ m/s. Furthemore, Gc at the initiation of the crack propagation is almost the same in the resin and in the composite.

Secondly, same testing has been made at 40°C. The temperature increase induces a translation of the Gc/velocities curve to higher crosshead speeds (time-temperature relation). So, at this temperature, the transition from unstable (stick-slip) to ductile stable cracking can be observed for a crack velocity of $2\ 10^{-5}$ m/s.

Then, the influence of moisture environment on the crack propagation has been studied. Testing has been made in distilled water at room temperature. At low crosshead speed (0.5 mm/mn) when water has time to diffuse at the crack tip, the hydrolisis of the polyester resin induces an embrittlement of both the composite and the bulk polymer. The crack propagates in a brittle-stable manner while a stick-slip phenomenon appears in room environment.

In conclusion, the polyester exhibits an unstable cracking in a large brittle/ductile transition. It seems that this stick-slip stage appears during β and α transitions which are very closed in polyester resins. The presence of water at the crack tip induces an embrittlement of the resin and so the stick-slip vanishes. This effect is the opposit as it has been observed in epoxy resins in which water induces a plastification at the crack tip and then increases the stick-slip phenomenon. Influence of moisture aging on the position of β and α pics is now studied.

INFLUENCE OF THE HYDROSTATIC TENSOR ON THE DEFORMATION OF PA11 NEAR T_g

K. Marchal*, L. Belec*, J.L. Gacougnolle*, P. Dang, Y. Meimon***, B. Dewimille*****

Mechanical behaviour of PA11 has been compared in tension, torsion and compression at 20°C and 60°C. Tests have been performed at controlled strain rate and under constant load. The yield stress σ_y does not depend on the mode of straining and the Von Mises criterion can be used without any term taking account of the hydrostatic tensor

Polyamide 11 is a semi-crystalline polymer with a low degree of cristallinity, less than 30%, so that the mechanical properties of the amorphous phase are preponderant for the behaviour of this polymer. With T_g at 45°C a crucial change in the mechanical behaviour of PA11 is expected between 18°C and 60°C. In view of building a constitutive law, experiments have been performed at constant strain rate and in creep under constant load in tension, torsion and compression.

In order to eliminate water from PA11, all the specimens are heated at 80°C for two days in vacuum, then they are kept at room temperature at least 3 weeks before testings. Dumbbell specimens, ISO R 527, have been used to make a systematic study of tensile tests and creep tests in tension between 18°C and 60°C. The comparison of behaviour in tension, torsion and compression has been made by using tubes of 39 mm diameter and 3 mm thickness.

At 18°C tensile curves exhibit four successive stages : the stress starts to increase in a quasi-elastic regime up to the flow stress σ_y, occurring at $\varepsilon_y \sim 3$ %, between 4 % and 8 % of strain this stress remains constant, then the strain-hardening takes place up to the necking occurring at a constant stress of 64 MPa and a strain of 35 % (Fig. 1). The flow stress increases with the strain rate but the stress of the necking is at 64 MPa whatever the strain rate, this stress depends only on the temperature.

During the plateau at σ_y the specimen is creeping at constant strain rate, this is a stationary creep. This stationary creep is also detected on creep curves obtained at lower stresses (Fig. 2). Contrary to the stationary creep observed on amorphous polymers, which is a transient

* L.M.P.M. - E.N.S.M.A., Téléport 2, B.P. 109, Chasseneuil-du-Poitou, 86960 Futuroscope cedex
** CERDATO, ATOCHEM, 27470 Serquigny
*** I.F.P., B.P. 311, 92506 Rueil Malmaison Cedex

creep between a stage at decreasing creep rate and a stage at accelerating creep rate, thestationary creep of PA11 is a transient creep between two stages at decelerating creep rates. Just after loading starts the logarithmic stage followed by the Andrade creep, also named KWW creep, these stages correspond two the viscoelastic increase of stress preceding σ_y (Fig. 3). Beyond the stationary creep begins a second logarithmic creep related to the strain hardening of tensile curves. The apparent activation volumes of both the plateau of stress in tensile curves and the stationary creep are identical, ~ 1800 $\mathring{A}^3$, suggesting that the physical aigin of these phenomena are the same.

Tests on tubes have been performed in tension up to a strain of 30 %, but in torsion and compression the onset of buckling limits the maximal strain at respectively 20 % and 8 %. The scatter of the tubes geometry induces a scatter between tests in each straining mode of ± 5 %. The comparison of stress-strain curves in different modes is made by using the known relations :

$$\sigma_{eq} = \sqrt{\sigma_{22}^2 + 3\sigma_{2\theta}^2} \qquad \varepsilon_{eq} = \sqrt{\frac{4}{9}\left(\varepsilon_{22} - \varepsilon_{\theta\theta}\right)^2 + \frac{4}{3}\,\varepsilon_{2\theta}^2}$$

and, in torsion-tension tests, the equivalent strain rate is defined by

$$\dot{\varepsilon}_{eq} = \sqrt{\varepsilon_{22}^2 + \frac{2}{3}\,\varepsilon_{2\theta}^2}$$

At $\dot{\varepsilon}_{eq} = 10^{-3} s^{-1}$ and within the scatter range the flow stress appears to be the same in tension, torsion and compression at temperatures below T_g (Fig. 4-5). Obviously the plateau of stress is also identical in the three modes of straining.

Creep curves in tension, torsion and compression and an equivalent stress of 25 MPa exhibit the same logarithmic kinetics during the first 100 s then they diverge progressively, the creep rate being higher in tension than in torsion and compression (Fig. 6). In the 3 strain modes the stationary creep can be reached but the stationary rate depends on the hydrostatic tensor as shown Figure 7, this is apparently in disagreement with the results obtained for the plateau of stress which does not depend on this tensor. The explanation may be given by the gap of strain rates : 10^{-3} s^{-1} in controlled straining and less than 10^{-5} s^{-1} in creep.

At 60°C no influence of the hydrostatic tensor can be detected neither in controlled straining (Fig. 8) nor in creep. This influence can probably be seen only under high pressure.

It is surprising that a semi-crystalline polymer with 70 % of amorphous phase exhibits a so small sensitivity to hydrostatic tensor. It is well know that the yield stress of amorphous polymers increases rapidly with hydrostatic pressure and the Coulomb yield criterion is the right criterion for these polymers (1). Nevertheless it has been shown (2) that PA6 also does not seem sensitive to the hydrostatic tensor.

(1) P.B. Bowden, J.A. Jukes, J. Mater. Sci. 3 183 (1968).
(2) R.K. Mittal, I.P. Singh, Poly. Eng. and Sci. 22, 358 (1982).

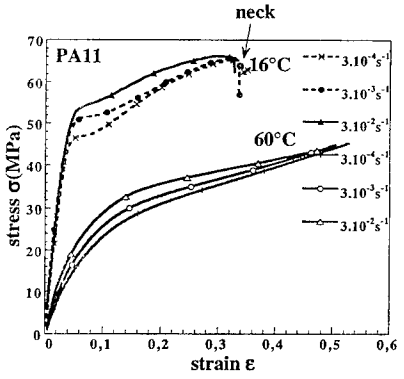

Fig.1: Tensile curves of PA11 at 16°C and 60°C

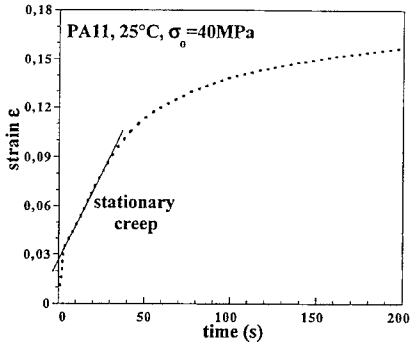

Fig.2: Creep curve at 25°C under 40MPa showing the stationary creep

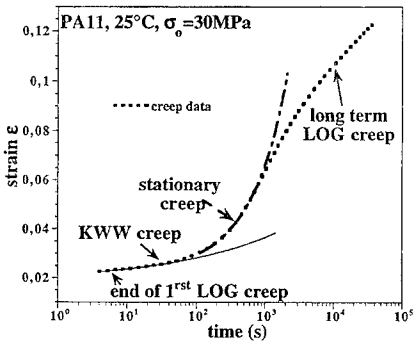

Fig. 3: Creep curve at 25°C under 30MPa: the four successive creep stages

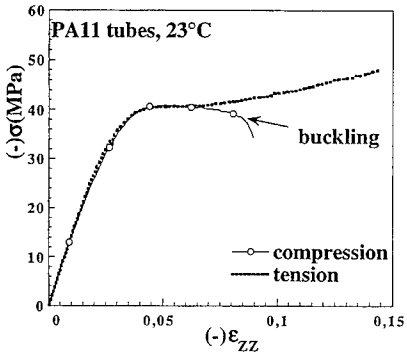

Fig.4: Tension and compression curves of tubes of PA11 at 23°C

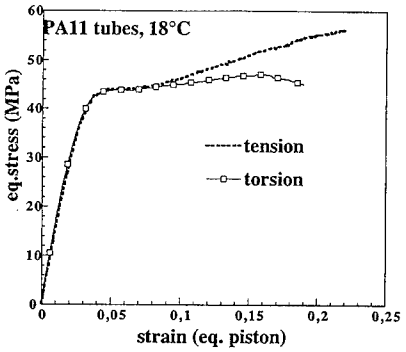

Fig.5: Torsion curve plotted in equivalent strain and stress compared to tensile curve at 18°C

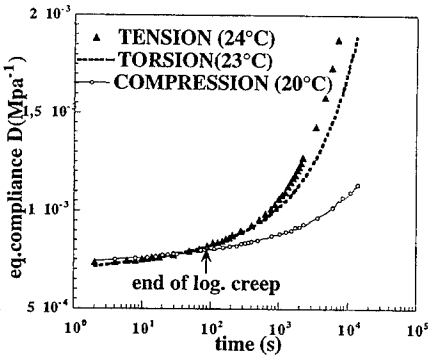

Fig.6: Comparison of creep curves of PA11 tubes in tension, torsion and compression plotted in equivalent compliance

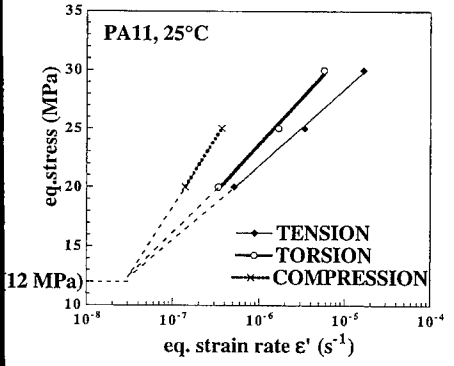

Fig.7: Equivalent strain rate of the stationary creep plotted versus equivalent creep stress in tension, torsion and compression

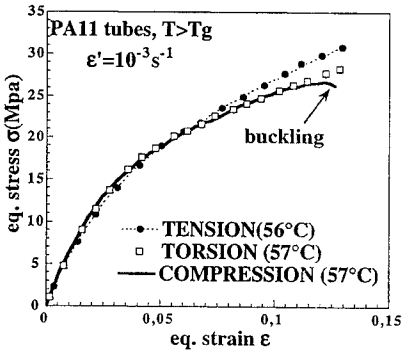

Fig.8: Tension, torsion and compression curves of tubes of PA11 at 60°C

Brittle-tough transition in high density polyethylene

S.J.K. Ritchie, P. Davis & P.S. Leevers
Imperial College, London

The existence of a brittle-tough transition in the fracture behaviour of polymers has been known for many years. However, little progress has been made in identifying its underlying micro-mechanisms, or in predicting its dependency on temperature, strain rate and geometry. This area has recently attracted increased industrial interest with the introduction of a new generation of modified high-density polyethylenes for pressure-pipe applications. Above a geometry-dependant brittle-tough transition temperature, it is impossible to sustain rapid crack propagation along a pipe, even at the highest available test pressure. The appearance of shear-lips adjacent to free boundaries of the fracture surface plays a controlling role. Suppression of the shear-lips by notching suppresses the transition: the material continues to fail in the brittle regime providing the deformation rate remains high. Therefore, in order to understand the brittle-tough transition, the mechanism of shear-lip formation must be investigated. A new 'Inverted Charpy' test method has been developed to study this process. The results, together with those from high-rate drawing tests, are used to investigate the dependency of shear lip formation on rate and temperature.

For some modified high-density polyethylenes, the brittle-tough transition of extruded pipe is sensitive to the thermal history to which it was subjected during processing. Spherulite size of the polymer is sensitive to cooling rate. By subjecting polymer test specimens to controlled cooling rates, the correlation between spherulite size and the brittle-tough transition temperature is examined.

The Use Of Fillers To Improve The Dynamic Fracture Resistance Of Medium Density Polyethylene.

J.C. Graham, S.J.K. Ritchie, X.Dong.

The use of particulate fillers to improve the resistance of brittle polymers to rapid fracture is well established: rubber toughening is used, for example, in epoxies and ABS. Thermoplastic polymers such as medium and high density polyethylenes, although tough under slow loading rates, can be susceptible to brittle fracture at high loading rates. There is therefore a motivation to attempt to use toughening agents in these polymers. An improvement in their resistance to rapid crack propagation is unfortunately elusive; rubber 'toughening' actually decreases the dynamic fracture resistance of polypropylene at high rates. The successful use of fillers in tough thermoplastics has been limited to the use of inexpensive particulates, in particular $CaCO_3$, as bulking agents. The use of such fillers at high loadings reduces cost, but at the expense of material properties. This decrease in performance is attributed to poor particle/matrix bonding.

The use of novel chemical pretreatment of the filler has allowed the manufacture of medium density polyethylene with $CaCO_3$ filler loadings up to 40 wt% and unimpaired mechanical properties; indeed, static and dynamic moduli are somewhat improved with filler loading.

Two tests have been used to measure dynamic fracture resistance. 'Frozen tongue' modified single edge notch tension tests have been performed over the temperature range 20 to -70 °C for compositions from 0 to 40 wt% $CaCO_3$. The results are analysed using a lumped mass-spring analytical model and a Finite Volume discretisation of the equations of motion. Split Hopkinson Pressure Bar tests are performed to allow the determination of dynamic stress-strain curves for use in the analyses of the frozen tongue test. High Speed Double Torsion tests have also been carried out for the same range of compositions over the temperature range 0 to -20 °C. The results are analysed using a 1D Finite Difference discretisation.

Dynamic fracture toughness is found to be at a minimum for 15 wt% loading and to be dramatically higher for 40% wt loading than for the pure material..

Statistical modeling of crack growth and reliability assessment of HDPE

Farrukh S. Qureshi, Zafarullah Khan, Anwar K. Sheikh, Mohiuddin Ahmad
Department of Mechanical Engineering
King Fahd University of Petroleum and Minerals
Dhahran 31261, Saudi Arabia

Solid polymers are increasingly being used in engineering applications. These applications require that the plastic parts be able to withstand static and dynamic stresses, temperature variations and temperature gradients. The increasing use of plastics in engineering applications mandates that reliable mechanical property data must be available to the engineers involved in design and manufacturing of components and structures made of plastics. Similarly, development of suitable reliability models and life prediction methodologies is essential to provide estimates of performance capabilities of these materials. Although enough data is available on the performance of plastics under static loading conditions, extensive data for the dynamic loading as well as reliability and life prediction models are not commonly available for plastic materials. The present study was aimed at generation of fatigue crack growth data of plastic materials, and employing a statistical modeling approach to characterize the fatigue crack growth behavior of plastic materials.

The specimens were hot pressed from virgin HDPE resin provided by the Saudi Arabian Basic Industries Corporation (SABIC). Ten replicates of the experiment were carried out by subjecting the specimens to cyclic loading at identical conditions of stress level and frequency. The crack growth was monitored with an increase in number of cycles. A considerable scatter in the crack growth was observed. The average ln(crack length(L)) was observed to increase linearly with lnN (where N is number of cycles), indicating a strong correlation. The standard deviation of lnL can also be treated as a linear function of lnN, although with a lesser degree of correlation. This led to postulate a recently proposed fatigue life reliability model whose basic assumptions are satisfied with above observation. The data of time to reach a critical level of crack length was fitted to that model and it was found to provide an excellent fit. Based on the interpretation of this model various reliability characteristics are developed.

FRACTURE OF POLYMERS AT SLOW STRAIN RATE WITH UV EXPOSURE

C T Kelly*, Li Tong† & J R White†

Injection moulded tensile bars made from polyethylene (PE), polypropylene (PP), polystyrene (PS) and polycarbonate (PC) have been tested at slow strain rate ($1.1\text{-}1.4 \times 10^{-7} s^{-1}$). When notched bars were exposed to ultraviolet irradiation (UV) during the slow strain rate test they failed sooner. Pre-exposure to UV caused further reduction in performance. PC was less affected by UV than the other materials. Stress-aided photo-oxidation probably assisted crack growth in PE, whereas in PP, orientation of the molecules at the crack tip appeared to provide some resistance to fracture. In PP failure was strongly influenced by cracking of the photo-degraded surface layer.

INTRODUCTION

The strategy normally adopted to evaluate polymer weatherability is to expose specimens (naturally or artificially) for different times then to measure their mechanical and/or chemical properties. Fracture tests on degraded bars are conducted in the laboratory and not in the climate under scrutiny. Artificial weathering tests distort the degradation process and do not lead to accurate prediction of service lifetime, as discussed by Kockott (1), Brown (2) and Turnbull and White (3). For example, if elevated temperature is used to obtain acceleration, the various degradation reactions are accelerated differently and the balance between them changes. An alternative strategy applied here is to conduct a mechanical test of increasing severity while under UV exposure so that failure occurs within an acceptably short time without the need for a subsequent test. Simultaneous application of stress and UV is common in service and this test is more likely to imitate service failure conditions than those in which UV exposure and the fracture test are separated. Failure by fracture nucleated at the surface is a common occurrence in service and the use of notched samples ensures some similarity. The notch causes a stress concentration and allows access of UV irradiation and oxygen to the process zone in which cracking and chemical degradation is concentrated.

EXPERIMENTAL

Slow strain rate tests

The slow strain rate test rigs followed the Parkins design for studying environmental stress cracking of metals and alloys (4,5) but with detailed differences to allow for the lower loads and higher deformations obtained with polymers. The tests reported here were run at strain rates in the range 1.12 to 1.37 x $10^{-7} s^{-1}$; figures 1-6 are for tests at 1.33 x $10^{-7} s^{-1}$. The

*Department of Chemical Engineering, The University of Queensland, Australia
†Materials Division, University of Newcastle upon Tyne

rigs were placed in a room designed to remain at a constant temperature (30°C) but some tests ran at slightly higher temperatures because the air circulation equipment could not cope with solar heating during a particularly hot spell. The crack growing from the notch tip was photographed at intervals. Crack development during critical stages of growth was monitored overnight using timer-operated exposures at pre-set intervals. Crack and craze lengths and the crack opening displacement were measured from the photographs. Selected samples were inspected in the scanning electron microscope (SEM) after failure in the slow strain rate test.

Exposure conditions

The UV was provided by fluorescent tubes type *UVA-340 (Q-Panel Company)* for which the output in the UV matches solar radiation spectrum at the Earth's surface fairly closely. They were used previously for artificial weathering studies by O'Donnell and White (6). The intensity used was 2.5-4Wm^{-2} in the wavelength range 295-320nm, that is the total radiation below 320nm wavelength, and corresponds to midsummer intensities at noon in hot climates. Some samples were exposed "side-on", with the broad moulded face towards the UV source. Other samples were exposed with the edge containing the notch facing the UV source ("edge-on"). Since the tubes provide an extended source, significant illumination fell onto the broad faces during edge-on exposures: the illumination was found to be of the order of 25% of that falling onto a plane facing the source and located at the same distance from it.

Materials and sample preparation

Tensile test bars, measuring approximately 190mm x 12.7mm x 3mm, were made by injection moulding into a single end-gated mould. The materials chosen for study were all provided free of charge by the manufacturers and were: (a) Linear low density polyethylene (PE): BP (experimental grade: M_n=17000, M_w=135000); (b) Polypropylene (PP): ICI GWM22; (c) Polystyrene (PS): BP H101; and (d) Polycarbonate - unstabilized (PC): Bayer Makrolon 2600. Samples were stored in the dark for at least one month prior to commencing a test. Notches were cut using a broaching tool giving one of the notch profiles specified in BS and ISO standards: notch depth = 2.7±0.1mm; radius of root of notch = 0.25mm; included angle between notch faces = 45°. Some samples were pre-exposed to UV in open frames for several weeks prior to conducting the slow strain rate test. Some were exposed side-on and others were exposed edge-on.

RESULTS AND DISCUSSION

Polyethylene

The PE bars behaved in a ductile manner. For all test conditions a crack grew from the tip of the notch and the notch hinged open (Kelly and White (7)). UV application resulted in lower load at any given deformation (fig.1). Samples tested at slow strain rate with UV exposure began to show advanced ductile fracture with a load drop after about 20mm extension (~20% strain) whereas PE tested unexposed continued to work harden well beyond this point (fig.1). In the later stages of the test (after a crosshead displacement of ~18mm) the crack opening displacement (COD) was much greater in the presence of UV (fig.2). It is speculated that photo-mechanical reaction causes rapid scission of stretched molecules at the crack tip. Samples which were pre-exposed formed surface cracks quite early on in the slow strain rate test (7). They failed at much lower loads and lower deformations (7).

Polypropylene

The PP bars showed many features similar to those with PE but there were some important differences. Samples tested at slow strain rate with no pre-exposure showed less ductility. When UV exposure was applied, lower loads were recorded at all stages and the sample failed earlier (fig. 3). The COD was insensitive to UV exposure (figure 4). It is believed that the bond rearrangements required during PP oxidation are more difficult to achieve when the molecule is extended, as at the crack tip (Rapoport *et al*(8)). When pre-exposed samples were tested they showed more ductility in the final stages of the test, but only after the load had gone through a maximum and then fallen steeply (7). Cracks grew in the surface of pre-exposed samples but they did not form patterns as prominent as those with pre-exposed PE (7). It was common for a dominant surface crack to grow across the wdth of the bar from the notch tip in the embrittled surface layer quite early on in the slow strain rate test (7). The effect of side-on pre-exposure was much greater than that of edge-on exposure. This is shown in figure 5 in which the energy dissipated during the slow strain rate test (measured using the area under the load-deformation plot) is plotted versus pre-exposure time.

Polystyrene

PS samples failed in a brittle manner after deforming less than 1mm (see Kelly *et al* (9). Crazes formed ahead of the notch tip after an incubation period then gradually accelerated until the end of the test. The crack grew slowly at first but then accelerated almost without warning and the final cracking, occupying more than half of the bar section, was completed in less than one second. The application of UV exposure caused premature failure (9).

Polycarbonate

The effect of UV exposure on the load-deformation characteristic in general and the onset of fracture in particular was quite small with PC (figure 6). Kelly *et al* (9) found that crack propagation was more sensitive to strain rate than to the UV exposure conditions. When the strain rate was increased by $<20\%$, from $1.12\text{x}10^{-7}\text{s}^{-1}$ to $1.33\text{x}10^{-7}\text{s}^{-1}$, the crack growth rate doubled. The fracture mechanism was apparently the same under all conditions tested. A shear band began to grow across the width of the bar from the notch quite early on in the test and had almost reached the far side before any significant crack growth was observed.

CONCLUSIONS

Slow strain rate testing of polymers with simultaneous application of UV may give useful information on weatherability. PC was least affected by UV in the test - in parallel with its behaviour outdoors. PE and PP showed differences in behaviour that may be due to conformation-controlled oxidation behaviour.

REFERENCES

1. Kockott, D, Polym.Degrad.Stab. 25 (1989) 181.
2. Brown, R P, Polymer Testing 10 (1991) 3.
3. White, J.R & Turnbull, A, J.Mater.Sci. 29 (1994) 584.
4. Parkins, R N, "Stress corrosion cracking - The slow strain-rate technique" ASTM STP 665 Eds. Ugiansky, G M & Payer, J H, (1979) p.5.

5. Parkins, R N, Corrosion 46 (1990) 178 (NACE 1990 Plenary Lecture)
6. O'Donnell, B & White, J R, J.Mater.Sci. 29 (1994) 3955.
7. Kelly, C T and White, J R, Polym.Degrad.Stab. (1997) *in press*
8. Rapoport, N Ya, Shibriaeva, L C, Zaikov, V E, Iring, M, Fodor, Zs & Tüdős, F, Polym.Degrad.Stab. 12 (1985) 191
9. Kelly, C T, Li Tong and White, J R, J.Mater.Sci. (1997) *in press*

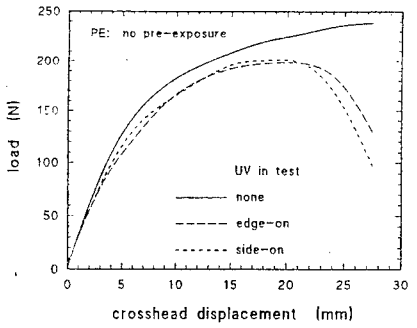

Fig.1 Load-deformation at slow strain rate: PE

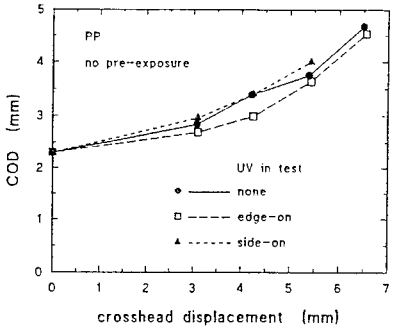

Fig.4 COD development in PP

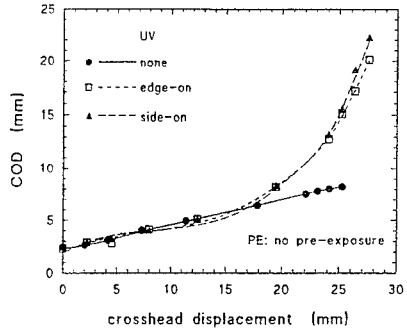

Fig.2 COD development in PE.

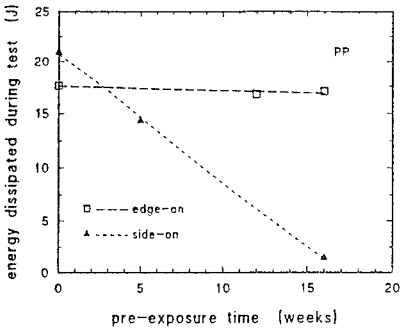

Fig.5 Energy dissipation vs. pre-exposure: PP

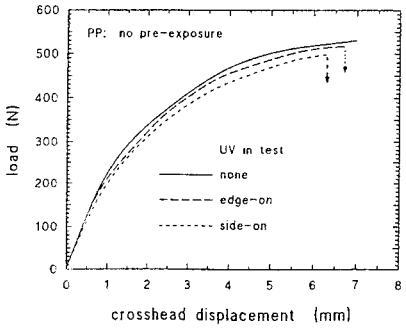

Fig.3 Load-deformation at slow strain rate: PP

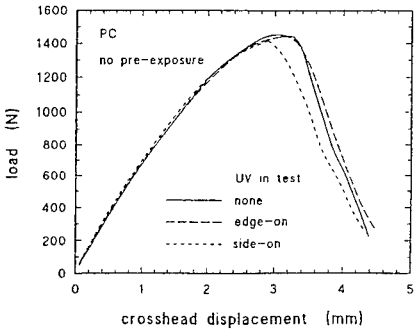

Fig.6 Load-deformation at slow strain rate: P

AN ASSESSMENT OF THE DEFECTS DAMAGES IN POLYETHYLENE GAS PIPES

A. OUAKKA[1,3], K. DANG VAN[1], D. GUEUGNAUT[2], P. BLOUET[2]

In order to analyze the risk of fracture in polyethylene pipe structures and to control the lifetime of the gas distribution network, GdF has undertaken a broad research program to evaluate the damage induced by scratches of various geometries which can be generated during the lay-in of the pipes. We illustrate here an application using a finite element code which gives a classification of the defects in terms of both shape and size.

INTRODUCTION

Polyethylene pipes used in gas distribution under medium pressure can be damaged by contact of sharp objects (stones,tools ...). These latters, by their shape and the way they come into contact with the pipe, generate external scratching, gouging, denting, scoring or other surface defects (fig. 1). From these defects, a slow crack growth (SCG) can occur then leading to irreversible incidents.

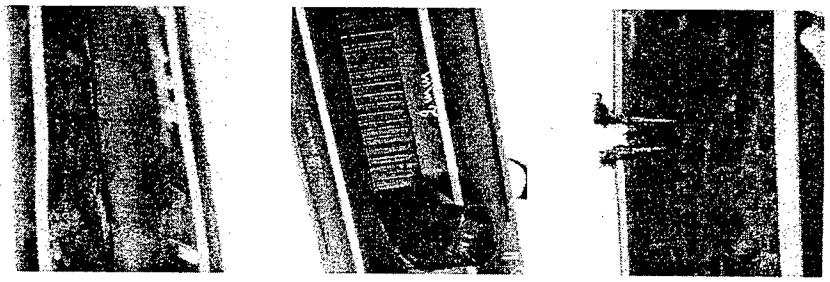

Figure 1: A variety of polyethylene gas pipes surface defects

In order to prevent such risks, GdF has set up a broad research program to evaluate the damage induced by these defects and their evolutions. This project, both numerical and experimental, consists in developping a local approach of fracture [1] and of damage mechanics by using an original rheological model of polyethylene which, naturally, takes into consideration all the aspects of the anelasticity effect of the material. This model has been incorporated into a GdF finite element code to simulate slow crack growth process in polyethylene (PE) pipes [2][3].

[1]Ecole Polytechnique, Laboratoire de Mécanique des Solides, Palaiseau, France
[2]Gaz de France, Research and Development Division, La Plaine Saint Denis, France
[3]Université de Fes, Laboratoire de Mécanique des Fluides et Energétique, Fes, Morocco

EXPERIMENTAL STUDY

The performance of a PE gas pipe resin is based on the resistance properties to SCG. There are various methods for measuring this SCG resistance. The Full Notch Creep Test (FNCT) greatly accelerates the time for brittle fracture processes and its results correlate with the hydrostatic pressure test on pipe. Using FNCT specimens, the SCG characteristics of PE can be quantified. Three different notches (meaning square, circular and V-shaped) FNCT specimens used in this study are shown in figure 2.

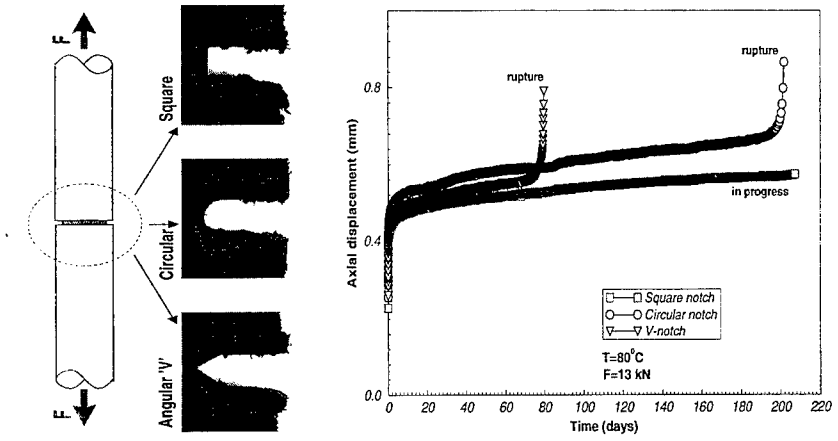

Figure 2: Schematic of FNCT test : shapes of the considered specimens and creep curves

Under the same test conditions (load and temperature), the measures show that the angular notch leads to the lowest failure meaning that the V-shaped notch is the most critical. At the opposite, the square-shape notch leads to a far longer failure time showing the lowest harmfulness of such defect.

Our aim is to reproduce this classification by a numerical simulation both on the FNCT specimens and on scratched pipes.

NUMERICAL SIMULATION OF DEFECTS' HARMFULNESS

The computation code developped to simulate the SCG in PE is based on :

- the realistic modelling of the PE behaviour taking into consideration the elasticity, the viscosity and the instantanous plasticity effects simultanously observed ;
- a local criterion defined by the anelastic strain ϵ^{ane} of the model.

Thus the simulation consists on comparing, for each defect on PE structure Ω and at each time t, the entire anelastic strain $\left[\max_{\Omega} ||\epsilon^{ane}(t)||\right]$ which evaluates the accumulated damage ahead of the crack tip.

APPLICATION TO FNCT SPECIMENS

Using an axisymmetrical modelling of FNCT method, the simulation was carried out on a half axisymmetrical specimen as shown in figure 3. This computation gives the highest level of damage for the angular notch and the lowest one for the square notch.

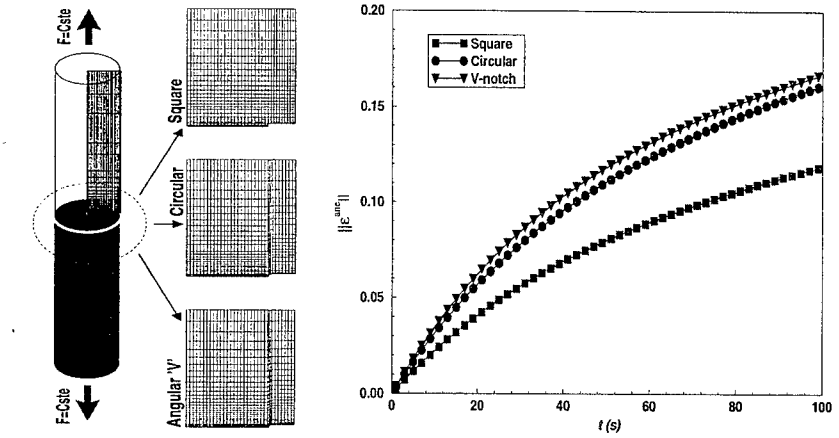

Figure 3: Numerical modelization of FNCT method

APPLICATION TO SCRATCHED PIPES

The evaluation of the damage induced by the three different notches on the pressurized pipe by using plane strain conditions, produces as above, the same classification of the defects in terms of their shapes (fig. 4).

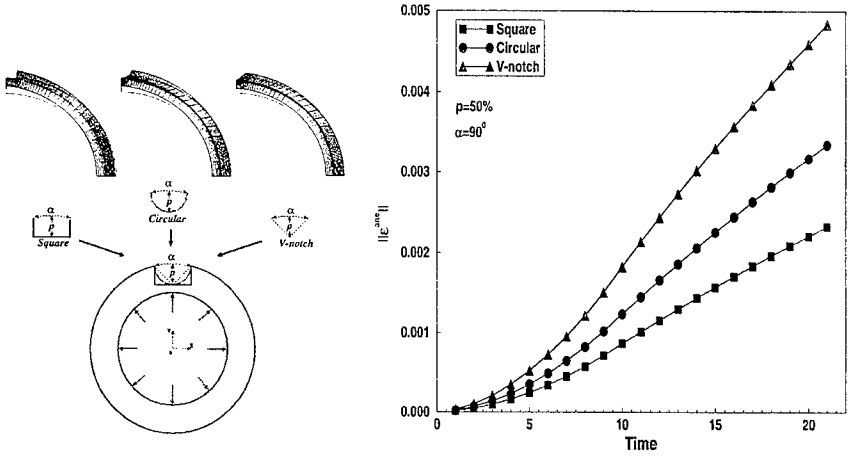

Figure 4: Damage due to the different geometries of notches on PE pipes

APPLICATION TO THE PREDICTION OF NOTCHED PIPES LIFETIME

For the PE pipe $\Omega_{\alpha,p}$ which presents a defect characterized by an opening angle α and a depth p, the numerical process which validity is prooved previously allows to realize, at a given pressure and temperature, the damage iso-curves defined by :

$$0 \leq Z(\alpha,p) = \frac{z(\alpha,p)}{\max\limits_{\alpha,p} z(\alpha,p)} \leq 1 \quad with \quad z(\alpha,p) = \max_{\Omega_{\alpha,p}} ||\epsilon^{ane}(t)|| \quad \text{and } t \text{ is the time from which crack initiation occurs for the deepest defect}$$

Let τ_0 be the failure time corresponding to notched pipe Ω_{α_0,p_0}. From the damage iso-curve $Z(\alpha_0,p_0)$, we can generate a set of notch dimensions (α,p) which induce a time to failure τ equal to τ_0. The aim is to define the admissible parameters (α_c,p_c) of the notch which will give the longest failure times. Figure 5 shows an example of the damage map for an angular notch.

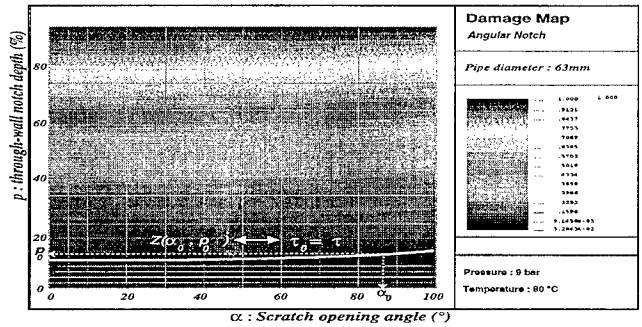

Figure 5: Damage map for an angular scratch on PE pipe

CONCLUSION

Both the experimental and the numerical studies give the same ranking of defects' harmfulness with respect to their shapes. These results indicate that the Full Notch Creep Test is a reliable method for reproducing brittle fractures similar to that occuring in service on notched pipes. The local approach of fracture allows one to relate damage and lifetime of notched pipes. Finally, the methodology presented gives an assessment of the safety conditions for notched PE pipes.

References

[1] H.D. Bui, K. Dang Van & E. de Langre: *"A Simplified Analysis of Creep Crack Growth Using Local Approach"*. Nuclear Engineering and Design, N°105, pp. 147-153, 1987.

[2] J. Kichenin : *"Comportement Thermomécanique du Polyéthylène. Application aux Structures Gazières"*. Thèse de l'Ecole Polytechnique, Janvier 1992.

[3] K.Boytard, A.Ouakka & K.Dang Van: *"A Modelling Tool for the Mechanical Behaviour of Polyethylene Pipe"*. Pipeline Technology, Vol.I, Ed. R.Denys, Elsevier Science, pp. 245-253, 1995.

THE PROPERTIES OF COPOLY(ETHER - ESTER)S/ POLYSTYRENE SYSTEM

R Jeziórska *, E Grzywa **, W Zieliński *

The polymer system state of the block copoly(ether-ester) elastomers (CPEE) with polystyrene (PS) which can be moulded by injection and extrusion techniques was obtained in the melt. The influence of polystyrene on thermal, processing, mechanical, morphological, rheological and utility properties of the system was investigated. The investigations were carried out using thermogravimetric (TG), differential scanning microcalorymetry (DSC), scanning electron microscopy (SEM) and dynamic rheometry methods. It was found that this system depending on the CPEE/PS concentration can behave as elastomer or thermoplastic polymer. The dynamic viscosity data for CPEE/PS melts are succesfully explained in terms of three-block copolymers where the domain structure is formed.

The unusual properties of polymer systems have motivated several studies (1-3) to characterize the morphological, mechanical and rheorogical behavior of these materials. This paper presents the study on some properties of the physical polymer system state of the block copoly(ether-ester) elastomers (CPEE) with polystyrene (PS) which are of interest from an application poin of view (4).

For the investigations the following materials were used: copoly(ether-ester)s - Polish product, named Elitel containing 50% (Elitel 4450), 60% (Elitel 4440) and 80% (Elitel 4420) of hard segments (CPEE, "Elana" Chemical Fibers, Toruń), polystyrene, low-impact, injection-grade (PS, "Xenon" Cooperative, Łódź).

On the basis of the above investigations it was found that CPEE/PS system has a multiphase structure. There is one soft phase with a single glass transition temperature in the low temperature region, T_{g1}, and two hard phases with two glass transition temperatures, T_{g2}, and one melting point T_m. The phase-separated microstructure is a typical morphological behavior of block copolymers with incompatible sequences (5,6), owing to the crystallization abbility of the CPEEs hard segments in the melt state. On the other hand, this can be also explained by the immiscibility of PS and the hard segments of CPEE.

* Department of Engineering Plastics and Specialty Polymers, Industrial Chemistry Research Institute, Warsaw, Poland
**Department of Polymers and Materials for Medicine, Industrial Chemistry Research Institute, Warsaw, Poland.

The dynamic viscosity data for CPEE/PS melts are correlated in a way that demonstrates the domain-type structure in the low frequency range and a thermoplastic behavior in the high frequency range. We suggest that the rheological properties of this system are comparable to the properties of ABA three-block copolymers where the domain structure is formed (6).

CPEE/PS system shows a wide range of mechanical properties and stiffness (Tab.1-3). It is characterized by improved impact strength, heat resistance and processability. The results of the investigations show that the increasing of mechanical properties is conected with a growing amount of PS. It was also highly dependent on the kind of Elitel used. An increase of the content of the hard segments of CPEE leads to a higher increase of the breaking and flexural strength, tensile and flexural modulus, hardness and deflaction temperature and a higher decrease of elongation at break and impact strength. The mechanical properties of the system are comparable to the properties of elastomers when the amount of PS is up to 20% and even up to 40% with the Elitel 4450. It is characterized by high impact strength and elongation at break, and low tensile and flexural modulus. When PS content is growing up the mechanical properties of the system are changing into thermoplastic polymers properties. This system shows good impact strength, low elongation at break and high tensile and flexural modulus.

This system can be utilized for market applications of high impact machine parts working at temperatures from -40^{0}C up to 100^{0}C, hydraulic hoses working at low temperatures, housings and parts of the domestic appliances, electrical and electronic flexible parts and cases, flexible couplings, etc.

REFERENCES

1. Lohmar, J., and Meyer, K., 1988, Die Makromol. Chem., Macromol. Symp., 16, 161-173
2. Ishizu, K., 1989, Polym.-Plast. Technol. Eng., 28 (5&6), 601-630
3. Zuchowska, D., and Steller, R., 1990, Die Angewandte Makromolekulare. Chemie, 175, 69-79
4. Pol. Pat. Appln. 311 022 (1995)
5. Freeguard, G.F., and Karmarkar, M., 1972, J. Appl. Polym. Sci., 16, 69-82
6. Arnold, K.R., and Meier, D.J., 1970, J. Appl. Polym. Sci., 14, 427-440

TABLE I - Some properties of the Elitel 4450/PS system

Property	PS amount, % by wt.								
	0	10	20	30	40	50	70	80	100
Breaking strength, MPa	9.0	14.0	14.3	14.6	14.8	17.6	24.0	25.0	42.0
Elongation at break, %	<590	<490	<490	222	84	26.0	23.0	21.0	2.6
Tensile modulus, MPa	135	180	224	236	396	736	2000	2330	3010
Flexural modulus, MPa	120	187	255	281	435	792	1980	2450	3000
Flexural strength, MPa	3.5	4.0	4.7	7.8	11.6	18.5	50.0	56.5	77.6
Impact strength Charpy at 23°C, kJ/m²	nb	nb	nb	nb	nb	nb	50% nb 46.2	39,4	24,8
Impact strength Charpy at -40°C, kJ/m²	nb	nb	nb	nb	nb	nb	42,5	36,2	17,6
Notched impact strength Charpy at 23°C, kJ/m²	nb	nb	nb	nb	26.0	12.7	5,2	4,2	1,9
Notched impact strength Charpy at -40°C, kJ/m²	nb	nb	nb	nb	16,0	9,1	5,0	3,2	1,5
Hardness Shore, °ShD	34	35	40	45	50	54	65	73	84
Deflection temperature under load of 0,45 MPa, °C	45	49	56	62	65	68	68	70	87

nb - not break

TABLE II - Some properties of the Elitel 4440/PS system

Property	PS amount, % by wt.								
	0	10	20	30	40	50	70	80	100
Breaking strength, MPa	17,0	17,8	18,8	20,8	21,6	23.0	37,0	38,0	42,0
Elongation at break, %	<450	<270	63	21	8.7	7.1	6.0	4,0	2.6
Tensile modulus, MPa	230	318	418	589	765	1110	2230	2410	3010
Flexural modulus, MPa	210	345	433	633	885	1220	2450	2575	3000
Flexural strength, MPa	5.9	11.1	12.1	18.2	24.7	29.8	61.0	67.4	77.6
Impact strength Charpy at 23°C, kJ/m²	nb	nb	nb	nb	nb	nb	29,9	28,5	24,8
Impact strength Charpy at -40°C, kJ/m²	nb	nb	nb	nb	40% nb 46.7	45.1	22,5	20,7	17,6
Notched impact strength Charpy at 23°C, kJ/m²	nb	nb	19,3	7,5	5,0	4.8	4,0	2,5	1,9
Notched impact strength Charpy at -40°C, kJ/m²	nb	18,4	10,0	6,4	3,2	2,5	2,0	1,9	1.5
Hardness Shore, °ShD	54	58	58	64	66	69	76	77	84
Deflection temperature under load of 0,45 MPa, °C	52	83	83	83	82	83	85	85	87

nb - not break

TABLE III - Some properties of the Elitel 4420/PS system

Property	PS amount, % by wt.								
	0	10	20	30	40	50	70	80	100
Breaking strength, MPa	24	25,2	28,7	30,8	31,2	38,0	40,0	45,0	42,0
Elongation at break, %	<330	<450	<390	19,0	12,0	5,7	4,0	2,6	2,6
Tensile modulus, MPa	570	625	830	1120	1490	1830	2700	2740	3010
Flexural modulus, MPa	460	498	693	939	1270	1610	2500	2620	3000
Flexural strength, MPa	18,0	19,8	20,3	26,3	35,1	45,5	49,0	49,8	77,6
Impact strength Charpy at 23°C, kJ/m²	nb	nb	nb	nb	nb	nb	53,9	48,3	24,8
Impact strength Charpy at -40°C, kJ/m²	nb	nb	nb	nb	nb	60% nb 33,8	32,5	26,2	17,6
Notched impact strength Charpy at 23°C, kJ/m²	nb	80% nb 37,9	21,3	11,8	9,8	6,6	5,0	4,0	1,9
Notched impact strength Charpy at -40°C, kJ/m²	7,5	12,2	11,0	8,9	5,3	4,6	3,8	3,0	1,5
Hardness Shore, °ShD	64	65	66	68	71	73	75	78	84
Deflection temperature under load of 0,45 MPa, °C	70	85	85	85	85	83	85	85	87

nb - not break

DEFORMATION BEHAVIOUR OF CUBIC BLOCK COPOLYMER MORPHOLOGIES WITH DISCRETE OR TRICONTINUOUS GLASSY MICRODOMAINS

BJ Dair*, E Prasman*, EL Thomas*, M Capel†

Large-strain deformation behaviour of highly oriented films of two cubic styrene-isoprene-styrene (SIS) triblock copolymers with spherical and double gyroid morphologies, respectively, were studied via synchrotron SAXS. The sphere morphology deforms as an ideal rubber, while the behaviour of the double gyroid morphology is more complex.

Introduction

Styrene-diene-styrene triblock copolymers, in which the styrene phase is the minority component, are industrially important materials because of their outstanding thermoelastic properties. The three classic morphologies in A/B diblock copolymers are spheres of the minority component in a matrix of the other, cylinders, and lamellae. Novel cubic phases have recently been discovered in copolymer systems (1-4), including the ordered tricontinuous double gyroid (DG) morphology (1,2). We have identified and obtained triblock copolymers which form the DG morphology, opening up the possibility of investigating the large strain mechanical properties of this new morphology.

The DG phase has a tricontinuous, triply periodic structure in which two interpenetrating, non-intersecting networks of the minority phase are embedded in the majority phase and conform to the symmetries of the $Ia\bar{3}d$ space group. The classic sphere morphology, in which discrete glassy spheres are arranged in the $Im\bar{3}m$ space group in the rubbery matrix.

Roll-casting is used to prepare oriented, near-single-crystal textured films (5-7). The comparison of the deformation of these two cubic morphologies provides insight into the deformation behavior of discrete versus continuous materials reinforcement.

Experimental

A tricontinuous cubic morphology is formed by a 34 wt% polystyrene SIS triblock copolymer with block molecular weights: 13.6K-46.4K-13.6K (6). The polymer was roll-cast from a concentrated cumene solution (1 wt/2 vol), dried overnight, and annealed at 120°C for 10 days. Tensile samples 2mm wide were cut from the resulting 0.67 mm - thick film.

A blend of Dexco Vector 4211D SIS triblock copolymer (block molecular weights: 14K-66K-14K; 30 wt% PS content with a cylinder morphology), and Penreco Drakeol 500 mineral oil was combined in a weight ratio of 60% to 40%, respectively. The overall composition of 18 wt% PS gives the discrete cubic morphology (7). This blend was roll-cast from a concentrated toluene solution (1 wt/2.5 vol). To avoid volatizing the mineral oil, the film was not annealed. Tensile samples 4.35 mm wide were cut from the resulting 0.88 mm-thick film.

Small Angle X-ray Synchrotron experiments were conducted at Brookhaven National Laboratory on beamline X12B using 1.54 Å x-rays and sample-to-detector distances ranging from 247 cm to 260 cm. Scattering patterns were collected using a custom-built 2D detector

* Department of Materials Science and Engineering, Massachusetts Institute of Technology, Cambridge, MA 02139, USA; † National Synchrotron Light Source, Brookhaven National Laboratory, Upton, NY 11973, USA

(8) with exposure times ranging from 5 s. to 10 min. A custom-built tensile stage with an attached 50 lb. load cell was used to deform tensile specimen at strain rates of 0.57 - 1.05 min^{-1}. In-situ SAXS patterns, along with simultaneous load-deformation curves, were taken as tensile specimens were loaded up to ~ 300 - 600% and unloaded to zero load.

Results and Discussion

Tricontinuous Cubic Morphology

Roll-casting aligns the [111] direction of the cubic crystal along the roll-cast flow direction. Figure 1a defines the unit cell axes relative to the tensile specimen. Figures 2a and 3a show the SAXS pattern of roll-cast oriented double gyroid before deformation, as viewed down the $[1\bar{1}0]$ ($\hat{x}$) and $[11\bar{2}]$ ($\hat{y}$) directions, respectively, with the vertical being the [111] ($\hat{z}$) direction. The samples are well ordered and highly anisotropic, as shown by the SAXS patterns.

The sample was stretched in the [111] direction. The stress-strain curve (figure 4a) for DG exhibits a yield point which is due to necking phenomenon. Up until yield, the SAXS patterns change little, except for fading of the Bragg peaks due to decreasing order in the sample. Necking occurs in the sample at 15% strain. After yield, the SAXS patterns of the polymer loses the characteristic gyroid Bragg reflections and exhibit "streaky lobe" patterns. Figures 2b and 3b show the x and y views, respectively, of the necked region in a sample stretched to 100% strain; the sample is still biaxial, as can be noted from the different characters of the lobe patterns in the two different views. Figures 2c and 3c show the x and y views, respectively, of the necked region in a sample stretched to 650% strain. Here, the two views of the sample are nearly identical; a tilt series between the two pictures shows similar patterns, suggesting that the sample exhibits fiber symmetry at this very high level of strain.

Upon unloading, a new SAXS pattern, dubbed the "tie-fighter", emerges with a much different character than that prior to deformation. Figures 2d and 3d show patterns the unloaded sample with 75% residual plastic deformation, as viewed down the x and y axes, respectively. The different characteristics of the two views demonstrate that the deformed sample is no longer fiber symmetric, implying that the structure has some memory of its original anisotropic nature, even after being deformed to very large strains. The deformed structure associated with the "tie-fighter" pattern is less ordered than the undeformed structure, as exemplified by streaks of intensity rather than discrete Bragg peaks.

The unloaded structure completely heals upon annealing; SAXS patterns for the annealed structure (figures 2e and 3e) are nearly identical to the original, implying that the interpenetrating PS networks are not completely destroyed when taken to high deformation and can reform into their original oriented state upon relaxation and further thermal treatment.

Discrete Cubic Morphology

Roll-casting a solution of triblock copolymer, mineral oil and toluene produces a highly ordered and oriented sample of PS spheres situated on a body-centered cubic lattice with approximate fiber symmetry about the [111] direction, which was aligned with the roll-casting flow direction (figure 1b). Figure 5a shows the roll-cast sample viewed along the y-direction.

The SAXS patterns exhibit a very clear zero of the form factor arising from the polystyrene spheres, from which the radius of the spheres can be determined to be R=104Å. The calculated volume fraction of spheres is 19.6%, and assuming mineral oil does not go into the polystyrene and neglecting the differences in densities of PS, PI and mineral oil, the crosslinking functionality of the spheres (PS chains per sphere) is approximately 200.

The sample was stretched in the [111] direction. The stress-strain curve (figure 4b) resembles that of an ideal rubber. Figures 5b-e show the SAXS patterns recorded at 30%, 60%, 100%, and 300% deformation. The (222) reflection is oriented along the direction of the applied force and allows precise determination of the local strain as a function of the

applied strain. For all values of applied strain, the local strain was found to be equal to the macroscopically measured strain, indicating that the deformation of the polystyrene sphere lattice is affine. SAXS data also show that the glassy polystyrene spheres remain spherical during deformation, and that the strain is accommodated only by the rubbery matrix. Recovery of the lattice from deformation is complete, but viscoelastic, requiring ~36 hours after unloading. Figure 5f shows the SAXS pattern of the recovered sample.

The [111] Poisson's ratio for the lattice was found to be between 0.45 and 0.5 for the whole range of strain values. The SAXS patterns show no streaking perpendicular to the direction of the applied force through the origin, indicating no cavitation occurs at any time during deformation. Taken together, these two observations imply an isovolume deformation.

The SAXS pattern in figure 5e shows a progressive horizontal 'streaking out' of the reflections as the strain increases, suggesting that the tensile deformation of the macroscopic sample in the [111] direction induces a progressive breakup of the original large grains in the transverse directions into subgrains. After removal of the strain, the streaks completely disappear, indicating that the subgrains have reformed large grains and the axial misregistration of the spheres is viscoelastically recovered after unloading.

Acknowledgments

We would like to thank C. Honeker for the stretching apparatus, help at the beamline, and scientific discussion; A. Avgeropoulos and N. Hadjichristidis for synthesizing the SIS triblock with tricontinuous morphology; Dexco for supplying the 4211D SIS triblock; Penreco for supplying the mineral oil; R. Albalak for the roll-caster; and C. Zimba for his cooperation at the X-ray beamline. This research was supported by the Air Force (AFOSR F49620-94-1-0224) and the National Science Foundation (NSF DMR 92-14853).

References

(1) Hajduk, D. A.; Harper, P. E.; Gruner, S. M.; Honeker, C. C.; Kim, G; Thomas, E. L.; Fetters, L. J., Macromol. **27** (1994) 4063.
(2) Schultz, M. F.; Bates, F. S.; Almdal, K.; Mortensen, K., Phys. Rev. Lett. **73** (1994) 86.
(3) Thomas, E. L.; Alward, D. B.; Kinning, D. J.; Martin, D. C.; Handlin, D. L.; Fetters, L. J., Macromol. **19** (1986) 2197.
(4) Hasegawa, H.; Tanaka, H.; Yamasaki, K.; Hashimoto, T., Macromol. **20** (1987) 1651.
(5) Albalak, R. J.; Thomas, E. L., J. Polym. Sci.: Part B: Polym. Phys. **31** (1993) 37.
(6) Avgeropoulos, A; Hadjichristidis, N.; Dair, B. J.; Thomas, E. L., in preparation.
(7) Prasman, E.; Thomas, E. L., submitted to J. Polym. Sci.: Part B: Polym. Phys.
(8) Capel, M. C.; Smith, G. C.; Yu, B., Rev. Sci. Instrum. **66** (1995) 2295.
(9) Odell, J. A.; Keller, A, Polym. Eng. and Sci. **17** (1977) 544.
(10) Fujimoto, M.; Hashimoto, T.; Kawai, H., Rub. Chem. & Tech. **51** (1978) 215.
(11) Honeker, C. C.; Thomas, E. L., Chem. Mat. **8** (1996) 1702.

Figures

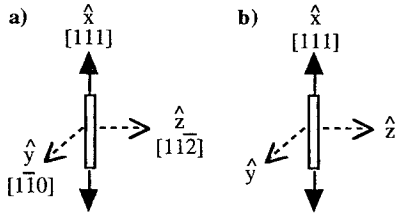

Figure 1a: Crystallographic directions of double gyroid sample relative to the tensile specimen axes

Figure 1b: Crystallographic directions of spheres sample relative to the tensile specimen axes; this sample has fiber symmetry and thus the x and y direction are identical

a) x view, at start

b) loaded to 100% strain

c) loaded to 650% strain

d) unloaded to 0 load

e) reannealed 5 days, 120 C

Figure 2: SAXS patterns of roll-cast DG undergoing tensile deformation in the [111] direction as viewed along the x-axis

a) y view, at start

b) loaded to 100% strain

c) loaded to 650% strain

d) unloaded to 0 load

e) reannealed 5 days, 120 C

Figure 3: SAXS patterns of roll-cast DG undergoing tensile deformation in the [111] direction as viewed along the y-axis

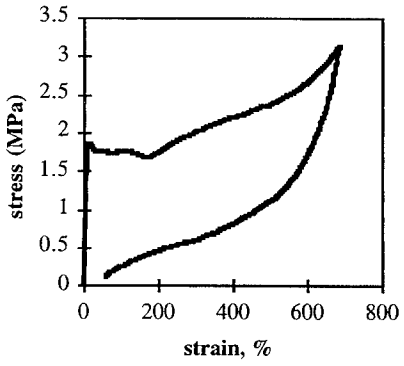

Figure 4a: Double Gyroid stress-strain curve

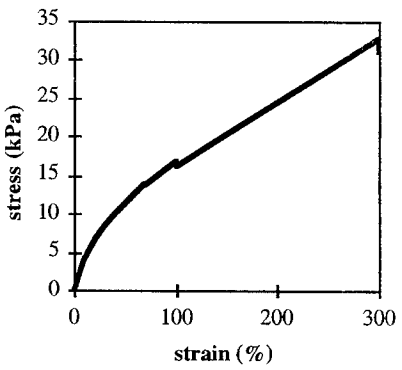

Figure 4b: Spheres stress-strain curve

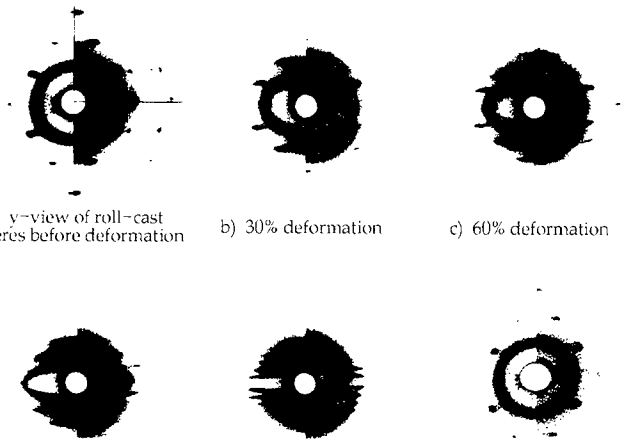

a) y-view of roll-cast spheres before deformation

b) 30% deformation

c) 60% deformation

d) 100% deformation

e) 300% deformation

f) unloaded and recovered

Figure 5: SAXS patterns of roll-cast spheres, deformed along the [111] direction and viewed along the y-direction

INFLUENCE OF MOLECULAR WEIGHT AND MINERAL OIL CONTENT ON THE FRACTURE TOUGHNESS OF COMMERCIAL POLYSTYRENES

J Pulda*

Results are presented of a study in which a relationships between the normally measured mechanical properties of commercial polystyrenes such as tensile strength and particularly impact strength on the one hand, and molecular characteristics (molecular weight averages, polydispersity), plasticizer level (mineral oil), and also viscosity of the melt on the other have been studied. The technique of non-linear multiple regression was applied to quantify these relationships. Very strong relationships between the mechanical properties and molecular characteristics and mineral oil content have been found. Interrelationships between mechanical properties and processability (viscosity and melt flow rate of the melt) are illustrated.

The failure properties, such as impact fracture or tensile strength, of thermoplastics are of the utmost importance in polymers. It is well known that these properties of polymers depend among others in particular on their molecular weight (MW), molecular weight distribution (MWD) and low molecular weight additives (other polymers, mineral oils etc.). General -purpose polystyrene finds use in numerous applications. Therefore, the polymer is available in different molecular weights and polydispersity indices, and with different plasticizer contents. As the traditional measures of molecular weight, such as M_n, M_w, and M_z, are unable to account for the variation of fracture and tensile properties with molecular characteristics, the multivariable power dependence [1] of polymer properties on molecular characteristics has been applied to molecular weight dependance of impact strength and tensile strength, and the content of mineral oil has been included into the relations. Mineral oil is often used to improve the processability of the polymers and it is important to understand how the oil affects the mechanical and rheological properties of commercial polystyrenes.

The main purpose of the work reported here, was to correlate impact strength and tensile strenght with molecular weight averages, polydispersity and mineral oil content. In addition the relationships between tensile and impact properties and viscosity of polymer melt have been studied because of their importance [2].

EXPERIMENTAL

Constant parameters of the regression equations have been calculated using experimental data measured on 31 polystyrene samples with broad MWD. Molecular characteristics of the samples were determined by gel permeation chromatography. The range of weight average molecular weight (M_w) was 240 000 - 380 000 g/mole and the range of polydispersity M_w/M_n

* Synthetic Rubber Research Institute, Kaučuk a.s., Kralupy nad Vltavou, Czech Republic

was 2,4 -3,3. The content of mineral oil was 0 - 4 wt.% (determined by gas chromatography). Charpy tester was used for impact testing. The tests were carried out on the specimens with notches. The specimens were prepared with an injection molding machine. Tensile strengths were measured at a crosshead speed of 50 mm/min. Melt flow rate (MFR) measurements were conducted using an extrusion plastometer and shear viscosity was measured on a capillary rheometer at two shear rates (100 and 1000 s^{-1}). The temperature of rheological measurements was 200 °C.

RESULTS

Many authors have related the weight average molecular weight to the fracture toughness (computed from the fracture impact tests) or tensile strength of polystyrenes [3, 4]. In order to include polydispersity and mineral oil content, non-linear relationship with several terms were tested. Correlation coefficient (R^2) was used to compare the fitting of equations. The following relations appeared to be very good to correlate various mechanical properties of polymers:

$$P = A\, M_w^{a1} (M_w/M_n)^{a2}\, Y^{a3} \quad \text{.....(1)}$$

$$P = A\, M_w^{a1} (M_z\, M_{z+1}/M_w^{2})^{a2}\, Y^{a3} \quad \text{.....(2)}$$

$$P = A\, M_w^{a1} (M_w/M_n)^{a2}\, Y^{a3}\, (M_z/M_w)^{a4} \quad \text{.....(3)}$$

where P denotes physical property, A, a1, a2, a3 are regression coefficients and M_{z+1}, M_z and M_n are molecular weight averages. Y is defined as $1/(1+x_i)$, where x_i denotes weight fraction of mineral oil. The regression and correlation coefficients are given in table I.

Table I - Regression and correlation coefficients for the equations (1), (2), (3).

equation	property	A	a1	a2	a3	a4	R^2
(1)	IS	$4.121*10^{-6}$	1.084	-0.383	5.072	-	0.920
	TS	4.578	0.205	-0.110	11.742	-	0.980
(2)	IS	$9.780*10^{-6}$	1.010	-0.206	4.763	-	0.914
	TS	4.797	0.188	0.025	11.480	-	0.980
(3)	IS	$4.521*10^{-6}$	1.078	-0.345	5.064	-0.090	0.922
	TS	2.950	0.234	-0.267	11.745	0.3814	0.984

where IS denotes Charpy impact strength and TS denotes tensile strength

Analysis of the data has shown that IS is proportional to M_w^1 and TS is proportional to $M_w^{0.2}$. Influence of mineral oil is strong, particularly on TS. For example, 1 wt.% of oil decreases IS by 5% and TS by 11%. Influence of polydispersity is not so strong. IS and TS decrease with increasing polydispersity. Good fit of the proposed equations is illustrated in Figure 1, where the Charpy impact strength values predicted by equation (3) are compared to the measured values.

Correlations between IS and TS on the one hand, and rheological properties on the other are illustrated in Figures 2 and 3. It has been found that IS is correlated well with MFR and TS with the viscosity at shear rate 1000 s^{-1}.

SYMBOLS USED

IS = Charpy tensile strength (kJ/m^2)

M_n = number average molecular weight (g/mole)

M_w = weight average molecular weight (g/mole)

M_z = z -average molecular weight (g/mole)

M_{z+1} = z+1 -average molecular weight (g/mole)

MFR = melt flow rate (g/10min)

TS = tensile strength (MPa)

x_i = weight fracture of mineral oil in the sample

η_{1000} = viscosity of polymer melt at shear rate 1000 s^{-1} (Pa s)

REFERENCES

1. Dobkowski, Z., 1981, Eur. Polym. J., 17, 1131

2. Crowder, M.L., Ogale, A.A., Moore, E.R., and Dalke,B.D., 1994, Polym. Eng. Sci., 1497

3. Greco, R., and Ragosta, G., 1987, Plast. Rubber Process. Applications, 7, 163

4. Wooden, D.C., Lamont, J.C., and Gorka, R., 1986, SPE Antec, 41, 675

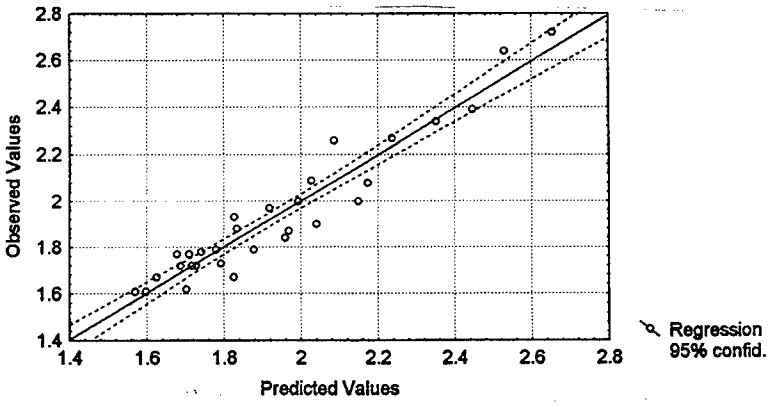

Figure 1. Charpy impact strength, measured vs. predicted values

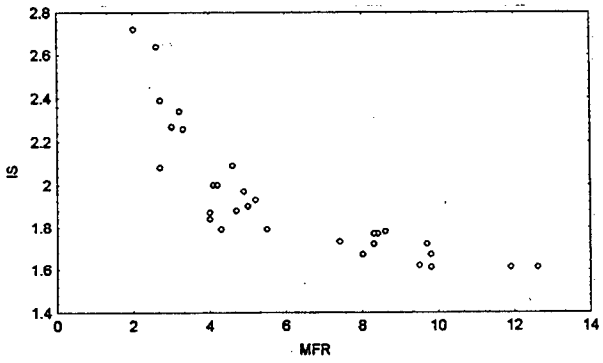

Figure 2. Relation between Charpy impact strength (IS) and melt flow rate (MFR)

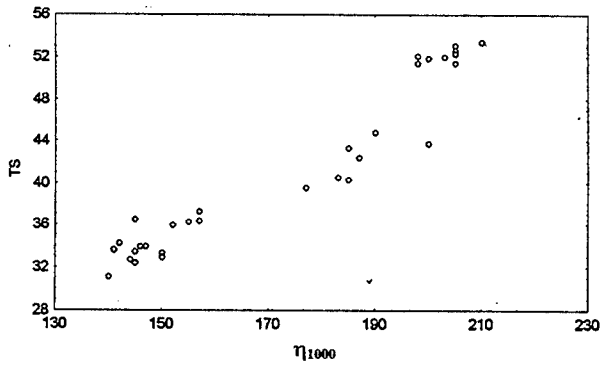

Figure 3. Relation between tensile strength (TS) and viscosity at shear rate 1000 s^{-1} (η_{1000})

FRACTURE TOUGHNESS OF CORE-SHELL PARTICLES MODIFIED POLYEPOXY NETWORKS

A. MAAZOUZ*, L. BECU, J.F. GERARD and H. SAUTEREAU

The yield and fracture behaviour of BDMA-catalyzed DGEBA/Dicy networks toughened with core-shell particles (CSR) - were studied. The considered core-shell particles were of three types :

i) poly(butadiene-co-styrene) core/carboxy-functionalized (CSR1) or not (CSR2) poly (methyl methacrylate-co-sytrene) shell,

ii) poly(butyl acrylate) core/carboxy functionalized (CSR3) poly(methyl methacrylate) shell.

The blends have been realized with well-defined processing conditions and the level of toughening depended on the state of dispersion of the particles in the matrix. Using linear elastic fracture mechanics (LEFM), the presence of CS particles in the epoxy networks led to an improvement of crack initiation and fatigue-crack propagation. The toughening mechanisms brought to the fore were cavitation and shear banding but no croiding was exhibit, probably due to the high crosslinking density of the matrix.

INTRODUCTION

Various ways of toughening epoxy thermosets have been already investigated. The main trend consists in the addition of rubbers or thermoplastics which are initially miscible in the epoxy system and display a phase separation during curing (1,2). Thus the final morphology of the dispersed phase is strongly dependent on the curing conditions (3,4). An other way consists in the addition of preformed particles to the reactive epoxy mixture (5-9). The aim of this paper is to investigate the influence of the core-shell (CSR) structure, especialy the shell composition and functionalization, on the degree of dispersion of the particles and consequently on toughness and fatigue crack propagation resistance of the modified materials.

EXPERIMENTAL

Preparation of blends and materials

Home-made core-shell particles have been previously prepared (5) but only in small quantities. Therefore, for the study of dispersion and fatigue characterization, industrial core-shell particles from Rohm & Hass were used.

The aggregates of dried CSR particles were added to the epoxy prepolymer diglycidylether of bisphenol A (DGEBA) and dicyandiamide (DDA) hardener reactive system without solvent. Benzyl-dimethyl-amine was used as initiator (see Table I). The mixture was obtained with an intermeshing corotating twin screw extruder (CLEXTRAL BC21).

Several trials have been made, changing screw profile, temperature and rotating speed in order to obtain the best dispersion of core-shell particles. All samples were finally obtained with the same screw profile at 90°C and 278 rpm.

Various volume fractions (8, 17, 24 %) of CSR1 and only 24 % vol. of CSR2 or CSR3 were considered here.

The synthesis was carried out with aminohydrogen to epoxy ratio equal to 0.6 in order to obtain the maximum glass transition temperature (curing 1 h at 120°C followed by 1h at 180°C). The detailed preparation of these materials was previously published (2).

* **Laboratoire des Matériaux Macromoléculaires - UMR CNRS n° 5627**
INSA Bât. 403 - 20, Avenue A. Einstein, 69621 Villeurbanne Cedex, France

TECHNIQUES

The characteristics of the two phase materials were studied by means of DSC, dynamic mechanical spectroscopy (DMS) and transmission electronic microscopy (TEM). The dispersion state of the particles in the final material was estimated using TEM and an image analysis software which gave us the value of the heterogenety factor of dispersion $\frac{\sigma}{m}$ (σ : standard deviation and m : average number). $\frac{\sigma}{m}$ decreases when the dispersion is improved. Young's modulus and yield stress at room temperature were obtained from uniaxial tensile and compression tests respectively. Fracture toughness (K_{Ic}) was determined using single-edge-notched (SEN) specimens in three points bending (3PB) geometry. Fatigue crack propagation tests were performed on compact-tension (CT) specimens at room temperature, at 5Hz, with a stress ratio close to zero (10).

RESULTS AND DISCUSSION

TEM analysis showed that the particles dispersion in the epoxy prepolymer was influenced by the chemical nature of the CSR particles.

A good dispersion of CSR1 particles ($\frac{\sigma}{m}$ = 9) was obtained with a carboxy fonctionalized shell, whereas a high level of aggregation ($\frac{\sigma}{m}$ = 70) was observed in the case of CSR2 particles (without functionalization). Good dispersion state is also observed for CSR3 ($\frac{\sigma}{m}$ = 10) (see Table II).

The rheological behaviour of the CSR/epoxy prepolymer mixtures was studied. It was also found very dependent on the dispersion state of the particles : the shell functionalization reduces, significantly the viscosity of the mixtures.

In order to study the influence of the particles nature or volume fractions on mechanical properties, only blends with a high level of dispersion were considered ($\frac{\sigma}{m} \approx 10$).

The DSC analysis reveals glass transition temperatures of 141 ± 2°C for all materials, indicating no change in the chemical structure of the epoxy matrix via CSR particles introduction. In the same way the Young's modulus at 25°C are only slighly decreased, and remain significantly higher than the modulus of CTBN-toughened epoxy networks (2-4). As shown in Table II, the fracture tougheness of the brittle matrix is increased by incorporation of CSR particles. However the materials exhibiting a high level of agglomeration show greatly dispersed K_{Ic} values. Only functionalized CSR1 and CSR3 particles ($\frac{\sigma}{m} \approx 10$) confer a large improvement with a small standard deviation of the K_{Ic} values. For 24 % volume fraction, K_{Ic} increases from 1.3 ± 0.5 for CSR2 ($\frac{\sigma}{m}$ = 60) to 1.4 ± 0.1 MPa.$\sqrt{m}$ for CSR1 ($\frac{\sigma}{m}$ = 10).

The effects of the volume fraction of well dispersed functionalized CSR1 particles were studied by fatigue crack propagation tests.

The experimental data for CSR1 materials were linearly well-fitted, in a log-log diagram, by the Paris law :

$$\frac{da}{dN} = C\,(\Delta K)^m$$

The presence of CSR particles shifts the FCP curve of the neat epoxy towards high ΔK values and improves significantly the resistance to fatigue crack propagation (see Figure 1).

Increasing the amount of core shell particles leads to the same effect. In addition, the m values decrease continuously in agreement with those found by Cowe *et al.* (11).

The improvement in FCP is the same we have obtained with 15 % CTBN (6) without the drawbacks of such materials (decrease in Tg and Young's modulus), due to partial miscibilty. The ΔK_{max} values obtained in FCP tests were well correlated to K_{Ic} values, suggesting then that the toughening mechanisms are nearly the same. The TEM of damaged zone exhibits cavitation of CSR particles and shear bonding but no croiding, this fact being probably related to the high crosslinking density of the epoxy network.

CONCLUSION

The use of a twin screw extruder allowed us to obtain a good dispersion of CSR particles in epoxy prepolymers, without the use of solvent or surfactant.
The shell functionalization improves the dispersion and then a high toughness value is obtained with a small standard deviation.
The introduction of CSR particles significantly increases the fatigue crack propagation resistance, which is well correlated to the static KIc values. Thus, the introduction of preformed particles is a good alternative way to toughen epoxy network without the drawbacks of rubber modified thermosets.
Works are now in progress to synthetize new core-shell particles with different functional groups and different chain length.

REFERENCES

1. Bascom R.T, Moulton R.J, Riew C.K, Siebert A.R, J. Mat. Sci (1981) 16, 3657
2. Maazouz A, Sautereau H, Gérard J.F, Polymer Networks & Blends (1992) 2, 65
3. Montarnal S, Pascault J.P., Sautereau H, *in* «Rubber Toughened Plastics», Adv. Chem. Ser. n° 222, Vol. 8, C.K. Riew, ed., ACS, New Orleans, p. 193 (1989)
4. Verchère D, Pascault J.P., Sautereau H., Moschiar S.M., Riccardi C.C., Williams R.J.J., J. Appl. Polym. Sci. (1991) 42, 701
5. Bécu L., Sautereau H., Maazouz A., Gérard J.F., Pabon M. and Pichot C., Polymer for Advanced Technologies (1994) 6, 316
6 Maazouz a., Sautereau H., Gérard J.F., Polym. Bull. (1994) 33, 67
7 Sue H.J., Garcia-Meitin E.I., Pickelman D.N., Young P.C. in «Rubber Toughened Plastics», Adv. Chem. Ser. n° 223, C.K. Riew and A.J. Kinloch, eds., ACS, Washington DC, 259 (1993)
8 Qian J.Y., Pearson R.A., Dimonies V.L., Zl-Aasser M.S. (1995) J. Appl. Polym. Sci., 58, 439
9 Lowel P.A. (1955) Macromol. Symp. 92, 71
10 Becu L, Maazouz A., Sautereau H., Gérard J.F. (submitted to J. Appl. Polym. Sci.) (accepted)
11 Lowe A., Know A.H., Mai Y.W. (1996) Polymer, 37, 565

Table I. Chemical products used in synthesis of materials

Name	Chemical formula	Supplier
DGEBA	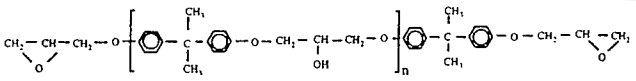 $\overline{Mn} = 380\ gmol^{-1}$	Bakelite 0164
Dicy	$H_2N\text{-}C(=N\text{-}C\equiv N)\text{-}NH_2$ Dicyandiamide	Bakelite VE 2560
BDMA	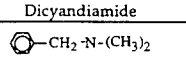 Catalyst or initiator	Aldrich

Table II. Mechanical properties at 25°C of pure and CSR modified epoxy networks

Materials	E (GPa)	σ_y (MPa)	K_{IC} MPa.$\sqrt{m}$	G_{IC} J.m^{-2}	ΔK^* MPa$\sqrt{M}$	$\frac{\sigma}{m}$ (Dispersion)
Pure epoxy	3,2	105	0.8±0.08	220	0.43	/
9.5 % vol. CSR1	2.65	95	1.1±0.05	490	0.44	12
17.5 % vol. CSR1	2.67	85	1.1±0.08	450	0.85	10
24 % vol. CSR1	2.17	72	1.4±0.1	800	0.86	9
24 % vol. CSR2	2.1	53	1.3±0.5	700	/	70
24 % vol. CSR3	2.2	71	1.7±0.09	1130	0.88	10

** for da/dN = 7.5.10^{-4} mm per cycle*

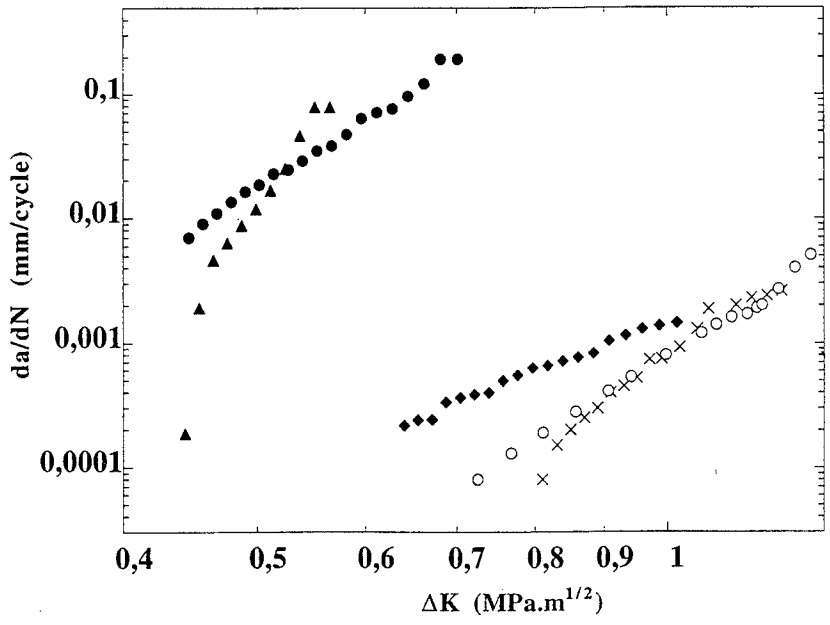

Figure 1 : FCP curves for the neat epoxy and CSR 1 / epoxy blends -the same epoxy matrix modified with (17,5 % Vol) of CTBN is given as reference-(○)- ; (▲): neat epoxy ; (●): 9,5 % vol. ; (◆): 17,5 % vol. ; (×): 24 % vol.

AUTHORS' INDEX

M Aboulfaraj 363
AM Adams 45
WW Adams ..... 23 ,330
M Ahmad 552
A Alderson 27,482
KL Alderson 531
VG Alekseev ..... *
E Allert ..... *
I Anguillesi 450
A Arbor 93
JC Arnold 294,298
EM Arruda 398,399
MS Arzhakov 72,313
SA Arzhakov 72
OV Arzhakova 310,317
FR Attenborough 27
A Aubert 363
Z Ayadi 220,367
D Ayre 179,462
HR Azimi 175
R Bagheri 175
L Bailey 290
D Baker 290
NF Bakeev 310,313,317
FI Baltá Calleja 347
T Bartischies 207
DC Bassett 338
L Becu 574
B Beghin 506
Ph Béguelin 286
JGJ Beijer 270
L Belec 546
J Bergstrom 379
C Bernal 246,250
N Billon 199,203,320
ML Bissiliat 203
P Blackie 539
P Blouet 557
DJ Blundell 45
J Boekholt 423
PN Bogdanovich 514
C Bonnebat 371
MC Boyce 63,375,379
WL Bradley 109,518
SW Bradley 114,518
WAM Brekelmans 494
C Briancon 359
BJ Briscoe 474
NW Brooks 53
LJ Broutman 342
N Brown 118
CP Buckley 45,83,435
CB Bucknall 179,458,462,466
MF Butler 41,157
E Butta ..... *
G Capaccio 101
M Capel 565
G Carcagno 250
CM Care 470
RM Casado 139
S Castagnet 535
G Castelein 49
JY Cavaillé 274
S Chambaudet 359
L Chazeau 274
W Chen 133
GX Cheng 237
M Chong 106
C Chui 375
DJ Cleaver 470
DM Colucci 411
G Coulon 49
D Crane 290
C Cunat 57,220,367
AM Cunha 320
R Daffara 506
A Dahoun 57
DJ Dair 565
P Dang 535,546
K Dang Van 557
M Davallo 191
OM Davies 298
P Davis 550
R Denidievel 274
B Dewimille 546
DJ Dijkstra 207
Y Doi 498
F Dolan 539
W Döll 347,351
AM Donald 41,177
X Dong 551
JA Donovan 258
PJ Dooling 83
M Douglas 106
J Du 254
DM Duan 216
RA Duckett 31,53,355
DS Dudis 23
DJ Earls 129
DT Edmonds 334
D Edwards 342
BR Eggen 27
SJ Eichhorn 228
S Elkoun 187
M Ensslen 31,351

* Paper not available at time of print

ML Ericson 306
S Etienne 371
R Ettelaie 470
KE Evans 27,482,531
BL Farmer 23,330
L Fasce 250
C Fond 161,478
P Frontini 246,250
W Fuller 45
N Fuwa 498
C G'Sell 359,363,367,371
JL Gacougnolle .. 53,545,546
AG Galushko ..... *
V Garcia Brosa 246
D Gardiner 242
G Gary 203
V Gaucher-Miri 187
C Gauthier 64,238,389
A Gavrus 199
RJ Gaymans 171,266
R Gensler 165
JF Gerard 574
DW Gidley 93
A Gilchrist 143
D Giuliani 446
JM Gloaguen 302
R Godehart ..... *
S Goerlitz 343
M Goldman 290
LE Govaert .. 87,423,427,494
JC Graham 551
W Grellmann 490
BV Grunkin 514
E Grzywa 561
D Gueugnaut 557
JL Hahnfeld 466
JL Halary 68
SM Halliwell 342
WY Hamad 224,228
H Hamada 328,329
HXY Han 31
M Hara 133
JP Harcup 101
IR Harrison 407
JL Harvie 435
JM Haudin 211
C He 157
RE Hefner Jr 129
MI Heggie 27
R Hellouin 371
N Heymans 403
JG Hilborn 390
S Hinduja 83
PJ Hine 338
G Hinrichsen 207
R Hiss 439
JM Hiver 363
HA Hristov 93
G Hu 510
Y-C Huang 175
JP Ibar 236
A Imad 506
H Inaba 394
EJ Ingham 110,454
VI Irzhak ..... *
A Ivankovic 526
BJP Jansen 153
F Jay 211
R Jeziórska 561
AF Johnson 31
DP Jones 45,355
VA Kapranov ..... *
A Karbach 207
HH Kausch 97,165,286
M Kawagoe 195,431,498
CT Kelly 553
AAJ Ketelaars 324
Z Khan 552
SD Khizhnyak 147
J Kiefer 390
R Kim 125
G-M Kim 486
K Kishimoto 394
JR Klepaczko 203
ETJ Klompen 87
L Könczöl 31,351
EJ Kramer 125
M Kravchenko 64
R Lach 490
J Lai 35
M Lamborn 114
NV Larionova ..... *
A Lazzeri 442,446,450
PS Leevers 106,526,550
JM Lefebvre 302
JF Legrand 274
PJ Lemstra 153
R Lenke 161
LH Lin 384
H Lindberg 306
H Lopez Montenegro 246
PA Lovell 139
X Lu 118
F Lumini 541
X Ma 133
A Maazouz 574
DH MacKerron ..... *
A Mahendrasingam 45

D Mainhard 57
? Marceron 210,567
Marchal 546
. Marchetti..... 450
GP Marshall 110,454
A Martin 45
E Massoni 199
RG Matthews 355
GB McKenna 69,411,415,419
DH McKerron..... 45
TCB McLeish 31
HEH Meijer 153,494
Y Meimon..... 546
G Mesmacque 506
GH Michler 343,347,351,486
NJ Mills 143,282
AA Mironova 310,317
G Mitchell 258
W Mizuno 431
B Monasse 211
L Monnerie 68
M Morita 195,498
A Morita 394
EJ Moskala 236
M Nait Abdelaziz 506
M Nakanishi 195
K Nakayama 324
X Nennig 545
TN Nesiolovskaya ..... *
M Notomi 394
PA O'Connel 415
B O'Connor 466
CK Ober 125
E Oleinik 64
RH Olley 338
G Orange 502
C Ortiz 125
A Ouakka 557
R Pachter 23,330
PM Pakhomov 147
G Parker 133
A Pavan 541
B Paysant-Le Roux ...57,367
RA Pearson 175
TJ Pecorini 278
T Peijs 427
E Pelillo 474
J Perez 64,238,389
NN Peschanskaya 185
CLG Plummer 97,165
A Plumtree 237
GM Podojil 330
E Prasman 565
L Pruitt 290
J Pulda 570
M Puricelli 541
J Qian 175
J Qiu 195,498
M Quehen 302
FS Quershi 552
S Rastogi 153
D Register 114
SJK Ritchie 550,551
G Robert 371
E Rodeghiero 125
A Roy 545
S Rudnev 64
AJ Ryan 41
O Salamatino 64
K Sasaki 482
JA Sauer ..... *
A Sauron 470
H Sautereau 250,574
P Scaramuzzino 97
R Schirrer 161,478
CR Schultheisz 419
G Schulze 351
R Séguéla 187
R Self 114
CG Sell..... 49,57
VP Shantarovich 215
Z Shao 264
AK Sheikh 552
T Shibuya 394
J Shirodkar 435
P Sigety 359
O Sindt 238
SK Sinha 474
T Slavetskaya 64
RJM Smit 427,494
M Song 510
JL Spoormaker 270
R Stadler 343
JL Stanford 139,191
AC Steenbrink 266
G Strobl 439
HJ Sue 127
S Sulley 298
K Takada 498
JE Taylor 294
D Taylor 540
P Terech 274
TA Tervoort 87
C Teuchert ..... *
L Tézé 68
N Thavarungkul 407
EL Thomas 565
JJ Thompson ..... *

SM Thorpe 383
MD Thouless 354
Y Tillier 199
PT Timmermans 87
L Tong 553
P Tordjeman 68
L Tsou 133
AP Unwin 53
CAC Van Aert 423
E Van der Giessen 35,266
A van der Wal 171
GP Venizelos 526
V Vettegren 539
JC Viana 320
AV Volkov 313
F Vollrath 262
AL Volynskii 310,313,317
PR Von Lockette 399
J Von Stebut 57
IM Ward 53,101,338,355
NJ Ward 31
RS Webber 531
R Weidisch 343
JR White 553
AN Wilkinson 191
JG Williams 106,216
AH Windle 383
R Wojnar 522
Y Xue 134
PN Yakushev 185
RJ Yan 338
HH Yang 458
LM Yarsheva 310,317
T Yasuda 498
M Ye Solovyov ..... *
AF Yee 93,254
Y Yoshida 394
RJ Young 139
L Yu Kabal'nova 310
J-P Yvard 506
HX Zhu 143,282
W Zieliński 561
AD Zjuzkov 514
AI Zubkov 147